Crystallography Reports, Vol. 49, No. 4, 2004, pp. 527–536. From Kristallografiya, Vol. 49, No. 4, 2004, pp. 599–609.
Original English Text Copyright © 2004 by Watanabe, Soma, Ito.

CRYSTALLOGRAPHIC SYMMETRY

A Quasi-Lattice Based on a Cuboctahedron. 1. Projection Method[1]

Y. Watanabe*, T. Soma, and M. Ito*****
** Department of Information Systems, Teikyo Heisei University, 2289 Uruido, Ichihara, Chiba, 290-0193 Japan*
e-mail: watanabe@thu.ac.jp
*** Computer and Information Division, Riken, Wako-shi, Saitama, 351-0198 Japan*
**** Faculty of Engineering, Gunma University, Aramaki, Gunma, 371-8510 Japan*

Received September 1, 2003

Abstract—A three-dimensional (3D) quasi-lattice (*QL*) based on a cuboctahedron is obtained by the projection from a seven-dimensional hypercubic base lattice space to a 3D tile-space. The projection is defined by a lattice matrix that consists of two projection matrices from the base lattice space to a tile-space and perp-space, respectively. In selecting points in the test window, the method of infinitesimal transfer of the test window is used and the boundary conditions of the test window are investigated. The *QL* obtained is composed of four kinds of prototiles, which are derived by choosing triplets out of seven basis vectors in the tile-space. The *QL* contains three kinds of dodecahedral clusters, which play an important role as packing units in the structure. A modification of the lattice matrix making the *QL* periodic in the *z* direction is also considered. *© 2004 MAIK "Nauka/Interperiodica".*

INTRODUCTION

The discovery of icosahedral quasicrystal in 1984 [1] stimulated both experimental and theoretical studies in this field [2, 3]. The theoretical study of quasiperiodic tiling, which was developed before the discovery of quasicrystals by de Bruijn [4] in connection with Penrose tiling, is based on the projection method. As methods of generating quasiperiodic tiling, the cut method and self-similar methods are known. The former is more general than the projection method and can generate a wider class of quasiperiodic tilings [5]. In this paper, a three-dimensional (3D) quasiperiodic tiling, or a quasi-lattice (*QL*), developed by the authors is presented and its method of generation and its properties are explained—based on a 7 × 7 lattice matrix derived from a cuboctahedron and showing quasi-eightfold symmetry in one of its two-dimensional (2D) projections (cf. [6–8]).

BASIS VECTORS, PROTOTILES, AND DODECAHEDRAL CLUSTERS

A 3D *QL* based on a projection from a seven-dimensional (7D) hypercubic lattice (base lattice space) to a 3D space (tile-space) is proposed. The seven basis vectors in the tile-space are derived from the cuboctahedron and grouped into two sets of vectors of different lengths: three vectors along the fourfold axis of relative length $1/\sqrt{3}$ and four vectors along the threefold axis of relative length $1/\sqrt{2}$. These are chosen so that the projection of vectors onto a plane perpendicular to the fourfold axis forms an eightfold star with relative length $1/\sqrt{3}$, which coincides with the configuration of basis vectors of a 2D octagonal pattern, or Beenker's tiling [9]. The geometry of the seven basis vectors is shown in Fig. 1.

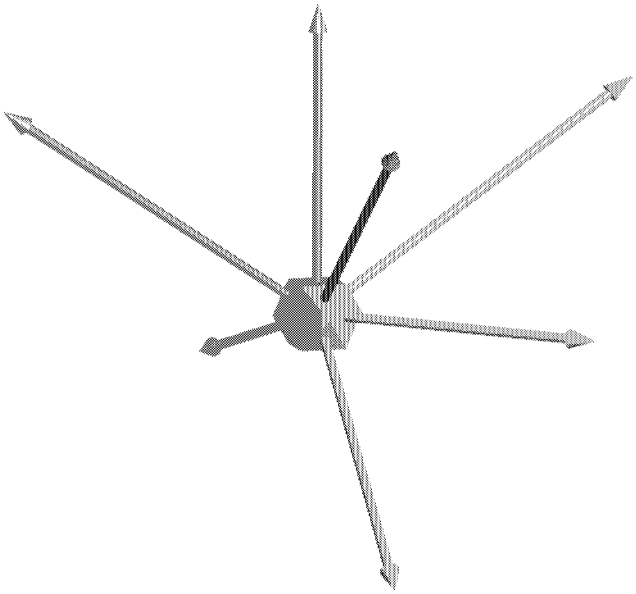

Fig. 1. Seven basis vectors derived from the normal of a cuboctahedron. They are grouped into two sets—three from the square facet and four from the triangular one—with a length ratio of $\sqrt{2}/\sqrt{3}$.

---

[1] This article was submitted by the authors in English.

Table 1. Prototile parameters of a 3D quasi-lattice

	a	b	c	$\cos\alpha$, (α, deg)	$\cos\beta$, (β, deg)	$\cos\gamma$, (γ, deg)	V
C	1	1	1	0, (90)	0, (90)	0, (90°)	1
S	1	1	$\frac{\sqrt{6}}{2}$	0, (90)	$\frac{\sqrt{3}}{3}$, (54.7)	$\frac{\sqrt{3}}{3}$, (54.7)	$\frac{\sqrt{2}}{2}$
P	$\frac{\sqrt{6}}{2}$	$\frac{\sqrt{6}}{2}$	1	$\frac{1}{3}$, (70.5)	$\frac{\sqrt{3}}{3}$, (54.7)	$\frac{\sqrt{3}}{3}$, (54.7)	1
R	$\frac{\sqrt{6}}{2}$	$\frac{\sqrt{6}}{2}$	$\frac{\sqrt{6}}{2}$	$-\frac{1}{3}$, (109.5)	$\frac{1}{3}$, (70.5)	$\frac{1}{3}$, (70.5)	$\sqrt{2}$

The constituent prototiles of the *QL* are derived by choosing three vectors out of seven basis vectors. The combinations of three basis vectors are restricted to four cases that make independent prototiles. They are a cube (*C*), a square parallelogram parallelepiped (*S*), a rhombic parallelogram parallelepiped (*P*), and a rhombohedron (*R*), as shown in Fig. 2 by a ball and stick model. The cell constants of these prototiles are listed in Table 1.

Three kinds of dodecahedra—a rhombic dodecahedron (*RD*), a rhombic parallelogram dodecahedron (*RPD*), and a square parallelogram dodecahedron (*SPD*)—that are assembled by different prototiles can be identified as the constituent clusters of the *QL*. These dodecahedra consist of prototiles ($RD = 4R$, $RPD = 2P + 2S$, and $SPD = C + 3S$, respectively). The geometrical packing arrangements of these dodecahedra are illustrated in Fig. 3. The shapes of the facets of the constituent prototiles are identified by small letters: *r* for the rhombus, *p* for the parallelogram, and *s* for the square, with parentheses showing the facet as seen from inside. The number following the letter indicates the shape

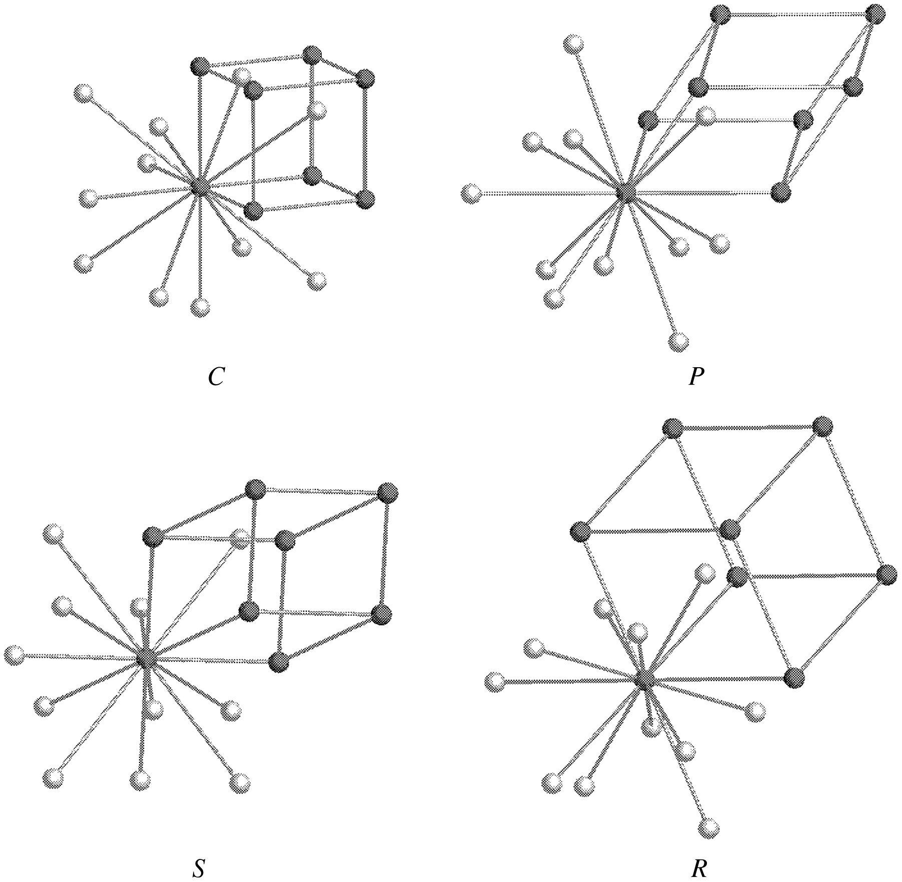

Fig. 2. Each figure includes a cuboctahedral star shown by balls and lines, with the prototile shown by dark balls.

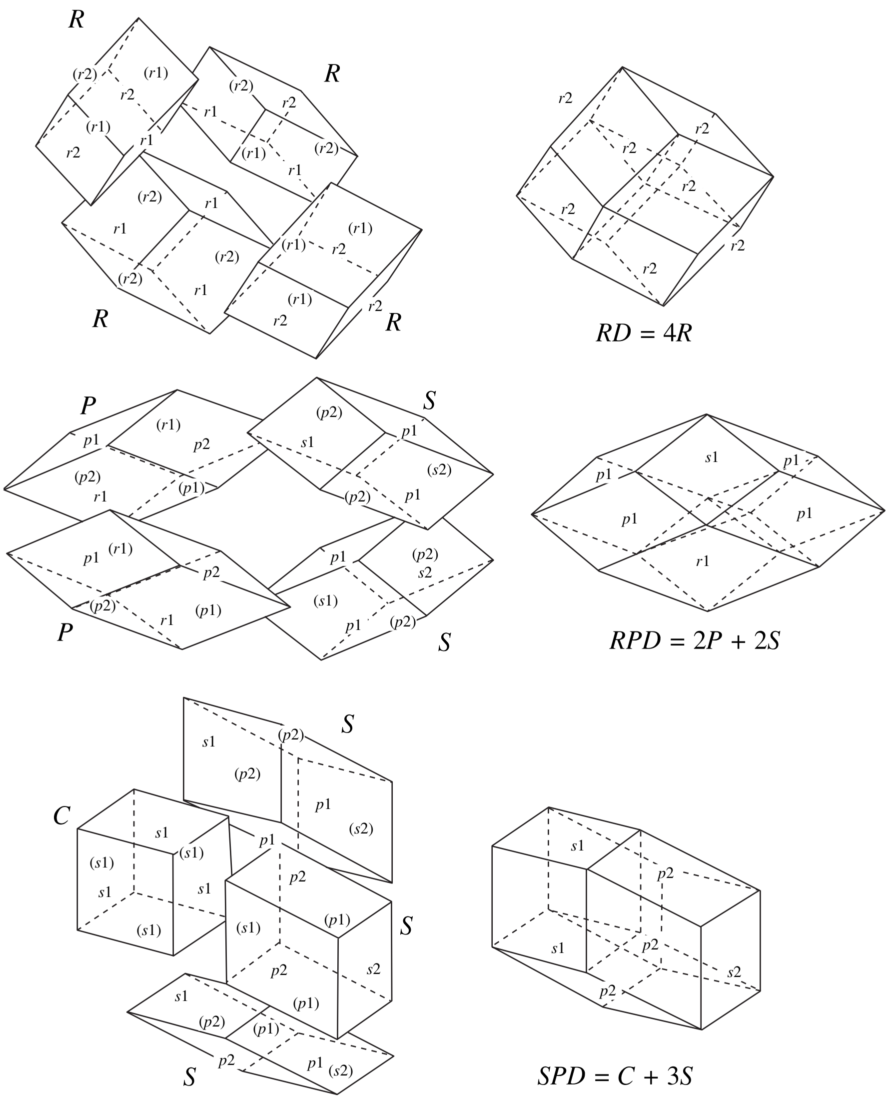

Fig. 3. Three kinds of dodecahedral clusters are shown (from top to bottom) in the right column and the expanded constituent prototiles in the left column.

type, and matching is allowed only with the facet of the same shape type. The shapes of the facet of contact play an important role in defining the inflation rules in the self-similar method of *QL* construction. This problem is discussed in detail elsewhere [10, 11].

PROJECTION METHOD AND THE BOUNDARY OF THE TEST WINDOW

In the projection method of generating quasiperiodic tiling, it is known that overlapping or absence of prototiles in the tiling is caused when a projected point in perp-space falls on the boundary of the test window and the boundary condition (open or closed) is not properly specified.

Since this problem is avoided by choosing an appropriate transfer vector of the window, no discussion is usually made except in the case of the method of selecting the proper transfer vector. Pleasants [12] proposed a method—called the infinitesimal transfer of test window to avoid overlapping or absence of prototiles—in which the test window is transferred infinitesimally in a direction not parallel to any of the facets of the window and in which the projected points that stay inside both the original and the transferred window are selected.

Figure 4 shows the case in which a one-dimensional (1D) tiling is generated by the projection from a 2D lattice space. The axis x is the tile-space and x' is the perp-space. If the test window obtained by projecting a unit square into the perp-space retains its initial position (zero transfer) and both ends are inside, the upper left and lower right corners of the unit square are inside the window and overlapping in the prototile occurs in the tiling. By infinitesimal transfer of the test window along the axis of the perp-space, shown by an arrow (no distinction being made in this case between the transfer

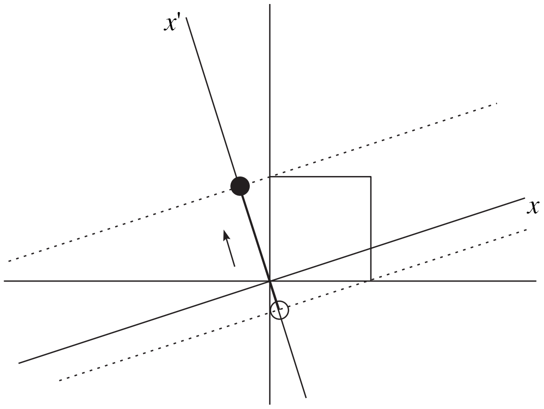

Fig. 4. Test window on perp-space x' for a 1D tiling.

and the infinitesimal transfer), the window becomes a line segment that is closed at the upper end (shown by a filled circle) and open at the lower end (shown by an open circle) and the overlapping of prototiles is avoided.

Figure 5 shows the unit polygon (a), or the projection of a four-dimensional (4D) unit cube to the tile-space, and the test window (b) of Beenker's tiling with zero transfer. Choose an infinitesimal transfer vector (shown by the outside arrow) so that all the basis vectors in the perp-space fall within the test window; then, the boundary condition becomes as is shown by the thick (inside) and thin (outside) line segments and the circles. Open and filled circles show points that are outside and inside, respectively. It is found that the test window in the perp-space is mirror symmetric with respect to the line bisecting the angle between vectors 1' and 4'. The tiling in the tile-space shown in Fig. 5c is also mirror symmetric with respect to the line bisecting the angle between vectors 1 and 4 and not eightfold symmetric with respect to the origin, although the shape of the test window is eightfold symmetric.

QUASIPERIODIC LATTICE BASED ON A CUBOCTAHEDRON

The 7×7 lattice matrix A in a 7D space is given in (1) in which the upper three rows correspond to the projection matrix to 3D tile-space (x, y, z) and the lower four rows correspond to that to 4D perp-space (x', y', z', w'):

$$A = \frac{1}{\sqrt{3}}\begin{pmatrix} 1/\sqrt{2} & 1/\sqrt{2} & -1/\sqrt{2} & 1/\sqrt{2} & 1 & 0 & 0 \\ 1/\sqrt{2} & 1/\sqrt{2} & 1/\sqrt{2} & -1/\sqrt{2} & 0 & 1 & 0 \\ 1/\sqrt{2} & -1/\sqrt{2} & 1/\sqrt{2} & 1/\sqrt{2} & 0 & 0 & 1 \\ -1/2 & -1/2 & 1/2 & -1/2 & \sqrt{2} & 0 & 0 \\ -1/2 & -1/2 & -1/2 & 1/2 & 0 & \sqrt{2} & 0 \\ -1/2 & 1/2 & -1/2 & -1/2 & 0 & 0 & \sqrt{2} \\ \sqrt{3}/2 & -\sqrt{3}/2 & -\sqrt{3}/2 & -\sqrt{3}/2 & 0 & 0 & 0 \end{pmatrix}. \quad (1)$$

The seven column vectors by upper three rows of matrix A represent the basis vectors in the tile-space shown in Fig. 1, and those by the lower four rows represent the basis vectors in the perp-space. It is known that the arrangement of basis vectors in Fig. 1 can be regarded as a combination of an octahedral star and a hexahedral star [13], and the projection matrix for tile-space can be lifted to an orthogonal frame of 7D space leading to matrix A [14]. The mixing ratio is $1 : \sqrt{2}$, and the projected points in the perp-space fill the test window uniformly, except for the w' axis—as explained below—and the tiling becomes quasiperiodic.

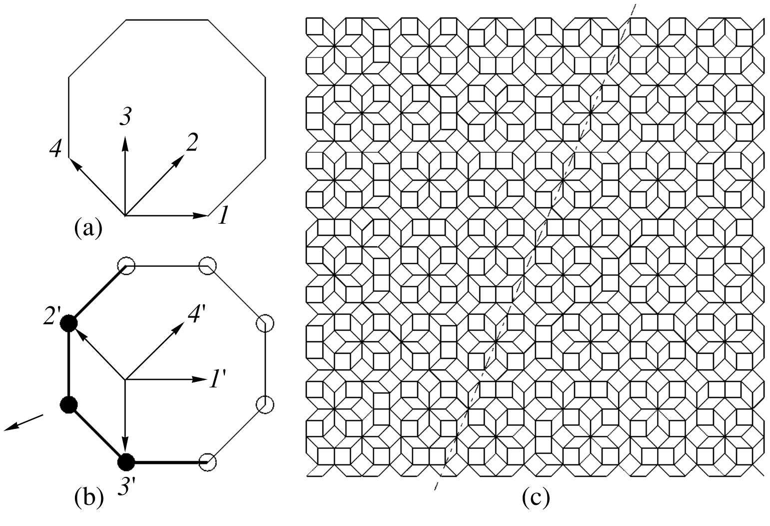

Fig. 5. Unit polygon (a) and test window (b) for Beenker's tiling. (c) A Beenker's tiling by the test window shown in (b) with the line of mirror symmetry shown by a dotted line.

The projection matrices $P_\parallel$ and $P_\perp$ defined in [15] for a 3D Penrose tiling are related, in general, to lattice matrix A as

$$P_\parallel = A^{-1}A_\parallel, \quad P_\perp = A^{-1}A_\perp \tag{2}$$

or

$$\tilde{A}_\parallel = \tilde{P}_\parallel\tilde{A} = P_\parallel\tilde{A}, \quad \tilde{A}_\perp = \tilde{P}_\perp\tilde{A} = P_\perp\tilde{A}, \tag{3}$$

where $A_\parallel$ is a matrix with nonzero rows from the tile-space part of A, and $A_\perp$ from the perp-space part of A [7]. $\tilde{A}_\parallel$, $\tilde{A}_\perp$, $\tilde{P}_\parallel$, and $\tilde{P}_\perp$ are transposed matrices of $A_\parallel$, $A_\perp$, $P_\parallel$, and $P_\perp$, respectively. $P_\parallel$ and $P_\perp$ are symmetric matrices; therefore, $\tilde{P}_\parallel = P_\parallel$ and $\tilde{P}_\perp = P_\perp$. It is easy to show that

$$P_\parallel = \frac{1}{3}\begin{pmatrix} 3/2 & 1/2 & 1/2 & 1/2 & 1/\sqrt{2} & 1/\sqrt{2} & 1/\sqrt{2} \\ 1/2 & 3/2 & -1/2 & -1/2 & 1/\sqrt{2} & 1/\sqrt{2} & -1/\sqrt{2} \\ 1/2 & -1/2 & 3/2 & -1/2 & -1/\sqrt{2} & 1/\sqrt{2} & 1/\sqrt{2} \\ 1/2 & -1/2 & -1/2 & 3/2 & 1/\sqrt{2} & -1/\sqrt{2} & 1/\sqrt{2} \\ 1/\sqrt{2} & 1/\sqrt{2} & -1/\sqrt{2} & 1/\sqrt{2} & 1 & 0 & 0 \\ 1/\sqrt{2} & 1/\sqrt{2} & 1/\sqrt{2} & -1/\sqrt{2} & 0 & 1 & 0 \\ 1/\sqrt{2} & -1/\sqrt{2} & 1/\sqrt{2} & 1/\sqrt{2} & 0 & 0 & 1 \end{pmatrix}, \tag{4}$$

$$P_\perp = \frac{1}{3}\begin{pmatrix} 3/2 & -1/2 & -1/2 & -1/2 & -1/\sqrt{2} & -1/\sqrt{2} & -1/\sqrt{2} \\ -1/2 & 3/2 & 1/2 & 1/2 & -1/\sqrt{2} & -1/\sqrt{2} & 1/\sqrt{2} \\ -1/2 & 1/2 & 3/2 & 1/2 & 1/\sqrt{2} & -1/\sqrt{2} & -1/\sqrt{2} \\ -1/2 & 1/2 & 1/2 & 3/2 & -1/\sqrt{2} & 1/\sqrt{2} & -1/\sqrt{2} \\ -1/\sqrt{2} & -1/\sqrt{2} & 1/\sqrt{2} & -1/\sqrt{2} & 2 & 0 & 0 \\ -1/\sqrt{2} & -1/\sqrt{2} & -1/\sqrt{2} & 1/\sqrt{2} & 0 & 2 & 0 \\ -1/\sqrt{2} & 1/\sqrt{2} & -1/\sqrt{2} & -1/\sqrt{2} & 0 & 0 & 2 \end{pmatrix}, \tag{5}$$

where $P_\parallel$ and $P_\perp$ have the following properties:

$$P_\parallel^2 = P_\parallel, \quad P_\perp^2 = P_\perp, \tag{6}$$

$$P_\parallel + P_\perp = I, \tag{7}$$

$$P_\parallel P_\perp = O, \tag{8}$$

where I is the unit matrix and O is the zero matrix of order 7.

The angles between the two basis vectors given in Table 1—109.5°, 70.5°, and 54.7°—are approximate, but the exact values can easily be obtained using the inner product of the selected two column vectors by the upper three rows of matrix A. Furthermore, it should be noted that the four vectors of length $1 : \sqrt{2}$ in the tile-space are linearly dependent with respect to the integer coefficient. This is reflected by the fact that the elements of the bottom row of (1) are 0 or 1/2 and that the w' coordinates of the projected points make a discrete set of a multiple of 1/2. Thus, the number of independent vectors in the tile-space is six, and the tiling can be generated by projection from six-dimensional (6D) to 3D space. The lattice matrix for this case is easily obtained by removing the first column vector corresponding to the basis vectors in (1) and taking the z axis to coincide with the direction of that vector, so that the projections of the other six vectors to the xy plane form two threefold stars. Details will be discussed elsewhere [16].

The test window is defined as a convex hull by 2^7 projected points in the perp-space corresponding to vertices of a 7D unit cube of the base lattice space. It has a boundary facet defined by a number of combinations of three out of seven basis vectors in the 4D perp-space. If no degeneracy occurs, all the combinations define the facets, that is, 70 or $2C_7^3$ facets should appear. However, degeneracy of the hyperplanes defining the facet arises in this case, because they have the same normals.

In fact, the polytope generated has 34 facets and 72 vertices in 4D space. The details of a method of finding the projected polytope in the perp-space that uses the program Qhull [18] is discussed elsewhere [17]. Table 2 shows the component (rounded numerical values) of normals of facets and the offsets from the center to each facet of the polytope. Figure 6 shows sections of the 4D polytope at $w' = -1, -1/2, 0, 1/2$, and 1 that are

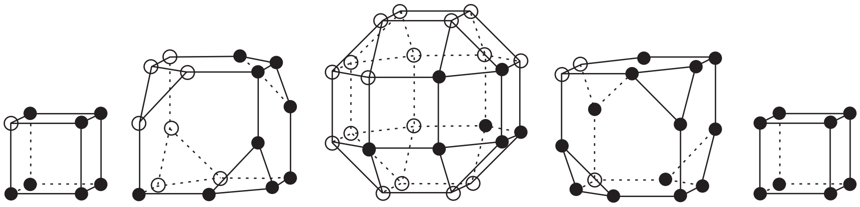

Fig. 6. Sections of a 4D test window polytope at $w' = -1$ (a), $-1/2$ (b), 0 (c), 1/2 (d), and 1 (e).

3D polyhedra of 6, 10, 26, 10, and 6 facets, respectively, as shown in Fig. 6. Circles on the vertices show inside and outside properties (refer to Fig. 5) of the test window for the infinitesimal transfer with a direction of (0.3, –0.5, –0.7, 2.0) and a transfer vector of (0, 0, 0, 0). In the same way, the unit polyhedron, or the projection of a 7D unit cube to the 3D tile-space, is obtained as a truncated rhombic dodecahedron with 18 facets and 32 vertices. It is shown in Fig. 7 with basis vectors.

A 3D quasiperiodic tiling obtained under the test window conditions shown in Fig. 6 with the domain of projection of a 7D unit cube is shown in Fig. 8. It consists of one *C*, eight *S*s, eight *P*s, and four *R*s, of which six *S*s and six *P*s constitute three *RPD* clusters and three *S*s and one *C* constitute one *SPD* cluster.

The projection of the 3D *QL* to 2D surface is shown in Figs. 9a–11a for the projection direction along the fourfold, threefold, and twofold symmetry axes of the unit polyhedron shown in Fig. 7. The original 3D *QL* is obtained with the domain of the projection in the base lattice space as $-2 \le x_i \le 2$, $i = 1, \ldots, 7$ and consists of 1404 vertex points.

The diffraction patterns shown in Figs. 9b–11b are calculated by the standard method using the direct Fourier transform for a 2D mask. Assuming that a Dirac measure exists at each vertex x of the 3D *QL* given above, the measure associated with the *QL* is $m = \Sigma_{KP}\delta_{\mathbf{x}}$. The Fourier transform is formally given by $m(\mathbf{k}) = \Sigma_{KP}\exp(2\pi i\mathbf{kx})$, where $\mathbf{kx}$ indicates the scalar product [15]. If $\mathbf{k}$ is restricted in plane P perpendicular to the asymmetry axis, the Fourier transform on the plane can be given with $\mathbf{x}$ replaced by $\mathbf{x}_P$, the projection of $\mathbf{x}$ to plane P. This shows that, taking the square of the Fourier transform, the diffraction pattern can be obtained by using a 2D program. In Fig. 9b, although the pattern is basically fourfold symmetric, bright spots forming regular octagons or quasiregular octagons can be noticed.

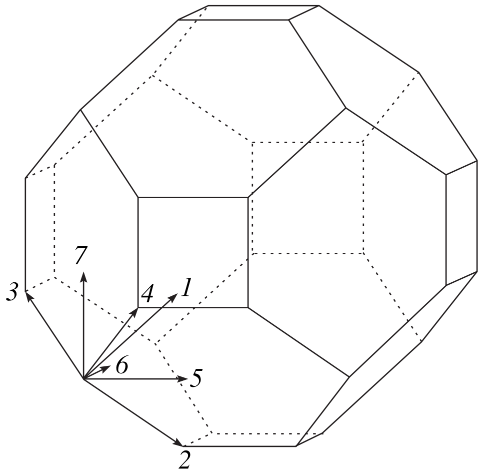

Fig. 7. A unit polyhedron by the projection of a 7D unit cube onto the tile-space is shown that is a truncated rhombic dodecahedron. Basis vectors, which are shown by arrows, are numbered according to the order of column vectors in (1).

DISTORTION OF THE QUASIPERIODIC LATTICE

The *QL* can be deformed so that it is periodic in one direction and quasiperiodic in the other two directions by introducing distortion parameter δ into matrix *A*

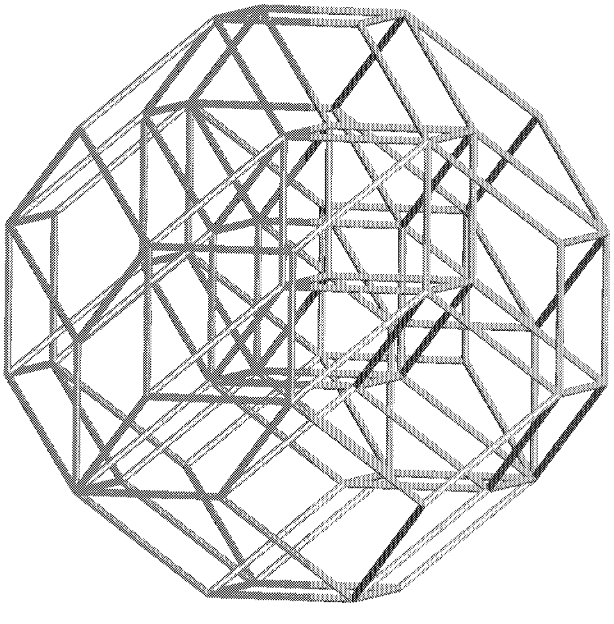

Fig. 8. A part of the 3D quasiperiodic tiling corresponding to the unit polyhedron generated using the test window shown in Fig. 6. It consists of prototiles: one *C*, eight *S*s, eight *P*s, and four *R*s.

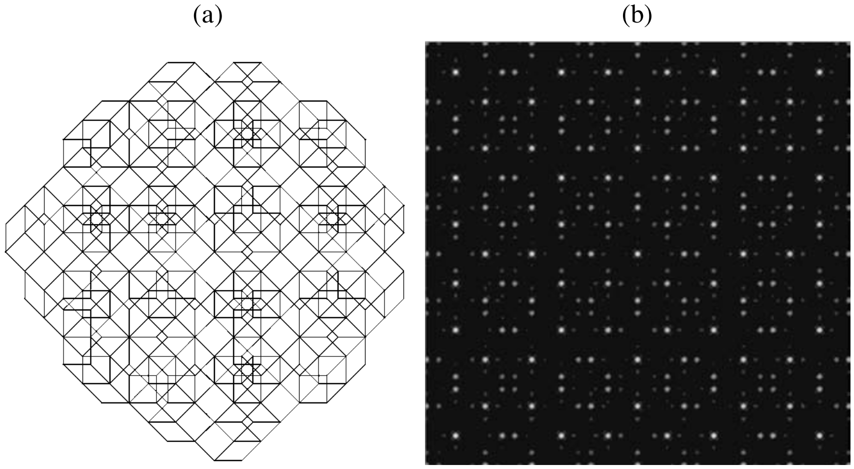

Fig. 9. Projections of a 3D *QL* to a plane perpendicular to a twofold symmetry axis of the unit polyhedron (a) and the corresponding diffraction pattern calculated by the direct Fourier transform using 1404 points (b).

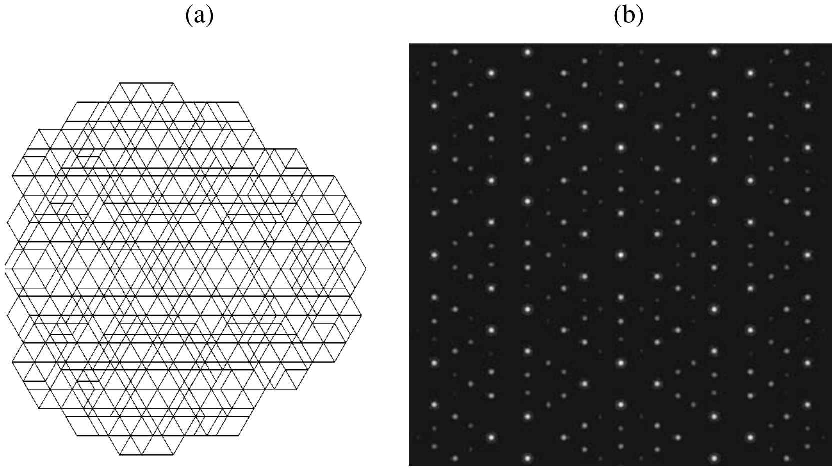

Fig. 10. Projections of a 3D *QL* to a plane perpendicular to a threefold symmetry axis of the unit polyhedron (a) and the corresponding diffraction pattern calculated by the direct Fourier transform using 1404 points (b).

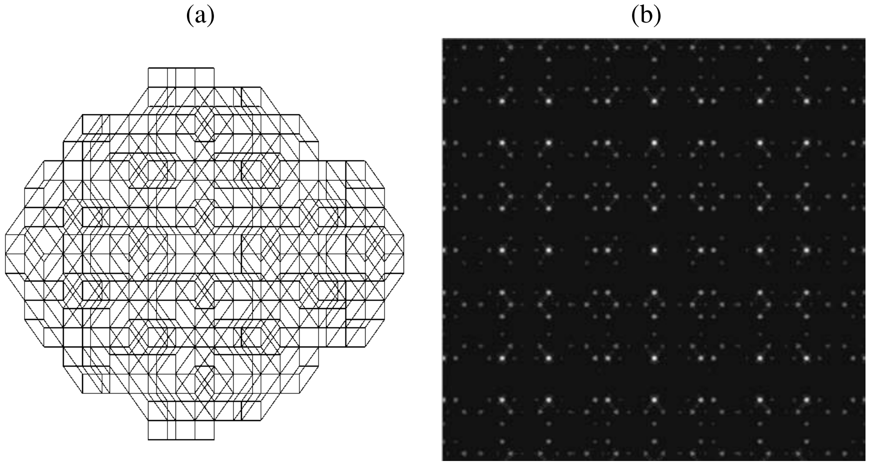

Fig. 11. Projections of a 3D *QL* to a plane perpendicular to a fourfold symmetry axis of the unit polyhedron (a) and the corresponding diffraction pattern calculated by the direct Fourier transform using 1404 points (b).

Table 2. Rounded numerical values of normals and offsets of the test window

No.	$n_{x'}$	$n_{y'}$	$n_{z'}$	$n_{w'}$	Offset
1	0.547723	–0.547723	0.547723	0.316228	0.987048
2	–0.547723	0.547723	–0.547723	–0.316228	0.987048
3	0.547723	–0.547723	–0.547723	–0.316228	0.987048
4	–0.547723	0.547723	0.547723	0.316228	0.987048
5	0.000000	0.000000	0.866025	0.500000	0.853553
6	0.000000	0.000000	–0.866025	–0.500000	0.853553
7	0.707107	–0.707107	0.000000	0.000000	0.985599
8	–0.707107	0.707107	0.000000	0.000000	0.985599
9	0.547723	0.547723	–0.547723	0.316228	0.987048
10	–0.547723	–0.547723	0.547723	–0.316228	0.987048
11	0.000000	0.707107	–0.707107	0.000000	0.985599
12	0.000000	–0.707107	0.707107	0.000000	0.985599
13	0.866025	0.000000	0.000000	0.500000	0.853553
14	–0.866025	0.000000	0.000000	–0.500000	0.853553
15	0.000000	0.866025	0.000000	0.500000	0.853553
16	0.000000	–0.866025	0.000000	–0.500000	0.853553
17	0.707107	0.000000	–0.707107	0.000000	0.985599
18	–0.707107	0.000000	0.707107	0.000000	0.985599
19	0.547723	0.547723	0.547723	–0.316228	0.987048
20	–0.547723	–0.547723	–0.547723	0.316228	0.987048
21	0.000000	0.866025	0.000000	–0.500000	0.853553
22	0.000000	–0.866025	0.000000	0.000000	0.853553
23	0.707107	0.000000	0.707107	0.000000	0.985599
24	–0.707107	0.000000	–0.707107	0.000000	0.985599
25	0.000000	0.707107	0.707107	0.000000	0.985599
26	0.000000	–0.707107	–0.707107	0.000000	0.985599
27	0.866025	0.000000	0.000000	–0.500000	0.853553
28	–0.866025	0.000000	0.000000	0.500000	0.853553
29	0.000000	0.000000	0.866025	–0.500000	0.853553
30	0.000000	0.000000	–0.866025	0.500000	0.853553
31	0.707107	0.707107	0.000000	0.000000	0.985599
32	–0.707107	–0.707107	0.000000	0.000000	0.985599
33	0.000000	0.000000	0.000000	1.000000	1.000000
34	0.000000	0.000000	0.000000	–1.000000	1.000000

(Eq. (1)). The geometry of the distortion considered is similar to those proposed for the 2D case [19]. Distorting the basis vector in the z direction, the lattice matrix A can be QL-modified as

$$A' = \frac{1}{\sqrt{3}}\begin{pmatrix} 1/\sqrt{2} & 1/\sqrt{2} & -1/\sqrt{2} & 1/\sqrt{2} & 1 & 0 & 0 \\ 1/\sqrt{2} & 1/\sqrt{2} & 1/\sqrt{2} & -1/\sqrt{2} & 0 & 1 & 0 \\ D_1/\sqrt{2} & -D_1/\sqrt{2} & D_1/\sqrt{2} & D_1/\sqrt{2} & 0 & 0 & D \\ -1/2 & -1/2 & 1/2 & -1/2 & \sqrt{2} & 0 & 0 \\ -1/2 & -1/2 & -1/2 & 1/2 & 0 & \sqrt{2} & 0 \\ -D/2 & D/2 & -D/2 & -D/2 & 0 & 0 & \sqrt{2}D_1 \\ \sqrt{3}/2 & -\sqrt{3}/2 & -\sqrt{3}/2 & -\sqrt{3}/2 & 0 & 0 & 0 \end{pmatrix}, \tag{9}$$

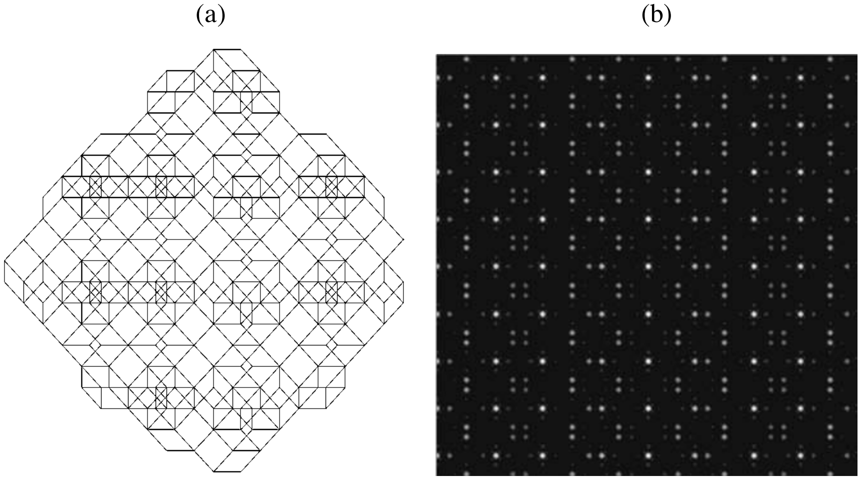

Fig. 12. *xz* plane projection of a distorted 3D tiling that is quasiperiodic in the *x* and *y* directions and periodic in the *z* direction (a) and the corresponding diffraction pattern calculated by the direct Fourier transform using 1282 points (b).

which satisfies the orthonormal condition, where $D = \sqrt{1-4\delta-2\delta^2}$ and $D_1 = 1+\delta$, from which the properties of the tiling can be derived. For $\delta \neq 0$ and $|\delta| < 1$, the basis vectors are grouped into three sets: four vectors from the first four, two from the fifth and sixth, and one from the last column vectors of (9). The number of prototiles becomes seven, and that of clusters six. It is interesting to note that, for $\delta = -1$, the elements of the third row corresponding to the *z* coordinate are zeroes, except for the last one, and that the projection of the tiling to the *xy* plane becomes a tiling with prototiles of Beenker's tiling. Details will be discussed elsewhere [20]. As an example, put $\delta = \sqrt{6/5} - 1$ into (9); then, matrix A' becomes

$$A' = \frac{1}{\sqrt{3}}\begin{pmatrix} 1/\sqrt{2} & 1/\sqrt{2} & -1/\sqrt{2} & 1/\sqrt{2} & 1 & 0 & 0 \\ 1/\sqrt{2} & 1/\sqrt{2} & 1/\sqrt{2} & -1/\sqrt{2} & 0 & 1 & 0 \\ \sqrt{3/5} & -\sqrt{3/5} & \sqrt{3/5} & \sqrt{3/5} & 0 & 0 & \sqrt{3/5} \\ -1/2 & -1/2 & 1/2 & -1/2 & \sqrt{2} & 0 & 0 \\ -1/2 & -1/2 & -1/2 & 1/2 & 0 & \sqrt{2} & 0 \\ -\sqrt{3/20} & \sqrt{3/20} & -\sqrt{3/20} & -\sqrt{3/20} & 0 & 0 & 4\sqrt{3/20} \\ \sqrt{3}/2 & -\sqrt{3}/2 & -\sqrt{3}/2 & -\sqrt{3}/2 & 0 & 0 & 0 \end{pmatrix}, \quad (10)$$

in which the z' coordinate in the perp-space is discrete (multiples of $1/2\sqrt{5}$) in addition to the w' coordinate (multiples of 1/2). Also, the *z* coordinate in the tile space is discrete (multiples of $1/\sqrt{5}$). Consequently, the 3D tiling is periodic along the *z* direction and quasiperiodic in the *xy* plane. A 3D tiling generated under similar conditions as the *QL* shown above can be obtained, and its projection onto the *xy* plane and the corresponding diffraction pattern are shown in Figs. 12a and 12b, respectively.

CONCLUSIONS

As an extension of 2D eightfold symmetric Beenker's tiling, a 3D quasiperiodic tiling based on a cuboctahedron is considered and its properties are investigated. Since a *QL* is composed of four kinds of prototiles, the structure appears complicated, but the symmetry of the *QL* reflects that of the cuboctahedron, namely, two-, three-, and fourfold symmetry. It is an interesting question whether a self-similar method of generation exists for the *QL* derived by the projection method. Ways of constructing a *QL* by self-similar method have been successfully found [10], and their details will be elucidated. The *QL* can be considered a quasicrystal model that gives fourfold symmetry. Furthermore, the tiling with the distortion parameters presented here may be applied to model an octagonal phase of some metal compounds by introducing an appropriate distortion parameter. Though, in this paper, the geometrical aspect is emphasized, further study is needed to take into account the physical and chemical aspects.

ACKNOWLEDGMENTS

The authors would like to deeply thank the late Prof. M.V. Jarić for his suggestion of distorting the basis vectors of QL and to Betsumiya and Ikegami for geometrical discussion and technical support for this work. One of the authors (T. Soma) thanks the University of the South Pacific for accepting him as a visiting research professor and providing him with an agreeable research environment while staying in Fiji. Also, the authors are grateful to the members of the Computer and Information Division of Riken, especially Dr. Himeno, the head, for their support. This work was partly supported by the Special Coordination Funds for Promoting Science and Technology.

REFERENCES

1. D. Schechtman, I. Blech, D. Gratias, and J. W. Cahn, Phys. Rev. Lett. **53**, 1951 (1984).
2. C. Janot, *Quasicrystals: a Primer*, 2nd ed. (Clarendon Press, Oxford, 1994).
3. M. Senechal, *Quasicrystals and Geometry* (Cambridge Univ. Press, Cambridge, 1995).
4. N. G. de Bruijn, Proc. Ned. Akad. Wet. A **43**, 39 (1981); Proc. Ned. Akad. Wet. A **43**, 53 (1981).
5. P. Bak and A. I. Goldman, *Introduction to Quasicrystals, Aperiodicity and Order,* Ed. by M. V. Jaric (Academic, New York, 1988), Vol. 1, p. 143.
6. Y. Watanabe, T. Soma, M. Ito, and T. Betsumiya, Mater. Sci. Forum **22–24**, 213 (1987).
7. T. Soma, Y. Watanabe, and M. Ito, in *Proceedings of 3rd International Meeting on Quasicrystals*, Ed. by M. Yacaman (World Sci., Singapore, 1990), p. 231.
8. T. Soma and Y. Watanabe, in *Proceedings of 6th International Conference on Quasicrystals*, *Yamada Conference XLVII*, Ed. by S. Takeuchi and T. Fujiwara (World Sci., Singapore, 1997), p. 156.
9. F. P. M. Beenker, Eindhoven Univ. Tech. Rep. 82-WSK-04 (1982).
10. Y. Watanabe and Y. Ikegami, in *Proceedings of China–Japanese Seminar*, Ed. by K. H. Kuo and T. Ninomiya (World Sci., Singapore, 1991), p. 204.
11. Y. Watanabe, Mater. Sci. Forum **150–151**, 167 (1994).
12. M. Baake, J. Hermisson, and P. Pleasants, J. Phys. A: Math. Gen. **30**, 3029 (1997).
13. T. Soma and Y. Watanabe, South. Pac. J. Natl. Sci. **15**, 145 (1997).
14. T. Soma and Y. Watanabe, Acta Crystallogr., Sect. A: Found. Crystallogr. **55**, 508 (1999).
15. A. Katz and M. Duneau, J. Phys. (Paris) **47**, 181 (1986).
16. T. Soma and Y. Watanabe, FORMA (2004) (in press).
17. T. Soma and Y. Watanabe, FORMA **15**, 67 (2000).
18. C. B. Barber, D. P. Dobkin, and H. Huhdanpaa, ACM Trans. Math. Softw. **22**, 469 (1996).
19. T. Soma and Y. Watanabe, Acta Crystallogr., Sect. A: Found. Crystallogr. **48**, 470 (1992).
20. T. Soma and Y. Watanabe, FORMA (2004) (in press).

Crystallography Reports, Vol. 49, No. 4, 2004, pp. 537–546. Translated from Kristallografiya, Vol. 49, No. 4, 2004, pp. 610–620.
Original Russian Text Copyright © 2004 by Chizhikov.

Quasicrystal as a Locally Deformed Crystal Structure

V. A. Chizhikov
Shubnikov Institute of Crystallography, Russian Academy of Sciences, Leninskiĭ pr. 59, Moscow, 119333 Russia
e-mail: chizhikov@ns.crys.ras.ru

Received November 10, 2003

Abstract—Lattice models for a two-dimensional octagonal quasicrystal and a three-dimensional icosahedral quasicrystal with the icosahedral–dodecahedral local order are introduced. It is shown that an octagonal quasicrystal may be obtained as a result of the local deformation of an ideal square atomic lattice. Possible paths of structural transformations between various phases of an AlPd crystal are determined. It is shown that icosahedral quasicrystals of aluminum alloys with transition metals can be considered to be a result of the local distortions of an ideal fcc lattice of elemental aluminum induced by a transition metal impurity. *© 2004 MAIK “Nauka/Interperiodica”.*

INTRODUCTION

As is well known, the diffraction pattern from an icosahedral quasicrystal consists of sharp Bragg peaks whose positions are completely described by a set of six integers (and not three, as in a conventional three-dimensional, crystal) [1–3]. This fact allows one to describe the structure of a quasicrystal by the methods of multidimensional crystallography developed for other types of incommensurate phases, such as, e.g., modulated crystals [4, 5]. Nevertheless, there are some important differences between quasicrystals and modulated crystals associated with their symmetry properties and methods used to obtain these structures. The main reason to consider quasicrystals as an individual class of structures is their unusual point symmetry inadmissible in periodic crystals. Contrary to quasicrystals, modulated crystals are considered a result of the distortion of the crystal structure under the action of one or several periodic modulations with periods incommensurate with respect to the periods of the initial crystal. Such a distortion makes the crystal aperiodic, so that it is necessary to introduce some new vectors into the basis of its reciprocal lattice—one vector per modulation. The structures in which the dimensionality of the reciprocal-lattice basis exceeds the dimensionality of space are called incommensurate or quasiperiodic. The possibility to single out the initial periodic lattice (so-called mean lattice) is reflected in the physical properties of modulated crystals. Thus, it is obvious that the point symmetry group of a modulated crystal should be a subgroup of the point group of the initial crystal; in other words, it cannot have unusual symmetry elements inherent in quasicrystals such as five-, eight-, ten-, and twelvefold axes. Another example is the presence in the diffraction pattern from modulated crystals of a system of main peaks corresponding to the mean lattice, whereas, in quasicrystals, all the incommensurate basis vectors of the reciprocal lattice are equivalent.

Taking what was said above into account, the aim of this work as declared in the article title, i.e., the description of a quasicrystal formed as a result of the local distortion of the periodic structure, seems to be unattainable. However, there are some facts that indicate that this is not true. Among these facts is, e.g., the experimental detection of the phase transitions of the crystal–quasicrystal type. Another purely theoretical example is the lattice model of a plane dodecagonal tiling of squares and equilateral triangles [6–8]. This paradox is explained by the fact that only specific modulations can give rise to an increase in the point symmetry of a crystal. One may readily find the restrictions imposed on the main reciprocal-lattice periods of incommensurate modulations, which, together with the main reciprocal-lattice periods of the initial crystal, should form the basis of the reciprocal lattice of a quasicrystal. For example, in order to obtain a structure with octagonal symmetry, the reciprocal-lattice basis of a square net, $\{(1, 0), (0, 1)\}$, should be complemented with the vectors $(1/\sqrt{2}, 1/\sqrt{2})$ and $(1/\sqrt{2}, -1/\sqrt{2})$. However, in order to describe the structure, knowledge of the reciprocal-lattice basis is not sufficient—one must also know the positions of individual atoms. Earlier, some attempts were made to describe the atomic structure of a quasicrystal with the aid of periodic structures with the same dimensionality as in a quasicrystal [9, 10]. Thus, the atomic positions of an octagonal quasicrystal were considered as those obtained by averaging the positions of the sites of two square lattices rotated by an angle of 45° with respect to one another [9]. The possibility to single out the fcc mean lattice in a three-dimensional icosahedral Penrose tiling was shown in [10].

The present work aims at the description of the atomic structure of some quasicrystals formed as a result of the local distortion of primitive periodic lat-

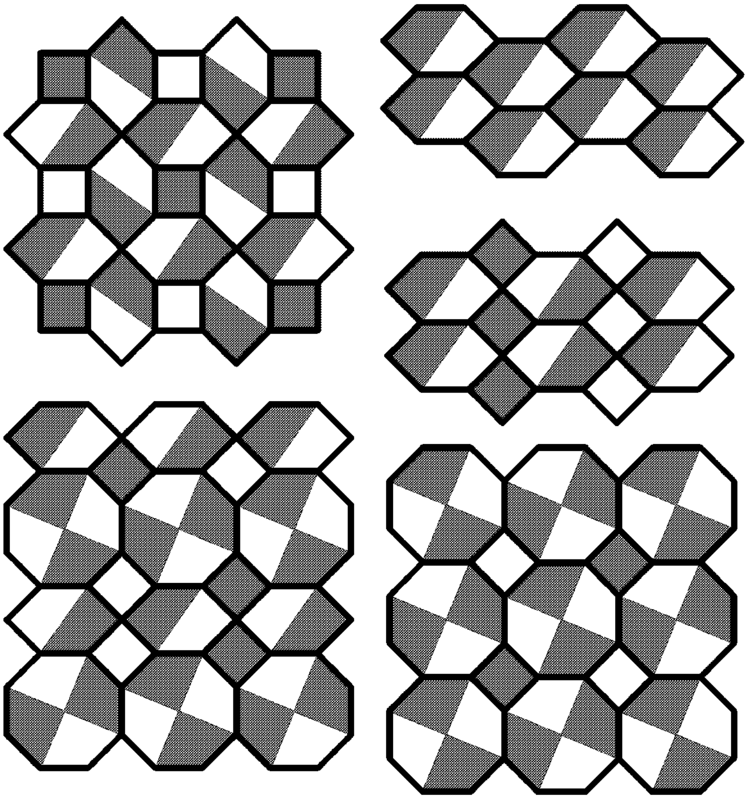

Fig. 1. Examples of plane periodic tilings composed by squares, regular octagons, and equilateral hexagons with the angles 90° and 135°. The light and dark figures indicate the possibility of the transition from tilings of the given class to lattices consisting of tetragons topologically equivalent to the square net.

tices. As examples, we consider plane octagonal tilings and, also, the class of structures with the so-called icosahedral–dodecahedral local order (IDLO).

A QUASIPERIODIC OCTAGONAL TILING AS A DEFORMED SQUARE LATTICE

As an example, consider a class of tilings on a plane composed of three types of tiles—squares, regular octagons, and equilateral hexagons with the angles 90° and 135°. Figure 1 shows several of the simplest tilings of such type. Any tiling of this class possesses one peculiar property—if one supplements the vertices already existing in the tiling with a site in the centers of all the octagons, then the system of sites thus obtained can be used to construct a net topologically equivalent to a square lattice. Indeed, as is seen from Fig. 1, each tiling can be divided into tetragons in such a way that each site of the structure (including the sites in the octagon centers) would be a vertex shared by four tetragons. This signifies that all the structures of the given class, with the atoms being located at square and hexagon vertices and octagon vertices and centers, can be considered a result of the local deformation of an ideal square lattice having no voids and interstitial atoms.

A similar property has long been known for another class of plane structures, namely, for tilings composed of squares and regular triangles. It has been shown that the latter are related in a similar way to a triangular net [6].

The tilings shown in Fig. 1 are examples of periodic structures, but the same tiles can also be used to construct aperiodic (including quasiperiodic octagonal) tilings. In order to determine the structure with the macroscopically octagonal symmetry, one may use, e.g., the rules of tiling inflation (Fig. 2).

We would like to explain the meaning of the term inflation related to the self-similarity property of some tilings, which reduces to the following. All the tiles of a certain tiling can be divided into similar smaller figures. Then, uniformly extending this pattern in such a way that the constituent figures would acquire again their initial dimensions, we arrive at a structure locally isomorphous to the initial one, in other words, the old and new tilings overlap within arbitrarily large regions. The inflation rules uniquely determine the class of locally isomorphous structures and can be used to describe quasiperiodic mosaics. The multiple inflation of the tiling allows one to obtain infinitely large regions of tilings, starting this procedure from only one or several tiles.

The tiles in Fig. 2 may be divided into figures similar to these tiles in accordance with their in-plane orientations. The orientations are indicated by auxiliary triangles on the figure sides. The similarity coefficient of the tiles for the old and new tilings is $\alpha = (1 + \sqrt{2})$. The number of squares equals the number of octagons. The ratio of the number of hexagons to the number of octagons equals $(\sqrt{2} - 1)$. The portion of the structure corresponding to these inflation laws is shown in Fig. 3. The tiling thus obtained is not the only possible octagonal structure built by squares, regular octagons, and equilateral hexagons with angles of 90° and 135° despite the fact that this tiling possesses some peculiar features [11]. First, all the sites of this structure are three-connected ones. Moreover, they all have the same nearest environment. Second, this tiling may also be obtained from the well-known Ammann–Beenker tiling [12, 13] constructed of squares and rhombuses with acute angles of 45° and the removal of some sites.

The octagonal tiling thus obtained may also be divided into tetragons by the method indicated above (Fig. 3). Thus, the given structure with the additional sites in the octagon centers is topologically equivalent to the square lattice. Decorating this structure with atoms, we arrive at a plane quasicrystal with octagonal symmetry (Fig. 4). It is seen that this quasicrystal may be considered a result of the local deformation of a plane crystal with the square lattice due to the replacement of some atoms $(3 - 2\sqrt{2} \sim 17\%)$ by impurity atoms with a large atomic radius.

The increase in the point symmetry of the crystal upon its deformation is rather amazing. It is worth mentioning the reverse process—lowering of the symmetry upon the quasicrystal–crystal transition. Similar to any phase transformation, lowering of the symmetry indicates the nonuniqueness of the transition, which can occur along different paths. Indeed, the constituent hexagons and octagons may be divided into tetragons in two ways that are symmetric with respect to one another. Each of these ways describes the transition to its own square lattice. The angle formed by these lattices in the octagonal tiling is 45°.

Thus, we showed that a quasiperiodic octagonal structure is simply related to a square lattice. Earlier, a similar property was demonstrated for another class of quasiperiodic structures, namely, for dodecagonal tilings composed by squares and equilateral triangles [8]. It was shown that these tilings can undergo transition to a triangular lattice, which is accompanied by lowering of the point symmetry to the hexagonal one. The atomic structures of quasicrystals are often described with the aid of the projection method—the atomic positions are determined as the projections of some sites of a multidimensional periodic lattice onto the physical space. In this case, the selection of a physical space determines the local environment of atoms in the structure. The transition from the quasiperiodic lattice to a periodic lattice of the same dimensionality considered here may also be described as a projection from the multidimensional space onto a subspace different from the physical one. Up to now, the octagonal tiling described here (Figs. 3, 4) and the dodecagonal tiling mentioned above [7] are the only known examples of quasiperiodic structures for which such projecting can be performed onto an ideal (without vacancies and interstitials) periodic lattice. However, if one does not require that the lattice onto which projection is made be ideal, this approach may also be applied to a very wide class of substances. In particular, this is true for the atomic structures of a number of icosahedral quasicrystals and their periodic approximants possessing the so-called icosahedral–dodecahedral local order considered in the following section. We suggest the method of projecting the atomic positions of these structures onto a primitive cubic lattice.

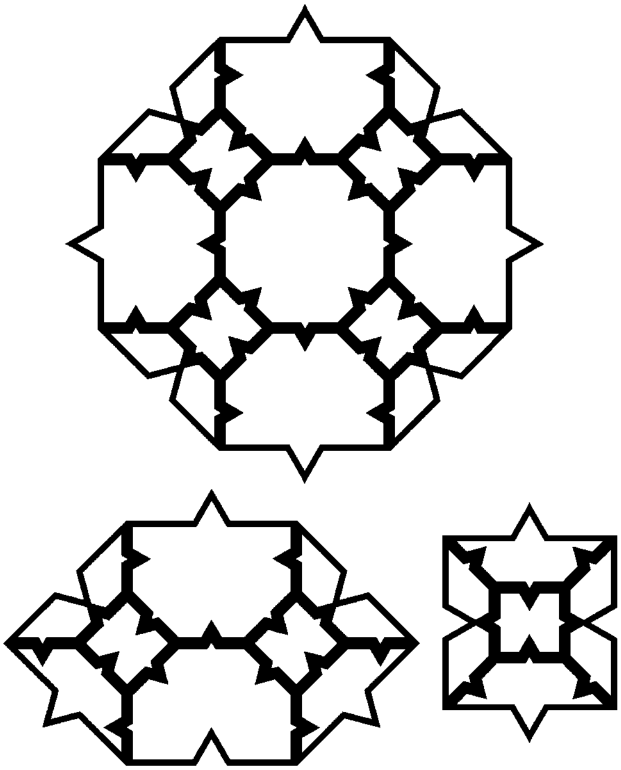

Fig. 2. Inflation rules for the octagonal tiling consisting of squares, regular octagons, and equilateral hexagons with the angles 90° and 135°. The tiles of the initial tiling (thin lines) are divided into figures similar to the initial ones of a new tiling (thick lines) in accordance with their in-plane orientations, indicated by the zigzags on the sides.

LATTICE MODEL OF STRUCTURES WITH ICOSAHEDRAL–DODECAHEDRAL LOCAL ORDER

Above, we showed that the atomic positions of a certain periodic or quasiperiodic structure can be pro-

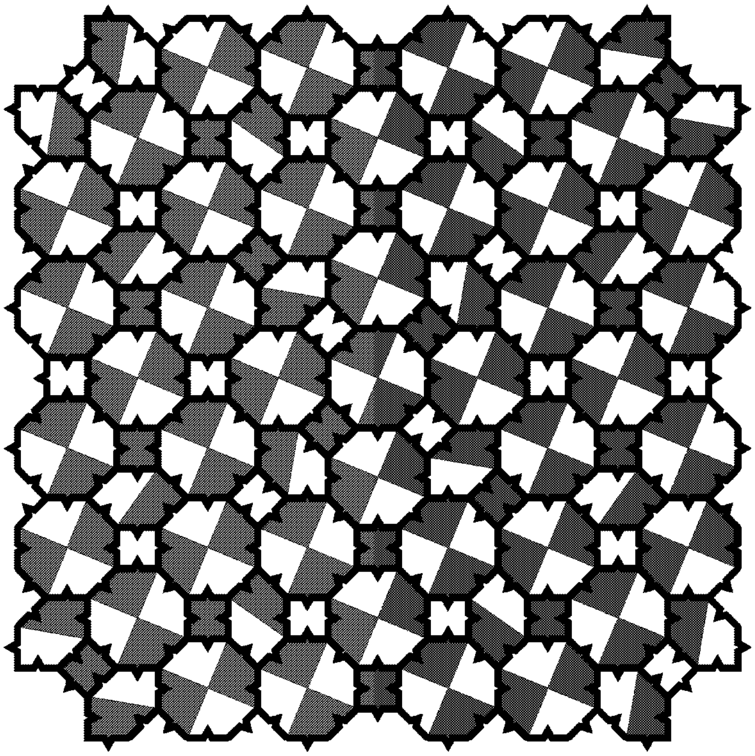

Fig. 3. A portion of the octagonal tiling with 3-connected sites obtained with the aid of the inflation rules. One can see the transition to the lattices consisting of tetragons topologically equivalent to a square net.

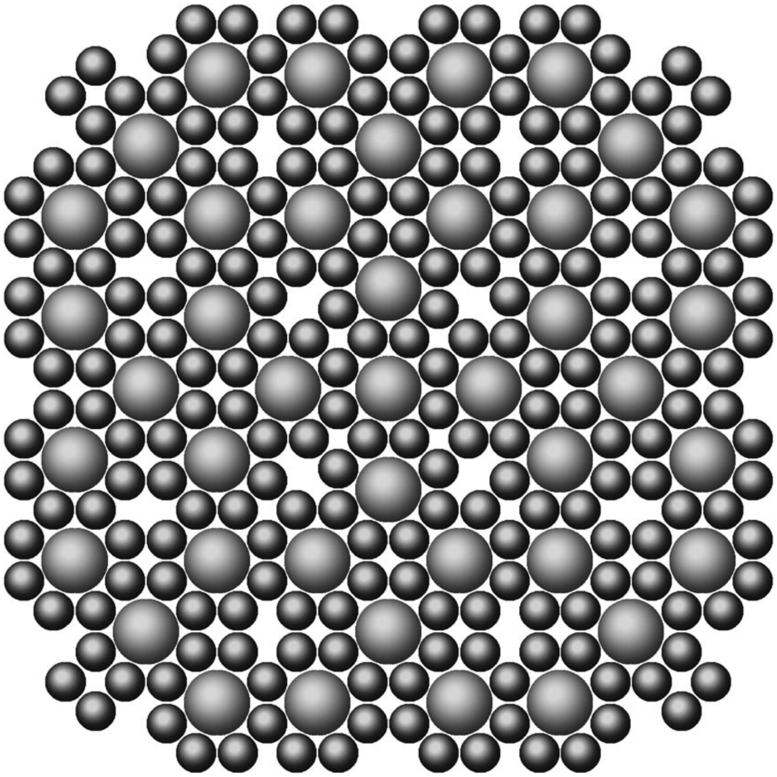

Fig. 4. A plane octagonal quasicrystal obtained with the aid of atomic decoration of the tiling shown in Fig. 3.

jected onto the sites of a primitive lattice of the same dimensionality, with the lattice type and the projective method being determined by the local order in the given structure. In what follows, the projective method and a lattice with the atoms thus projected are referred to as a lattice model. In this section, we introduce the lattice model for a class of icosahedral quasicrystals and their periodic approximants characterized by the same icosahedral–dodecahedral local order (IDLO) in the arrangement of atoms.

The nearest neighbors of each atom in an ideal structure with the IDLO are located at the distances r_3, r_5, and r_2 ($r_3 < r_5 < r_2$) along the three-, five-, and twofold symmetry axes of an icosahedron. In this case, the connectivity of the structure with the IDLO is attained only with the aid of the r_3 and r_5 vectors. In other words, one may construct a chain of atoms between any two atoms of the structure in such a way that the distance between two neighbors in the chain would be determined either by a vector of the r_3 or the r_5 type. The only exceptions seem to be two simplest structures—bcc and diamond ones. The IDLO is never rigorously obeyed in crystals, and yet, for a number of reasons, the IDLO may be used as an idealized description of a really existing mutual arrangement of atoms in a number of substances. Possible interatomic bonds in a structure are determined by a set of 62 vectors of approximately equal lengths ($r_2/r_3 = 2/\sqrt{3}$) that can be used to approximate the real interatomic distances in many real structures. However, the icosahedral symmetry of this set of vectors makes the use of IDLO especially convenient for the description of the structures of icosahedral quasicrystals and their periodic approximants [14, 15].

It should be noted that the connectivity of the structure with the IDLO may also be attained by using the vectors of only one type, r_3 or r_5. In the first case, we arrive at the dodecahedral local order (DLO) and, in the second case, the icosahedral local order (ILO). The DLO is encountered in some simple crystals, i.e., in bcc and diamond lattices, crystals of the FeSi type, etc. The ILO in its pure form is encountered in three-dimensional Penrose tilings [16] and also in a cubic $Al_{12}Mn$ crystal. There are grounds to believe that real icosahedral quasicrystals and their higher-order crystal approximants are connected DLO structures with a small number of additional atoms in the positions of the so-called icosahedral holes related to their nearest environment by vectors of the r_5 type [14, 15].

In conventional length units ($r_2/2 \equiv 1$), 20 r_3 vectors have the form $(\pm1, \pm1, \pm1)$ or $(\pm\tau, 0, \pm1/\tau)\circlearrowright$; 12 r_5 vectors, the form $(\pm\tau, \pm1, 0)\circlearrowright$; and 30 r_2 vectors, the form $(\pm2, 0, 0)\circlearrowright$ or $(\pm\tau, \pm1/\tau, \pm1)\circlearrowright$, where the plus or minus signs are selected independently for each coordinate and the sign $\circlearrowright$ indicates the allowed cyclic permutations. Here $\tau = (\sqrt{5} + 1)/2$ is the golden mean. Thus, the distance between any two A and B atoms in the IDLO structure is represented by the vector

$$\mathbf{r}_{AB} = (n_x\tau + m_x, n_y\tau + m_y, n_z\tau + m_z), \tag{1}$$

where n_i and m_i are integers.

Now, introduce the lattice model for IDLO structures by making the change

$$\tau \longrightarrow 1. \tag{2}$$

Then, the vector $\mathbf{r}_{AB}$ is transformed into the vector $\mathbf{r}^*_{AB}$ with the integral coordinates

$$\mathbf{r}^*_{AB} = (n_x + m_x, n_y + m_y, n_z + m_z), \tag{3}$$

In other words, we perform projection onto a primitive cubic lattice. It is interesting to follow how the 62 vectors that describe the positions of the neighboring atoms are changed after this operation: the vectors r_3 are transformed into the $(\pm1, \pm1, \pm1)$ and $(\pm1, 0, 0)\circlearrowright$ vectors, the vectors r_5, into the $(\pm1, \pm1, 0)\circlearrowright$ vectors, and the vectors r_2, into the $(\pm2, 0, 0)\circlearrowright$ and $(\pm1, 0, \pm1)\circlearrowright$ vectors. Here, we used the ratio $1/\tau = \tau - 1$ valid for the golden mean. It is seen that the atoms of the initial IDLO structure spaced from one another by the distances r_5 and r_2 are projected onto the same fcc sublattice of the primitive cubic lattice, whereas the atoms spaced by the distance r_3, are projected onto the different fcc sublattices. This fact will be used in the discussion of the structures of real icosahedral quasicrystals in the system aluminum–transition metal.

Generally speaking, calling the transition from $\mathbf{r}_{AB}$ to $\mathbf{r}^*_{AB}$ a projecting, we implicitly assume the use of a certain multidimensional formalism. Indeed, $\mathbf{r}_{AB}$ and $\mathbf{r}^*_{AB}$ can be considered as the projections of a six-dimensional vector, $\mathbf{N} = (n_x, n_y, n_z, m_x, m_y, m_z)$, onto various three-dimensional subspaces.

Now, consider possible constraints that may be imposed onto the lattice model under study. Obviously, the transition from $\mathbf{r}_{AB}$ to $\mathbf{r}^*_{AB}$ is not a mutually unique transformation: each of the vectors of type (3) is the projection of an infinite number of vectors of type (1). Generally speaking, two IDLO vectors, $\mathbf{r}_1$ and $\mathbf{r}_2$, are projected onto the same site of a primitive cubic lattice then, and only then, if their difference has the form $\mathbf{r}_1 - \mathbf{r}_2 = (1/\tau)(k_x, k_y, k_z)$, with k_i being integers. Therefore, the condition for the applicability of the given model seems to be the absence of interatomic distances of the $(1/\tau)(k_x, k_y, k_z)$ type in an IDLO structure. This condition is not fulfilled, e.g., for a three-dimensional Penrose tiling in which the short diagonal of a oblate rhombohedron may have the form $(1/\tau, 1/\tau, 1/\tau)$; whence it follows that, being projected, the vertices located at the ends of the given diagonal will merge into one point. However, the length of this diagonal, r_3/τ, is considerably shorter than the main distance, r_5, between the sites of this structure. Thus, the condition of the applicability of the suggested lattice model to one or another

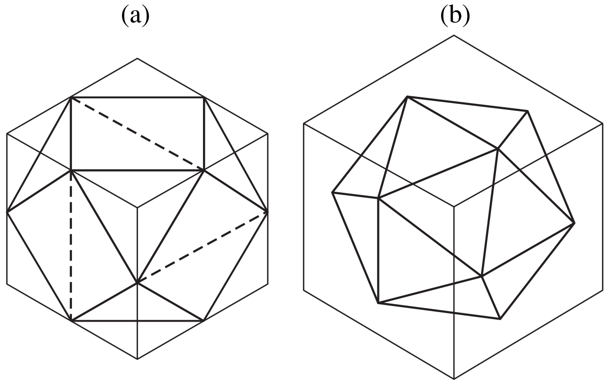

Fig. 5. Transformation of the (a) local environment of an atom in the fcc structure into (b) an icosahedron. Interatomic bonds indicated by solid lines have the same lengths. The icosahedron is inscribed in a cube. The cube edges depicted on the left and on the right are related as $\sqrt{2}/\tau$. The dashed lines indicate the interatomic bonds restored in the transition to an icosahedron.

IDLO structure may coincide with the purely physical requirement of the absence of interatomic distances in this structure that are too short.

As was shown above, the $(\pm 2, 0, 0)\circlearrowright$ vectors directed along the twofold axes of an icosahedron remain intact when projecting the IDLO structure onto a primitive cubic lattice. On the one hand, the $(\pm 2, 0, 0)\circlearrowright$ vectors differ from the other r_2 vectors, since they are located along the coordinate axes of the cubic lattice onto which projecting is made. However, on the other hand, the selection of only 3 from the total 15 twofold axes of an icosahedron is quite arbitrary and depends only on the initial choice of the coordinate system. Altogether, there are five possible sets of three twofold axes normal to one another that are related by the symmetry elements of the symmetry group of an icosahedron. Each of these sets has its own coordinate system for the IDLO structure and, therefore, also its own cubic lattice onto which the projecting can be made. If the IDLO structure is an icosahedral quasicrystal, then it is unimportant which of the five cubic lattices is used for projecting, because the symmetry of the initial structure makes all the projections equivalent. However, if the initial structure is a periodic approximant, then the projections onto different cubic lattices are different. In what follows, this property is used to consider certain well-known crystals with IDLO.

The application of the above lattice model to real IDLO crystals is illustrated by several simple examples.

APPLICATION OF THE LATTICE MODEL TO WELL-KNOWN CRYSTALS WITH IDLO

Cubic $Al_{12}M$ crystal has a bcc lattice. Two manganese atoms occupy the vertex and the center of the cubic unit cell and are surrounded with the aluminum icosahedra. The $Al_{12}Mn$ structure is an example of icosahedral local order and, as was shown above, the absence of r_3 bonds results in the fact that all the atoms are projected onto the same fcc sublattice of a primitive cubic lattice. The 12 aluminum atoms surrounding each manganese atom are projected onto the local environment of the site of the fcc lattice (cuboctahedron), also consisting, as is well known, of 12 atoms (Fig. 5). As was indicated above, the application of the lattice model described by Eq. (2) to a periodic structure depends on the choice of the cubic lattice onto which the projecting is made. Let us consider it using the example of $Al_{12}Mn$.

The length of the edge of the cubic unit cell in the selected conventional units is $2\tau^2$. If the coordinate system of the lattice onto which the structure is projected coincides with the initial coordinate system of the cubic crystal, the crystal periods $(2\tau^2, 0, 0)\circlearrowright$ are transformed into the periods $(4, 0, 0)\circlearrowright$ of the lattice. A cube with an edge length of 4 has 32 sites in one fcc sublattice, whereas the unit cell of an $Al_{12}Mn$ crystal contains only 26 atoms. Thus, the projection considered is an fcc lattice with a large number of defects—there is only one manganese atom and three vacancies per 12 aluminum atoms. The result would be different if we were projecting onto another cubic lattice. Thus, it is possible to select the coordinate system in which the edges of the cubic unit cell of an $Al_{12}Mn$ crystal are represented by the vectors $(\tau^3, -\tau, \tau^2)\circlearrowright$. They are projected onto the periods $(3, -1, 2)\circlearrowright$ of the cubic lattice (we used here the relations $\tau^3 = 2\tau + 1$ and $\tau^2 = \tau + 1$). The volume of a rhombohedron built on these periods equals 52; in other words, this rhombohedron has exactly 26 sites in one fcc sublattice.

Thus, the second method of projecting gives an fcc containing no vacancies, i.e., all its sites are occupied by aluminum and manganese atoms. This allows us to consider an $Al_{12}Mn$ crystal as a result of the local deformation of an ideal fcc aluminum lattice accompanied by the replacement of some sites by manganese impurity. Indeed, the replacement of an aluminum atom in one of the sites of the fcc lattice by a manganese atom results in the distortion of the nearest environment of this site. Since the Al–Mn bond length is somewhat less than the Al–Al bond length, the 12 aluminum atoms surrounding the site strive to approach the central manganese atom, which is hindered by bonds existing between the aluminum atoms, whose lengths should remain constant. Nevertheless, deformation without changing the Al–Al bonds is also possible, unless each of the aluminum atoms would acquire an additional bond (Fig. 5). In the latter case, the 12 aluminum atoms form an icosahedron with the manganese atom in the center.

The distortion of the local environment of impurity atoms and formation of icosahedral $Al_{12}Mn$ clusters result in the deformation of the whole structure. In this case, some Al–Al bonds formed by aluminum atoms from different clusters are broken, but most of the

Ideal DLO structures of the crystalline AlPd phases

Sp. gr., lattice parameters	Lattice periods	Position multiplicity and atomic species	Atomic coordinates of the IDLO structure
$Pm\bar{3}m$ ($B2$), $a = r_2$	$(2, 0, 0)\circlearrowright$	1(Al)	(0, 0, 0)
		1(Pd)	(1/2, 1/2, 1/2)
$P2_13$ ($B20$), $a = \tau r_2$	$(2\tau, 0, 0)\circlearrowright$	4(Al)	$(\tau^{-1}/4, \tau^{-1}/4, \tau^{-1}/4)$
		4(Pd)	$(1 - \tau^{-1}/4, 1 - \tau^{-1}/4, 1 - \tau^{-1}/4)$
$R\bar{3}$ (26 atoms), $a = \tau\sqrt{2+\tau}\, r_2$, $\cos\alpha = -1/\sqrt{5}$	$(\tau^2, -\tau^3, \tau + 2)\circlearrowright$	1(Al)	(0, 0, 0)
		1(Pd)	(1/2, 1/2, 1/2)
		6(Al)	$(1 - \tau^{-1}/4, 1/2 + \tau^{-2}/4, 1/2 + \tau^{-3}/4)$
		6(Pd)	$(1/2 - \tau^{-1}/4, \tau^{-2}/4, \tau^{-3}/4)$
		6(Al)	$(1/2 + \tau^{-1}/4, \tau^{-2}/4, 1/4)$
		6(Pd)	$(\tau^{-1}/4, 1/2 + \tau^{-2}/4, 3/4)$

Note: Crystal periods are given in arbitrary length units ($r_2/2 \equiv 1$).

bonds remain unchanged, which allows us to state that the deformation has a local character. In order to obtain the sought structure of $Al_{12}Mn$ crystal, manganese atoms should occupy the sites of the rhombohedral sublattice with the periods $(3, 0, -1)\circlearrowright$ (as earlier, the period of the fcc lattice is assumed to be equal to two).

It is striking that two cubic structures (fcc aluminum crystal and bcc $Al_{12}Mn$ crystal) have only one common threefold axis. This signifies that the lattice transformation considered above cannot be described within the framework of the conventional theory of phase transformations, because, in the process of this transition, the cubic symmetry is first lost and, then, restored again, with the intermediate phase having the rhombohedral symmetry.

Transitions between AlPd crystalline phases. In the Al–Pd system, three crystalline phases are revealed in the vicinity of the point of equal concentrations of aluminum and palladium atoms. These phases may be described by the dodecahedral local order—these are the cubic phases with the $B2$ and $B20$ structures (sp. gr. $Pm\bar{3}m$ and $P2_13$, respectively) and the rhombohedral structure (sp. gr. $R\bar{3}$ with 26 atoms per unit cell) [17]. The table gives the description of the ideal DLO structures of these crystals. It has been shown [18] that the ideal atomic positions determined by the DLO approximation are rather close to the experimental positions. All the three crystals have similar structural characteristics. First, aluminum and palladium atoms in the structure alternate: each aluminum atom is surrounded by palladium atoms and vice versa. Second, the aluminum and palladium sublattices in each crystal are related by a certain symmetry transformation. Making no distinctions between the atomic species, we increase the structure symmetry—the $Pm\bar{3}m$ space group is transformed into $Im\bar{3}m$; the $P2_13$ space group, into $Pa\bar{3}$; and the $R\bar{3}$ space group, into $R\bar{3}$, with a corresponding double decrease in the unit-cell volume [19, 20]. Later, we shall show that the three AlPd phases can transform into one another via the local structural transformations, with the transition between the $B2$ and $B20$ structures being simply described within the lattice model given by Eq. (2).

Writing the atomic coordinates of the $B2$ structure in the selected coordinate system natural for a cubic crystal, we avoid the use of τ (see table) and, therefore, in this case, the lattice model coincides with the structure. However, it is interesting to consider this crystal in a rotated coordinate system in which the edges of the cubic unit cell are set by the vectors $(\tau, -1/\tau, 1)\circlearrowright$. These vectors are projected to form the periods $(1, 0, 1)\circlearrowright$ of a simple cubic lattice. A rhombohedron built on these periods has a volume equal to two, which corresponds to the number of atoms in the cubic unit cell of the $B2$ structure. Thus, it is shown that the $B2$ structure may be "densely" projected onto a primitive cubic lattice without any vacancies. With due regard made for the atomic species, the space group of the projection is $Fm\bar{3}m$. Figure 6 shows (a) a cubic unit cell of the $B2$ structure and (b) a rhombohedron representing its projection onto the cubic lattice. It should be emphasized that, although both structures (initial structure $B2$ and its projection) possess the cubic symmetry, they have only one common threefold symmetry axis.

Lattice model (2), being applied to the $B20$ structure, transforms the periods $(2\tau, 0, 0)\circlearrowright$ of this crystal into the periods $(2, 0, 0)\circlearrowright$ of a primitive cubic lattice. A cube with such edges has a volume equal to eight, which corresponds to the number of atoms in the unit cell of the $B20$ structure. Thus, the $B20$ and $B2$ structures may be densely projected onto a primitive cubic lattice. With due regard made for the fact that the lattice model may be considered as the local distortion of a

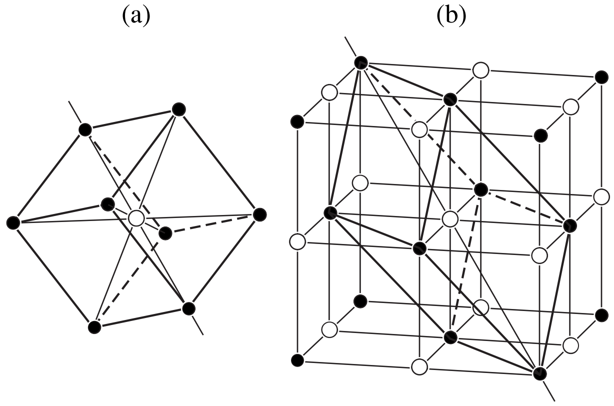

Fig. 6. (a) Cubic unit cell of the *B*2 structure and (b) its projection onto the fcc lattice. The common threefold symmetry axis is shown.

crystal, we can state that the *B*2 and *B*20 phases of an AlPd crystal may be related by a phase transition accompanied by the local deformation of the structure. In this case, the two cubic phases have only one common threefold axis; in other words, this transition would occur via the formation of a certain intermediate phase having rhombohedral symmetry.

A rhombohedral AlPd crystal has the same structural feature as the *B*2 phase—the atoms form similar chains of alternating aluminum and palladium atoms along the threefold axis. The similar and distinguishing features of these two phases can readily be illustrated by the projections of the crystal onto the plane normal to the threefold axis (Fig. 7). It is seen that the transition to the rhombohedral phase is associated with the displacement of the projections of atoms from the sites of the ideal triangular lattice onto which the *B*2 structure is projected. Also, the atomic chains show relative displacements along the direction normal to this plane. Some atomic bonds (not more than one per atom) are broken. The periods $(\tau^2, -\tau^3, \tau + 2)\circlearrowright$ of the rhombohedral crystal have corresponding periods $(2, -4, 4)\circlearrowright$ in the *B*2 structure. At the same time, the lattice model described by (2) transforms the period $(\tau^2, -\tau^3, \tau + 2)$ into the vector $(2, -3, 3)$ (here, the equations $\tau^2 = \tau + 1$ and $\tau^3 = 2\tau + 1$ were used). Thus, it is seen that the transition from the rhombohedral AlPd crystal to crystals with the *B*2 structure cannot be described within the framework of the suggested lattice model. This seems to be explained by the fact that, in the course of this transition, some bond angles are considerably distorted.

Thus, it was shown that all the three phases of an AlPd crystal are related and that, in principle, the phase transitions are possible between these phases.

Icosahedral quasicrystals in the system aluminum–transition metal. Most of the known quasicrystals were discovered in aluminum alloys with transition metals (TMs). Among them is the first icosahedral quasicrystal, $Al_{86}Mn_{14}$, discovered in 1984 [1]. Therefore, the application of the suggested lattice model to these systems is of great interest. The experimental data show that there is a characteristic bond-length ratio, which is also confirmed by the *ab initio* pair interaction potentials [21, 22]: the Al–TM bond lengths are slightly

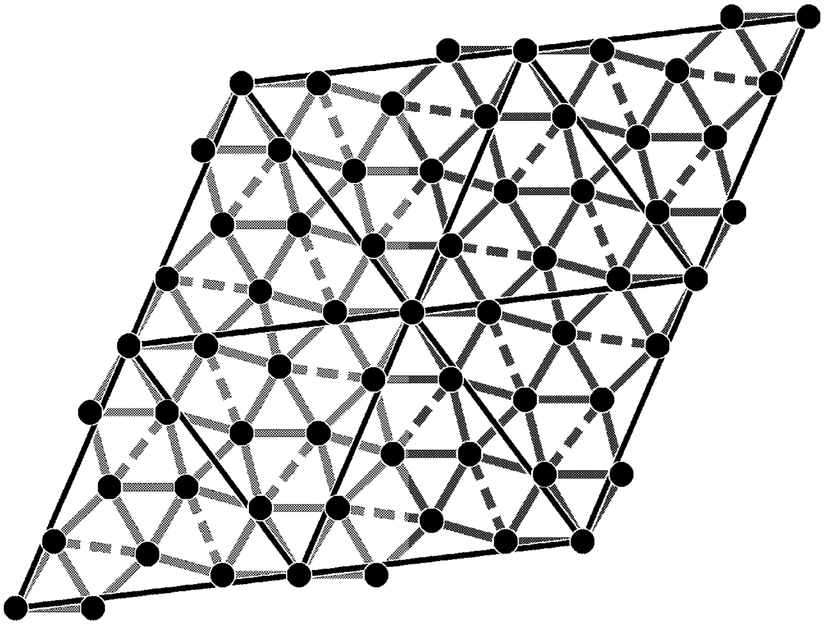

Fig. 7. The structure of the rhombohedral AlPd structure projected onto the plane normal to the threefold axis of the crystal. The circles indicate the chains of atoms along the threefold axis. Thin lines show the projections of the unit-cell edges (periods), the solid lines, the projections of the interatomic bonds. Dashed lines indicate the bonds absent in the orthorhombic phase which were restored during the transition to the *B*2 structure.

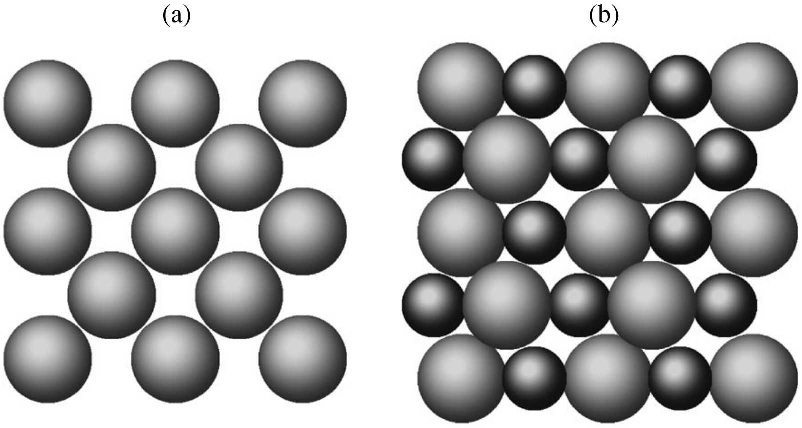

Fig. 8. Comparison of the atomic layers normal to the [100] axis in (a) the fcc structure of elemental aluminum and (b) in cubic AlPd with the *B*20 structure. It is seen that the fcc structure of elemental aluminum can be considered a result of the local deformations of the cubic AlPd structure because of the filling of the atomic voids with palladium atoms.

shorter than the TM–TM and Al–Al bond lengths. Thus, it has been shown [21] that the main minimum values of the pair Al-TM potentials are about 2.34 Å for Al–TM, 2.55 Å for TM–TM, and 2.74 Å for Al–Al bond lengths. The ratio of these bond lengths equals $l_{\mathrm{Al-TM}} : l_{\mathrm{TM-TM}} : l_{\mathrm{Al-Al}} = 1 : 1.09 : 1.17$. At the same time, the ratio of the distances in the IDLO structures is $r_3 : r_5 : r_2 = 1 : 1.10 : 1.15$. It is seen that $l_{\mathrm{Al-TM}}/l_{\mathrm{Al-Al}} \sim r_3/r_2$. Thus, it is possible to assume that, if the alloy in the Al–Tm system is characterized by the structure with IDLO, then the Al–TM bonds correspond to the vectors r_3 and r_5; to the TM–TM bonds, the vectors r_3, r_5, and r_2; and to the Al–Al bonds, the vectors r_5 and r_2. Obviously, this assumption is true for the $Al_{12}Mn$ and AlPd crystals considered above. However, as was shown earlier, the application of the lattice model to the IDLO structure results in the fact that the atoms spaced by the distances r_5 and r_2 are projected onto one fcc sublattice of a primitive cubic lattice. Thus, within the lattice model of the alloy in the Al–TM system, aluminum atoms would occupy the sites of one fcc sublattice, whereas the transition metal atoms may be located at the sites of different fcc sublattices. This allows one to put forward the hypothesis that icosahedral quasicrystals in aluminum alloys with transition metals and their periodic approximants may be considered as having structures obtained by distortion of an ideal fcc aluminum lattice due to incorporation of transition metal impurity. In this case, impurity atoms can replace the aluminum atoms (as in $Al_{12}Mn$) or be incorporated into the vacancies of another sublattice dual to the fcc lattice (as in AlPd). Figure 8 shows the changes in the atomic layer normal to the [100] axis with the transition from elemental aluminum to the *B*20 phase of the AlPd alloy. Each aluminum atom in the initial fcc lattice is related to 12 other aluminum atoms, whereas, in the *B*20 structure, each aluminum atom has only 6 neighboring aluminum atoms. Nevertheless, any two aluminum atoms in an AlPd crystal can be bound by a chain consisting of aluminum atoms alone, i.e., the connectivity of the structure with respect to aluminum is preserved. In quasicrystals, where the relative aluminum concentration is higher, the connectivity of the structure with respect to aluminum atoms should be more pronounced.

CONCLUSIONS

A simple lattice model of icosahedral quasicrystals with the icosahedra–dodecahedral local order and their periodic approximants is suggested. The model allows one to describe the structures of such substances by setting the function of the displacements of the sites of a simple cubic structure. It should be noted that the transformation inverse to lattice model (2) is somewhat ambiguous, because the integral coordinate n related to the cubic lattice is transformed into the coordinate $(n - m) + m\tau$ of the IDLO structure with the integer m that can take various values. This ambiguity allows one to describe a large number of structures by the same method.

On the other hand, if two different structures are described by the same lattice model, this model can be used as a criterion determining the possibility of the occurrence of the phase transition between these structures, as was demonstrated using the example of the *B*2 and *B*20 phases of an AlPd crystal. In particular, this criterion seems to be also applicable to the description of a possible crystal–quasicrystal phase transition widely discussed in the literature.

ACKNOWLEDGMENTS

The author is grateful to V.E. Dmitrienko, M. Kléman, S.B. Roshal, and S.B. Astaf'ev for fruitful discussions. The study was supported by the Russian Foundation for Basic Research (project no. 02-02-16275a), the Centre National de la Recherche Scientifique, France

(CNRS–RAS agreement nos. 4058 and 16377), and the Russian Science Support Foundation.

REFERENCES

1. D. Shechtman, I. Blech, D. Gratias, *et al.*, Phys. Rev. Lett. **53**, 1951 (1984).
2. C. L. Henley, Comments Condens. Matter Phys. **13**, 59 (1987).
3. C. Janot, *Quasicrystals—A Primer* (Clarendon Press, Oxford, 1997).
4. T. Janssen, Acta Crystallogr., Sect. A: Found. Crystallogr. **42**, 261 (1986).
5. P. Bak, Phys. Rev. Lett. **56**, 861 (1986).
6. H. Kawamura, Prog. Theor. Phys. **70**, 352 (1983).
7. P. Stampfli, Helv. Phys. Acta **59**, 1260 (1986).
8. M. Oxborrow and C. L. Henley, Phys. Rev. B **48**, 6966 (1993).
9. S. B. Roshal and I. V. Lebedyuk, Kristallografiya **45** (3), 518 (2000) [Crystallogr. Rep. **45**, 473 (2000)].
10. W. Steurer and T. Haibach, Acta Crystallogr., Sect. A: Found. Crystallogr. **55**, 48 (1999).
11. V. A. Chizhikov, Kristallografiya **47** (6), 967 (2002) [Crystallogr. Rep. **47**, 897 (2002)].
12. F. P. M. Beenker, Technical Report 82-WSK-04 (Eindhoven Univ., 1982).
13. R. Ammann, B. Grunbaum, and G. C. Shephard, Discrete Comput. Geom. **8**, 1 (1992).
14. V. E. Dmitrienko, Acta Crystallogr., Sect. A: Found. Crystallogr. **50**, 515 (1994).
15. V. E. Dmitrienko, Mater. Sci. Forum **150–151**, 199 (1994).
16. P. Kramer and R. Neri, Acta Crystallogr., Sect. A: Found. Crystallogr. **40**, 580 (1984).
17. T. Matkovic and K. Schubert, J. Less-Common Met. **55**, 45 (1977).
18. V. E. Dmitrienko, in *Proceedings of Workshop on Aperiodic Structures* (Krakow, 1996), p. 28.
19. V. A. Chizhikov, Kristallografiya **44** (6), 1094 (1999) [Crystallogr. Rep. **44**, 1024 (1999)].
20. V. A. Chizhikov, Kristallografiya **45** (1), 128 (2000) [Crystallogr. Rep. **45**, 122 (2000)].
21. T. Tei-Ohkawa, K. Edagawa, and S. Takeuchi, J. Non-Cryst. Solids **189**, 25 (1995).
22. M. Mihalkovic, I. Al-Lehyani, E. Cockayne, *et al.*, Phys. Rev. B **65**, 104205 (2002).

Translated by L. Man

Crystallography Reports, Vol. 49, No. 4, 2004, pp. 547–552. Translated from Kristallografiya, Vol. 49, No. 4, 2004, pp. 621–627.
Original Russian Text Copyright © 2004 by Dmitrienko, Chizhikov, Astaf'ev, Kléman.

THEORY OF CRYSTAL STRUCTURES

Intensity and Width of Bragg Reflections from Imperfect Icosahedral Quasicrystals Obtained by Simulating Atomic Growth

V. E. Dmitrienko*, V. A. Chizhikov*, S. B. Astaf'ev*, and M. Kléman**
** Shubnikov Institute of Crystallography, Russian Academy of Sciences,*
Leninskiĭ pr. 59, Moscow, 119333 Russia
e-mail: dmitrien@ns.crys.ras.ru
*** Laboratoire de Mineéralogie–Cristallographie, Universités Paris VI et Paris VII, 4 Place Jussieu,*
Paris Cedex 05, 75252 France

Received December 29, 2003

Abstract—The Bragg reflections from icosahedral quasicrystals obtained in the course of a computer experiment on the simulation of crystal growth have been studied. The computer experiments based on the theory developed earlier allow one to "grow" in a computer the imperfect quasicrystals of nanometer dimensions. It is shown that the absolute value of the structure factor can be close to the maximum possible one for crystals, i.e., to the structure factor in the case where all the atoms scatter in phase. The spectral width of Bragg reflections is studied, and it is shown that the reflection width depends not only on the quasicrystal dimensions in the physical space but, also, on the perpendicular component of the reciprocal-lattice vectors. The data obtained are compared with the known experimental data. *© 2004 MAIK "Nauka/Interperiodica".*

INTRODUCTION

Usually, the formation of Bragg reflections is associated with the long range order, i.e., with crystal periodicity. In turn, the periodicity imposes severe restrictions onto the crystal symmetry. In particular, the periodicity in a three-dimensional space is incompatible with the icosahedral symmetry. Therefore, immediately after the discovery of icosahedral quasicrystals in metal alloys that yielded diffraction patterns with sharp maxima and, at the same time, possessing the icosahedral symmetry [1], the question arose whether aperiodic structures can give rise to the formation of Bragg peaks described by δ functions. The answer turned out to be positive, although, in the general case, the scattering patterns from aperiodic structures were rather unusual and became the subject of intense study.

In terms of mathematics, the construction of an aperiodic function in a space meets no difficulties. It is sufficient to use the sum of the harmonic functions with the number D of *linearly independent* wave vectors exceeding the space dimensionality d. Mathematicians have studied these almost periodic and quasi-periodic functions for quite a long time [2] and shown that the quasi-periodic functions (i.e., the functions with finite D) could be considered *irrational* sections of D–dimensional *periodic* functions. This property is very useful for description of modulated structures and computation of their diffraction patterns [3]. The interest in the noncrystallographic symmetry considerably increased after Penrose publication in which he showed that it was possible to tile the space with pairs of specially selected figures only aperiodically. The point symmetry of such a *Penrose tiling* turned out to be decagonal, which cannot be realized in crystals [4, 5]. One of the first studies of Penrose tilings in crystallography and computations of the corresponding diffraction patterns had been made by Mackay prior to the discovery of real quasicrystals [6].

Strictly speaking, quasicrystals are structures in which aperiodicity is a consequence of a noncrystallographic point symmetry. In addition to three-dimensional icosahedral quasicrystals, octagonal [7], decagonal [8], and dodecagonal [9] quasicrystals were found in which quasiperiodicity was observed in two dimensions, whereas, along the third dimension, these quasicrystals were periodic. The respective point symmetry groups contain eight-, ten-, and twelvefold rotation or screw symmetry axes.

The atomic structure of ideal quasicrystals with icosahedral symmetry can be determined using a special projection of a six-dimensional (D = 6) cubic lattice onto a three-dimensional physical space [10], with the Bragg peaks from such a structure being described by δ functions. Another approach to the description of quasicrystal structures is based on the principles of generalized symmetry [11, 12]. However, the real quasicrystals have much more complicated structures: they differ from the ideal ones by the presence of specific phason defects. The latter defects manifest themselves in the diffraction patterns as reflection broadening and displacements. Unlike the phonon deformations inherent in crystals, the broadening and displacements of reflections are dependent, not on the reciprocal-lattice vectors in the physical space, but on the components of these vectors in the perpendicular space.

Below, we consider the effect of phason defects on the diffraction patterns from quasicrystals using the microscopic approach based on simulation of growth of icosahedral quasicrystals and direct computation of their spatial Fourier harmonics, i.e., diffraction reflections. This mode of growth is physically well justified and, therefore, we hope that phason point defects arising in this model are close to those formed in real quasicrystals. On the other hand, *a priori*, this model contains no dislocations and phonon-induced deformations that may distort the respective diffraction patterns.

SIMULATION OF QUASICRYSTAL GROWTH

In order to compute the diffraction spectrum, we must know the positions of all the atoms, because it is impossible to select a unit cell in quasicrystals. We considered a rather large quasicrystal (containing slightly more than 10^7 atoms) grown in the course of a computer experiment on growth simulation. Despite the complexity and aperiodicity of the structures of icosahedral crystals, the model of their growth should be sufficiently simple to be used to describe growth at a rather high rate and rapid cooling (up to 10^6 deg/S). At the same time, this model should be universal, because quasicrystals are observed in numerous metal alloys. The latter signifies that the model should not be too sensitive to the choice of the atomic-interaction potential.

Two major assumptions justified in terms of physics [13, 14] underlie our model.

1. It is assumed that the short range order of atoms in quasicrystals and their crystalline approximants are described by the dodecahedral and icosahedral local order (DLO and ILO, respectively). In other words, the nearest neighbors of each atom are located at distances r_3, r_5, and r_2 from this atom along the three-, five-, and twofold axes, respectively. Some additional geometrical justification of DLO can be found in [14], whereas the argument in favor of ILO is its high density. Since the periodic approximants of quasicrystals are characterized by the same type of order, the use of this approximation alone is insufficient. One must exclude (with the aid of a certain physical mechanism) possible growth of these approximants.

2. Earlier, we suggested using the oscillations of the dependence of the atomic-interaction potential on distance (the so-called Friedel oscillations) as a mechanism for suppression of growth of simple crystal structures. The point is that the quasicrystals and approximants are described by different radial distribution functions of atoms, which is especially clearly seen for the second coordination sphere [15]. Because of the screening effect of the conduction electrons, the interaction potential between ions in metals acts within a rather short distance, so that its effect is taken into account at distances of an order of two interatomic distances, i.e., at about $1.8r_2$. It is important that the conduction electrons form a quantum system and, therefore, screening has oscillations depending on the distance whose period is inversely proportional to the Fermi momentum and, thus, depends on the electron concentration. As a result, within some distances, the interaction potential is positive, so these distances become energetically disadvantageous and should be suppressed during growth. In this study, we applied the model potential used earlier in [15]. The potential oscillations were selected in such a way as to make more advantageous the distances τr_5 and τr_2—inherent in the quasicrystal and related to the so-called Mackay shell—and to suppress the distances typical of crystals in the space between the first coordination sphere and the Mackay shell and immediately beyond this shell.

Once the local order and atomic-interaction potential are selected, the growth process may be simulated in different ways. In order to grow a crystal of the maximum possible size, we used the simple Eden model and the following algorithm.

1. A small seed (consisting of less than 100 atoms) is constructed as a piece of an ideal quasicrystal with DLO–ILO having an almost spherical shape.

2. In accordance with DLO–ILO, all the possible new atomic positions (the so-called "waiting positions") are calculated.

3. In accordance with the selected potential, the binding energies of all the waiting positions are calculated.

4. Then, a new atom is added to the waiting position with the minimum energy, and the procedure is repeated beginning with step 2.

Thus, unlike in the Monte Carlo method, new atoms can be added to the model but cannot be subtracted from it, which allows one to grow large quasicrystals for a reasonably short computational time.

MILLER INDICES OF RECIPROCAL-LATTICE VECTORS OF AN ICOSAHEDRAL QUASICRYSTAL

It is well known that the position of each reflection of the diffraction pattern from any three-dimensional periodic crystal is determined by three Miller indices, which are the coefficients of the decomposition of the reciprocal-lattice vector corresponding to the chosen reflection along the three basis vectors. The diffraction pattern from an icosahedral quasicrystal can be described mainly by the same method; however, in this case, the reciprocal-lattice basis consists of six vectors so that one has to use six, and not three, Miller indices. The reciprocal-lattice basis of an icosahedral quasicrystal is usually selected as 6 vectors directed along the fivefold axes and setting 6 of the total 12 vertices of an icosahedron. The positions of the icosahedron vertices are written in the most convenient form, with the axes of the Cartesian coordinate system being directed along the twofold axes of the icosahedron. In such a setting, the icosahedron vertices are determined by the vectors $(\pm\tau, 0, \pm1)$ in the arbitrary length units. Here $\tau = (\sqrt{5} + 1)/2$ is the golden mean, the plus and minus signs are selected independently for each coordinate, and all the cyclic permutations are admissible. With due regard for the fact that fivefold axes can be indicated in an arbitrary order and that two vertices lie on each of these axes on both sides of the icosahedron center, the reciprocal-lattice basis may be chosen by $6! \cdot 2^6 = 46080$ ways, with the Miller indices being dependent on this choice. We used the following reciprocal-lattice basis:

$$\begin{aligned} \mathbf{Q}_1 &= (q_2/2)(1, \tau, 0), & \mathbf{Q}_2 &= (q_2/2)(1, -\tau, 0), \\ \mathbf{Q}_3 &= (q_2/2)(0, 1, \tau), & \mathbf{Q}_4 &= (q_2/2)(0, 1, -\tau), \\ \mathbf{Q}_5 &= (q_2/2)(\tau, 0, 1), & \mathbf{Q}_6 &= (q_2/2)(-\tau, 0, 1). \end{aligned} \tag{1}$$

Here, q_2 is the length of one of the reciprocal-lattice vectors lying on a twofold axis [the extreme left peak in Fig. 1b; the Miller indices are (110 000)] and $q_2 = 2\pi\tau^3/(a_R\sqrt{1+\tau^2})$, where $a_R = \tau r_5$ is the parameter of the quasi-lattice. The reciprocal-lattice vector thus chosen can be represented as

$$\mathbf{Q}_{\parallel}(\mathbf{H}) = \sum_{i=1}^{6} h_i \mathbf{Q}_i. \tag{2}$$

Here, $\mathbf{H} = (h_1h_2h_3h_4h_5h_6)$, where h_1–h_6 are the Miller indices and the sign $\parallel$ indicates the $\mathbf{Q}_{\parallel}$ vector is the projection of the six-dimensional vector **H** onto the three-dimensional space of the reciprocal lattice, hereafter called the parallel space.

It is also useful to consider the projection of the vector **H** onto the three-dimensional subspace orthogonal to the parallel subspace of the reciprocal lattice. This additional subspace is termed the perpendicular space of the reciprocal lattice. An arbitrary vector of the perpendicular space can be written in the form

$$\mathbf{Q}_{\perp}(\mathbf{H}) = \sum_{i=1}^{6} h_i \mathbf{Q}_i^{\perp}, \tag{3}$$

where $\mathbf{Q}_i^{\perp}$, with $i = 1$–6, are the basis vectors of the perpendicular space set by the equations

$$\begin{aligned} \mathbf{Q}_1^{\perp} &= (q_2/2)(\tau, -1, 0), & \mathbf{Q}_2^{\perp} &= (q_2/2)(\tau, 1, 0), \\ \mathbf{Q}_3^{\perp} &= (q_2/2)(0, \tau, -1), & \mathbf{Q}_4^{\perp} &= (q_2/2)(0, \tau, 1), \\ \mathbf{Q}_5^{\perp} &= (q_2/2)(-1, 0, \tau), & \mathbf{Q}_6^{\perp} &= (q_2/2)(1, 0, \tau). \end{aligned} \tag{4}$$

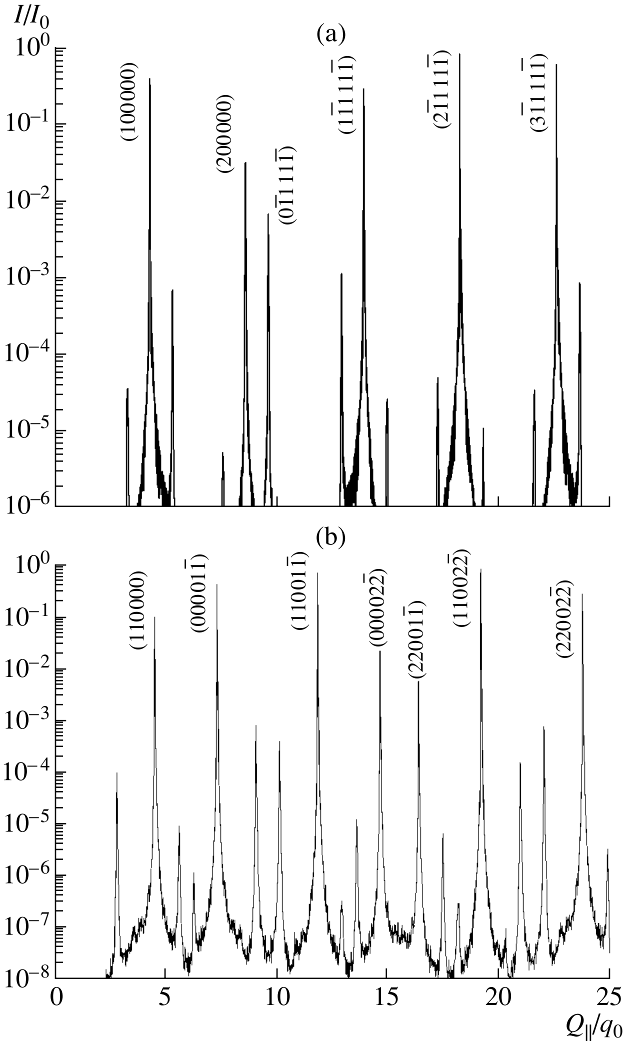

Fig. 1. Diffraction spectra from a quasicrystalline cluster grown in the computer experiment along the (a) fivefold and (b) twofold axes. The intensity is given on the logarithmic scale so as to be able to distinguish weak peaks. The six-dimensional Miller indices of the reflections are indicated.

To each $\mathbf{Q}_{\parallel}$, there corresponds one and only one $\mathbf{Q}_{\perp}$.

ANALYSIS OF DIFFRACTION PATTERNS

A diffraction spectrum of a quasicrystal (structure factor) was calculated by the standard formula

$$F(\mathbf{H}) = N^{-1}\sum_j \exp[i(\mathbf{k}' - \mathbf{k})\mathbf{r}_j], \tag{5}$$

where **k** and **k**' are the wave vectors of the incident and scattered waves, respectively; $\mathbf{r}_j$ are the atomic positions; and the summation is performed over all the N atoms assumed to be of the same species (which allows us to neglect the atomic scattering factor, also dependent on $\mathbf{k}' - \mathbf{k}$). If all the atoms scatter in phase, all the

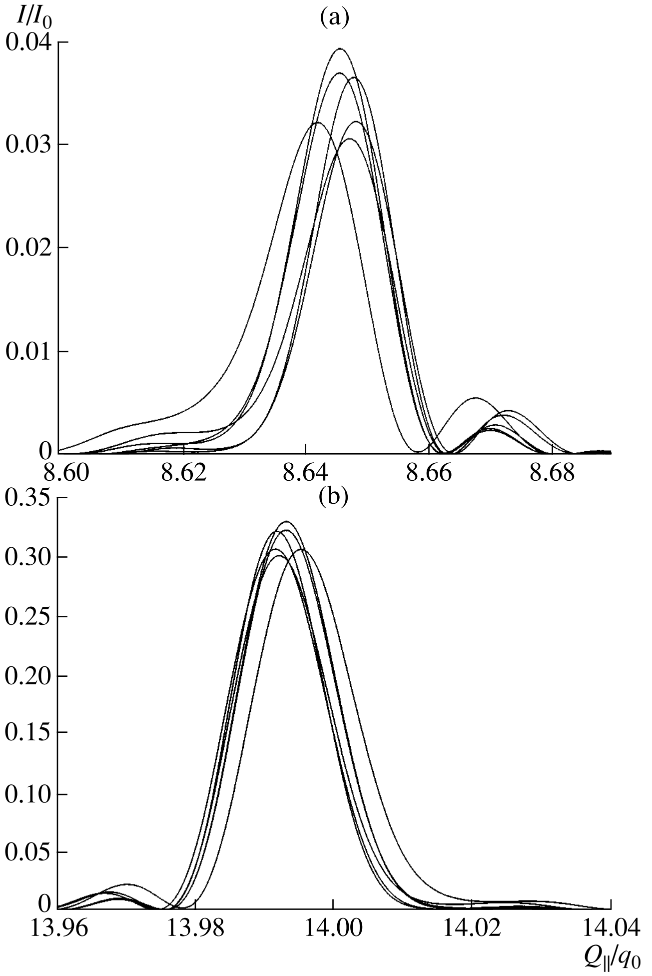

Fig. 2. Diffraction peaks along the fivefold symmetry axes: (a) (200000) and (b) ($1\bar{1}111\bar{1}$). The curves are calculated along all the six fivefold axes.

exponents in the above equation are equal to unity, and the structure factor attains its maximum value—unity.

We studied the reflections with the wave vectors directed along all the six fivefold symmetry axes and all the 15 twofold axes of the icosahedral point group of the quasicrystal. Therefore, the difference between the wave vectors $\mathbf{Q} = \mathbf{k}' - \mathbf{k}$ was also directed along either fivefold or twofold axes. The diffraction width of the reflections in the planes orthogonal to these axes was not studied, because it would be too time consuming.

Figure 1 shows the diffraction spectra calculated along the five- and twofold symmetry axes. The wave-vector lengths measured in arbitrary units, $q_0 = (2/r_2)$, are plotted along the abscissa. Since dimensionality D of the reciprocal-lattice basis is higher than dimensionality d of the space of wave vectors, then, generally speaking, the whole reciprocal space is densely filled with peaks of various intensities. Nevertheless, as we see from the plots, there is a discrete set of pronounced intensity peaks, which, on the whole, is characteristic of quasicrystals. The seeming controversy is caused by the fact that the reflection intensities rapidly decrease with an increase in the modulus of the wave-vector projection onto the perpendicular reciprocal-lattice space. The peaks observed on the diffraction pattern correspond to relatively low $Q_{\perp}$ values, whereas the intensities of the remaining peaks are negligible.

An inflation property that is important for the analysis of the diffraction pattern can be understood based on the following reasoning. If we consider two wave vectors, $\mathbf{Q}_{\|}^{(1)}$ and $\mathbf{Q}_{\|}^{(2)} = n\mathbf{Q}_{\|}^{(1)}$, which differ by an integral factor; their Miller indices, and; therefore, the corresponding vectors in the perpendicular space also differ by the same factor, $\mathbf{H}^{(2)} = n\mathbf{H}^{(1)}$ and $\mathbf{Q}_{\perp}^{(2)} = n\mathbf{Q}_{\perp}^{(1)}$. However, an increase in $\mathbf{Q}_{\perp}$ results in a decrease in reflection intensity. Thus, of the two reflections, $\mathbf{Q}_{\|}^{(1)}$ and $\mathbf{Q}_{\|}^{(2)}$, the latter has a lower intensity, with the intensity ratio being the higher, the higher the n value is. Thus, the intensities of the peaks with the moduli of the wave vector $\mathbf{Q}_{\|}/q_0$ equal to 4.32 and 8.65 (Fig. 1a), and the wave vectors $(q_2/2)(1, \tau, 0)$ and $(q_2/2)(2, 2\tau, 0)$ differ by a factor of two, whereas the peak with the modulus of the wave vector $\mathbf{Q}_{\|}/q_0$ equal to 12.98 and the wave vector $(q_2/2)(3, 3\tau, 0)$ is so weak that we did not index it at all.

Another mathematical fact, although it is not so obvious, can be readily obtained from Eqs. (1)–(4) and reduces to the fact that, if we have two wave vectors, $\mathbf{Q}_{\|}^{(1)}$ and $\mathbf{Q}_{\|}^{(2)} = \tau\mathbf{Q}_{\|}^{(1)}$, then the situation for the respective vectors in the perpendicular space is opposite, $\mathbf{Q}_{\perp}^{(2)} = (1/\tau)\mathbf{Q}_{\perp}^{(1)}$. This signifies that the intensity of the second peak in this case is higher. Consider, e.g., the sequence of peaks with $\mathbf{Q}_{\|}/q_0$ equal to 4.55, 7.35, 11.90, and 19.26 (Fig. 1b). The absolute values of their wave vectors are q_2, τq_2, $\tau^2 q_2$, and $\tau^3 q_2$, respectively, whereas the intensities of the corresponding peaks approach the maximum possible intensity. This property can, conventionally, be called the τ-inflation.

However, not all the peaks possess this property. For example, the sequence of reflections along the fivefold axis (Fig. 1a) begun with the peak at 4.32 has no reflections corresponding to the wave vectors exceeding that of the first one by factors of τ and τ^2, and the following peak at 18.32 of this sequence has the wave vector exceeding that of the first peak by a factor of τ^3. This property can conventionally be called the τ^3 inflation. The absence of some peaks is explained by the fact that the corresponding wave vectors cannot be represented as the integral combinations of basis vectors (1). The properties of the τ and τ^3 inflation of the reflections is the characteristic feature of icosahedral quasicrystals with a primitive six-dimensional lattice. In particular, the inflation property allows one to distinguish between

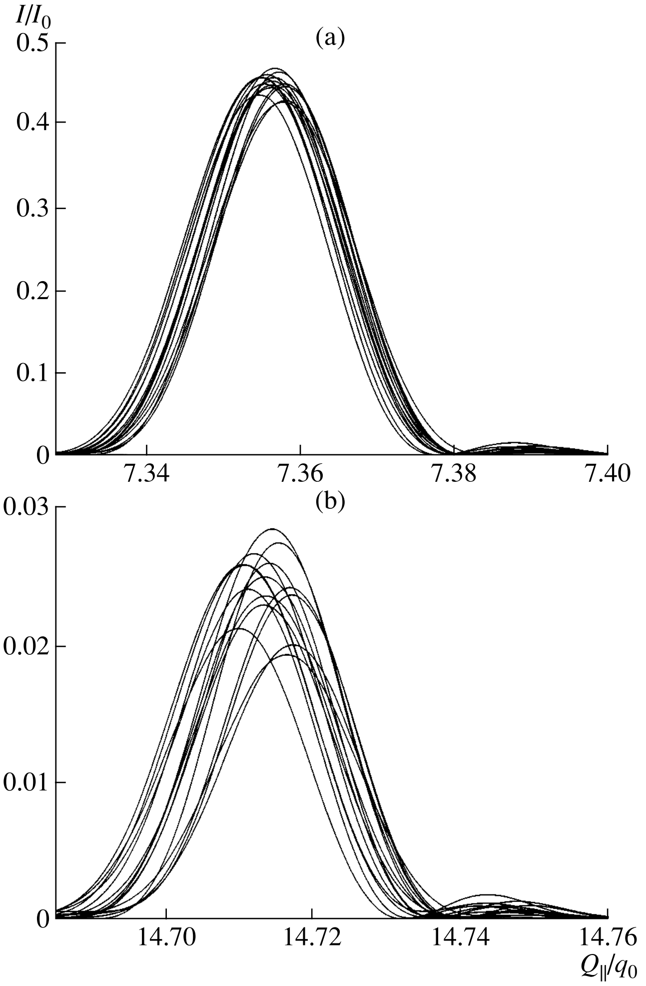

Fig. 3. Diffraction peaks along the twofold symmetry axes: (a) $(00001\bar{1})$ and (b) $(00002\bar{2})$. The curves were calculated along all the fifteen twofold axes.

the icosahedral and crystalline phases using the method of powder diffractometry.

Figure 2 shows one strong and one weak reflection located along the fivefold symmetry axes of the diffraction pattern. To demonstrate the influence of phason defects, we measured the intensity curves along all the six axes (reflections with the opposite wave vectors have the same intensities). For an ideal quasicrystal, all the curves should have the same shape, but, because of phason defects, the real reflections are asymmetric and have different positions and widths.

As has to be expected, the influence of phason defects is stronger the more pronounced the wave-vector modulus in the perpendicular space $Q_\perp$ is. The reflections with comparatively law $Q_\perp$ values have almost symmetric shapes, and their width is determined mainly by the finite dimensions of the quasicrystal considered. A similar behavior is also observed for reflections along the twofold axis in Fig. 3.

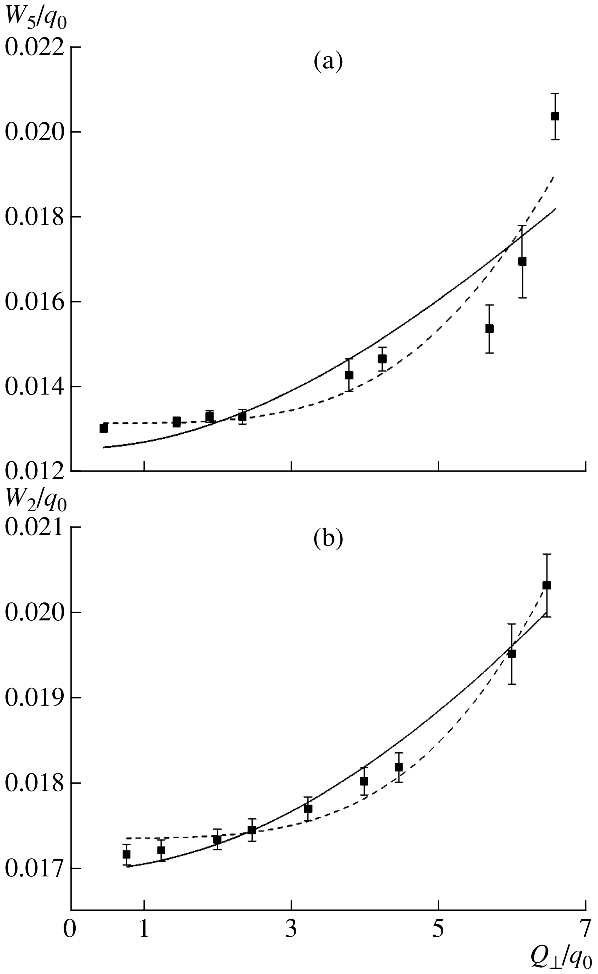

Fig. 4. Spectral width of reflections as a function of the magnitude of the perpendicular wave-vector component $Q_\perp$ for reflections located along the (a) fivefold and (b) twofold axes. Squares indicate the calculated values, and solid and dashed lines indicate the curves calculated in the $W_{ph}(Q_\perp) \propto Q_\perp$ and $W_{ph}(Q_\perp) \propto Q_\perp^2$ approximations, respectively.

In the general case, the reflection intensity is lower for the wave vectors with pronounced perpendicular components. This effect is observed experimentally for both perfect and imperfect quasicrystals. Theoretically, this effect is a direct consequence of the finite dimensions of perfect and imperfect quasicrystals in the perpendicular space [13–15].

It should also be indicated that the main reflections also have weak satellites formed alternatively on the right and left sides of the main reflection (Figs. 2, 3). Analysis showed that the formation of satellites is associated with an inhomogeneous distribution of phason defects. Indeed, the dimension of a quasicrystal in the perpendicular space and, therefore, the number of phason defects slightly decreases with an increase in the quasicrystal radius [13–15]. In other words, the number of defects on the periphery is larger than in the center. Such an inhomogeneity results in the satellite formation. Similar satellites also appear in real quasicrystals, but they are usually associated with the presence of an additional incommensurate modulation.

It is also interesting to analyze the dependence of the spectral width on the perpendicular reflection component (Fig. 4). It is seen from Fig. 4 that the width regularly increases with an increase in the perpendicular component of the reciprocal-lattice vector. The finite width of the reflection at $Q_\perp \longrightarrow 0$ is explained by the finite dimensions of the "grown" quasicrystal. To confirm this statement, we performed diffraction experiments along the two- and fivefold axes using quasicrystals of various dimensions, which explains different widths of the diffraction peaks at $Q_\perp \longrightarrow 0$. It is possible to assume that the observed broadening is explained by the finite dimensions of the quasicrystal and the presence in it of phason defects. These factors give independent contributions to the reflection width

$$W(Q_\perp) = \sqrt{W_f^2 + W_{ph}^2(Q_\perp)},$$

where W_f and $W_{ph}(Q_\perp)$ are values of broadening due to the finite dimensions of the quasicrystal and phason defects, respectively. The solid and dashed lines in Fig. 4 correspond to $W_{ph}(Q_\perp) \propto Q_\perp$ and $W_{ph}(Q_\perp) \propto Q_\perp^2$. Obviously, the dependence of W on $Q_\perp$ cannot be described sufficiently well by such simple functions.

CONCLUSIONS

The simulation of diffraction scattering from quasicrystals allows us to draw the conclusion that the presence of phason defects gives rise to broadening and asymmetry of diffraction peaks and that these phenomena are strongly dependent on the wave-vector components in the perpendicular space. Strong reflections with low value of the perpendicular component are characterized by weak asymmetry, whereas the reflection width is determined mainly by the finite dimensions of the quasicrystal studied. The reflections with large perpendicular components show a pronounced asymmetry, and their averaged width increases with an increase in the value of the perpendicular component. The displacements of the peaks from the positions dictated by the icosahedral symmetry are much less than the peak width, and, therefore, they were not analyzed.

Despite the fact that we considered a rather simple model, it had all the properties of real quasicrystals and could readily be extended to more complicated situations. Thus, an Eden model can be replaced by a more realistic Monte Carlo model [15, 16], but this considerably increases the time necessary for computations, whereas the results thus obtained are almost the same. It would also be interesting to see how the presence of various atomic species would influence the diffraction pattern and use the experimental data obtained for determining the positions of the given species in the physical and perpendicular spaces.

ACKNOWLEDGMENTS

This study was supported by the Russian Foundation for Basic Research (project no. 02-02-16275a) and the Agreement Between the Centre National de la Recherche Scientific (CNRS, France) and the Russian Academy of Sciences (project nos. 4058 and 16377). One of us, V.A. Chizhikov, is also grateful to the Russian Science Support Foundation.

REFERENCES

1. D. Shechtman, I. Blech, D. Gratias, and J. W. Cahn, Phys. Rev. Lett. **53**, 1951 (1984).
2. H. Bohr, Acta Math. **45**, 29 (1924); Acta Math. **46**, 101 (1925); Acta Math. **47**, 237 (1927).
3. P. M. de Wolff, Acta Crystallogr., Sect. A: Cryst. Phys., Diffr., Theor. Gen. Crystallogr. **30**, 777 (1974).
4. R. Penrose, Math. Intell. **2**, 32 (1979).
5. M. Gardner, *Penrose Tile to Trapdoor Ciphers* (Freeman, New York, 1989; Mir, Moscow, 1993).
6. A. L. Mackay, Kristallografiya **26**, 910 (1981) [Sov. Phys. Crystallogr. **26**, 517 (1981)].
7. N. Wang, H. Chen, and K. H. Kuo, Phys. Rev. Lett. **59**, 1010 (1987).
8. L. Bendersky, Phys. Rev. Lett. **55**, 1461 (1985).
9. T. Ishimasa, H.-U. Nissen, and Y. Fukano, Phys. Rev. Lett. **55**, 511 (1985).
10. P. A. Kalugin, A. Yu. Kitaev, and L. S. Levitov, Pis'ma Zh. Éksp. Teor. Fiz. **41**, 119 (1985) [JETP Lett. **41**, 145 (1985)].
11. V. A. Koptsik, Comput. Math. Appl. **16**, 407 (1988).
12. V. A. Koptsik, Lect. Notes Phys. **382**, 588 (1991).
13. V. E. Dmitrienko and S. B. Astaf'ev, Pis'ma Zh. Éksp. Teor. Fiz. **61**, 316 (1995) [JETP Lett. **61**, 331 (1995)].
14. V. E. Dmitrienko and S. B. Astaf'ev, Phys. Rev. Lett. **75**, 1538 (1995).
15. V. E. Dmitrienko, S. B. Astaf'ev, and M. Kléman, Phys. Rev. B **59**, 286 (1999).
16. V. E. Dmitrienko, S. B. Astaf'ev, and M. Kléman, *Physics of Crystallization* (Fizmatlit, Moscow, 2002), p. 263.

Translated by L. Man

Crystallography Reports, Vol. 49, No. 4, 2004, pp. 553–558. Translated from Kristallografiya, Vol. 49, No. 4, 2004, pp. 628–633.
Original Russian Text Copyright © 2004 by Smirnova.

THEORY OF CRYSTAL STRUCTURES

Combinatorial Analysis of Crystals

N. L. Smirnova
Moscow State University, Vorob'evy gory, Moscow, 119992 Russia
e-mail: snl194@mail.ru

Received November 4, 2002

Abstract—The alphabetical, specific, partial, and complete codes of vertices are determined for diamond crystals and a number of Schlegel projections. The codes obtained are compared with the codes of the types of atomic environment. *© 2004 MAIK "Nauka/Interperiodica".*

In the early 20th century, crystallographers revealed and described superstructures formed through ordering of atoms over positions of the closest packings; such superstructures are also known as ordered isomorphs. Moreover, a number of structures of layered silicates consisting of a small number of layers were identified at that time. These layers, which were subsequently referred to as "*serdechnik*" ("core") and "*kol'chuga*" ("chain armor") by N.V. Belov, are combined to form mixed layers that alternate with intermediate layers. This leads to the formation of ordered or disordered isomorphs. The design of the possible superstructures on the basis of the universal law of polarity, the principle of nonindifference (preference), and the law of small numbers has offered a small number of models of parent superstructures and limited (or continuous) polytype and heteropolytype series between them. A comparison of the obtained models with approximately 100 identified structural types and their cationic and anionic motifs confirmed the view that the phenomenon of polarity, the principle of nonindifference, and the law of small numbers are the universal laws governing the organization of the system of structural types. In the 1950s, the conclusion was drawn that all structural types are formed through ordered isomorphism (combinatorics) of systems of elements (atoms, rods, layers, frameworks, etc.) with different dimensions ranging from zero to three [1].

The enumeration and combinatorial analysis of the variety of crystallographic simple forms and their combinations (external forms) for diamond crystals were carried out by Voytekhovsky [2] in the framework of the Curie principle. It should be noted that the Curie principle accounts for the special case of the general mechanism of interaction between any object and a medium as two matrices that can have a mutual influence on each other during interaction [3]. The enumeration enables one to determine the number of theoretically possible and really existing objects. The set of really existing objects can be complemented.

The main objective of the present work was to describe a system of diamond crystals in terms of an attribute according to which the number of constituents changes from one to four. The relevant constituents were considered earlier in [4, 5]. These are triangles, tetragons, pentagons, and hexagons, which were also treated in [6]. Hereinafter, these constituents will be denoted by *t*, *q*, *p*, and *h*, respectively. Moreover, the alphabetical and specific codes are introduced for vertices, partial vertexons, and complete vertexons. In what follows, by a "vertexon" we mean a set of vertices of a polyhedron with faces shared by these vertices. The code of a vertex will be considered to mean a combination of polygons shared by this vertex and their number. For example, the alphabetical code *tqp* implies that trigonal, tetragonal, and pentagonal faces are shared by the vertex under consideration. The specific code of a vertex involves not only the type of adjacent faces but also their numbers. In particular, the specific code *tqp*⟨211⟩ means that two trigonal, one tetragonal, and one pentagonal faces are shared by the vertex. The specific code of a vertex can also be written using only numerals. For this purpose, the numerals corresponding to the numbers of triangles, tetragons, pentagons, and hexagons shared by the vertex are placed in the first, second, third, and fourth positions, respectively. For example, the specific code *tqp*⟨211⟩ of a vertex can be represented as 2110 (zero indicates the absence of hexagons). By adding the number of such vertices in an external form, i.e., ⟨2⟩, to the vertex code 2110, we obtain the code 2110⟨2⟩ of the partial vertexon. The vertexon of an external form of a crystal, the vertexon of a coordination polyhedron, and the vertexon of an atomic environment and their codes are referred to as simple when they consist of one partial vertexon and as complex when they involve several partial vertexons. The combination of partial vertexons of a simple or complex vertexon (and their code) is termed the complete vertexon (the complete code). Examples of codes of vertexons for a tetrahedron, an octahedron, and a cube are given below. The vertices of a tetrahedron, an octahedron, and a cube have the alphabetical codes *t*, *t*, and *q* and the specific codes *t*⟨3⟩, *t*⟨4⟩, and *q*⟨3⟩ (or 30, 40, and 03), respectively. The partial vertexons of a tet-

Table 1. Partial codes of vertices for 31 types of diamond crystals

Alphabetical vertex code	Number of faces I*a* *f*	Specific vertex code	Number of vertices (indices of specific codes of partial vertexon)	Number of different vertexons *D* and total number of all vertexons *A*	Number of all vertices I*a* *v*	Type of partial vertexon
tqp	3	1110	2, 2, 2, 4, 4, 4	2-6	18	Tetragon, tetragon
tqh	3	1101	1, 2, 2, 4, 6	4-5	15	Hexagon
tqh	3	1011	2, 3, 4, 4, 6, 8	5-6	27	Tetragon, tetragon, hexagon, cube
qph	3	0111	1, 2, 4	3-3	7	Tetrahedron
tq	3	12	1, 1, 2, 3, 4, 4, 6	5-7	21	Tetragon, tetragon, trigonal prism
tp	3	1020	1, 1, 2, 2, 3, 3, 3, 4, 5, 6, 6	6-11	36	Tetragon, dihedron, trigonal prism, octahedron
th	3	1002	2, 2, 12	2-3	16	Laves polyhedron
qp	3	0120	1, 1, 2, 2, 3, 4	4-6	13	Tetragon
qp	3	0210	1, 1, 1, 2, 2, 2, 3, 3, 4, 4, 10	5-11	33	Tetragon, tetragon, pentagonal prism
qh	3	0201	1, 2, 2, 4, 12	4-5	21	Tetragon, hexagonal prism
tqp	4	1210	1, 1, 1, 2	2-4	5	Partial vertexon with one or two vertices
tqp	4	2110	1, 2, 2	2-3	5	Partial vertexon with one or two vertices
tp	4	22	1, 2, 2, 3, 4	4-5	12	Tetragon
h	4	2020	1	1-1	1	Partial vertexon with one vertex
t	3	30	4	1-1	4	Tetrahedron
q	3	03	1, 1, 1, 2, 2, 3, 4, 8, 8	5-9	30	Tetragon, tetragonal prism, tetragonal prism
p	3	0030	1, 1, 1, 6	2-4	9	Octahedron
tp	4	13	1, 2	2-2	3	Partial vertexon with one or two vertices
tp	4	31	3	1-1	3	Triangle
h	4	3010	3	1-1	3	Triangle
t	4	40	6	1-1	6	Octahedron
Σ	68	21		62-95	288	

Note: Zeros situated at the last two positions in the codes are not presented.

rahedron, an octahedron, and a cube are described by the codes 30⟨4⟩, 40⟨6⟩, and 03⟨8⟩, respectively. The complete vertexons of a tetrahedron, an octahedron, and a cube consist of one partial vertexon, and, hence, their codes are identical to the codes of the partial vertexons. The code of faces characterizes a combination of trigonal, tetragonal, pentagonal, and hexagonal faces and their number. For example, the face codes of a tetrahedron, an octahedron, and a cube can be represented as 3⟨4⟩, 3⟨8⟩, and 4⟨6⟩, respectively.

Earlier [6], it was demonstrated that atomic environments can be characterized by 14 theoretically possible alphabetical codes of vertices that are composed of different combinations of letters (*t*, *q*, *p*, and *h*) and 47 theoretically possible specific codes: *t*⟨1, 2, 3, 4, 5⟩, *q*⟨1, 2, 3⟩, *tq*⟨(1, 2, 3, 4)1, (1, 2)2, 13⟩, *p*⟨1, 2, 3⟩, *tp*⟨(1, 2, 3, 4)1, (1, 2)2⟩, *qp*⟨(1, 2)1, 12⟩, *tqp*⟨(1, 2)11, 121⟩, *h*⟨1, 2⟩, *th*⟨(1, 2, 3)1, 12⟩, *qh*⟨(1, 2)1, 12⟩, *tqh*⟨(1, 2)11⟩, *ph*⟨(1, 2)1, 12⟩, *tph*⟨(1, 2)11⟩, and *qph*⟨111⟩. In the above notation, for example, the code *qh*⟨(1, 2)1, 12⟩ corresponds to the combination of codes *qh*⟨11⟩, *qh*⟨21⟩, and *qh*⟨12⟩. These codes were obtained for triangles, tetragons, pentagons, and hexagons with angles of 60°, 90°, 109°, and 120°, respectively. Real crystals can also be characterized by the aforementioned codes. However, in this case, there can appear additional codes that are differ-

Table 2. Complete vertex codes of diamond crystals

Face code of crystals	Point group *G*	Arity *Ar* of the face code of vertexons	Number I*a* of faces and vertices	Complete alphabetical code of crystals	Complete specific code of crystals
+3⟨4⟩	$\bar{4}3m$	1-1	4-4	1*t*	+30 ⟨4⟩
+3⟨8⟩	*m*3*m*	1-1	8-6	1*t*	+40 ⟨6⟩
4⟨6⟩a	2*mm*	1-1	6-8	1*t*	+03 ⟨8⟩
4⟨6⟩b	$\bar{3}m$	1-1	6-8	1*t*	+03 ⟨8⟩
+3-4⟨2-3⟩	3*m*	1-1	5-6	1*tq*	+12 ⟨6⟩
3-4⟨4-4⟩	*mmm*	2-2	8-8	2*tq*	12-22 ⟨4-4⟩
+3-4⟨2-4⟩	2*mm*	2-3	6-7	1*q*2*tTe*	03-12-22 ⟨2-4-1⟩
3-4⟨2-5⟩	*m*	2-3	7-8	1*q*2*tTe*	03-12-22 ⟨4-2-2⟩
3-4⟨4-3⟩	3*m*	2-3	7-7	1*q*2*tTe*	03-12-31 ⟨1-3-3⟩
3-5⟨2-6⟩	$\bar{3}m$	2-2	8-12	1*t*1*tp*	0030-1020 ⟨6-6⟩
3-5⟨5-3⟩	3*m*	2-2	8-9	2*tp*	1020-3010 ⟨6-3⟩
4-5⟨5-2⟩	*m*	2-1	7-10	1*qp*	0210 ⟨10⟩
3-4-5⟨1-3-3⟩	*m*	3-4	7-10	1*q*1*tp*2*qp*	03-1020-0210-0120 ⟨1-3-3-3⟩
3-4-5⟨1-5-1⟩	$\bar{1}$	3-4	7-9	1*q*1*tq*1*tp*1*t*q*p*	03-13-0210-1110 ⟨3-1-3-2⟩
+3-4-5⟨2-2-2⟩	*mm*2	3-3	6-8	1*tp*1*qp*1*tqp*	1020-0210-1110 ⟨2-2-4⟩
3-4-5⟨3-1-3⟩	*m*	3-4	7-9	1*tp*1*qp*2*tqp*	1020-0120-1110-2110 ⟨5-1-2-1⟩
3-4-5⟨3-2-3⟩	*m*	3-5	8-10	1*tq*1*tp*2*qp*1*tqp*	12-1020-0120-0210-2110 ⟨1-4-2-1-2⟩
3-4-5⟨2-2-4⟩	*m*	3-5	8-11	1*p*1*tp*1*qp*2*tqp*	0030-1020-0120-1110-1210 ⟨1-3-4-2-1⟩
3-4-5⟨2-4-2⟩	2/*m*	3-3	8-10	1*qp*2*tqp*	0210-1110-1210 ⟨4-4-2⟩
3-4-5⟨3-3-1⟩	*m*	3-4	7-8	2*tq*1*qp*1*tqp*	22-12-0210-1110 ⟨2-1-1-4⟩
3-6⟨4-4⟩	$\bar{4}3m$	2-1	8-12	1*th*	1002 ⟨12⟩
4-6⟨6-2⟩	$\bar{3}m$	2-1	8-12	1*qh*	+0201 ⟨12⟩
3-4-6⟨2-5-1⟩	*m*	3-4	8-10	1*q*1*tq*1*qh*1*tqh*	03-13-0201-1101 ⟨2-2-2-4⟩
3-4-6⟨4-3-1⟩	3*m*	3-2	8-9	1*tq*11*tqh*	22-1101 ⟨3-6⟩
3-4-5-6⟨1-5-1-1⟩	*m*	4-4	8-11	1*qp*1*tqp*1*qh*1*tqh*	0210-1210-0201-1101 ⟨4-1-4-2⟩
3-5-6⟨3-3-1⟩	3*m*	3-3	7-10	1*p*1*tp*1*tph*	0030-1020-1011 ⟨1-3-6⟩
3-5-6⟨4-2-2⟩	*mm*2	3-3	8-11	1*tp*1*th*1*tph*	2020-1002-1011 ⟨1-2-8⟩
3-4-5-6⟨4-1-2-1⟩	*m*	4-4	8-10	1*tp*1*tqp*1*tqh*1*tph*	1020-2110-1101-1011 ⟨2-2-2-4⟩
3-4-5-6⟨1-3-3-1⟩	*m*	4-7	8-12	1*p*1*tp*2*qp*1*qh*1*tph*1*qph*	0030-1020-0210-0120-0201-1011-0111 ⟨1-1-2-2-2-2-2⟩
3-4-5-6⟨2-2-2-2⟩	2*mm*	4-4	8-12	1*qp*1*th*1*tph*1*qph*	0210-1002-1011-0111 ⟨2-2-4-4⟩
3-4-5-6⟨2-3-2-1⟩	1	4-9	9-11	1*q*1*tp*2*qp*1*tqp*1*qh* 1*tqh*1*tph*1*qph*	03-1020-0210-0120-1210-0201-1101-1011-0111 ⟨1-1-1-1-1-1-1-1-3⟩
D = 31	*D* = 10	*A* (faces) = 79	*A* (faces) = 226	*D* = 27	*D* = 30
A = 31	*A* = 31	*A* (vertices) = 95	*A* (vertices) = 288	*A* = 31	A = 31

Note: *D* is the number of different objects (symmetry groups, faces, vertices, codes), and *A* is the number of all objects.

ent from those listed above, because the corresponding angles of polygons in real crystals can differ from the angles in regular polygons.

For diamond crystals, 21 specific vertex codes can be represented as follows: *t* ⟨+3, +4⟩ for a triangle; *q* ⟨+3⟩, *tq* ⟨+12, +22, +13, +31⟩ for a tetragon; *p* ⟨+3⟩, *tp* ⟨+12, 31, 22⟩, *qp* ⟨12, 21⟩, *tqp* ⟨111, 211, 121⟩ for a pentagon; and *h*, *th* ⟨12⟩, *qh* ⟨+21⟩, *ph*, *tqh* ⟨111⟩, *tph* ⟨111⟩, and *qph* ⟨111⟩ for a hexagon. The vertex codes designated by the plus sign are similar to the

Table 3. Codes of partial vertexons of the Schlegel projections of the simplest dodecahedra

Specific vertex code	25	37	40	42	44	7362	49	54	94	7488	*D*-*A*
q⟨03⟩									1		1-1
p⟨0030⟩	1						1				2-2
q⟨0210⟩		2	1		1		2	3	2		6-11
q⟨0120⟩	2	1		3			1	2			5-9
tqp⟨1110⟩									1		1-1
h⟨0003⟩									1		1-1
qh⟨0201⟩	1	2	1	2	2				2		6-10
qh⟨0102⟩		2	1	2	3				2		5-10
ph⟨0021⟩	1	1	2	1	1		1				6-7
ph⟨0012⟩	2	2	1	2	1	1			1		7-10
tph⟨1011⟩						4					1-4
qph⟨0111⟩	6	3	7	3	5		3		3		7-30
s⟨00003⟩										1	1-1
ts⟨10002⟩										1	1-1
qs⟨02001⟩							2				1-2
qs⟨01002⟩										1	1-1
tqs⟨11001⟩										1	1-1
ps⟨00201⟩								3			1-3
ps⟨00102⟩										1	1-1
tps⟨10101⟩										4	1-4
qps⟨01101⟩							1	4			2-5
hs⟨00021⟩						2					1-2
ths⟨10011⟩						2					1-2
qhs⟨010011⟩							1				1-1
*phs*00111⟩						1	1				2-2
Σ*D*-*A*	6-13	7-13	6-13	6-13	6-13	5-10	9-13	4-12	8-13	6-9	63-122

Note: The number of the vertexon is given in the upper row, *D* is the number of different codes, and *A* is the number of all codes.

codes derived in [6] for the types of atomic environments. The total number of sets of indices (numerals in angle brackets) indicating the number of identical and different faces shared by the vertex under consideration is equal to seven, namely, 3, 4, 12, 22, 13, 111, and 112. The number of different types of polygons shared by one vertex cannot be more than three: the code of the vertex involves indices 3 and 4 for one type of polygons; indices 12, 22, and 13 for two types of polygons; and indices 111 and 112 for three types of polygons. The total number of polygons shared by one vertex can be equal either to three (indices 3, 12, 111) or four (indices 4, 22, 13, 112). The polygons shared by vertices with indices 22 and 112 can be located in different ways and, hence, characterized by different combinations: 22 *ttqq*, *tqtq*, 2020 *tptp*, 211 *ttqp*, 121 *tqqp*, *tqtp*, and *tqpq*. In this case, both the combination *ttpp* and any combination with two *H* are not found.

In a crystal, each vertex can be repeated 1, 2, 3, 4, 5, 6, 8, 10, or 12 times, thus forming partial vertexons. These numbers complement the codes of vertices and form partial specific codes of partial vertexons (for example, 1110⟨2⟩). A partial vertexon can be represented by one point; two points; a triangle; a tetragon; a hexagon; a trigonal, tetragonal, pentagonal, or hexagonal prism; a tetrahedron; an octahedron; and even a Laves polyhedron. For 31 types of diamond crystals, there are 62 different partial vertexons and the total number of all partial vertexons is equal to 95. The total number of vertices in these vertexons is 288. The specific codes of partial vertexons, which were determined for 31 types of diamond crystals, are listed in Table 1. Table 1 also presents the alphabetical and specific codes of vertices, the numbers of vertices in partial vertexons, the type of partial vertexons (namely, a tetragon; a hexagon; a cube; a dihedron; an octahedron; a trigonal, tetragonal, pentagonal, or hexagonal prism; a vertexon with one, two, or three vertices; etc.), the number of faces shared by one vertex (I*af*), the total number of all vertexons (*A*), the number of different vertexons

(*D*), and the total number of vertices in vertexons (I*a* *v*).

The complete specific codes of vertexons (external forms) of diamond crystals are listed in Table 2. The complete codes involve from one to nine partial specific codes. The complete code of a crystal can be written as a combination of partial codes of different vertices (for example, 12-22-03) and the number of vertices (for example, ⟨4-1-2⟩); i.e., it can be represented in the form 12-22-03⟨4-1-2⟩. This means that the complete code of a crystal consists of three partial specific codes, namely, 12⟨4⟩, 22⟨1⟩, and 03⟨2⟩. The simple codes of diamond crystals (single-arity codes) are composed of one partial code, and the complex codes (*n*-arity codes) contain several partial codes. Among the 31 codes, the arity is equal to 1 for 8 codes, 2 for 4 codes, 3 for 7 codes, 4 for 7 codes, 5 for 2 codes, 7 for 1 code, and 9 for 1 code. Furthermore, among the eight simple codes of vertices of the crystals, only six codes are similar to the codes obtained in [6] for atomic environments (in Table 2, these codes are denoted by the plus sign).

In [2], the variety of real octahedra corresponding to 30 combinatorially different forms of diamond crystals, one of which is represented by two affinely nonequivalent species, was characterized by the combinatorial symmetry, i.e., the point symmetry groups of the most symmetric representatives of the same combinatorial type. All these forms were described by the face formulas, which were composed of numerals indicating trigonal, tetragonal, pentagonal, and hexagonal faces and indices corresponding to the number of faces of each type in the crystal (Table 2).

Out of 32 point groups, 10 groups are realized. Among the 31 crystal types, 3 types are cubic, 8 types are hexagonal, 6 types are orthorhombic, 12 types are monoclinic, and 2 types are triclinic.

In [7], a classification was proposed for polyhedra of structural types according to the type of faces. A scheme (table) composed of numbers with indices was made up for different systems. All the face formulas determined in [2] are consistent with the scheme proposed in [7]. However, among the 31 formulas obtained, only 5 were known previously, whereas the other formulas with large indices were derived for the first time.

Voytekhovsky [2] described the Schlegel projections of the ten simplest dodecahedra involving faces with an identical nearest environment. In this case, polygons are elements. The partial and complete vertex codes determined for these projections are presented in Table 3. The vertices located inside the Schlegel projection were taken into account. The alphabetical codes include five types of faces, namely, *t*, *q*, *p*, *h*, and *s* (heptagon). Each projection involves no more than four different faces. This implies that the Schlegel projections under consideration obey the law of small numbers. It should be noted that the law of small numbers also manifests itself in the fact that any convex polyhedron necessarily has a tetrad, a triad, a pair, or three pairs of single-type faces [8]. The complete codes include from 4 to 9 different codes and 9, 10, 12, or 13 partial codes. The data obtained for 10 projections of all 122 vertices and their partial specific codes (including 63 different codes) are summarized in Table 3.

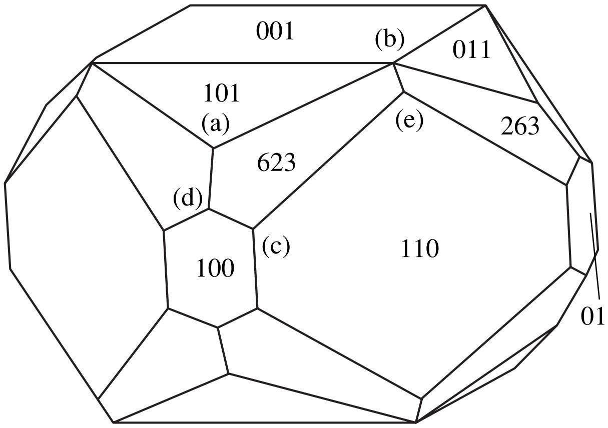

External form of the (Na,K) variety of merlinoite. The codes of vertices are as follows: (a) *tp* ⟨1020⟩, (b) *tqp* ⟨2120⟩, (c) *ph* ⟨0012⟩, and (d, e) *ph* ⟨0021⟩.

An external form of the (Na,K) variety of merlinoite (Kukisvumchorr, Khibiny) [8] is shown in the figure. The crystal has the {101} trigonal, {001} tetragonal, {236} pentagonal, {100} hexagonal, and {110} hexagonal faces. The face code of the crystal can be written in the form 3-4-5-6⟨8-2-16-8⟩ (the numbers of faces are given in angle brackets). The vertices are described by three partial alphabetical codes: *tp* (vertex a), *tqp* (vertex b), and *ph* (vertices c, d, e). Moreover, these vertices are described by four partial specific codes: *tp* ⟨1020⟩ (vertex a), *tqp* ⟨2120⟩ (vertex b), *ph* ⟨0012⟩ (vertex c), and *ph*⟨0021⟩ (vertices d, e). The crystal is characterized by the complete alphabetical vertex code 1*tp*1*tqp*2*ph* and the complete specific code 1020-2120-0012-0021 ⟨8-8-16-16⟩. The number of simple vertex forms with due regard for symmetry is five (vertices a–e), and the number of partial vertexons without regard for symmetry is four (vertices a, b, c, and d = e). This example clearly illustrates the difference between complex forms of vertexons and complex vertexons.

Earlier [6], attempts to reveal the alphabetical codes *qp*, *tqp*, *ph*, *tph*, *qph*, and *tqph* for real crystals were not successful. In the present work, all 14 theoretically possible variants for real crystals are revealed. Moreover, in [6], the theoretically possible specific codes *q* ⟨02⟩, *tq* ⟨+11, +23⟩, *p* ⟨001, 002⟩, *tp* ⟨1010, 2010, +2020⟩, *qp* ⟨0110, +0210, +0120⟩, *tqp* ⟨+1110, +1210⟩, *h* ⟨0002⟩, *th* ⟨1001, 3001, +1002⟩, *qh* ⟨0101, +0102⟩, *tqh* ⟨+1101⟩, *ph* ⟨0011, +0021, +0012⟩, *tph* ⟨+1011, 1021⟩, and *qph* ⟨+0111⟩ were not established for crystals. In this work, many of the aforementioned codes proved to be realized. These codes are denoted by the plus sign. Among the 47 possible variants, only 12 codes remain nonrealized. The specific codes *h* ⟨+0003⟩ and *tqp* ⟨+2120⟩ are forbidden theoretically. The sum of the angles for the former variant is close to the maximum permissible value (360°). The sum of the ideal angles for the latter variant is considerably larger (428°). It should be noted that other codes are also possible, because the theoretical calculation was performed for regular polygons, whereas real faces can be distorted significantly.

The alphabetical, specific, partial, and complete codes derived for diamond crystals, the variety of merlinoite, and Schlegel projections, as well as the results obtained in a number of recent works [9–16], are of particular interest for the development of the theory of coordination polyhedra, external crystal forms, and their symmetry (asymmetry) and can be used for solving applied problems. This information is of considerable importance in studying polyhedra with unknown symmetry.

ACKNOWLEDGMENTS

The author would like to thank M.I. Shtogrin for fruitful discussions.

REFERENCES

1. N. L. Smirnova, Kristallografiya **4** (1), 13 (1959) [Sov. Phys. Crystallogr. **4**, 10 (1959)].
2. Yu. L. Voytekhovsky, in *Proceedings of III International Mineralogical Seminar “New Ideas and Conceptions in Mineralogy”* (Geoprint, Syktyvkar, 2002), p. 240.
3. A. A. Bogdanov, *Tectology (General Organization Science)* (Ékonomika, Moscow, 1987 and 1989), Vols. 1 and 2.
4. N. L. Smirnova, Kristallografiya **21** (4), 822 (1976) [Sov. Phys. Crystallogr. **21**, 468 (1976)].
5. J. L. C. Daams and P. Villars, J. Alloys Compd. **215**, 1 (1994).
6. N. L. Smirnova, Vestn. Mosk. Univ., Ser. 4: Geol., No. 4, 39 (2000).
7. N. L. Smirnova, Kristallografiya **44** (5), 786 (1999) [Crystallogr. Rep. **44**, 726 (1999)].
8. O. V. Yakubovich, V. Massa, I. V. Pekov, and Ya. V. Kucherinenko, Kristallografiya **44** (5), 835 (1999) [Crystallogr. Rep. **44**, 776 (1999)].
9. N. L. Smirnova, in *Proceedings of IV All-Russian Meeting on Mineralogy of Ural* (Miass, 2003), p. 240.
10. N. L. Smirnova, in *Proceedings of International Conference “Carbon: Mineralogy, Geochemistry, and Astrochemistry”* (Syktyvkar, 2003), p. 25.
11. N. L. Smirnova, in *Proceedings of XV International Conference on X-ray Diffraction* (St. Petersburg, 2003), p. 54.
12. N. L. Smirnova, in *Proceedings of Joint International Scientific Conference on New Geometry of Nature* (Kazan. Gos. Univ., Kazan, 2003), Vol. 1, p. 201.
13. N. L. Smirnova, in *Proceedings of the 2003 Anniversary Fedorov’s Session* (St. Petersburg, 2003), p. 67.
14. N. L. Smirnova, in *Mineralogy, Gemmology, and Art* (S.-Peterb. Gos. Univ., St. Petersburg, 2003), p. 67.
15. N. L. Smirnova, in *Proceedings of Annual Session of Moscow Division of the Mineralogical Society* (IGEM Ross. Akad. Nauk, Moscow, 2003), p. 109.
16. N. L. Smirnova, in *Proceedings of the XXII Academician N. V. Belov Scientific Readings* (Nizhegor. Gos. Univ., Nizhni Novgorod, 2003), p. 24.

Translated by O. Borovik-Romanova

Crystallography Reports, Vol. 49, No. 4, 2004, pp. 559–572. Translated from Kristallografiya, Vol. 49, No. 4, 2004, pp. 634–648.

CRYSTAL CHEMISTRY

Principles and Criteria for the Choice and Refinement of Structural Models in Inorganic Crystal Chemistry

V. S. Urusov

Moscow State University, Vorob'evy gory, Moscow, 119992 Russia
e-mail: urusov@geol.msu.ru

Received January 22, 2003

Abstract—A hierarchical approach to the choice of the most probable structural models of a compound with a specified chemical composition and to the subsequent refinement of these models with the use of different methods is analyzed. Most attention is given to one of the first stages of the choice of the starting model (on the basis of the principles of total and local crystal electroneutrality) and to the solution of the problem of construction and determination of the bond graphs and connectivity matrices. Simple criteria for the most stable configurations of chemical bonds are introduced reasoning from the principles of minimum dissymmetrization and maximum informational entropy. *© 2004 MAIK "Nauka/Interperiodica".*

INTRODUCTION

Despite the considerable advances achieved in many fields of science and technology at the end of the 20th century due to intensive computerization of scientific research, the basic problem of crystal chemistry, namely, the prediction of the probability of existence and stability of a particular crystal structure for a specified chemical composition, remains far from solved. This is why many researchers have focused their efforts on this area of investigation. Modern approaches and methods used for predicting the most probable structure of a compound with a specified chemical composition can be grouped in the following hierarchical order:

(i) The topological selection, according to which only a relatively small number of combinations of main structural units (coordination polyhedra) are regularly repeated in different crystal structures. In particular, according to the Pauling rule of parsimony, the number of essentially different structural units in a crystal tends to be minimum.

(ii) Analysis of the symmetry and geometric constraints for which the preference of particular space symmetry groups over other space groups plays an important but not clearly understood role.

(iii) The use of the principle of closest packing, tolerance factor, sorting diagrams of structural types, and other factors in order to construct the starting structural model.

(iv) The introduction of the probability criteria for the existence of the chosen topological configuration (starting structure) on the basis of the principles of electroneutrality and the best valence and coordination matching (balance), the construction of the connectivity matrices and bond graphs and the calculation of the bond valences and lengths of ideal (unstrained) bonds, and comparison of different models in the framework of the concepts of minimum distortion of bonds and polyhedra and maximum entropy.

(v) The refinement of the most probable topological configuration with the use of a number of empirical and semiempirical methods, such as strained-bond, distance-least-squares, valence-least-squares, and distance–valence-least-squares methods (see below).

(vi) The search for the atomic configuration corresponding to a minimum cohesive energy of a crystal and computer simulation of the structure and properties (elastic, thermodynamic, etc.) in terms of atomistic potentials of interatomic interaction.

(vii) First-principles (*ab initio*) quantum-chemical calculations of the atomic structure, interatomic energy, electron density distribution, and main properties of the crystal.

In principle, all the aforementioned stages of the theoretical analysis and the determination of the structure and properties of a crystal can be used sequentially, because each higher level of such an analysis substantially narrows the scope of the search. In this respect, the purpose of the present work was to develop an algorithm for solving the problem associated with the choice of the most probable topological characteristics of a crystalline compound of a specified stoichiometric composition on the basis of a minimum set of initial data and the subsequent structure refinement with the use of modern crystal chemical methods. The principles of such an algorithm have already been proposed in a number of recent works (see, for example, [1–3]) and call for further elaboration and refinement.

PRINCIPLES OF TOTAL AND LOCAL VALENCE (AND COORDINATION) BALANCES. MODERN BOND-VALENCE METHOD

At this stage of constructing the topological model of a crystal structure, the problem can be solved through an exhaustive search for all allowable combinations of valences V and coordination numbers of cations A and anions X in the formula A_nX_m. Here, A_n stands for all cationic components and X_m stands for all anionic components, including atoms of the same chemical element in nonequivalent crystallographic positions (Wyckoff positions). In the course of the exhaustive search, the following two conditions must be satisfied: (a) the condition of electroneutrality of the crystal (or its formula unit),

$$\sum_i^n V_i = -\sum_j^m V_j, \qquad (1)$$

where the left-hand side is the sum of the valences over all cations and the right-hand side is the sum of the valences over all anions; and (b) the balance of coordination numbers (bond numbers),

$$\sum_i^n \nu_{ij} = \sum_j^m \nu_{ji}, \qquad (2)$$

where ν_{ij} is the number of the jth anions in the nearest environment of the ith cation (the coordination number of the ith cation) and ν_{ji} is the number of the ith cations in the nearest environment of the jth anion (the coordination number of the jth anion). Equality (2) corresponds to the obvious condition that the number of bonds from the cations to the anions must be exactly equal to the number of bonds from the anions to the cations. In this case, more electropositive atoms (cations) must be surrounded only by more electronegative atoms (anions). However, the chemical bonds in the compound do not need to be completely ionic in nature and the effective charges of cations and anions do not need to be equal to their formal valences. Therefore, conditions (1) and (2) are satisfied for the vast majority of inorganic compounds and minerals. It is evident that the exceptions are provided by intermetallic and polycationic (polyanionic) compounds.

An exhaustive search for all valences and coordination numbers even for a specified relatively simple stoichiometric composition (for example, ABX_3) requires a long time if this process is not controlled. A similar problem was previously solved using the bond graphs by Rao and Brown [2] and the connectivity matrices in my earlier work [3]. The most consistent variant of the latter method was proposed by O'Keeffe [4]. The modern version of this method [3, 5] makes it possible to predict the bond lengths in individual coordination polyhedra and to introduce criteria for the appropriate choice of the most probable structures among the large number of structures that, in principle, are allowed.

As an example, we will analyze the system studied earlier by Rao and Brown [2], who considered the coordination numbers of cations $A^{[8]}$ (the A atom is located in the eight-vertex polyhedron AX_8) and $B^{[6]}$ (the B atom resides in the environment of six anions; i.e., it is involved in the BX_6 structural unit). For this system, from the coordination balance (2), we obtain the following mean coordination number of X anions:

$$\bar{\nu}(X) = (8 + 6)/3 = 14/3.$$

The nonintegral value of $\bar{\nu}$ indicates that the anions should occupy not one but two or even more nonequivalent positions. For example, the sought structure can involve three nonequivalent anionic positions corresponding to the aforementioned mean coordination number. In particular, the combinations $X1^{[2]}X2^{[4]}X3^{[8]}$, $X1^{[3]}X2^{[5]}X3^{[6]}$, $X1^{[3]}X2^{[4]}X3^{[7]}$, and some others do not contradict the coordination number balance. This situation will be analyzed below. Now, we consider a simpler case and, as was done in [2], assume that there exist only two coordinationally nonequivalent types of anions, namely, $X1$ and $X2$. However, in contrast to the inferences made in [2], we assume that the coordination number of anions can vary not from two to six but over a wider range (i.e., from two to ten), because no geometric constraints are imposed at this stage. Furthermore, if we also assume that the valence $V(X)$ is equal to two (typical valence of oxygen, sulfur, and their analogues), the valence V of cations, according to the electroneutrality condition (1), can vary from one to five.

Let us consider the situation in which the valences of cations in the specified stoichiometric formula are equal to two for A atoms and four for B atoms. As a result, the traditional chemical formula can be written in the form $A^{2+}B^{4+}X1_2^{2-}X2^{2-}$, where the plus and minus signs indicate the electropositive and electronegative characters of the corresponding particles. In our model, the construction and solution of the connectivity matrix is reduced to the following procedure. Initially, we determine the mean bond valences $\bar{s}$, which coincide with the Pauling bond strengths of cations: $\bar{s}(A) = V_A/\nu_A = 2/8 = 0.25$ and $\bar{s}(B) = V_B/\nu_B = 4/6 = 0.67$. For the special case when the coordination numbers of the $X1$ and $X2$ anions are equal to four and six, respectively, Table 1 presents all the possible coordination environments of both anions and the deviations of the anion valences from the sum of the bond strengths of the surrounding cations (the deviations from the exact values determined in the framework of the second Pauling rule), that is,

$$\Delta V_j = V'_j - V_j = \sum_{i=1}^{\nu} \bar{s}_i - V_j. \qquad (3)$$

In turn, according to the sum rule of the bond-valence model, the true valences of the anions are equal to the sum of the valences of all unstrained (ideal) bonds:

$$V_j = \sum_{i=1}^{\nu} s_{ij}. \tag{4}$$

As follows from the electroneutrality condition (1) of the crystal, the allowable combinations of nearest environments of the anions must satisfy the equality $\sum_j^m \Delta V_j = 0$. This circumstance considerably restricts the number of possible crystal chemical formulas and the number of the corresponding connectivity matrices. With the values of ΔV_j taken from Table 1, it is easy to demonstrate that only four variants of the bond distribution are possible in our case. These variants of the bond distribution can be represented by the following matrices:

$$\text{I)}\quad \begin{array}{ccc} & 2X1 & X2 \\ A^{2+} & 6s_{11} & 2s_{12} \\ B^{4+} & 2s_{21} & 4s_{22}, \end{array}$$

$$\text{II)}\quad \begin{array}{ccc} A^{2+} & 4s_{11} & 4s_{12} \\ B^{4+} & 4s_{21} & 2s_{22}, \end{array}$$

$$\text{III)}\quad \begin{array}{ccc} A^{2+} & 2s_{11} & 6s_{12} \\ B^{4+} & 6s_{21} & 0, \end{array}$$

$$\text{IV)}\quad \begin{array}{ccc} A^{2+} & 8s_{11} & 0 \\ B^{4+} & 0 & 6s_{22}. \end{array}$$

Here, numerals indicate the number of bonds and s_{ij} are the bond valences, which are unknowns. The last two variants, *III* and *IV*, can be immediately rejected, because they do not provide bonding between AX_8 and BX_6 structural units. Indeed, their linkedness L, which is defined as the fraction of anions common to both polyhedra (among the total number of anions) [3], is equal to zero: $L = 0$. For variant *IV*, the above result directly follows from the connectivity matrix. In the case of matrix *III*, from three equations for the sums of the bond valences $V = \sum s_{ij}$, we obtain the valences $s_{11} = 0$, $s_{12} = 0.33$, and $s_{21} = 0.67$. Therefore, the value of L is also equal to zero.

For matrices *I* and *II*, each containing four unknowns s_{ij}, the solutions can be found from the three independent equations for the sums of the bond valences and one equation of the bond loop (closed contour) [2, 3]:

$$s_{11} - s_{21} + s_{22} - s_{21} = 0. \tag{5}$$

It should be noted that, in relationship (5), the bond valences are treated as vectors whose signs can be reversed depending on the direction of the bonds (from cations to anions or from anions to cations). By solving the system of four linear equations, we obtain the following bond valences: $s_{11} = 0.308$, $s_{12} = 0.077$, $s_{21} = 1.077$, and $s_{22} = 0.461$ for variant *I* and $s_{11} = 0.280$, $s_{12} = 0.220$, $s_{21} = 0.720$, and $s_{22} = 0.560$ for variant *II*.

Table 1. Possible cationic environments of $X1$ and $X2$ anions for the structural model $A^{2+}B^{4+}X1_2^{[4]}X2^{[6]}$ and the corresponding deviations ΔV from the Pauling rule

$X1$	ΔV	$X2$	ΔV
4*A*	–1.00	6*A*	–0.50
3*A*, *B*	–0.58	5*A*, *B*	–0.08
2*A*, 2*B*	–0.16	4*A*, 2*B*	0.34
A, 3*B*	0.25	3*A*, 3*B*	0.76
4*A*	0.68	2*A*, 4*B*	1.18
		A, 5*B*	1.60
		6*B*	2.00

For variants *I* and *II*, the linkednesses proved to be $L = 1$, because all three anions are involved in the formation of bonds with both cations. However, in order to choose the most probable bond distribution between the remaining variants, it is necessary to introduce a comparison criterion. This criterion represents a deviation (distortion) of bonds from an ideal variant, namely, the root-mean-square deviation of the calculated bond valences from their mean Pauling values (distortion index); that is,

$$D = \langle \Delta s_{ij}^2 \rangle^{1/2}, \tag{6}$$

where $\Delta s_{ij} = s_{ij} - \bar{s}$. As a result, we find $D = 0.22$ for variant *I* and $D = 0.05$ for variant *II*. This implies that the second distribution mode of bonds between the cations and anions is substantially more preferential than the first distribution.

By generalizing all the foregoing, we can argue that the stable crystal structure should obey the *principle of minimum dissymmetrization*. This principle is considered to mean a minimum deviation of the real bond distribution from the idealized (most symmetric) model of bond distribution in all the coordination polyhedra involved.

SYSTEMATIC ANALYSIS OF THE BOND VALENCE DISTRIBUTION AND PREDICTION OF THE APPLICABILITY OF STRUCTURAL MODELS

The results of the calculations carried out according to the above procedure for all possible sets of valences of both cations and for all possible sets of coordination numbers of both anions (z and y) in a compound with the crystal chemical formula $A^{[8]}B^{[6]}X1_2^{[z]}X2^{[y]}$ are presented in Table 2. In this table, numerals in parentheses

Table 2. Bond valences and stability criteria of all allowable structural matrices for compounds of the general crystal chemical formula $A^{[8]}B^{[6]}X1_2^{[z]}\,X2_2^{[y]}$

$A^{n+}B^{m+}$	$z; y$	$s(A{-}X1)$	$s(A{-}X2)$	$s(B{-}X1)$	$s(B{-}X2)$	D	$-S$
$A^{+}B^{5+}$	2; 10	(2)0.275	(6)0.075	(2)1.725	(4)0.388	0.42	1.529
	2; 10	(0)	(8)0.125	(4)01.000	(2)0.500	0.15	0.220
	4; 6	(6)0.163	(2)0.011	(2)1.511	(4)0.495	0.33	0.887
	4; 6	**(4)0.133**	**(4)0.117**	**(4)0.867**	**(2)0.765**	**0.03**	**0.011**
	5; 4	(8)0.125	(0)	(2)1.5	(4)0.5	0.31	0.744
	5; 4	**(6)0.123**	**(2)0.131**	**(4)0.815**	**(2)0.869**	**0.02**	**0.004**
	6; 2	(8)0.125	(0)	(4)0.750	(2)1.000	0.08	0.050
$A^{2+}B^{4+}$	2; 10	(2)0.823	(6)0.059	(2)1.176	(4)0.412	0.35	1.990
	3; 8	(4)0.400	(4)0.100	(2)1.200	(4)0.400	0.27	0.978
	3; 8	(2)0.374	(6)0.209	(4)0.813	(2)0.374	0.15	0.287
	4; 6	(6)0.308	(2)0.077	(2)1.077	(4)0.461	0.22	0.535
	4; 6	**(4)0.280**	**(4)0.220**	**(4)0.720**	**(2)0.560**	**0.05**	**0.041**
	5; 4	(8)0.250	(0)	(2)1.000	(4)0.500	0.15	0.233
	5; 4	**(6)0.242**	**(2)0.275**	**(4)0.637**	**(2)0.725**	**0.03**	**0.003**
	6; 2	(8)0.250	(0)	(4)0.500	(2)1.000	0.15	0.233
$A^{3+}B^{3+}$	2; 10	(2)0.971	(6)0.176	(2)1.029	(4)0.235	0.36	1.824
	3; 8	(4)0.373	(4)0.176	(2)0.853	(4)0.323	0.22	0.761
	3; 8	(2)0.661	(6)0.280	(4)0.670	(2)0.161	0.27	0.677
	4; 6	(6)0.432	(2)0.203	(2)0.703	(4)0.318	0.12	0.233
	4; 6	**(4)0.450**	**(4)0.300**	**(4)0.550**	**(2)0.400**	**0.07**	**0.090**
	4; 6	(2)0.500	(6)0.333	(6)0.500	(0)	0.05	0.052
	5; 4	(8)0.375	(0)	(2)0.500	(4)0.500	0.00	0.000
	5; 4	**(6)0.356**	**(2)0.432**	**(4)0.466**	**(2)0.568**	**0.04**	**0.038**
	5; 4	(4)0.250	(4)0.500	(6)0.500	(0)	0.10	0.170
	6; 2	(3)0.375	(0)	(4)0.250	(2)1.000	0.23	0.693
	6; 2	(6)0.167	(2)1.000	(6)0.500	(0)	0.27	1.151
$A^{4+}B^{2+}$	2; 10	(2)1.233	(6)0.256	(2)0.767	(4)0.116	0.38	1.989
	3; 8	(4)0.731	(4)0.269	(2)0.538	(4)0.231	0.30	0.622
	3; 8	(2)1.023	(6)0.326	(4)0.488	(2)0.023	0.27	1.251
	4; 6	**(6)0.535**	**(2) 0.395**	**(2)0.395**	**(4)0.302**	**0.05**	**0.044**
	4; 6	(4)0.615	(4)0.385	(4)0.385	(2)0.231	0.10	0.131
	4; 6	(2)1.000	(6)0.333	(6)0.333	(0)	0.22	0.535
	5; 4	**(6)0.465**	**(2)0.605**	**(4)0.302**	**(2)0.395**	**0.05**	**0.045**
	5; 4	(4)0.500	(4)0.500	(6)0.333	(0)	0.00	0.000
	6; 2	(6)0.333	(2)1.000	(6)0.333	(0)	0.22	0.535
$A^{5+}B^{+}$	2; 10	(2)1.602	(6)0.299	(2)0.398	(4)0.051	0.44	2.142
	2; 10	(4)1.000	(4)0.250	(0)	(6)0.167	0.28	0.964
	3; 8	0.873	(4)0.377	(2)0.255	(4)0.123	0.19	0.471
	3; 8	1.509	(6)0.330	(4)0.245	(2)0.009	0.39	1.718
	4; 6	(2)1.500	(6)1.333	(6)0.167	(0)	0.40	1.369
	4; 6	(4)0.802	(4)0.448	(4)0.198	(2)0.104	0.14	0.241
	4; 6	**(6)0.614**	**(2)0.659**	**(2)0.159**	**(4)0.171**	**0.01**	**0.003**
	5; 4	(6)0.569	(2)0.793	(4)0.114	(2)0.207	0.07	0.062
	5; 4	(4)0.750	(4)0.500	(6)0.167	(0)	0.10	0.101
	6; 2	(6)0.500	(2)1.000	(6)0.167	(0)	0.16	0.271

Table 3. Comparison of the bond valences calculated using three methods for compounds of the crystal chemical formula $A^{[8](4+)}B^{[6](2+)}X1_2^{[4](2-)}X2^{[6](2-)}$

s_{ij}	Bond valences calculated according to relationships		
	(5)	(7)	(8)
s_{11}	0.789	0.804	0.802
s_{12}	0.461	0.446	0.448
s_{21}	0.211	0.196	0.198
s_{22}	0.078	0.108	0.104

indicate the numbers of the corresponding bonds. The bond distributions for which $L = 0$ and the structural models cannot be realized are not included in Table 2. The bond valences s_{ij} calculated in this work and in [2] for identical structural models (except for the models with the ratios of the coordination numbers of anions $z : y = 2 : 10$ and $3 : 8$, which were not analyzed in [2]) almost coincide, even though the techniques used for solving the system of linear equations differ substantially. In [2], the loop equation was written in the form

$$\ln s_{11} - \ln s_{12} + \ln s_{22} - \ln s_{21} = 0$$

or

$$s_{11}/s_{12} = s_{21}/s_{22}. \tag{7}$$

This approach (conversion to logarithms of s_{ij}) makes it possible to avoid the appearance of unphysical negative values of s_{ij} for weak bonds in the case of large differences between the valences of the cations. For the same purpose, in the present work, we used the weighting scheme

$$s_{11}/\bar{s}_{11} - s_{12}/\bar{s}_{12} + s_{22}/\bar{s}_{22} - s_{21}/\bar{s}_{21} = 0, \tag{8}$$

where $\bar{s}_{ij}$ are the mean (Pauling) bond valences for the corresponding coordination polyhedra. It is evident that the following equalities are satisfied: $\bar{s}_{11} = \bar{s}_{12}$ and $\bar{s}_{21} = \bar{s}_{22}$. This approach (introduction of the weighting scheme) also provides a means for avoiding negative bond valences that have no physical meaning. Different methods for solving this problem, which belongs to the class of ill-posed problems, were compared and analyzed in my previous work [6]. It was demonstrated that, in general, different approaches developed to date have offered consistent solutions. In particular, the difference between the bond valences s_{ij} determined using the loop equations (7) and (8) does not exceed several units in the third decimal place. The results obtained upon solving one of the connectivity matrices by three different methods [with the use of loop equations (5), (7), and (8), respectively] are presented in Table 3. These data confirm the above inference.

The distortion criteria D and stability criteria S for each solution are listed in Table 2. The stability criterion (proposed by Rao and Brown [2]) is expressed in terms of the informational entropy (Shannon–Janes entropy) of the bond graph, that is,

$$S = -\sum s_{ij} \ln(s_{ij}/p_{ij}), \tag{9}$$

where p_{ij} are the *a priori* estimates of the bond valences. In [2], the values of p_{ij} were taken to be equal to unity. In our calculations, the mean bond valences (Pauling bond strengths) for cation polyhedra were used as the initial data: $p_{ij} = \bar{s}_{ij}$. According to the concept of maximum entropy [7, 8], the most stable configuration correspond to the smallest magnitude of the entropy $|S|$ (because $S < 0$).

It can be seen from Table 2 that the minimum-distortion criteria D and the maximum-entropy criteria S lead to qualitatively identical results. The most probable configurations are marked with bold type in Table 2. As can be seen from Table 2, these configurations do not contain odd numbers of bonds, because the linkedness L of configurations with odd numbers of bonds is always less than unity. In these situations, even at $D = 0$ and $S = 0$ (one case for each of the $A^{3+}B^{3+}$ and $A^{4+}B^{2+}$ combinations of cation valences), a lower stability should be expected for the corresponding hypothetical crystal structures. It can also be seen from Table 2 that, irrespective of the ratios between the cation valences, the most stable configurations of bonds correspond to the minimum difference between the coordination numbers of anions (4, 6; 5, 4). Therefore, the environments of two types of anions $X1$ and $X2$ tend to be similar to each other to a maximum degree, which does not contradict the principle of minimum dissymmetrization.

Now, we compare the experimental data with the aforementioned theoretical predictions. It follows from Table 2 that, for compounds with the $A^{+}B^{5+}$ combination of cation valences, there are two most probable bond distributions with distortion indices $D = 0.03$ and 0.02 and configurational entropies $-S = 0.011$ and 0.004, respectively. The second variant according to both criteria is more preferential. Actually, sodium uranate $NaUO_3$ crystallizes in the orthorhombic structure (space group *Pbnm*), which is characterized by the following nearest environments of cations and anions: Na (6O1 + 2O2); U (4O1 + 2O2); O1 (3Na + 2U); and O2 (2Na + 2U). This bond distribution is in complete agreement with our prediction.

For compounds with the $A^{2+}B^{4+}$ combination of cation valences, there exist also two most probable bond distributions with distortion indices $D = 0.05$ and 0.03 and entropies $-S = 0.041$ and 0.003, respectively. As before, it is clear that the second variant is substantially more appropriate than the first variant. Indeed, many double oxides, such as $CaSnO_3$, $SrSnO_3$, $CaGeO_3$, $SrZrO_3$, and $CdTiO_3$ (one out of four polymorphic

Table 4. Bond valences and distortion indices *D* for allowable combinations of cation valences and coordination numbers of anions in compounds of the general crystal chemical formula $A^{[8]}B^{[6]}X1^{[x]}X2^{[y]}X3^{[z]}$

$A^{n+}B^{m+}$	$x; y; z$	Numbers of bonds (in parentheses) and bond valences						
		A–*X*1	*A*–*X*2	*A*–*X*3	*B*–*X*1	*B*–*X*2	*B*–*X*3	*D*
A^+B^{5+}	2; 4; 8	(0)	(2)0.148	(6)0.117	(2)1.000	(2)0.852	(2)0.648	0.09
	2; 5; 7	(0)	(3)0.134	(5)0.119	(2)1.000	(2)0.800	(2)0.701	0.08
	3; 5; 6	(1)0.144	(3)0.126	(4)0.119	(2)0.928	(2)0.810	(2)0.762	0.05
	5; 5; 4	**(3)0.123**	**(3)0.123**	**(2)0.131**	**(2)0.869**	**(2)0.815**	**(2)0.815**	**0.02**
$A^{2+}B^{4+}$	3; 5; 6	(0)	(3)0.231	(5)0.259	(3)0.667	(2)0.646	(1)0.707	0.01
	3; 5; 6	(0)	(4)0.294	(4)0.206	(3)0.667	(1)0.823	(2)0.588	0.06
	3; 4; 7	(0)	(2)0.288	(6)0.237	(3)0.667	(2)0.712	(1)0.576	0.03
	3; 4; 7	(1)0.334	(1)0.250	(6)0.250	(2)0.833	(3)0.586	(1)0.575	0.08
	3; 4; 7*	(0)	(1)0.000	(7)0.286	(3)0.667	(3)0.667	(0)	0.07
	4; 4; 6	**(2)0.280**	**(2)0.280**	**(4)0.220**	**(2)0.720**	**(2)0.720**	**(2)0.560**	**0.05**
	5; 5; 4	**(3)0.242**	**(3)0.242**	**(2)0.275**	**(2)0.637**	**(2)0.637**	**(2)0.725**	**0.03**
$A^{3+}B^{3+}$	3; 5; 6	(3)0.667	(2)0.455	(3)0.364	(0)	(3)0.364	(3)0.303	0.09
	4; 4; 6	(2)0.450	(2)0.450	(4)0.300	(2)0.550	(2)0.550	(2)0.400	0.07
	4; 4; 6	(1)0.500	(1)0.500	(6)0.333	(3)0.500	(3)0.500	(0)	0.05
	5; 5; 4	(4)0.375	(4)0.375	(0)	(1)0.500	(1)0.500	(4)0.500	0.00
	5; 5; 4	**(3)0.356**	**(3)0.356**	**(2)0.432**	**(2)0.466**	**(2)0.466**	**(2)0.568**	**0.04**
$A^{4+}B^{2+}$	**4; 4; 6**	**(3)0.535**	**(3)0.535**	**(2)0.395**	**(1)0.395**	**(1)0.395**	**(4)0.302**	**0.05**
	5; 5; 4	**(3)0.465**	**(3)0.465**	**(2)0.605**	**(2)0.302**	**(2)0.302**	**(2)0.395**	**0.05**
	5; 5; 4	(2)0.500	(2)0.500	(4)0.500	(3)0.333	(3)0.333	(0)	0.00
$A^{5+}B^{+}$	3; 4; 7	(3)0.667	(3)0.609	(2)0.586	(0)	(1)0.172	(5)0.166	0.03
	3; 4; 7	(3)0.667	(2)0.780	(3)0.480	(0)	(2)0.220	(4)0.140	0.09
	3; 5; 6	(3)0.667	(2)0.712	(3)0.525	(0)	(3)0.192	(3)0.142	0.06
	4; 4; 6	**(3)0.614**	**(3)0.614**	**(2)0.659**	**(1)0.159**	**(1)0.159**	**(4)0.171**	**0.01**
	5; 5; 4	(3)0.569	(3)0.569	(2)0.793	(2)0.147	(2)0.147	(2)0.207	0.07

* Low degree of linkedness $L = 1/3$ and a decrease in the coordination number of the *A* cation to seven.

modifications); double sulfides (for example, $BaZrS_3$); and double fluorides (with halved valences of all atoms), for example, neighborite $NaMgF_3$, crystallize in the orthorhombic structure (space group *Pbnm*) with a bond distribution identical to that considered in the preceding case. It is interesting to note that the high-pressure phase (which is hypothetically stable under the conditions of the Earth's lower mantle), the so-called magnesian silicate perovskite $MgSiO_3$, has the same crystal structure.

As regards compounds of the $A^{3+}B^{3+}X_3$ type, either of the two structural configurations marked with bold type in Table 2 for these compounds is obviously more preferable in accordance with the criteria $D = 0.04$ and $-S = 0.038$. Actually, there exist many representatives of such compounds with a $GdFeO_3$ structure (space group *Pbnm*), whose coordination number and bond distributions are identical to those for all the above examples. In particular, these are heavy rare-earth, relatively light rare-earth, and yttrium aluminates; high-pressure phase $ScAlO_3$; etc.

It seems likely that crystalline compounds of the $A^{4+}B^{2+}X_3$ and $A^{5+}B^{+}X_3$ types do not exist because of the geometric hindrances, which will be considered in the next section.

The exhaustive search for all possible combinations of three anions nonequivalent in the environment for the same coordination numbers of the $A^{[8]}$ and $B^{[6]}$ cations reveals a number of allowable crystal chemical formulas: $X1^{[2]}X2^{[3]}X3^{[9]}$, $X1^{[2]}X2^{[4]}X3^{[8]}$, $X1^{[2]}X2^{[5]}X3^{[7]}$, $X1^{[3]}X2^{[4]}X3^{[7]}$, and $X1^{[3]}X2^{[5]}X3^{[6]}$. It is also necessary to take into account that identical coordination numbers can be observed for two anions nonequivalent in symmetry or (and) the nearest environment, such as $X1^{[5]}X2^{[5]}X3^{[4]}$, $X1^{[4]}X2^{[4]}X3^{[6]}$, etc. The total number of crystal chemical formulas $A^{[8]}B^{[6]}X1X2X3$ allowed according to the electroneutrality condition (1) is more than 300, namely, 47 for the $A^{+}B^{5+}$ combination of cation valences, 64 for the

$A^{2+}B^{4+}$ combination, 76 for the $A^{3+}B^{3+}$ combination, 58 for the $A^{4+}B^{2+}$ combination, and 67 for the $A^{5+}B^{+}$ combination.

However, the calculated valences s_{ij} of individual bonds for all possible combinations of cation valences and coordination numbers of anions show that, for the most part, these variants are characterized by large distortion indices D. Only a rather small number of combinations have $D \leq 0.10$, which allows for the possibility of forming the corresponding crystal structures. These combinations are given in Table 4.

It is clearly seen from analyzing the data presented in Table 4 that, among the combinations of coordination numbers of anions with small distortion indices D, the four aforementioned configurations (5, 5, 4), (4, 4, 6), (3, 5, 6), and (3, 4, 7) are considerably predominant. It is easy to see that, as in the previous case (Table 2), these configurations correspond to closer coordination numbers of anions. The only exception is provided by compounds of the $A^{+}B^{5+}X_3$ type with a maximum difference between the cation valences. In this case, there appear combinations in which the coordination number of the $X1$ anion is equal to two. It is interesting to note that, in these situations, the $X1$ anion is not involved in the environment of the univalent A^{+} cation but forms a bridge between pentavalent cations with the maximum bond valence $s = 1.00$ for the configurations under consideration. In general, the anion with the lowest coordination number (two, three) predominantly occurs in combination with a more multiply charged cation (B^{5+}, B^{4+}, A^{5+}, A^{4+}). For compounds of the $A^{3+}B^{3+}X_3$ type with the same cation valences, this anion appears to be completely or predominantly in the environment of the B^{3+} cations with a smaller coordination number and a higher bond valence (these compounds are absent in Table 4, because their distortion indices D are always larger than 0.10). As a consequence, the small degree of linkedness $L = 2/3$ and even 1/3 is observed for the majority allowed combinations of coordination numbers of anions (the numbers of bonds in the corresponding raw of Table 4 are equal to zero). A structural configurations with nonuniform distributions of bonds from particular anions to different cations (odd numbers of bonds in parentheses) also cannot exist, because such a distribution is inconsistent with the principle of minimum dissymmetrization and, hence, strongly reduces the probability of forming similar crystal structures. Therefore, a relatively high probability of formation should be observed only for several combinations of anions (4, 4, 6) and (5, 5, 4) with the closest coordination numbers. These combinations are marked with bold type in Table 4.

An analysis of the ICSD-2000 Database revealed the sole compound described by one of the structural configurations marked with bold type in Table 4. This is the monoclinic polymorphic modification $CdTiO_3$ (space group $Pbn2_1$) that has three nonequivalent positions of oxygen atoms [the coordination numbers of oxygen atoms are equal to five for O1 and O2 (3Cd + 2Ti) and four for O3 (2Cd + 2Ti)] and the following nearest environments of cations: Cd (3O1 + 3O2 + 2O3) and Ti (2O1 + 2O2 + 2O3). This corresponds to compounds with an $A^{2+}B^{4+}$ combination of cation valences in the last row of Table 4. It is interesting to note that, despite the lower symmetry, the coordination numbers and the bounding distribution in coordination polyhedra under consideration are identical to those found for all the above examples. The anions with a coordination number of four form an identical number of bonds with octahedra and eight-vertex polyhedra, and the anions with a coordination number of five form two bonds with octahedra and three bonds with eight-vertex polyhedra. Consequently, this monoclinic structure can be assigned to the same $GdFeO_3$ structure type, which includes all the aforementioned crystal structures with orthorhombic symmetry.

PRINCIPLE OF MINIMUM DISSYMMETRIZATION. PSEUDOSYMMETRY

By generalizing the inferences made above, we can state that the stable crystal structure should correspond to the principle of minimum dissymmetrization, which is considered to mean a minimum deviation of the real bond distribution from the idealized (most symmetric) model of bond distribution in all coordination polyhedra. It is assumed that, in the ideal model, all coordination polyhedra have a regular structure and the lengths of all similar bonds are equal to each other. This situation becomes possible in the case when different coordination polyhedra in the crystal structure are topologically similar to each other, i.e., when they are linked together in an equivalent manner. Let us now assume that the oxide structure involves only regular octahedra with symmetry $m\bar{3}m$. There exist only two cubic structure types that completely satisfy the above condition. These are the NaCl-type structure for bivalent elements in which all octahedra are shared by the edges and the ReO_3-type structure in which all oxygen octahedra around hexavalent cations are joined through all vertices into a framework. In all other cases (trivalent, tetravalent, pentavalent cations), it is impossible to construct a stable structure from topologically equivalent octahedra [9]. According to the general principles of the symmetry theory [10], the dissymmetrization requires an expansion of the system through the breaking of its isolation: only material agents that are external with respect to the fixed system can lead to a reduction of the symmetry. In our case, the appearance of A atoms with a lower valence in large-sized holes of the framework of the ReO_3-type structure and an attendant decrease in the valence of B atoms within the octahedra break the “chemical isolation” of the structure and are predominantly responsible for the typical lowering of symmetry in the compounds belonging to the perovskite structure type. These compounds can remain cubic

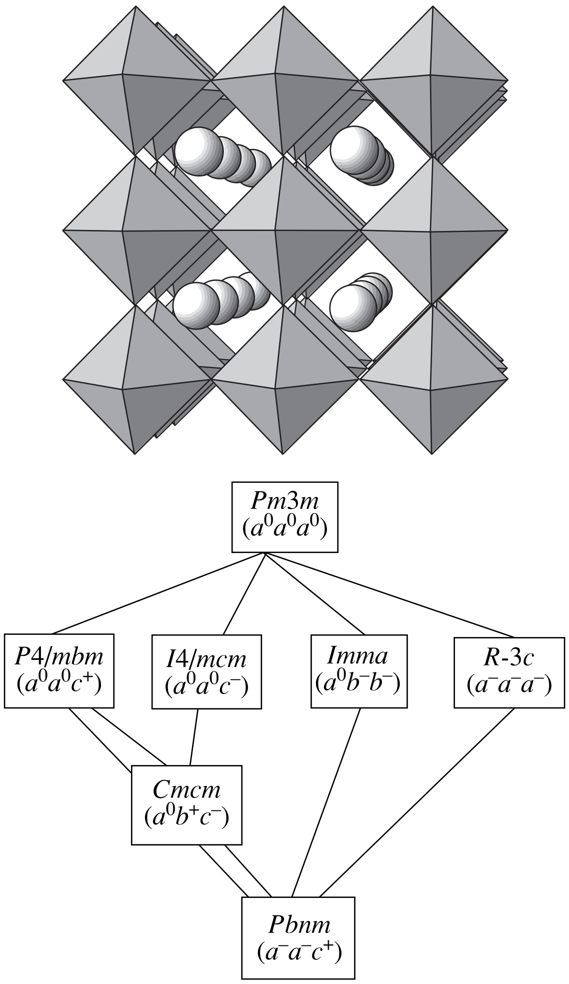

Fig. 1. Sequence of transitions from the parent cubic perovskite structure $Pm3m$ to the orthorhombic distorted structure $Pbnm$ through the rotations of the octahedra (according to the Glazer notation [11]).

only in special cases (especially at high temperatures) but, as a rule, have pseudocubic structures with tetragonal, trigonal, orthorhombic, or monoclinic symmetry.

Figure 1 shows the ideal structure of cubic perovskite (space group $Pm\bar{3}m$), the systems of octahedral tilting according to the Glazer notation [11] (see below), and a sequence of transitions to tetragonal, trigonal, and orthorhombic structures. The pseudocubic structure of all derivatives of the initial cubic structure is retained as a result of the minimum permissible distortion and partial loss of symmetry (minimum dissymmetrization). The concept of *pseudosymmetry* can also be useful for describing similar situations.

Moreover, the analysis of the data presented in Tables 2 and 4 demonstrates that, according to the principle of minimum dissymmetrization, among the numerous possible structural variants, the most favorable structures are as follows:

(i) structures with close coordination numbers of crystallographically nonequivalent atoms (occupying different Wyckoff positions) of the same chemical element;

(ii) structures with the most uniform (and the most symmetric) distribution of bonds between single-type nonequivalent atoms of the same chemical element and geometrically different coordination polyhedra; and

(iii) structures with the highest linkedness of different polyhedra (with a maximum degree of participation of crystallographically different atoms in the bonding of individual structural units).

It should also be emphasized that the above statements are corollaries to the Pauling rule of parsimony. According to this rule, the number of nonequivalent crystallographic positions of atoms of the same chemical element tends to a minimum. Now, this rule can be complemented by the following corollary: if atoms of the same chemical element occupy different Wyckoff positions, these atoms tend to be crystallographically similar to each other, i.e., to have identical or close coordination numbers and symmetries as similar as possible.

GEOMETRIC CONSEQUENCES AND CONSTRAINTS. PROBABLE SYMMETRY OF THE PREDICTED STRUCTURE

Undeniably, the valence and coordination constraints considered above lead to a sharp decrease in the number of structures that can exist in the crystal form. However, these constraints themselves are insufficient for definitive prediction. This can be judged from the lack of examples of $A^{[8]}B^{[6]}X_3$ compounds with the $A^{4+}B^{2+}$ and $A^{5+}B^{+}$ variants of cation valences, for which there exist numerous configurations that are allowed in accordance with the principles of valence and coordination number balance (Tables 2, 4). This situation can be simply explained by the fact that multiply charged cations with sizes larger than these of univalent and bivalent cations are either absent or almost absent. As a consequence, small-sized cations cannot occupy positions with a larger coordination number.

From analyzing the most stable topology of the bond distribution, which was revealed in the preceding section, we can make a number of inferences regarding the geometry of the hypothetical structure. Initially, we consider the octahedral environment of the B atom. This environment consists of four $X1$ anions and two $X2$ anions. In turn, anions of each type have two octahedral cations B as their nearest neighbors. Therefore, this structure should be characterized by a three-dimensional framework formed by vertex-shared octahedra, as is the case in the ReO_3 and $CaTiO_3$ perovskite structure types (Fig. 1). However, unlike the cubic structures of ReO_3 and perovskite (space group $Pm\bar{3}m$), whose frameworks consist of regular octahedra with symme-

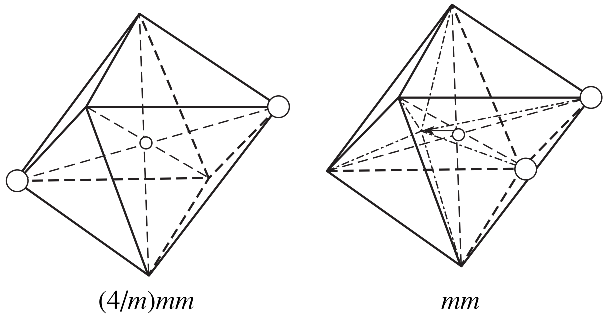

Fig. 2. Tetragonal and orthorhombic distortions of the octahedra with two vertices occupied by anions of the other type (shown by large circles). The *B* atoms are located at the centers of the octahedra. The possible shift of the B atom from the center is indicated by the arrow.

try $m\bar{3}m$, our model structure should be composed of distorted octahedra, because their vertices are occupied by anions of two different types. Depending on the mutual arrangement of *X*1 and *X*2 anions in octahedron vertices, the point symmetry of the octahedron can be either tetragonal (4/*m*)*mm* for the *trans* orientation of two *X*2 anions or orthorhombic *mm* for the *cis* orientation of these anions (Fig. 2). According to the principle of minimum dissymmetrization, we can assume that the proper symmetry of the octahedra is tetragonal. Furthermore, owing to the difference between the coordination numbers of the anions, the interatomic distance *R*(*B*-*X*1) should differ from the distance *R*(*B*-*X*2). Since the coordination number of five for the *X*1 anion is larger than the coordination number of four for the *X*2 anion, the radius of the former anion is somewhat greater than the radius of the latter anion and, hence, $R(B - X2) < R(B - X1)$. In turn, in order to retain the linkedness of the framework formed by these distorted octahedra, the adjacent octahedra undergo tilting. As a result, the cubic symmetry of the initial framework of a ReO_3 type is reduced and becomes no higher than tetragonal symmetry (Fig. 3). It can be seen from Fig. 3 that four neighbors of the central octahedron are rotated about the [001] axis through the same angle in the opposite directions with respect to the central octahedron. There are two variants of tetragonal distortions, which are designated as $a^0a^0c^-$ (Fig. 3b) and $a^0a^0c^+$ (Fig. 1) according to the Glazer notation [11]. The superscript 0 indicates that no rotations occur about the *a* axes. The superscript "–" and "+" on *c* signify that the octahedra lying above or below the layer depicted in the figure are rotated in the (001) plane in the opposite and same directions, respectively.

Using this line of reasoning, we can demonstrate that the symmetry of the framework composed of tilting octahedra with tetragonal symmetry (4/*m*)*mm* should become orthorhombic. Indeed, Fig. 4 shows the arrangement of the *X*2–*X*2 axial directions of the adjacent octahedra, which form a chain along the diagonal of the tetragonal cell. In order to prevent ineffective transformation of the framework structure into a layered structure, the *X*1–*X*1 diagonals of the equatorial planes of the octahedra in adjacent chains should lie along the diagonal of the tetragonal cell and the axial bonds *X*2–*B*–*X*2 should be aligned with the [001] axis perpendicular to the figure plane. This implies that the tilting of the octahedra should involve all three axial directions of the initial cell. Then, the new cell depicted in Fig. 3c becomes orthorhombic and, according to the Glazer notation, can be designated as one of the following tilting systems: $a^+b^+c^-$, $a^+a^+c^+$, $a^+b^-b^-$, or $a^+a^-a^-$ [11].

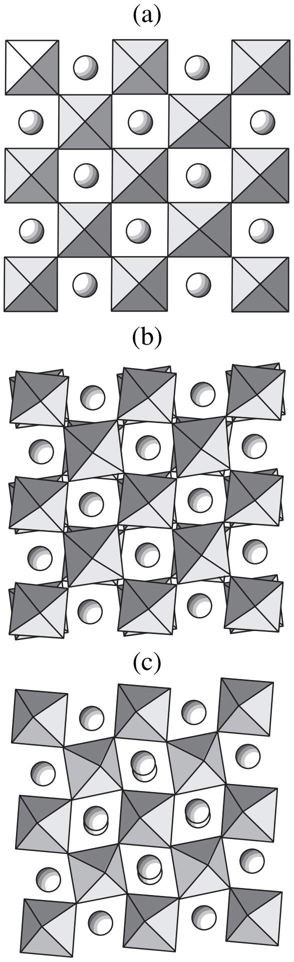

Fig. 3. Projections of (a) cubic, (b) tetragonal, and (c) orthorhombic perovskite structures along the [001] axis.

The problem regarding the geometry of coordination polyhedra around *A* atoms with larger sizes requires a comparative analysis of the most commonly encountered eight-vertex polyhedra, such as a cube, tetragonal antiprism, dodecahedron, and bicapped trigonal prism. A cube as a candidate for the coordination polyhedron should be rejected, because it has six tetragonal faces that cannot be brought into coincidence with trigonal faces of adjacent octahedra. Note that,

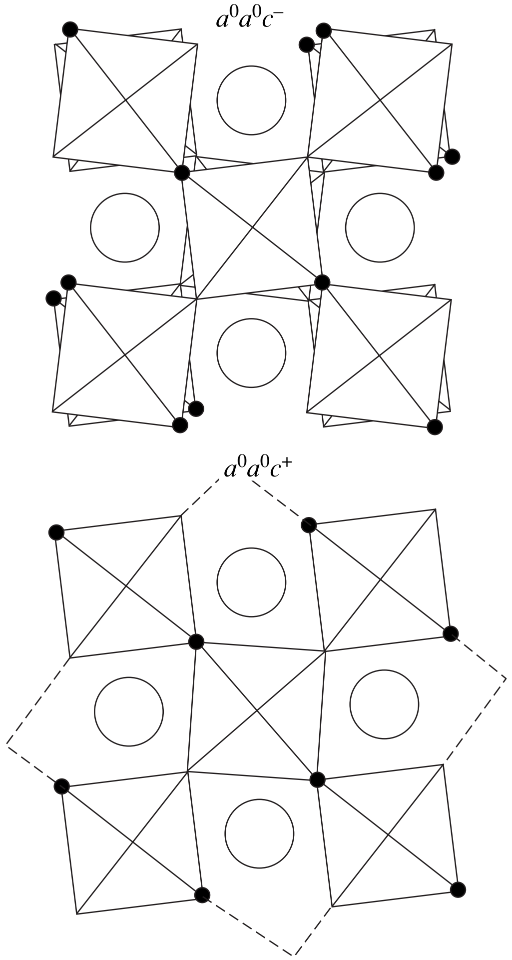

Fig. 4. Schematic diagram illustrating the formation of the inclined plane and orthorhombic distortion in two adjacent layers of the initial tetragonal structure due to a regular alternation of anions of two types (empty vertices and closed circles).

since two $X2$ and six $X1$ anions occupy the cube vertices, the cube is necessarily distorted and its ideal symmetry $m\bar{3}m$ is lowered to trigonal symmetry $\bar{3}m$ (for the *trans* orientation of $X2$ anions) or orthorhombic symmetry $mm2$ (mm).

A dodecahedron has 12 trigonal faces. This exceeds the number of faces necessary for filing a hole between eight adjacent octahedra. A bicapped trigonal prism is not an isometric figure, has one tetragonal and eight trigonal faces, and, apparently, also cannot fit into the octahedral three-dimensional framework without gaps. Consequently, owing only to a very strong distortion, such a coordination polyhedron around an A atom can become a probable environment.

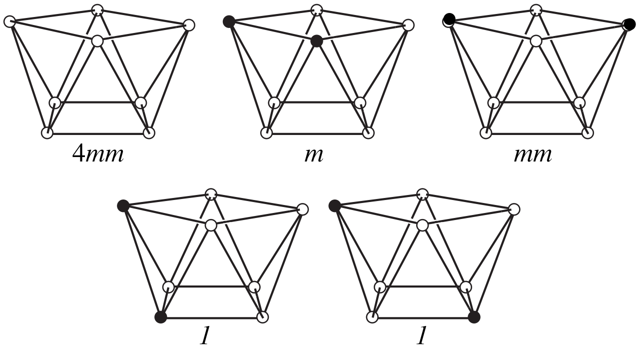

Fig. 5. Tetragonal antiprism and its orthorhombic and triclinic distortions due to a change in the nature of two vertices (shown by closed circles).

A tetragonal antiprism has two tetragonal faces and eight trigonal faces. Consequently, this polyhedron is a quite probable candidate for participation in the design (formation) of the structure. However, it should be taken into account that, since six $X1$ and two $X2$ anions occupy vertices of the polyhedron in our case, its ideal tetragonal symmetry (4*mm*) is lowered either to orthorhombic symmetry *mm*, or to monoclinic symmetry *m*, or even to triclinic symmetry 1 (Fig. 5). In the first case (symmetry *mm*), both $X2$ anions should occupy the *trans* positions. In the second case (symmetry *m*), both $X2$ anions should be located at the *cis* positions on one of the tetragonal faces, which renders the octahedral structural framework inhomogeneous. Therefore, we assume that symmetry of this polyhedron is lowered to triclinic symmetry. In this situation, both $X2$ anions are located on the opposite tetragonal faces and different edges of trigonal faces so as to provide a maximum distance between each other.

For the variant with proper triclinic symmetry of eight-vertex polyhedra, chains of octahedra with $X2$–$X2$ axial directions are aligned along the diagonal of the cell, which can result in the appearance of an inclined plane. Therefore, the space group *Pbnm* is the most probable group. Glazer [11] and Woodward [12] showed that this space groups is associated with the system of tilting $a^+b^-b^-$ in three directions with two identical rotation angles. It should be noted that this space-group symmetry is observed for all compounds crystallizing in the $GdFeO_3$ structure type (see the preceding section). The projection of the high-pressure perovskite-type structure $MgSiO_3$ with the space group *Pbnm* is depicted in Fig. 6. It is interesting to note that 65% of all the known perovskites are described by this space group [13], which ranks second in occurrence among all the orthorhombic space groups [14].

One more argument in favor of a considerable distortion of the cubic initial structure is provided by the Goldschmidt tolerance factor,

$$t = (r_A + r_O)/[2^{1/2}(r_B + r_O)], \quad (10)$$

where r_A and r_B are the octahedral radii of cations and r_O is the oxygen radius. Compounds of the perovskite structure type with different symmetries are characterized by a wide range of tolerance factors, namely, $1.05 > t > 0.78$. However, cubic structures are stable only at tolerance factors very close to unity: $1.05 > t > 0.99$. At tolerance factors in the range $0.99 > t > 0.78$, symmetry is necessarily lowered through the tilting of octahedra about small-sized A cations. For example, the magnesian silicate perovskite $MgSiO_3$ has the tolerance factor $t = 0.83$, which is close to the lower limit of the existence of the perovskite structure type (more precisely, this structure belongs to the orthorhombic $GdFeO_3$ structure type, which is a derivative of the perovskite type) [15]. Therefore, the $MgSiO_3$ perovskite is stable only at very high pressures.

STAGES OF REFINING THE CHOSEN STRUCTURAL MODEL

Let us consider the methods and procedures used for refining the starting structural model, which were chosen on the basis of the general crystal chemical principles described above. At the last stages, it is possible not only to refine the structure but also to predict many properties of a crystal. As an example, we will again analyze the orthorhombic structure of the $MgSiO_3$ magnesian silicate perovskite (which is important from the geochemical and geophysical standpoints), which, most likely, represents one of the main crystalline phases of the Earth's lower mantle.

Bond-Valence Method

The bond-valence method considered above makes it possible to determine the interatomic distances R_{ij} from the calculated valences s_{ij} of individual bonds with the use of the basic equation of the method:

$$R_{ij} = R_1 - b\ln s_{ij}, \tag{11}$$

where b is the empirical constant, which is usually equal to a universal (mean) value of 0.37 Å, and R_1 is the standard distance corresponding to the bond with the unit valence $s_{ij} = 1$. The distances R_1 are tabulated for many bonds [5].

The connectivity matrix for the $MgSiO_3$ perovskite is written according to the bond distribution for the $GdFeO_3$ structure type; that is,

$$\begin{array}{lcc} & \mathrm{O1} & \mathrm{2O2} \\ \mathrm{Mg}^{2+} & 2s_{11} & 6s_{12} \\ \mathrm{Si}^{4+} & 2s_{21} & 4s_{22}. \end{array}$$

The calculated bond valences are as follows: s(Mg–O1) = 0.275, s(Mg–O2) = 0.242, s(Si–O1) = 0.725, and s(Si–O2) = 0.637. With the use of the distances R_1(Mg–O) = 1.693 Å and R_1(Si–O) = 1.624 Å and Eq. (11), we find the bond lengths R(Mg–O1) = 2.171(×2), R(Mg–O2) = 2.218(×6), R(Si–O1) = 1.743(×2), and R(Si–O2) = 1.791 Å(×4). A comparison of the results of calculations with the experimental data on the interatomic distances (Table 5) demonstrates that, although they are in qualitative agreement, the bond-valence method leads to an underestimation of the degree of structural distortion and to higher symmetry of coordination polyhedra.

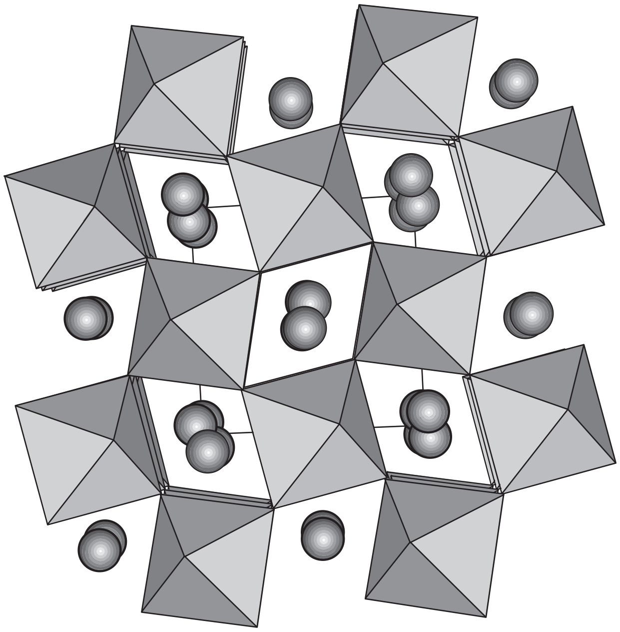

Fig. 6. Projection of the structure of the orthorhombic magnesian silicate perovskite $MgSiO_3$.

Distance-Least-Squares and Valence-Least-Squares Methods

The empirical distance-least-squares method is based on the least-squares fitting of interatomic distances to some preliminarily chosen typical distances. The function to be minimized has the form

$$\psi(x) = \sum_{i=1}^{m} \omega_i (R_i - R_{\mathrm{O}i})^2, \tag{12}$$

where $R_{\mathrm{O}i}$ are the specified typical interatomic distances, R_i are the same distances calculated for the chosen model from the atomic coordinates x and the unit cell parameters, and ω_i are the weighting factors assigned to the ith distance. Table 5 presents the results of calculations from this method with the experimental unit cell parameters $a = 4.732$ Å, $b = 4.892$ Å, and $c = 6.836$ Å for the $MgSiO_3$ perovskite and the distances $R_{\mathrm{O}i}$ calculated using the bond-valence method for regular polyhedra SiO_6 (1.774 Å) and MgO_8 (2.143 Å). The equilibrium O–O distance was taken to be equal to 2.500 Å. The weighting scheme is given in Table 5, in which the atomic coordinates and interatomic distances are compared with the experimental data. It can be seen from Table 5 that, although the theoretical and experimental data are in reasonable agreement, the distance-least-squares method underestimates the degree of distortion of eight-vertex polyhedra around Mg atoms.

Table 5. Results of the distance-least-squares refinement of the structure of the magnesian silicate perovskite $MgSiO_3$

Atom	Theoretical coordinates			Experimental coordinates		
	x	*y*	*z*	*x*	*y*	*z*
Mg	0.526	0.605	0.25	0.514	0.557	0.25
Si	0.5	0	0.5	0.5	0	0.5
O1	0.093	0.502	0.25	0.102	0.465	0.25
O2	0.184	0.189	0.547	0.195	0.208	0.555

Bond	*R*(theor), Å	*R*(exp), Å	Bond	*R*(theor), Å	*R*(exp), Å
Si–O1	(2)1.765	(2)1.784	Mg–O1	2.022	1.999
Si–O2	(2)1.782	(2)1.767	Mg–O1	2.108	2.070
Si–O2	(2)1.785	(2)1.784	Mg–O2	(2)2.139	(2)2.030
			Mg–O2	(2)2.196	(2)2.252
			Mg–O2	(2)2.295	(2)2.413

Note: The weighting scheme is as follows: ω(Si–O) = 2.0, ω(Mg–O) = 1.5, and ω(O–O) = 1.0.

The valence-least-squares method is based on the minimization of the functional [formally similar to functional (12)]

$$\varphi(x) = \sum_{i=1}^{m} \omega_i (V_i - V_{Oi})^2, \qquad (13)$$

where $V_j = \sum_{i=1}^{\nu} s_{ij}$ and V_{Oi} is the true valence of the ith atom. Here, the valences s_{ij} are functions of the interatomic distances or atomic coordinates at specified (usually experimental) unit cell parameters. This method should be used with care, at least until the parameters R_1 and b (in the bond-valence method) are unknown for each type of bonds. For example, our analysis of a number of recently refined structural data for the magnesian silicate perovskite (according to the ICSD-2000 Database) shows that the experimental sums of the valences of eight Mg–O bonds (2.15–2.30 valence units) are regularly larger than two valence units, whereas the sums of the valences of six Si–O bonds (3.80–3.94 valence units) are regularly smaller than four valence units. This suggests that, most likely, it is not sufficiently correct to use the universal parameter $b = 0.37$ Å for bonds with such a substantial difference in strength (rigidity). Actually, when this parameter is slightly decreased to 0.35 Å for the Mg–O bond and is increased to 0.40 Å for the Si–O bond, the bond valence sum rule is almost exactly satisfied for both cations.

Strained-Bond Model

Energetically, the distance-least-squares method can be simply justified by expanding interatomic interaction energy ε into a power series in the vicinity of the equilibrium position

$$\varepsilon(R) = \varepsilon_0 + (k/2)(R - R_0)^2 + \dots. \qquad (14)$$

Here, R_0 is the equilibrium distance and k is the quasi-elastic constant (bond rigidity), which is equal to the second derivative of the energy with respect to the distance at R_0; that is,

$$k = \varepsilon'' = (\partial^2\varepsilon/\partial R^2)_{R = R_0}. \qquad (15)$$

By summing changes in the energy over all pair interactions in the crystal, we find in the harmonic approximation that

$$\Delta\varepsilon(R) = \sum[\varepsilon(R) - \varepsilon_0] = \sum(k/2)(R - R_0)^2. \qquad (16)$$

A comparison of relationships (14), (16), and (12) demonstrates that the quantity (k/2) plays the role of a weighting factor in the distance-least-squares method. *A priori* estimations of this quantity involve the most considerable difficulties. In [16, 17], this quantity was taken to be proportional to the ratio between the valence and the coordination number of cations, i.e., to the Pauling bond strength $k \sim \gamma\bar{s}_i \sim = \gamma V_i/\nu_i$, where γ is a constant with the dimension of force. Then, the bond rigidity ratio, for example, for a perovskite of the $A^{2+}B^{4+}X_3$ type with a coordination number of 12 for A cations and a coordination number of 6 for B cations is estimated to be $k_B/k_A \simeq 8$. The same ratio can be obtained using an independent empirical method with due regard for the fact that, at 0 K, the following thermodynamic relationship is satisfied:

$$\varepsilon'' = 9VK/R^2, \qquad (17)$$

where V is the molar volume and K is the bulk modulus of the crystal. With the use of the known experimental data for periclase MgO and stishovite SiO_2, we obtain ε''(MgO) = 3670 kJ/mol · $Å^{-2}$ and ε''(SiO_2) = 14800 kJ/mol · $Å^{-2}$. In this approximation, the bond rigidity ratio $k_B/k_A \sim 4$, with allowance made for the correction for an increase in the coordination number of Mg from six in periclase to eight in the $MgSiO_3$ perovskite and the corresponding increase in the mean distance, should increase by no less than 40%: $k_B/k_A \sim 5.5$.

In the strained-bond model [16, 17], the mean parameter $\langle a\rangle$ of a pseudocubic perovskite unit cell per molecular unit can be determined by minimizing the strain energy of cation–anion bonds:

$$\Delta\varepsilon = 8k_A[(\langle a\rangle/2^{1/2}) - R_{0A}]^2 + 6k_B[(\langle a\rangle/2) - R_{0B}]^2. \qquad (18)$$

Here, R_{0A} and R_{0B} are the lengths of ideal (unstrained) bonds, which were calculated from formula (11) within the bond-valence method: Si–O = 1.774 Å and Mg–O = 2.143 Å for the regular octahedron and eight-vertex polyhedron, respectively. The equilibrium unit cell parameter is determined through the minimization of the strain energy (18) with respect to $\langle a\rangle$; that is,

$$\partial(\Delta\varepsilon)/\partial\langle a\rangle = 0.$$

As a result, we have

$$\langle a \rangle = (16k_A R_{0A}/\sqrt{2} + 6k_B R_{0B})/(8k_A + 3k_B). \quad (19)$$

Substitution $k_B \simeq 5.5k_A$ into expression (19) gives $\langle a \rangle \simeq$ 3.38 Å and a volume of 38.6 Å^3 per molecular unit. Then, the volume of the unit cell with $Z = 4$ is equal to 154.6 Å^3. The experimental unit cell volume for the orthorhombic $MgSiO_3$ perovskite is 162.45 Å^3. Therefore, the theoretical and experimental data are in satisfactory agreement, with due regard for a rough estimation of parameters in the strained-bond model.

Structure and Properties Determined by Minimizing the Cohesive Energy of a Crystal

The most advanced crystal chemical approach to the determination of an equilibrium atomic configuration and the properties of a crystal consists in finding the cohesive energy (lattice energy, atomization energy) at the minimum. The cohesive energy is written as the sum of pair potentials (in some cases, multiparticle interactions are also taken into account) in the form

$$U_{ij}(R_{ij}, f) = z_i z_j f^2/R_{ij} + \lambda \exp(-R_{ij}/\rho) - c_{ij}/R_{ij}^6. \quad (20)$$

Here, z_i and z_j are the atomic charges (valences), f is the degree of bond ionicity, $z_i f$ and $z_j f$ are the effective atomic charges, λ and ρ are the parameters of the repulsive potential, and c_{ij} is the van der Waals energy parameter.

The parameters of potential (20) can be *a priori* specified and then can be refined together with the atomic coordinates and unit cell parameters during the energy minimization. Such potentials [described by relationship (20)] has been repeatedly used to minimize the energy and to refine the structure of the orthorhombic $MgSiO_3$ perovskite (no less than six times by the late 1980s [18]). Since then, there have appeared approximately ten works devoted to calculations based on semiclassical potentials similar to that described by formula (20) [19]. As an example, we present the results obtained by Oganov in the last work [19]. The following parameters of the potentials were used at the last stage of calculations: $zf_{\text{Mg}} = +1.9104$, $zf_{\text{Si}} = +2.9043$, $zf_{\text{O}} = -1.6049$, $\lambda_{\text{Mg–O}} = 1007.526$ eV, $\rho_{\text{Mg–O}} = 0.2866$ Å, $\lambda_{\text{Si–O}} = 1108.983$ eV, $\rho_{\text{Si–O}} = 0.2827$ Å, $\lambda_{\text{O–O}} = 2023.8$ eV, $\rho_{\text{O–O}} = 0.2674$ Å, and $c_{\text{O–O}} = 13.83$ eV Å^6. The results of calculations of the structure (unit cell parameters, unit cell volume, atomic coordinates) and many properties (elastic constants C_{ij}, bulk modulus K, shear modulus G, Debye temperature ϑ, thermal expansion coefficient α, heat capacity C_V, entropy S) are compared with the experimental data in Table 6. The reader can easily see that the model structural parameters and the model properties of the crystal under investigation agree well with the true quantities. This gives grounds to turn to the determination of thermoelastic properties of the crystal and the construction of the equation of state at high temperatures and pressures, which provides a way of solving a number of fundamental problems associated with the geophysics and geochemistry of the Earth's depth.

Table 6. Comparison of the structural parameters and properties simulated by the semiclassical (atomistic) potentials and first-principles (*ab initio*) methods and experimental data for the magnesian silicate perovskite $MgSiO_3$

Property		Atomistic Potentials	*Ab initio*	Experiment
V_0, Å^3		162.31	157.87	162.45
a_0, Å		4.7822	4.7272	4.7747
b_0, Å		4.8960	4.8889	4.9319
c_0, Å		6.9322	6.8311	6.8987
Mg	x	0.5056	0.5160	0.5143
	y	0.5267	0.5576	0.5556
	z	1/4	1/4	1/4
Si (x, y, z)		(0; 1/2, 0)	(0; 1/2, 0)	(0; 1/2, 0)
O1	x	0.1026	0.1044	0.1037
	y	0.4620	0.4654	0.4655
	z	1/4	1/4	1/4
O2	x	0.1982	0.1969	0.1974
	y	0.2014	0.2015	0.2011
	z	0.5526	0.5539	0.5538
C_{11}	GPa	500	499	482
C_{22}		509	561	537
C_{33}		398	466	485
C_{12}		116	123	144
C_{13}		210	137	147
C_{23}		188	142	146
C_{44}		174	217	204
C_{55}		189	186	186
C_{66}		102	160	147
K, GPa		270.4	258.3	264.0
G, GPa		146.3	187.3	178.4
C_V		80.88		80.6
α		2.09		1.57 : 2.2
C_1, m/s		–	10953	11042
S		61.81		57.2
θ_n, K		984	1097	1078

Note: The thermal expansion coefficient α is expressed in terms of 10^{-5} K^{-1}, and the quantities C_V and S are given in terms of J/(mol K).

First-Principles (Ab Initio) Calculations of the Structure and Properties of Crystals

In recent years, increased interest has been expressed by researchers in calculations of the structure and properties of crystals with the use of modern *ab initio* (first-principles) quantum-mechanical methods.

Among them, the Hartree–Fock self-consistent field method and the density-functional theory method used in different variants (beginning with the local-density approximation to more exact generalized gradient approximations) are the most universally employed techniques. It is evident that these methods are beyond the scope of crystal chemical approaches; hence, the predictions and inferences made in the framework of the crystal chemistry can be only tentatively useful when choosing the most probable structural models.

In this respect, without going into the description of the comparative capabilities and computational procedures of the *ab initio* methods, we can illustrate their applicability by using the results of the calculations of the structure and many properties of the $MgSiO_3$ orthorhombic perovskite (Table 6), which were performed within the simplest local-density approximation of the density-functional theory [19]. As can be seen from Table 6, the structure and properties calculated within this approach are in good agreement with the experimental data, which, undeniably, suggest an excellent future for *ab initio* methods as applied to structural calculations. Moreover, the use of molecular-dynamics methods offers strong possibilities for predicting the behavior of crystals over the entire range of their stability, which, in turn, makes it possible to construct the complete equation of state and to investigate the conditions for stability of crystalline phases.

CONCLUSIONS

After reading the last sections of this paper, the impression can arise that classical methods and procedures of the crystal chemistry have already given way to more precise techniques for solving the basic structural chemical problem concerning the prediction of the structure and properties of a crystal with a known chemical composition. However, this is by no means the case, because the necessity of limiting the number of examined models, as before, remains an important problem. This can be explained by the fact that the time required to perform calculations with the use of semiclassical (atomistic) methods for minimizing the energy and, especially, first-principles calculations remains long and expensive. On the other hand, the simple methods and approaches developed in the framework of the classical crystal chemistry are considerably more economical and, which is particularly important, can be readily automated using personal computers. Thus, it is my opinion that only the use of an appropriate combination of all currently available methods, procedures, and approaches can provide the most efficient and economical way to achieve the main objective of crystal chemistry.

ACKNOWLEDGMENTS

I would like to thank my disciples L.S. Dubrovinskiĭ, N.A. Dubrovinskiĭ, N.N. Eremin, A.R. Oganov, I.Yu. Kantor, and others, who, at different times and different stages, took part in solving the problem. I am also grateful to L.E. Terent'eva for her assistance in preparing the manuscript.

This work was supported by the Russian Foundation for Basic Research (project nos. 96-15-98315, 99-05-65139, 02-05-64845, 00-15-98582), the State Program in Support of Leading Scientific Schools (project no. 1955.2003), and the International Association of Assistance for the promotion of cooperation with scientists from the New Independent States of the former Soviet Union (project no. INTAS 97-32174).

REFERENCES

1. T. S. Bush, C. R. A. Catlow, and P. D. Battle, J. Mater. Chem. **5**, 1269 (1995).
2. G. H. Rao and I. D. Brown, Acta Crystallogr., Sect. B: Struct. Sci. **54**, 221 (1998).
3. V. S. Urusov, Z. Kristallogr. **216**, 10 (2001).
4. M. O'Keeffe, Struct. Bonding (Berlin) **71**, 161 (1989).
5. V. S. Urusov and I. P. Orlov, Kristallografiya **44**, 736 (1999) [Crystallogr. Rep. **44**, 686 (1999)].
6. V. S. Urusov, Dokl. Akad. Nauk **380** (4), 506 (2001).
7. G. I. Daniel, *Maximum Entropy in Action*, Ed. by D. Buck and V. A. Macaulay (Clarendon Press, Oxford, 1991).
8. M. V. Vol'kenshteĭn, *Entropy and Information* (Nauka, Moscow, 1986).
9. V. S. Urusov, N. A. Dubrovinskaya, and L. S. Dubrovinskiĭ, *Design of Probable Crystal Structures of Minerals* (Mosk. Gos. Univ., Moscow, 1990).
10. A. V. Shubnikov and V. A. Koptsik, *Symmetry in Science and Art* (Nauka, Moscow, 1972).
11. A. M. Glazer, Acta Crystallogr., Sect. B: Struct. Crystallogr. Cryst. Chem. **28**, 3384 (1972).
12. P. M. Woodward, Acta Crystallogr., Sect. B: Struct. Sci. **53**, 32 (1997).
13. M. W. Lufaso and P. M. Woodward, Acta Crystallogr., Sect. B: Struct. Sci. **57**, 725 (2001).
14. V. A. Blatov, A. P. Shevchenko, and V. N. Serezhkin, Kristallografiya **42**, 773 (1997) [Crystallogr. Rep. **42**, 707 (1997)].
15. S. Sasaki, C. T. Prewitt, and R. C. Liebermann, Am. Mineral. **68**, 1189 (1983).
16. V. M. Talanov, *Energetic Crystal Chemistry of Multisublattice Crystals* (Rostov. Gos. Univ., Rostov-on-Don, 1986).
17. V. P. Sakhnenko, N. V. Dergunova, and L. A. Reznichenko, *Energetic Crystal Chemistry of Solid Solutions of the Oxygen-Octahedral Type Compounds and Design of Piezoceramic Materials* (Rostov. Gos. Univ., Rostov-on-Don, 1999).
18. V. S. Urusov and L. S. Dubrovinskiĭ, *Computer Simulation of the Structure and Properties of Minerals* (Mosk. Gos. Univ., Moscow, 1989).
19. A. R. Oganov, *Computer Simulation Studies of Minerals* (Univ. of London, London, 2002).

Translated by O. Borovik-Romanova

Crystallography Reports, Vol. 49, No. 4, 2004, pp. 573–578. Translated from Kristallografiya, Vol. 49, No. 4, 2004, pp. 649–654.
Original Russian Text Copyright © 2004 by Osaulenko, Repnikova, Makarov, Suvorova.

DIFFRACTION AND SCATTERING OF IONIZING RADIATION

X-ray Study of the Structure of Multicomponent Glasses Based on Mining-Industry Waste

R. N. Osaulenko*, E. A. Repnikova*, V. N. Makarov, and O. V. Suvorova****

** Petrozavodsk State University, pr. Lenina, Petrozavodsk, 185640 Karelia, Russia*
e-mail: erepn@psu.karelia.ru
*** Institute of Rare Element and Mineral Chemistry and Technology, Kola Research Center, Russian Academy of Sciences,*
ul. Fersmana 14, Apatity, Murmansk oblast, 184200 Russia

Received September 4, 2000; in final form, May 17, 2002

Abstract—The short-range order and microinhomogeneity structure of laboratory samples of glasses belonging to the diopside–orthoclase–apatite system with different percentages of components were investigated by X-ray diffraction and small-angle scattering. A correlation between a change in the chemical composition of a glass, causing its segregation, and the short-range order parameters was ascertained: an increase in the apatite content leads to a change in the short-range order parameters. The use of the X-ray small-angle scattering technique made it possible to reveal inhomogeneities of electron density in the glasses under study and the dependence of the sizes of inhomogeneities on the glass composition. © *2004 MAIK “Nauka/Interperiodica”*.

INTRODUCTION

In recent years, the field of application of basalt fibers and casting has been significantly widened. In particular, they can be used for production of heat-insulating mats and cords and sound-absorbing and filter materials. Due to its high chemical durability, basalt casting can be used in the chemicals industry. The application of mining-industry waste significantly reduces the cost of such materials. The development of industrial technologies in this field depends on obtaining glasses with the desired properties. In this context, prediction of these properties—depending on the chemical composition of a glass and conditions of its preparation—plays an important role. In particular, multicomponent glasses are of interest. Information on the structure of these glasses is important both from the scientific point of view and for their practical use in new material production technologies. To date, information obtained in this field is rather scarce.

In this paper, we report the results of investigations of the short-range order and microinhomogeneities in diopside–orthoclase–apatite glasses by X-ray diffraction analysis. Previous studies [1] showed that, when the content of apatite in the glasses of this system is increased to a certain value, a transition from the homogeneous state to a state characterized by two immiscible phases occurs. It is of interest to find out how this phenomenon is related to changes in the microstructure of the objects studied.

EXPERIMENTAL SAMPLES

Figure 1 shows the phase diagram of the diopside–orthoclase–apatite system, where points *1*, *2*, *3*, and *4* denote the chemical composition of the studied glass samples. The curve in the diagram represents the boundary, below which (at a corresponding concentration of the components) the glass structure is homogeneous; above this boundary, the glass separates into two immiscible phases.

Samples of apatite ($Ca_3(PO_4)_3F$), diopside ($CaMgSi_2O_6$), and orthoclase ($KAlSi_3O_8$) were prepared, respectively, from apatite concentrate (AO Apatite), a monomineral fraction of diopside extracted from phlogopite–diopside rocks of the

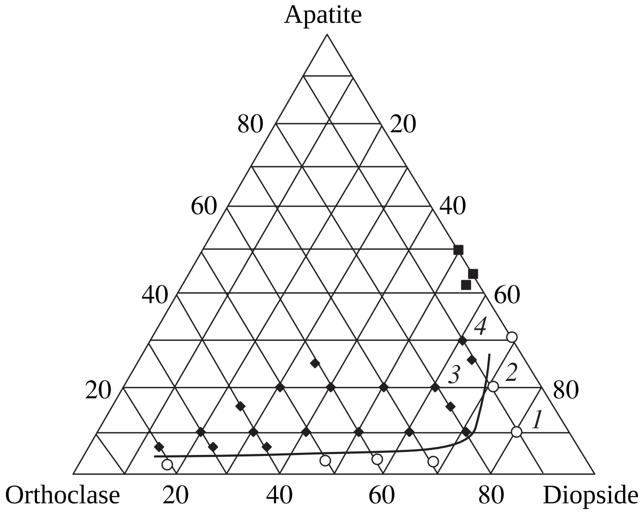

Fig. 1. Solubility of apatite in the apatite–orthoclase–diopside system. (○) Homogeneous melt at 1400°C, (◆) two liquid immiscible phases, (■) melt and crystals at the same temperature.

1063-7745/04/4904-0573$26.00 © 2004 MAIK “Nauka/Interperiodica”

Kovdor phlogopite deposit [1], and a monomineral fraction of potassium feldspar from the Kovdor deposit. The chemical compositions of diopside and potassium feldspar (orthoclase) somewhat differ from ideally stoichiometric (Table 1). Based on the percentages of oxides in the minerals under investigation, we calculated the formula compositions of the samples:

1: $O_{0.608}Si_{0.184}Al_{0.012}K_{0.008}Ti_{0.0008}Ca_{0.092}Fe_{0.0077}P_{0.0155}F_{0.0052}Mg_{0.0631}Na_{0.0024}$
2: $O_{0.6108}Si_{0.1645}Al_{0.0116}K_{0.008}Ti_{0.00077}Ca_{0.099}Fe_{0.0067}P_{0.031}F_{0.01}Mg_{0.055}Na_{0.0023}$
3: $O_{0.6121}Si_{0.1545}Al_{0.0113}K_{0.008}Ti_{0.00072}Ca_{0.102}Fe_{0.0063}P_{0.039}F_{0.013}Mg_{0.0514}Na_{0.0022}$
4: $O_{0.6134}Si_{0.1446}Al_{0.011}K_{0.0081}Ti_{0.00066}Ca_{0.105}Fe_{0.0058}P_{0.047}F_{0.016}Mg_{0.048}Na_{0.0021}$

With regard to the effect of temperature on the solubility of apatite in aluminosilicate melts, the blend was prepared in corundum crucibles at the same temperature (1400°C) [1]. The melt was kept at this temperature for 3 h for complete homogenization. In order to relieve stresses, the prepared glass was annealed at 600°C. The glass-transition temperature was approximately the same for all the samples (in the vicinity of 750°C).

EXPERIMENTAL AND CALCULATION TECHNIQUES

The short-range order parameters were determined by X-ray diffraction analysis on a DRON-3.0 automated diffractometer in MoK_α radiation with monochromatization of the primary and diffracted beams in reflection geometry and in the s range ($s = 4\pi\sin\theta/\lambda$, where s is the diffraction vector, θ is the diffraction angle, and λ is the radiation wavelength) from 0.35 to 16.6 Å^{-1}. Fused quartz was used as a reference. The experimental values of the reflection intensities were corrected to scattering from air, polarization, and Compton scattering, after which the short-range order parameters were calculated by the Warren–Finback method.

Table 1. Chemical compositions of diopside and orthoclase

Oxide	Weight content, %	
	diopside	orthoclase
SiO_2	55.36	62.93
TiO_2	0.40	–
Al_2O_3	1.30	17.75
$FeO + Fe_2O_3$	3.50	–
MgO	14.51	0.02
CaO	24.63	0.16
Na_2O	0.20	2.65
K_2O	0.10	16.76

According to Warren [2, 3], the distribution of pair functions is constructed in the form

$$\sum_i\sum_j \frac{N_{ij}}{r_{ij}}P_{ij}(r) = 2\pi^2 r\rho_e\sum_j Z_j + \int_0^{s_{\max}} I_i(s)\exp(-\alpha^2 s^2)g^{-2}(s)\sin(sr)ds, \tag{1}$$

where N_{ij} is the number of atoms of type j on the ith coordination sphere; r_{ij} is the radius of the ith coordination sphere for j-type atoms; ρ_e is the electron density; Z_j is the atomic number of the elements forming a material; $I_i(s)$ is the interference function of the i-type atoms; $\exp(-\alpha_1^2 s^2)$ is the decay factor, the action of which manifests itself in the reduction of the influence of experimental errors; and $g^{-2}(s)$ is the sharpening factor, which ensures a higher contrast of the interference pattern at large values of s. The pair functions have the form

$$P_{ij}(r) = \int_0^{s_{\max}} f_i f_j \sin(sr_{ij})\exp(-\alpha^2 s^2)g^{-2}(s)\sin(sr)ds, \tag{2}$$

where $f_i f_j$ are the atomic scattering functions of the i- and j-type atoms.

The pair function characterizes the distribution of the electron density of a particular pair of atoms and depends on the types of atoms forming the pair. The left-hand side of (1) is calculated from the experimental intensities. Let us denote it as $D(r)$ and the integrand as $H(s)$. Then, $D(r) = 2\pi^2 r\rho_e\sum_j Z_j + \int_0^{s_{\max}} H(s)\sin(sr)ds$. $D(r)$ is the distribution of the sum of pair functions $P_{ij}(r)$ and characterizes the distribution of electron density in a material. The positions of peaks on the curve $D(r)$ give the corresponding interatomic distances. In real noncrystalline materials, the widths of the maxima of the pair functions $P_{ij}(r)$ increase due to the dispersion σ_{ij} of interatomic distances with respect to the average value of r_{ij}. These values are fitted by the method of successive approximations; the criterion is a sufficiently good coincidence between the left- and the

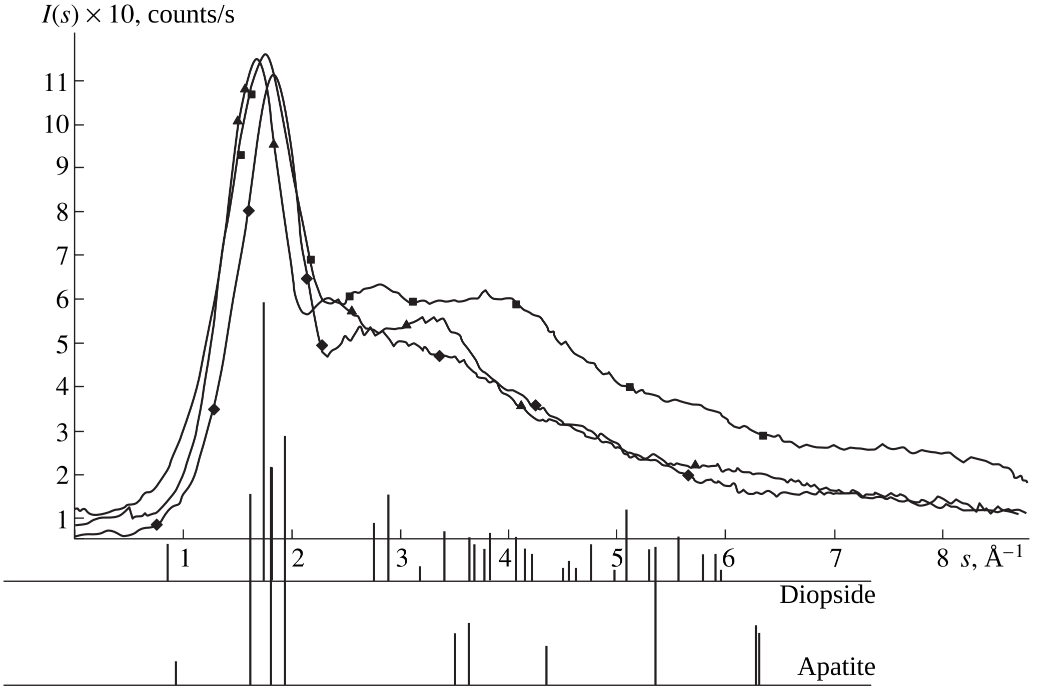

Fig. 2. Dependence of the scattering intensity *I* on the diffraction vector *s* for samples (■) 1, (▲) 2, and (◆) 3 and the bar graphs for diopside and apatite crystals.

right-hand sides of Eq. (1). The coordination numbers for the chosen pairs of atoms were determined by the least-squares method. The Warren–Finback method, being fairly informative, makes it possible to analyze the differences in the short-range order structure on a large number of coordination spheres with high accuracy [4–6]. The error in determining the short-range order parameters amounted to 3–5%.

The microinhomogeneous structure of the glass samples was investigated by the method of small-angle scattering (SAS) of X-rays in a KRM-1 X-ray chamber using copper, Ni-filtered, radiation. Glassy carbon was used as a reference. The angle dependences of the scattering intensity were obtained in the range of angles ε from 7 min of arc to 7° with step $d\varepsilon$ = 1–10 min of arc. The values of the scattering intensity measured from different samples were normalized to the same thickness. The portion of the curve $I(\varepsilon)$ on which the scattering intensity becomes angle-independent was used to determine the intensity of thermal diffuse scattering with subsequent subtraction of the found value from the total scattering intensity for each sample. In addition, in calculating the intensity, we introduced a collimation correction using the method proposed by Filipovich [7] in the approximation of an infinite X-ray beam. The radii of gyration of inhomogeneities of electron density were calculated by the Guinier method [8]. According to this method, the logarithmic dependence $\ln I(\varepsilon) = f(\varepsilon^2)$ for a monodisperse system is a straight line with the slope α, for which

$$\tan\alpha = -\frac{4\pi^2}{3\lambda^2}R_0^2, \qquad (3)$$

where R_0 is the radius of gyration of a void and λ is the X-ray radiation wavelength.

Then, the radius of gyration of an inhomogeneity can be written as

$$R_0 = \frac{\lambda}{2\pi}\sqrt{|3\tan\alpha|}. \qquad (4)$$

The value of R_0 can be easily determined by plotting the dependence $\ln I(\varepsilon) = f(\varepsilon^2)$ and measuring its slope. In the case of a polydisperse system with a small number of fractions of inhomogeneities, this dependence is a polygonal line. With an increase in the number of fractions, it becomes smoother. In this case, the so-called method of tangents is used, in which portions of a curve are approximated by tangents. It should be noted that the accuracy of this method is rather low; thus, it allows one only to estimate the presence and sizes of inhomogeneities in a sample. In order to minimize experimental error, the SAS data were averaged over several X-ray diffraction patterns. The error in the values of the quantitative parameters obtained by the SAS method was 5–10%.

RESULTS AND DISCUSSION

Figure 2 shows the distributions of the scattering intensity $I(s)$ for samples 1, 2, and 3 and, for comparison, the bar graphs of diopside and apatite crystals. It is obvious that the samples of the minerals under study are amorphous and that the form of the first maximum in the $I(s)$ curve is well described by the corresponding maxima characteristic of the crystalline modifications

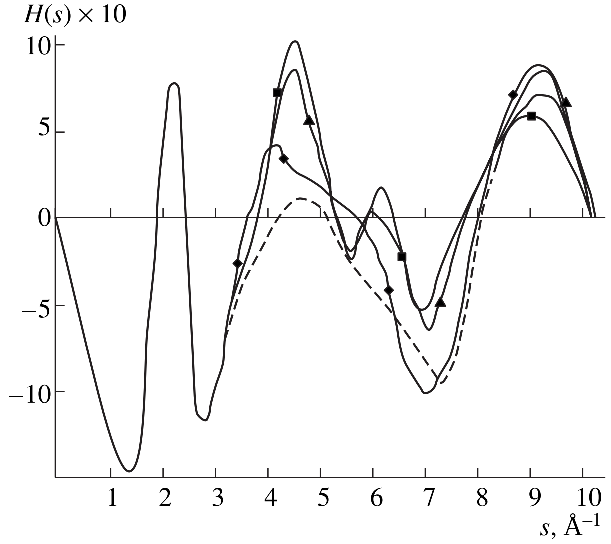

Fig. 3. Dependences $H(s)$ for samples (▲) 1, (■) 2, (◆) 3, and (dashed line) 4.

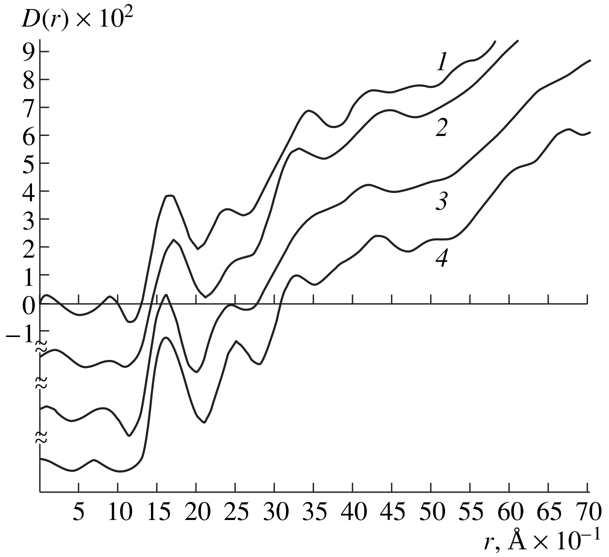

Fig. 4. Dependences $D(r)$ for samples (*1*) 1, (*2*) 2, (*3*) 3, and (*4*) 4.

of these minerals. The differences in the diffraction patterns are more pronounced in the curves $H(s)$ (Fig. 3). The calculated values of the function $H(s)$ were used to obtain the distributions of the pair functions $D(r)$ in the studied samples (Fig. 4). The positions of the first maxima for samples 1 and 2 are close to each other and lie in the vicinity of $r \sim 1.6$ Å (Fig. 4), which is characteristic of the interatomic distance Si–O in a silicon–oxygen tetrahedron. For large values of r, the difference in the shape of the curves $D(r)$ can be clearly seen, which indicates the difference in the short-range order for samples with different chemical compositions. For samples 3 and 4, the first maximum is shifted somewhat to the left as compared to samples 1 and 2, which is indicative of the decrease in the corresponding interatomic distance.

The simulation of the short-range order in glasses 1 and 2 was performed by the method of smearing the diopside lattice, since the percentage of diopside significantly exceeds that of apatite in these samples. Stoichiometric diopside belongs to the chain silicates; it has a monoclinic structure (sp. gr. $C2/c$) with the unit cell parameters $a = 9.799$ Å, $b = 9.029$ Å, $c = 5.274$ Å, and $\beta = 106°$. The atomic coordinates, lattice constants, and angles between the X, Y, and Z axes were used to calculate the weighted mean values of the interatomic distances and coordination numbers for diopside crystals (Table 2). The results obtained for sample 1 (listed in the same table) suggest that the interatomic distances corresponding to the coordination spheres Si–O, Ca–O, O–O, and Ca–Mg in the glasses under study correspond to similar coordination spheres in crystalline diopside. At the same time, the radii of the coordination spheres of the Si–Si and Ca–Si types decrease. The change in the length of the Si–Si bond indicates a decrease in the Si–O–Si angles. In addition, a significant increase in the dispersion of interatomic distances in the vitreous state in comparison with the crystalline phase is observed. Figure 5 shows the function $D(r)$ for sample 1, the first seven contributions from the corresponding spheres, and the theoretical curve $D(r)$ calculated for the final fitting (Table 2). Simulation of the short-range order for sample 2, the chemical composition of which corresponds to the homogeneity region, showed that the short-range order parameters differ insignificantly from the corresponding parameters for sample 1.

Table 2. Short-range order parameters: r_{ij}, $N_{ij} \pm \Delta N_{ij}$, and σ_{ij} for sample 1; and r_{ij}, N_{ij}, and Δr_{ij} for diopside crystals

Type of sphere	Sample 1			Diopside crystal		
	r_{ij}, Å	$N_{ij} \pm \Delta N_{ij}$, atoms	σ_{ij}, Å	r_{ij}, Å	N_{ij}, atoms	Δr_{ij}, Å
Si–O	1.65	3.9 ± 0.1	0.005	1.63	4.0	0.00
Fe–O	1.83	5.6 ± 0.5	0.25	1.76	6.0	0.04
Ca–O	2.31	8.0 ± 0.2	0.28	2.31	8.0	0.04
O–O	2.67	4.1 ± 0.1	0.3	2.67	4.0	0.05
Si–Si	2.89	4.1 ± 0.2	0.2	3.15	4.2	0.01
Ca–Si	3.26	8.1 ± 0.4	0.25	3.32	8.1	0.02
Ca–Mg	3.56	2.8 ± 0.2	0.1	3.54	2.5	0.05

The short-range order in samples 3 and 4, the chemical composition of which corresponds to the segregation region, significantly differs from that in samples 1 and 2. Simulation of the function of radial distribution of the electron density $D(r)$ by smearing the diopside lattice led to a considerable disagreement between the theoretical and experimental dependences. The reason

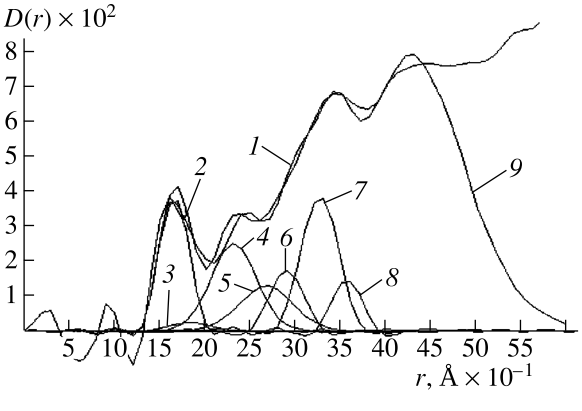

Fig. 5. Experimental dependence $D(r)$ and partial distribution functions for sample 1: (*1*) $D_{\text{exper}}(r)$, (*2*) Si–O, (*3*) Fe–O, (*4*) Ca–O, (*5*) O–O, (*6*) Si–Si, (*7*) Ca–Si, (*8*) Ca–Mg, and (*9*) $D_{\text{theor}}(r)$.

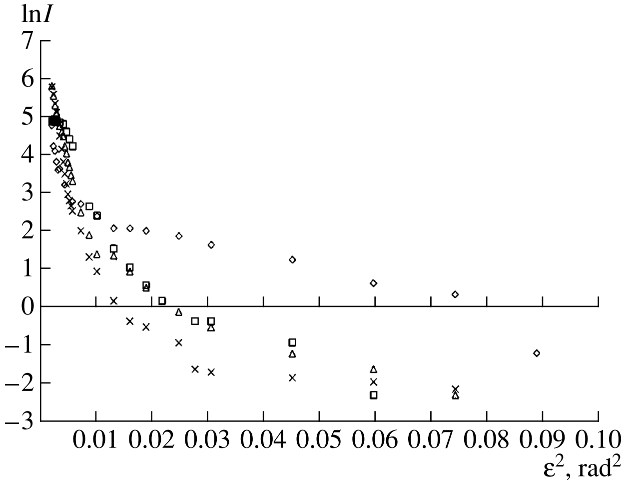

Fig. 6. Dependences of the logarithm of small-angle scattering intensity on the squared scattering angle for samples (◇) 1, (□) 2, (△) 3, and (×) 4.

for this is the contribution of atomic pairs (which were previously ignored) to the dependence $D(r)$. When the apatite content in a glass exceeds 20 wt %, the largest contribution to the function $D(r)$ is from the P–O pairs, for which r_{1j} = 1.55 Å and N_{1j} = 6.2 atoms. According to the calculations, 1 P–O band is for 16 Si–O bonds. In addition, the dispersion of interatomic distances decreases. The final results of calculation of the short-range-order parameters of samples 3 and 4 are listed in Tables 3 and 4. The listed values of the Si–O distance are averaged for cation–oxygen polyhedra with Si, Al, and P cations; therefore, it should be considered the real interatomic distance in a silicon–oxygen tetrahedron. The values of r_{ij}, N_{ij}, and Δr_{ij} for diopside and apatite crystals were calculated by combining the coordination spheres similar in r_{ij}. The data of Tables 3 and 4 suggest that, with a change in the chemical composition of a glass in the segregation region, the radii of the coordination spheres do not change significantly, while the dispersion σ_{ij} continues to decrease. This is indicative of the increase in the degree of ordering with increasing the apatite content in the glass.

Figure 6 shows the dependences of the logarithm of the SAS intensity on the squared scattering angle. The shape of the scattering curves indicates the presence of a polydisperse system of electron-density inhomogeneities in the samples under investigation. Two size fractions of inhomogeneities can be selected from the SAS curves with a large degree of reliability (Table 5). On the basis of the above results, we can conclude that the radius of gyration of inhomogeneities belonging to the small-size fraction R_1 is approximately the same for all the glass samples, whereas, for the large-size fraction R_2, the radius of gyration increases from samples 1 and 2 to samples 3 and 4 by about a factor of three. Apparently, the limited solubility of apatite in the diopside-

Table 3. Short-range order parameters r_{ij}, $N_{ij} \pm \Delta N_{ij}$, and σ_{ij} for sample 3 and theoretically calculated and combined parameters for diopside and apatite crystals

Type of sphere	Sample 3			Diopside and apatite crystals		
	r_{ij}, Å	$N_{ij} \pm \Delta N_{ij}$, atoms	σ_{ij}, Å	r_{ij}, Å	N_{ij}, atoms	Δr_{ij}, Å
Si–O	1.61	4.53 ± 0.10	0.005	1.62	4.85	0.01
Fe–O	1.83	6.1 ± 0.2	0.02	1.76	6.0	0.08
Ca–O	2.37	7.5 ± 0.1	0.2	2.33	8.2	0.09
O–O	2.68	3.9 ± 0.1	0.02	2.67	4.1	0.05
Si–Si	2.95	3.8 ± 0.3	0.09	3.15	4.2	0.01
Ca–Si	3.24	8.0 ± 0.1	0.25	3.28	8.3	0.03
Ca–Mg	3.60	4.4 ± 0.4	0.08	3.54	2.5	0.08

Table 4. Short-range order parameters r_{ij}, $N_{ij} \pm \Delta N_{ij}$, and σ_{ij} for sample 4

Type of sphere	Sample 4			Diopside and apatite crystals		
	r_{ij}, Å	$N_{ij} \pm \Delta N_{ij}$, atoms	σ_{ij}, Å	r_{ij}, Å	N_{ij}, atoms	Δr_{ij}, Å
Si–O	1.62	4.88 ± 0.15	0.005	1.62	4.85	0.01
Fe–O	1.79	6.2 ± 0.1	0.01	1.76	6.0	0.08
Ca–O	2.37	7.7 ± 0.1	0.31	2.33	8.2	0.09
O–O	2.70	4.9 ± 0.1	0.005	2.67	4.1	0.05
Si–Si	2.94	4.1 ± 0.2	0.05	3.15	4.2	0.01
Ca–Si	3.24	6.5 ± 0.12	0.05	3.28	8.3	0.03
Ca–Mg	3.60	4.7 ± 0.3	0.01	3.54	2.5	0.08

Table 5. Radii of gyration of inhomogeneities in small-size and large-size fractions, R_1 and R_2

Sample no.	$R_1 \pm \Delta R$, Å	$R_2 \pm \Delta R$, Å
1	10 ± 2	83 ± 5
2	18 ± 2	76 ± 5
3	14 ± 2	210 ± 10
4	16 ± 2	230 ± 10

containing silicate melt leads to the occurrence (at an apatite content of more than 20 wt %) of a "glass-in-glass" structure. Since diopside and apatite have different densities (3.3 and 4.1 g/cm^3, respectively), we can suggest that the found inhomogeneities are regions with a composition similar to the composition of apatite and are distributed in the matrix of supercooled silicate melt.

CONCLUSIONS

It has been ascertained that multicomponent diopside–orthoclase–apatite glasses based on mining-industry waste have an amorphous structure similar to the structure of diopside when the content of the latter in a glass exceeds 65 wt %. An increase in apatite content by more than 20 wt % significantly affects the character of the short-range ordering of atoms in the glass. In samples 3 and 4, the increase in the influence of phosphor–oxygen bonds and the decrease in the dispersion of interatomic distances within the coordination spheres under consideration are pronounced. Apparently, the decrease in the dispersion is related to the occurrence of a more ordered structure in segregated glasses. The short-range order in these glasses corresponds to the positions of atoms in crystalline apatite.

The studied glasses have a microinhomogeneous structure, which manifests itself in the SAS dependences. With an increase in the apatite content of more than 20 wt %, the radii of gyration of electron-density inhomogeneities belonging to the large-size fraction increase noticeably.

REFERENCES

1. V. N. Makarov and O. V. Suvorova, Steklo Keram., No. 2, 18 (1997).
2. B. E. Warren, *X-ray Diffraction* (Addison-Wesley, Reading, Mass., 1969).
3. B. E. Warren, Kristallografiya **16** (6), 1262 (1971) [Sov. Phys. Crystallogr. **16**, 1106 (1971)].
4. E. A. Repnikova, Kristallografiya **43** (2), 361 (1998) [Crystallogr. Rep. **43**, 327 (1998)].
5. E. A. Repnikova and V. A. Gurtov, Kristallografiya **35** (2), 422 (1990) [Sov. Phys. Crystallogr. **35**, 242 (1990)].
6. L. A. Aleshina and A. D. Fofanov, *X-ray Analysis of Amorphous Materials* (Petrozavod. Gos. Univ., Petrozavodsk, 1987).
7. V. N. Filipovich, Zh. Tekh. Fiz. **27** (5), 1029 (1975) [Sov. Phys. Tech. Phys. **2**, 938 (1975)].
8. A. Guinier, *Théorie et Technique de la Radiocristallographie* (Dunod, Paris, 1956; Fizmatgiz, Moscow, 1961).

Translated by Yu. Sin'kov

Crystallography Reports, Vol. 49, No. 4, 2004, pp. 579–584. Translated from Kristallografiya, Vol. 49, No. 4, 2004, pp. 655–661.
Original Russian Text Copyright © 2004 by Zanin, Aleĭnikova, Antipin, Afanas'ev.

Analysis of Chemical Bonding in Zn_3P_2 Crystals from X-ray Diffraction Data

I. E. Zanin*, K. B. Aleĭnikova*, M. Yu. Antipin, and M. M. Afanas'ev***

** Voronezh State University, Universitetskaya pl. 1, Voronezh, 394006 Russia*
e-mail: zie@main.vsu.ru
*** Nesmeyanov Institute of Organoelement Compounds, Russian Academy of Sciences, ul. Vavilova 28, Moscow, 117813 Russia*

Received May 20, 2003

Abstract—The refined data on the crystal structure of Zn_3P_2 (**I**) provide evidence for a tetrahedral coordination of metal atoms, which is characteristic of covalent structures with sp^3-hybridized orbitals. Deformation-electron-density maps for crystal **I**, which were constructed from high-precision X-ray diffraction data, confirm the predominantly covalent character of bonds in this compound. The deformation-density maps clearly show covalent bridges with their peaks shifted toward electronegative phosphorus atoms. The longer the bond, the larger the shift. The presence of delocalized electrons indicates that the bonding mechanism is partially metallic. *© 2004 MAIK "Nauka/Interperiodica".*

INTRODUCTION

The Zn–P phase diagram is a simple system containing two chemical compounds [1]. One of these compounds, which has formula composition Zn_3P_2, satisfies the normal rules of valence. Another compound, with composition ZnP_2, follows the rule of four electrons and is an analogue of the Group IV elements. The structure of the ZnP_2 compound, which has two polymorphs, has been studied repeatedly [2, 3]. The chemical interactions in both polymorphs have been analyzed in detail [4]. The structure of Zn_3P_2 has not been refined since 1935 [5]. In terms of properties, this compound belongs to the indirect-gap semiconductors; the band-gap width is ~1.20 eV.

Previously, it was assumed [6] that Zn_3P_2 can be assigned to compounds with a predominantly ionic bond character. The bonding scheme for compound **I** is shown in Fig. 1. According to this scheme, zinc and phosphorus atoms acquire positive and negative charges, respectively (two $4s^2$ valence electrons pass from each of three zinc atoms to two phosphorus atoms, giving rise to a $3s^23p^6$ configuration of their valence shells). The ionic component of the chemical bond makes the major contribution to the chemical interaction.

However, data on the crystal structure (a tetrahedral coordination of metal atoms) and semiconducting properties of Zn_3P_2 are indicative of a substantial contribution made by the covalent component to the chemical bond.

With the aim of studying the characteristic features of the chemical interaction between atoms in Zn_3P_2 crystals on the basis of high-precision X-ray diffraction data, we constructed deformation-electron-density maps at Zn–P bonds of different lengths.

EXPERIMENTAL

Prismatic Zn_3P_2 single crystals were grown by vapor-phase deposition and ground to ~0.3-mm spheres. X-ray diffraction data (30 115 reflections) were collected on an automated Smart-CCD diffractometer (MoK_α radiation, graphite incident-beam monochromator, $\theta < 75°$, full sphere of reciprocal space) at 173 K (at the Center of X-ray Diffraction Studies of the Nesmeyanov Institute of Organoelement Compounds of the Russian Academy of Sciences, Moscow). The **I** crystals are tetragonal, sp. gr. $P4_2/nmc$, $Z = 8$, $a = b = 8.0785(2)$ Å, $c = 11.3966(4)$ Å. The structure was

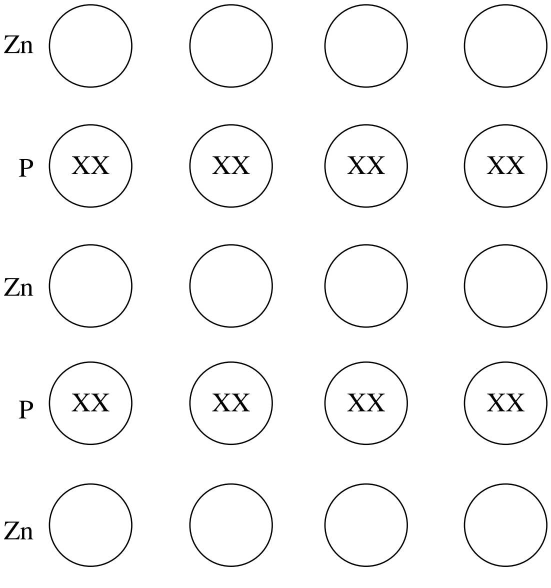

Fig. 1. Bonding scheme in the Zn_3P_2 crystal on the assumption of an ionic bonding character.

Table 1. Atomic coordinates and isotropic thermal parameters (Å^2) for the crystal structure of **I**

Atom	x	y	z	U_{iso}
Zn(1)	0.53251(2)	0.75000	0.13336(2)	0.002
Zn(2)	0.25000	0.50333(2)	0.10381(2)	0.002
Zn(3)	0.46763(2)	0.75000	–0.14323(2)	0.003
P(1)	0.25000	0.75000	–0.00292(5)	0.001
P(2)	0.49572(3)	0.50428(3)	0.25000	0.001
P(3)	0.75000	0.75000	–0.00571(4)	0.001

Table 2. Bond lengths d (Å) in the Zn_3P_2 crystal structure

Bond	d	Bond	d
Zn(1)–P(3)	2.3662(3)	P(1)–Zn(3)	2.3765(4)
Zn(1)–P(2*a*)	2.4074(2)	P(1)–Zn(1*c*)	2.7606(4)
Zn(1)–P(2*j*)	2.4074(2)	P(1)–Zn(1)	2.7606(4)
Zn(1)–P(1)	2.7606(4)	P(2)–Zn(3)	2.4058(2)
Zn(2)–P(3*f*)	2.3320(3)	P(2)–Zn(3*g*)	2.4058(2)
Zn(2)–P(1)	2.3346(4)	P(2)–Zn(1*d*)	2.4074(2)
Zn(2)–P(2*a*)	2.5916(2)	P(2)–Zn(1*h*)	2.4074(2)
Zn(2)–P(2*n*)	2.5916(2)	P(2)–Zn(2*d*)	2.5916(2)
Zn(3)–P(1)	2.3765(4)	P(2)–Zn(2*h*)	2.5916(2)
Zn(3)–P(2)	2.4058(2)	P(3)–Zn(2*e*)	2.3320(3)
Zn(3)–P(2*l*)	2.4058(2)	P(3)–Zn(2*h*)	2.3320(3)
Zn(3)–P(3)	2.7676(3)	P(3)–Zn(1)	2.3662(3)
P(1)–Zn(2*c*)	2.3346(4)	P(3)–Zn(1*b*)	2.3662(3)
P(1)–Zn(2)	2.3346(4)	P(3)–Zn(3*b*)	2.7676(3)
P(1)–Zn(3*c*)	2.3765(4)	P(3)–Zn(3)	2.7676(3)

Note: The atoms labeled by letters are generated from the basis atoms by the following symmetry transformations: $a = 1/2 - y, x, -1/2 + z$; $f = 1/2 + x, 1 - y, -z$; $b = 1/2 - x, 1/2 - y, z$; $g = 1/2 + y, -1/2 + x, 1/2 - z$; $c = 3/2 - x, 1/2 - y, z$; $h = 1 - x, -1/2 + y, -z$; $d = y, 1/2 - x, 1/2 + z$; $l = 1/2 + y, 1 - x, 1/2 - z$; $e = -1/2 + x, 1 - y, -z$; $n = 1/2 + x, 1/2 + y, -z$.

solved by the heavy-atom method and refined anisotropically by the full-matrix least-squares method with the use of a SHELXTL PLUS 4.2 software package [7] (refinement against F_0^2). An empirical absorption correction was applied using Smart-CCD software. The absolute structure was confirmed by calculation of the Flack parameter [8]. The final R factor was 2.67% (based on 2158 independent reflections with $F > 4\sigma(F)$. The atomic coordinates, bond lengths, and bond angles are listed in Tables 1, 2, and 3, respectively. The structure of crystal **I** was described in detail in [9].

RESULTS AND DISCUSSION

Chemical analysis of Zn_3P_2 crystals [9] has shown that phosphorus atoms form a cubic close packing in which three-quarters of the tetrahedral sites are occupied by zinc atoms. The figure of merit calculated from positions corresponding to the sites of the ideal close packing is 60%. This structure can be considered an imperfect antifluorite structure from which one-quarter of the metal atoms have been removed. In the real structure, phosphorus atoms are located in the centers of weakly distorted cubes (Fig. 2). Six out of eight vertices of each cube are occupied by three independent zinc atoms—Zn(1), Zn(2), and Zn(3) (two atoms of each type)—located in the 8*g* sites of the space group $P4_2/nmc$. Metal atoms of each independent type occupy two vertices of the coordination cube on the face diagonals. Two unoccupied vertices are also located at the ends of the face diagonal of this coordination polyhedron. The P(1) (4*c* site) and P(3) (4*d* site) atoms each form two long bonds with the Zn(1) and Zn(3) atoms (2.7606(4) and 2.7676(3), respectively) and four very short bonds with other zinc atoms. The latter bond lengths (2.3346(4)–2.3765(4) and 2.3320(3)–2.3662(3) Å; the average values are 2.3556(4) and 2.3491(3) Å, respectively; see Table 2) are smaller than the sum of the tetrahedral radii of these elements (2.41 Å, according to [6]). Taking into account the nearly identical coordination environment (two long and four short bonds with zinc atoms) and a good correlation between the bond angles (see Tables 2, 3), these two independent P atoms in the structure of **I** can be considered analogous atoms. The atom P(2) (8*f* site) differs substantially from the two aforementioned phosphorus atoms and is characterized by the presence of six "balanced" bonds, their lengths (2.4058(2)–2.5916(2) Å; the average value is 2.4683(2) Å) being approximately equal to the sum of the tetrahedral radii.

Analysis of the coordination polyhedra demonstrated that Zn_3P_2 crystals have a highly ordered structure (many planar sections containing numerous atoms can be distinguished). In each coordination polyhedron (pseudocube) of a phosphorus atom, one can construct a (110)-type plane containing five atoms simultaneously, four zinc atoms and a central phosphorus atom (see Fig. 2). The deviations of the atoms from the plane are smaller than 0.008 Å. The sum of the bond angles around the central phosphorus atom is 360°. For the analogous P(1) and P(3) atoms, both the longest and shortest bonds are located in this plane.

The zinc atoms are located in weakly distorted tetrahedra formed by phosphorus atoms (Fig. 3). Each of three independent zinc atoms forms two bonds with a P(2) atom (their lengths being approximately equal to the sum of the tetrahedral radii), one bond with a P(1) atom, and one bond with a P(3) atom. The Zn(1)–P(3) and Zn(3)–P(1) bonds are short and have nearly identical lengths (2.3662(3) and 2.3765(3) Å, respectively). The Zn(1)–P(1) and Zn(3)–P(3) bonds are also similar in length (2.7606(4) and 2.7676(3) Å, respectively) and are the longest of all the Zn–P bonds. The bond angles at these two atoms also correlate well with each other.

Table 3. Bond angles (deg) in an **I** crystal

P(1)–Zn(1)–P(3)	103.70(3)	P(1)–Zn(1)–P(2*a*)	102.04(2)	P(1)–Zn(1)–P(2*j*)	102.04(2)
P(3)–Zn(1)–P(2*a*)	117.49(1)	P(3)–Zn(1)–P(2*j*)	117.49(1)	P(2*a*)–Zn(1)–P(2*j*)	111.07(2)
P(1)–Zn(2)–P(2*a*)	109.40(2)	P(1)–Zn(2)–P(3*f*)	119.98(3)	P(1)–Zn(2)–P(2*n*)	109.40(2)
P(2*a*)–Zn(2)–P(3*f*)	108.12(2)	P(2*a*)–Zn(2)–P(2*n*)	99.98(2)	P(3*f*)–Zn(2)–P(2*n*)	108.12(2)
P(1)–Zn(3)–P(2)	115.54(1)	P(1)–Zn(3)–P(3)	103.23(3)	P(1)–Zn(3)–P(2*l*)	115.54(1)
P(2)–Zn(3)–P(3)	100.66(2)	P(2)–Zn(3)–P(2*l*)	117.29(2)	P(3)–Zn(3)–P(2*l*)	100.66(2)
Zn(1)–P(1)–Zn(2)	72.96(2)	Zn(1)–P(1)–Zn(3)	76.52(1)	Zn(1)–P(1)–Zn(1*c*)	111.53(3)
Zn(1)–P(1)–Zn(2*c*)	72.96(2)	Zn(1)–P(1)–Zn(3*c*)	171.95(3)	Zn(2)–P(1)–Zn(3)	110.52(1)
Zn(2)–P(1)–Zn(1*c*)	72.96(2)	Zn(2)–P(1)–Zn(2*c*)	117.21(4)	Zn(2)–P(1)–Zn(3*c*)	110.52(1)
Zn(3)–P(1)–Zn(1*c*)	171.95(3)	Zn(3)–P(1)–Zn(2*c*)	110.52(1)	Zn(3)–P(1)–Zn(3*c*)	95.43(3)
Zn(1*c*)–P(1)–Zn(2*c*)	72.96(2)	Zn(1*c*)–P(1)–Zn(3*c*)	76.52(1)	Zn(2c)–P(1)–Zn(3*c*)	110.52(1)
Zn(3)–P(2)–Zn(1*d*)	105.98(2)	Zn(3)–P(2)–Zn(2*d*)	168.16(2)	Zn(3)–P(2)–Zn(3*g*)	92.62(2)
Zn(3)–P(2)–Zn(1*h*)	114.18(1)	Zn(3)–P(2)–Zn(2*h*)	76.48(1)	Zn(1*d*)–P(2)–Zn(2*d*)	75.06(1)
Zn(1*d*)–P(2)–Zn(3*g*)	114.18(1)	Zn(1*d*)–P(2)–Zn(1*h*)	120.57(2)	Zn(1*d*)–P(2)–Zn(2*h*)	73.93(2)
Zn(2*d*)–P(2)–Zn(3*g*)	76.48(1)	Zn(2*d*)–P(2)–Zn(1*h*)	73.93(2)	Zn(2*d*)–P(2)–Zn(2*h*)	114.73(2)
Zn(3*g*)–P(2)–Zn(1*h*)	105.98(2)	Zn(3*g*)–P(2)–Zn(2*h*)	168.16(2)	Zn(1*h*)–P(2)–Zn(2*h*)	75.06(1)
Zn(1)–P(3)–Zn(3)	76.55(1)	Zn(1)–P(3)–Zn(1*b*)	95.87(3)	Zn(1)–P(3)–Zn(3*b*)	172.42(3)
Zn(1)–P(3)–Zn(2*e*)	108.72(1)	Zn(1)–P(3)–Zn(2*h*)	108.72(1)	Zn(3)–P(3)–Zn(1*b*)	172.42(3)
Zn(3)–P(3)–Zn(3*b*)	111.03(3)	Zn(3)–P(3)–Zn(2*e*)	74.26(2)	Zn(3)–P(3)–Zn(2*h*)	74.26(2)
Zn(1*b*)–P(3)–Zn(3*b*)	76.55(1)	Zn(1*b*)–P(3)–Zn(2*e*)	108.72(1)	Zn(1*b*)–P(3)–Zn(2*h*)	108.72(1)
Zn(3*b*)–P(3)–Zn(2*e*)	74.26(2)	Zn(3*b*)–P(3)–Zn(2*h*)	74.26(2)	Zn(2*e*)–P(3)–Zn(2*h*)	122.74(4)

Hence, the Zn(1) and Zn(3) atoms in this structure can be considered analogous. Unlike these atoms, the Zn(2) atom forms the two shortest bonds with the P(3) and P(1) atoms (2.3320(3) and 2.3346(4) Å, respectively) and two bonds with the P(2) atom (2.5916(2) Å). Four of the six bond angles at the Zn(2) atom are virtually

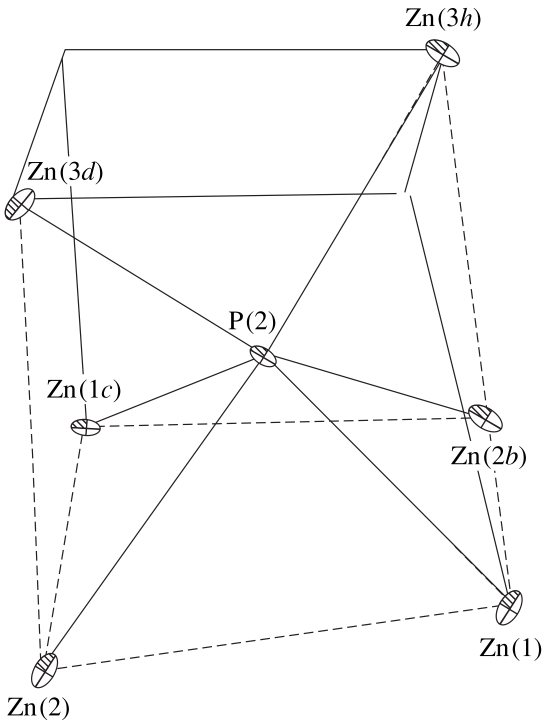

Fig. 2. Coordination polyhedron of the P(2) atom in the structure of **I**.

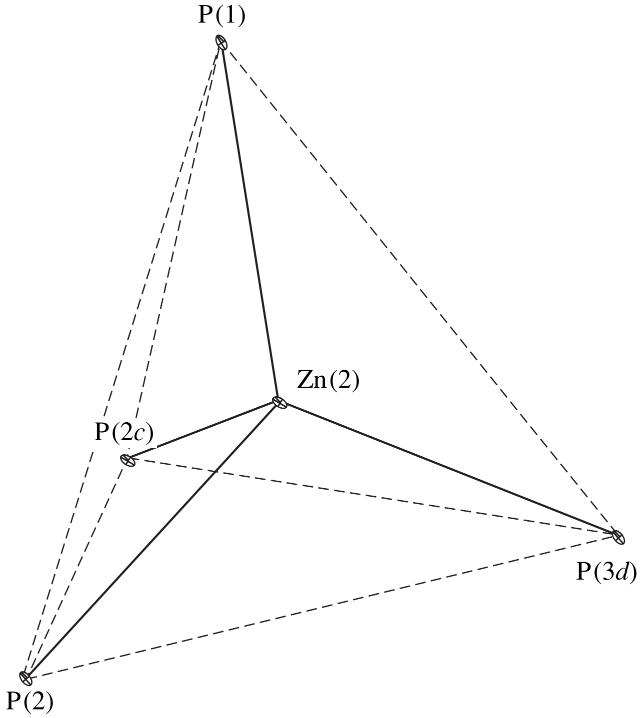

Fig. 3. Coordination polyhedron of the Zn(2) atom in the structure of **I**.

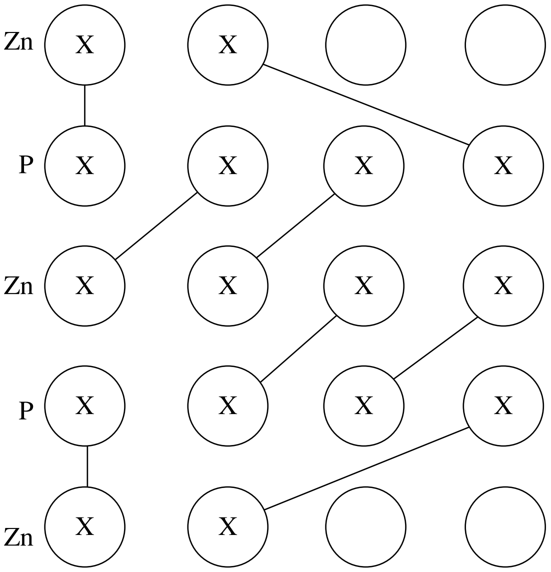

Fig. 4. Bonding scheme in the Zn_3P_2 crystal on the assumption of the covalent bonding character.

equal to the tetrahedral angle (109.3°), whereas the two other angles have the maximum and minimum values (119.98° and 99.98°, respectively) of all the P–Zn–P bond angles.

Reasoning from the tetrahedral coordination of zinc atoms and nearly tetrahedral coordination of two of the three independent phosphorus atoms in Zn_3P_2 (which are typical of covalent structures with sp^3-hybridized orbitals), we propose a new bonding scheme for this compound based on sp^3-hybridized orbitals (see Fig. 4).

This scheme accounts for the nonequivalence of the zinc atoms that occupy the same 8*g* sites but differ in the geometry of their chemical bonds and explains the nearly tetrahedral coordination of atoms and pronounced semiconducting properties of this compound. An increase in the coordination number of the Zn(1) and Zn(2) atoms from two to four (according to the number of occupied and unoccupied orbitals) and an increase in the coordination number of the phosphorus atoms from four to six can be attributed to the resonance between the unoccupied and occupied orbitals [10]. Unoccupied metal orbitals of atoms do not impart the metallic properties to a compound if these atoms do not interact with each other in the compound structure. Actually, Zn(1) and Zn(2), as well as Zn(3) and Zn(2), atoms may be considered as interacting because the interatomic distances are 3.0098–3.0489(3) and 3.0967(3) Å, respectively. These atoms occupy adjacent tetrahedral sites in the cubic close packing. By contrast, the Zn(1) and Zn(3) atoms occupy tetrahedral sites in a diamond pattern and, hence, cannot interact with each other. The distance between these atoms is no less than 3.1954(5) Å (the sum of the metallic radii being ~2.8 Å).

In order to analyze in detail the chemical interactions between zinc and phosphorus atoms in the Zn_3P_2 crystal with the use of the X-ray diffraction data, we constructed maps of deformation-electron-density distribution at the Zn–P bonds of different lengths. To obtain the most informative valence-electron-density maps at the bonds, the small-angle scattering limit was chosen empirically. The chemical bonding was analyzed using deformation-density maps devoid of atomic asymmetry. For the **I** structure and the experi-

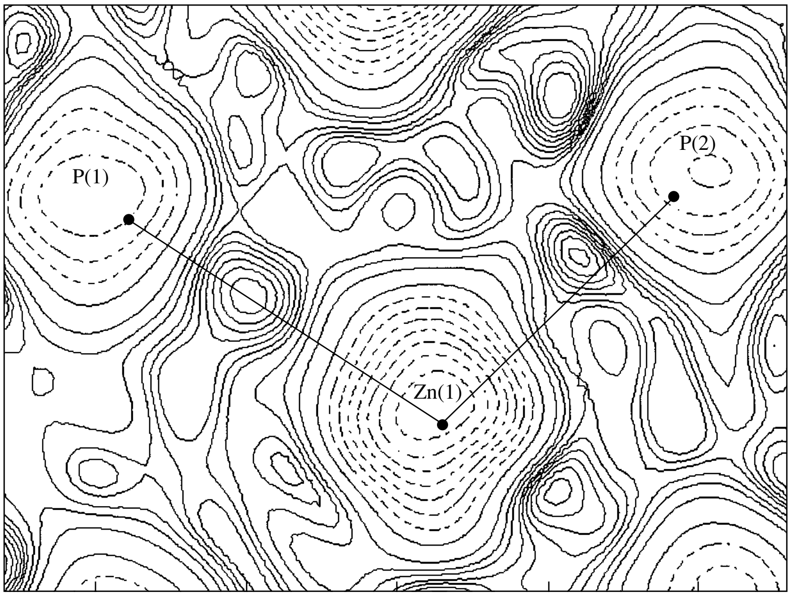

Fig. 5. Deformation electron density in the plane through the P(1)–Zn(1)–P(2) bonds.

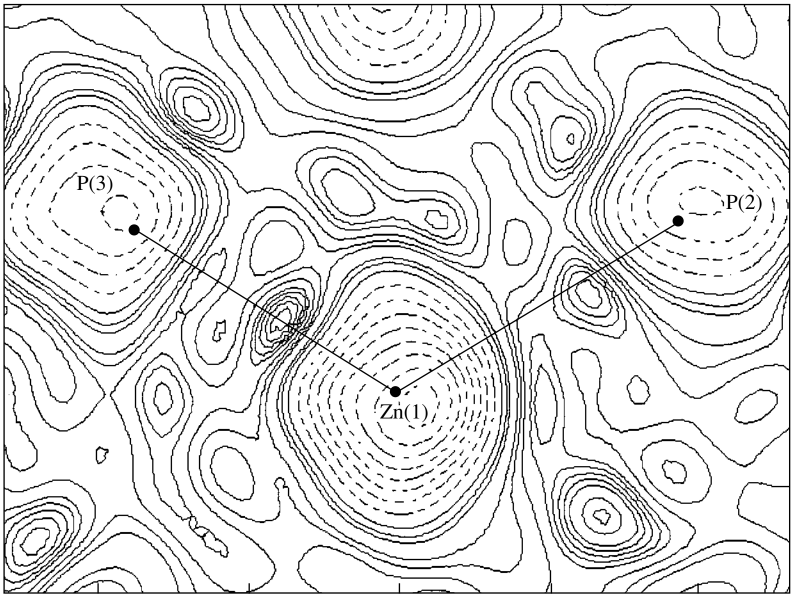

Fig. 6. Deformation electron density in the plane through the P(2)–Zn(1)–P(3) bonds.

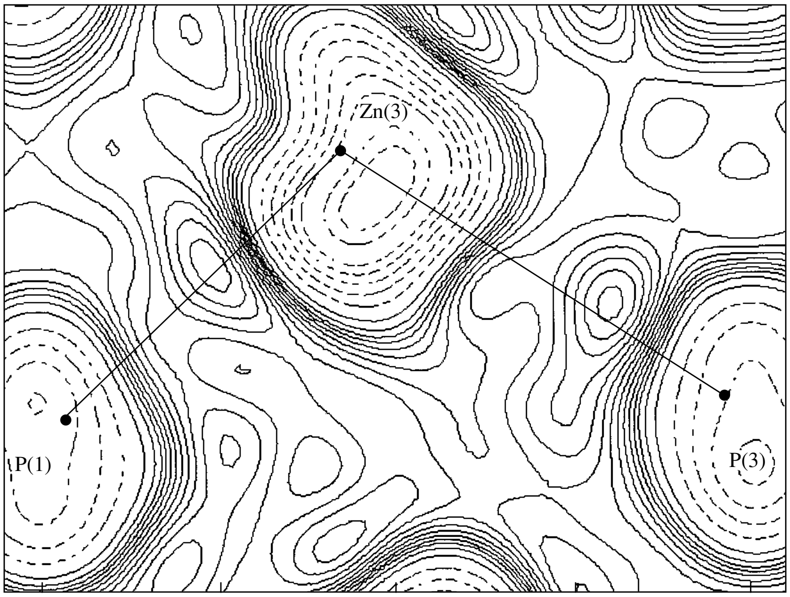

Fig. 7. Deformation electron density in the plane through the P(1)–Zn(3)–P(3) bonds.

mental data obtained in this study, this condition was met in the $(\sin\theta)/\lambda$ range from 0.85 to 1.34 Å^{-1}.

In the longest Zn–P bonds, i.e., Zn(1)–P(1) (2.7606(4) Å) and Zn(3)–P(3) (2.7676(3) Å), well-formed bond bridges can clearly be seen. These bridges shift toward the electronegative phosphorus atoms, so that the distance between the electron-density peaks and the phosphorus atoms are equal to one-third of the Zn–P bond length (Fig. 5), which may be indicative of an ionic component of the bond.

The lengths of the Zn(1)–P(2) and Zn(3)–P(2) bonds (2.4074(2) and 2.4058(2) Å, respectively) are almost equal to the sum of the tetrahedral radii. These bonds (see Fig. 6) exhibit high deformation-electron-density peaks shifted toward the electronegative phosphorus atom.

For the shortest bonds involving the analogous atoms, i.e., Zn(1)–P(3) (2.3662(3) Å) and Zn(3)–P(1) (2.3765(4) Å), the covalent bridges are located in the bond lines. The corresponding electron-density peaks

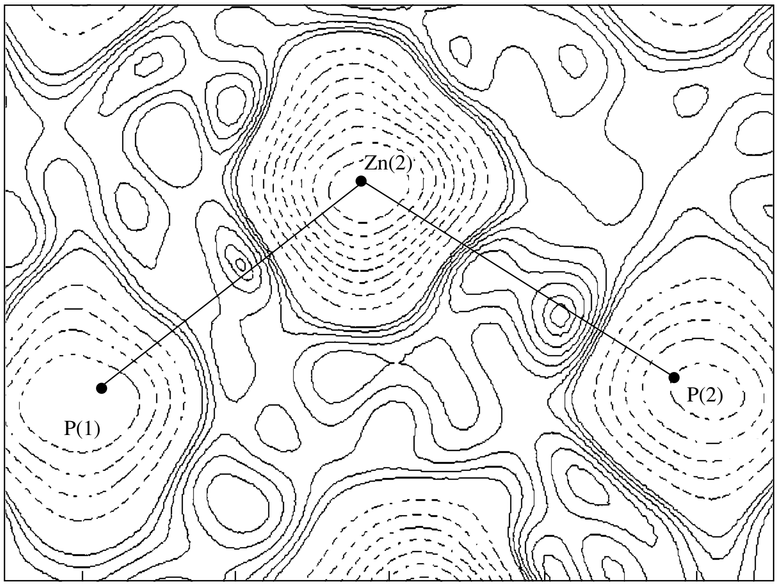

Fig. 8. Deformation electron density in the plane through the P(1)–Zn(2)–P(2) bonds.

are high (Fig. 7), well-formed, and located virtually midway between the zinc and phosphorus atoms.

A small negative charge in the vicinity of the zinc atom is observed in the Zn(2)–P(2) bond (2.5916(4) Å) with a length larger than the sum of the tetrahedral radii of these elements. The main covalent bridge is well-formed, rather high, and shifted toward the electronegative phosphorus atom (Fig. 8). All other Zn(2)–P bonds are also typically covalent with a substantial ionic-component contribution, the peaks in the shortest Zn(2)–P bonds being shifted to the midpoints of the bonds.

It should be noted that all the deformation-density maps clearly show the presence of delocalized electrons, which in places are accumulated to form weak peaks. This indicates that a metallic component makes a substantial contribution to the bonds, which results in smoothing of the lattice potential and a decrease in the band gap width.

CONCLUSIONS

Analysis of deformation-density maps confirmed the predominantly covalent character of chemical bonding in Zn_3P_2 and, consequently, the bonding scheme we proposed on the basis of this assumption.

In most of the deformation-density maps, the peaks of covalent bridges shift toward the electronegative phosphorus atoms, which is indicative of the presence of an ionic component of the bond. For the crystallographically independent analogous Zn(1) and Zn(3) atoms, the longer the Zn–P bond, the larger this shift and, consequently, the ionicity. In the shortest Zn–P bonds, the deformation-density peaks are located virtually midway between the zinc and phosphorus atoms, which is characteristic of purely covalent bonding.

ACKNOWLEDGMENTS

This study was supported by the Russian Foundation for Basic Research, project no. 03-03-32233.

REFERENCES

1. M. Hansen and K. Anderko, *Constitution of Binary Alloys*, 2nd ed. (McGraw-Hill, New York, 1958; Metallurgizdat, Moscow, 1962).
2. J. G. White, Acta Crystallogr. **18**, 217 (1965).
3. M. E. Fleet and T. A. Mowles, Acta Crystallogr., Sect. A: Found. Crystallogr. **40**, 1778 (1984).
4. I. E. Zanin, K. B. Aleĭnikova, and M. Yu. Antipin, Kristallografiya **48** (2), 232 (2003) [Crystallogr. Rep. **48**, 199 (2003)].
5. M. Stackelberg and R. Paulus, Z. Phys. Chem. Abt. B **28**, 429 (1935).
6. J. P. Suchet, *Chemical Physics of Semiconductors* (Dunod, Paris, 1962; Van Nostrand, New York, 1965; Metallurgiya, Moscow, 1969).
7. G. M. Sheldrick, *SHELXTL PLUS. Release 4.2* (Siemens Analytical Instruments, Madison, Wisconsin, USA, 1991).
8. H. D. Flack, Acta Crystallogr., Sect. A: Found. Crystallogr. **39**, 876 (1983).
9. I. E. Zanin, K. B. Aleinikova, M. Yu. Antipin, and M. M. Afanas'ev, Elektronnyĭ Zhurnal Issledovano v Rossii, No. 169, 2059 (2003); http://zhurnal.ape.relam.ru/articles/2003/169.pdf.
10. B. F. Ormont, *Introduction to Physical and Crystal Chemistry of Semiconductors* (Vysshaya Shkola, Moscow, 1982).

Translated by T. Safonova

Crystallography Reports, Vol. 49, No. 4, 2004, pp. 585–590. Translated from Kristallografiya, Vol. 49, No. 4, 2004, pp. 662–667.
Original Russian Text Copyright © 2004 by Maksimov, Kazantsev, Molchanov, Verin, Mill.

Crystal Structure and Microtwinning of Monoclinic $La_3SbZn_3Ge_2O_{14}$ Crystals of the Langasite Family

B. A. Maksimov*, S. S. Kazantsev*, V. N. Molchanov*, I. A. Verin*, and B. V. Mill**

* *Shubnikov Institute of Crystallography, Russian Academy of Sciences,*
Leninskiĭ pr. 59, Moscow, 119333 Russia
e-mail: maximov@ns.crys.ras.ru
** *Faculty of Physics, Moscow State University,*
Vorob'evy gory, Moscow, 119992 Russia
e-mail: mill@plms.phys.msu.ru

Received February 19, 2004

Abstract—The crystal structure of monoclinic $La_3SbZn_3Ge_2O_{14}$ crystals from the langasite family is determined by X-ray diffraction analysis [$a = 5.202(1)$ Å, $b = 8.312(1)$ Å, $c = 14.394(2)$ Å, $\beta = 90.02(1)°$, sp. gr. $A2$, $Z = 2$, and $R/R_w = (5.2/4.6)\%$]. The structure is a derivative of the $Ca_3Ga_2Ge_4O_{14}$-type structure ($a = 8.069$ Å, $c = 4.967$ Å, sp. gr. $P321$, $Z = 1$). The crystal studied is a polysynthetic twin with the twin index $n = 2$, whose monoclinic components are related by pseudomerohedry by a threefold rotation axis of the supergroup $P321$. *© 2004 MAIK “Nauka/Interperiodica”.*

INTRODUCTION

Piezoelectric crystals of the langasite family with the $Ca_3Ga_2Ge_4O_{14}$ structure ($a = 8.069$ Å, $c = 4.967$ Å, sp. gr. $P321$, and $Z = 1$) attract an ever-increasing interest because of the possibility of their use in frequency-selective devices and detectors [1]. Recently, it has been established that some compounds of this family undergo phase transitions both under high pressures and high temperatures [2]. One of these compounds is $La_3SbZn_3Ge_2O_{14}$ (LSZG) [3].

The X-ray powder diffraction pattern of an LSZG crystal was first indexed in a trigonal system with unit cell parameters characteristic of the compounds of the langasite family, $a = 8.305$ Å and $c = 5.199$ Å [4]. A more detailed study of the X-ray powder diffraction pattern of this crystal showed that the lattice has a slight, presumably orthorhombic, distortion [5]. In terms of possible phase transitions with lowering of the symmetry in the crystals of the langasite family [2], one of the most probable space groups of LSZG crystals seems to be sp. gr. $A2$. Below, we consider the results of the complete X-ray diffraction study of LSZG single crystals.

EXPERIMENTAL

Small, needlelike LSZG crystals were obtained by melting of the phase with a small excess of Sb_2O_5 preliminarily synthesized in closed platinum crucibles and subsequent slow cooling of the melt.

The X-ray diffraction experiments were performed on small rather isometric pieces of a crystal. The measurements were made on a CAD-4F diffractometer (MoK_α radiation). An automated search for diffraction reflections and their indexing yields the hexagonal metrics of a lattice whose refined parameters are $a = b = 8.312(1)$ Å and $c = 5.202(1)$ Å. No considerable distortions of the reflection profiles and the angles between the basis lattice vectors indicating deviations from the trigonal to the monoclinic symmetry characteristic of the langasite family were revealed at this stage.

An experimental array consisting of 9636 diffraction reflections with $\sin\theta/\lambda \le 0.97$ Å^{-1} was collected within the complete sphere of the reciprocal space. After rejection of the reflections whose intensities did not satisfy the conditions $I > 2\sigma(I)$, the initial set reduced to 8536 reflections. To introduce the absorption correction, the sample was approximated by a sphere with a diameter of 0.12 mm. Thermal motion of all the atoms was described in the anisotropic harmonic approximation. The calculation of the extinction corrections according to the isotropic Becker model showed a slight prevalence of the first type of extinction. We used, in our calculations, the atomic scattering curves for neutral atoms. Processing of the experimental data and all the subsequent computations were performed using the JANA 2000 crystallographic complex of programs [6].

Averaging of the symmetrically equivalent reflections within the Laue group $\bar{3}m$ (characteristic of the crystals of the langasite family) yielded a rather high reliability factor, $R_{av(I)} = 10.6\%$. The transition from the trigonal P to the monoclinic A unit cell with the parameters $a = 5.202(1)$ Å, $b = 8.312(1)$ Å, $c = 14.394(2)$ Å, and $\beta = 90.02(1)°$ with the use of the matrix (00–1/010/210) and the subsequent averaging of the reflec-

Table 1. Characteristics of X-ray diffraction experiment and crystallographic data for LSZG crystals

Chemical formula	$La_3SbZn_3Ge_2O_{14}$
Diffractometer	CAD-4F
Radiation	MoK_α $\lambda = 0.71069$ Å
Monochromator	Pyrolytic graphite
Scanning mode	$\omega/2\theta$
Ranges of *h*, *k*, *l* variation	$-10 \le h \le 10$; $-16 \le k \le 16$; $-28 \le l \le 28$
Sp. gr.	*A*2
a, Å	5.2022(6)
b, Å	8.312(1)
c, Å	14.394(2)
β, deg	90.02(1)
V, $Å^3$	622.4(1)
Number of formula units	2
$\rho_{X\text{-}ray}$, g/cm^3	5.88
Crystal radius, mm	0.06
μ_{Mo}, mm^{-1}	22.69
Max $\sin\theta/\lambda$ ($Å^{-1}$)	0.97
Number of measured reflections	9636
Number of reflections used in refinement	8536
Extinction coefficient, ρ	0.0053(1)
Criterion of significance	$I > 2\sigma(I)$
Weighting scheme	$1/(\sigma F)^2$
Number of independent parameters	108
R/R_w, %	5.2/4.6
GOOF, %	2.6/2.9
Flack parameter	0.012

Note: The Flack parameter shows the relative volume of the inverted component and characterizes the reliability of the determination of the absolute structure model.

tion intensities within the Laue group 2/*m* did not considerably reduce the *R* factor of averaging, $R_{av(I)}$ = 9.4%.

The results of averaging did not give sufficient evidence in favor of monoclinic symmetry, but indicated the existence of pseudosymmetry along axis *3* and possible twinning of the crystal by the same symmetry element (axis *3*) in the presumed Laue group 2/*m*. The final choice of monoclinic symmetry was dictated by the comparison of the refined structure model of an LSZG crystal within the sp. gr. *P*321 (trigonal model) and *A*2 (monoclinic model, pseudoorthohexagonal unit cell) with and without allowance made for twinning. The structure models were refined using the non averaged set of structure factors.

The main crystallographic characteristics of the crystal, the experimental parameters, and the final values of the reliability factors for the monoclinic model are indicated in Table 1.

TRIGONAL STRUCTURE MODEL

The $Ca_3Ga_2Ge_4O_{14}$-type structure can be described as a mixed framework of two kinds of oxygen tetrahedra [small 2*d* tetrahedra (position symmetry *3*) and larger 3*f* tetrahedra (position symmetry *2*)] and 1*a* octahedra (position symmetry 32). The coordination polyhedron of large cations (Na^+, Ca^{2+}, Sr^{2+}, Ba^{2+}, Pb^{2+}, and Ln^{3+}) occupying the framework voids has eight oxygen vertices and can be represented as a dodecahedron with triangular faces.

Most compounds of the langasite family have disordered structures with the crystallographic positions being occupied by mixed cations. Similar to $Sr_3TaGa_3Si_2O_{14}$, an LSZG crystal should possess an ordered structure with the positions being occupied by one cation species. It is natural to assume that the La^{3+} ions in the trigonal model of the LSZG structure would occupy the 3*e* position; the Sb^{5+} ions, the 1*a* position; the Zn^{2+} ions, the 3*f* position; and the Ge^{4+} ions, the 2*d* position. To refine the LSZG model, we used this cation distribution and the positional parameters from [7].

At the first stage of the refinement, we established a considerable deficit of oxygen in the O(2) position ($q \sim 0.66$). The difference electron-density syntheses showed the additional oxygen position O(2–1) with the residual electron density 4.7 e/$Å^3$ (Fig. 1). The simultaneous independent refinement of the main and additional positions showed that the sum of their occupancies ($q \sim 0.66$ and ~0.33, respectively) was close to unity. The final R/R_w values, with due regard for the thermal motion of all the atoms of the trigonal model in the anisotropic approximation, were (7.5/6.2)%. The shortest O–O distance between the O(2) and O(2–1) positions was about 0.9 Å, and the distance between the O(2) positions related by the threefold rotation axis was ~2 Å. The corresponding coordinate and thermal parameters are listed in Table 2.

MONOCLINIC STRUCTURE MODEL

Obviously, the coefficients of oxygen distribution over the O(2) and O(2–1) positions indicate that the transition from the statistical trigonal structure model of an LSZG crystal (sp. gr. *P*321) to the ordered model (sp. gr. *A*2) should result in the loss of the threefold symmetry axis and, as a result, in lowering of the symmetry to monoclinic. In the monoclinic model, one of the faces of a Ge tetrahedron (parallel basal plane in the trigonal model) should be formed with the participation of two oxygen atoms from the main O(2) position ($q = 0.66$) and one oxygen atom from the new O(2–1) position ($q = 0.33$). Thus, the Ge tetrahedron can have three orientations, which creates the conditions for merohedral twinning.

In the transition to the monoclinic model, the axes of the direct lattice of the trigonal model are transformed to the centered pseudoorthohexagonal *A* lattice with the use of the (00–1/010/210) matrix, and the coordinates of the points are transformed with the use of the (001/–1/210/1/200) matrix. The monoclinic model was refined both without and with allowance made for twinning. Finally, after the comparison of the results of the above two refinements, we made the choice in favor of merohedral twinning in the crystal.

At the stage of analysis of the difference electron-density synthesis and the refinement of the position occupancies, we localized a system of maxima corresponding to the mean statistical trigonal model of the LSZG structure. The R/R_w value for this monoclinic model, (7.4/6.4)%, is practically the same as for the trigonal model. These results confirmed, once again, our assumption that the crystal studied is a pseudomerohedral twin with the monoclinic components being related by a threefold rotation axis.

The refinement of the monoclinic model with due regard made for twinning resulted in a considerable reduction of the R/R_w value [down to (5.2/4.6)%]. The difference and residual electron-density synthesis showed no traces of the statistical distribution of anions

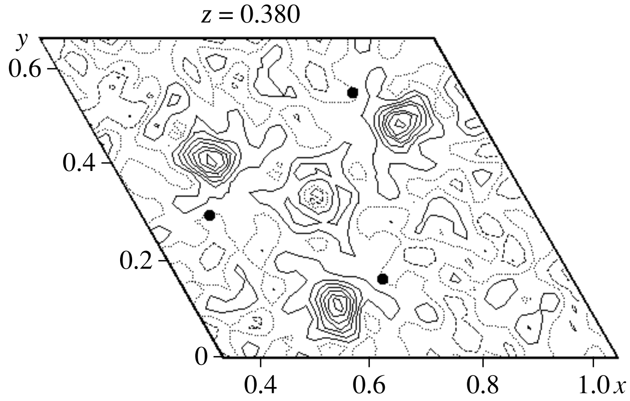

Fig. 1. The (x, y, 0.380) section of the difference electron-density synthesis constructed by the coordinates of the trigonal model and showing the maxima of the additional O(2–1) position (4.7 e/Å^3). The isolines are spaced by 0.5 e/Å^3. The filled circles indicate the atoms in the O(2) position in the section z = 0.29.

Table 2. Positional and thermal parameters of the atoms of two structure models of LSZG crystals

The average trigonal model (sp. gr. *P*321, *Z* = 1)

Atom	Wyckoff position	Occupancy, *q*	*x*/*a*	*y*/*b*	*z*/*c*	B_{eq}, Å^2
La	3*e*	1	0.42277(5)	0	0	0.46(1)
Sb	1*a*	1	0	0	0	1.49(1)
Ge	2*d*	1	1/3	2/3	0.5381(2)	1.48(1)
Zn	3*f*	1	0.75968(9)	0	1/2	1.55(2)
O(1)	2*d*	1	1/3	2/3	0.1991(9)	1.9(1)
O(2)	6*g*	0.66	0.4622(7)	0.2897(9)	0.2909(8)	2.1(2)
O(2–1)	6*g*	0.33	0.5184(12)	0.4067(16)	0.3774(17)	1.9(1)
O(3)	6*g*	1	0.2274(5)	0.0896(5)	0.7850(5)	1.5(3)

Monoclinic model with allowance for twinning (sp. gr. *A*2, *Z* = 2)

Atom	Wyckoff position	Occupancy, *q*	*x*/*a*	*y*/*b*	*z*/*c*	B_{eq}, Å^2
La(1)	2*a*	1	0	0.4227(3)	0	1.23(2)
La(2)	4*c*	1	−0.0015(2)	0.2888(3)	0.28857(5)	1.87(1)
Sb	2*a*	1	0	0.0	0	1.63(2)
Zn(1)	2*b*	1	1/2	0.7614(4)	0	1.66(5)
Zn(2)	4*c*	1	0.5013(3)	0.1218(3)	0.1201(1)	1.39(3)
Ge	4*c*	1	0.4618(1)	0.5004(4)	0.1665(1)	1.59(2)
O1	4*c*	1	0.8030(9)	0.493(2)	0.1697(8)	2.4(2)
O(2)^2	4*c*	1	0.708(2)	0.826(1)	0.3610(6)	1.4(1)
O(3)^2	4*c*	1	0.712(1)	0.118(1)	0.4230(5)	2.4(2)
O(4)$^{2-1}$	4*c*	1	0.625(1)	0.142(1)	0.2500(5)	2.6(2)
O(5)^3	4*c*	1	0.217(2)	0.970(1)	0.1105(6)	1.6(2)
O(6)^3	4*c*	1	0.202(2)	0.334(1)	0.4299(7)	2.1(2)
O(7)^3	4*c*	1	0.225(2)	0.683(2)	0.4536(8)	2.4(2)

Note: The superscripts in the notation of oxygen atoms correspond to the O(2), O(2–1), and O(3) positions of the trigonal model.

Table 3. Interatomic distances (Å) in the LSZG structure

Anionic environment of La atoms				Sb octahedron	
La(1)–O(7) (×2)	2.40(1)	La(2)–O(6)	2.32(1)	Sb–O(5) (×2)	1.96(1)
O(3) (×2)	2.47(1)	O(4)	2.36(1)	O(6) (×2)	2.01(1)
O(2) (×2)	2.64(1)	O(5)	2.37(1)	O(7) (×2)	2.03(1)
O(1) (×2)	2.71(1)	O(1)	2.62(1)	average distance	2.00(1)
average distance	2.55(1)	O(2)	2.66(1)		
		O(1')	2.73(1)		
		O(3)	2.82(1)		
		average distance	2.55(1)		
Zn(1) tetrahedra		**Zn(2) tetrahedra**		**Ge tetrahedra**	
Zn(1)–O(6) (×2)	1.94(1)	Zn(2)–O(7)	1.85(1)	Ge–O(2)	1.74(1)
O(3) (×2)	1.96(1)	O(5)	1.95(1)	O(4)	1.74(1)
average distance	1.95(1)	O(4)	1.98(1)	O(1)	1.777(5)
		O(2)	2.04(1)	O(3)	1.85(1)
		average distance	1.95(1)	average distance	1.78(1)
O(3)–O(6) (×2)	2.81(2)				
O(6') (×2)	3.20(1)				
O(3)–O(3')	3.13(1)	O(4)–O(2)	2.81(1)	O(1)–O(2)	3.03(1)
O(6)–O(6')	3.70(2)	O(7)	3.05(1)	O(4)	2.80(1)
		O(5)	3.25(1)	O(3)	3.17(1)
		O(2)–O(5)	3.01(1)	O(2)–O(4)	3.10(1)
		O(7)	3.08(1)	O(3)	2.59(2)
		O(5)–O(7)	3.53(1)	O(3)–O(4)	2.54(1)

characteristic of the previous models. The relative volumes of the monoclinic twin components related by a threefold axis were equal to 0.29, 0.32, and 0.39, which agreed with the results of averaging performed within the framework of the trigonal space group at the first stages of the analysis of experimental data. The positional and thermal parameters of the monoclinic model are indicated in Table 2 and the interatomic distances in Table 3.

RESULTS AND DISCUSSION

Comparing the results of the refinement of the structure models of LSZG crystals in the trigonal and monoclinic space groups, we see that LSZG crystals are crystallized in the monoclinic system with the pseudoorthohexagonal lattice metrics. This indicates merohedral twinning of these crystals. In addition to considerably lower *R* factors, the refinement in the monoclinic space group with due regard for twinning allowed us to reduce the extinction factor. It also improved the convergence of the results obtained after the refinement and considerably "purified" the residual electron-density syntheses. At the concluding stage of the refinement, the maximum heights of the residual density amounted to 1.7 e/Å^3, whereas, in the trigonal structure model, this indicator of the quality of the structure model was higher by a factor of 4.3; for the monoclinic model without allowance for twinning, it was higher by a factor of 2.

The structure of a monoclinic LSZG crystal is a derivative of the trigonal $Ca_3Ga_2Ge_4O_{14}$-type structure, with the preservation of all the main characteristics of the latter (Fig. 2). Lowering of the symmetry is accompanied by considerable displacements of O atoms up to 1 Å (the displacements of cations are considerably less). This results in a decrease of the coordination number of La(2) atoms from 8 to 7 and in certain changes in the character of polyhedron connection. Figure 3 compares the geometric characteristics of the layer of Sb octahedra and two types of La polyhedra (eight- and seven-vertex polyhedra) in the monoclinic LSZG crystals and, also, of the layer of (Nb,Ga) octahedra and eight-vertex La polyhedra in the trigonal $La_3Nb_{0.5}Ga_{5.5}O_{14}$ crystals [8].

In the transition from the trigonal to monoclinic model (Table 2), each of the 3*e* and 3*f* positions of the sp. gr. *P*321 in the LSZG structure generates the special [La(1) and Zn(1) on the *2* axis] and general [La(2) and

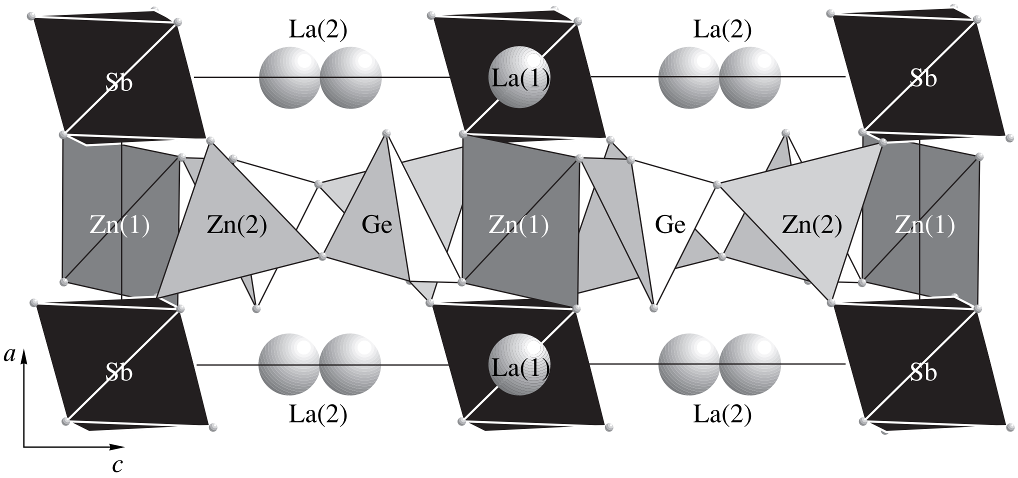

Fig. 2. Projection of the LSZG crystal structure onto the *xz* plane.

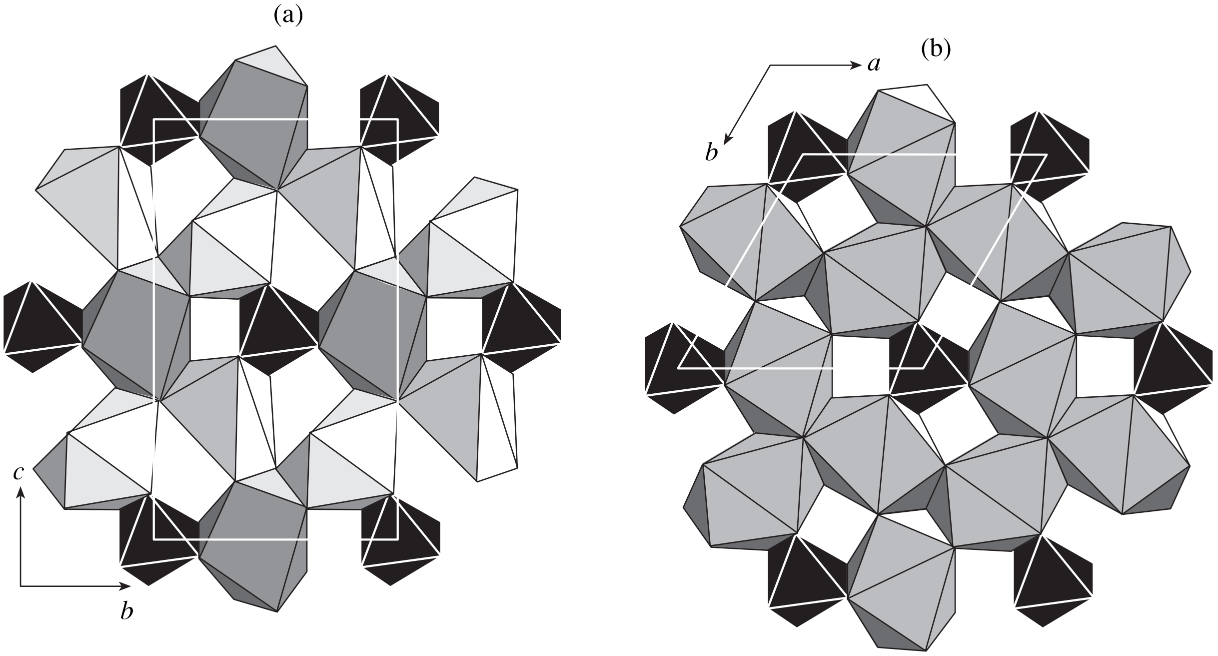

Fig. 3. (a) The polyhedral layer consisting of SbO_6 octahedra and two types of La polyhedra in a monoclinic LSZG crystal and (b) the layer consisting of $(Nb,Ga)O_6$ octahedra and LaO_8 polyhedra in the trigonal $La_3Nb_{0.5}Ga_{5.5}O_{14}$ crystals.

Zn(2)] positions. The O and Ge atoms are located in the general position, and the Sb atoms occupy the special position with the symmetry *2*. The oxygen polyhedron around La(1) is a distorted Thomson cube with flat bases in distinction from a triangular dodecahedron in the trigonal $Ca_3Ga_2Ge_4O_{14}$-type structure. The scatter in the La(1)–O distances (0.31 Å) is less than in the dodecahedra of the trigonal structure of the known compounds of the langasite family. The polyhedron around the La(2) atom is a seven-vertex polyhedron that can be described as a considerably distorted pentagonal bipyramid with the axial O(4) and O(6) vertices. The eighth atom, O(4), shared by the dodecahedron and the GeO_4 tetrahedron, is spaced 3.52 Å from La(2). As a result of the displacement of O(4), the Ge tetrahedron shares only two short O–O edges with $La(1)O_8$ and $La(2)O_7$ polyhedra, whereas the third edge increases to a value of 3.10 Å. The $La(1)O_8$ polyhedron shares edges with four neighboring $La(2)O_7$ polyhedra. The environment of $La(2)O_7$ is built by two $La(1)O_8$ (which share edges) and two $La(2)O_7$ (which share vertices). The SbO_6 octahedron shares three edges with La polyhedra, with the Sb–O distances being almost constant. The Zn–O and Ge–O distances in the tetrahedra correspond to the ionic radii of Zn^{2+} and Ge^{4+} and confirm the ordered occupancy of tetrahedra with these ions. As earlier, the tetrahedra in the tetrahedral layer share oxygen vertices. The O(1) atom is shared by the Ge tetrahedron and three La polyhedra and, as in the trigonal structure, does not participate in condensation of tetrahedra inside the layer.

Concluding this article, we should like to indicate that, probably, the results obtained are not final. This is indicated by the insufficiently low R/R_w values, considerable errors in the atomic coordinates and interatomic distances, high B_j values for the cationic part of the structure (comparable with the thermal parameters of anions), and some features of the diffraction patterns that require a more detailed study.

ACKNOWLEDGMENTS

This study was supported by the Russian foundation for Basic Research (project no. 03-02-17075) and the Federal Program on Support of Prominent Scientists the Leading Scientific Schools (project NSh 1642.2003.2).

REFERENCES

1. B. V. Mill and Yu. V. Pisarevsky, in *Proceedings of 2000 IEEE/EIA International Frequency Control Symposium* (Kansas City, Missouri, USA, 2000), p. 133.
2. B. V. Mill’, B. A. Maksimov, Yu. V. Pisarevskiĭ, *et al.*, Kristallografiya **49** (1), 65 (2004) [Crystallogr. Rep. **49**, 60 (2004)].
3. A. Pavlovska, J. Schneider, S. Werner, *et al.*, Z. Kristallogr. **218**, 187 (2003).
4. B. V. Mill’ and T. Fukuda, Zh. Neorg. Khim. **43** (4), 538 (1998).
5. S. Ivanov and V. Zhurov, ICDD **51**, 51 (2001).
6. V. Petriček and M. Dusek, in *Proceedings of JANA 2000* (Inst. of Physics, Acad. Sci. Czech Rep., Praha, 2000).
7. H. Takeda, J. Sato, T. Kato, *et al.*, Mater. Res. Bull. **35**, 245 (2000).
8. V. N. Molchanov, B. A. Maksimov, D. F. Kondakov, *et al.*, Pis’ma Zh. Éksp. Teor. Fiz. **74** (4), 244 (2001) [JETP Lett. **74**, 222 (2001)].

Translated by L. Man

Crystallography Reports, Vol. 49, No. 4, 2004, pp. 591–597. Translated from Kristallografiya, Vol. 49, No. 4, 2004, pp. 668–675.
Original Russian Text Copyright © 2004 by Ryzhova, Molchanov, Artyukhov, Simonov, Sobolev.

Growth and Defect Crystal Structure of CdF_2 and Nonstoichiometric $Cd_{1-x}R_xF_{2+x}$ Phases (R = Rare Earth Elements and In). 2. Methods of Structure Refinement of $Cd_{0.90}R_{0.10}F_{2.10}$ Phases Using the Example of $Cd_{0.90}Tb_{0.10}F_{2.10}$. Structure of Nanodimensional Clusters in $Cd_{0.90}Tb_{0.10}F_{2.10}$ Crystal

E. A. Ryzhova*, V. N. Molchanov*, A.A. Artyukhov, V. I. Simonov*, and B. P. Sobolev***
** Shubnikov Institute of Crystallography, Russian Academy of Sciences, Leninskiĭ pr. 59, Moscow, 119333 Russia*
e-mail: rahelen@ns.crys.ras.ru
*** Kurchatov Institute, Russian Research Center, pl. Kurchatova 1, Moscow, 123182 Russia*

Received December 24, 2003

Abstract—The structures of the CdF_2 and $Cd_{0.90}Tb_{0.10}F_{2.10}$ crystals, the first representatives of the family of nonstoichiometric CdF_2-based $Cd_{1-x}R_xF_{2+x}$ phases (R = La–Lu, Y), are determined by X-ray diffraction analysis. The structures belong to the CdF_2 structure type. The nonstoichiometric CaF_2 phases have structural defects—interstitial fluorine atoms and vacancies in the main anionic motif. The structural data allowed us to establish for the first time the simultaneous presence in $Cd_{0.90}Tb_{0.10}F_{2.10}$ of two types of clusters—electrically neutral $[CdTb_3F_{26}]$ and charged $[Cd_2Tb_2F_{26}]^{1-}$—and to determine their structure. The cluster charge is compensated with the vacancies in the positions of the main fluorine atoms, which may give rise to superionic conductivity in $Cd_{1-x}R_xF_{2+x}$ crystals. *© 2004 MAIK “Nauka/Interperiodica”.*

INTRODUCTION

The present publication continues a series of publications dedicated to the synthesis and study of CdF_2 single crystals and $Cd_{1-x}R_xF_{2+x}$ fluorite phases (R = RE and In) [1]. The second part is devoted to the methods of localization of structural defects in $Cd_{1-x}R_xF_{2+x}$ phases by X-ray diffraction using the example of a $Cd_{0.90}Tb_{0.10}F_{2.10}$ crystal.

X-ray diffraction studies of the atomic structure of nonstoichiometric fluorite phases of the composition $M_{1-x}R_xF_{2+x}$ (M = Ca, Sr, Ba) were started long ago. The methods of analysis of the experimental X-ray diffraction data are well developed. The specific feature of these heterovalent solid solutions is association of RE into complexes called *clusters*. Elementary clusters have nanometer dimensions, which allowed one to consider fluorite phases as nanostructural crystals [2].

The history of the concept of association of structural defects in nonstoichiometric fluorite phases is considered elsewhere [3]. It is based on an assumption [4] of the isostructurality of the $Ca_{8-\delta}R_{5+\delta}F_{31+\delta}$ phases and $Na_7Zr_6F_{31}$ [5], a compound in which the $[M_6F_{37}]$ group was first found. The core of this group is a $\{F_{12}\}$ cuboctahedron surrounded with six square $[MF_8]$ antiprisms. The center of a fluorine cuboctahedron is occupied by a fluorine atom. Later, $[R_6F_{36(37)}]$ groups, which are called octahedral rare earth clusters (because of the arrangement of RE ions at the octahedron vertices), were found experimentally in the form of structurally ordered blocks in the Ca_2RF_7 [6] and some other phases.

Comprehensive study of the changes in the defect structures of the fluorite $M_{1-x}R_xF_{2+x}$ phases along the cationic series M = Ca, Sr, Ba, Cd, Pb and R = Y, La-Lu, with RF_3 content ranging within 10–50 mol % (x = 0.1–0.5), by X-ray and neutron diffraction analysis was started at the Institute of Crystallography in 1969 [7]. The data known by 1985 and the changes in the defect structures of the $M_{1-x}R_xF_{2+x}$ phases with M = Ca, Sr, and Ba were analyzed and generalized in [8]. In [8], the two simplest cluster configurations in the $M_{1-x}R_xF_{2+x}$ solid solutions were considered. One of them is the well known octahedral configuration in which RE cations are located according to the octahedral motif. The center of the cationic octahedron is occupied by an empty $\{F_{12}\}$ cuboctahedron whose fluoride anions occupy the position with multiplicity 48 at the twofold symmetry axis. This configuration was confirmed by structural studies of the ordered Ca_2RF_7 and $Ba_4R_3F_{17}$ phases (R = Y, Yb). The second configuration is a tetrahedron of four RE ions and, therefore, is called a tetrahedral cluster. The core of this cluster is the tetrahedral group of fluoride anions occupying the 32*f* position on the threefold axis in sp. gr. $Fm3m$. In the ordered phases possessing structure derived from the fluorite one, no tetrahedral RE configurations were found. However, interstitial fluoride ions in the 32*f* position were observed in some nonstoichiometric fluorites.

It turned out that, in the first approximation, the transition from octahedral to tetrahedral clusters depends on the ratio of the ionic radii of isomorphously substituted M^{2+} and R^{3+} cations with different valences: at $r(R^{2+})/r(M^{3+}) < 0.95$, octahedral clusters are observed, whereas at $r(R^{2+})/r(M^{3+}) > 0.95$, tetrahedral ones are established [8].

Later, the cluster evolution in the $Ca_{0.68}R_{0.32}F_{2.32}$ phases was studied by the neutron powder diffraction method [9]. The EXAFS method was used to study $Ca_{0.90}R_{0.10}F_{2.10}$ [10] and, later, also $Ca_{0.68}R_{0.32}F_{2.32}$ [11]. The properties of the fluorite-type phases with the composition $M_{1-x}R_xF_{2+x}$, and, first of all, their spectroscopic properties were interpreted based on various cluster configurations, whose total number amounts to 30. The most detailed review of the clusters suggested for the interpretation of the properties of the fluorite phases (known by 1991) was made in [12]. Energy consideration of the stable cluster configurations in $M_{1-x}R_xF_{2+x}$ solid solutions was started in [13–15]. The problem was generalized in [16]. The variations in the defect structure of $Ba_{1-x}R_xF_{2+x}$ crystals along the row of the cerium subgroup (from La to Nd) were studied by neutron diffraction in [17–19]. The short review of the evolution of the defect structure in the fluorite phases of the composition $M_{1-x}R_xF_{2+x}$ with M = Ca, Sr, and Ba can be found in Chapter 7 of the book written by Sobolev [20]. Unfortunately, there are no structural data on the fluorite $Cd_{1-x}R_xF_{2+x}$ phases. The present series of publications aims to fill this gap.

The association of RE ions in $Cd_{1-x}R_xF_{2+x}$ solid solutions is indirectly confirmed by nonuniform broadening of the luminescence spectra of Nd^{3+} in $Cd_{1-x}Y_xF_{2+x}$ crystals observed in [21], but no spectrum analysis aimed at the determination of possible new configurations and structures of the associates was performed.

The determination of the cluster structure of $Cd_{1-x}R_xF_{2+x}$ based on the structural data known for these phases reduces to the localization of interstitial fluoride anions compensating the difference in the cation valences of the fluorite matrix (Cd^{2+}) and the impurity (R^{3+}) and, also, of the vacancies in the main anionic motif and the fluorine atoms pushed out from the main positions into interstitials.

The coordinates of the positions occupied by interstitial anions and their occupancies allow one to draw conclusions about the structure of nanodimensional clusters of structural defects in the matrix of the initial CdF_2 structure. It is more reliable to refine low occupancies of the interstitial-fluorine positions by neutron diffraction data. However, it is impossible to use neutron diffraction for the structural study of the $Cd_{1-x}R_xF_{2+x}$ phases because of extremely pronounced neutron absorption by the natural mixture of cadmium isotopes.

Below, we consider the method used for the refinement of the structure of the $Cd_{1-x}R_xF_{2+x}$ phases from the X-ray diffraction data. The main shortcoming of the analysis of the structural experiment on the nonstoichiometric fluorite $M_{1-x}R_xF_{2+x}$ phases, in general, and on $Cd_{1-x}R_xF_{2+x}$, in particular, is the strong correlations between the parameters to be refined. The analysis of possible cluster configurations is performed based on the data obtained, and the atomic model of the structures of two nanodimensional defect clusters in $Cd_{1-x}R_xF_{2+x}$ crystals is suggested.

EXPERIMENTAL

The $Cd_{0.90}Tb_{0.10}F_{2.10}$ single crystals were grown from melt in an atmosphere of helium and the products of tetrafluoroethylene pyrolysis by the Bridgman method. The 3-mm-thick disks were cut out from the middle part of a crystalline boule normally to the growth axis. After optical polishing, the disks were studied in polarized light. The growth methods, crystal morphology, and methods of sample preparation are described elsewhere [1].

Homogeneous regions of the disks were used to prepare spherical samples with a diameter of about 150 μm for X-ray analysis. The spheres were glued to glass fibers with a solution of polystyrene in isoamyl acetate. The experiment was performed on an automated CAD-4 (Enraf Nonius) diffractometer (MoK_α radiation) with a graphite monochromator at the temperature 295 K. Reflections with $\sin\Theta/\lambda \le 1.2$ from a $Cd_{0.90}Tb_{0.10}F_{2.10}$ crystal were recorded over the whole reflection sphere. Reflections with $\sin\Theta/\lambda \le 1.2$ from a CdF_2 crystal were recorded within 3/4 of the reflection sphere. The stability of the diffractometer operation was periodically checked (after recording of each 300 reflections) by measuring the intensities of the three control reflections. The orientation matrix of the sample was checked after every hour of the diffractometer operation. The lattice parameters were refined by the least squares method using 24 symmetry-related 337-type reflections.

The structural computations were performed by the JANA2000 programs [22]. The array of the experimental intensities was corrected for absorption in a spherical sample, polarization, and the Lorentz factor. The analysis of the diffraction experiment from CdF_2 and $Cd_{0.90}Tb_{0.10}F_{2.10}$ single crystals revealed no deviations from cubic symmetry. The systematic extinctions uniquely indicated a F Bravais lattice and the diffraction class $m3mF$ corresponding to the space groups $Fm3m$, $F432$, and $F\bar{4}3m$.

The data obtained uniquely indicated the CaF_2 structure type and, therefore, the further structure analysis was performed within the sp. gr. $Fm3m$. The refined structural data confirmed the choice of this space group. Averaging of the symmetry-equivalent squared structure factors is characterized by the reliability factors R_{av} = 2.41 and 2.03% for CdF_2 and $Cd_{0.90}Tb_{0.10}F_{2.10}$, respectively. In the course of the refinement, we also introduced the correction for isotropic secondary extinction in the Becker–Coppens approximation (type I, the Lorentzian angular distribution of mosaics blocks) [23]. In the refinement of the anharmonic thermal atomic vibrations, we expanded the temperature factor into the Gram–Charlier series [24]. The refinement of the structural parameters by the least squares method was made using the $|F|$ moduli and the atomic scattering curves and corrections for anomalous scattering [24]. The parameters of the diffraction experiment for the CdF_2 and $Cd_{0.90}Tb_{0.10}F_{2.10}$ crystals are listed in Table 1.

It was very important to determine *the chemical composition of a* $Cd_{1-x}Tb_xF_{2+x}$ *single crystal* because the $Cd_{0.90}Tb_{0.10}F_{2.10}$ compound melts incongruently (with decomposition), which may result in nonuniform terbium distribution along the crystalline boule.

Earlier, the compositions of the single crystals of the fluorite phases of the $M_{1-x}R_xF_{2+x}$ family selected for structural studies were determined using the concentration dependence of the unit-cell parameter. For the $Cd_{1-x}R_xF_{2+x}$ solid solutions, the RE content was determined from the equation $x = (a - a_0)/k$, where x is the molar fraction of RF_3, a is the lattice parameter of the solid solution, and a_0 is the lattice parameter of CdF_2. The values of coefficient k for the $Cd_{1-x}R_xF_{2+x}$ solid solutions were taken from [25]. For the $Cd_{1-x}Tb_xF_{2+x}$ sample, the TbF_3 content calculated from the established lattice parameter of the crystal studied [a = 5.433(4) Å] amounts to 13 mol %.

To refine the terbium content in the fragment of the single crystal boule used to cut out the sample for structural studies, we analyzed this fragment by atomic emission spectroscopy with inductively coupled plasma (ICP–AES). This analysis showed that the terbium fluoride content in the sample amounted to 10 ± 0.5 mol % or $x = 0.10 \pm 0.005$ mole fractions. Thus, within the accuracy of the analysis, the composition of the crystal coincided with the charge composition. This is the first determination of the composition in the middle part of the boule made by chemical analysis for the phases of the $Cd_{1-x}R_xF_{2+x}$ family. It shows that, similar to some other crystals of the $M_{1-x}R_xF_{2+x}$ composition (M = Ca, Sr, and Ba), the growth process in the middle part of the boule becomes stationary and the content of the RF_3 impurity is close to its content in the charge.

Taking into account the approximate values of coefficient k in the concentration dependence of the lattice parameter, we used in the calculations the composition $Cd_{0.90}Tb_{0.10}F_{2.10}$ obtained by spectroscopic analysis.

Table 1. Main characteristics of diffraction experiments on CdF_2 and $Cd_{0.90}Tb_{0.10}F_{2.10}$ single crystals

Sample	CdF_2	$Cd_{0.90}Tb_{0.10}F_{2.10}$
Diffractometer	CAD-4 Enraf Nonius	
Radiation, λ, Å	MoK_α, λ = 0.71069	
T, K	295	
Radius of spherical sample, μm	205(5)	156(5)
Absorption coefficient, mm^{-1}	13.37	16.24
Range of ω/2θ scanning, deg	0.80 + 0.35tan(θ)	
Maximum sinθ/λ, $Å^{-1}$	1.2	
Number of measured reflections	1601	2394
Number of independent reflections	88	88
$R_{av}(Int)$, %	2.41	2.03
Sp. gr.	*Fm*3*m*	
Lattice parameter, Å	5.393(3)	5.433(4)

REFINEMENT OF CdF_2 AND $Cd_{0.90}Tb_{0.10}F_{2.10}$ STRUCTURES

Refinement of the CdF_2 *structure.* Figure 1 shows the (110) sections of residual electron-density for a CdF_2 crystal. For fluorite phases, this is the most informative section, because all the basis and interstitial atoms of the structure are located in this section. Hereafter, we always consider these sections in the process of structure refinement. The residual electron-density synthesis shown in Fig. 1a is constructed after the subtraction of Cd and F atoms in the harmonic approximation of the atomic thermal vibrations. In the vicinity of the fluorine position, one can see the characteristic electron-density maximum and minimum indicating the deviation of the thermal vibrations of fluorine atoms from the harmonic law along the [111] direction. The introduction of third-order anharmonism of thermal vibrations of fluorine atoms removes these features of the electron-density synthesis. The corresponding section is shown in Fig. 1b. The structural parameters and the reliability factor obtained after the concluding refinement are shown in Table 2. The syntheses in Fig. 1 show the residual electron density at the point with the coordinates (0.5, 0.5, 0.5), which corresponds to the center of the empty cube of the structure. Detailed analysis showed that this maximum is due to the series termination.

In the CdF_2 structure, the Cd atoms occupy the centers of fluorine cubes. The Cd–F distances are equal to 2.335 Å, the cube edges F–F are equal to 2.697 Å, and the Cd–Cd distances are equal to 3.813 Å.

Refinement of the $Cd_{0.90}Tb_{0.10}F_{2.10}$ *structure.* The initial model for the refinement of this solid solution was the CdF_2 structure with due regard for the (Cd,Tb) and F atoms and 100% position occupancies. For the iso-

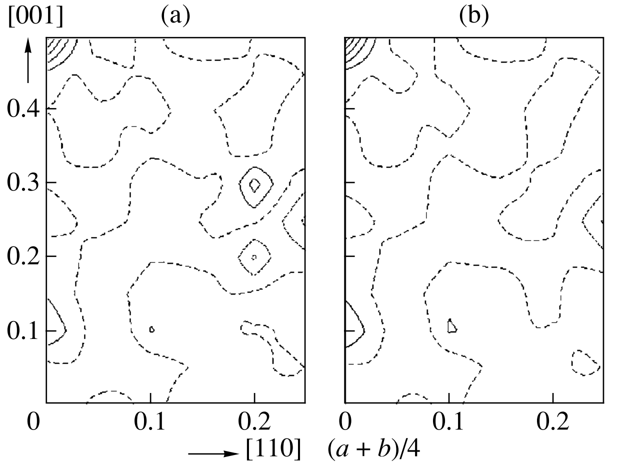

Fig. 1. The (110) section of the residual electron-density synthesis of the CdF_2 structure with removed Cd and F atoms. Isolines are separated by 0.1 e/Å^3. Solid lines indicate positive electron density; dotted lines, negative electron density; and the dashed line indicates the zero level. The synthesis is constructed (a) in the harmonic approximation of atomic thermal vibrations and (b) with due regard for the third-order anharmonicity of thermal vibrations of fluorine atoms.

morphous mixture (Cd,Tb), one mixed scattering curve was used. The difference electron-density synthesis obtained after the refinement of this model is shown in Fig. 2a. The synthesis was constructed using all the reflections of the experimental array except for 111 and 220. These most intense reflections were excluded from the least square procedure because the Becker–Coppens extinction correction for them did not eliminate the extinction effect and the moduli $|F_{obs}|$ of these reflections were considerably less than $|F_{calcd}|$.

The next variant of the difference electron-density synthesis is shown in Fig. 2b. It is constructed after the refinement of the occupancy of the position of the main fluorine. The details of this synthesis indicate the existence of the anharmonic component in the thermal vibrations of both cations (Cd, Tb) and fluorine. The allowance for the fourth-order anharmonicity in the thermal vibrations of (Cd, Tb) (synthesis in Fig. 2c) and third-order anharmonicity in the thermal vibrations of fluorine atoms (synthesis in Fig. 2d) considerably improves the synthesis.

Table 2. Results of the structure refinement for a CdF_2 crystal with allowance for third-order anharmonicity of thermal vibrations of F atoms

Atom	Parameters to be refined	Parameter values
Cd (0, 0, 0)	B_{iso}, Å^2	0.598(2)
F (1/4, 1/4, 1/4)	B_{11}, Å^2	0.00841(5)
	C_{123} 10^3, Å^2	0.0009(2)
Number of independent structure factors		88
Number of parameters to be refined		5
R, %		0.59
R_w, %		0.43

The difference synthesis in Fig. 2d has two pronounced electron-density maxima at the threefold symmetry axis in the position 32*f* of the sp. gr. $Fm3m$. These maxima are attributed to fluorine atoms of the tetrahedral core of the cluster and some of fluorine atoms relaxed (displaced) from the main positions along the threefold axis toward the centers of the empty cubes of the structure. The fluorine atoms in the main position are hereafter denoted as F_{main} and the relaxed ones, as F_{rel}. The position occupied by the fluorine atoms of the cluster core are called the additional position, and the fluorine atoms in this position are denoted as F_{add}. One should bear in mind that only some of these atoms are really additional to the CdF_2 stoichiometry. The coordinates of the F_{add} – (w, w, w) atoms are w, w, w, while those of the F_{rel} atoms are u, u, u, with $u < w$. The F_{rel} peak in Fig. 2d is approximately twice as high as the F_{add} peak.

The interstitial fluorine atoms detected by the X-ray diffraction method indicate the defect structure of $Cd_{0.90}Tb_{0.10}F_{2.10}$ crystals. The positions on threefold axes occupied by these atoms unambiguously indicate the tetrahedral configuration of the anionic core of the cluster described in [8].

The tetrahedral anionic core of the cluster is formed in the following way. One F_{main} atom leaves its position, and the cavity thus formed by the four adjacent empty cubes incorporates the tetrahedral group of four F_{add} atoms. One of these atoms compensates for the F_{main} atom that left its position, whereas the three other atoms should compensate for the difference in the valences between the cations of the Cd^{2+} matrix and the Tb^{3+} impurity. The formation of such a tetrahedral anionic core of the cluster is illustrated by Fig. 3.

Four cationic polyhedra around the anionic core of the cluster may incorporate two, three, or four Tb atoms. Thus, the composition of the tetrahedral clusters can be represented as $[Cd_{4-n}Tb_nF_{22+4}]$ ($n = 2, 3, 4$).

The cluster of the composition $[Cd_2Tb_2F_{26}]^{-1}$ ($n = 2$) has a negative charge that can be compensated for only with the vacancies in the main fluorine position. If the cluster has three Tb atoms, its composition is $[CdTb_3F_{26}]$ ($n = 3$). This cluster is electrically neutral. If we admit the existence of clusters with the composition $[Tb_4F_{26}]^{+1}$ ($n = 4$), then the excessive positive charge of the crystal would require the presence of four, and not three, additional fluorine atoms per cluster.

Studying the structure of the $Ca_{1-x}R_xF_{2+x}$ phases (from the lattice geometry of the phases close to $Cd_{1-x}R_xF_{2+x}$), one often assumes that a low electron-density peak in the center of the cubic void (Fig. 2d) should be attributed to an additional fluorine atom. This position has the coordinates (0.5, 0.5, 0.5) and is

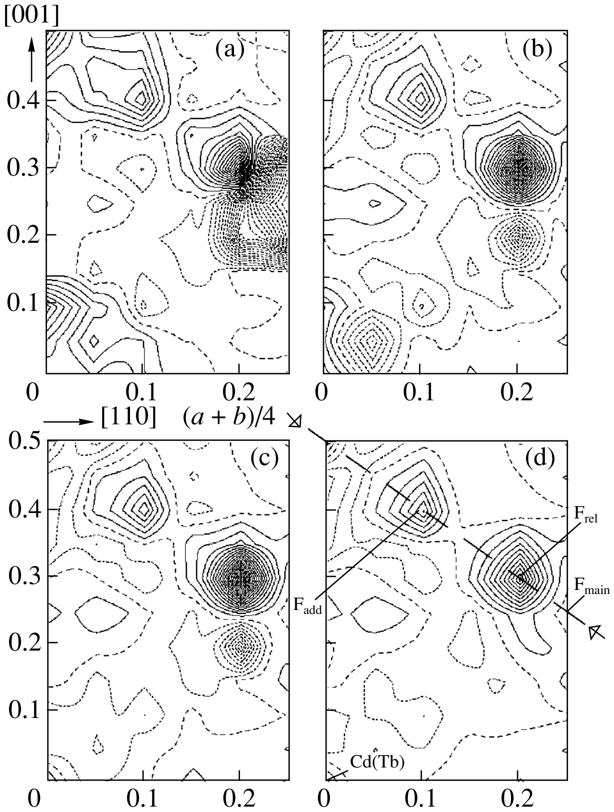

Fig. 2. The (110) section of the difference electron-density synthesis for the $Cd_{0.90}Tb_{0.10}F_{2.10}$ structure. Isolines are spaced by 0.05 e/Å^3. The synthesis is constructed (a) with the subtracted (Cd,Tb) atoms and fluorine atoms in the main structure position with 100% occupancy, (b) after the refinement of the occupancies of the main structural fluorine position, (c) after the allowance for the fourth-order anharmonism of (Cd,Tb) thermal vibrations, and (d) after the additional allowance for the third-order anharmonism of thermal vibrations of fluorine atoms.

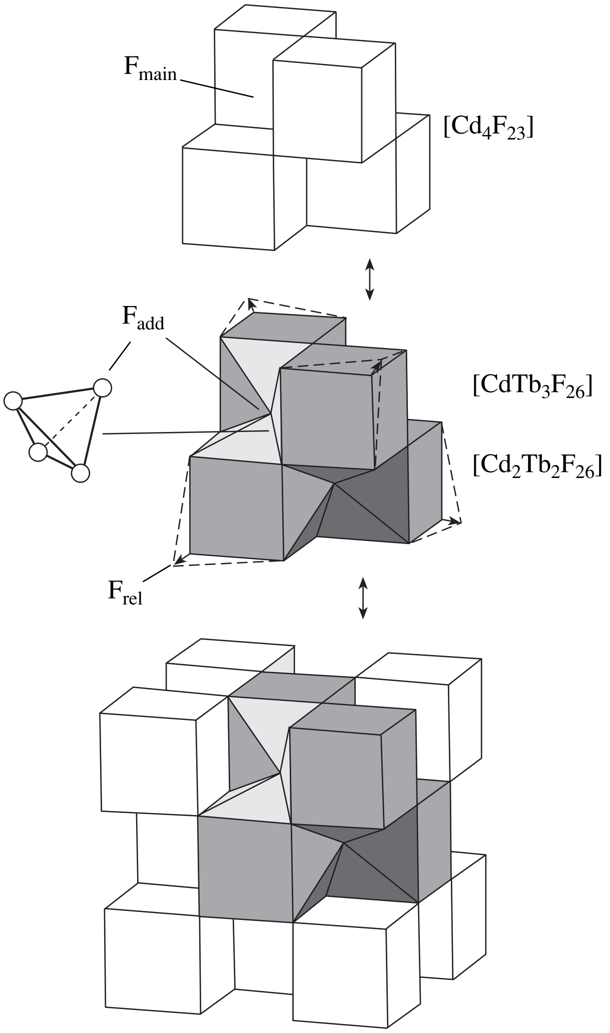

Fig. 3. Schematic of formation of $[Cd_{4-n}Tb_nF_{22+4}]$ clusters (n = 2, 3) in the crystal structure of the $Cd_{0.90}Tb_{0.10}F_{2.10}$ solid solution.

equally spaced from six heavy (Cd,Tb) atoms of the structure located around the void over the vertices of a regular octahedron. To check whether this peak is due to the series termination, we increased the real temperature factor in the experimental array by 25%. This procedure improved the series convergence and resulted in the complete disappearance of the peak indicated above. Thus, the $Cd_{0.90}Tb_{0.10}F_{2.10}$ solid solution has no $[Tb_4F_{26}]$ clusters.

At the next stage of the structure refinement, we constructed the section of the difference electron-density synthesis with the removed F_{main} and F_{add} atoms. This difference synthesis is shown in Fig. 4a.

At the final stage of the refinement, we also took into consideration the relaxed fluorine atoms F_{rel}. In this case, the total occupancy of all the fluorine positions was recorded in accordance with the chemical analysis of the solid solution at a level of 8.40 atoms per unit cell. The final difference synthesis of the electron density after the refinement of this model is shown in Fig. 4b. The structural parameters and the reliability factors obtained after this stage of the refinement are listed in Table 3.

DISCUSSION OF RESULTS

The main result obtained in our study is the determination of the total occupancy for the main and relaxed fluorine atoms, 6.90 + 0.96 = 7.86 atoms per unit cell. The multiplicity of the main fluorine position equals eight, which signifies that these positions contain up to 2% of the vacancies. It is these vacancies that may give rise to superionic conductivity of the $Cd_{1-x}R_xF_{2+x}$ solid solutions. The ionic transport in these crystals will be considered in one of the following publications of this series.

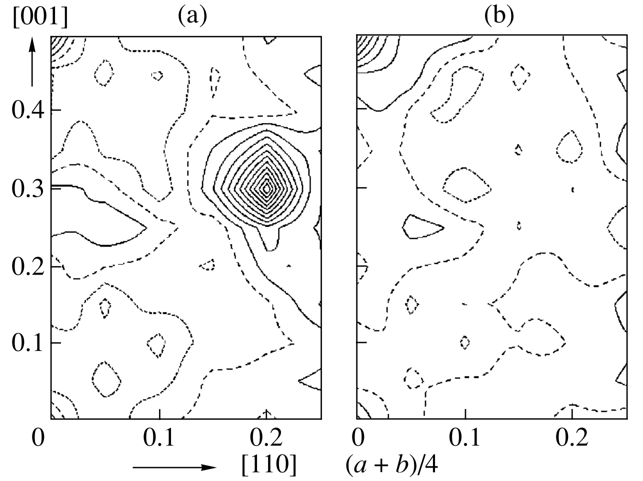

Fig. 4. The (110) sections of the difference electron-density syntheses for the $Cd_{0.90}Tb_{0.10}F_{2.10}$ structure. Isolines are spaced by 0.05 e/Å^3. (a) Difference synthesis constructed with the subtraction of (Cd,Tb), F_{main}, and F_{add} atoms; (b) difference synthesis constructed with the subtraction of all the atoms of the structure. One can see only the maximum due to series termination.

The determination of the occupancy of the position with F_{add} atoms allows us to obtain the additional information on the nature of the clusters of structural defects in the single crystal studied. Irrespective of the Cd/Tb ratio, each tetrahedral cluster has an anionic core formed by four interstitial fluorine atoms. It was shown above that there are no $[Tb_4F_{26}]$ clusters in the $Cd_{0.90}Tb_{0.10}F_{2.10}$ solid solution. So, we have only to consider the general case—the simultaneous presence of the $[CdTb_3F_{26}]$ and $[Cd_2Tb_2F_{26}]$ clusters in a single crystal.

Table 3. Results of the final refinement of the structure of a $Cd_{0.90}Tb_{0.10}F_{2.10}$ single crystal

Atom	Parameters to be refined	Parameter values
$(Cd_{0.90}Tb_{0.10})$	B_{11}, Å^2	0.00695(2)
(0, 0, 0)	$D_{1111} \times 10^4$, Å^2	0
	$D_{1122} \times 10^4$, Å^2	−0.000060(8)
F_{main}	Q, at/unit cell	6.90(7)
(1/4, 1/4, 1/4)	B_{11}, Å^2	0.0117(1)
	$C_{123} \times 10^3$, Å^2	0.0029(3)
F_{rel}	Q, at/unit cell	0.96(7)
(u, u, u)	u	0.305(2)
	B_{iso}, Å^2	2.1(2)
F_{add}	Q, at/unit cell	0.54(7)
(w, w, w)	w	0.418(2)
	B_{iso}, Å^2	1.4(2)
Number of independent structure factors		88
Number of parameters to be refined		13
R, %		0.25
R_w, %		0.28

The number of F_{add} atoms per unit cell obtained after the refinement of the structure of the $Cd_{0.90}Tb_{0.10}F_{2.10}$ single crystal equals 0.54. In this case, one cluster is shared by 4/0.54 = 7.41 unit cells. Proceeding from the chemical analysis, 7.41 unit cells contain 2.96 Tb atoms. We assume that the fraction of the $[CdTb_3F_{26}]$ clusters equals q and, respectively, the fraction of the $[Cd_2Tb_2F_{26}]$ clusters equals $(1 - q)$. After the solution of the equation $3q + 2(1 - q) = 2.96$, we obtain that the $Cd_{0.90}Tb_{0.10}F_{2.10}$ solid solution has 96% neutral clusters of the composition $[CdTb_3F_{26}]$ and 4% clusters of the composition $[Cd_2Tb_2F_{26}]$ with the negative unit charge. The vacancies in the main fluorine position are formed to compensate this negative charge and give rise to superionic conductivity with respect to fluorine.

The ratio of the number of fluorine atoms relaxed from the main positions to the number of the additional fluorine atoms obtained after the final refinement of the $Cd_{0.90}Tb_{0.10}F_{2.10}$ structure is ~1.8 : 1. Proceeding from the analysis of the interatomic distances in the $Cd_{0.90}Tb_{0.10}F_{2.10}$ structure, one may assume that it is the fluorine atoms of the main position that would be first to relax from this position. These atoms belong to the cluster and have no direct contact with additional fluorine atoms. The cluster has four such atoms and four additional fluorine atoms (Fig. 3). Since the number of relaxed fluorine atoms is higher than the number of the additional ones by a factor of 1.8, the other fluorine atoms related to the cluster also relax. Which these relaxing atoms are depends which cluster cations (Cd or Tb) they contact. The X-ray diffraction data cannot directly answer this question, because, in this case, one is dealing with one unit cell averaged over the whole single crystal.

All the interatomic distances related to the unit cell averaged over the crystal have admissible values. The distances between the (Cd, Tb) cation and the fluorine atoms in the main positions are 2.352 Å, and the distances of these cations to the additional fluorine atoms are 2.357 Å. The relaxed fluorine atoms are spaced from three cations by somewhat reduced distances of 2.234 Å and spaced from one cation by a longer distance of 2.870 Å. One may assume that, in the Tb polyhedron, the distances to the three additional fluorine atoms are equal to 2.357 Å and, to the six fluorine atoms in the main position, 2.352 Å. In this case, the tenth fluorine atom (a relaxed one) is spaced from terbium by a longer distance of 2.870 Å. This atom can be excluded from the polyhedron, and, then, the coordination number of Tb^{3+} in the $Cd_{0.90}Tb_{0.10}F_{2.10}$ structure becomes 9. This agrees with the conclusions drawn in [26] about the reduced coordination number of RE cations because of a decrease in their ionic radii in the row from La to Lu in the series of RE trifluorides. Three reduced

(Cd,Tb)–F_{rel} distances are equal to 2.234 Å and seem to be the distances to the Cd atoms surrounding the Tb polyhedron. The distances between the main fluorine atoms are 2.716 Å; those between the additional ones are 2.581 Å. The latter distances seem to be reduced, because these edges are shared by Tb polyhedra. The intercationic (Cd, Tb)– (Cd,Tb) distance equals 3.841 Å.

CONCLUSIONS

It is established by X-ray diffraction analysis that CdF_2 and $Cd_{0.90}Tb_{0.10}F_{2.10}$ crystals belong to the fluorite structure type. The refinement of the structure of $Cd_{0.90}Tb_{0.10}F_{2.10}$ single crystals using difference electron-density syntheses showed the presence of F_{add} fluorine atoms in the $32f$ (w, w, w) position on the threefold axis with the coordinates $w = 0.418$ of the sp. gr. $Fm3m$. The existence of relaxed F_{rel} fluorine atoms (displaced from the main positions along the threefold axes) is also established. These atoms occupy the position $32f$ $Fm3m$ (u, u, u) with $u = 0.305$. The number of fluorine atoms per unit cell localized in the main F_{main} positions is 6.90, that in the relaxed F_{rel} positions is 0.96, and that in the additional F_{add} positions is 0.54. The considerable prevalence (by a factor of about 1.8) of relaxed fluorine F_{rel} atoms over the additional fluorine F_{add} atoms is established in the fluorite $M_{1-x}R_xF_{2+x}$ phases (M = Ca, Sr, Ba, Cd; R = RE) for the first time. This seems to be the characteristic feature of the $Cd_{1-x}R_xF_{2+x}$ solid solutions.

The possible cluster configurations in the $Cd_{0.90}Tb_{0.10}F_{2.10}$ solid solution are analyzed. It is shown that the single crystal studied contains 96% electrically neutral clusters with the composition $[CdTb_3F_{26}]$ and 4% the charged clusters with the composition $[Cd_2Tb_2F_{26}]^{-1}$. The formation of these clusters is accompanied by the formation of vacancies with a concentration up to 2% in the main anionic motif of the structure. These vacancies may give rise to superionic conductivity with respect to fluorine in $Cd_{1-x}R_xF_{2+x}$ single crystals.

ACKNOWLEDGMENTS

The authors are grateful to L.P. Otroshchenko and A.M. Golubev for valuable remarks and discussions. The study was supported by the International Scientific–Technological Center (project no. 2136), and the Grant of the President of the Russian Federation to Scientific Schools (NSh-1642.2003.5 and NSh-1954.2003.2).

REFERENCES

1. I. I. Buchinskaya, E. A. Ryzhova, M. O. Marychev, and B. P. Sobolev, Kristallografiya **49** (3), 544 (2004) [Crystallogr. Rep. **49**, 544 (2004)].
2. B. P. Sobolev, A. M. Golubev, and P. Herrero, Kristallografiya **48** (1), 148 (2003) [Crystallogr. Rep. **48**, 141 (2003)].
3. O. Greis and J. M. Haschke, in *Handbook on the Physics and Chemistry of Rare Earths*, Ed. by Karl A. Gscheidner, Jr. and LeRoy Eyring (North-Holland, Amsterdam, 1982), Vol. 5, Chap. 45, p. 387.
4. O. Greis, Dissertation (Br. Albert-Ludwigs-Universität, Freiburg, 1976).
5. J. H. Burns, R. D. Ellison, and H. A. Levy, Acta Crystallogr., Sect. B: Struct. Crystallogr. Cryst. Chem. **24** (2), 230 (1968).
6. D. J. M. Bevan, O. Greis, and J. Strahle, Acta Crystallogr., Sect. A: Cryst. Phys., Diffr., Theor. Gen. Crystallogr. **36** (6), 889 (1980).
7. V. B. Aleksandrov and L. S. Garashina, Dokl. Akad. Nauk SSSR **189** (2), 307 (1969) [Sov. Phys. Dokl. **14**, 1040 (1969)].
8. L. A. Muradyan, B. A. Maksimov, and V. I. Simonov, Koord. Khim. **12** (10), 1398 (1986).
9. J. P. Laval, A. Mikou, and B. Frit, Solid State Ionics **28–30**, 1300 (1988).
10. C. R. A. Catlow, A. V. Chadwick, G. N. Greaves, *et al.*, Nature **312**, 601 (1984).
11. J. P. Laval, A. Abaouz, B. Frit, *et al.*, J. Solid State Chem. **85** (1), 133 (1990).
12. P. P. Fedorov, Butll. Soc. Catalanas Cien. Fis. Quim. Mat. **12** (2), 349 (1991).
13. V. V. Osiko, Fiz. Tverd. Tela (Leningrad) **7** (5), 1294 (1965) [Sov. Phys. Solid State **7**, 1047 (1965)].
14. C. R. A. Catlow, J. Phys. C: Solid State Phys. **6**, L64 (1973).
15. C. R. A. Catlow, J. Phys. C: Solid State Phys. **9**, 1859 (1976).
16. C. R. A. Catlow, Rev. Inorg. Chem. **2**, 1 (1980).
17. L. P. Otroshchenko, V. B. Alexandrov, L. A. Muradian, *et al.*, Butll. Soc. Catalanas Cien. Fis. Quim. Mat. **12** (2), 383 (1991).
18. B. P. Sobolev, V. B. Alexandrov, L. P. Otroshchenko, *et al.*, Butll. Soc. Catalanas Cien. Fis. Quim. Mat. **100**, 323 (1995).
19. L. E. Fykin, L. P. Otroschenko, V. B. Alexandrov, *et al.*, Physica B (Amsterdam) **234–236** (1), 121 (1997).
20. B. P. Sobolev, *The Rare Earth Trifluorides*, Part II: *Introduction to Materials Science of Multicomponent Metal Fluoride Crystals* (Inst. d'Estudis Catalans, Barcelona, 2001).
21. Kh. S. Bagdasarov, O. E. Izotova, A. A. Kaminskiĭ, *et al.*, Dokl. Akad. Nauk SSSR **188** (5), 1042 (1969) [Sov. Phys. Dokl. **14**, 939 (1970)].
22. V. Petricek and M. Dusek, in *Proceedings of JANA 2000* (Inst. of Physics, Acad. Sci. Czech Rep., Praha, 2000).
23. P. J. Becker and P. Coppens, Acta Crystallogr., Sect. A: Cryst. Phys., Diffr., Theor. Gen. Crystallogr. **30** (2), 129 (1974).
24. *International Tables for Crystallography,* Ed. by A. J. C. Wilson (Kluwer Academic, Dordrecht, 1992), Vol. C.
25. P. P. Fedorov and B. P. Sobolev, Kristallografiya **37** (5), 1210 (1992) [Sov. Phys. Crystallogr. **37**, 651 (1992)].
26. L. S. Garashina, B. P. Sobolev, and V. B. Aleksandrov, Kristallografiya **25** (2), 294 (1980) [Sov. Phys. Crystallogr. **25**, 171 (1980)].

Translated by L. Man

Crystallography Reports, Vol. 49, No. 4, 2004, pp. 598–602. Translated from Kristallografiya, Vol. 49, No. 4, 2004, pp. 676–680.
Original Russian Text Copyright © 2004 by Grigor'ev, Fedoseev, Budantseva, Bessonov, Krupa.

STRUCTURE OF INORGANIC COMPOUNDS

Synthesis and X-ray Diffraction Study of Complex Neptunium(VI) Potassium Chromate $K_2[(NpO_2)_2(CrO_4)_3(H_2O)] \cdot 3H_2O$

M. S. Grigor'ev*, A. M. Fedoseev*, N. A. Budantseva*, A. A. Bessonov*, and J.-C. Krupa**

** Institute of Physical Chemistry, Russian Academy of Sciences, Leninskiĭ pr. 31, Moscow, 119991 Russia*
e-mail: grigoriev@ipc.rssi.ru
*** Institute of Nuclear Physics, Orsay Cedex, 91406 France*

Received January 22, 2003

Abstract—The crystal structure of the $K_2[(NpO_2)_2(CrO_4)_3(H_2O)] \cdot 3H_2O$ compound was established. The structure consists of anionic layers $[(NpO_2)_2(CrO_4)_3(H_2O)]_n^{2n-}$, between which K+ ions and crystallization water molecules are located. The coordination polyhedra of Np atoms are distorted pentagonal bipyramids. All chromate ions are bound in a tridentate-bridging fashion. *© 2004 MAIK "Nauka/Interperiodica".*

Many uranyl chromates have been synthesized, and the structures of the majority of these compounds have been determined [1]. The $H_2O–Cs_2CrO_4–UO_2CrO_4$ system appeared to be rather simple, and, in this system, the formation of only two complexes with compositions $Cs_2[(UO_2)_2(CrO_4)_3]$ and $Cs_2[UO_2(CrO_4)_2(H_2O)]$ was observed [2].

In solutions of potassium chromate, uranyl undergoes hydrolysis to form the $K[UO_2CrO_4OH] \cdot 1.5H_2O$ complex [3]. The synthesis of complex uranyl chromates with the use of potassium bichromate gave rise to $K_2[(UO_2)_2(CrO_4)_3(H_2O)_2] \cdot 4H_2O$ [4] and $K_2[UO_2(CrO_4)_2(H_2O)] \cdot 3H_2O$ [5]. Of chromate compounds of transuranium elements in the oxidation state +6, only the neptunyl chromate carbamide complex $[NpO_2CrO_4\{OC(NH_2)_2\}_2]$ has been described [6]. In this complex, the chromate ion is coordinated in a tridentate-bridging fashion. It has also been noted that the behavior of hexavalent U, Np, and Pu is substantially different with respect to polymerization in the course of their hydrolysis, whereas these valence forms have very similar first hydrolysis constants [7]. However, this observation has found no explanation. Hence, it was of interest to study the behavior of neptunium(VI) (at least) in solutions of potassium chromate and compare it with the behavior of uranyl, because, under these conditions, the complex formation is accompanied by hydrolysis. In principle, these "yl" ions can be expected to show somewhat different behavior under the same conditions.

Chromate compounds of transuranium elements in the oxidation state +6 are also of interest from the viewpoint of crystal chemistry, because chromate ions in some uranyl chromates [8–10] are in an anomalous bidentate-chelating-bridging coordination mode. In this case, one of the oxygen atoms of the chromate ion serves as a bridge between two uranium atoms. As a result, the coordination polyhedra of the uranium atoms (pentagonal bipyramids) are linked by sharing an equatorial edge. This coordination mode is as yet unknown for other doubly charged tetrahedral oxo anions in uranyl compounds. The linking of coordination polyhedra by sharing equatorial edges through the bridging oxygen atoms is typical of Np(V) compounds. However, chromate ions in these compounds are also highly prone to chelating-bridging coordination [11–13].

EXPERIMENTAL

Synthesis

The starting solutions and instrumentation have been described previously [14].

A 0.4 M K_2CrO_4 solution was added dropwise to a 0.4 M solution of neptunyl nitrate devoid of free acid, which gave rise to a finely crystalline precipitate. This precipitate was dissolved upon vigorous stirring. When kept at room temperature even for a short time (~1 h), a solution containing equimolar amounts of chromate and neptunyl yielded small crystals, which slowly (for 20–30 h) recrystallized into relatively large rectangular plate-like dark red crystals. Their composition was determined as $K_2[(NpO_2)_2(CrO_4)_3(H_2O)_2] \cdot 8H_2O$ by X-ray diffraction. The crystal structure of this compound will be described elsewhere. It should be noted that the formation of crystalline products from a solution of neptunyl nitrate substantially slows down in the presence of even small amounts (0.05–0.1 M) of nitric acid. Under analogous conditions, uranyl forms the $K_2[(UO_2)_2(CrO_4)_3(H_2O)_2] \cdot 4H_2O$ complex, which has been established by powder X-ray diffraction analysis [4].

Prolonged storage of $K_2[(NpO_2)_2(CrO_4)_3(H_2O)_2] \cdot 8H_2O$ under a layer of a supernatant led to the slow formation of yet another crystalline compound. Its composition was determined by X-ray diffraction analysis and is described by the formula $K_2[(NpO_2)_2(CrO_4)_3(H_2O)] \cdot 3H_2O$ (**I**). In this study, we report the results of an X-ray diffraction study of complex **I**.

X-ray Diffraction Analysis

X-ray diffraction data were collected from a single crystal $0.25 \times 0.14 \times 0.08$ mm^3 in size on an automated CAD4 diffractometer (λMoK_α radiation, graphite monochromator). The monoclinic unit-cell parameters were determined based on 16 reflections with $2\theta > 26°$ at 20°C: $a = 10.797(5)$, $b = 10.492(6)$, $c = 16.121(7)$ Å, $\beta = 90.61(4)°$, sp. gr. $P2_1/c$, $Z = 4$, and $d_{calcd} = 3.707$ g/cm^3. A total of 2362 reflections ($2\theta_{max} = 48°$), of which 1965 independent reflections were with $I > 2\sigma(I)$, were measured. The experimental intensities were corrected for absorption using azimuthal scan curves [15] for seven reflections ($\mu = 13.33$ mm^{-1}; the maximum and minimum transmittances are 0.846 and 0.412, respectively). The structure was solved by a direct method (SHELXS86 [16]) and refined by the full-matrix least-squares method on F^2 (SHELXL93 [17]) with anisotropic thermal parameters for all non-hydrogen atoms. The hydrogen atoms of three out of four water molecules were located using a difference Fourier synthesis and refined isotropically with the fixed O–H distances. The final refinement (268 parameters) converged to $R(F) = 0.0255$ and $wR(F^2) = 0.0631$ (based on reflections with $I > 2\sigma(I)$). The atomic coordinates for the structure of **I** are given in Table 1. Selected interatomic distances and bond angles are listed in Table 2.

RESULTS AND DISCUSSION

The coordination polyhedra of both crystallographically independent Np atoms in the structure of **I** are distorted pentagonal bipyramids. The apical positions of the bipyramids are occupied by the “yl” O atoms. NpO_2 groups are almost linear and symmetrical, and all Np–O distances in these groups have close values (Table 2). One of the positions in the equatorial environment around the Np(1) atom is occupied by the coordinated water molecule O*w*(1). All other positions in the equatorial environment around both NpO_2 groups are occupied by the O atoms of three crystallographically independent tridentate-bridging CrO_4 groups and the symmetrically related groups (Fig. 1). The Np–O distances in the equatorial planes of the neptunyl groups vary from 2.318(7) to 2.408(6) Å for the O atoms of chromate ions and are equal to 2.498(7) Å for the coordinated water molecule.

Each NpO_2 group is linked to six other NpO_2 groups through chromate ions, forming anionic layers

Table 1. Atomic coordinates ($\times 10^4$) and equivalent (isotropic) thermal parameters (Å^2, $\times 10^3$) for the structure of **I**

Atom	*x*	*y*	*z*	$U_{eq(iso)}$
Np(1)	3901(1)	4645(1)	7684(1)	15(1)
Np(2)	9120(1)	5665(1)	8211(1)	15(1)
Cr(1)	6018(1)	6779(1)	8779(1)	17(1)
Cr(2)	2084(2)	7645(1)	7658(1)	19(1)
Cr(3)	992(1)	4173(1)	6534(1)	18(1)
K(1)	3168(3)	3967(3)	4022(2)	52(1)
K(2)	1067(3)	7345(3)	5073(2)	54(1)
O(1)	2721(6)	4330(6)	8375(4)	26(2)
O(2)	5100(6)	4958(6)	7012(4)	27(2)
O(3)	9858(6)	5138(6)	9113(4)	29(2)
O(4)	8373(6)	6194(7)	7312(4)	29(2)
O(11)	4850(6)	5749(6)	8758(4)	21(2)
O(12)	7303(6)	5958(6)	8957(4)	24(2)
O(13)	6087(6)	7521(6)	7881(4)	26(2)
O(14)	5819(7)	7762(7)	9523(4)	34(2)
O(21)	3309(6)	6742(6)	7459(4)	25(2)
O(22)	900(6)	6723(6)	7735(5)	34(2)
O(23)	1899(6)	8665(6)	6886(4)	30(2)
O(24)	2274(7)	8397(7)	8501(4)	40(2)
O(31)	2463(6)	4534(6)	6623(4)	25(2)
O(32)	340(6)	4263(6)	7443(4)	25(2)
O(33)	809(6)	2680(5)	6188(4)	22(2)
O(34)	363(7)	5114(7)	5894(5)	36(2)
O*w*(1)	5116(7)	3084(7)	8520(4)	28(2)
O*w*(2)	3323(8)	8747(7)	5156(5)	32(2)
O*w*(3)	1352(10)	2321(8)	4437(6)	68(3)
O*w*(4)	3306(12)	5823(10)	5196(6)	70(3)
H(1*A*)	5460(80)	3210(90)	8960(30)	20(30)
H(1*B*)	5460(80)	2610(70)	8190(50)	20(30)
H(2*A*)	3770(110)	8870(160)	4760(60)	90(60)
H(2*B*)	3250(100)	9410(50)	5410(60)	30(30)
H(4*A*)	3240(130)	5430(110)	5630(50)	60(50)
H(4*B*)	3940(80)	6160(150)	5030(100)	80(60)

Table 2. Selected interatomic distances (d) and bond angles (ω) in compound **I**

Distance	d, Å	Angle	ω, deg
Np(1)–O(1)	1.748(7)	O(1)–Np(1)–O(2)	178.8(3)
Np(1)–O(2)	1.745(7)		
Np(1)–O(11)	2.321(6)	O(11)–Np(1)–O(21)	76.5(2)
Np(1)–O(21)	2.321(6)	O(21)–Np(1)–O(31)	75.2(2)
Np(1)–O(31)	2.318(7)	O(11)–Np(1)–O*w*(1)	72.1(2)
Np(1)–O*w*(1)	2.498(7)	O(31)–Np(1)–O(13*A*)	71.4(2)
Np(1)–O(13*A*)	2.408(6)	O*w*(1)–Np(1)–O(13*A*)	65.9(2)
Np(2)–O(3)	1.747(6)	O(3)–Np(2)–O(4)	179.6(3)
Np(2)–O(4)	1.748(6)		
Np(2)–O(12)	2.360(6)	O(12)–Np(2)–O(23*A*)	75.5(2)
Np(2)–O(22*B*)	2.382(6)	O(22*B*)–Np(2)–O(32*B*)	69.4(2)
Np(2)–O(23*A*)	2.382(6)	O(23*A*)–Np(2)–O(32*B*)	71.6(2)
Np(2)–O(32*B*)	2.351(6)	O(12)–Np(2)–O(33*C*)	72.2(2)
Np(2)–O(33*C*)	2.327(6)	O(22*B*)–Np(2)–O(33*C*)	71.7(2)
Cr(1)–O(11)	1.677(6)	O(11)–Cr(1)–O(12)	108.3(3)
Cr(1)–O(12)	1.675(7)	O(11)–Cr(1)–O(13)	109.3(3)
Cr(1)–O(13)	1.645(6)	O(11)–Cr(1)–O(14)	108.6(4)
Cr(1)–O(14)	1.599(6)	O(12)–Cr(1)–O(13)	110.3(3)
		O(12)–Cr(1)–O(14)	108.9(4)
		O(13)–Cr(1)–O(14)	111.3(4)
Cr(2)–O(21)	1.679(7)	O(21)–Cr(2)–O(22)	108.8(3)
Cr(2)–O(22)	1.625(7)	O(21)–Cr(2)–O(23)	108.3(3)
Cr(2)–O(23)	1.652(6)	O(21)–Cr(2)–O(24)	110.3(4)
Cr(2)–O(24)	1.584(7)	O(22)–Cr(2)–O(23)	110.6(4)
		O(22)–Cr(2)–O(24)	109.2(4)
		O(23)–Cr(2)–O(24)	109.7(4)
Cr(3)–O(31)	1.664(7)	O(31)–Cr(3)–O(32)	110.0(3)
Cr(3)–O(32)	1.641(7)	O(31)–Cr(3)–O(33)	110.7(3)
Cr(3)–O(33)	1.674(6)	O(31)–Cr(3)–O(34)	109.3(4)
Cr(3)–O(34)	1.581(7)	O(32)–Cr(3)–O(33)	107.4(3)
		O(32)–Cr(3)–O(34)	110.8(4)
		O(33)–Cr(3)–O(34)	108.5(4)

Note: The coordinates of the atoms labeled by additional letters *A*, *B*, and *C* are related to those listed in Table 1 by the symmetry transformations $(1 - x, 0.5 - y, 1.5 - z)$, $(1 + x, y, z)$, and $(1 - x, 0.5 + y, 1.5 - z)$, respectively.

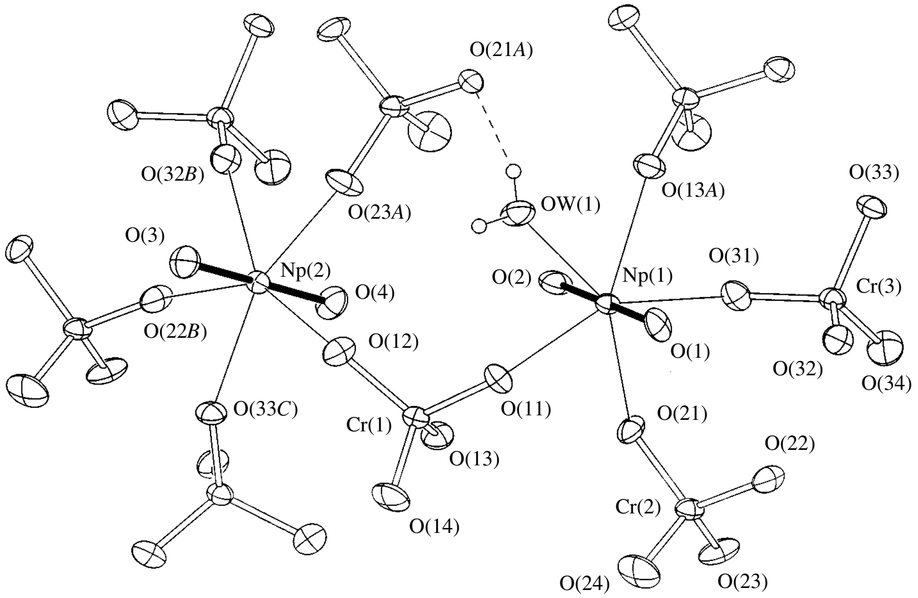

Fig. 1. Environment around Np atoms in the structure of **I**. The thermal ellipsoids are drawn at the 50% probability level. Hydrogen atoms are shown by spheres of arbitrary radius.

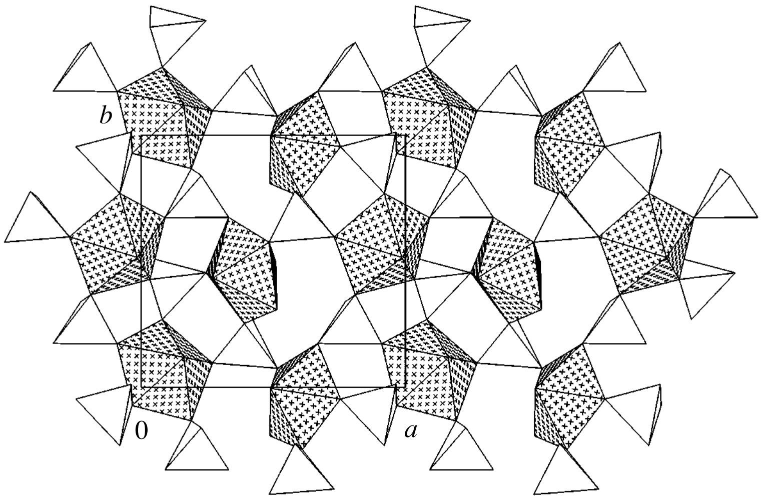

Fig. 2. Anionic layer $[(NpO_2)_2(CrO_4)_3(H_2O)]_n^{2n-}$ in the structure of **I**.

$[(NpO_2)_2(CrO_4)_3(H_2O)]_n^{2n-}$ (Fig. 2), between which K^+ ions and crystallization water molecules are located. The mean planes of the anionic layers coincide with the gliding planes (y = 1/4 and y = 3/4). The equatorial planes of the coordination polyhedra of Np atoms are not parallel to the mean plane of the anionic layer. The corresponding dihedral angles are 52.8° [Np(1)] and 34.6° [Np(2)]. It is probable that a large angle of rotation of the coordination polyhedron of the Np(1) atom is related to the presence of a hydrogen bond between the coordinated water molecule O*w*(1) and the water molecule O*w*(2) of crystallization located between the layers. The characteristics of this and other hydrogen bonds are listed in Table 3. The adjacent anionic layers are linked by hydrogen bonds in which the crystallization water molecules, O*w*(2) and O*w*(3), serve as proton donors.

It should be emphasized that the coordination mode of the chromate ions in complex **I** is analogous to that observed in many uranyl compounds. However, the composition and structure of **I** differ substantially from those of the uranyl chromates studied earlier.

The environment around K atoms is formed by the O atoms of the chromate ions, NpO_2 groups, coordinated water molecules, and crystallization water mole-

Table 3. Characteristics of hydrogen bonds in the structure of **I**

D(–H)···A	d(D–H)	d(H···A)	d(D···A)	DHA, deg	Symmetry operation for A
Ow(1)–H(1A)···Ow(2)	0.82(2)	2.02(4)	2.810(11)	164(10)	$-x + 1, y - 0.5, -z + 1.5$
Ow(1)–H(1B)···O(21)	0.82(2)	1.94(3)	2.742(9)	164(9)	$-x + 1, y - 0.5, -z + 1.5$
Ow(2)–H(2A)···O(11)	0.82(2)	2.06(2)	2.872(10)	178(17)	$x, -y + 1.5, z - 0.5$
Ow(2)–H(2B)···O(12)	0.81(2)	2.02(3)	2.815(10)	168(11)	$-x + 1, y + 0.5, -z + 1.5$
Ow(3)···O(1)			2.871(10)		$x, -y + 0.5, z - 0.5$
Ow(3)···O(33)			2.916(11)		x, y, z
Ow(4)–H(4A)···O(31)	0.82(2)	2.05(5)	2.832(12)	160(14)	x, y, z

cules. The coordination numbers of K atoms are 7 [K(1)] and 10 [K(2)]. The K–O distances vary from 2.72 to 3.05 Å and from 2.80 to 3.39 Å, respectively. The coordination polyhedra of K atoms are linked to each other by shared edges and vertices. The "yl" O(3) atom, the Ow(3) and Ow(4) atoms of the crystallization water molecules, and two of the three "free" atoms of the CrO_4–O(24) tetrahedra [O(24) and O(34)] serve as bridges.

In conclusion, let us compare the structure of **I** with the structures of other actinide complexes. Of compounds containing dioxo cations of actinides and tetrahedral doubly charged anions, a complex anion with a similar composition was found only in the structure of $(H_3O)_2[(UO_2)_2(SeO_4)_3(H_2O)] \cdot 5H_2O$ [18]. All the selenate ions in this structure are also coordinated in a tridentate-bridging mode, but the complex anion has a three-dimensional structure.

The X-ray diffraction study was carried out at the X-ray Structural Center of the Nesmeyanov Institute of Organoelement Compounds of the Russian Academy of Sciences, headed by M.Yu. Antipin.

REFERENCES

1. L. B. Serezhkina, Doctoral Dissertation in Chemistry (Moscow, 1996), pp. 70–71, 87–90.
2. L. B. Serezhkina, Zh. Neorg. Khim. **33**, 2966 (1988).
3. L. B. Serezhkina, V. K. Trunov, L. N. Kholodkovskaya, *et al.*, Koord. Khim. **16**, 1288 (1990).
4. N. V. Kuchumova, L. B. Serezhkina, and V. N. Serezhkin, Radiokhimiya **30**, 317 (1988).
5. V. N. Serezhkin, E. Yu. Grigor'eva, and N. V. Boĭko, Zh. Neorg. Khim. **30**, 717 (1985).
6. G. B. Andreev, M. Yu. Antipin, A. M. Fedoseev, and N. A. Budantseva, Kristallografiya **46** (3), 433 (2001) [Crystallogr. Rep. **46**, 383 (2001)].
7. G. R. Choppin and J. N. Marthur, Radiochim. Acta **52/53**, 25 (1991).
8. Yu. N. Mikhaĭlov, Yu. E. Gorbunova, E. A. Demchenko, *et al.*, Zh. Neorg. Khim. **43**, 1831 (1998).
9. Yu. N. Mikhaĭlov, Yu. E. Gorbunova, E. A. Demchenko, *et al.*, Zh. Neorg. Khim. **44**, 1444 (1999).
10. Yu. N. Mikhaĭlov, Yu. E. Gorbunova, E. A. Demchenko, *et al.*, Dokl. Akad. Nauk **358**, 360 (1998).
11. M. S. Grigor'ev, N. A. Baturin, A. M. Fedoseev, and N. A. Budantseva, Radiokhimiya **33** (5), 53 (1991).
12. M. S. Grigor'ev, T. E. Plotnikova, N. A. Baturin, *et al.*, Radiokhimiya **37**, 102 (1995).
13. M. S. Grigor'ev, T. E. Plotnikova, N. A. Baturin, *et al.*, Radiokhimiya **38**, 136 (1996).
14. A. Fedosseev, N. Budantseva, A. Bessonov, *et al.*, J. Alloys Compd. **271–273**, 154 (1998).
15. A. C. T. North, D. C. Phillips, and F. S. Mathews, Acta Crystallogr., Sect. A: Cryst. Phys., Diffr., Theor. Gen. Crystallogr. **24**, 351 (1968).
16. G. M. Sheldrick, Acta Crystallogr., Sect. A: Found. Crystallogr. **46**, 467 (1990).
17. G. M. Sheldrick, *SHELXL93. Program for the Refinement of Crystal Structures* (Univ. of Göttingen, Germany, 1993).
18. V. A. Blatov, L. B. Serezhkina, V. N. Serezhkin, and V. K. Trunov, Koord. Khim. **14**, 1705 (1988).

Translated by T. Safonova

Crystallography Reports, Vol. 49, No. 4, 2004, pp. 603–613. Translated from Kristallografiya, Vol. 49, No. 4, 2004, pp. 681–691.
Original Russian Text Copyright © 2004 by Belokoneva, Ivanova, Stefanovich, Dimitrova, Kurazhkovskaya.

STRUCTURE OF INORGANIC COMPOUNDS

New *Ln*[$B_6O_9(OH)_3$] Borates (*Ln* = Sm–Lu): Structure, Properties, and Structural Relation to Cationic $Li_4[B_7O_{12}]Cl$ Conductors (Li-Boracites)

E. L. Belokoneva, A. G. Ivanova, S. Yu. Stefanovich, O. V. Dimitrova, and V. S. Kurazhkovskaya

Moscow State University, Vorob'evy gory, Moscow, 119992 Russia
e-mail: elbel@geol.msu.ru

Received February 6, 2003

Abstract—Crystals of new rare earth borates of the composition *Ln*[$B_6O_9(OH)_3$] (*Ln* = Sm–Lu), sp. gr. *R3c* are synthesized under hydrothermal conditions. Their crystal structures are determined on single crystals with *Ln* = Ho, Gd without preliminary determination of their chemical formulas. The polar anionic framework of the crystals consists of BO_3 triangles and BO_4 tetrahedra and has wide channels along the threefold axis of the structure, which are similar to the channels along the *a*, *b*, and *c* axes in cubic $Li_4[B_7O_{12}]Cl$ boracite with Li conductivity. Rare earth atoms are arranged in the structure over the cubic F pseudolattice, whereas the analogous positions in Li boracites are filled with Cl anions. The squared optical nonlinearity of the new crystals is comparable with the nonlinearity of quartz, whereas the electrical conductivity in borates at 300°C exceeds 10^{-6} S/cm. © *2004 MAIK "Nauka/Interperiodica".*

INTRODUCTION

The continuing demand in technology for new effective nonlinear-optical and lasing materials is stimulating the further synthesis of noncentrosymmetric crystals in complex borate systems with rare earth elements and the study of their structures and properties. Some promising dehydrated rare earth borates have already been discovered in these systems [1, 2]. At present, only three aqueous borates are known—mineral braitshite (complicated calcium- and *Ln*-containing borate) with unknown structure [3], synthetic LiNd[$BO_3(OH)$] crystals [4], and recently synthesized and studied *Ln*[$B_4O_6(OH)_2$]Cl (Ln = Pr, Nd) borates [5] showing high optical nonlinearity. Below, we describe the study of the structure and dielectric and nonlinear optical properties of Ho and Gd borates (denoted as **I** and **II**, respectively).

SYNTHESIS OF CRYSTALS AND THEIR PROPERTIES

Single crystals of new *Ln* borates were obtained during the study of phase formation in Ln_2O_3–B_2O_3–H_2O systems (*Ln* = Sm, Eu, Gd, Ho, Tm, Yb, and Lu). The experiments were performed in standard 5–6-cm^3-large Teflon-futerated autoclaves. The synthesis parameters were $t = 270$–$280°C$, $P \sim 70$ atm; the lowest temperature was limited by the kinetics of the hydrothermal reaction, and the highest temperature, by the apparatus used. The experiment duration (18–20 days) was selected to ensure the reaction completion. The filling coefficient of the autoclave was selected in such a way as to maintain a constant pressure during the whole experiment. The weight ratio of the oxides was $Ln_2O_3 : B_2O_3 = 1 : 1$. The mineralizers were Cl^- and CO_3^{2-} ions. The highest transparency was recorded for 4-mm-long pale yellow or colorless Ho- and Gd-containing crystals with a cubic habit.

The diffraction patterns of all the phases with the Ln elements indicated above were identical and had no analogues in the PDF database, which allowed us to consider these crystals as new crystals. To determine the composition of crystals **I**, qualitative X-ray spectral analysis of the crystals was performed on a CAMSCAN 4DV scanning electron microscope with an attachment for energy-dispersive analysis (LINK Co.) at the Department of Petrography of the Geology Faculty of Moscow State University. The presence of Ho atoms in crystals **I** indicated the formation of a new borate, whereas the phases isostructural to this borate were borates containing the elements from the middle and end parts of the Ln series.

The powder samples were tested for noncentrosymmetricity by the method of second harmonic generation. The measurements on **I** and **II** crystals performed with the use of the pulsed Nd-activated YAG laser (backscattering scheme) [6] showed that, depending on the powder dispersion, the second-harmonic yield ranged within one to three and five to ten units of the quartz standard for crystals **I** and **II**, respectively. This uniquely indicated the absence of center of inversion in the structure. A more pronounced signal from crystals **II** in comparison with that from crystals **I** correlates with a higher transparency of crystals **II** in the green range of the spectrum at the wavelength of the second

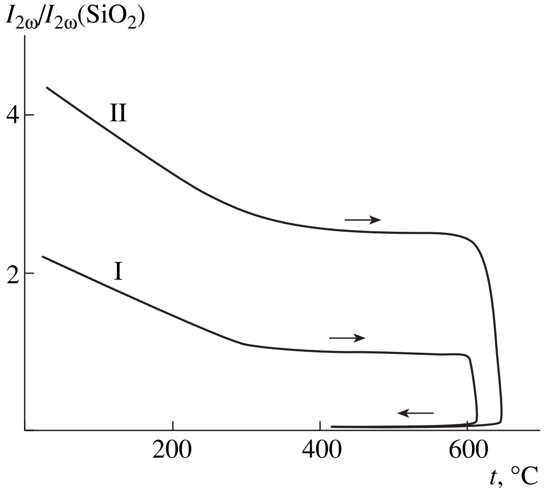

Fig. 1. Intensity of the second-harmonic generation in the units of quartz standard for grinded $HoB_6O_9(OH)_3$ (**I**) and $GdB_6O_9(OH)_3$ (**II**) crystals during heating and cooling (the direction of the temperature variation is indicated by arrows).

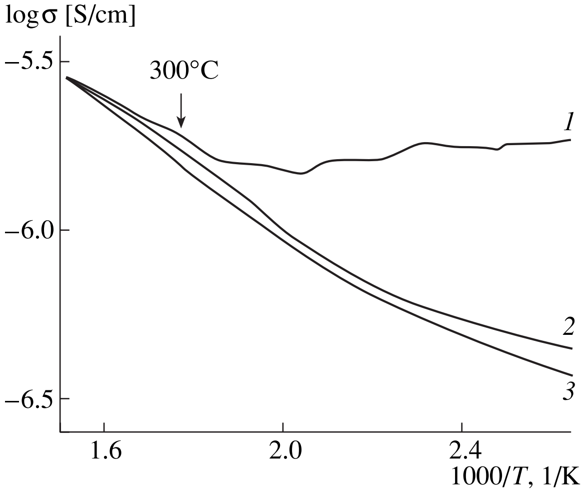

Fig. 2. Conductivity of the $HoB_6O_9(OH)_3$ polycrystal at a frequency of 1 MHz in different modes: (*1*) the first heating, (*2*) cooling, and (*3*) subsequent heating.

harmonic, $\lambda_{2\omega} = 0.532$ μm. The comparable intensities of the second-harmonic generation obtained on very fine powders of compounds **I** and **II** and on a quartz powder with the same dispersion (3–5 μm) allows us to state that the effective optical nonlinearity of newly synthesized borates is close to the value of nonlinear coefficient d_{11} of quartz, 0.364 pm/V. A relatively weak increase in the effect of the second-harmonic generation in the transition from finely-dispersed powders to powders with coarse particles (up to 30 μm) indicates the absence of the phase synchronism of neodymium-activated YAG laser radiation.

With an increase in temperature up to 300°C, the nonlinear optical activity of crystals **I** and **II** decreases, then attains a constant value, and, finally, at temperatures exceeding the critical temperature, t_{cr} (~610°C for **I** and 630°C for **II**), it irreversibly disappears (Fig. 1). Heating to the temperatures higher than T_c results in crystal turbidity and cracking, i.e., in effects usually accompanying the decomposition of hydrated compounds.

The electrical conductivity was measured on a polycrystalline sample of compound **I** having the form of a dense intergrowth of randomly oriented small single crystals. The intergrowth was used to prepare a 2.1 × 2.4 × 0.8-mm-plate with large surfaces metallized at room temperature by the application of Degussa silver-containing paste. The electrical measurements were made in the temperature range 20–400°C using an E7–12 a.c. bridge at a frequency of 1 MHz. Grown crystals **I** showed an elevated conductivity of the order of 10^{-6} S/cm characteristic of numerous ionic and, in particular, protonic conductors. An important fact is that crystals **I** showed elevated conductivity in the above temperature range only after the first cycle of heating (Fig. 2). The following heating–cooling cycles did not result in such a high conductivity in the low-temperature range, but the conductivity was preserved above 300°C. The temperature dependence of conductivity was similar to the temperature dependence characteristic of ionic conductors with low activation energies (~0.2 eV).

STRUCTURAL STUDY

The parameters of as-grown **I** and **II** crystals were determined and refined on a Syntex P-1 diffractometer (λMoK_α, graphite monochromator). Of all the possible vectors, we chose three mutually perpendicular vectors with the length ~11.9 Å corresponding to a possible cubic unit cell. The refinement of angles showed that the differences between the *a*, *b*, and *c* values exceed the standard deviations and that the angles between the vectors considerably differ from 90° (in tenths of a degree), which indicates the pseudocubicity of the crystals and that the true symmetry of the crystals is lower than cubic (hexagonal, orthorhombic, or, probably, monoclinic). In experiments with an Sm-containing crystal, its habit corresponded to a half-cube with a fused base and the body diagonal being parallel to the threefold axis. This brought us to the assumption that the lattice has a trigonal distortion. Single crystal **I** selected for the diffraction experiment also corresponded to a half-cube with the edge ~0.125 mm. A single crystal of compound **II** was selected for the diffraction experiment under a polarization microscope, where most of the crystals examined showed a twin boundary along the diagonal of the cube face. The dimensions of the selected crystal having the appropriate quality and the shape of a flattened cube were ~0.175 × 0.175 × 0.1 mm. In the pseudocubic *F* lattice of crystals **I** and **II**, some vectors corresponded to the

Table 1. Crystallographic data for $Ln[B_6O_9(OH)_3]$, where Ln = Ho (**I**) and Gd (**II**), and the characteristics of the experiment

	I	**II**
Brutto formula	$H_3O_{12}B_6Ho$	$H_3O_{12}B_6Gd$
Sp. gr., Z	$R3c$, 6	
a, Å	8.385(9)	8.410(4)
c, Å	20.71(4)	20.72(1)
V, $Å^3$	1261(5)	1269(2)
ρ_{calcd}, g/cm^3	3.35(1)	3.296(5)
μ, cm^{-1}	98.39	95.49
Weighting scheme	$1/[\sigma(F) + 0.001(F)]^2$	
Number of the parameters to be refined	58	58
2θ, $\sin\theta/\lambda_{max}$	100.25 & 1.080	100.37 & 1.081
Number of reflections with $F > 4\sigma(F)$	2740	2516
$R(F)$, R_w	0.0267, 0.0291	0.0485, 0.0521
S	0.970	1.690
Absolute scale	0.583(3)	0.569(6)

hexagonal (rhombohedral) lattice in which the direction of the trigonal distortion of the unit cell is the threefold axis, which coincides with one of the body diagonals of the cube [7]. In a number of variants, some vectors corresponded to an orthorhombic unit cell. The refinement of possible hexagonal parameters for several body diagonals of the cube revealed the unique direction of the trigonal distortion and the true axes. In all the cases (except for one), the scatter in the a and b parameters exceeded the standard deviations and the angles considerably differed from 90° and 120° (tenths of a degree). For Gd borate (**II**), the unit-cell parameters were slightly larger than those for the Ho borate (**I**) (Table 1), which is explained by the different ionic radii of these rare earth elements associated with the lanthanide contraction.

The experimental three-dimensional array of I_{hkl} used for the structure determination of compounds **I** and **II** was obtained in the reciprocal-space region $0 \le h \le 16$, $-16 \le k \le 16$, and $0 \le l \le 41$. The processing of intensities and their conversion into F^2_{hkl} was made using the PROFIT program [8], with all further computations being performed by the CSD complex. The extinction rules were: for hkl reflections, $-h + k + l = 3n$, and, for $h\bar{h}l$ reflections, $l = 2n$. With due regard for the crystal noncentrosymmetricity, these extinctions uniquely determined the polar space group $R3c - C^6_{3v}$. The structure of Ho borate (**I**) was determined by the heavy-atom method. The analysis of the P_{uvw} function revealed Ho atoms in the special 000 position (the origin of the space group was fixed by the z coordinate). The refinement of the thermal parameters with due regard for the scale factor yielded $R_{hkl} \sim 12.5\%$. The remaining two B and four O atoms were localized from the difference Fourier syntheses. The balance of valence strengths showed that the most “underloaded” atom is O(1); therefore, it was assumed to be an OH group, which allowed us to write the electrically neutral formula of new borate **I** as $Ho[B_6O_9(OH)_3]$. The least square refinement (using $F(hkl)$) of the positional and anisotropic thermal parameters with due regard for anomalous scattering of the Mo radiation, the variations of the weighting scheme, and the correction for absorption introduced by the DIFABS program [9] resulted in the final values listed in Table 1. The structure model of compound **II** was confirmed by computations (Tables 1, 2, and 3). This indicates the isostructurality of the compounds studied. A higher reliability factor for **II** is explained by the fact that crystal **I** had larger dimensions and an anisotropic shape, which hindered the correct allowance for absorption.

To determine the position of the H atom in compound **I**, we calculated the residual electron-density synthesis, which revealed a maximum with the coordinates $x = 0.24$, $y = 0.00$, and $z = 0.00$ and the O(1)–H distance 1.64 Å. This distance is larger than the conventional O–H distance and indicates the cationic function of hydrogen. The O(2)–H distance was 1.84 Å, which may be interpreted as the existence of the second O–H bond. The O(3)–H distance was 1.88 Å. The refinement of the H position results in its displacement [x = 0.24(1) Å, y = –0.02(1) Å, z = – 0.028(3) Å] toward the donor O(1) atom up to the attainment of the distance 1.1 Å, with the distance to the acceptor O(4) atom being 1.84 and the bond angle O(1)–H···O(4) being 107.3(6)°. However, it should be indicated that the refinement of the H positions in the structures of inorganic compounds by X-ray diffraction data often requires their displacement of H toward donor atoms, and the atomic coordinates obtained from high-resolu-

Table 2. Coordinates of basis atoms and their thermal parameters for $Ln[B_6O_9(OH)_3]$, where Ln = Ho (**I**) and Gd (**II**)

Atom	x/a	y/b	z/c	B_{eq}
Ho	0	0	0.00000	0.317(3)
Gd*	0	0	0	0.311(8)
O(1)	0.4322(5)	0.1612(4)	0.2577(2)	0.57(7)
	0.425(1)	0.158(1)	0.2603(4)	0.5(2)
O(2)	0.4238(4)	0.0111(5)	0.8497(2)	0.58(7)
	0.4243(9)	0.009(1)	0.8531(3)	0.6(2)
O(3)	0.0887(5)	0.2241(5)	0.0807(2)	0.59(7)
	0.0915(9)	0.225(1)	0.0841(4)	0.5(1)
O(4)	0.1348(5)	0.3335(5)	0.2991(2)	0.63(7)
	0.138(1)	0.334(1)	0.3015(3)	0.6(2)
B(1)	0.3701(6)	0.0401(7)	0.9148(2)	0.46(9)
	0.370(1)	0.037(1)	0.9176(5)	0.4(1)
B(2)	0.2445(7)	0.0101(6)	0.1328(3)	0.54(10)
	0.240(1)	0.007(1)	0.1355(5)	0.3(2)

* The second line in the entries indicates the atomic coordinates in the structure of Gd borate (**II**).

$T = \exp[-1/4(B_{11}a^{*2}h^2 + \ldots + 2B_{23}b^*c^*kl)]$,

$B_{eq} = 1/3[B_{11}a^{*2}a^2 + \ldots + 2B_{23}b^*c^*bc\cos\alpha]$.

tion syntheses are often more correct than the refined coordinates.

Powder diffraction patterns of the samples annealed at 350 and 600°C were the same as the patterns from the as-grown crystals. The diffraction pattern of compound **I** annealed at 650°C showed worse crystallinity—it contained some reflections corresponding to the $RbVF_3$- and $TlGaF_6$-type phases (PDF database).

The X-ray diffraction study of a single crystal annealed at 350°C showed that the unit-cell parameters correspond to the trigonal system and practically coincide with the unit-cell parameters of the initial sample. The refinement of the model obtained earlier in the same sp. gr. $R3c$ in the anisotropic approximation of atomic thermal vibrations and with due regard for absorption yielded the reliability factors $R = 0.0326$ and $R_w = 0.0336$ at $S = 0.98$. The residual electron-density synthesis had no peak corresponding to the position of the H atom, but, proceeding from the principle of electrical neutrality, the model of the structure of the new borate requires the presence of this atom.

To establish the existence of the proton–oxygen bonds in **I** and to determine the state of the crystals after heating above t_{cr}, we studied the corresponding IR spectra of these crystals. The spectra were recorded on a Specord-75 IR spectrophotometer by the method of fine-disperse films on KBr substrates in the frequency ranges of 3800–3000 and 1800–400 cm^{-1} (Fig. 3).

The valence vibrations of the B–O and B–O–B bonds of condensed BO_3 and BO_4 ions are responsible for the 1400–1250 and 1030–930 cm–1 bands (Fig. 3a). These bands have the same intensities; therefore, it is possible to assume that there are the same numbers of triangular and tetrahedral groups in the structure. The bands in the range 750–500 cm^{-1} are related to the deformation vibrations of the BO_3 and BO_4 ions. In the

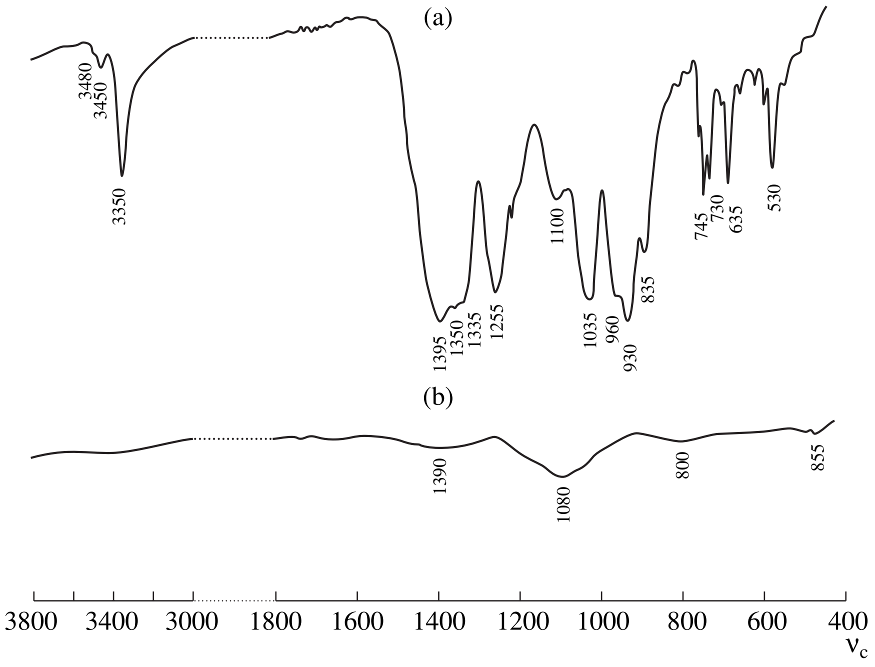

Fig. 3. Infrared spectrum of (a) the as-grown $Ho[B_6O_9(OH)_3]$ crystal and (b) product of its decomposition.

Table 3. Main interatomic distances *d* between cations and anions in the $Ln[B_6O_9(OH)_3]$ structures, where *Ln* = Ho (**I**) and Gd (**II**)

Nine-vertex polyhedron					
Bond	*d*, Å	Bond	*d*, Å	Bond	*d*, Å
Ho–O(1)	2.359 × 3 2.368 × 3*	Ho–O(2)	2.462 × 3 2.491 × 3	Ho–O(3)	2.341 × 3 2.399 × 3
B(1) tetrahedron		B(2) triangle			
Bond	*d*, Å	Bond	*d*, Å		
B(1)–O(1)	1.451(13) 1.43(1)	B(2)–O(2)	1.37(3) 1.37(1)		
B(1)–O(2)	1.48(4) 1.47(2)	B(2)–O(3)	1.39(3) 1.37(1)		
B(1)–O(3)	1.506(10) 1.51(1)	B(2)–O(4)	1.369(10) 1.37(1)		
B(1)–O(4)	1.48(3) 1.48(2)				

* The second line in the entries indicate the interatomic distances in the structure of Gd borate (**II**).

range of vibrations of O–H bonds in the borate spectrum, there is an intense band at 3350 cm^{-1} and a weak band at 3450 cm^{-1} with the shoulder at 3480 cm^{-1}. The band at 1100 cm^{-1} corresponds to the in-plane deformation vibrations of B–OH, and the band at ~835 cm^{-1} corresponds to the out-of-plane deformation vibrations. The existence of two additional weak bands in addition to the main intense band of OH vibrations indicates a certain misorientation of OH bonds. For crystals annealed at temperatures slightly lower than 600°C, the band structure of the spectra and the band intensities remain unchanged.

The IR spectrum of the product of decomposition of Ho-containing borate is shown in Fig. 3b. It is characteristic of holmium borate glass. A broad diffuse band with the maximum at 1390 cm^{-1} corresponding to the B–O vibrations of triangular ions is much less intense than the band of BO_4 vibrations at 1080 cm^{-1}. The vibration band of BO_3 ions (~800 cm^{-1}) is diffuse and has a low intensity. The change of the triangular coordination to the tetrahedral one is characteristic of borate glasses with an elevated content of cations, e.g., of alkali, alkali earth, or Pb ions [10]. The shift of the band to higher frequencies due to vibrations of tetrahedral ions can be explained by an increase in the electron-density contribution of trivalent holmium to the B–O bond because of the bond polarization.

RESULTS AND DISCUSSION

In crystal structures **I** and **II**, the Ln atoms (Ho, Gd) are coordinated by nine oxygen atoms (Table 3) at distances of 2.5 Å, of which six atoms [three O(3) and three O(1)] form a trigonal prism whose side faces are centered by O(2) atoms. Such a polyhedron is called a tricapped prism and is well known for Ln cations. The Ln polyhedra in the structure are isolated. In accordance with the ionic radii of Ho and Gd, the average interatomic Gd–O distances in **II** are larger by 0.065 Å than the corresponding Ho–O distances in **I** (2.419 and 2.354, respectively).

The anionic part of the structure consists of boron atoms in the triangular and tetrahedral coordination. Two independent polyhedra, the B(1) tetrahedron and B(2) triangle, are multiplied by the symmetry elements of the structure (threefold axes, *c* planes, and lattice translations *R*) and share their vertices to form the $[B_6O_9(OH)_3]^{3-}$ framework. This framework consists of hexagonal $[B_6O_{12}(OH)_3]^{9-}$ rings with symmetry *3* formed by alternating tetrahedra and triangles, which share the O(3) and O(4) vertices (altogether, three tetrahedra and three triangles). The tetrahedra and triangles have a polar orientation along the *c* axis (Figs. 4a, 4b). The polar rings are connected along the *c* axis via the O(2) oxygen vertices and form the polar framework. The O(1) atoms form dangling vertices of tetrahedra looking outside the rings. Their charge is compensated with B(1) and Ho and H atoms. The framework has six *z*-levels: ~0.10, ~0.27, ~0.44, ~0.60, ~0.77 and ~0.94 (Fig. 4b), at which the rings are located. The framework has through channels with ditrigonal section along the *c* axis (Fig. 4c) whose centers are occupied by Ln atoms. The channels are formed by the above rings (narrower in the cross section) and three pairs of triangles and tetrahedra that form open rings (wider in the cross section) (Fig. 4a). In addition to the vertical channels, the framework also has narrower horizontal channels (Fig. 4b), which allows us to relate the compound framework to the so-called zeolite-type open frameworks. Figure 4d shows the structure in the pseudocu-

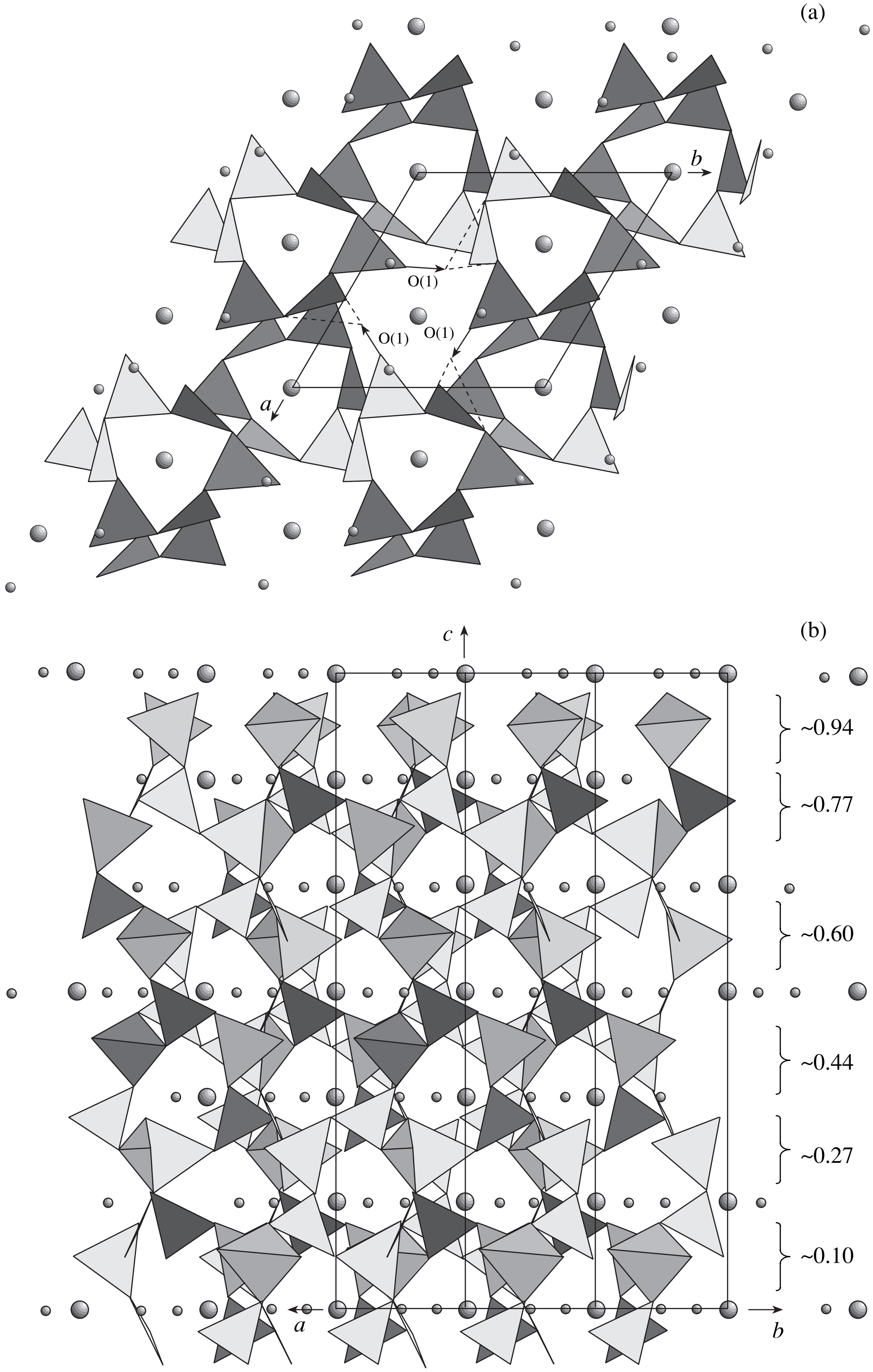

Fig. 4. Crystal structure of $Ln[\mathrm{B_6O_9(OH)_3}]$ (*Ln* = Sm–Lu),B] compounds (*Ln* = Ho and Gd). One can see B tetrahedra and B triangles; the Ho and H atoms are indicated by larger and smaller circles, respectively. (a) The *ab* projection showing two framework levels along the *c* axis and boron-oxygen rings, (b) side projection of the framework showing six levels of the rings along the *x* axis, (c) the *ab* projection, and (d) the trigonal unit cell in the pseudocubic setting.

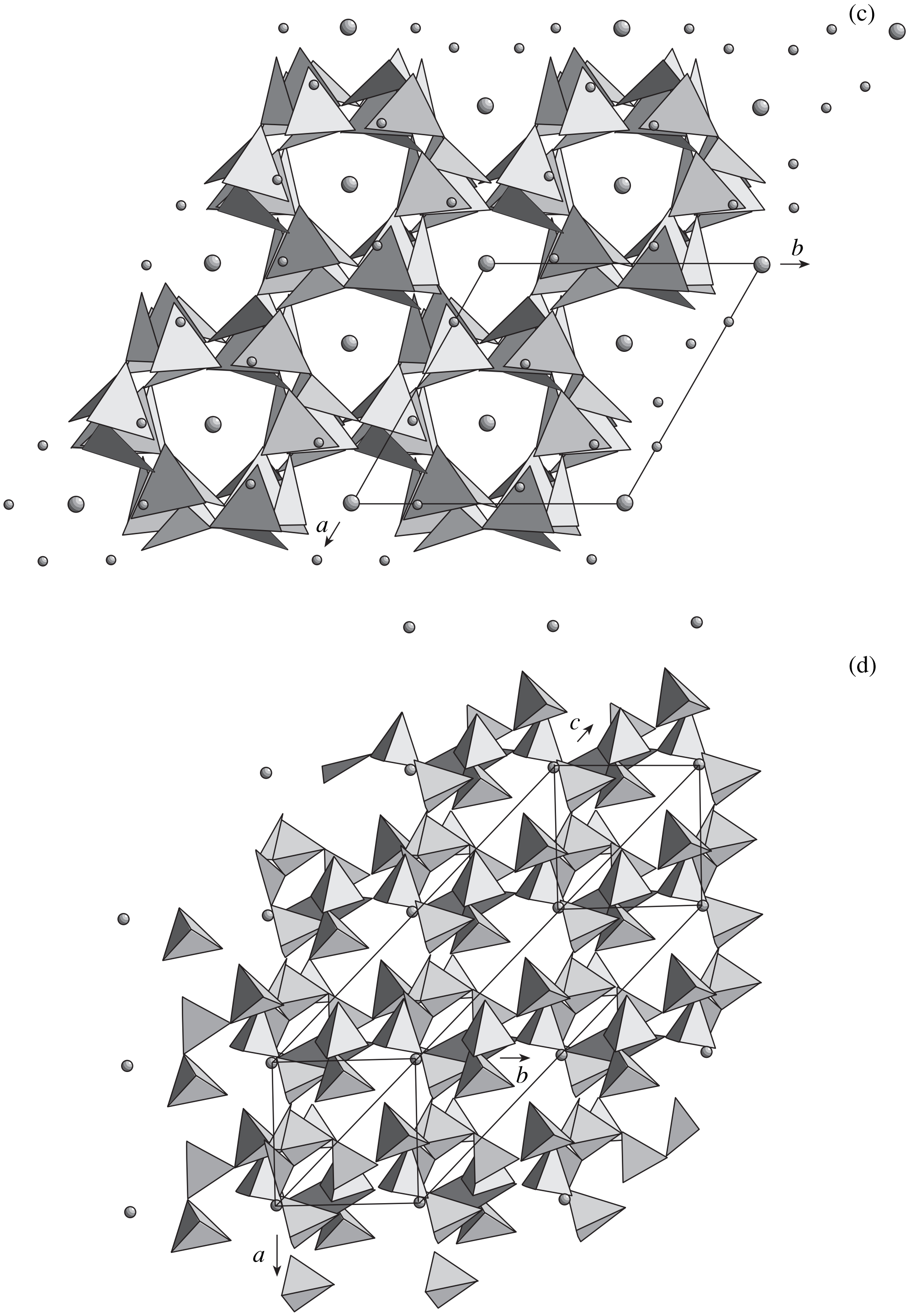

Fig. 4. (Contd.)

bic setting. The Ho atoms satisfy the law of the cubic *f* lattice, but the anionic boron–oxygen framework does not obey the cubic symmetry.

According to the classification principles described in [11], new Ln borates should be related to hexaborates. Their structures are based on the hexaborate fundamental building blocks in the shape of rings, $6[3\triangle + 3T] - [B_6O_{12}(OH)_3]^{9-}$. For the first time, such a block incorporated into the framework was revealed in the structures of synthetic Li boracites of the composition $Li_4[B_7O_{12}]Cl$ (Figs. 5a, 5b).

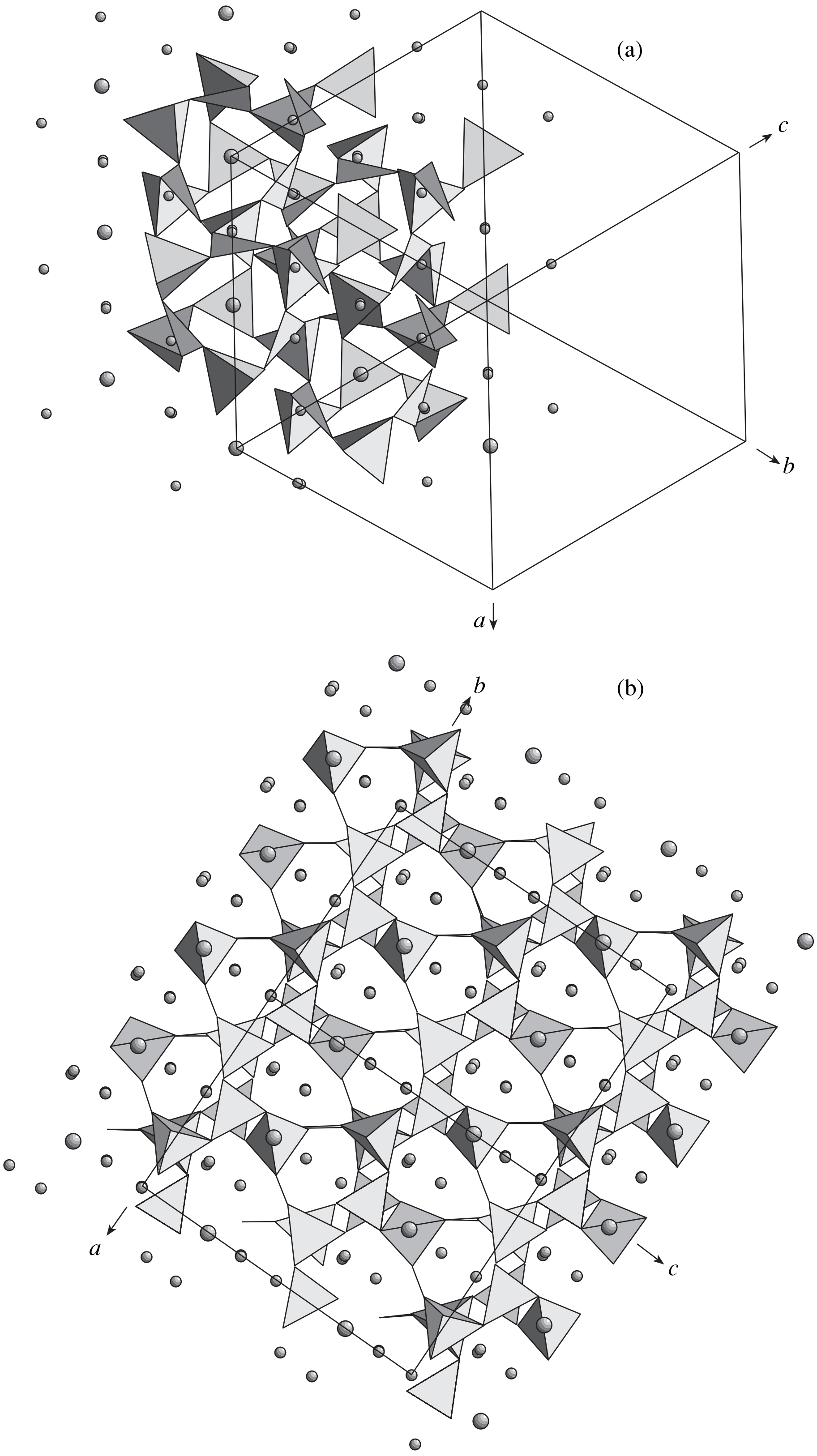

Fig. 5. Crystal structure of the $Li_4[B_7O_{12}]Cl$ compound showing B tetrahedra and B triangles; Cl and Li atoms are shown by large and small circles, respectively. (a) Structure fragment in the hexagonal setting, (b) side projection of the framework in a setting similar to that shown in Fig. 4b, (c) the *ab* projection.

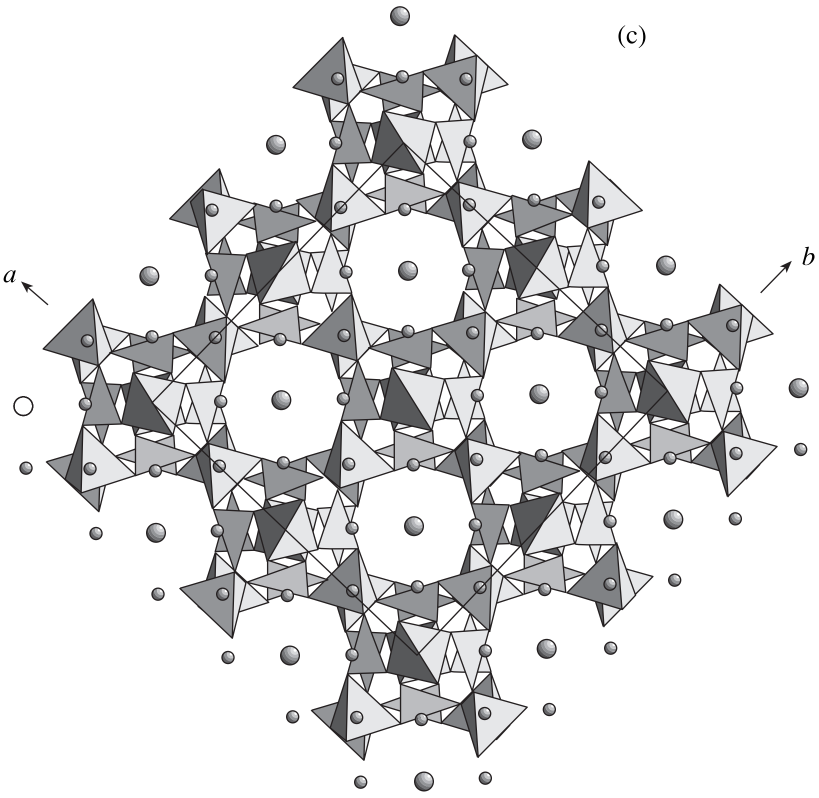

Fig. 5. (Contd.)

New Ln hexaborates show obvious similarity to Li boracites. As was indicated above, one can single out pseudocubic parameters ~12 Å in their lattices. The positions of Ln elements correspond to the positions of Cl anions (Fig. 5c). The framework of the cubic γ phase of Li boracite is somewhat different from the frameworks of new borates—the through channels are directed along the coordinate axes, and all the oxygen vertices are shared by B tetrahedra and B triangles. Thus, cubic boracite has no dangling vertices compensated in **I** and **II** with protons. A higher cationic conductivity with respect to Li is characteristic of the high-temperature cubic γ phase formed from the tetragonal and rhombohedral $Li_4[B_7O_{12}]Cl$ modifications as a result of several successive displacive-type phase transitions [12].

As was indicated in [12], the structures of synthetic $Mg_3[B_7O_{13}]Cl$, $Cr_3[B_7O_{13}]Cl$, and $Ni_3[B_7O_{13}]Cl$ boracites have additional O atoms lying in the centers of rings. As a result, the B triangles share the O vertex and the B coordination increases to tetrahedral. If the block topology is preserved, its formula can be written as 6[6T]. The block is connected with the framework via the additional B triangle. Such a block was found not only in synthetic but also in natural boracites—cubic, trigonal, rhombohedral (congolite), and orthorhombic (chambersite).

There exists a third variety of the hexaborate block with such a topology. In this block, three tetrahedra share one common oxygen atom and three end B tetrahedra are replaced by B triangles, so that the block formula is written as 6[3△ + 3T]. This block is the basis of the structures of a number of natural and synthetic hexaborates [13, 14]. The existence of a large family of minerals based on the 6[3△ + 3T] block seems to be associated with its high stability, rigidity, low charge, and, thus, energetically advantageous structure.

Among the compounds with the open zeolite framework, there is the well-known orthorhombic rubidium beryllosilicate [15], in which one can single out six-membered $Rb_2[Be_2Si_2O_7]$ rings composed of three (Si^{4+}) tetrahedra and three ($[Be_3Si_3O_{10.5}]^{3-}$) triangles similar to those observed in borates considered above, in which these positions are occupied by Be^{2+} ions. In other words, we encounter here the classical scheme of heterovalent isomorphism. The framework projections of both structures are similar. One can see wide channels centered either by Ho (in borate) or Rb (in beryllosilicate) atoms. The frameworks have different topologies because of the polar orientation of the B tetrahedra in new borate, whereas, in beryllosilicates, Si tetrahedra are oriented with their vertices alternatively up and down and the Be triangles are in the planes of the triangular bases of Si tetrahedra (Figs. 6a, 6b). Both struc-

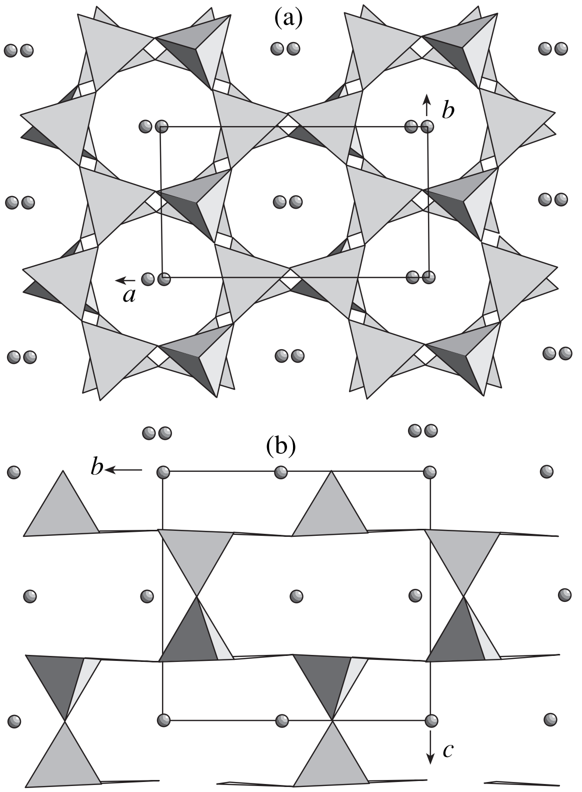

Fig. 6. Crystal structure of the $Rb_2Be_2Si_2O_7$ compound. (a) The *ab* projection and (b) the *bc* projection.

tures have different metrics and belong to different systems.

At the same time, the frameworks built by tetrahedra in the structures of kalsilite and, especially, beryllonite types (Fig. 7) [15] are topologically close to the framework of compound **I**. It is possible to represent the structural transformation of the framework of **I** (consisting of tetrahedra and triangles) under pressure into the purely tetrahedral framework. This transformation should be accompanied by the compression of open rings and small displacement of the O(1) atom (the dangling vertex of the B tetrahedron) and its incorporation into the coordination of the B triangle accompanied by the transformation of triangles into tetrahedra (Fig. 4a). In this case, the positions of Ln atoms and H cations are preserved. The metrics of the unit cells of beryllonite $NaBePO_4$ and new borate correlate with one another. Indeed, three parameters along the monoclinicity axis *b* of beryllonite (7.818 Å) form the *c* parameter of new borate; the pseudohexagonal axes *c* with the lattice parameter ~8.18 Å (the *a* axis of beryllonite) can readily be selected in the perpendicular plane.

CONCLUSIONS

The analysis of the temperature studies of the second-harmonic generation, the structural data, and the IR spectra shows their consistency and indicates the stability of new holmium and gadolinium borates over wide temperature ranges with the preservation of H atoms and their bonds mainly with O(1) atoms and, to a lesser degree, also with O(2) atoms at temperatures up to t_{cr} = 610 (630)°C. The decomposition of the above compounds at temperatures above t_{cr} results in the formation of borate glass in which the Ho concentration is higher than its concentration in the as-grown crystal. The Ho distribution in borate glass is close to the arrangement of Rb and Tl atoms in the compounds indicated above. This process is accompanied by a change of the triangular coordination of B atoms to the tetrahedral coordination.

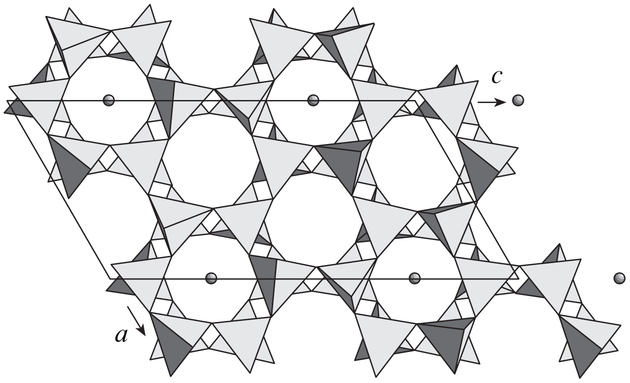

Fig. 7. Crystal structure of beryllonite $NaBePO_4$, the *ac* projection,

The enhanced thermal vibrations of H^+ ions revealed at 350°C give rise to diffusion of the proton position, but not to its removal. The indicated partial proton delocalization at high temperatures manifests itself in weakening of the second-harmonic generation effect and in a rather high conductivity and a low activation energy. The first indications of the structural disorder of protons in the frameworks of $HoB_6O_9(OH)_3$ and $GdB_6O_9(OH)_3$ crystals require detailed study of proton transport in larger single-crystal and polycrystal samples.

ACKNOWLEDGMENTS

The authors are grateful to N.A. Korotaeva for determination of the chemical composition of the crystals. This work was supported by the Russian Foundation for Basic Research, project no. 02-03-33316.

REFERENCES

1. N. I. Leonyuk and L. I. Leonyuk, *Crystal Chemistry of Anhydrous Borates* (Mosk. Gos. Univ., Moscow, 1983).
2. P. A. Arsen’ev, L. M. Kovba, Kh. S. Bagdasarov, *et al.*, in *Compounds of Rare-Earth Elements: Systems with the Oxides of Elements from Groups I–III*, Ed. by P. A. Arsen’ev and L. M. Kovba (Nauka, Moscow, 1983).

3. O. B. Raup, A. J. Gude, E. J. Awornik, *et al.*, Am. Mineral. **53**, 1081 (1968).
4. G. K. Abdullaev, G. G. Dzhafarov, and Kh. S. Mamedov, Kristallografiya **29** (6), 1084 (1984) [Sov. Phys. Crystallogr. **29**, 635 (1984)].
5. E. L. Belokoneva, S. Yu. Stefanovich, O. V. Dimitrova, and A. G. Ivanova, Zh. Neorg. Khim. **47** (3), 370 (2002).
6. S. Yu. Stefanovich, in *Extended Abstracts of European Conference on Lasers and Elecrto-Optics (CLEO-Europe'94)* (Amsterdam, 1994), p. 249.
7. Yu. K. Egorov-Tismenko and G. P. Litvinskaya, *Theory of Crystal Symmetry* (GEOS, Moscow, 2000), p. 393.
8. V. A. Strel'tsov and V. E. Zavodnik, Kristallografiya **34** (6), 1369 (1989) [Sov. Phys. Crystallogr. **34**, 824 (1989)].
9. N. Walker and D. Stuart, Acta Crystallogr., Sect. A: Found. Crystallogr. **39**, 158 (1983).
10. *The Infrared Spectra of Minerals*, Ed. by V. C. Farmer (Mineralogical Society, London, 1974), p. 206.
11. H. Strunz, Eur. J. Mineral. **9**, 225 (1997).
12. W. Jeitschko, T. A. Bither, and P. E. Bierstedt, Acta Crystallogr., Sect. B: Struct. Crystallogr. Cryst. Chem. **33**, 2767 (1977).
13. E. L. Belokoneva, T. A. Korchemkina, and O. V. Dimitrova, Zh. Neorg. Khim. **44** (6), 951 (1999).
14. E. L. Belokoneva, S. Yu. Stefanovich, T. A. Borisova, and O. V. Dimitrova, Zh. Neorg. Khim. **46** (11), 1788 (2001).
15. P. A. Sandomirskiĭ and N. V. Belov, *Crystal Chemistry of Mixed Anionic Radicals* (Nauka, Moscow,1984).

Translated by L. Man

Crystallography Reports, Vol. 49, No. 4, 2004, pp. 614–618. Translated from Kristallografiya, Vol. 49, No. 4, 2004, pp. 692–696.
Original Russian Text Copyright © 2004 by Trubach, Beskrovnyĭ, A. Orlova, V. Orlova, Kurazhkovskaya.

STRUCTURE OF INORGANIC COMPOUNDS

Synthesis and Investigation of the New Phosphates $K_2LnZr(PO_4)_3$ (Ln = Ce–Yb, Y) with Langbeinite Structure

I. G. Trubach*, A. I. Beskrovnyĭ, A. I. Orlova*, V. A. Orlova*, and V. S. Kurazhkovskaya*****

**Nizhni Novgorod State University, pr. Gagarina 23, Nizhni Novgorod, 630950 Russia*
***Joint Institute for Nuclear Research, Dubna, Moscow oblast, 141980 Russia*
****Moscow State University, Vorob’evy gory, Moscow, 119899 Russia*

Received February 13, 2003

Abstract—New orthophosphates of potassium, zirconium, and rare earth elements $K_2LnZr(PO_4)_3$ (Ln = Ce–Yb, Y) that crystallize in a langbeinite structure (cubic system, sp. gr. $P2_13$, $Z = 4$) were prepared and investigated by X-ray diffraction and IR spectroscopy. The structure of the $K_2PrZr(PO_4)_3$ phosphate was refined by the Rietveld method using neutron powder diffraction data (DN-2 time-of-flight diffractometer, Joint Institute for Nuclear Research, Dubna). This structure is characterized by a mixed framework $[PrZr(PO_4)_3]$ with large cavities in which potassium cations are located. Pr^{3+} and Zr^{4+} cations are distributed in order over two independent crystallographic positions. The limits of the incorporation of lanthanide cations into the anionic framework in phosphates with sodium–zirconium phosphate and langbeinite structures are considered. *© 2004 MAIK “Nauka/Interperiodica”.*

INTRODUCTION

Crystalline compounds with a framework structure of the $[T_2(PO_4)_3]^{n-}$ type (T are elements with an oxidation state from +1 to +5, and n is the framework charge) constitute a significant part of a large number of inorganic orthophosphates. The number of structural types into which compounds with these frameworks crystallize is limited and is determined by the possible character of the connection between discrete PO_4 and TO_6 polyhedra (the discreteness of these two kinds of polyhedra is due to the ratio $T : P = 2 : 3$ [1]) and depends on the types of T cations and cations compensating the framework charge, as well as on their combination in the compound composition. Among the well-known structural types, the sodium–zirconium phosphate $NaZr_2(PO_4)_3$ (NZP or NASICON) is most widespread; however, depending on the nature of the cations and their ratio, other structural types may also arise.

One of the structural modifications of the $[T_2(PO_4)_3]$ framework is a cubic structure of langbeinite type. The mineral langbeinite, $K_2Mg_2(SO_4)_3$, forms a family of isostructural analogs—sulphates described by the general formula $M_2^{+}M_2^{2+}(SO_4)_3$, where M^+ = K, Rb, Cs, Tl, and NH_4 and M^{2+} = Mg, Ca, Mn, Co, Ni, Zn, Cd, and Fe.

At present, phosphates with a langbeinite structure are only represented by separate compounds. In most of them, the framework is formed by small multiply charged Ti^{3+}, Ti^{4+}, Cr^{3+}, and Fe^{3+} cations (although Y, Gd [2], and Bi [3] cations, which are larger in size, can also form the framework), while cavities are occupied by large low-charge cations Na^+, K^+, and Ba^{2+} cations: $KTi_2(PO_4)_3$ [4], $K_{1.75}Ti_2(PO_4)_3$ [5], $K_2Ti_2(PO_4)_3$ [5, 6], $Na_2CrTi(PO_4)_3$, $Na_2FeTi(PO_4)_3$ [7], $KBaFe_2(PO_4)_3$ [8], and $KBaCr_2(PO_4)_3$ [9]. The number of similar representatives containing zirconium or hafnium is smaller (the NZP type is more typical of them). In this case, along with zirconium cations, yttrium, gadolinium, or bismuth cations of larger size are also involved in the framework formation: $K_2YZr(PO_4)_3$, $K_2GdZr(PO_4)_3$ [2], and $K_2BiHf(PO_4)_3$ [3].

The combination of zirconium and trivalent lanthanides is not typical of framework compounds with relatively high concentrations of the latter: in phosphates with an NZP structure, the fraction of framework positions occupied by lanthanides does not exceed 0.5 for the smallest lanthanide cation and significantly decreases with an increase in the REE-cation radius [10]. At the same time, the phosphate $K_2GdZr(PO_4)_3$ is known, and it crystallizes in a langbeinite structure. In this structure, REE cations occupy half of the framework positions (for comparison, in phosphates of the $Na_{1+x}Gd_xZr_{2-x}(PO_4)_3$ series, the maximum gadolinium content is $x_{max} = 0.3$). The existence of the $K_2GdZr(PO_4)_3$ phosphate suggests the existence of isoformula phosphates with a langbeinite structure containing other lanthanides. The synthesis and properties of these compounds are of interest from the point of view of crystal chemistry, since they supplement ideas of the isomorphism of trivalent lanthanides in framework structures and provide new information on their anion-forming function in phosphates with a framework structure.

The purpose of this study was to synthesize and study phosphates of potassium, zirconium, and trivalent

Table 1. Unit-cell parameters of $K_2LnZr(PO_4)_3$ phosphates

Ln	R_{Ln}, Å	Sample color	*a*, Å	*V*, Å^3
Pr	0.99	Light green	10.3528(10)	1109.61
Sm	0.96	Light yellow	10.324(4)	1100(1)
Eu	0.95	White	10.328(4)	1101(1)
Gd	0.94	White	10.306(4)	1094(1)
Dy	0.91	White	10.323(4)	1100(1)
Ho	0.90	White	10.297(4)	1091(1)
Y	0.90	White	10.296(4)	1092(1)
Er	0.89	Light pink	10.271(4)	1083(1)
Tm	0.88	White	10.266(4)	1081(1)
Yb	0.87	White	10.266(4)	1081(1)
Lu	0.86	White	10.249(4)	1077(1)

Table 2. Crystallographic data and refinement parameters for the structure of the $K_2PrZr(PO_4)_3$ phosphate

Space group	$P2_13$
Z	4
d range, Å	0.75–3.79
Number of reflections	290
R_{exp}	2.45
R_{wp}	2.34
R_p	2.7
χ^2	3.6
Number of refined parameters	39

Table 3. Coordinates and thermal factors B_{iso} of atoms in the structure of the $K_2PrZr(PO_4)_3$ phosphate

Atom	Position	*x*	*y*	*z*	B_{iso}, Å^2
K(1)	4*a*	0.0416(16)	0.0416(16)	0.0416(16)	3.5
K(2)	4*a*	0.2907(14)	0.2907(14)	0.2907(14)	3.5
Pr	4*a*	0.5705(12)	0.5705(12)	0.5705(12)	2.6
Zr	4*a*	0.8547(7)	0.8547(7)	0.8547(7)	2.5
P	12*b*	0.6243(9)	0.4658(6)	0.2582(10)	0.2
O(1)	12*b*	0.6682(10)	0.5180(7)	0.3801(11)	2.7
O(2)	12*b*	0.7352(10)	0.4658(7)	0.1629(9)	2.8
O(3)	12*b*	0.5883(9)	0.3281(6)	0.2615(7)	1.7
O(4)	12*b*	0.5217(7)	0.5566(8)	0.1975(9)	2.0

lanthanides with the general formula $K_2LnZr(PO_4)_3$ (*Ln* = Ce–Lu) by X-ray powder diffraction and IR spectroscopy and refine the structure of the $K_2PrZr(PO_4)_3$ phosphate by neutron powder diffraction.

EXPERIMENTAL

The samples were synthesized by the sol–gel method. One-molar aqueous solutions of KCl, $ZrOCl_2$, $Ln(NO_3)_3$, and H_3PO_4 were used as starting reagents. In the initial stage of synthesis, a calculated amount of orthophosphoric acid was slowly added, with stirring, to solutions of metal salts taken in a stoichiometric ratio. The sol obtained was dried at 95°C, dispersed in an agate mortar, and heated successively at 400, 600, 800, 1000, 1100, and 1200°C with intermediate dispersion in each stage.

The samples were investigated by X-ray powder diffraction on a DRON-2.0 X-ray diffractometer using filtered CoK_α radiation (Fe filter, λ = 1.78892 Å) in the range of reflection angles 2θ = 10°–60°. IR spectra were recorded on a Specord-75IR spectrophotometer in the range of wave numbers from 1400 to 400 cm^{-1} (samples were prepared by deposition of a fine-dispersed suspension in isopropyl alcohol on a KBr substrate with subsequent drying).

The neutron diffraction pattern of a powder sample placed in a cylindrical container (*d* = 10 mm) was measured at room temperature on a DN-2 time-of-flight diffractometer installed in the base of the IBR-2 pulsed fast neutron reactor (Joint Institute for Nuclear Research, Dubna). The structure was refined by the Rietveld method using the Mria program [11].

RESULTS AND DISCUSSION

The samples obtained were either white or colored powders (Table 1). The X-ray diffraction patterns of all the samples heated at 800°C contained reflections characteristic of the $K_2YZr(PO_4)_3$ phosphate, which crystallizes in the langbeinite structure. In the case of lanthanum-, cerium-, or neodymium-containing samples,

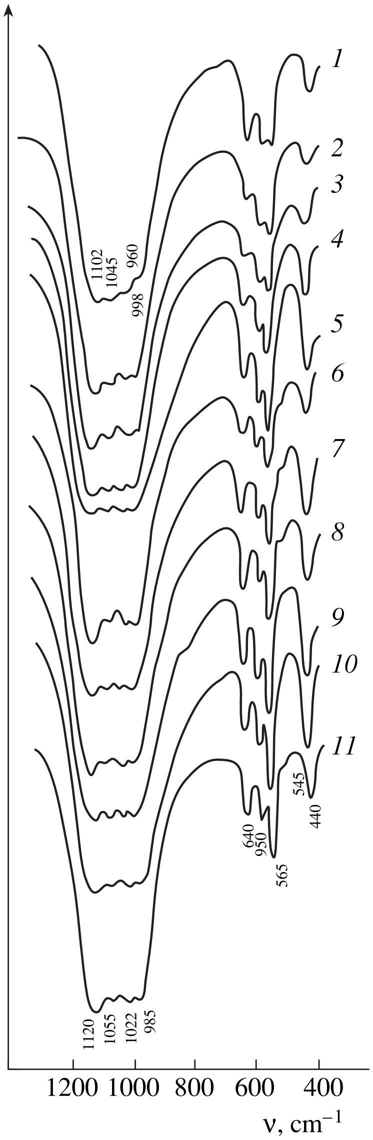

Fig. 1. IR spectra of the $K_2LnZr(PO_4)_3$ phosphates: Ln = (*1*) Pr, (*2*) Sm, (*3*) Eu, (*4*) Gd, (*5*) Dy, (*6*) Ho, (*7*) Y, (*8*) Er, (*9*) Tm, (*10*) Yb, and (*11*) Lu.

along with the reflections from the langbeinite phase, we also observed reflections from the double potassium–zirconium phosphate $KZr_2(PO_4)_3$ and the simple phosphate of the corresponding lanthanide, $LnPO_4$. Further heating at 1000 and 1100°C resulted in an increased crystallinity of the samples and made it possible to obtain them in the form of single-phase products (except for the La-, Ce-, and Nd-containing samples).

The X-ray diffraction data indicate that, at 1200°C, partial decomposition of the compounds occurs with formation of the simple phosphate $LnPO_4$ and ZrO_2. Heating at 1300°C led to the complete decomposition of the phosphates under study. Using the $K_2YZr(PO_4)_3$ phosphate as a structural analog, we performed analytical indexing of the X-ray diffraction patterns of the compounds obtained and calculated the unit-cell parameters (Table 1).

The IR spectroscopy data indicates that the compounds obtained belong to the orthophosphate class (Fig. 1). The spectra of the compounds contain all the absorption bands that can be predicted by the theory of groups for phosphorus tetrahedra in a crystal lattice with the sp. gr. $P2_13$. Asymmetric stretching and bending vibrations (ν_3 and ν_4) of phosphorus tetrahedra give rise to three bands per each type in the frequency ranges 1120–990 and 640–560 cm^{-1}, respectively; symmetric stretching vibrations (ν_1) give rise to one band (985–960 cm^{-1}); and symmetric stretching vibrations (ν_2) give rise to a weak band at ~440 cm^{-1}. In going from the praseodymium-containing phase to the lutetium-containing one, a systematic shift of all the spectral bands (especially bands due to stretching vibrations) to higher frequencies is observed, which is related to the decrease in the REE-cation radius. In the IR spectra of the compounds containing REEs from Ho to Lu (Fig. 1, curves *6*–*11*), an additional shoulder (or a weak band) arises in the region of bending ν_4 vibrations at 545 cm^{-1}.

The structure of the $K_2PrZr(PO_4)_3$ phosphate was refined using the neutron powder diffraction data. The values of the coordinates of atoms in the $K_2YZr(PO_4)_3$ phosphate reported in [8] were used as a starting model to refine the structural characteristics. The unit-cell parameters and the results of refining the structure of $K_2PrZr(PO_4)_3$ are listed in Table 2. The experimental and theoretical profiles of the neutron diffraction pattern of a sample under study and the difference curve, normalized to the standard deviation at a point, are shown in Fig. 2. The calculated positional and thermal parameters, as well as the corresponding values of interatomic distances and the bond angles, are listed in Tables 3 and 4.

A fragment of the structure of $K_2PrZr(PO_4)_3$ is shown in Fig. 3. It is based on the mixed anionic framework $[PrZr(PO_4)_3]$ constructed from discrete PrO_6, ZrO_6, and PO_4 polyhedra. A characteristic fragment of this framework is a group (dimer) formed of two octahedra linked by three bridge tetrahedra $\{M_2(PO_4)_3\}^{2-}$. Sharing oxygen atoms, these dimers form a three-dimensional network with large cavities.

Pr^{3+} and Zr^{4+} cations are distributed over two nonequivalent structural positions 4*c*, being located in distorted MO_6 octahedra. Potassium cations completely occupy framework cavities and are coordinated by nine oxygen atoms. In comparison with the analog, the compound under study shows greater distortion of the phosphate tetrahedron, which is, apparently, due to the incorporation of large praseodymium cations into the framework and the corresponding significant strains.

In contrast to the isoformula phosphates $K_2LnZr(PO_4)_3$ and $K_2GdZr(PO_4)_3$, for which the statistical characters of distribution of zirconium cations and the trivalent element have been ascertained [2],

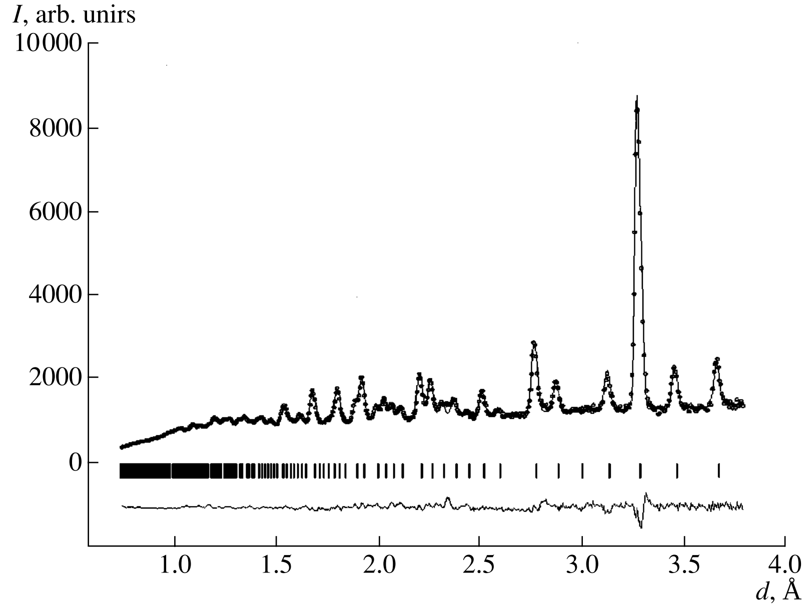

Fig. 2. Experimental (circles), theoretical (solid line), and difference (experiment minus calculation) profiles, normalized to the standard deviation at point, of the neutron diffraction pattern of a $K_2PrZr(PO_4)_3$ sample. Vertical bars are the calculated positions of diffraction peaks.

praseodymium and zirconium cations are completely ordered over the framework positions in the compound under study. Such a distribution of these cations seems to be very likely if we take into account the significant difference in their nature (the electronic shell structure), as well as the significant difference in their sizes (37.5%).

Thus, the data obtained indicate that all the phosphates of potassium, zirconium, and trivalent REE, described by the general formula $K_2LnZr(PO_4)_3$, are crystallized in the cubic langbeinite structure. Lanthanide cations, along with zirconium ones, are involved in the formation of the complex anionic framework. Lanthanide cations have an octahedral environment in LnO_6 polyhedra, which is not typical of them. It should be noted that, in the case of isoformula sodium compounds $Na_2LnZr(PO_4)_3$, only one phosphate with *Ln* = Yb (*R* = 0.87 Å), crystallizing in the NZP structure [10], was obtained as a single-phase product. Thus, the highest molar fraction of trivalent lanthanides involved, along with zirconium, in the framework formation is obtained for the potassium compounds $K_2LnZr(PO_4)_3$, which are formed for all REEs independent of their ionic radii. Obviously, the type of alkali compensating cations significantly affects the character of the obtained structure.

Table 4. Selected interatomic distances (Å) and bond angles (deg) in the structure of the $K_2PrZr(PO_4)_3$ phosphate

$K(1)O_9$ polyhedron		$K(2)O_9$ polyhedron		PO_4 tetrahedron			
K(1)–O(1)	3.12 × 3	K(2)–O(2)	3.40 × 3			O(1)–P–O(2)	109.3
K(1)–O(2)	2.92 × 3	K(2)–O(3)	3.12 × 3	P–O(1)	1.45	O(1)–P–O(3)	114.9
K(1)–O(4)	2.68 × 3	K(2)–O(4)	3.11 × 3	P–O(2)	1.51	O(1)–P–O(4)	110.0
⟨K–O⟩	⟨2.91⟩	⟨K–O⟩	⟨3.21⟩	P–O(3)	1.47	O(2)–P–O(3)	101.9
MO_6 octahedron				P–O(4)	1.55	O(2)–P–O(4)	104.8
Pr–O(1)	2.28	Zr–O(3)	2.20	⟨P–O⟩	⟨1.50⟩	O(3)–P–O(5)	115.0
Pr–O(2)	2.26	Zr–O(4)	2.03			⟨O–P–O⟩	⟨109.3⟩
⟨Pr–O⟩	⟨2.27⟩	⟨Zr–O⟩	⟨2.12⟩				

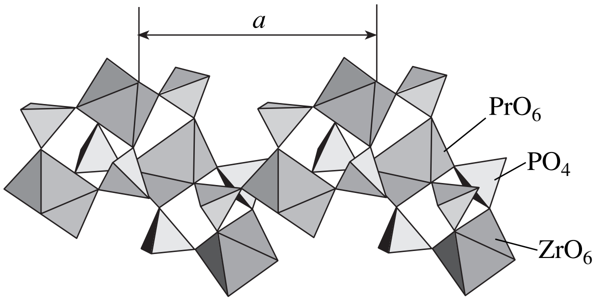

Рис. 3. Фрагмент каркаса фосфата $K_2PrZr(PO_4)_3$.

ACKNOWLEDGMENTS

This study was supported by the Russian Foundation for Basic Research (project nos. 01-03-33013 and 02-03-06007) and the Ministry of Industry, Science, and Technology of the Russian Federation (a grant in support of the development of unique equipment in Russia).

REFERENCES

1. A. A. Voronov, V. V. Ilyukhin, and N. V. Belov, Kristallografiya **20** (3), 556 (1975) [Sov. Phys. Crystallogr. **20**, 340 (1975)].
2. H. Wulff, U. Guth, and B. Loescher, Powder Diffr. **7**, 103 (1992).
3. E. R. Losilla, S. Bruque, M. A. G. Aranda, *et al.*, Solid State Ionics **112**, 53 (1998).
4. R. Masse, A. Durif, J. C. Guitel, and I. Tordjman, Bull. Soc. Fr. Mineral. Crystallogr. **95**, 47 (1972).
5. A. Leclaire, A. Benmoussa, M. M. Borel, *et al.*, J. Solid State Chem. **78**, 227 (1989).
6. E. S. Lunezheva, B. A. Maksimov, O. K. Mel’nikov, and L. A. Muradyan, Kristallografiya **34** (3), 611 (1989) [Sov. Phys. Crystallogr. **34**, 363 (1989)].
7. J. Isasi and A. Daidouh, Solid State Ionics **133**, 303 (2000).
8. P. D. Battle, A. K. Cheetham, W. T. A. Harrison, and G. J. Long, J. Solid State Chem. **62**, 16 (1986).
9. P. D. Battle, T. C. Gibb, S. Nixon, and W. T. A. Harrison, J. Solid State Chem. **75**, 21 (1988).
10. Y. Miyajima, T. Miyoshi, J. Tamaki, *et al.*, Solid State Ionics **124**, 201 (1999).
11. V. B. Zlokazov and V. V. Chernyshev, J. Appl. Crystallogr. **25**, 447 (1992).

Translated by Yu. Sin’kov

Crystallography Reports, Vol. 49, No. 4, 2004, pp. 619–625. Translated from Kristallografiya, Vol. 49, No. 4, 2004, pp. 697–703.
Original Russian Text Copyright © 2004 by Sidorov.

Specific Features of Structure and Ferroelectric Properties of $BaTiO_3$ Phases

T. A. Sidorov

Lebedev Physical Institute, Russian Academy of Sciences, Leninskiĭ pr. 53, Moscow, 119333
e-mail: sidta@mail.ru

Received November 20, 2000; in final form, February 25, 2003

Abstract—Analysis of the interatomic Ti–O distances in the asymmetric Ti–O··Ti bridges in the ferroelectric barium titanate phases showed that the rhombohedral, orthorhombic, and tetragonal $BaTiO_3$ phases consist of TiO_3^{2-}, TiO_2, and TiO^{2+} groups, respectively. The groups show strong electrostatic interaction and, so, orient along one direction, which gives rise to spontaneous polarization of these phases. In each phase, polarization switching under the action of a rather strong electric field proceeds via transfer of the oxygen atoms from one titanium atom to another with simultaneous change of the group orientation to the opposite one. *© 2004 MAIK "Nauka/Interperiodica".*

INTRODUCTION

Interatomic Ti–O bonds in some Ti–O–Ti bridges of the ferroelectric barium titanate phases have different lengths. However, the asymmetry of the Ti–O–Ti bridges has not received enough attention from researchers. The analysis made in the present study showed that the ferroelectric barium titanate phases are formed by groups of atoms possessing dipole moments. These groups are bound to one another by strong electrostatic forces giving rise to unidirectional orientations of these groups and, thus, spontaneous polarization of these phases.

ASYMMETRIC Ti–O··Ti BRIDGES

The structures of ferroelectric barium titanate phases are rather well studied. The structures of rhombohedral [1], orthorhombic [2], and tetragonal [3, 4] phases were studied by neutron diffraction on barium titanate single crystals. The structure of single crystals of the tetragonal phase was also studied by the X-ray diffraction method [4–7]. Finally, the structures of all the three $BaTiO_3$ phases were studied by neutron diffraction on polycrystals, with the structure of each phase being determined at several temperatures [8]. Table 1 summarizes the data obtained in the above studies and shows that, despite some scatter in the interatomic distances, the Ti–O distances in the ferroelectric phases of barium titanate may be divided into three groups—short distances ranging within 1.83–1.90 Å, long distances ranging within 2.11–2.21 Å, and intermediate distances ranging within 2.00–2.03 Å. The intermediate bonds form symmetric Ti–O–Ti bridges that are found in the orthorhombic and tetragonal phases but absent in the rhombohedral phase. The short and long bonds form only asymmetric Ti–O··Ti bridges recorded in all the three phases.

To make the representation clear, we indicate short bonds by solid line, as is usually done for chemical bonds; the bonds with the intermediate lengths, by the broken line and the long ones, by the dotted line. Then, the nearest environment of a titanium atom (six bridging Ti–O–Ti bonds in the ferroelectric $BaTiO_3$ phases) has the form shown in Fig. 1. It is seen that each barium

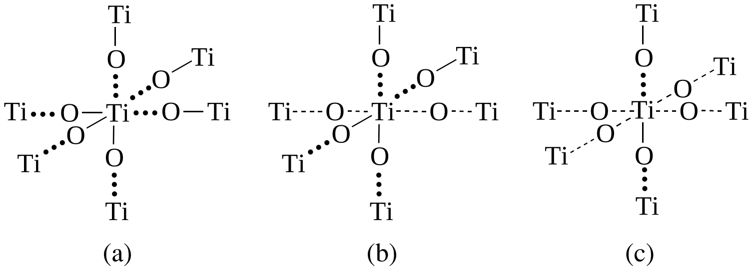

Fig. 1. Schematic representation of the nearest environment of a titanium atom in (a) rhombohedral, (b) orthorhombic, and (c) tetragonal phases.

Table 1. Ti–O bond lengths (d, Å) and their numbers (N) in ferroelectric barium titanate phases

Phase	T, K	Type of bond					
		short		intermediate		long	
		d	N	d	N	d	N
R[1]	132	1.890	3	–	–	2.122	3
R[8]	130	1.874	3	–	–	2.136	3
O[2]	263	1.90	2	2.00	2	2.11	2
O[8]	270	1.863	2	1.999	2	2.157	2
T[3]	295	1.877	1	2.001	4	2.166	1
T[4]	295	1.862	1	2.030	4	2.172	1
T[5]	298	1.860	1	2.002	4	2.174	1
T[7]	298	1.87	1	2.004	4	2.15	1
T[8]	300	1.829	1	2.000	4	2.206	1

Note: R indicates rhombohedral, O, orthorhombic, and T, tetragonal phases; the corresponding references are given in square brackets.

Table 2. Interatomic $d(M–X)$ and $d(M\cdot\cdot X)$ distances (in Å) and asymmetry coefficients K_a (in %) of the $M–X\cdot\cdot M$ bridges in molecular crystals and barium and lead titanates

Type of crystal	Compound	Type of bridge	Bridge		K_a	Reference
			$d(M–X)$	$d(M\cdot\cdot X)$		
OM	Hydrocarbons	C–H···C	1.09	2.90	166	[9]
		C–C···C	1.54	3.40	120	[9]
CH	HIO_3	O–H···O	0.99	1.78	80	[9]
	H_2O	O–H···O	1.01	1.75	73	[9]
	$B(OH)_3$	O–H···O	1.02	1.70	67	[9]
SH	$NaHC_2O_4 \cdot H_2O$	O–H···O	1.036	1.537	48	[10]
	KD_2AsO_4	O–D···O	1.03	1.49	45	[9]
	KH_2AsO_4	O–H···O	1.06	1.46	38	[9]
	KH_2PO_4	O–H···O	1.12	1.47	31	[11]
	$KH(HCO_2)_2$	O–H···O	1.16	1.28	10	[10]
	$HCl \cdot 2H_2O$	O–H···O	1.19	1.28	8	[10]
	$HBr \cdot 2H_2O$	O–H···O	1.17	1.22	4	[10]
IM	$SbCl_3$	Sb–Cl···Sb	2.34	3.46	48	[11]
	HgI_2	Hg–I···Hg	2.62	3.51	44	[12]
	I_2	I–I···I	2.72	3.50	29	[11]
BT	$BaTiO_3$ R*	Ti–O···Ti	1.874	2.136	14	[8]
	$BaTiO_3$ O*	Ti–O···Ti	1.863	2.157	16	[8]
	$BaTiO_3$ T*	Ti–O···Ti	1.829	2.206	21	[8]
	$PbTiO_3$ T*	Ti–O···Ti	1.78	2.38	34	[11]

Note: OM—organic molecular crystals, CH—molecular crystals with conventional hydrogen bonds, SH—crystals with strong hydrogen bonds, IM—inorganic molecular crystals, and BT—barium and lead titanates.

titanate phase has groups of atoms strongly bound with one another and much weaker bounds with the atoms of the neighboring groups. These are TiO_3, TiO_2, and TiO groups, encountered in the rhombohedral, orthorhombic, and tetragonal phases, respectively.

It is expedient to compare this structure with analogous structures with intragroup bonds shorter than intergroup ones. These structures have characteristic asymmetric $M–X\cdot\cdot M$ bridges, where $M–X$ is the short distance between the atoms of one group and $X\cdot\cdot M$ is

Table 3. Interatomic Ti–O and O–H distances (in Å) in the free (d_f) and crystalline (d_b) states and their relative differences (in %) for the corresponding compounds

Compound	Molecule	Distance		Difference
		d_f	d_b	$(d_b - d_f)/d_f$
$BaTiO_3$–*T*	TiO	1.620* [14]	1.829 [8]	13
$BaTiO_3$–*O*	TiO_2	1.62** [14]	1.863 [8]	15
ROH	H_2O	0.9567* [14]	0.97–1.16*** [10, 15]	1.5–22

* Spectroscopic study in the gas phase.
** Study by the molecular beam.
*** Neutron diffraction study of crystals with hydrogen O–H···O bonds.

the long distance between the atoms of the neighboring groups. To compare the compounds having different compositions and structures, it is expedient to introduce asymmetry coefficient K_a for a $M–X\cdots M$ bridge, which is defined as the ratio of the difference between the interatomic distances in the asymmetric $M–X\cdots M$ bridge to the short interatomic distance in percentage points

$$K_a = [d(M\cdots X) - d(M - X)]/d(M - X).$$

Table 2 lists the interatomic distances and the asymmetry coefficients for $M–X\cdots M$ bridges in barium and lead titanates and for crystals of four types—(1) molecular crystals with van der Waals bonds, (2, 3) crystals with conventional and strong intermolecular hydrogen bonds, and (4) crystals of inorganic molecular compounds. It is seen that crystals of type 1 have the asymmetry coefficient exceeding 100%; crystals of type 2, the asymmetry coefficient ranging within 100–50%; crystals of type 3, the asymmetry coefficient ranging within 50–4%; and the crystals of type 4, the asymmetry coefficient ranging within 48–29%. The close maximum values of the asymmetry coefficients for crystals of types 3 and 4 indicate that inorganic compounds of type 4 are molecular crystals with strong intermolecular bonds. This confirms the conclusion about strong intermolecular interactions in crystalline I_2 [11], which is based on the fact that the intermolecular distance between the iodine atoms from neighboring molecules is less than the sum of the van der Waals radii of iodine atoms. The asymmetry coefficients in barium and lead titanates range within 34–14%, i.e., they lie in the same ranges as the asymmetry coefficients of the molecular crystals of inorganic compounds. This allows us to draw the conclusion that the strong interaction between the atomic groups in barium and lead titanate crystals is similar to the intermolecular interaction in molecular crystals with strong hydrogen bonds and in molecular crystals of the inorganic compounds considered above.

The strong interaction between the atomic groups in the barium titanate phases can be interpreted based on the concept of the repulsion of electron pairs of the valence shell [13]. According to this concept, an atom in a compound has a core consisting of a nucleus and the electrons of the inner shells and binding electrons and lone electron pairs of the external valence shell. If the atomic core is sufficiently large (as in the case of titanium, in which the core radius equals 0.68 Å), then this core is weakly screened by the binding electron pairs. As a result, the positively charged atomic core attracts the negatively charged lone electron pair of the oxygen atom from the neighboring atomic group, which results in strong bonding between the groups, mainly of an electrostatic nature.

It is important to note that the compounds with strong hydrogen bonds include such well-known ferroelectrics indicated in Table 2 as potassium dihydrophosphate, dihydroarsenate, and dideuteroarsenate with $H_2PO_4^-$, $H_2AsO_4^-$ and $D_2AsO_4^-$ groups bound by strong hydrogen bonds. This shows the close structural relation of the barium titanate phases and the above ferroelectrics—all these structures are formed by strongly interacting atomic groups.

TiO AND TiO_2 MOLECULES IN THE ISOLATED STATE AND IN CRYSTALS

As is well known, the transition from free molecules to molecules related by hydrogen bonds is accompanied by a considerable decrease in the frequency of the stretching vibrations of the intramolecular O–H bond and a certain increase in its bond length. Analogous

Table 4. Frequencies of stretching vibrations of the Ti–O and O–H bonds in the free (ν_f) and crystalline (ν_b) states

Compound	Phase	Molecule	Frequency, cm^{-1}		$(\nu_f - \nu_b)/\nu_f$, %
			ν_f	ν_b	
$BaTiO_3$	*T*	TiO	1008	725	26
$BaTiO_3$	*O*	TiO_2	962	720	25
ROH [15]		H_2O	3650	3000–2000	18–45

Note: The data for the TiO molecules (gas phase) and TiO_2 (isolated molecules in the neon matrix) are borrowed from [14]; the data for the tetragonal and orthorhombic phases are borrowed from [16] and [17], respectively.

Table 5. Parameters of atomic thermal vibrations U_{eq} (Å^2, $\times 10^3$) in the barium titanate phases [8]

Phase	U_{eq} (Ba)	U_{eq} (Ti)	U_{eq} (O_{as})	U_{eq} (O_s)
R	–0.6	2.8	2.6	
O	1.0	5.0	3.4	5.3
T	3.4	5.9	–1.7	8.7

Note: The O_{as} and O_s are oxygen atoms in the asymmetric and symmetric Ti–O–Ti bridges, respectively. *R* indicates rhombohedral, *O* indicates orthorhombic, and *T* indicates tetragonal phases.

effects should also be expected for the barium titanate phases if these phases, like the compounds with hydrogen bonds, are formed by strongly interacting groups. Indeed, Tables 3 and 4 confirm the existence of these effects in the barium titanate phases. These effects show good qualitative and quantitative agreement with the analogous effects in molecular compounds with hydrogen bonds.

SYMMETRIC Ti–O··Ti BRIDGES

Up to now, we have restricted our consideration to asymmetric Ti–O··Ti bridges observed in all the three ferroelectric $BaTiO_3$ phases. However, the orthorhombic and tetragonal phases have, in addition to asymmetric bridges, also symmetric Ti··O··Ti bridges. To understand the difference between the asymmetric and symmetric bridges, one has to consider the thermal motion of oxygen atoms in these bridges. Table 5 lists the U_{eq} values equal to one third of the spur of the tensor of the anisotropic thermal vibration for an oxygen atom. Each U_{eq} value is averaged over the temperatures at which the structure determinations of these phases were made. Comparing the U_{eq} values for oxygen atoms in the asymmetric and symmetric bridges of the orthorhombic and tetragonal phases, we see that oxygen atoms in the symmetric bridges of both phases vibrate with a higher amplitude than in the asymmetric bridges.[1]

Above, we established the analogy between the barium titanate phases and the structures of compounds with strong hydrogen bonding; therefore, we may also expect that the potential energy of an oxygen atom in the Ti–O··Ti bridge will be close to the potential energy of a proton in the hydrogen O–H··O bridge. In other words, the potential energy of an oxygen atom is the symmetric W-like curve with two minima separated by a low potential barrier [10]. The oxygen atom in an asymmetric bridge is located in the vicinity of one of the Ti atoms. In the rhombohedral phase, which has only asymmetric bridges, three oxygen atoms are located in the vicinity of each titanium atom. At the temperature of the transition from the rhombohedral to the orthorhombic phase, one of the three oxygen atoms in the potential well starts jumping between the neighboring wells. Such a behavior of the oxygen atom is equivalent to the bridge symmetrization and an increase in the amplitude of its thermal vibrations. In the transition from the orthorhombic to the tetragonal phase, one more oxygen atom starts jumping between the neighboring wells, which is also equivalent to the bridge symmetrization and an increase in the amplitude of its thermal vibrations. Thus, in the vicinity of a titanium atom, one can always find one, two, and three oxygen atoms in the tetragonal, orthorhombic, and rhombohedral phases, respectively. Moreover, in the orthorhombic and tetragonal phases, there are also one or two jumping oxygen atoms that can be found in the vicinity of the given titanium atom only for a certain period of time.

The structure of the barium titanate phases consisting of atomic groups and the existence of two types of oxygen atoms should also be reflected in the chemical formulas of barium titanate, which should be written as $Ba(TiO_3)$ for the rhombohedral phase, $Ba(TiO_2)O$ for the orthorhombic phase, and $Ba(TiO)O_2$ for the tetragonal phase. The oxygen atoms from the groups are indicated in brackets, i.e., they can be found in the vicinity of the titanium atom at all times, whereas the oxygen atoms outside the brackets can be found alternatively either in the vicinity of one or another titanium atom.

RHOMBOHEDRAL PHASE

Rhombohedral barium titanate is described by the sp. gr. $R3m$, $Z = 1$. The unit-cell parameters of the rhombohedral unit cell at 132 K are $a = 4.004$ Å and $\alpha = 89.87°$ [1]; the parameters of the corresponding hexagonal unit cell are $a = 5.649$ Å and $c = 6.942$ Å [18]. The structure of the rhombohedral barium titanate is shown in Fig. 2 [1]. A complex TiO_3^{2-} anion has the shape of a pyramid with the OTiO angle equal to 95.23°.

In Fig. 2, a titanium atom located at the z axis lies above three oxygen atoms strongly bound to it. This titanium is bound to three titanium atoms of the three complex anions lying below the initial one via these three oxygen atoms. In turn, this titanium atom is weakly bound to three oxygen atoms of the above TiO_3^{2-} anions. As a result, the structure has a three-dimensional framework consisting of TiO_3^{2-} anions bound by strong electrostatic interactions. The framework voids are occupied by Ba^{2+} cations, which neutralize the negative charge of the framework.

Since each complex anion has a dipole moment associated with the polarity of the titanium–oxygen bond, the equal orientations of these anions result in spontaneous polarization of the crystal. Thus, spontaneous polarization is the result of the equivalent orientations of the complex TiO_3^{2-} anions with dipole

---

[1] Negative U_{eq} values show that the determination of these quantities was insufficiently accurate.

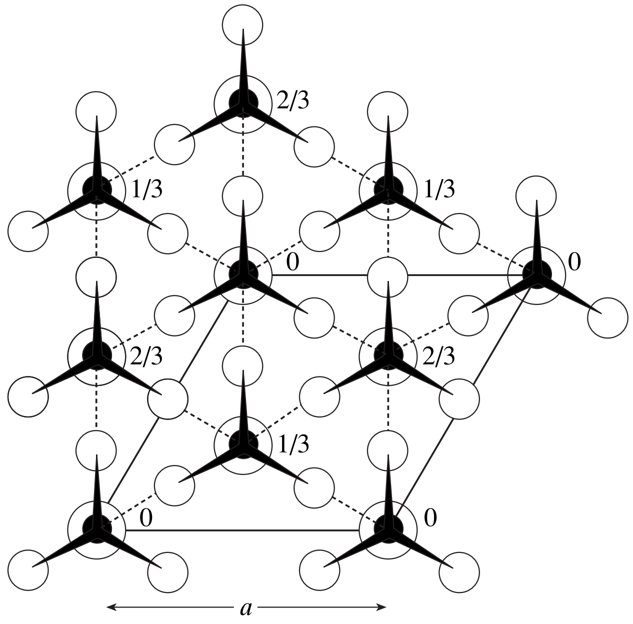

Fig. 2. Structure of the rhombohedral barium titanate phase projected onto the (001) plane of the hexagonal unit cell. Small filled circles indicate titanium atoms; medium white ones, oxygen atoms; and large empty ones, barium atoms. Solid lines show the intragroup and broken lines the intergroup titanium–oxygen bonds. The numbers indicate the heights of the titanium atoms in fractions of parameter *c* of the hexagonal unit cell.

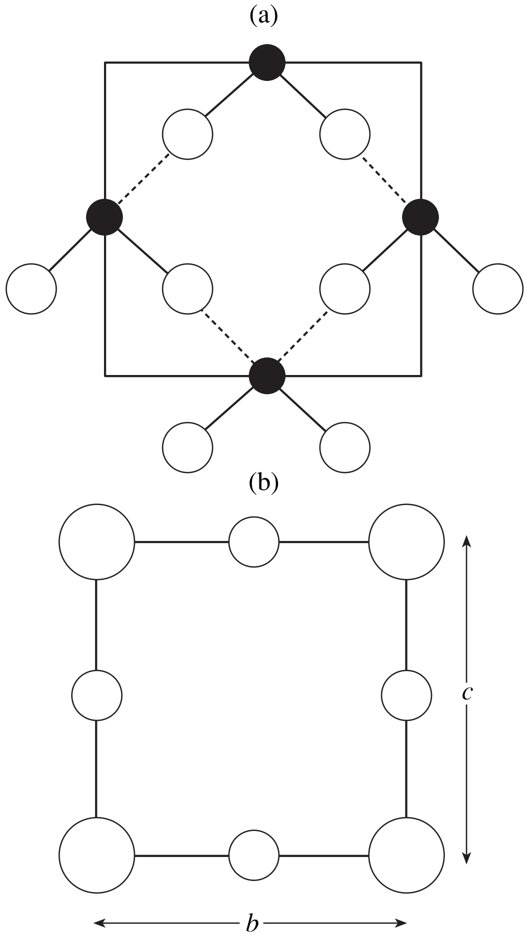

Fig. 3. Structure of the orthorhombic phase of barium titanate projected onto the (100) plane. (a) Arrangement of TiO_2 groups in the *yz* plane at a height $x = 1/2$ and (b) arrangement of jumping oxygen atoms and Ba^{2+} cations in the same plane at the height $x = 0$. For notation, see Fig. 2.

moments and is a result of strong electrostatic interaction giving rise to the parallel orientation of all complex TiO_3^{2-} anions along the threefold axis.

ORTHORHOMBIC PHASE

Orthorhombic barium titanate is described by the sp. gr. *Amm*2, $Z = 2$. The unit cell parameters at 263 K are $a = 3.990$ Å, $b = 5.669$ Å, and $c = 5.682$ Å [2]. The structure of the orthorhombic phase [2] is shown in Fig. 3, where TiO_2 groups are indicated. A bent TiO_2 group has the OTiO angle equal to 94.9°.

Each TiO_2 group is bound by Ti··O bonds to four neighboring in-plane TiO_2 groups. The O atoms participating in different bridges are located above and below the Ti atoms and, together with the Ba^{2+} cations, form the planes alternating with the planes of TiO_2 groups. Spontaneous polarization of the orthorhombic phase along the *c* axis is explained by the same orientation of the TiO_2 groups with dipole moments along the *c* axis associated with the interactions between these groups.

TETRAGONAL PHASE

Tetragonal barium titanate is described by the sp. gr. *P*4*mm*, $Z = 1$. The unit-cell parameters determined at 295 K are $a = 3.99095$ Å and $c = 4.0352$ Å [4]. The structure of the tetragonal phase [4] is shown in Fig. 4. Each of the $[TiO]^{2+}$ groups is bound by Ti··O bonds with two other similar groups. Thus, the linear chains are formed along the *c* axis. Each chain is located inside a channel built by symmetry-related oxygen atoms and Ba^{2+} cations and having the square cross section. The same orientation of the dipole $[TiO]^{2+}$ groups along the *c* axis is explained by the forces acting between the groups along this axis. Similar chains formed by the $[TiO]^{2+}$ groups whose Ti and O atoms are bound by strong covalent bonds are also revealed in another ferroelectric—$KTiOPO_4$ [19]. The ferroelectric properties of the latter seem to be associated with these chains. Linear chains consisting of diatomic TiO groups, with the atoms being related by covalent bonds, were also found in the narsarsukite, a silicate of the composition $Na_2TiOSi_4O_{10}$ [20].

SWITCHING OF POLARIZATION IN THE PHASES

As was indicated above, the potential energy of oxygen atoms in the Ti–O··Ti bridge is represented by a

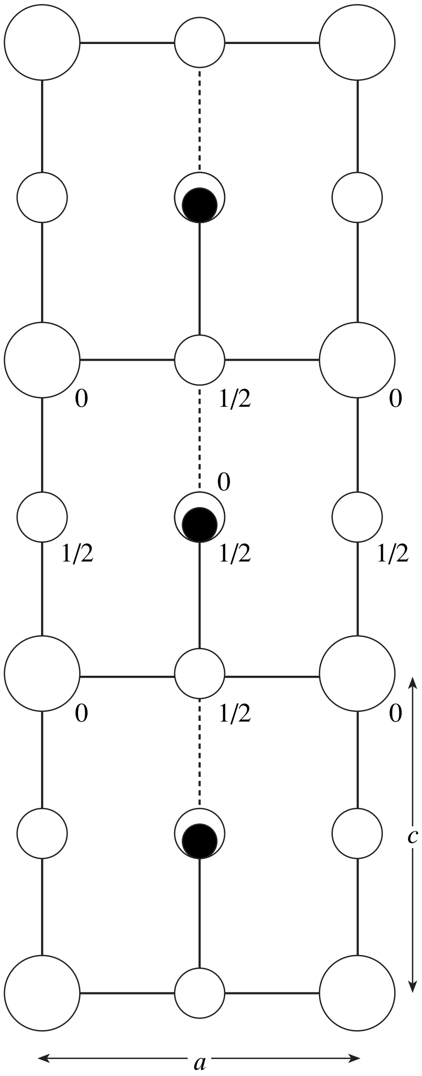

Fig. 4. Structure of the tetragonal barium titanate phase projected onto the (010) plane. The numbers indicate the heights of the atoms in fractions of unit-cell parameter *b*. For notation see Fig. 2.

symmetric W-like curve with two minima separated by a low potential barrier. The application of an electric field directed opposite to the spontaneous-polarization vector decreases the height of the low barrier, and, if the field intensity is sufficiently high, the oxygen atom is detached from one titanium atom and is attached to another titanium atom. As a result, the intragroup bonds are transformed into the intergroup ones and the intergroup bonds are transformed into the intragroup ones, which results in the reversal of the sign of spontaneous polarization, i.e., polarization switching.

As is well known, the crystalline potassium niobate phases, $KNbO_3$, have structures similar to the structure of the corresponding barium titanate phases [21–23]. Using arguments similar to those considered for barium titanate, we may assume that the potassium niobate phases are also formed by the NbO_3^-, NbO_2^+, and NbO^{3+} groups in the rhombohedral, orthorhombic, and tetragonal phases, respectively.

CONCLUSIONS

Comparing the relative differences between the long and short Ti–O distances in the asymmetric Ti–O··Ti bridges revealed in all the ferroelectric $BaTiO_3$ phases with relative differences between the O··H and O–H bonds in the asymmetric O–H··O bridges in compounds with strong hydrogen bonds, we came to the conclusion that the ferroelectric $BaTiO_3$ phases may be described in a way similar to phases consisting of TiO_3^{2-}, TiO_2, and TiO^{2+} groups in the rhombohedral, orthorhombic, and tetragonal phases, respectively. These groups are bound by strong intergroup bonds and form a three-dimensional framework in the rhombohedral phase, layers in the orthorhombic phase, and chains in the tetragonal phase. Strong interactions between the groups orient these groups in one direction in each phase, and, since each of these groups has a dipole moment (because the titanium–oxygen bonds are polar), each phase shows spontaneous polarization. In an intense electric field opposite to the direction of the spontaneous-polarization vector, the oxygen atom (located between two titanium atoms) is detached from one titanium and attached to another titanium atom because of a low barrier between these titanium atoms. This results in the transformation of the intragroup bonds to intergroup ones and vice versa and the change of the group orientation to the opposite one, i.e., switching of the crystal polarization. The above description of the barium and potassium niobate structures reveals their similarity to the structures of other ferroelectrics, e.g., potassium dihydrophosphate, which also consists of strongly bound atomic groups, which are related by weaker bonds.

ACKNOWLEDGMENTS

The author is grateful to A.V. Arakcheeva for fruitful discussion and N.T. Sidorova and A.A. Koplevenko for their help in preparation of illustrations.

REFERENCES

1. W. Schildkamp and K. Fischer, Z. Kristallogr. **155**, 217 (1981).
2. G. Shirane, H. Danner, and R. Pepinsky, Phys. Rev. **105**, 856 (1957).
3. B. C. Frazer, H. Danner, and R. Pepinsky, Phys. Rev. **100**, 745 (1955).
4. J. Harada, T. Pedersen, and Z. Barnea, Acta Crystallogr., Sect. A: Cryst. Phys., Diffr., Theor. Gen. Crystallogr. **26**, 336 (1970).
5. H. T. Evans, Acta Crystallogr. **4**, 377 (1951).
6. H. T. Evans, Acta Crystallogr. **14**, 1019 (1961).

7. R. H. Buttner and E. N. Maslen, Acta Crystallogr., Sect. B: Struct. Sci. **48**, 764 (1992).
8. G. H. Kwei, A. C. Lawson, S. J. L. Billinge, and S.-W. Cheong, J. Phys. Chem. **97**, 2368 (1993).
9. S. S. Batsanov, *Experimental Foundations of Structural Chemistry* (Izd. Standartov, Moscow, 1986).
10. J. Emsley, Chem. Soc. Rev. **9**, 91 (1980).
11. A. Wells, *Structural Inorganic Chemistry* (Clarendon Press, Oxford, 1984; Mir, Moscow, 1987), Vol. 2.
12. A. Wells, *Structural Inorganic Chemistry* (Clarendon Press, Oxford, 1984; Mir, Moscow, 1987), Vol. 3.
13. R. J. Gillespie, *Molecular Geometry* (Van Nostrand Reinhold, New York, 1972; Mir, Moscow, 1975).
14. K. S. Krasnov, N. V. Filippenko, V. A. Bobkova, N. L. Lebedeva, E. V. Morozov, T. I. Ustinova, and G. A. Romanova, *Molecular Constants of Inorganic Compounds: Handbook* (Khimiya, Leningrad, 1979).
15. G. C. Pimentel and A. L. McClellan, *The Hydrogen Bond* (Freeman, San Francisco, 1960; Mir, Moscow, 1964).
16. L. H. Robins, D. L. Kaiser, L. D. Potter, *et al.*, J. Appl. Phys. **76**, 7487 (1994).
17. M. Laabidi, M. D. Fontana, and B. Jannot, Solid State Commun. **76**, 765 (1990).
18. H. F. Kay and P. Vousden, Philos. Mag. **40**, 1019 (1949).
19. B. V. Andreev, V. A. D'yakov, N. I. Sorokina, *et al.*, Solid State Commun. **80**, 777 (1991).
20. D. R. Peacor and M. J. Buerger, Am. Mineral. **47**, 539 (1962).
21. A. W. Hewat, J. Phys. C: Solid State Phys. **6**, 2559 (1973).
22. M. Athee and A. W. Hewat, Acta Crystallogr., Sect. A: Cryst. Phys., Diffr., Theor. Gen. Crystallogr. **34**, 309 (1978).
23. V. A. Shuvaeva and M. Yu. Antipin, Kristallografiya **40**, 511 (1995) [Crystallogr. Rep. **40**, 466 (1995)].

Translated by L. Man

Crystallography Reports, Vol. 49, No. 4, 2004, pp. 626–630. Translated from Kristallografiya, Vol. 49, No. 4, 2004, pp. 704–709.
Original Russian Text Copyright © 2004 by Troyanchuk, Karpuk, Mantytskaya, Szymczak.

High-Pressure Synthesis and Magnetic Properties of $Bi_{0.5}D_{0.5}MnO_3$ (D = Pb, Ba) Solid Solutions

I. O. Troyanchuk*, M. K. Karpuk*, O. S. Mantytskaya*, and H. Szymczak**

**Institute of Solid-State and Semiconductor Physics, Belarussian Academy of Sciences, ul. Brovki 17, Minsk, 220072 Belarus*
e-mail: troyan@ifttp.bas-net.by

***Institute of Physics, Polish Academy of Sciences, Al. Lotnikow 32/46, 02-668, Warsaw, Poland*

Received September 19, 2002; in final form, March 18, 2003

Abstract—Perovskites $Bi_{0.5}D_{0.5}MnO_3$ (D = Pb, Ba) were prepared under high pressure (4 GPa) at 1200–1300°C. According to the X-ray diffraction data, crystalline $Bi_{0.5}Pb_{0.5}MnO_3$ has a tetragonal unit cell with the parameters $a = 3.940$ Å and $c = 3.800$ Å, whereas $Bi_{0.5}Ba_{0.5}MnO_3$ crystals are cubic with $a = 3.940$ Å. It is concluded from magnetic studies that lead-containing manganite is an antiferromagnet with $T_N = 120$ K, whereas $Bi_{0.5}Ba_{0.5}MnO_3$ is a spin glass with spin-freezing temperature $T_f = 38$ K. Both compounds are decomposed upon heating in air at temperatures above 500°C. With the use of synthesis in air, $Bi_{0.5}Ca_{0.5-x}D_xMnO_3$ solid solutions with x as high as 0.25 were obtained. © *2004 MAIK “Nauka/Interperiodica”.*

INTRODUCTION

The manganites $Bi_{1-x}D_xMnO_3$ (D = Ca, Sr) have attracted much of the attention of researchers due to the effect of charge ordering, which manifests itself at unusually high temperatures [1]. Charge ordering is a phenomenon of crucial importance for understanding the relationship between the magnetic and electrical properties of manganites, as well as the effect of giant magnetoresistance, which, in some cases, manifests itself as an effect of “melting” of the charge-ordered state in an external magnetic field. In this case, the sample resistivity may change by seven to nine orders of magnitude in an external field of 3–4 T [2]. It is well known that the charge ordering in the rare-earth manganites $R_{0.5}Sr_{0.5}MnO_3$ and $R_{0.5}Ca_{0.5}MnO_3$ (R is a rare-earth ion) occurs at temperatures of 150–250 K as a first-order phase transition. At an ordering of Mn^{3+} and Mn^{4+} ions in a 1 : 1 ratio, the stripes containing Mn^{3+} and Mn^{4+} ions alternate along the a axis simultaneously with the ordering of the d_z^2 orbitals of Mn^{3+} ions [3]. Models describing the commensurate ordering of Mn^{3+} and Mn^{4+} stripes were also proposed for $x = 2/3$ and 3/4 [4]. For $x = 2/3$, one Mn^{3+} stripe alternates with two Mn^{4+} stripes, whereas, for $x = 3/4$, one Mn^{3+} stripe alternates with three Mn^{4+} stripes. Incommensurate ordering of these stripes has been observed for irrational values of x [4].

Recently, it has been established by the neutron- and electron-diffraction methods that the charge-ordering temperatures for the bismuth manganites $Bi_{0.5}Ca_{0.5}MnO_3$ and $Bi_{0.5}Sr_{0.5}MnO_3$ are 335 and 500 K, respectively; i.e., much higher than the corresponding temperatures for rare-earth manganites [1]. For $Bi_{0.5}Sr_{0.5}MnO_3$, a model of charge ordering was proposed, in which two stripes of Mn^{3+} ions alternate with two Mn^{4+} stripes [5]. This is one of the possible reasons for the high stability of the charge-ordered phase. Anomalous magnetic properties are another specific feature of bismuth-containing manganites. It is well known that lanthanide manganites are antiferromagnets, whereas bismuth manganite is a ferromagnet [6–8]. The substitution of lanthanide ions by rare-earth ions leads to the appearance of magnetic properties, while a similar substitution for systems based on bismuth manganites destroys ferromagnetic ordering. To better understand the anomalous properties of bismuth manganites, the properties of new perovskite-like systems based on $BiMnO_3$ should be studied. In this paper, we report the preparation of new $Bi_{0.5}D_{0.5}MnO_3$ (D = Pb^{2+}, Ba^{2+}) compounds with the use of a high-pressure technique.

EXPERIMENTAL

Samples of $Bi_{0.5}D_xCa_{0.5-x}MnO_3$ solid solutions (D = Pb^{2+} or Ba^{2+}, $x \leq 0.25$) were prepared using conventional ceramic technology at t = 900–1100°C. The temperature of synthesis decreased with increasing contents of Ba and Pb, which is, obviously, caused by the decrease in the stability in air of the solid solutions under study. We failed to prepare single-phase samples with $x > 0.25$ in air despite a wide variety of the synthesis conditions. The $Bi_{0.5}Ba_{0.5}MnO_3$ and $Bi_{0.5}Pb_{0.5}MnO_3$ samples were prepared by synthesis under a high pressure of 4 GPa at a temperature near 1200°C. X-ray diffraction analysis was performed on a DRON-3 diffractometer (CrK_α radiation, graphite monochromator). The error in determining the unit-cell parameters did not exceed ±0.002 Å. The magnetization was measured on a QI-3001 commercial magnetometer in the temper-

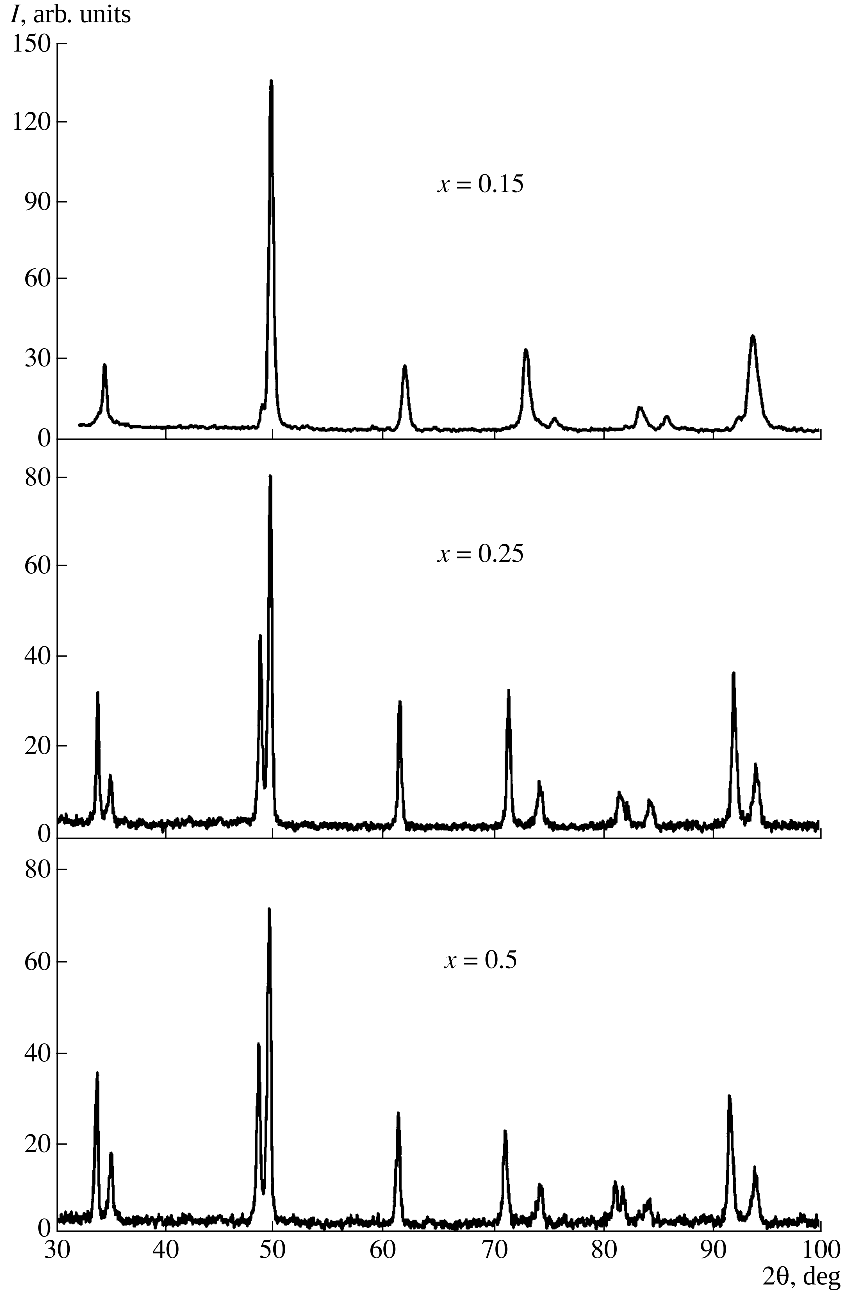

Fig. 1. X-ray powder diffraction patterns of the $Bi_{0.5}Ca_{0.5-x}Pb_xMnO_3$ samples, measured at room temperature.

ature range of 4.2–300 K. Resistivity was measured using a standard four-probe method on 2 × 2 × 10 mm^3 samples. The contacts were formed by ultrasonic deposition of indium.

RESULTS AND DISCUSSION

X-ray diffraction analysis showed that $Bi_{0.5}Ca_{0.5}MnO_3$ has a monoclinically distorted unit cell ($a = 3.866$ Å, $b = 3.764$ Å, $c = 3.897$ Å, and $\beta = 90.5°$), which corresponds to the data in [9]. The substitution of calcium by lead leads to a gradual stabilization of tetragonal distortions (sp. gr. $P4/mmm$). The samples of $Bi_{0.5}Ca_{0.5}Pb_{0.15}MnO_3$ and $Bi_{0.5}Ca_{0.25}Pb_{0.25}MnO_3$ had a tetragonally distorted unit cell ($a = 3.865$ Å, $c = 3.805$ Å, and $a/c = 1.016$ and $a = 3.929$ Å, $c = 3.795$ Å, and $a/c = 1.035$, respectively). The sample of $Bi_{0.5}Pb_{0.5}MnO_3$, which was prepared under high pressure, showed a further increase in the tetragonal distortions: $a = 3.940$ Å, $c = 3.800$ Å, $a/c = 1.037$ (Fig. 1). The sample of $Bi_{0.5}Ca_{0.25}Ba_{0.25}MnO_3$, which was prepared in air, was characterized by broad lines in its X-ray diffraction pattern. The value of the unit-cell parameter $a = 3.868$ Å was obtained, if we assume a pseudocubic symmetry.

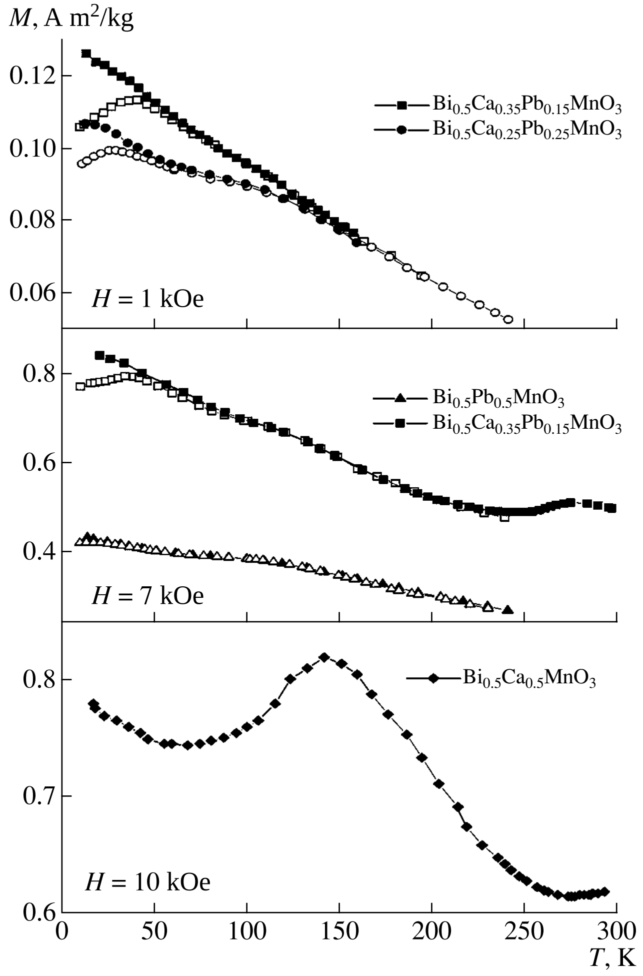

Fig. 2. Temperature dependences of magnetization for the $Bi_{0.5}Pb_{0.5}MnO_3$ samples (filled and open symbols stand for the FC and ZFC magnetizations, respectively).

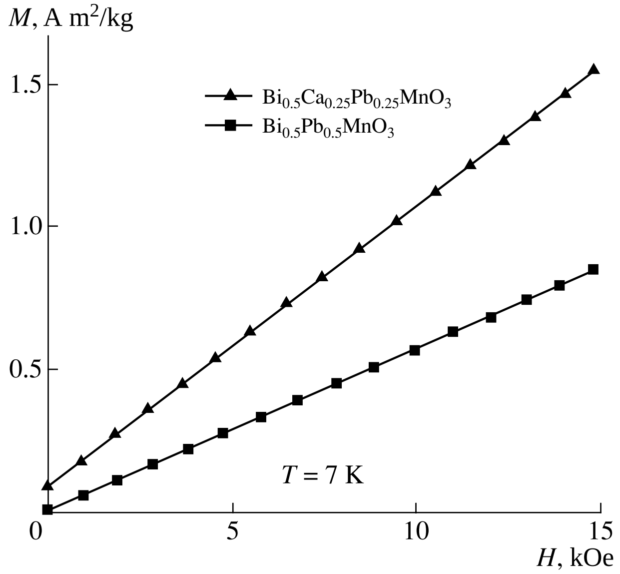

Fig. 3. Field dependences of magnetization at $T = 7$ K for $Bi_{0.5}Ca_{0.5-x}Pb_xMnO_3$ ($x = 0.25, 0.5$) samples, measured after cooling in field $H = 15$ kOe.

The $Bi_{0.5}Ba_{0.5}MnO_3$ sample that was grown under high pressure showed narrow unsplit lines, which unambiguously indicated a cubic symmetry with the unit-cell parameter $a = 3.940$ Å. The substitution of Ca^{2+} ions by either Ba^{2+} or Pb^{2+} ions leads to a significant increase in the unit-cell volume, which is caused by the much larger ionic radii of Pb^{2+} and Ba^{2+} in comparison with Ca^{2+}. Indeed, according to [10], the ionic radius of Ca^{2+} is 1.48 Å for the coordination number 12, whereas the ionic radii of Pb^{2+} and Ba^{2+} are 1.63 and 1.75 Å, respectively.

The temperature dependences of the magnetization of $Bi_{0.5}Ca_{0.5-x}Pb_xMnO_3$ manganites, measured after either cooling in a magnetic field (field cooling (FC)) or cooling in the absence of a field (zero-field cooling (ZFC)), are shown in Fig. 2. For the $Bi_{0.5}Ca_{0.5}MnO_3$ sample, the FC dependence has a clearly pronounced peak near 140 K. At $T = 270$ K, the magnetization begins to increase again with increasing temperature, which indicates a phase transition occurring somewhat above room temperature. According to [1], this transition is due to a charge ordering at $T = 335$ K. The substitution of Ca^{2+} ions by Pb^{2+} ions results in the disappearance of the magnetization peak near 140 K. However, a slightly pronounced anomalous behavior of magnetization was observed near $T_N = 120$ K. The ZFC dependences show a peak near $T_f = 40$ K. Below this temperature, the ZFC and FC dependences of magnetization diverge even in rather high magnetic fields (about 10 kOe), which suggests a high magnetic anisotropy. For the $Bi_{0.5}Pb_{0.5}MnO_3$ sample, the FC and ZFC dependences almost coincide. Near 120 K, a break is observed in the FC and ZFC curves. It should be noted that the $Bi_{0.5}Ca_{0.35}Pb_{0.15}MnO_3$ sample also showed anomalous FC dependence behavior near room temperature (caused by the charge ordering): the magnetization increased with increasing temperature (Fig. 2). Unfortunately, we could not study the behavior of the magnetization above 300 K for technical reasons. The field dependences of magnetization are almost linear at liquid-helium temperatures (Fig. 3), which is characteristic of paramagnets and antiferromagnets. However, a very low spontaneous magnetization (about 0.01 μ_B per formula unit) was observed for $Bi_{0.5}Ca_{0.25}Pb_{0.25}MnO_3$.

The substitution of calcium by barium ions in the $Bi_{0.5}Ca_{0.5-x}Ba_xMnO_3$ system led to the complete disappearance of the anomalous magnetization behavior near both 140 K and room temperature (Fig. 4). However, the peak of magnetic susceptibility at $T_f = 38$ K observed upon heating in a magnetic field of 100 Oe after zero-field cooling is much more clearly pronounced than in the case of the lead system. As for lead-containing perovskites, the difference between the ZFC and FC curves below 40 K is retained in high fields, which suggests a high magnetic anisotropy. The depen-

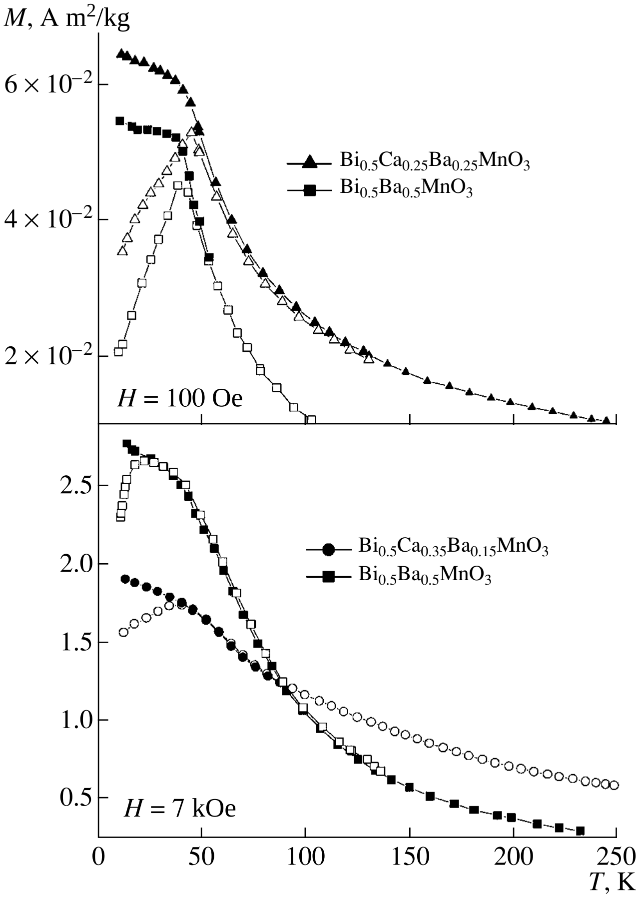

Fig. 4. Temperature dependences of magnetization for the $Bi_{0.5}Ca_{0.5-x}Ba_xMnO_3$ samples (filled and open symbols stand for the FC and ZFC magnetizations, respectively).

dences of magnetization on an external magnetic field at $T = 7$ K are nonlinear in the field range 0–15 kOe.

However, it is very difficult to evaluate the spontaneous magnetization because of the high magnetic anisotropy. Figure 5 shows a minor hysteresis loop for the $Bi_{0.5}Ca_{0.25}Ba_{0.25}MnO_3$ sample obtained after cooling from room temperature in field $H = 5$ kOe. It turned out that a field of 15 kOe is too weak to induce magnetization reversal in the sample. It should be noted that the magnetic susceptibility at low temperatures increases with increasing the barium content, whereas, at high temperatures, the compounds with a high calcium content have a high susceptibility.

The $Bi_{0.5}D_{0.5}MnO_3$ (D = Pb, Ba) samples have a rather high resistivity (about $10^2\ \Omega$ cm) at room temperature. With a decrease in temperature, the resistivity increases sharply, as it does in the case of semiconductors.

At the current time, compounds doped with calcium and strontium are the most studied manganites. The reason for this is the existence of complete series of both $RMnO_3$–$CaMnO_3$ and $RMnO_3$–$SrMnO_3$ solid solutions, as well as a thoroughly developed technique

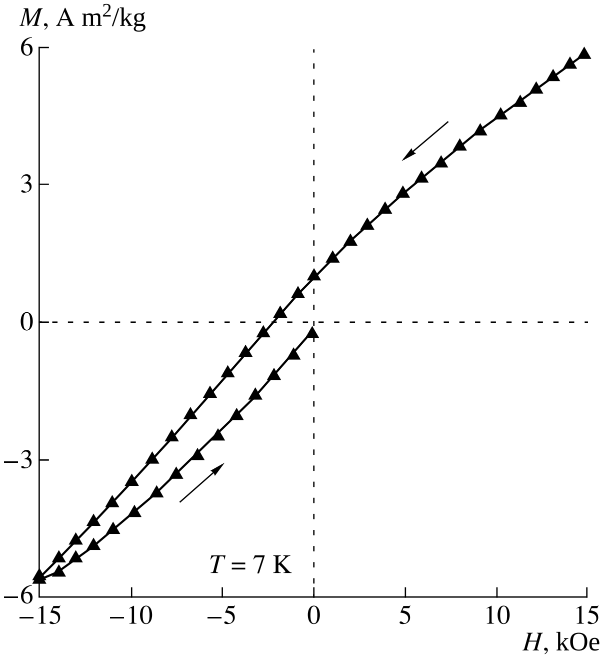

Fig. 5. A minor hysteresis loop for $Bi_{0.5}Ca_{0.25}Ba_{0.25}MnO_3$, obtained after cooling in field $H = 15$ kOe.

of preparing high-quality samples. The magnetic and electric properties of lead-doped manganites have been studied much less. It is well known that lead ions may substitute for lanthanide ions under synthesis at normal pressure, forming $R_{1-x}Rb_xMnO_3$ (R = La, Pr, Nd) solid solutions, at least, up to $x = 0.45$ [11]. The compounds with $x = 0.45$ are ferromagnetic metals below the Curie temperature. The manganites with R = Sm and Eu show properties intermediate between those of ferromagnets and spin glasses, whereas the samples with heavy rare-earth ions are spin glasses [11]. Apparently, the region of existence of solid solutions becomes somewhat narrowed with decreasing the lanthanide ionic radius. The main magnetic state of $Bi_{0.5}Pb_{0.5}MnO_3$ appears to be antiferromagnetic, which sharply distinguishes the properties of this compound from those of the other compounds in the $R_{0.5}Pb_{0.5}MnO_3$ series. The crystal structures also strongly differ, since the $R_{1-x}Pb_xMnO_3$ samples have, as a rule, either O-orthorhombic ($a < c/\sqrt{2} < b$) or rhombohedral distortions. The Néel temperature seems to be approximately 120 K, where a slightly pronounced anomalous magnetization behavior was observed. In our opinion, the appearance of very weak spontaneous magnetization in $Bi_{0.5}Ca_{0.5-x}Pb_xMnO_3$ solid solutions below 40 K is due to a chemical inhomogeneity of these compounds. Fragments of these compounds containing an excess of bismuth ions appear to reveal spin-glass properties. It is well known that $BiMnO_3$ is a ferromagnet, but doping with alkaline-earth Ca and Sr ions suppresses the ferromagnetic component and stabilizes the spin-glass properties until a charge-ordered stripe structure begins to form.

It is interesting to note that the tetragonal distortion in $Bi_{0.5}Pb_{0.5}MnO_3$ exceeds that in $Bi_{0.5}Sr_{0.5}MnO_3$. Indeed, the ratio c/a = 1.03 and 1.037 for $Bi_{0.5}Sr_{0.5}MnO_3$ and $Bi_{0.5}Pb_{0.5}MnO_3$, respectively. Therefore, the transition into the cubic phase for the lead-containing compound should occur at a higher temperature as compared to the strontium-containing one. The transition from the tetragonal to the cubic phase at 500 K in $Bi_{0.5}Sr_{0.5}MnO_3$ is related to charge ordering. This solid solution showed the highest charge ordering temperature among transition-metal oxides. The similarity of the unit-cell parameters of $Bi_{0.5}Sr_{0.5}MnO_3$ and $Bi_{0.5}Pb_{0.5}MnO_3$ suggests that the charge ordering also occurs in $Bi_{0.5}Pb_{0.5}MnO_3$, and the temperature of the charge-order–disorder transition in the lead compound should be even higher than in the strontium one.

In barium-doped manganites $R_{1-x}Ba_xMnO_3$, the transitions from the antiferromagnetic to the ferromagnetic state (R = La, Pr, Nd; $x \sim 0.1$) and direct transitions from the antiferromagnetic state to the spin-glass state (R = Sm, Eu, Gd, Tb; $x \sim 0.1$) were observed [12]. It is noteworthy that the compounds with a high barium content ($x > 0.4$) have a cubic structure despite the large difference in the ionic radii of lanthanides and barium. In contrast to $Bi_{0.5}Pb_{0.5}MnO_3$, the crystal structure and magnetic properties of $Bi_{0.5}Ba_{0.5}MnO_3$, obviously, do not differ radically from the corresponding characteristics of $R_{0.5}Ba_{0.5}MnO_3$ solid solutions, where R = Sm, Eu, or a heavy rare-earth element. A long-range order in $Bi_{0.5}Ba_{0.5}MnO_3$ appears to be absent, as in the aforementioned lanthanides, and the spin-glass component shows up at temperatures below 40 K. It should be noted that $T_f \sim 40$ K is the characteristic temperature at which a spin-glass-like state evolves in manganites independently of the type of distortions of the crystal structure and the ratio of the average ionic radii of the ions occupying positions A and B in the perovskite structure ABO_3. At present, the difference in the radii of ions in A positions is considered to be of critical importance for the magnetic properties of manganites. The magnetic state of manganites can be predicted to some extent by the formula

$$\sigma^2 = \sum x_i r_i^2 - \langle r_A \rangle^2,$$

where x_i is the number of ith ions in the A sublattice and r_i is the corresponding ionic radius [13, 14]. The critical temperature T_C decreases with decreasing σ^2. The greater the difference between the ionic radii, the more likely the spin-glass-like magnetic state is. It seems that the large difference in ionic radii also leads to the stabilization of the cubic structure, since the $R_{0.5}Ba_{0.5}MnO_3$ (R = Sm, Eu, Gd, Tb) manganites have a cubic structure [15]. In the case of bismuth compounds, apart from the value of the ionic radius, which for Bi^{3+} ions is closer to that of lanthanum than that of samarium ions, the capability of bismuth ions to form anisotropic *sp*-covalent bonds plays an important role. In particular, this specific feature invalidates the interpretation of the magnetic properties and crystal structure of bismuth manganites based on the values of ionic radii and their ratios.

ACKNOWLEDGMENTS

This study was supported by the Belarussian Foundation for Basic Research (project no. F01-014).

REFERENCES

1. J. L. Garcia-Muñoz, C. Fronterra, M. A. G. Aranda, *et al.*, Phys. Rev. B **63**, 64415 (2001).
2. C. N. Rao, A. Arulraj, A. K. Cheetham, and B. Raveau, J. Phys.: Condens. Matter **12**, 83 (2000).
3. P. G. Radaelli, D. E. Cox, L. Capogna, *et al.*, Phys. Rev. B **59**, 14440 (1999).
4. S. Mori, C. Y. Chen, and S.-W. Cheong, Nature **392**, 473 (1998).
5. M. Hervieu, A. Maignan, C. Martin, *et al.*, Chem. Mater. **13**, 1356 (2001).
6. V. A. Bokov, I. E. Myl’nikova, S. A. Kizhaev, *et al.*, Fiz. Tverd. Tela (Leningrad) **7**, 3695 (1966) [Sov. Phys. Solid State **7**, 2993 (1966)].
7. F. Sugawara, S. I. Y. Syono, and S. Akimoto, J. Phys. Soc. Jpn. **25**, 1553 (1968).
8. H. Chiba, T. Atou, and Y. Syono, J. Solid State Chem. **132**, 139 (1997).
9. V. A. Bokov, N. A. Grigorian, and M. F. Brizhina, Phys. Status Solidi **20**, 745 (1967).
10. *Modern Crystallography*, Vol. 2: *Structure of Crystals*, Ed. by B. K. Vaĭnshteĭn, V. M. Fridkin, and V. L. Indenbom (Nauka, Moscow, 1979).
11. V. N. Derkachenko, I. O. Troyanchuk, and S. N. Pastushonok, Fiz. Nizk. Temp. **17**, 239 (1991).
12. I. O. Troyanchuk, D. D. Khalyavin, S. V. Trukhanov, and H. Szymczak, J. Phys.: Condens. Matter **11**, 8707 (1999).
13. P. V. Vanitha, P. N. Santhosh, R. S. Singh, and C. N. R. Rao, Phys. Rev. B **59**, 13539 (1999).
14. L. M. Rodriguez-Martinez and J. P. Attfield, Phys. Rev. B **54**, 15622 (1996).
15. S. V. Trukhanov, I. O. Troyanchuk, and H. Szymczak, Phys. Rev. B **66**, 184424 (2002).

Translated by T. Dmitrieva

Crystallography Reports, Vol. 49, No. 4, 2004, pp. 631–634. Translated from Kristallografiya, Vol. 49, No. 4, 2004, pp. 710–713.
Original Russian Text Copyright © 2004 by Prokhorskiĭ, Fofanov, Aleshina, Nikitina.

STRUCTURE OF INORGANIC COMPOUNDS

Structure of Amorphous Oxide Al_2O_3: Results of a Molecular-Dynamics Experiment

M. E. Prokhorskiĭ, A. D. Fofanov, L. A. Aleshina, and E. A. Nikitina
Petrozavodsk State University, pr. Lenina 33, Petrozavodsk, 185640 Karelia, Russia
e-mail: office@mainpgu.karelia.ru

Received April 3, 2002

Abstract—The structure of amorphous aluminum oxide was simulated by the molecular-dynamics method. A random distribution of Al^{3+} and O^{2-} ions over the volumes of cubes with sides of 21 and 24 Å was used as a starting configuration. The character of the distribution of cations in the anion subsystem was analyzed. It was shown that formation of voids in model clusters is possible when the average electron density is underestimated *© 2004 MAIK “Nauka/Interperiodica”.*

INTRODUCTION

To date, a large amount of experimental data on the structure of amorphous Al_2O_3 has been stored [1–6]. The experimental results require theoretical justification. One of the methods for simulation of the atomic structure is the molecular-dynamics method.

It was noted in [1] that the short-range order character in amorphous anodic Al_2O_3 films is most similar to the structure of γ'-Al_2O_3, where Al^{3+} cations are randomly distributed over octahedral and tetrahedral positions of the oxygen fcc sublattice in the ratio 70 : 30. It was shown later that the ratio of the numbers of cations in different positions depends on the conditions of formation of anodic aluminum oxide films; the distribution of cations differs from equiprobable and has a large correlation range [5]. In addition, the character of ordering in the cation subsystem of amorphous aluminum oxide differs from both the character of location of cations in well-known crystalline modifications of Al_2O_3 [7] and the distribution of cations in the case of random occupation of octahedral and tetrahedral positions, when the occupation of neighboring tetrahedral and octahedral voids of fcc oxygen packing by aluminum ions is forbidden [8].

Thus, the purposes of this study were as follows:

(i) Using the molecular-dynamics method, to confirm or disprove the presence of cations located at distances smaller than 2 Å from one another in clusters. Here, we mean the distances between the centers of neighboring octahedral and tetrahedral positions (1.71 Å) and between the centers of neighboring tetrahedral positions (1.975 Å) in the fcc oxygen packing in crystalline phases of aluminum oxide.

(ii) To analyze the features of the atomic structure of clusters formed as a result of the molecular dynamic experiment.

TECHNIQUE OF THE EXPERIMENT AND PROCESSING OF THE RESULTS

Computer simulation of the ordering of a system of randomly located aluminum and oxygen ions was performed by the molecular-dynamics method. In the initial state, 1000 ions (400 cations and 600 anions, which corresponds to the composition of Al_2O_3) were randomly distributed in a cubic volume. The only constraint imposed on the positions of ions relative to each other in the starting configuration was that the distance between any two ions must not be smaller than 1.5 Å. Periodic boundary conditions were used. Calculations were performed for cubic cells with sides of 21 and 24 Å. The average electron density for such cubes is equal to 0.72 and 1.08 electron/Å^3, respectively. The latter value corresponds to the electron density of amorphous aluminum oxide.

The interaction potential was chosen in the form of the Born–Higgins–Mayer potential [9]:

$$U(r_{ij}) = q_i q_j e_0^2/r_{ij} + A_{ij}\exp(-r_{ij}/\rho_{ij}) - C_{ij}/r_{ij}^6, \quad (1)$$

where r_{ij} is the distance between ions of the i and j types; q_i and q_j are the charges (in elementary charge units e_0) of ions of the i and j types, respectively; and A_{ij}, ρ_{ij}, and C_{ij} are coefficients, the values of which were taken from [9] (table).

The cutoff radii of the interaction potential came to 11 and 10 Å for cells 24 and 21 Å in size, respectively. The time step was 10^{-15} s; the temperature at which the experiments were performed (300 K) was maintained

Coefficients of the interaction potential [9]

	A_{ij}, eV	ρ_{ij}	C_{ij}, eV Å^{-6}
Al^{3+}–O^{2-}	1460.3	0.29912	0
O^{2-}–O^{2-}	22764.0	0.149	27.88

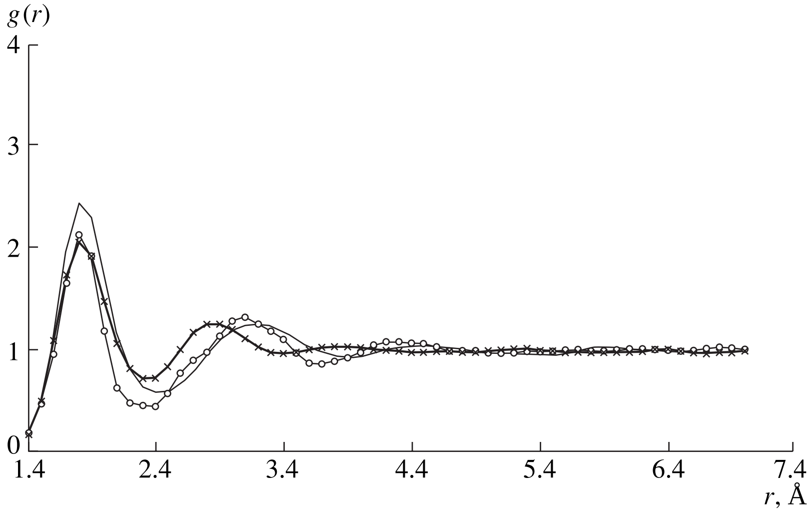

Fig. 1. Pair correlation functions: experimental data (solid line) and the results obtained by the molecular-dynamics method for clusters with sizes of 24 (circles) and 21 Å (crosses).

by the corresponding normalization of the atomic velocities. The molecular-dynamics experiment was performed using 10000 steps.

The functions of radial distribution $D(r)$ were calculated for the obtained clusters. With this purpose, we calculated the angular distribution of X-ray scattering intensity $I(s)$ by the Debye formula (on the assumption that scattering occurs from a set of identical clusters that are randomly oriented with respect to each other):

$$I(s) = \sum_{p=1}^{N} f_p f_p^* + \sum_{p=1}^{N-1}\sum_{q=p+1}^{N}(f_q f_p^* + f_p f_q^*)\sin(sr_{pq})/sr_{pq}. \quad (2)$$

Here, s is the magnitude of the diffraction vector, r_{pq} is the distance between paired atoms with indices p and q in a cluster, N is the total number of atoms, and f_p and f_q are the atomic scattering amplitudes. Then, from the dependences $I(s)$, the pair-interaction function $D(r)$ and the pair correlation functions $g_l(r)$ were calculated [10] and, then, compared with the corresponding experimental curves.

RESULTS AND DISCUSSION

Figure 1 shows the curves $g(r)$ for model clusters 21 and 24 Å in size and the experimental curve for an anodic aluminum oxide film formed in an oxalate electrolyte [5]. For all the three curves, the first peaks, which are due to the Al and O atoms located at shortest distances from each other, have identical positions. The second maximum on the curve $g(r)$ for 21-Å clusters is significantly shifted to smaller interatomic distances, whereas the second maximum on the curve corresponding to 24-Å clusters is closer to that on the experimental curve.

Analysis of the arrangement of atoms in clusters showed that, when atoms are located in a cube with a side of 24 Å, fairly large voids arise in the model volume (Fig. 2). The obtained result is in agreement with the data in the literature: it is known that Al_2O_3 films have a high porosity [11]. Investigations of Al_2O_3 oxides by small-angle X-ray scattering showed that their porosity may be as high as 11% and that voids are formed specifically in the stage of oxide growth [11].

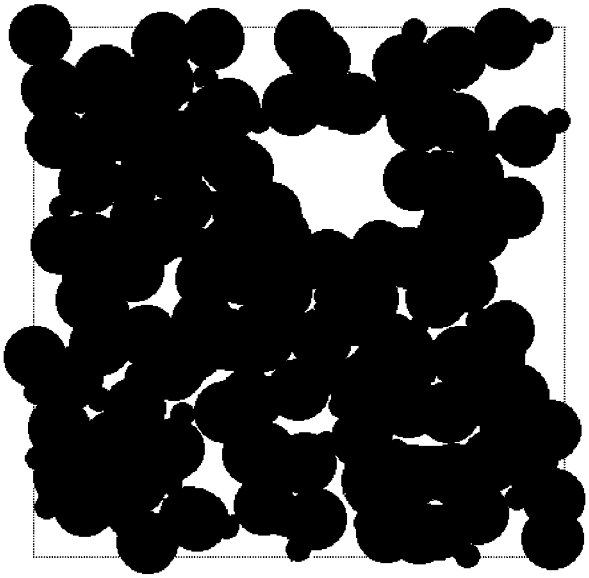

Fig. 2. Voids in a cluster. Projection of a layer 6 Å thick of a model 24-Å cluster on the *xy* plane. Aluminum cations (R_{Al} = 0.6 Å) and oxygen anions (R_O = 1.4 Å) are shown by circles.

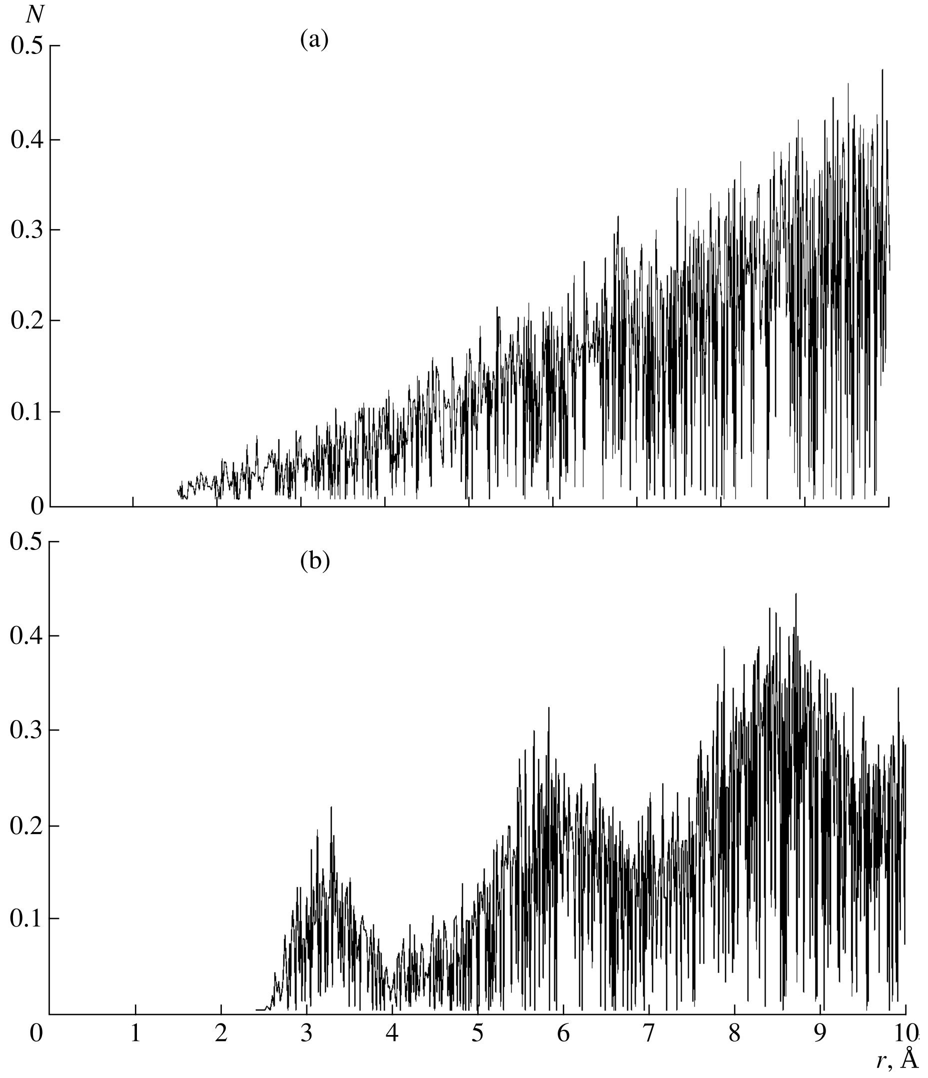

Fig. 3. Dependence of the number of Al–Al pairs per formula unit (Al_2O_3) on the interatomic distance (a) in the initial cluster and (b) after the molecular-dynamics experiment.

We plotted the dependences of the number of Al–Al cation pairs on the distance between paired atoms at the beginning (Fig. 3a) and end (Fig. 3b) of the computer experiment. The behavior of the curve in Fig. 3a shows that the number of pairs of Al atoms steadily increases with an increase in the interatomic distance, which is quite reasonable for random distribution of atoms over the volume. The curve obtained after the molecular-dynamics experiment exhibits well-formed peaks at 3.2, 6.0, and 8.6 Å. Provided the oxygen subsystem contains cations in neighboring tetrahedral positions (these oxygen tetrahedra, containing Al cations, share edges), the first peak in the dependence of the number of Al–Al pairs on distance would be observed in the vicinity of 2 Å. In the case of location of cations in the octahedral and tetrahedral voids sharing a face, we would observe a peak near 1.7 Å. The curve shown in Fig. 3b indicates that the number of pairs of Al atoms is zero in the range 0–2.5 Å; therefore, Al cations are located in neither neighboring tetrahedral nor neighboring tetrahedral and octahedral positions, which is in agreement with the interpretation of the experimental data for amorphous aluminum oxides given in [5].

For both clusters, we performed an analysis of distribution of anions around cations in a spherical layer between 1.6 and 2.2 Å before and after the molecular-dynamics experiment. As the analysis showed, cations in the initial cluster (for random and uniform volume distribution) may have any number of neighboring anions within a range of from one to six. Most cations have only two neighboring oxygen atoms. After the molecular-dynamics experiment, the number of aluminum cations with one or two neighboring oxygen anions is zero.

In a 24-Å cluster, cations have three, four, five, or six neighboring anions, which is indicative of the formation of tetrahedral and octahedral environment. However, most cations are surrounded by four neighboring oxygen atoms. The presence of three oxygen neighbors means that the formation of a tetrahedron is not completed; i.e., some fraction of the tetrahedra are either distorted or incomplete. In the case of five oxygen neighbors, we have incomplete octahedra. Obviously, the presence of voids in a cluster affects the average characteristics of the nearest ionic environment, since the ions located at the walls of voids have a smaller number of neighbors.

In the cube with a side of 21 Å, the number of Al cations with three, four, or five neighbors is smaller than in the cube with a side of 24 Å, while the number of Al cations in the octahedral environment is much larger. However, cations with seven of eight neighbors arise. Thus, in a cluster with electron density corresponding to the experimental value for amorphous aluminum oxides, the oxygen environment of cations is inconsistent with the entire set of well-known experimental data since, as is well known, aluminum cations cannot have more than six neighbors.

Thus, a decrease in the average electron density of a cluster leads to the following: (i) no more than six oxygen anions can be observed in the environment of aluminum cations and (ii) voids arise in the model volume. During the model relaxation, voids become stable inside a cluster, leading to the formation of some number of incomplete oxygen tetrahedra and octahedra around aluminum cations.

REFERENCES

1. N. M. Yakovleva and A. D. Fofanov, Izv. Akad. Nauk SSSR, Neorg. Mater. **21** (1), 48 (1985).
2. Y. Oka, T. Takahashi, K. Okada, and Sh. Inai, J. Non-Cryst. Solids **30**, 349 (1997).
3. R. Kniep, P. Lamparter, and S. Steeb, Chem. Adv. Mater. **101**, 30 (1989).
4. R. Manaila, A. Devenyi, and E. Candet, Thin Solid Films **116**, 289 (1989).
5. L. A. Aleshina, E. A. Nikitina, and A. D. Fofanov, Kristallografiya **42** (5), 906 (1997) [Crystallogr. Rep. **42**, 836 (1997)].
6. I. A. Popova, Izv. Akad. Nauk SSSR, Neorg. Mater. **14** (10), 1934 (1978).
7. L. A. Aleshina and E. A. Nikitina, Available from VINITI, No. 566-V 92.
8. L. A. Aleshina, K. L. Kovalev-Troitskiĭ, E. A. Nikitina, and A. D. Fofanov, Kristallografiya **38** (6), 158 (1993) [Crystallogr. Rep. **38**, 795 (1993)].
9. C. R. A. Catlow, R. James, W. C. Mackrodt, and R. F. Stewart, Phys. Rev. B **25**, 1006 (1982).
10. L. A. Aleshina and A. D. Fofanov, *X-ray Analysis of Amorphous Materials* (Petrozavod. Gos. Univ., Petrozavodsk, 1987).
11. V. V. Petrova, *Microporosity of Anodic Aluminum Oxide Films* (Petrozavod. Gos. Univ., Petrozavodsk, 1992).

Translated by Yu. Sin'kov

Crystallography Reports, Vol. 49, No. 4, 2004, pp. 635–642. Translated from Kristallografiya, Vol. 49, No. 4, 2004, pp. 714–721.

STRUCTURE OF INORGANIC COMPOUNDS

Crystal Structure of a New Representative of the Cancrinite Group with a 12-Layer Stacking Sequence of Tetrahedral Rings

K. A. Rozenberg*, A. N. Sapozhnikov, R. K. Rastsvetaeva***, N. B. Bolotina***, and A. A. Kashaev******

** Faculty of Geology, Moscow State University, Vorob'evy gory, Moscow, 119992 Russia*

*** Vinogradov Institute of Geochemistry, Siberian Branch, Russian Academy of Sciences, ul. Favorskogo 1a, Irkutsk, 664033 Russia*

**** Shubnikov Institute of Crystallography, Russian Academy of Sciences, Leninskiĭ pr. 59, Moscow, 119333 Russia*

e-mail: rast@ns.crys.ras.ru

***** Irkutsk State University of Transport Communications, ul. Chernyshevskogo 15, Irkutsk, 664074 Russia*

Received February 17, 2004

Abstract—The crystal structure of a 12-layer tounkite-like mineral of the cancrinite group was determined for the first time by single-crystal X-ray diffraction analysis (the unit-cell parameters are a = 12.757 Å, c = 32.211 Å). The structure was refined in the space group $P3$ to R = 0.035 using 3834 reflections with $|F| > 2\sigma(F)$. Si and Al atoms occupy tetrahedral framework positions in an ordered fashion. The average distances in the tetrahedra are $\langle$Si–O$\rangle$ = 1.611 Å and $\langle$Al–O$\rangle$ = 1.723 Å. The stacking sequence of the layers is described as *CACACBCBCACB*, where A, B, and C are six-membered rings arranged around the [2/3 1/3 z], [1/3 2/3 z], and [0 0 z] axes, respectively. In the structure of the mineral, the columns along the [0 0 z] axis are composed of cancrinite cages. The columns along the [2/3 1/3 z] and [1/3 2/3 z] axes contain alternating cancrinite, bystrite, and liottite cages. © *2004 MAIK "Nauka/Interperiodica".*

INTRODUCTION

The mineral tounkite was discovered as bottle-green crystals in the Malo-Bystrinskoe lazurite deposit (Lake Baikal region, Russia) and described in [1]. However, we failed to obtain a reliable structural model of this mineral because of structural disorder, as evidenced by the diffusion character of the hkl reflections with $l \neq 3n$. Later, a tounkite-like mineral, which we tentatively named ordered tounkite [2], was discovered in lazurite-bearing rocks of the Tultuĭskoe deposit in association with calcite, diopside, afghanite, and anisotropic lazurite. This mineral forms more perfect columnar bluish crystals up to 1 cm long. The aim of this study was to establish the structure of these crystals.

EXPERIMENTAL

The chemical composition of a specimen was studied by electron-probe X-ray microanalysis on a JCXA-733 microanalyzer. The empirical formula calculated for 12 (Si + Al) and Z = 6 is $(Ca_{2.58}Na_{5.18}K_{0.15})_{7.91}(Si_{5.99}Al_{6.01})_{12}O_{24}\,(SO_4)_{1.79}Cl_{1.33}$.

The unit-cell parameters a = 12.755(3) Å and c = 32.218(5) Å were determined by the photographic method and refined on an automated Bruker Platform diffractometer equipped with a CCD detector (Toledo, United States). X-ray diffraction data were collected on the same diffractometer. The X-ray data set corresponded to the trigonal system. However, the choice of the space group presented difficulties because of several alternatives. Of these space groups, only the space group $P31c$ has translational symmetry elements. However, 86 reflections with intensities $|F| > (3–10)\sigma$ are in contradiction with systematic absences of the hhl reflections with $l = 2n$, which should be observed for the space group $P31c$. Therefore, we rejected this space group in subsequent calculations. The best results were obtained within the space group $P3$ (the diffraction class $\bar{3}$). The principal characteristics of the crystal and details of the X-ray diffraction study are listed in Table 1. All calculations were carried out using the AREN crystallographic software package [3].

We failed to determine the structure of the mineral by direct methods due to the presence of a strong pseudotranslation (most hkl reflections are those with $l = 6n$). A structural model containing 114 independent atoms was constructed based on the analysis of the structures of tetrahedral frameworks of minerals belonging to the cancrinite group (bystrite, liottite, and afghanite), in which discrete six-membered rings form a close packing [4]. The cages in the framework were filled with extraframework cations and anions accord-

Table 1. Characteristics of the crystal and details of X-ray diffraction study

Characteristic	Data and conditions
Trigonal unit-cell parameters, Å	$a = 12.757(3)$
	$c = 32.211(5)$
Unit-cell volume, Å^3	$V = 4539.75$
Space group	$P3$
Radiation; λ, Å	MoK_α; 0.71073
ρ_{calcd}, g/cm^3	2.48
Crystal dimensions, mm	0.15 × 0.3 × 0.4
Diffractometer	Bruker
Ranges of indices of measured reflections	$-14 < h < 14$;
	$0 < k < 17$;
	$0 < l < 44$
$\sin\theta/\lambda$	<0.699
Total number of reflections	29457 $F > 3\sigma(F)$
Number of independent reflections	3834 $F > 3\sigma(F)$
R factor for merging	0.019
R factor upon refinement	0.035
Program for structure refinement	AREN [3]
Program for absorption correction	SADABS

ing to the distribution found in the structures of cancrinite-like minerals and taking into account the real chemical composition of the mineral under study. Several refinement cycles confirmed the validity of the model. Then, the calculated difference electron density maps additionally revealed two Ca and Cl positions, oxygen atoms coordinated to sulfur, and several split sodium positions. The compositions and occupancies of the extraframework positions were refined, taking into account the mixed atomic scattering curves. The structural model was refined with anisotropic atomic displacement parameters to $R = 0.035$. Details of the X-ray diffraction study are given in Table 1. The final coordinates and thermal parameters of the framework and extraframework atoms are listed in Tables 2 and 3, respectively. The interatomic distances for sulfur atoms are given in Table 4.

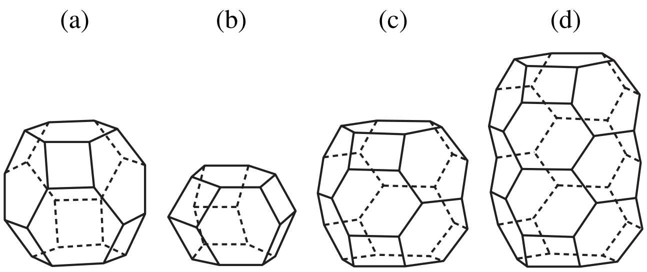

Fig. 1. Cages in the frameworks of the minerals of the cancrinite group: (a) a sodalite cage (cuboctahedron), (b) a cancrinite cage (hexagonal cuboctahedron), (c) a bystrite cage, and (d) a liottite cage.

RESULTS AND DISCUSSION

Complete X-ray diffraction analysis of the tounkite-like mineral gave the crystal-chemical formula ($Z = 1$) $[Si_{36}Al_{36}O_{144}]$ $[Na_{31.1}Ca_{3.94}K_{0.96}(SO_4)_{9.3}(SO_3)_{0.7}][Ca_{12}Cl_8]$, where the compositions of the framework and cages are enclosed in brackets. Silicon and aluminum atoms occupy tetrahedral framework positions in an ordered fashion, as evidenced by the average cation–anion distances in the tetrahedra ($\langle$Si–O$\rangle$ = 1.611 Å, $\langle$Al–O$\rangle$ = 1.723 Å).

The aluminosilicate framework of the mineral under study, like the frameworks of other cancrinite-like minerals, consists of six-membered rings of (Si,Al) tetrahedra arranged in layers. The layers are shifted with respect to each other along the c axis. Cancrinite and related minerals [5–10] differ in both the number of layers, labeled by letters A, B, and C, and their stacking sequence. For uniformity and to avoid ambiguity when comparing the stacking sequences of layers in different minerals, it was suggested [10] that the six-membered rings around the [2/3 1/3 z], [1/3 2/3 z], and [0 0 z] axes [10] to be denoted by A, B, and C, respectively. Then, the stacking sequences of layers in the structures of the minerals can be described as follows: a two-layer *AB* sequence in cancrinite, a four-layer *ACBC* sequence in bystrite, a six-layer *ACBCBC* sequence in liottite, an eight-layer *ACACBCBC* sequence in afghanite, and a ten-layer *ABCABACABC* sequence in franzinite. In these minerals, the parameter $c \sim 5n$ ($n = 1$–5) varies correspondingly from 5.1 to 26.5 Å. The order in which the layers alternate determines the shapes and positions of cages in the structure. The cancrinite, bystrite, and liottite structures have three types of cages—the so-called cancrinite, bystrite, and liottite cages (Fig. 1)—linked in columns. The cancrinite cage is the smallest one. This cage is formed in structures, where only one layer is sandwiched between two identical layers. In such structures, the medium layer differs from the two other layers in orientation and is present either singly or in combination with other layers. In the sodalite cage, two layers, which are shifted with respect to each other, are located between two identical layers. The bystrite cage appears in structures in which three layers are sandwiched between two identical layers. The bulky liottite cage contains five differently oriented layers. The afghanite structure consists of alternating liottite and cancrinite cages. By contrast, the columns along the [0 0 z] axis in bystrite, liottite, and afghanite are of the same type and are composed of cancrinite cages. Sodalite cages are involved in the formation of columns in the franzinite structure. In this structure, sodalite and

Table 2. Coordinates and equivalent atomic displacement parameters for the tetrahedral framework positions

Atom	x/a	y/b	z/c	B_{eq}, Å^2	Atom	x/a	y/b	z/c	B_{eq}, Å^2
Si(1)	0.2570(1)	0.0019(1)	0.0000(1)	0.4(1)	O(13)	0.5479(5)	0.4521(4)	0.2483(1)	1.3(5)
Si(2)	0.9245(1)	0.5856(1)	0.0840(1)	0.5(1)	O(14)	0.7733(5)	0.2039(4)	0.2473(1)	1.4(4)
Si(3)	0.0036(1)	0.2553(1)	0.1659(1)	0.4(1)	O(15)	0.3407(6)	0.3418(6)	0.2865(1)	1.9(5)
Si(4)	0.9249(1)	0.5854(1)	0.2477(1)	0.5(2)	O(16)	0.6728(4)	0.6744(5)	0.2912(1)	1.3(5)
Si(5)	0.0003(1)	0.2543(1)	0.3318(1)	0.7(1)	O(17)	0.8852(5)	0.1194(5)	0.3324(1)	1.9(4)
Si(6)	0.3409(1)	0.4152(1)	0.4156(1)	0.7(1)	O(18)	0.1178(5)	0.8872(5)	0.3291(1)	1.5(5)
Si(7)	0.2552(1)	0.0039(1)	0.4975(1)	0.5(2)	O(19)	0.3434(5)	0.3482(5)	0.3734(1)	1.8(5)
Si(8)	0.3390(1)	0.4140(1)	0.5803(1)	0.6(2)	O(20)	0.6650(5)	0.6695(5)	0.3704(1)	1.4(5)
Si(9)	0.2532(1)	−0.0024(1)	0.6642(1)	0.7(2)	O(21)	0.4511(5)	0.5474(5)	0.4131(2)	2.0(4)
Si(10)	0.9249(2)	0.5866(1)	0.7477(1)	0.9(2)	O(22)	0.2091(4)	0.7696(4)	0.4181(1)	0.9(4)
Si(11)	0.2534(1)	0.0001(1)	0.8319(1)	0.7(1)	O(23)	0.3480(5)	0.3384(5)	0.4535(1)	0.9(4)
Si(12)	0.5870(1)	0.9236(2)	0.9165(1)	0.8(2)	O(24)	0.6744(5)	0.6603(5)	0.4574(2)	2.0(6)
Al(1)	0.7405(2)	−0.0005(2)	−0.0014(1)	0.86(6)	O(25)	0.1266(5)	0.8875(5)	0.4979(2)	1.7(4)
Al(2)	0.4026(2)	0.0779(2)	0.0838(1)	0.53(5)	O(26)	0.8853(4)	0.1151(5)	0.4978(2)	1.5(6)
Al(3)	0.2627(2)	0.2601(2)	0.1650(1)	0.71(6)	O(27)	0.3449(5)	0.3354(5)	0.5401(1)	1.4(5)
Al(4)	0.4025(2)	0.0780(2)	0.2476(1)	0.43(5)	O(28)	0.6734(5)	0.6631(5)	0.5369(1)	1.4(6)
Al(5)	0.2597(2)	0.2599(1)	0.3319(1)	0.65(5)	O(29)	0.4564(5)	0.5476(5)	0.5820(2)	1.9(5)
Al(6)	0.0772(2)	0.4020(2)	0.4154(1)	0.75(5)	O(30)	0.2153(5)	0.7763(4)	0.5774(2)	1.5(5)
Al(7)	0.0033(2)	0.7405(2)	0.4982(1)	0.70(5)	O(31)	0.3441(4)	0.3476(6)	0.6216(1)	1.4(5)
Al(8)	0.0773(2)	0.4021(2)	0.5805(1)	0.69(5)	O(32)	0.6681(5)	0.6743(4)	0.6235(2)	1.4(5)
Al(9)	0.7423(2)	0.0005(2)	0.6661(1)	1.05(5)	O(33)	0.1163(4)	0.8878(5)	0.6648(2)	1.5(4)
Al(10)	0.4020(2)	0.0767(1)	0.7483(1)	0.74(5)	O(34)	0.8844(5)	0.1209(5)	0.6643(1)	2.0(4)
Al(11)	0.7399(1)	0.0005(1)	0.8319(1)	0.58(4)	O(35)	0.3443(6)	0.3451(5)	0.7047(2)	2.2(6)
Al(12)	0.0786(1)	0.4030(2)	0.9160(1)	0.37(5)	O(36)	0.6705(4)	0.6772(5)	0.7042(1)	1.2(6)
O(1)	0.1205(5)	0.8817(5)	0.0020(2)	1.6(5)	O(37)	0.5465(5)	0.4578(5)	0.7489(2)	2.6(5)
O(2)	0.8903(5)	0.1134(5)	−0.0017(2)	1.8(6)	O(38)	0.7739(5)	0.2146(5)	0.7474(2)	1.9(5)
O(3)	0.3495(6)	0.3463(5)	0.0398(2)	1.8(5)	O(39)	0.3432(6)	0.3412(5)	0.7883(1)	1.7(5)
O(4)	0.6730(5)	0.6657(5)	0.0367(2)	1.6(5)	O(40)	0.6707(6)	0.6664(6)	0.7902(2)	2.3(6)
O(5)	0.5501(5)	0.4530(5)	0.0857(2)	1.7(5)	O(41)	0.1213(5)	0.8869(5)	0.8329(1)	1.8(4)
O(6)	0.7777(5)	0.2118(5)	0.0855(1)	1.4(5)	O(42)	0.8882(4)	0.1196(5)	0.8349(1)	1.3(4)
O(7)	0.3336(5)	0.3455(5)	0.1206(1)	1.4(4)	O(43)	0.3420(5)	0.3416(6)	0.8734(1)	1.4(5)
O(8)	0.6633(5)	0.6756(6)	0.1237(2)	2.0(5)	O(44)	0.6690(5)	0.6695(5)	0.8698(1)	1.8(5)
O(9)	0.8841(4)	0.1239(4)	0.1659(1)	0.8(4)	O(45)	0.4577(5)	0.5481(5)	0.9196(2)	2.0(4)
O(10)	0.1154(5)	0.8833(5)	0.1670(1)	1.3(4)	O(46)	0.2108(5)	0.7774(5)	0.9174(2)	1.7(4)
O(11)	0.3407(5)	0.3454(5)	0.2076(1)	1.4(5)	O(47)	0.3432(5)	0.3436(5)	0.9555(2)	1.8(6)
O(12)	0.6638(4)	0.6710(5)	0.2031(1)	1.3(5)	O(48)	0.6761(5)	0.6704(4)	0.9564(1)	1.0(5)

Table 3. Coordinates and equivalent atomic displacement parameters of the framework atoms, multiplicities (Q), and occupancies (q) of positions

Position	x/a	y/b	z/c	B_{eq}, Å^2	Q	q
Ca(1)	0	0	0.0010(1)	1.21(7)	1	1
Ca(2)	0	0	0.1667(1)	0.81(7)	1	1
Ca(3)	0	0	0.3314(1)	1.21(6)	1	1
Ca(4)	0	0	0.4988(1)	0.67(7)	1	1
Ca(5)	0	0	0.6660(1)	1.08(7)	1	1
Ca(6)	0	0	0.8331(1)	1.15(6)	1	1
Ca(7)	0.6667	0.3333	0.0864(1)	1.60(7)	1	1
Ca(8)	0.6667	0.3333	0.2497(1)	1.92(7)	1	1
Ca(9)	0.6667	0.3333	0.7489(1)	3.17(6)	1	1
Ca(10)	0.3333	0.6667	0.4163(1)	1.19(6)	1	1
Ca(11)	0.3333	0.6667	0.9255(1)	1.85(6)	1	1
Ca(12)	0.3333	0.6667	0.5778(1)	1.63(6)	1	1
Cl(1)	0	0	0.0844(1)	5.5(5)	1	1
Cl(2)	0	0	0.2498(1)	6.5(5)	1	1
Cl(3)	0.3333	0.6667	0.4976(1)	5.4(5)**	1	1
Cl(4)	0	0	0.4162(1)	4.9(3)	1	1
Cl(5)	0	0	0.5805(1)	5.3(4)	1	1
Cl(6)	0.6667	0.3333	0.1711(4)	5.8(1)**	1	1
Cl(7)	0	0	0.7481(1)	4.5(3)	1	1
Cl(8)	0	0	0.9171(2)	4.9(3)	1	1
Na(1)	0.5056(3)	0.5036(3)	−0.0009(1)	2.8(1)	3	1
Na(2*a*)	0.2181(5)	0.4271(6)	0.0827(1)	3.84(7)	3	0.86
Na(2*b*)	0.169(2)	0.334(3)	0.0767(9)	3.2(3)	3	0.14
Na(3)	0.4783(4)	0.5307(3)	0.1629(1)	3.4(1)	3	1
Na(4)	0.2208(4)	0.4395(4)	0.2458(1)	3.6(1)	3	1
Na(5)*	0.5049(5)	0.4996(5)	0.3319(2)	3.79(7)	3	1
Na(6)	0.4326(4)	0.2180(3)	0.4153(1)	2.87(9)	3	1
Na(7)*	0.5260(3)	0.4818(3)	0.4964(1)	3.87(7)	3	1
Na(8)	0.4415(4)	0.2245(4)	0.5789(1)	3.53(8)	3	1
Na(9)*	0.4987(3)	0.5099(3)	0.6652(1)	3.52(6)	3	1
Na(10*a*)*	0.2265(4)	0.4460(4)	0.7509(1)	3.63(7)	3	0.80
Na(10*b*)	0.213(2)	0.411(2)	0.7398(9)	4.5(3)	3	0.20
Na(11)	0.5040(5)	0.5075(5)	0.8328(2)	2.92(6)	3	1
Na(12*a*)*	0.4413(4)	0.2238(4)	0.9156(1)	3.65(6)	3	0.75
Na(12*b*)	0.360(3)	0.186(2)	0.9129(6)	6.6(3)	3	0.25
S(1)	0.3333	0.6667	0.0213(2)	5.24(1)	1	1
O(49)	0.220(1)	0.614(1)	0.0510(4)	5.6(2)	3	0.70
O(50)	0.237(3)	0.615(3)	0.9951(9)	3.6(4)	3	0.30
O(51)	0.3333	0.6667	0.062(3)	6.8(4)**	1	0.30
S(2)	0.3333	0.6667	0.1713(2)	4.0(1)	1	1
O(52)	0.235(2)	0.618(3)	0.2023(7)	7.4(4)	3	0.50
O(53)	0.3333	0.6667	0.129(2)	7.9(4)**	1	0.50
O(54)	0.272(2)	0.559(1)	0.1550(8)	8.9(1)	3	0.50
O(55)	0.3333	0.6667	0.215(2)	6.8(4)**	1	0.50

Table 3. (Contd.)

Position	x/a	y/b	z/c	B_{eq}, Å^2	Q	q
S(3)	0.6667	0.3333	0.4991(1)	2.59(8)	1	1
O(56)	0.558(1)	0.280(2)	0.4774(4)	4.6(1)	3	0.50
O(57)	0.6667	0.3333	0.5443(8)	6.6(4)**	1	0.50
O(58)	0.5705(2)	0.253(3)	0.5239(9)	5.4(3)**	3	0.50
O(59)	0.6667	0.3333	0.4544(8)	6.2(4)**	1	0.50
S(4)	0.6667	0.3333	0.6382(1)	3.39(8)	1	1
O(60)	0.600(1)	0.390(1)	0.6313(4)	8.3(1)	3	1
O(61)	0.6667	0.3333	0.681(1)	6.4(2)**	1	1
S(5)	0.6667	0.3333	0.8492(1)	3.02(8)	1	1
O(62)	0.627(1)	0.407(2)	0.8701(8)	4.7(2)**	3	1
O(63)	0.6667	0.3333	0.805(1)	6.7(2)**	1	1
S(6)	0.3333	0.6667	0.3068(1)	3.3(1)	1	1
O(64)	0.212(1)	0.603(1)	0.2885(5)	7.6(2)	3	1
O(65)	0.3333	0.6667	0.3471(7)	7.5(1)**	1	1
S(7)	0.3333	0.6667	0.6846(1)	3.07(1)	1	1
O(66)	0.211(1)	0.597(2)	0.6969(9)	5.8(2)**	3	1
O(67)	0.3333	0.6667	0.647(1)	7.2(2)**	1	1
S(8)	0.3333	0.6667	0.8141(1)	2.99(9)	1	1
O(68)	0.2075(9)	0.592(1)	0.8019(4)	7.6(2)	3	1
O(69)	0.3333	0.6667	0.8553(5)	8.7(1)	1	1
S(9)	0.6667	0.3333	0.3575(1)	2.44(8)	1	1
O(70)	0.609(1)	0.399(1)	0.3669(6)	5.7(3)**	3	1
O(71)	0.6667	0.3333	0.3166(5)	5.8(3)**	1	1
S(10)	0.6667	0.3333	0.9786(1)	2.63(7)	1	1
O(72)	0.610(1)	0.396(1)	0.9634(4)	6.9(1)	3	1
O(73)	0.6667	0.3333	0.0214(7)	5.0(1)**	1	1

Note: The occupancies of the positions were determined with an accuracy of 0.01.
* The positions with mixed composition $Na_{0.65}Ca_{0.35}$; the composition of the Na(10a) position is $Na_{0.6}K_{0.4}$.
** Isotropic thermal parameters.

cancrinite cages alternate along the [0 0 z] axis, and sodalite and bystrite cages alternate along two other axes.

The structure of the new member of the cancrinite group is more complicated and is formed by the rings packed in the sequence *CACACBCBCACB* (Fig. 2), which produces three types of cages comprising columns. The columns along the [0 0 z] axis, like those in the above-described structures, consist only of cancrinite cages. Two other columns along the [1/3 2/3 z] (Fig. 3) and [2/3 1/3 z] (Fig. 4) axes are characterized by sets of cancrinite, bystrite, and liottite cages and differ in the order in which they alternate with each other. Therefore, the crystal structure of the tounkite-like mineral determined in this study has features in common with the afghanite structure that also manifest themselves in the IR spectrum (this spectrum was recorded by N.V. Chukanov). In both minerals, the columns along the [0 0 z] direction consist of cancrinite cages. In the afghanite structure, the cancrinite and liottite cages alternate along two other axes, whereas bystrite cages

Table 4. Interatomic distances in the SO groups

S(1)–O(49)	1.57(1) × 3	S(5)–O(62)	1.44(2) × 3
	⟨1.57⟩	–O(63)	1.42(2)
–O(50)	1.35(3) × 3		⟨1.44⟩
–O(51)	1.31(3)	S(6)–O(64)	1.46(1) × 3
	⟨1.34⟩	–O(65)	1.29(2)
S(2)–O(52)	1.47(2) × 3		⟨1.42⟩
–O(53)	1.36(2)	S(7)–O(66)	1.40(1) × 3
	⟨1.44⟩	–O(67)	1.21(3)
–O(54)	1.30(1) × 3		⟨1.35⟩
–O(55)	1.41(2)	S(8)–O(68)	1.45(1) × 3
	⟨1.33⟩	–O(69)	1.32(1)
S(3)–O(56)	1.38(1) × 3		⟨1.42⟩
–O(57)	1.46(1)	S(9)–O(70)	1.40(1) × 3
	⟨1.40⟩	–O(71)	1.31(1)
–O(58)	1.39(3) × 3		⟨1.38⟩
–O(59)	1.44(1)	S(10)–O(72)	1.40(1) × 3
	⟨1.40⟩	–O(73)	1.37(2)
S(4)–O(60)	1.38(1) × 3		⟨1.39⟩
–O(61)	1.38(2)		
	⟨1.38⟩		

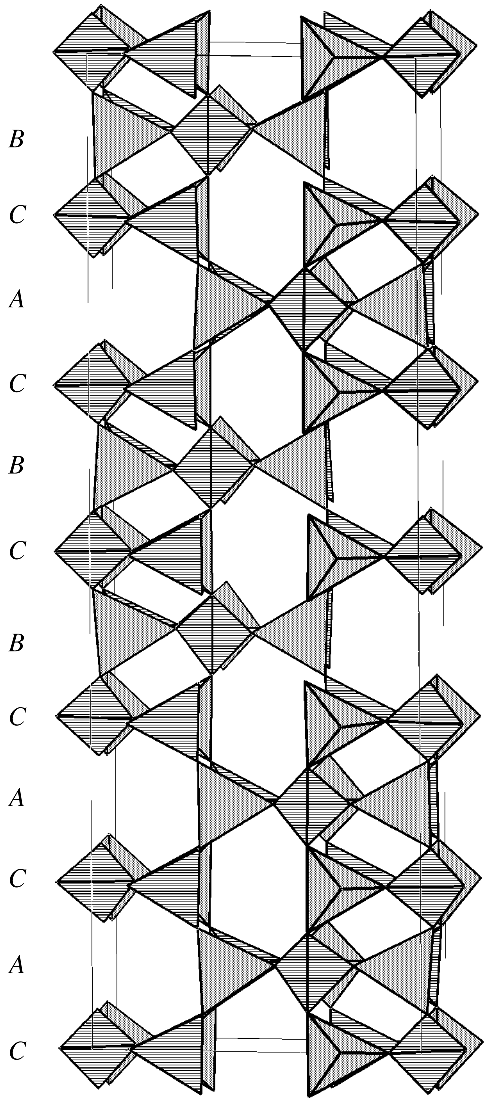

Fig. 2. Aluminosilicate framework projected onto the ($ca\sin\gamma$) plane. The Si tetrahedra are hatched. The layers perpendicular to the z axis are labeled with letters.

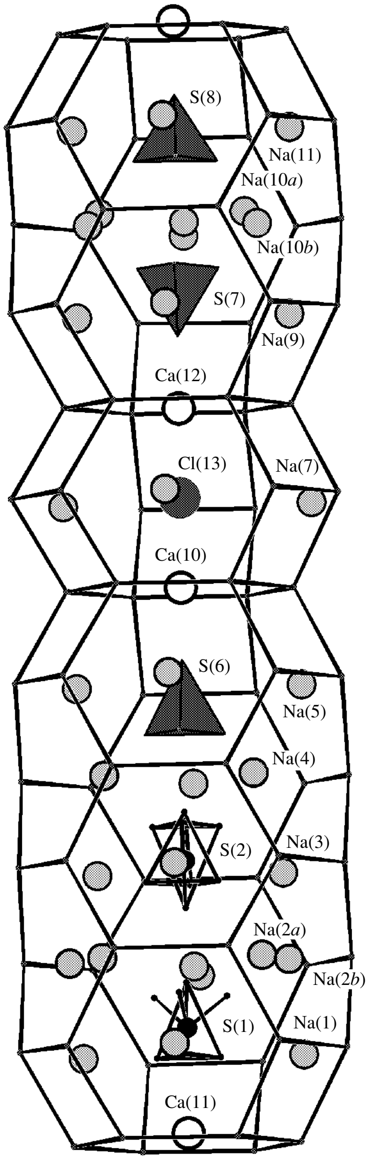

Fig. 3. Column of cages along the [1/3 2/3 z] axis. The SO_4 tetrahedra are shaded gray. Large cations and Cl are represented by circles.

are additionally involved in the formation of analogous columns in the tounkite-like mineral.

Large cations, anions, and anionic groups occupy the cages of all three types of columns in different fashions. In the cancrinite cages arranged along the [0 0 z] direction, calcium atoms are located at the centers of six-membered rings and large chlorine atoms occupy the centers of the cages to form infinite –Ca–Cl–Ca– chains. Fragments of these chains are also retained in discrete cancrinite cages of the columns.

The hexagonal bases of the cages forming columns along the [2/3 1/3 z] axis contain Ca(7), Ca(8), and Ca(9) atoms. Three SO_4 groups, one of which is statistically disordered over two orientations, occupy the liottite cage. The liottite cage contains the Na(6) and Na(8) positions, as well as mixed positions occupied by Na and Ca atoms, which are denoted as Na(5)*, Na(7)*, and Na(9)* and belong simultaneously to a column that extends along another axis. In the bystrite cage, two SO_4 groups are located on the threefold axis. The split Na(12*a*)* and Na(12*b*) positions in this cage, as well as the Na(1) and Na(11) positions shared with the adjacent column, are arranged around the threefold axis.

In the liottite cages arranged along the [1/3 2/3 z] axis, the S(1) atoms statistically occupy tetrahedral sites and have, in part, a triangular coordination

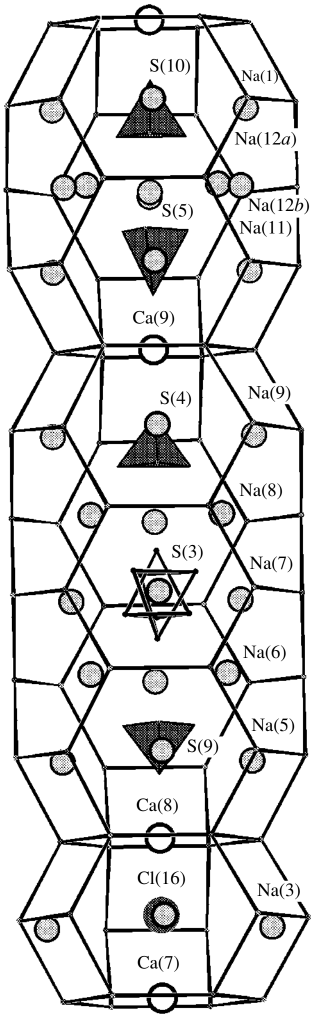

Fig. 4. Column of cages along the [2/3 1/3 *z*] axis. The notations are the same as in Fig. 3.

[$(SO_4)_{0.3}$ and $(SO_3)_{0.7}$, respectively]. One of the SO_4 tetrahedra has two orientations relative to the threefold axis with statistically disordered arrangement of O atoms. The Na(1), Na(2*a*), Na(2*b*), Na(3), and Na(4) positions, as well as the mixed Na(5) position (occupied by Na and Ca atoms), are located within the liottite cage around the [1/3 2/3 *z*] axis. The Na(1), Na(3), and Na(5)* positions are shared with the adjacent columns. Ca atoms lie in the hexagonal bases of the cage. In the cancrinite cage, the Cl(3) atom is located on the threefold axis and the Ca(10) and Ca(12) atoms occupy the bases. The mixed Na(7)* positions are located around the axis and belong simultaneously to the liottite cages of the adjacent columns. The bystrite cage contains two SO_4 tetrahedra on the threefold axis, which are randomly oriented in opposite directions. The Na(10*a*) position occupied by Na and K atoms, the Na(10*b*) position, and the mixed Na(9)* position occupied by Na and Ca atoms are arranged around the axis. The latter position is shared with the liottite cage of an adjacent column. The Na(11) position is also shared with the bystrite cage of an adjacent column.

Thus, the chemical composition of the tounkite-like mineral (as regards to the framework atoms) determined by X-ray diffraction analysis is in complete agreement with the results of chemical analysis. The missed sulfur atoms (0.75 atom per unit cell) belong, apparently, to sulfide groups and are spread over framework anionic positions. On the whole, the cages are identically occupied. However, it should be noted that the liottite cage in the column along the [2/3 1/3 *z*] axis contains a larger number of Ca atoms. On the contrary, the bystrite and cancrinite cages in the column along the [1/3 2/3 *z*] axis are more enriched in Ca than the corresponding cages in the above-mentioned column. In addition, S^{4+} is located in the liottite cage of the same column. These differences underline the low symmetry of the structure as a whole.

CONCLUSIONS

Like the tounkite and tounkite-like minerals, the new mineral marinellite [11] is characterized by a 12-layer stacking sequence of tetrahedral rings (c = 31.761 Å). The latter mineral is similar in chemical composition to the tounkite-like mineral. However, it differs in its lower Ca and S contents and higher K content, as well as in the presence of water with chlorine. Marinellite differs from the tounkite-like mineral in symmetry ($P31c$) and the layer stacking sequence (*CABABACBABAB*). The preliminary data [11] showed that marinellite also differs from tounkite. In the marinellite structure, liottite cages are arranged along the [0 0 *z*] axis and sodalite and cancrinite cages alternate along the [1/3 2/3 *z*] and [2/3 1/3 *z*] axes. At the same time, the IR spectra indicate substantial structural differences between the tounkite and tounkite-like minerals. Therefore, both minerals of the cancrinite group, characterized by a 12-layer stacking sequence, have different crystal structures and are, apparently, polymorphs of tounkite.

ACKNOWLEDGMENTS

We are grateful to Dr. Yusheng Chen for his help in obtaining experimental data. This study was supported by the Russian Foundation for Basic Research (project nos. 02-05-64080 and 03-05-65108) and the Grant for Support of Leading Scientific Schools (project no. NSh-1087-2003-5).

REFERENCES

1. V. G. Ivanov, A. N. Sapozhnikov, L. F. Piskunova, and A. A. Kashaev, Zap. Vseross. Mineral. O–va, No. 2, 92 (1992).
2. A. N. Sapozhnikov, A. A. Kashaev, N. B. Bolotina, *et al.*, in *Proceedings of XV International Workshop on X-ray*

Diffraction Analysis and Crystal Chemistry of Minerals (St. Petersburg, 2000), p. 199.

3. V. I. Andrianov, Kristallografiya **32** (1), 228 (1987) [Sov. Phys. Crystallogr. **32**, 130 (1987)].
4. A. A. Kashaev and A. N. Sapozhnikov, *Crystal Chemistry of Minerals* (Nauka, Leningrad, 1981), p. 7.
5. E. A. Pobedimskaya, L. E. Terent'eva, A. N. Sapozhnikov, *et al.*, Dokl. Akad. Nauk SSSR **319** (4), 873 (1991) [Sov. Phys. Dokl. **36**, 553 (1991)].
6. P. Ballirano, S. Merlino, E. Bonaccorsi, and A. Maras, Can. Mineral. **34** (6), 1021 (1996).
7. P. Ballirano, E. Bonaccorsi, A. Maras, and S. Merlino, Eur. J. Mineral. **9** (1), 21 (1997).
8. P. Ballirano, E. Bonaccorsi, A. Maras, and S. Merlino, Can. Mineral. **38** (4), 657 (2000).
9. P. Ballirano, A. Maras, and P. R. Buseck, Am. Mineral. **81**, 1003 (1996).
10. R. K. Rastsvetaeva, E. A. Pobedimskaya, L. E. Terent'eva, and A. N. Sapozhnikov, Kristallografiya **38** (2), 94 (1993) [Crystallogr. Rep. **38**, 185 (1993)].
11. E. Bonaccorsi and P. Orlandi, Eur. J. Mineral. **15** (6), 1019 (2003).

Translated by T. Safonova

Crystallography Reports, Vol. 49, No. 4, 2004, pp. 643–648. Translated from Kristallografiya, Vol. 49, No. 4, 2004, pp. 722–727.
Original Russian Text Copyright © 2004 by Antsyshkina, Sadikov, Sergienko, Poznyak.

Crystal Structure of SrFe(*EDTA*)Cl · $5H_2O$

A. S. Antsyshkina*, G. G. Sadikov*, V. S. Sergienko*, and A. L. Poznyak**

**Kurnakov Institute of General and Inorganic Chemistry, Russian Academy of Sciences,*
Leninskiĭ pr. 31, Moscow, 119991 Russia

e-mail: antas@igic.ras.ru

***Institute of Molecular and Atomic Physics, Belarussian Academy of Sciences,*
pr. F. Skoriny 70, Minsk, 220072 Belarus

Received July 4, 2002

Abstract—The crystal structure of the SrFe(*Edta*)Cl · $5H_2O$ (**I**) complex is determined. The crystals are monoclinic, $a = 7.530(4)$ Å, $b = 10.575(3)$ Å, $c = 23.308(10)$ Å, $\beta = 95.75(4)°$, $Z = 4$, and space group $P2_1/c$. The structural units of **I** are infinite ribbons of the molecular type that are formed by tetranuclear fragments. A tetranuclear fragment involves the centrosymmetric positively charged dimer group $[Sr(H_2O)_4Cl]_2^{2+}$ at the center and the $[Fe(Edta)(H_2O)]^-$ anionic complexes, which compensate for the positive charge of the dimer group, at the periphery. These constituents are bound via bridging oxygen atoms of the *Edta* ligands. The coordination number of the Sr atom is nine. The Sr–O bond lengths lie in the range between 2.552 and 2.766 Å, the Sr–Cl bond length is 3.216(3) Å, and the Sr···Sr distance is 4.371(1) Å. The parameters of the $[Fe(Edta)(H_2O)]^-$ group are within the range of values observed in such complexes: Fe–O, 1.996–2.086(3) Å; Fe–O(*w*), 2.110(4) Å; and Fe–N, 2.289(4) and 2.327(4) Å. Separate ribbons are linked by hydrogen bonds involving all H_2O molecules and terminal oxygen atoms of the *Edta* ligand. *© 2004 MAIK "Nauka/Interperiodica".*

INTRODUCTION

Among the large number of structurally characterized compounds that contain ethylenediaminetetraacetic acid (H_4Edta) as a ligand, there are many ethylenediaminetetraacetates with the central Fe(III) atom. A series of complexes consisting of the $[Fe(Edta)(H_2O)]^-$ anion and a singly charged counterion (such as Li^+ [1], Na^+ [2–4], K^+ [4], Rb^+ [1, 5], Ag^+ [3], Tl^+ [3], $[(C_2H_5)_4N]^+$ (organic) [6], or $(CN_3H_6)^+$ (organic) [1, 7]) has been investigated to date. All of them form mononuclear cationic–anionic structures of the island type, in which the $[Fe(Edta)(H_2O)]^-$ anion is the hexadentate seven-coordinate complex with symmetry close to C_2.

It is known that the changeover from singly charged cations to doubly or more multiply charged cations encourages cation–anion bonding and, as a consequence, the formation of heteronuclear polymeric structures through bridging atoms of the aminopolycarboxylate ligand. A similar situation is observed, for example, in calcium ethylenediaminetetraacetates with doubly charged cations, namely, Ca[Ca(*Edta*)] · $7H_2O$ [8] and Sr[Ca(*Edta*)] · $5H_2O$ [9].

The crystal structure of barium ethylenediaminetetraacetatoaquaferrate $BaFe_2(Edta)_2 \cdot 6H_2O$ [10] is of the same polymeric type as that of the above complexes with doubly charged cations.

It is of interest to answer the questions as to (i) whether this situation is typical of other compounds, (ii) whether it is retained in compounds with other doubly charged cations, and (iii) how the introduction of additional ligands affects the crystal structure.

For this purpose, we performed an X-ray diffraction study of the SrFe(*Edta*)Cl · $5H_2O$ (**I**) complex.

EXPERIMENTAL

Synthesis. Compound **I** (empirical formula, $C_{10}H_{22}ClFeN_2O_{13}Sr$) was prepared by the reaction of aqueous solutions of $Sr[Fe(Edta)(H_2O)]_2$ and HFe(*Edta*) in the presence of $SrCO_3$ and an excess amount of $SrCl_2$. Slow evaporation of the solution due to heating resulted in the precipitation of a mixture of small-sized yellow prismatic crystals of **I** and large-sized brown aggregates of $Sr[Fe(Edta)(H_2O)]_2$.

X-ray diffraction analysis. Crystals **I** are monoclinic, $a = 7.530(4)$ Å, $b = 10.575(3)$ Å, $c = 23.308(10)$ Å, $\beta = 95.75(4)°$, $V = 1846.8(1.4)$ Å^3, $M = 557.2$, $F(000) = 1124$, $\rho_{calcd} = 2.00$ g/cm^3, $\mu_{Mo} = 3.89$ mm^{-1}, $Z = 4$, and space group $P2_1/c$.

The X-ray experimental reflections were collected on an Enraf–Nonius CAD4 diffractometer at room temperature (λMoK_α, graphite monochromator, $\theta/2\theta$ scan mode, $2\theta_{max} = 56°$).

Table 1. Atomic coordinates and thermal parameters in structure **I**

Atom	x	y	z	U_{eq}/U_{iso}, Å^2	Atom	x	y	z	U_{eq}/U_{iso}, Å^2
Sr(1)	0.3768(1)	0.9784(0)	0.0804(0)	0.0217(1)	C(6)	1.1723(7)	1.3151(5)	0.1786(2)	0.023(1)
Fe(1)	0.7718(1)	1.2643(1)	0.1775(0)	0.0138(2)	C(7)	0.6521(6)	1.1836(5)	0.0597(2)	0.0186(9)
Cl(1)	0.2242(2)	1.2430(2)	0.0285(1)	0.0429(4)	C(8)	0.7438(7)	1.3032(5)	0.0448(2)	0.023(1)
N(1)	1.0174(5)	1.3922(4)	0.1916(2)	0.0179(8)	C(9)	0.9930(7)	1.5066(5)	0.1549(2)	0.020(1)
N(2)	0.7634(5)	1.3892(4)	0.0951(2)	0.0166(8)	C(10)	0.9270(7)	1.4681(5)	0.0943(2)	0.024(1)
O(1)	0.8750(5)	1.2380(3)	0.2618(1)	0.0246(7)	H(22)	1.14(1)	1.456(6)	0.265(3)	0.04(2)
O(2)	1.0418(5)	1.3039(4)	0.3393(2)	0.0326(9)	H(41)	0.49(1)	1.425(7)	0.078(3)	0.05(2)
O(3)	0.6301(5)	1.4149(3)	0.1977(1)	0.0215(7)	H(42)	0.616(9)	1.544(6)	0.077(3)	0.03(2)
O(4)	0.4680(6)	1.5828(4)	0.1700(2)	0.0339(9)	H(61)	1.24(1)	1.313(7)	0.211(3)	0.05(2)
O(5)	0.9618(4)	1.1527(3)	0.1515(1)	0.0204(7)	H(62)	1.233(8)	1.353(6)	0.150(3)	0.03(2)
O(6)	1.2478(5)	1.1024(3)	0.1623(2)	0.0238(7)	H(81)	0.670(7)	1.341(5)	0.009(2)	0.02(1)
O(7)	0.6137(4)	1.1720(3)	0.1118(1)	0.0196(7)	H(82)	0.849(9)	1.271(6)	0.040(3)	0.04(2)
O(8)	0.6156(5)	1.1015(3)	0.0227(1)	0.0246(8)	H(91)	0.924(6)	1.558(4)	0.169(2)	0.00(1)
O(*w*1)	0.2529(7)	0.7479(5)	0.0929(2)	0.055(1)	H(92)	1.08(1)	1.551(7)	0.154(3)	0.05(2)
O(*w*2)	0.0344(7)	0.9632(6)	0.0574(3)	0.062(1)	H(101)	0.890(7)	1.549(5)	0.067(2)	0.01(1)
O(*w*3)	0.4816(8)	0.8813(5)	0.1859(2)	0.055(1)	H(102)	1.016(6)	1.416(4)	0.083(2)	0.00(1)
O(*w*4)	0.6411(6)	0.8264(5)	0.0873(2)	0.041(1)	H(1*w*1)	0.32(2)	0.70(1)	0.13(1)	0.13(4)
O(*w*5)	0.5838(6)	1.1553(4)	0.2173(2)	0.0301(9)	H(2*w*1)	0.13(2)	0.76(1)	0.11(1)	0.13(4)
C(1)	0.9836(7)	1.3155(5)	0.2882(2)	0.022(1)	H(1*w*3)	0.44(1)	0.889(9)	0.214(4)	0.08(3)
C(2)	1.0330(7)	1.4266(5)	0.2531(2)	0.023(1)	H(1*w*4)	0.75(1)	0.830(6)	0.111(3)	0.04(2)
C(3)	0.5660(6)	1.4932(4)	0.1599(2)	0.0198(9)	H(2*w*4)	0.69(1)	0.806(9)	0.064(4)	0.06(3)
C(4)	0.6033(7)	1.4668(5)	0.0978(2)	0.023(1)	H(1*w*5)	0.597(8)	1.130(6)	0.248(3)	0.03(2)
C(5)	1.1265(6)	1.1789(5)	0.1636(2)	0.0185(9)	H(2*w*5)	0.493(9)	1.143(5)	0.201(3)	0.02(2)

The structure was solved by direct methods. The hydrogen atoms [except for the H(1*w*2), H(2*w*2), and H(2*w*3) atoms] were located from difference Fourier syntheses. The least-squares refinement was performed using 4194 unique nonzero reflections. The non-hydrogen atoms were refined in the anisotropic approximation, and the hydrogen atoms were refined isotropically. The final discrepancy factors are as follows: $R_1 = 0.0420$ and $wR_2 = 0.1072$ for 3087 reflections with $F_o \geq 4\sigma(F_o)$, $R_1 = 0.0740$ and $wR_2 = 0.1220$ for all 4194 reflections, $GOOF = 1.014$; and $\Delta\rho_{max} = 1.386$ e/Å^3 and $\Delta\rho_{min} = -0.637$ e/Å^3.

All the calculations were performed with the SHELXS86 [11] and SHELXL93 [12] program packages.

The coordinates and thermal parameters of atoms in structure **I** are listed in Table 1.

RESULTS AND DISCUSSION

The structural units of crystal **I** are infinite ribbons of the molecular type that are aligned along the shortest axis *a* of the crystal. A ribbon is composed of centrosymmetric tetranuclear fragments consisting of the central doubly charged dimer fragment $[Sr(H_2O)_4Cl]_2^{2+}$ and two terminal anionic complexes $[Fe(Edta)(H_2O)]^-$ (Fig. 1).

In structure **I**, the multifunctional ligand $Edta^{4-}$ (O^{210001}, according to the notation proposed by Serezhkin and coauthors [13]) is coordinated to the central Fe atom via the N(1), N(2), O(1), O(3), O(5), and O(7) atoms and to two Sr atoms via the O(7) and O(8) atoms. One of the acetate arms of *Edta* plays a dominant role in the formation of the tetranuclear fragment and fulfills the function of a triple bridge. The distances from the Sr atom to the terminal O(8) atom and its centrosymmetric analogue, namely, O(8)', are equal to 2.689(3)

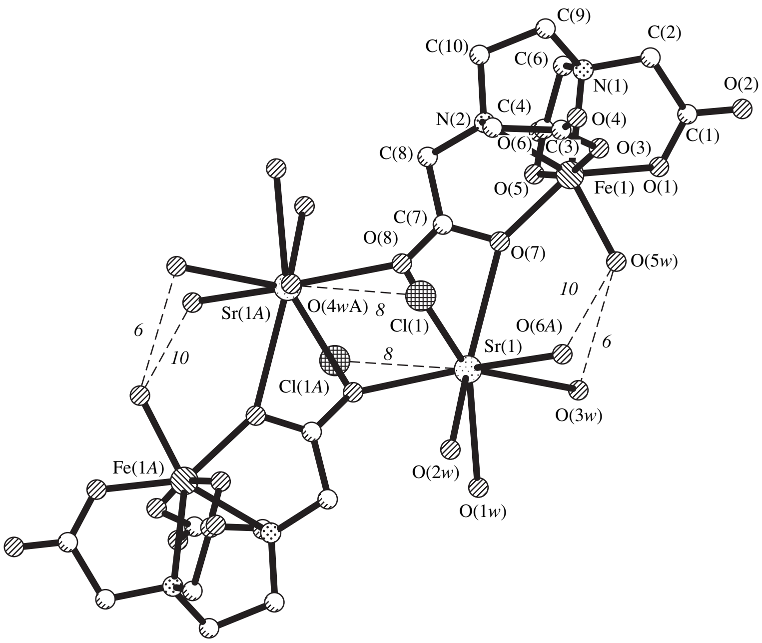

Fig. 1. Tetranuclear fragment of structure **I** in the projection onto the plane close to the mean plane of nine central rings formed by two $Edta^{4-}$ ligands with the Fe and Sr atoms.

and 2.554(3) Å, respectively. The bond between the Sr atom and the other bridging O(7) atom (coordinated to Fe) is significantly elongated [2.766(3) Å]. Apart from the aforementioned atoms [O(7), O(8), O(8)'], the coordination sphere of the Sr atom includes the bridging O(6) atom [Sr–O, 2.583(3) Å]; the Cl atom [Sr–Cl, 3.216(2) Å]; and the O(*w*1), O(*w*2), O(*w*3), and O(*w*4) atoms of four water molecules. The Sr–O(*w*1), Sr–O(*w*2), Sr–O(*w*3), and Sr–O(*w*4) bond lengths fall in the range 2.552(5)–2.718(5) Å. In this case, the water molecules are located in one part of the nine-vertex coordination polyhedron. No immediate interaction between the strontium atoms in the dimer occurs: the Sr···Sr distance is 4.371(1) Å.

In structure **I**, the $[Fe(Edta)(H_2O)]^-$ anionic fragment, like the other ethylenediaminetetraacetates, has a local symmetry close to C_2. The bond lengths are as follows: Fe–N, 2.289 and 2.327(4) Å; Fe–O(*Edta*), 1.996–2.086(3) Å; and Fe–O(H_2O), 2.110(4) Å. As usual, the five metallocycles are closed and all the four acetate arms are involved in the chelate formation. The ethylenediamine chelate ring (*En*) has an asymmetric *gauche* structure: two C atoms deviate from the Fe(1)N(1)N(2) plane by 0.16 and –0.51 Å. The glycinate *G* rings (in the plane of the *En* ring) form angles of 9° and 21° with the Fe(1)N(1)N(2) plane, and the *R* rings (perpendicular to the *En* plane) form angles of 96° and 90° with the same plane.

Table 2. Geometric parameters of hydrogen bonds in structure **I**

No.	O–H···*A* bond	Distances, Å			OH*A* angle, deg	Symmetry codes for the *A* atom
		O···*A*	O–H	H···*A*		
1	O(*w*1)–H(1*w*1)···O(4)	2.888(7)	1.1(1)	1.8(1)	157(9)	1 –*x*, –0.5 + *y*, 0.5 – *z*
2	O(*w*1)–H(2*w*1)···O(2)	2.910(7)	1.1(1)	1.9(1)	162(9)	1 –*x*, –0.5 + *y*, 0.5 – *z*
3	O(*w*2)···O(*w*2)	2.778(9)				1 – *x*, 2 – *y*, 0.5 – *z*
4	O(*w*2)···Cl(1)	3.427(6)				–*x*, 2 – *y*, 0.5 – *z*
5	O(*w*3)–H(1*w*3)···O(3)	2.935(6)	0.8(1)	2.15(9)	161(9)	1 –*x*, –0.5 + *y*, 0.5 – *z*
6	O(*w*3)···O(*w*5)	3.064(7)				*x*, *y*, *z*
7	O(*w*4)–H(1*w*4)···O(2)	2.803(6)	0.95(7)	1.86(7)	150(8)	2 –*x*, –0.5 + *y*, 0.5 – *z*
8	O(*w*4)–H(2*w*4)···Cl(1)	3.066(5)	0.70(9)	2.38(9)	165(9)	1 –*x*, 2 – *y*, 0.5 – *z*
9	O(*w*5)–H(1*w*5)···O(4)	2.800(5)	0.75(7)	2.10(7)	157(9)	1 –*x*, –0.5 + *y*, 0.5 – *z*
10	O(*w*5)–H(2*w*5)···O(6)	2.776(5)	0.76(7)	2.02(7)	175(8)	*x* – 1, *y*, *z*

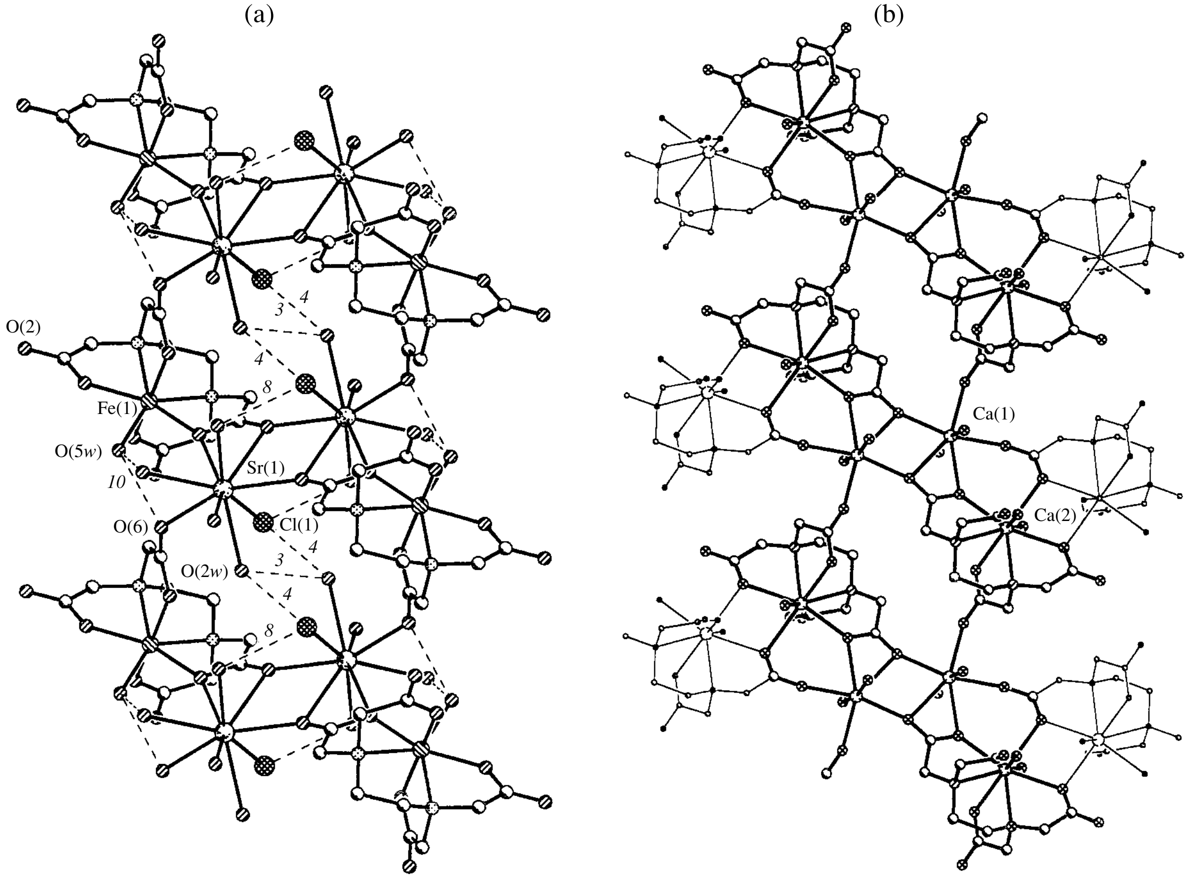

Fig. 2. Comparison of structures **I** and **II**. (a) Infinite ribbons of the molecular type in structure **I**. Dashed lines indicate hydrogen bonds (the numbering corresponds to that in Table 2). (b) Structure of the layer in **II**. A fragment of the ribbon is shown by heavy lines.

This does not exhaust the structural function of the *Edta*$^{4-}$ ligand. The terminal O(6) atoms bridge the tetranuclear units to form hexanuclear Fe··Sr··Sr··Fe··Sr··Sr rings, which, in turn, share the Sr··Sr sides to form infinite ribbons (Fig. 2a). The Sr–O(6) distance [2.583(3) Å] is one of the shortest distances in this structure.

The polymeric structural units are additionally stabilized by inner hydrogen bonds (Table 2). Hydrogen bonds 6, 8, and 10 strengthen the tetranuclear fragment: hydrogen bonds 6 and 10 link the coordination spheres of the Sr and Fe atoms, whereas the centrosymmetric pair of hydrogen bond 8 links two halves of the tetranuclear fragment at their center. This bond lies in the plane perpendicular to the plane of the tetranuclear fragment, which includes nine rings (in Fig. 1, this plane is almost parallel to the plane of the figure). The centrosymmetric pairs of hydrogen bonds 4 and 3 link adjacent tetranuclear fragments at the centers of hexanuclear rings inside the ribbons. The basal planes of the adjacent tetranuclear fragments are inclined with respect to the direction of extension of the ribbons, and the hexanuclear (··Fe··Sr···) rings are nonplanar; therefore, the ribbons are puckered.

According to our considerations in [14], the compounds with the same conformation of complexes are expected to form closely similar crystal structures. The conformation of **I** (Λλ or Δδ for the complex related by the inversion center) is the same as in Ca[Ca(*Edta*)] · $7H_2O$ (**II**) [8]. The alternative conformation (Λδ or Δλ) is observed in Sr[Ca(*Edta*)] · $5H_2O$ (**III**) [9]. The similarity can be revealed even if other important parameters are different.

In structures **I** and **II** under comparison, the coordination numbers (CNs) of metal atoms are essentially different: $CN_{Fe} = 7$ and $CN_{Sr} = 9$ in structure **I** and $CN_{Ca} =$ 8 and 7 in structure **II**. Moreover, the coordination sphere of the Sr(1) atom additionally includes the large-sized Cl(1) atom, which forms a hydrogen bond with the O(H_2O) atom of the neighboring tetranuclear dimer. Nonetheless, the ribbons in **I** are analogous to the fragments distinguished in structure **II** (Fig. 2b). In **II**, similar six-membered rings are formed by components of the tetranuclear associates. The ribbon fragments in **I**

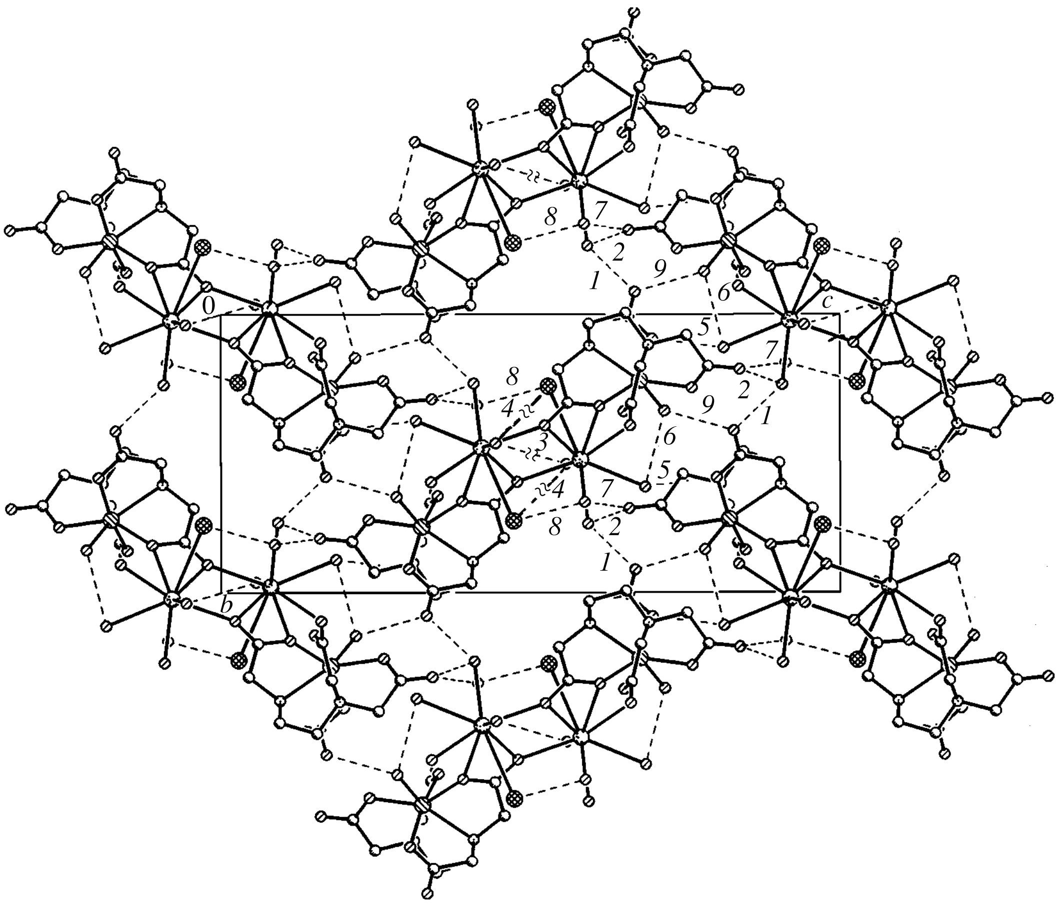

Fig. 3. Hydrogen bonds and packing of ribbons in structure **I**.

and **II** are formed in the same manner. The difference between the structures is in the packing of the ribbons in the crystal.

In **I**, the ribbons are packed according to the parquet motif (Fig. 3). The contacts between the ribbons are due to hydrogen bonds (hydrogen bonds 1, 2, 3, 5, 7, and 9). No other short contacts are observed in the structure. In the structural regions where van der Waals interactions could be expected, there exist relatively wide channels (4.7 Å in diameter).

In distinction to **I**, in which the ribbons are linked only by hydrogen bonds, the ribbons in **II** are associated into layers. The mechanism of association is very similar to the hypothetical mechanism discussed in [15]. The terminal ethylenediamine complexes of tetranuclear fragments are bound into dimeric associates. In **II**, the formation of the coordination (rather than hydrogen) bonds between the dimers brings about the formation of layers. In **III** (with a different conformation of the ethylenediamine complexes), the polymerization leads to the formation of a framework structure.

A comparison between structures **I** and **II** revealed that the hypothetical transition considered in [15], which is accompanied by the transformation of the discrete complex into the dimer, takes place in the concrete morphotropic transition and that the energy expended for forming the contact due to the totality of hydrogen bonds can be equivalent or comparable to that due to traditional coordination bonds.

In conclusion, it should be noted that the formation of heteronuclear polymeric structures frequently occurs via bridging atoms of aminopolycarboxylate ligands. This situation is typical of different doubly charged cations. The introduction of additional ligands (in our case, chlorine) does not produce an essential effect on the general strategy of crystal construction.

REFERENCES

1. M. D. Lind, J. L. Hoard, M. J. Hamor, *et al.,* Inorg. Chem. **3** (1), 34 (1964).
2. N. V. Novozhilova, T. N. Polynova, and M. A. Poraĭ-Koshits, Zh. Strukt. Khim. **16** (5), 865 (1975).
3. J. M. Lopez-Alcala, M. C. Puerta-Vizcaino, F. Gonzalez-Vilchez, *et al.*, Acta Crystallogr., Sect. C: Cryst. Struct. Commun. **40** (6), 939 (1984).

4. X. Solans, M. Font-Altaba, and J. Garcia-Oricain, Acta Crystallogr., Sect. C: Cryst. Struct. Commun. **40** (4), 635 (1984).
5. J. L. Hoard, M. D. Lind, and J. V. Silverton, J. Am. Chem. Soc. **83** (12), 2770 (1961).
6. Ya. M. Nesterova, T. N. Polynova, and M. A. Poraĭ-Koshits, Koord. Khim. **1** (7), 966 (1975).
7. X. Solans, M. Font-Altaba, and J. Garcia-Oricain, Acta Crystallogr., Sect. C: Cryst. Struct. Commun. **41** (4), 525 (1985).
8. B. L. Barnett and V. A. Uchtman, Inorg. Chem. **18** (10), 2674 (1979).
9. E. Passer and J. L. White, Inorg. Chim. Acta **24**, 13 (1977).
10. X. Solans, M. Font-Altaba, and J. Garcia-Oricain, Afinidad **41**, 572 (1984).
11. G. M. Sheldrick, Acta Crystallogr., Sect. A: Found. Crystallogr. **46**, 467 (1990).
12. G. M. Sheldrick, *SHELXL93: Program for the Refinement of Crystal Structures* (Univ. of Göttingen, Germany, 1993).
13. V. N. Serezhkin, T. N. Polynova, and M. A. Poraĭ-Koshits, Koord. Khim. **21** (4), 253 (1995).
14. G. G. Sadikov, A. S. Antsyshkina, A. L. Poznyak, and V. S. Sergienko, Zh. Neorg. Khim. **47** (1), 54 (2002).
15. A. S. Antsyshkina, G. G. Sadikov, A. L. Poznyak, and V. S. Sergienko, Zh. Neorg. Khim. **47** (1), 43 (2002).

Translated by I. Polyakova

Crystallography Reports, Vol. 49, No. 4, 2004, pp. 649–652. Translated from Kristallografiya, Vol. 49, No. 4, 2004, pp. 728–731.
Original Russian Text Copyright © 2004 by Sinyakov, Aleksandrov, Ovchinnikova.

STRUCTURE OF ORGANIC COMPOUNDS

Synthesis and Crystal Structure of *trans*-Tetrachloro(*C*,*C*-Dichloro-*C*-Phenyl-Methyl-Nitrido)(phenylnitrilo)tungsten(VI), *trans*-[$WCl_4(NCCl_2Ph)(NCPh)$]

A. E. Sinyakov, G. G. Aleksandrov, and N. A. Ovchinnikova

Kurnakov Institute of General and Inorganic Chemistry, Russian Academy of Sciences,
Leninskiĭ pr. 31, Moscow, 119991 Russia
e-mail: talan@igic.ras.ru

Received November 18, 2002

Abstract—A product of the insertion, namely, *trans*-tetrachloro(*C*,*C*-dichloro-*C*-phenyl-methyl-nitrido)(phenylnitrilo)tungsten(VI), *trans*-[$WCl_4(NCCl_2Ph)(NCPh)$] (**I**), is synthesized by the reaction of WCl_6 with *Ph*CN in CCl_4 under refluxing for 2 h. Judging from the characteristic IR bands ν(C≡N) and ν(W≡N), the complex synthesized is identical to the compound prepared earlier at room temperature. The crystal structure of complex **I** is determined using X-ray diffraction analysis. It is revealed for the first time that the coordination polyhedron of the tungsten atom in complex **I** is a distorted octahedron with four chlorine atoms in the equatorial plane. The axial positions are occupied by the N(1) atom [W–N(1), 2.265(13) Å] of the coordinated benzonitrile group and the N(2) atom [W–N(2), 1.732(13) Å] of the multiply bonded ligand $NCCl_2Ph$. *© 2004 MAIK "Nauka/Interperiodica".*

INTRODUCTION

As is known [1], the addition of nitriles to tungsten hexachloride is accompanied by the transfer of two chlorine atoms to the carbon atom of the nitrile group with the formation of products of the insertion, namely, [$WCl_4(NCCl_2R)(NCR)$]. It should be noted that derivatives of this type with $R = CH_3$– and CH_3CH_2– are relatively unstable and represent intermediate products in the reactions of reduction of tungsten hexachloride and the formation of nitrile adducts [$WCl_4(NCR)_2$]. According to Fowles *et al.* [1], the formation of [$WCl_4(NCR)_2$] nitrile adducts is promoted by heat treatment of the reaction mixture. In other works, insertion reactions resulting in the formation of stable complexes have been investigated only at room temperature. However, among the 11 known products of the insertion of nitriles into tungsten hexachloride, only the [$WCl_4(NC_2Cl_5)(NCCl_3)$] complex with trichloroacetonitrile was structurally characterized by Drew *et al.* [2].

In this respect, it was of interest to perform the reaction of tungsten hexachloride with benzonitrile at high temperatures and then to compare the obtained results with the available data in order to elucidate how the temperature conditions of the synthesis affect the crystal structure (in the case of the formation of a crystalline product) and composition of the product.

EXPERIMENTAL

Synthesis. The reactions were carried out with the following reactants: (i) tungsten hexachloride WCl_6 (commercial grade) purified from impurities through vacuum distillation at a temperature of 90°C and (ii) benzonitrile *Ph*CN (chemically pure) and carbon tetrachloride CCl_4 (chemically pure) purified from impurities by distillation over P_4O_{10}. All the procedures were performed in a dry argon atmosphere.

The elemental composition of the reaction product was determined using a Carlo Erba EA 1108 C,H,N,S-microanalyzer. The IR absorption spectra were recorded on a Specord 75 IR spectrophotometer in the range 4000–400 cm^{-1} (KBr pellets). Samples were prepared as suspensions in vaseline oil.

Benzonitrile *Ph*CN (1.21 ml) was added to a suspension of tungsten hexachloride (5.91 mmol, 2.34 g) in carbon tetrachloride (20 ml). The reaction mixture was boiled in a flask on an oil bath for 2 h. The flask was equipped with a reflux condenser and a tube with $CaCl_2$. Immediately after cooling, brown crystals of the [$WCl_4(NCCl_2Ph)(NCPh)$] compound (**I**) precipitated from the solution. The solid phase was isolated from the mother solution through decantation, washed several times with carbon tetrachloride, and dried under vacuum.

For $C_{8.75}Cl_6H_{6.25}N_{1.25}W$, anal. calcd. (%): N, 3.33; C, 20.00; H, 1.20.

Found (%): N, 3.22; C, 20.22; H, 1.05.

IR (cm^{-1}): 2256 s, 1282 s, 1154 m b, 992 m b, 872 w, 818 w, 784 m, 754 m, 716 s, 680 m, 634 w, 548 s, 498 m.

X-ray diffraction analysis. The X-ray experimental reflections were collected according to a standard procedure [3] on a Bruker AXS SMART 1000 diffrac-

Table 1. Crystal data, data collection, and refinement parameters for the crystal structure of complex **I**

Empirical formula	$C_{14}H_{10}Cl_6N_2W$
Molecular weight	602.79
Crystal size, mm	$0.05 \times 0.08 \times 0.15$
Crystal system	Monoclinic
Space group	$P2_1/n$
Unit cell parameters:	
a, Å	10.286(7)
b, Å	15.493(14)
c, Å	12.471(10)
β, deg	109.25(3)
V, Å^3	1876(3)
Z	4
ρ_{calcd}, g/cm^3	2.134
μ, cm^{-1}	7.008
F(000)	1136
Diffractometer	SMART
T, K	110
Radiation (λ, Å)	MoK_α (0.71073), graphite monochromator
Scan mode	ω
θ range, deg	2.17–30.00
Index ranges	$-14 \le h \le 14$, $-21 \le k \le 21$, $-12 \le 1 \le 17$
Total number of reflections measured	9476
Number of unique reflections	7241 [R_{int} = 0.1000]
T_{min}, T_{max}	0.99, 0.54
Number of parameters refined	139
Goodness-of-fit on F_2	1.000
R [$I > 2\sigma(I)$]	R_l = 0.1062, wR_2 = 0.2685
R (for all reflections)	R_l = 0.1144, wR_2 = 0.2816
Maximum and minimum residual electron densities, eÅ^{-3}	11.900 and –3.817

Table 2. Coordinates of the non-hydrogen atoms ($\times 10^4$) and their equivalent isotropic thermal parameters U_{eq} (Å$^2 \times 10^3$) for the crystal structure of complex **I**

Atom	x	y	z	U_{eq}, Å
W(l)	–2932(1)	3472(1)	7480(1)	19(1)
Cl(l)	–2078(4)	2493(2)	8963(4)	26(1)
C1(2)	–2858(4)	2387(2)	6227(4)	26(1)
Cl(3)	–4243(4)	4271(3)	5935(4)	29(1)
Cl(4)	–3592(4)	4385(3)	8691(4)	29(1)
C1(5)	887(4)	4234(3)	9274(4)	32(1)
C1(6)	–708(4)	5605(2)	7835(4)	28(1)
N(1)	–4977(13)	2857(8)	7344(13)	25(3)
N(2)	–1368(13)	3959(9)	7623(14)	28(3)
C(l)	–6014(15)	2557(10)	7308(16)	25(4)
C(2)	–7336(14)	2203(10)	7300(14)	19(3)
C(3)	–7703(16)	2276(11)	8281(16)	26(4)
C(4)	–8944(15)	1905(10)	8308(17)	28(4)
C(5)	–9711(17)	1455(11)	7373(16)	27(4)
C(6)	–9400(16)	1381(10)	6399(16)	24(4)
C(7)	–8122(15)	1756(10)	6356(16)	26(4)
C(8)	–176(14)	4471(10)	7867(14)	18(3)
C(9)	593(13)	4377(9)	7013(14)	17(3)
C(10)	1912(14)	4682(11)	7263(16)	27(4)
C(11)	2543(15)	4594(10)	6434(15)	24(4)
C(12)	1907(14)	4226(9)	5397(15)	22(3)
C(13)	622(15)	3890(10)	5188(15)	24(3)
C(14)	–79(16)	3966(11)	5961(16)	27(4)

tometer equipped with a CCD detector (ω scan mode; scan step, 0.3°; exposure time per frame, 30 s; $2\theta_{max}$ = 60°).

Semiempirical correction for absorption was introduced with the SADABS software package [4]. The structure was solved by direct methods with the SHELXS97 software package [5] and refined using the least-squares procedure in the full-matrix anisotropic approximation (the calculated positions of the hydrogen atoms were kept constant; U_H = 0.08 Å^2) with the SHELXL97 software package [6]. The standard methods, as applied to the solution and refinement of the crystal structure, led to a very large discrepancy factor (~16%). The repeated analysis of the experimental diffraction reflections (collected on the same diffractometer) with the use of the RLATT and GEMENI programs [7] revealed that the crystal is a twin (more precisely, the crystal is twinned along the b axis). The F^2 array was obtained by subtracting the contribution from part of the overlapping reflections. The structure refinement with this data array led to the following final factors: R_1 = 0.1062 and $R_w(F_o^2)$ = 0.2685 for reflections with $F_o > 4\sigma(F_o)$. Apparently, the large discrepancy factor can be explained by the insufficiently correct inclusion of the crystal twinning in the calculation.

The crystal data, data collection, and refinement parameters for the crystal structure of complex **I** are presented in Table 1. The coordinates of the non-hydrogen atoms and their equivalent isotropic thermal parameters are given in Table 2. The selected interatomic distances and the bond angles are listed in Table 3.

Table 3. Selected bond lengths *d* (Å) and angles ω (deg) for the crystal structure of complex **I**

Bond	*d*	Bond	*d*
W(1)–N(2)	1.732(13)	W(1)–N(1)	2.265(13)
W(1)–C1(3)	2.313(5)	W(1)–C1(2)	2.314(4)
W(1)–C1(1)	2.329(4)	W(1)–C1(4)	2.327(4)
C1(5)–C(8)	1.773(16)	C1(6)–C(8)	1.837(16)
N(1)–C(1)	1.151(19)	N(2)–C(8)	1.406(18)
C(1)–C(2)	1.46(2)	C(8)–C(9)	1.53(2)
Angle	ω	Angle	ω
N(2)–W(1)–N(1)	178.2(7)	N(2)–W(1)–Cl(3)	96.8(5)
N(1)–W(1)–Cl(3)	83.7(4)	N(2)–W(1)–Cl(2)	98.6(5)
N(1)–W(1)–Cl(2)	83.1(4)	Cl(3)–W(1)–Cl(2)	88.04(17)
N(2)–W(1)–Cl(1)	96.2(5)	N(1)–W(1)–Cl(1)	83.3(4)
Cl(3)–W(1)–Cl(1)	166.87(15)	Cl(2)–W(1)–Cl(1)	88.58(16)
N(2)–W(1)–Cl(4)	97.4(5)	N(1)–W(1)–C1(4)	80.9(4)
Cl(3)–W(1)–Cl(4)	90.04(17)	C1(2)–W(1)–C1(4)	164.01(14)
Cl(1)–W(1)–Cl(4)	89.71(16)	C(1)–N(1)–W(1)	177.7(14)
C(8)–N(2)–W(1)	169.0(13)	N(1)–C(1)–C(2)	177.4(18)
N(2)–C(8)–C(9)	114.2(13)	N(2)–C(8)–C1(5)	107.9(11)
C(9)–C(8)–Cl(5)	112.2(9)	N(2)–C(8)–Cl(6)	107.6(10)
C(9)–C(8)–Cl(6)	107.1(10)	Cl(5)–C(8)–Cl(6)	107.5(8)

RESULTS AND DISCUSSION

Our investigations demonstrated that the interaction of tungsten hexachloride with benzonitrile (taken in twofold excess) in carbon tetrachloride under refluxing for 2 h results in the formation of a product of the insertion, namely, complex **I**. According to the IR spectroscopic data, this product is similar to the compound synthesized at room temperature without heating. Actually, the IR absorption spectrum of complex **I** contains the ν(C≡N) band at a frequency of 2256 cm^{-1}, which is associated with the stretching vibrations of the coordinated benzonitrile group, and the ν(W≡N) band at a frequency of 1282 cm^{-1}, which is attributed to the stretching vibrations of the imido ligand. Similar bands were observed (at frequencies of 2262 and 1282 cm^{-1}, respectively) in the IR absorption spectrum of the $[\text{WCl}_4(\text{NCCl}_2Ph)(\text{NC}Ph)]$ complex synthesized at room temperature [1]. This allows us to assume that, in the case under consideration, the temperature conditions do not affect the final product of the reaction, unlike the reaction of tungsten hexachloride with ethyl isocyanate studied in our previous works [8, 9], in which we revealed thermal isomerization of the resultant ligand.

In complex **I**, the coordination polyhedron of the tungsten atom is a distorted octahedron with four chlorine atoms in the equatorial plane (figure). The axial positions of the octahedron are occupied by the N(1) atom [W–N(1), 2.265(13) Å] of the coordinated benzonitrile group and the N(2) atom of the multiply bonded ligand NCCl_2Ph. The distortion manifests itself in a displacement of the W atom from the equatorial plane to the N(1) atom by 0.29 Å. The angles formed by the Cl(1)–Cl(4) plane with the planes of the phenyl groups are equal to 91.4° and 83.4°. The angle between the planes of the phenyl groups is equal to 8.4°.

The W–N(2) distance [1.732(13) Å] in structure **I** lies in the range of the W–N(imido) distances (1.703–1.749 Å; mean distance, 1.726 ± 0.023 Å) in structures of five compounds of the general formula $[\text{WCl}_4(\text{NC}R_1)(\text{N}R_2)]$ (where $R_1 = Me$; $R_2 = \text{C}_6\text{Cl}_2\text{F}_6\text{N}$, SO_2NH_2, Cl, SCH_3 [10–13]; and $R_1 = \text{CCl}_3$, $R_2 = \text{C}_2\text{Cl}_5$ [2]). The nitrogen atom of the imido ligand in the above complexes forms a triple bond with the central atom due to the p_π–d_π interaction of the lone electron pair of the nitrogen atom with a free *d* orbital of the metal atom. The value of the W–N(2)–C(8) angle (169.0°) in complex **I** indicates that the lone electron pair of the nitrogen atom is incompletely involved in the bond with the tungsten atom. Therefore, the W–N(2) bond should be more correctly treated as a virtually triple bond.

A comparison of the data obtained for the products of low-temperature [1] and high-temperature syntheses shows that the temperature conditions do not affect the composition and structure of the resultant compounds. However, the boiling of the reaction mixture makes it possible to decrease the reaction time substantially.

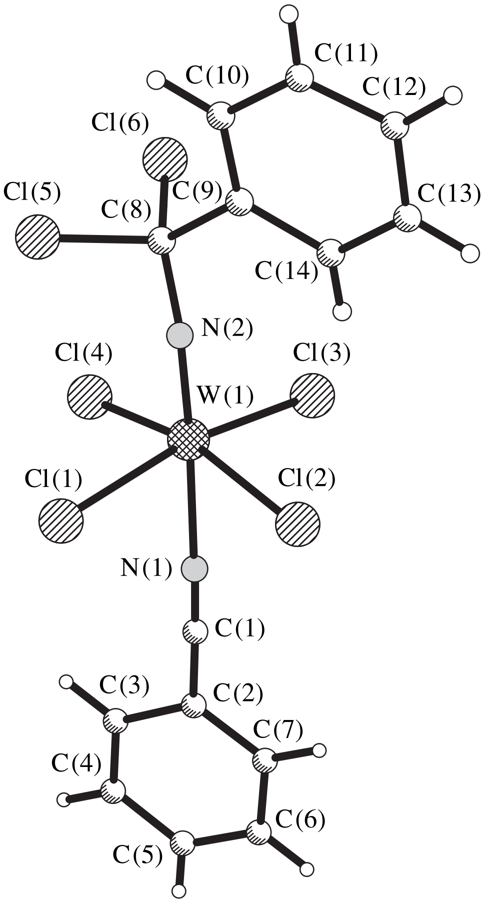

Molecular structure of complex **I**.

Judging from the elemental analysis data, treatment of complex **I** under vacuum results in the formation of a compound with nonstoichiometric composition. A decrease in the intensity of the $\nu(C\equiv N)$ band in comparison with the intensity of the $\nu(W\equiv N)$ band in the IR spectrum of complex **I** suggests that, in the course of treatment under vacuum, the coordinated nitrile groups are partially displaced from the coordination sphere with the formation of the $WCl_4(NCCl_2Ph)(NCPh)_{0.25}$ compound.

We have now investigated the reactivity of complex **I** with respect to organic isocyanates, isothiocyanates, and sulfur and carbon dioxides.

ACKNOWLEDGMENTS

We would like to thank the leader and staff of the Center of X-ray Powder Diffraction Analysis (Nesmeyanov Institute of Organoelement Compounds, Russian Academy of Sciences) for providing an opportunity to collect the X-ray experimental data on a SMART diffractometer (Russian Foundation for Basic Research, project no. 00-03-32807).

This work was supported by the Russian Foundation for Basic Research, project no. 00-15-97432.

REFERENCES

1. G. W. A. Fowles, D. A. Rice, and K. J. Shanton, J. Chem. Soc. Dalton Trans., 1212 (1977).
2. M. G. B. Drew, K. S. Moss, and N. Rolfe, Inorg. Nucl. Chem. Lett. **7** (12), 1219 (1971).
3. *SMART (Control) and SAINT (Integration) Software, Version 5.0* (Bruker AXS, Madison, WI, 1997).
4. G. M. Sheldrick, *SADABS: Program for Scaling and Correction of Area Detector Data* (Univ. of Göttingen, Germany, 1997).
5. G. M. Sheldrick, *SHELXS97: Program for the Solution of Crystal Structures* (Univ. of Göttingen, Germany, 1997).
6. G. M. Sheldrick, *SHELXL97: Program for the Refinement of Crystal Structures* (Univ. of Göttingen, Germany, 1997).
7. *RLATT and GEMENI (Twinning Solution Program Suite), Version 1.0* (Bruker AXS, Madison, WI, 1997).
8. N. A. Ovchinnikova, A. E. Sinyakov, A. M. Reznik, *et al.*, Koord. Khim. **28** (9), 716 (2002).
9. N. A. Ovchinnikova, A. E. Sinyakov, and V. S. Sergienko, J. Coord. Chem. (in press).
10. R. W. Roesky, H. Plenio, K. Keller, *et al.*, Chem. Ber. **119**, 3150 (1986).
11. M. Witt, H. W. Roesky, M. Noltemeyer, and G. M. Sheldrick, Z. Naturforsch. B **42**, 519 (1987).
12. A. Görge, K. Dehnicke, and D. Fenske, Z. Naturforsch. B **43**, 677 (1988).
13. A. Görge, U. Patt-Siebel, U. Müller, and K. Dehnicke, Z. Naturforsch. B **44**, 903 (1989).

Translated by O. Borovik-Romanova

Crystallography Reports, Vol. 49, No. 4, 2004, pp. 653–659. Translated from Kristallografiya, Vol. 49, No. 4, 2004, pp. 732–738.
Original Russian Text Copyright © 2004 by Smirnov, Natkaniec, Savenko, Kozlenko, Kichanov, Dlouha, Vratislav, Martinez-Sarrion, Mestres, Herraiz, Shuvalov.

LATTICE DYNAMICS AND PHASE TRANSITIONS

Neutron Studies of the Structure and Dynamics of $Rb_{1-x}(NH_4)_xI$ Mixed Crystals

L. S. Smirnov[1,2], I. Natkaniec[2,6], B. N. Savenko[2], D. P. Kozlenko[2], S. E. Kichanov[2], M. Dlouha[4], S. Vratislav[4], M. L. Martinez-Sarrion[5], L. Mestres[5], M. Herraiz[5], and L. A. Shuvalov[6]

[1]*Institute of Theoretical and Experimental Physics, Moscow, 117218 Russia*
e-mail: lsmirnov@nf.jinr.ru
[2]*Joint Institute for Nuclear Research, Dubna, Moscow oblast, 141980 Russia*
[3]*Niewodniczanski Institute of Nuclear Physics, Krakov, 31-342 Poland*
[4]*Faculty of Nuclear Science and Physical Engineering, Department of Solid State Engineering, Prague, Czech Republic*
[5]*Departament de Quimica Inorganica, Universitat de Barcelona, Barcelona, 08028 Spain*
[6]*Shubnikov Institute of Crystallography, Russian Academy of Sciences, Leninskiĭ pr. 59, Moscow, 119333 Russia*

Received June 3, 2003

Abstract—The structural and dynamical properties of the *x*–*T* phase diagram of the system of $Rb_{1-x}(NH_4)_xI$ mixed crystals is of great interest, because such solid solutions are almost free of internal stresses due to almost equal ionic radii of ammonium and rubidium. The *x*–*T* phase diagram of $Rb_{1-x}(NH_4)_xI$ is studied on samples with ammonium concentration ranging from 0.01 to 0.73 over the temperature range from 15 to 300 K by the methods of powder neutron diffraction and inelastic incoherent neutron scattering. The results obtained by powder neutron diffraction show that the α–β phase transition at low temperature is rather extended and occurs at the ammonium concentrations $x = 0.50$ and 0.66. The region of orientational state glass is determined by inelastic incoherent neutron scattering at the concentrations $x = 0.29$ and 0.40 at the temperature $T = 20$ K. *© 2004 MAIK “Nauka/Interperiodica”.*

INTRODUCTION

The study of the *x*–*T* phase diagram of $Rb_{1-x}(NH_4)_xI$ mixed crystals is very important for better understanding the possible influence of internal stresses. In the last decade, the *x*–*T* phase diagram of $K_{1-x}(NH_4)_xI$ mixed crystals was studied in detail and it was shown that the specific features of this system at low temperatures may be explained by the internal stresses caused by different ionic radii of potassium and ammonium [1–6]. This difference may be responsible for the formation of the ε phase with a new crystal structure on the *x*–*T* phase diagram of $K_{1-x}(NH_4)_xI$ mixed crystals.

Whereas KI undergoes no phase transitions prior to the attainment of low temperatures, NH_4I undergoes a number of following phase transitions with lowering of the temperature [7, 8]:

$$\begin{gathered}\alpha\text{-phase} \Leftrightarrow 255.4\text{ K} \Leftrightarrow \beta\text{-phase} \\ 231.4\text{ K} \Leftrightarrow \gamma\text{-phase}.\end{gathered} \tag{1}$$

The crystal structures of these phases were studied by both X-ray and neutron diffraction methods [9, 10]. The cubic α phase is described by the sp. gr. $Fm3m\text{-}O_h^5$, $Z = 4$; the ammonium ions in this phase are orientationally disordered. The cubic β phase is described by the sp. gr. $Pm3m\text{-}O_h^1$, $Z = 1$; in this phase, ammonium ions are also orientationally disordered. The tetragonal γ phase has a structure with ordered ammonium ions and is described by the sp. gr. $P4/nmm\text{-}D_{4h}^7$, $Z = 2$.

Depending on the ammonium concentration, the *x*–*T* phase diagram of $K_{1-x}(NH_4)_xI$ mixed crystals at low temperatures is represented by the following phases

$$\begin{gathered}\text{KI} \Leftrightarrow \alpha\text{-phase} \Leftrightarrow \text{phase OC} \Leftrightarrow \varepsilon\text{-phase} \\ \Leftrightarrow \beta\text{-phase} \Leftrightarrow \beta\text{-phase} \Leftrightarrow NH_4I.\end{gathered} \tag{2}$$

The *x*–*T* phase diagram of $K_{1-x}(NH_4)_xI$ mixed crystals at low temperatures also has the phase of orientational glass located between the α and ε phases. The crystal structure of the ε phase, determined by single crystal neutron diffraction at $T = 14$ K, is described by the sp. gr. $R3m$, $Z = 4$ [4].

The ionic radii of rubidium and ammonium are practically the same. RbI and KI crystals are isomorphous. Like KI, the RbI crystal does not undergo any phase transitions up to the attainment of low temperatures. RbI and NH_4I form solid solutions over the whole concentration range at room temperatures [11].

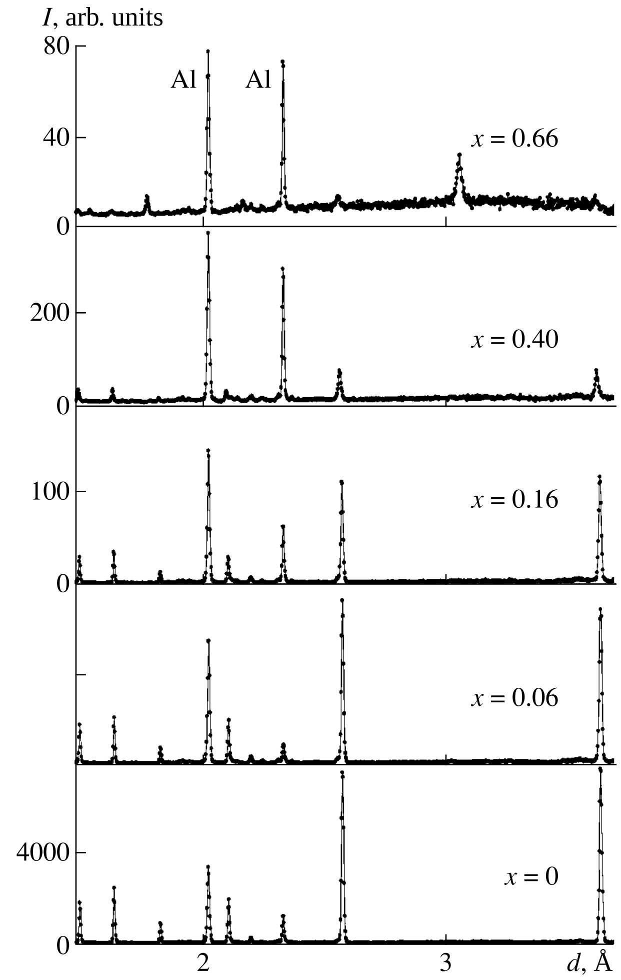

Fig. 1. Neutron powder diffraction spectra of $\mathrm{Rb}_{1-x}(\mathrm{NH}_4)_x\mathrm{I}$ crystals at various concentrations of ammonium ions obtained on a NERA-GH time-of-flight spectrometer at 20 K.

Below, we present the results of powder neutron diffraction and inelastic incoherent neutron scattering studies of the characteristics of the *x*–*T* phase diagram of $\mathrm{Rb}_{1-x}(\mathrm{NH}_4)_x\mathrm{I}$ mixed crystals. These studies were undertaken to reveal the ε phase and the shift of the phase boundaries in comparison with those on the *x*–*T* phase diagram of $\mathrm{K}_{1-x}(\mathrm{NH}_4)_x\mathrm{I}$ mixed crystals.

EXPERIMENTAL STUDIES AND RESULTS

The powder samples of $\mathrm{Rb}_{1-x}(\mathrm{NH}_4)_x\mathrm{I}$ mixed crystals with various ammonium concentrations were prepared by slow evaporation of aqueous solutions with the corresponding stoichiometric concentrations. The concentrations in the prepared powder samples were controlled by special chemical methods and X-ray phase analysis.

The crystal structure of $\mathrm{Rb}_{1-x}(\mathrm{NH}_4)_x\mathrm{I}$ mixed crystals and the dynamics of ammonium ions were studied by powder neutron diffraction (PND) and inelastic incoherent neutron scattering (IINS). This complex method allows one not only to study the properties of $\mathrm{Rb}_{1-x}(\mathrm{NH}_4)_x\mathrm{I}$ mixed crystals, but also the specific features of the *x*–*T* phase diagram, and establish general relations between the crystal structure, the lattice dynamics, and structural relaxation of individual lattice complexes. For $\mathrm{Rb}_{1-x}(\mathrm{NH}_4)_x\mathrm{I}$ mixed crystals, it is also possible to examine the influence of various types of disorder on the crystal structure and ammonium dynamics in different phases by the methods of inelastic incoherent neutron scattering.

Diffraction Studies

The crystal structure of $\mathrm{Rb}_{1-x}(\mathrm{NH}_4)_x\mathrm{I}$ mixed crystals was refined depending on ammonium-ion concentration and temperature using the data of spectrometric and diffractometric measurements (NERA-PR spectrometer and the DN-12 diffractometer (IBR-2, LNF, JINR, Dubna) by the time-of-flight method [12, 13] and also the data obtained on the diffractometer of a stationary reactor (CTU, Rzhezh, Czech Republic) by the conventional method [14]. The *x*–*T* phase diagram of the $\mathrm{Rb}_{1-x}(\mathrm{NH}_4)_x\mathrm{I}$ mixed crystals was studied on the samples with different ammonium concentrations, $x = 0.01$, 0.02, 0.06, 0.10, 0.16, 0.29, 0.40, 0.50, 0.66, and 0.77, in the temperature range from room temperature to 10 K.

The neutron diffraction experiments on a DN-12 diffractometer [13] with the scattering angle being $2\theta = 45°$ were performed on ~20-mm^3-large powder samples. The diffractometer resolution was $\Delta d/d = 0.022$ for $d = 2$ Å. To create low temperatures on samples, we used a special cryostat designed on the basis of a helium refrigerator with a closed helium cycle. The typical time of measuring a diffraction spectrum at each temperature point was 3 h.

The *x*–*T* phase diagram of the $\mathrm{Rb}_{1-x}(\mathrm{NH}_4)_x\mathrm{I}$ mixed crystals was studied along the concentration cut at a temperature ranging within 10–20 K for various diffraction spectra. The studies of the *x*–*T* phase diagram of $\mathrm{Rb}_{1-x}(\mathrm{NH}_4)_x\mathrm{I}$ mixed crystals by the powder neutron diffraction are illustrated by figures.

The results of the powder neutron diffraction study of the dependence on the ammonium concentration at 20 K made on an NERA-PR spectrometer are shown in Fig. 1. It is seen that the crystal structure of $\mathrm{Rb}_{1-x}(\mathrm{NH}_4)_x\mathrm{I}$ mixed crystals at $x = 0.0$, 0.06, 0.16, and 0.40 has a long-range order corresponding to the α phase. It should be noted that the α–β phase transition has no sharp boundary and is observed within the concentration range $\sim 0.50 < x < 0.66$ in which both these phases coexist (the PND spectrum obtained at $x = 0.50$ is not shown in Fig. 1). For the sample with $x = 0.66$, the NPD spectrum has a small contribution of the α phase.

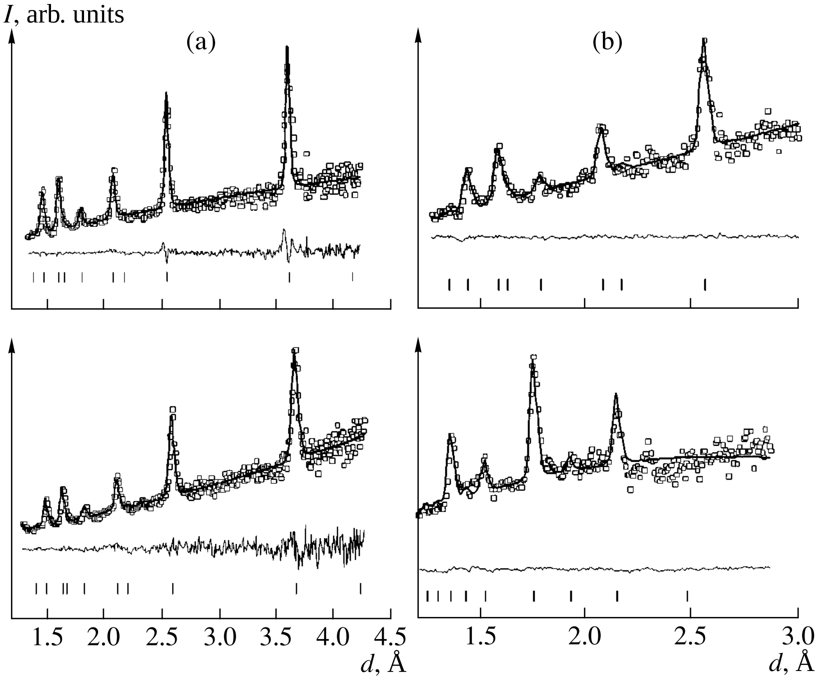

Fig. 2. (a) Portion of the diffraction spectrum of a $Rb_{0.71}(NH_4)_{0.29}I$ crystal at 283 K (sp. gr. *Fm*3*m*) and 15 K (sp. gr. *Fm*3*m*). (b) Portion of the diffraction spectrum of $Rb_{0.23}(NH_4)_{0.77}I$ crystals at 283 K (sp. gr. *Fm*3*m*) and 25 K (sp. gr. *Pm*3*m*).

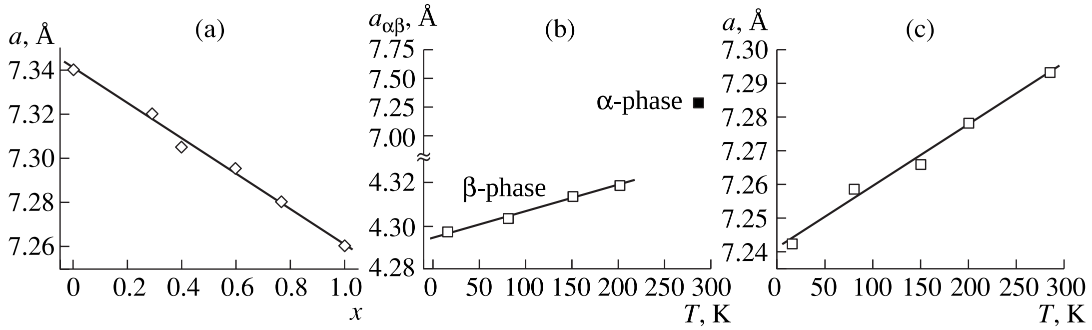

Fig. 3. Lattice parameter of the (a) cubic $Rb_{1-x}(NH_4)_xI$ unit cell as a function of the concentration of NH_4^+ ions at room temperature, (b) $Rb_{0.71}(NH_4)_{0.29}I$ crystals as a function of temperature, and (c) $Rb_{0.23}(NH_4)_{0.77}I$ crystals as a function of temperature. The linear interpolation was performed by the least squares method. The experimental errors do not exceed the symbol dimensions (b, c).

The samples of the $Rb_{1-x}(NH_4)_xI$ mixed crystals with the ammonium concentrations $x = 0.29$, 0.40, 0.66, and 0.77 were studied at room and low temperatures on a DN-12 diffractometer. The refinement of the NPD spectra was usually performed by the MRIA program [15]. The portions of the diffraction spectra of the samples with $x = 0.29$ and 0.77 and the results of their Rietveld full profile analysis are shown in Figs. 2a and 2b, which show the experimental points, the calculated profile, and the difference curve for various phases. The dependences of the lattice parameters on the temperature and concentration for various phases are shown in Figs. 3a–3c. The crystal structure of the $Rb_{1-x}(NH_4)_xI$ mixed crystals was studied on a CTU diffractometer at the ammonium concentrations $x = 0.01$, 0.02, 0.06, 0.10, 0.16, 0.40, and 0.66 in the temperature range from 10 to 300 K. The results of the structural studies of the samples with various ammonium concentrations at several temperatures are listed in the table.

Studies by Inelastic Incoherent Neutron Scattering

The IINS spectra from $Rb_{1-x}(NH_4)_xI$ mixed crystals were measured on a NERA-PR time-of-flight spectrometer of the inverted geometry (IBR-2 source, Dubna) [12]. An NERA-PR spectrometer allows one to measure the IINS spectra in the range of the transferred

Structural parameters of $Rb_{1-x}(NH_4)_xI$ mixed crystals depending on the ammonium concentration and temperature (K)

x	0.29	0.40	0.66	0.77
Temperature	280	280	280	280
Sp. gr.	*Fm*3*m*	*Fm*3*m*	*Fm*3*m*	*Fm*3*m*
Unit-cell parameter a, Å	7.3130(6)	7.2923(4)	7.2918(6)	7.2849(3)
$H1$–32(f)–(x)	0.5710(8)	0.5703(9)	0.5743(2)	0.5743(7)
$H2$–96(k)–(x, z)	0.5164(7)	0.5164(7)	0.5255(9)	0.5367(9)
	0.3672(3)	0.3651(6)	0.3421(3)	0.3549(6)
Temperature	200			200
Sp. gr.	*Fm*3*m*			*Pm*3*m*
Unit-cell parameter a, Å	7.3074(5)			4.3498(5)
$H1$–32(f)–(x)	0.5689(5)			0.3685(8)
$H2$–96(k)–(x, z)	0.5140(2)			
	0.3604(6)			
Temperature	150			150
Sp. gr.	*Fm*3*m*			*Pm*3*m*
Unit-cell parameter a, Å	7.2998(6)			4.3475(6)
$H1$–32(f)–(x)	0.5689(5)			0.3665(6)
$H2$–96(k)–(x, z)	0.5140(2)			
	0.3504(9)			
Temperature	15			15
Sp. gr.	*Fm*3*m*			*Pm*3*m*
Unit-cell parameter a, Å	7.2967(6)			4.3343(7)
H–8(g)–(x)				0.3635(8)
$H1$–32(f)–(x)	0.5627(8)			
$H2$–96(k)–(x, z)	0.5140(2)			
	0.3604(9)			

energies up to 150 meV using crystals–analyzers from pyrolytic graphite with a resolution of 0.6 meV at the elastic-scattering wavelength $\lambda_0 = 4.15$ Å.

Ammonium dynamics in $Rb_{1-x}(NH_4)_xI$ mixed crystals was studied along the concentration section of the x–T phase diagram at the temperature $T = 20$ K in the samples with $x = 0.01$, 0.02, 0.06, 0.10, 0.16, 0.29, 0.40, 0.50, and 0.66. The IINS spectra obtained for samples with different ammonium concentrations are shown in Figs. 4a and 4b. The spectra in Fig. 4a show a pronounced contribution of quasi-elastic incoherent neutron scattering (QENS) on wings of the profile of the elastic-scattering line from crystals–analyzers. The IINS contribution increases with an increase in ammonium concentration up to $x = 0.06$, 0.10, and 0.16. Then, beginning with the ammonium concentration in the samples from $x = 0.29$ to 0.40, the QENS contribution decreases, whereas the contribution from the low-energy modes becomes more pronounced. This may be explained as follows. The $Rb_{1-x}(NH_4)_xI$ mixed crystals with the ammonium concentration $x = 0.06$, 0.10, 0.16 lie inside the dynamically orientationally disordered α phase, and the QENS contribution corresponds to neutron scattering caused by reorientation of ammonium ions. An increase in the ammonium concentration is accompanied by changes of the height of the potential barriers of reorientation because of stronger ammonium–ammonium interactions. This leads to changes in the short-range order between ammonium ions, which start playing the key role in the formation of orientational state glass. Thus, on the x–T phase diagram, the $Rb_{1-x}(NH_4)_xI$ mixed crystals with the ammonium concentrations $x = 0.29$ and 0.40 are located in the region of orientational state glass.

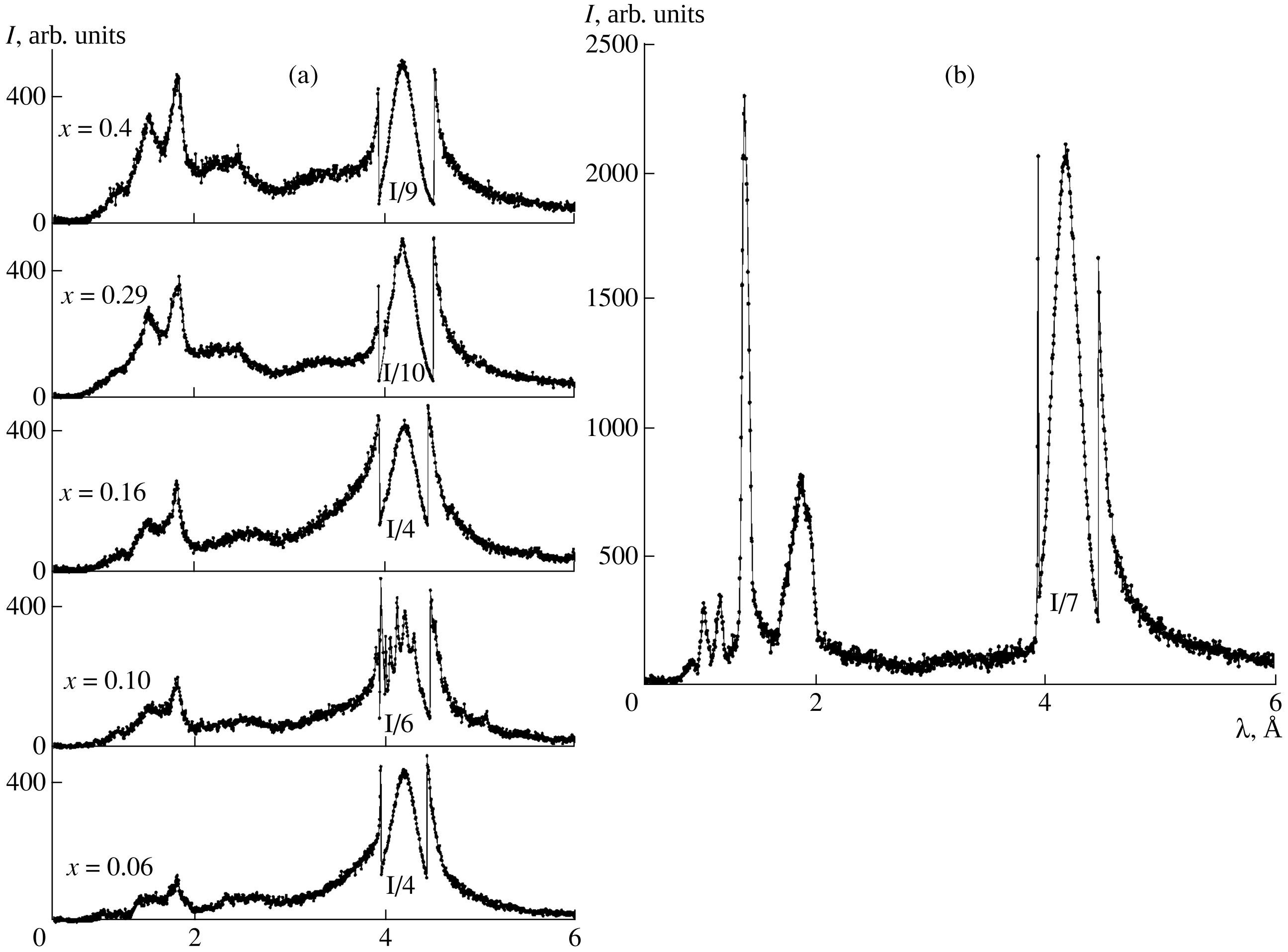

Fig. 4. Portions of the inelastic incoherent neutron scattering (IINS) spectra of (a) $Rb_{1-x}(NH_4)_xI$ and (b) $Rb_{0.34}(NH_4)_{0.66}I$ crystals at $T = 20$ K.

The diffraction study showed that the long-range order in this concentration range corresponded to the cubic crystal structure described by the sp. gr. *Fm*3*m*. Although the ammonium ions in the crystal structure of the β phase are orientationally ordered, there is no QENS contribution from the sample with such a structure. This indicates the low frequency of reorientation in the β phase at low temperatures, which cannot be observed on an NERA-PR spectrometer because of its resolution.

Generalized Density of Phonon States

Usually, the measured QENS spectra can be converted into the generalized density of phonon states $G(E)$ in the single-phonon incoherent approximation with the aid of a special program [16]. The $G(E)$ spectra of the $Rb_{1-x}(NH_4)_xI$ mixed crystals at 20 K at the ammonium concentrations $x = 0.0$, 0.06, 0.16, 0.40, and 0.66 are shown in Fig. 5.

The comparison of the $G(E)$ spectra shows the appearance of additional modes in the $Rb_{1-x}(NH_4)_xI$ mixed crystals with energies higher than the energy of the optical mode in RbI. In mixed crystals, these modes are called local and are related to the ammonium dynamics. The mode with the energy ~20 meV is the local translation mode ν_5, whereas the mode with the energy ~30 meV is the local libration mode ν_6 of ammonium ions. The $G(E)$ spectra from the samples with the ammonium concentrations $x = 0.06$, 0.16, and 0.40 have modes with energies ~2.5 and 10 meV not observed in RbI, but appearing in the continuous phonon spectrum of $Rb_{1-x}(NH_4)_xI$ mixed crystals. They are called the resonance modes and are denoted by E_r^1 and E_r^2, respectively. The resonance and local modes are observed in the mixed crystals at low temperatures (Fig. 6) inside the concentration ranges on the *x*–*T* phase diagram that correspond to the dynamically disordered α phase and the phase of orientational glass (or the phase of static disorder). The resonance modes are not observed at 20 K in the $G(E)$ spectrum of $Rb_{1-x}(NH_4)_xI$ mixed crys-

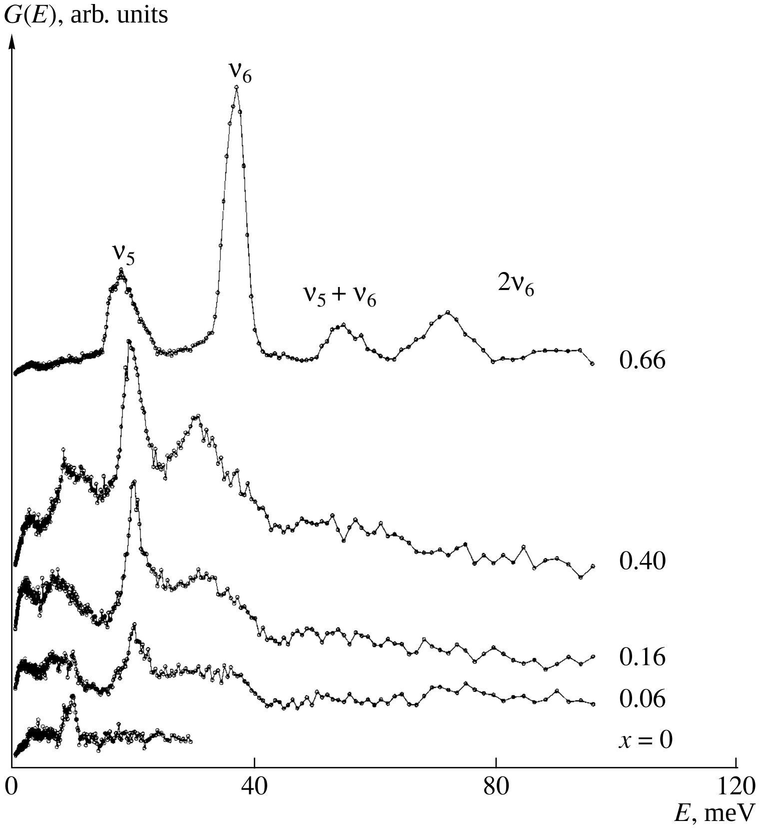

Fig. 5. Generalized phonon density of states $G(E)$ in $Rb_{1-x}(NH_4)_xI$ crystals at 20 K.

tals with the concentration $x = 0.66$ corresponding to the β phase. It should be noted that the $Rb_{1-x}(NH_4)_xI$ mixed crystals in the β phase at 20 K have the combination mode $\nu_5 + \nu_6$ and the second harmonic of the libration mode $2\nu_6$ not observed in the α phase.

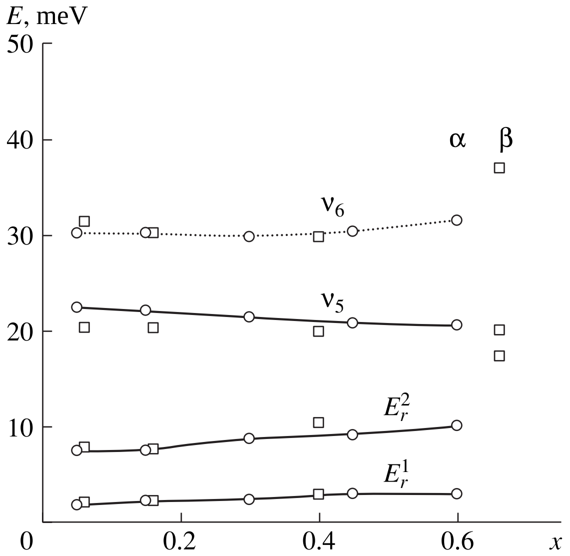

Fig. 6. Comparison of the energies of the observed modes in $K_{1-x}(NH_4)_xI$ (circles) and $Rb_{1-x}(NH_4)_xI$ (squares) mixed crystals at 10 and 20 K, respectively.

CONCLUSIONS

Thus, the combined method of neutron scattering including powder neutron diffraction and incoherent inelastic scattering yields great possibilities for detailed studies. The neutron studies performed allowed us to determine the concentration ranges of the existence of orientational state glass, which cannot be made by the method of powder neutron diffraction. The results obtained lead to certain conclusions on the properties of the x–T phase diagram of $Rb_{1-x}(NH_4)_xI$ mixed crystals, namely:

—$Rb_{1-x}(NH_4)_xI$ mixed crystals are in the α phase over the whole concentration range $0.0 < x < 1.0$ at room temperature;

—the long-range order in the structure of the α-phase is preserved in the concentration range of ammonium up to $x = 0.29$ at temperatures from room temperature to 20 K;

—$Rb_{1-x}(NH_4)_xI$ с x mixed crystals with $x = 0.77$ are characterized by the long-range order of the β phase at low temperature, which is transformed into the α phase in the temperature range 200–280 K;

—the α–β phase transition has no sharp boundaries, and the sequence of the transitions has the form

$$\begin{aligned} &\alpha\text{-phase } (0.01 \le x \le 0.16) \\ &\Leftrightarrow \text{phase OC } (0.29 \le x \le 0.40) \Leftrightarrow \alpha\text{-phase} \\ &+ \beta\text{-phase } (0.50 \le x \le 0.66) \Leftrightarrow \beta\text{-phase } (x = 0.77); \end{aligned} \quad (3)$$

—in $Rb_{1-x}(NH_4)_xI$ mixed crystals, there is no concentration range where there exists the crystal structure of the ε phase established earlier in $K_{1-x}(NH_4)_xI$ mixed crystals.

The x–T phase diagram of $Rb_{1-x}(NH_4)_xI$ mixed crystals is not considered in this article over the whole concentration range of ammonium ions, because study of the concentration ranges of the β and γ phases is under way. The problem of the existence of the ε phase of $Rb_{1-x}(NH_4)_xI$ mixed crystals on the x–T phase diagram is not solved completely. This phase was determined on the x–T phase diagram of $K_{1-x}(NH_4)_xI$ mixed crystals by the method of single-crystal neutron diffraction. The absence of the ε phase in $Rb_{1-x}(NH_4)_xI$ mixed crystals may be explained by the absence of internal stresses typical of $K_{1-x}(NH_4)_xI$ crystals.

It should be emphasized that the energy of the libration mode of ammonium ions in the ε phase should be close to the energy of the libration mode of ammonium in the α phase, but should be different from this energy in the β and γ phases. Different energies of ammonium libration modes are explained, first of all, by different numbers of iodine atoms in the nearest environment of ammonium ions. An ammonium ion interacts with only six iodine atoms both in the α and ε phases, whereas, in the β and γ phases, it interacts with eight iodine atoms. However, it is expedient to continue the search for the ε phase in the system of $Rb_{1-x}(NH_4)_xI$ mixed crystals by the method of neutron diffraction from single crystals.

ACKNOWLEDGMENTS

This study was supported by CICYT MAT 95-0218, the Russian Foundation for Basic Research (project nos. 02-02-17330 and 00-02-17199), the Ministry of Industry, Science and Technology of the Russian Federation (project nos. 40.012.1.1. 1148, and NSh-1514.2003.2).

REFERENCES

1. I. Fehst, R. Böhmer, W. Ott, *et al.*, Phys. Rev. Lett. **64**, 3139 (1990).
2. J. F. Berret, C. Bostoen, and B. Hennion, Phys. Rev. B **46**, 13747 (1992).
3. M. Winterlich, R. Böhmer, and A. Loidl, Phys. Rev. Lett. **75**, 1783 (1995).
4. M. Paasch, G. J. McIntyre, M. Reehuis, *et al.*, Z. Phys. B **99**, 339 (1996).
5. M. Ohl, M. Reehuis, and A. Krimmel, *BENSC Experimental Reports* (1998), p. 150.
6. F. Guthoff, M. Ohl, M. Reehuis, and A. Loidl, Physica B (Amsterdam) **266**, 310 (1999).
7. H. C. Perry and R. P. Lowndes, J. Chem. Phys. **51**, 3648 (1969).
8. N. G. Parsonage and L. A. K. Stavely, *Disorder in Crystals* (Clarendon Press, Oxford, 1978; Mir, Moscow, 1982), pp. 311–388.
9. H. A. Levy and S. W. Peterson, J. Am. Chem. Soc. **75**, 1536 (1953).
10. R. S. Seymour and A. W. Pryor, Acta Crystallogr., Sect. B: Struct. Crystallogr. Cryst. Chem. **26**, 1487 (1970).
11. R. J. Havighurst, E. Mack, Jr., and F. C. Blake, J. Am. Chem. Soc. **47**, 29 (1925).
12. I. Natkaniec, S. I. Bragin, J. Brankowski, and J. Mayer, in *Proceedings of ICANS-XII* (Abingdon, 1993), RAL Report 94-025, Vol. 1, p. 89.
13. V. L. Aksenov, A. M. Balagurov, V. P. Glazkov, *et al.*, Physica B (Amsterdam) **265**, 258 (1999).
14. M. Dlouha, S. Vratislav, D. Janeba, and V. Bosacek, in *Proceedings of the Workshop 95, CTU, Prague* (1995), p. 435.
15. V. B. Zlokazov and V. V. Chernyshev, J. Appl. Crystallogr. **25**, 447 (1992).
16. E. F. Sheka, I. V. Markichev, I. Natkanets, and V. D. Khavryuchenko, Fiz. Élem. Chastits At. Yadra **27**, 493 (1996) [Phys. Part. Nucl. **27**, 204 (1996)].

Translated by L. Man

Crystallography Reports, Vol. 49, No. 4, 2004, pp. 660–663. Translated from Kristallografiya, Vol. 49, No. 4, 2004, pp. 739–742.
Original Russian Text Copyright © 2004 by Sidorov, Palatnikov, Golubyatnik.

Raman Spectroscopy of the Ferroelectric–Antiferroelectric Phase Transition in $Li_{0.12}Na_{0.88}Ta_{0.2}Nb_{0.8}O_3$ Ceramic Solid Solution

N. V. Sidorov, M. N. Palatnikov, and N. A. Golubyatnik

Institute of Rare Element and Mineral Chemistry and Technology, Kola Research Center, Russian Academy of Sciences,
ul. Fersmana 14, Apatity, Murmansk oblast, 184200 Russia
e-mail: info@chemy.kolasc.net.ru

Received May 23, 2002

Abstract—The phase transition in the $Li_{0.12}Na_{0.88}Ta_{0.2}Nb_{0.8}O_3$ ceramic solid solution has been studied by Raman scattering spectroscopy at 350°C. A considerable broadening of the lines due to translational vibrations of cations in octahedral and cuboctahedral voids and to vibrations of the oxygen framework, as well as the decrease to zero of the intensity of the line due to bridge stretching vibrations of oxygen atoms of BO_6 octahedral anions, was revealed as the temperature of the solution approached the transition point from below. It was found that the solution loses its ferroelectric properties due to the preferential increase in the anharmonicity of vibrations of cations in octahedral voids. © *2004 MAIK “Nauka/Interperiodica”.*

INTRODUCTION

As was found in [1–6], the concentration structural phase transitions of a ferroelectric into the centrosymmetric antiferroelectric state (ferroelectric–antiferroelectric transitions) that occur at constant temperature with a change in concentrations x and y in systems of perovskite ceramic solid solutions described by the general formula $Li_xNa_{1-x}Ta_yNb_{1-y}O_3$ (LNTN) are accompanied by (1) the broadening of the line in the Raman scattering spectrum due to bridge stretching vibrations of oxygen atoms (B–O–B) in octahedral BO_6 anions (B = Nb, Ta) and (2) the vanishing of this line in the vicinity of the transition point. It is of interest to elucidate to what extent the intensity of this line (which is sensitive to violations of the central symmetry of the crystal structure) can be a measure of the order parameter in the system of LNTN solid solutions at thermal structural phase transitions to the centrosymmetric state. In this paper, we report the results of a study of temperature variations in the Raman spectra at the ferroelectric–antiferroelectric transitions in $Li_{0.12}Na_{0.88}Ta_{0.2}Nb_{0.8}O_3$ solid solutions.

EXPERIMENTAL

The samples of solid solutions were prepared by the conventional ceramic technique [1] in the form of pellets from high-purity-grade reagents by double firing (with intermediate grinding and stirring of the cakes) and sintering the ceramics at 1200–1280°C. The phase and chemical composition of the solid solution was determined from the ratio of the starting components and controlled by X-ray phase analysis and atomic absorption analysis. No impurity phases of other compounds were found. In the Raman spectra of the samples under study, as well, no additional lines corresponding to impurity phases were observed over the entire temperature range (below and above the transition point).

Raman spectra were recorded on a modified DFS-24 spectrometer using excitation by the 488.0-nm line (with power 0.05 W) of an ILA-120 argon laser. The frequency, width, and intensity of the line were measured accurate to ±1, ± 3 cm^{-1}, and 5%, respectively. Temperature was maintained constant accurate to ±0.5 K and controlled by a Pt–Pt,Rh thermocouple.

RESULTS AND DISCUSSION

The disordering of the structure of LNTN antiferroelectrics consists in the antiparallel orientation of the dipole moments of individual noncentrosymmetric octahedral BO_6 anions. The total dipole moment of such a crystal is zero. Thus, the structure of the antiferroelectric (consisting of noncentrosymmetric BO_6 anions) can be characterized by an “effective” centrosymmetric octahedral BO_6 anion. In the spectrum of this anion, transitions related to bridge stretching vibrations of the B–O–B bonds are forbidden [1]. The antiferroelectric character of dipole ordering in the high-temperature phase is confirmed by the temperature dependences of the second-harmonic intensity $I_{2\omega}(T)$ and the activation energy of polar clusters in the medium being centrosymmetric as a whole [1]. In antiferroelectric phases, $E_d \sim 0.05–0.2$ eV; in paraelectric “crumpling” phases, $E_d \sim 1$ eV [7].

The basic properties of solid solutions and ferroelectric–antiferroelectric phase transitions in LNTN systems have been studied previously by different methods [1–6, 8–10]. However, the mechanism of transformation in $Li_{0.12}Na_{0.88}Ta_{0.2}Nb_{0.8}O_3$ needs clarification. Interest in this compound is aroused not only by

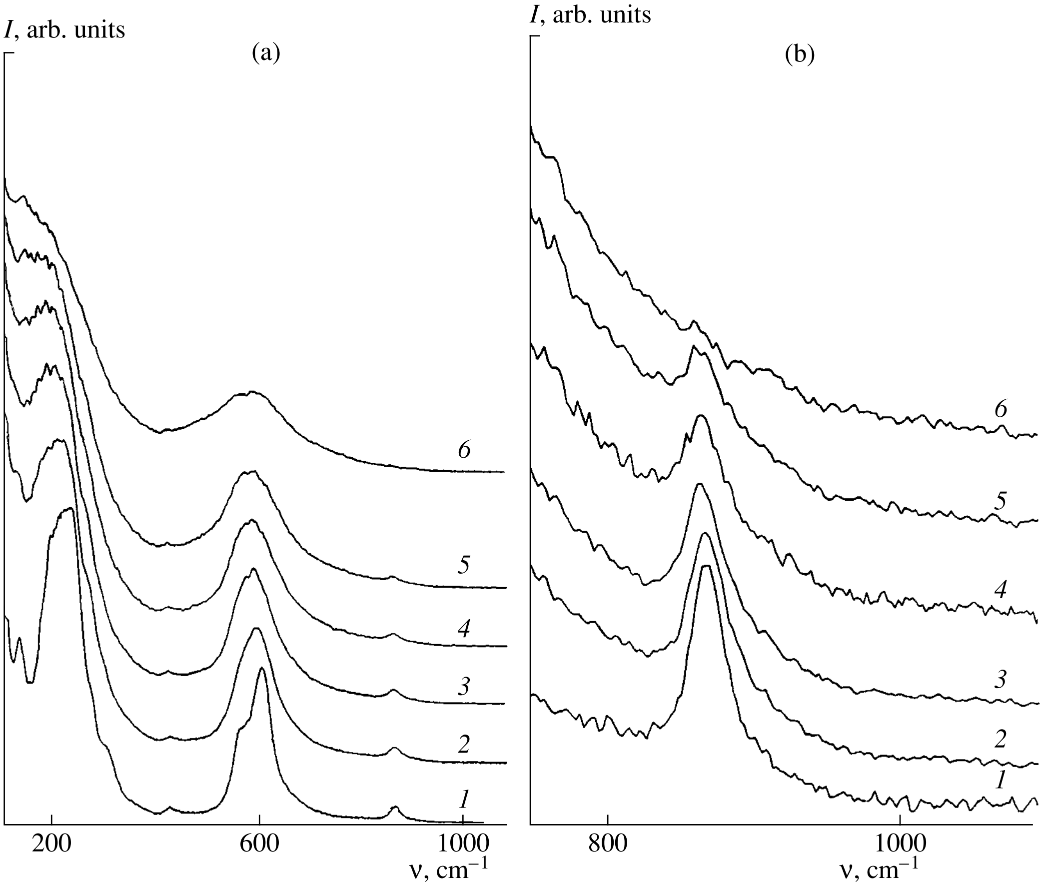

Fig. 1. (a) Temperature changes in the Raman spectrum of the $Li_{0.12}Na_{0.88}Ta_{0.2}Nb_{0.8}O_3$ ceramic solid solution and (b) the region of bridge stretching vibrations of oxygen atoms (B–O–B) in octahedral BO_6 anions. The temperature is (*1*) 20, (*2*) 185, (*3*) 250, (*4*) 320, (*5*) 325, and (*6*) 530°C.

the presence of the ferroelectric–antiferroelectric phase transition—it seems likely that cations in $Li_{0.12}Na_{0.88}Ta_{0.2}Nb_{0.8}O_3$ crystals are ordered so that the positions in the alkali metal sublattice that are unoccupied by Na^+ ions form peculiar conductivity channels, which, in turn, offers the prospect of phase transition into the superionic state at temperatures above the ferroelectric–antiferroelectric transition [1, 9, 10]. It is also worth noting that, at room temperature, the ferroelectric solid solution $Li_{0.12}Na_{0.88}Ta_{0.2}Nb_{0.8}O_3$ is in the region of the morphotropic phase transition, where phases with monoclinic and rhombohedral distortions of the perovskite subcell coexist (sp. grs. *Pbcm* and *R*3*c*). At a temperature of ~110°C, the phase transition $R3c \longrightarrow Pbcm$ is observed; at a temperature of ~350°C, the transition from the structure with orthorhombic symmetry *Pbcm* to the centrosymmetric antiferroelectric phase occurs [1]. The structure of the high-symmetry phase is not known with certainty. By analogy with the $NaTa_yNb_{1-y}O_3$ solid solution, one can suggest that the structure of the antiferroelectric phase is described by the sp. gr. *Pmnm* [11].

Figure 1 shows the temperature changes in the Raman spectra of the ceramic solid solution $Li_{0.12}Na_{0.88}Ta_{0.2}Nb_{0.8}O_3$ at the ferroelectric–antiferroelectric phase transition at ~350°C. This transition shows up in the spectrum, first of all, in the disappearance of the line at 875 cm^{-1}, which is due to bridge stretching vibrations of oxygen atoms in BO_6 (B = Nb,Ta) octahedral anions. Simultaneously, the entire Raman spectrum is broadened considerably (both the lines due to cation vibrations in octahedral and cuboctahedral voids (0–400 cm^{-1}) and the lines due to vibrations of BO_6 oxygen octahedra (550–900 cm^{-1}). This broadening indicates substantial thermal disordering of the structure in the centrosymmetric phase. It can be inferred that the disordering of the structure caused by heating and the phase transition to the centrosymmetric antiferroelectric state in $Li_{0.12}Na_{0.88}Ta_{0.2}Nb_{0.8}O_3$ are, in this case, due to the increase in the anharmonicity of several types of lattice vibrations (first and foremost, of the vibrations of ions in octahedral and cuboctahedral voids). Since the line due to bridge stretching vibrations of oxygen atoms in octahedral BO_6 anions is the only one that disappears above the ferroelectric–antiferroelectric transition point with the other lines retained

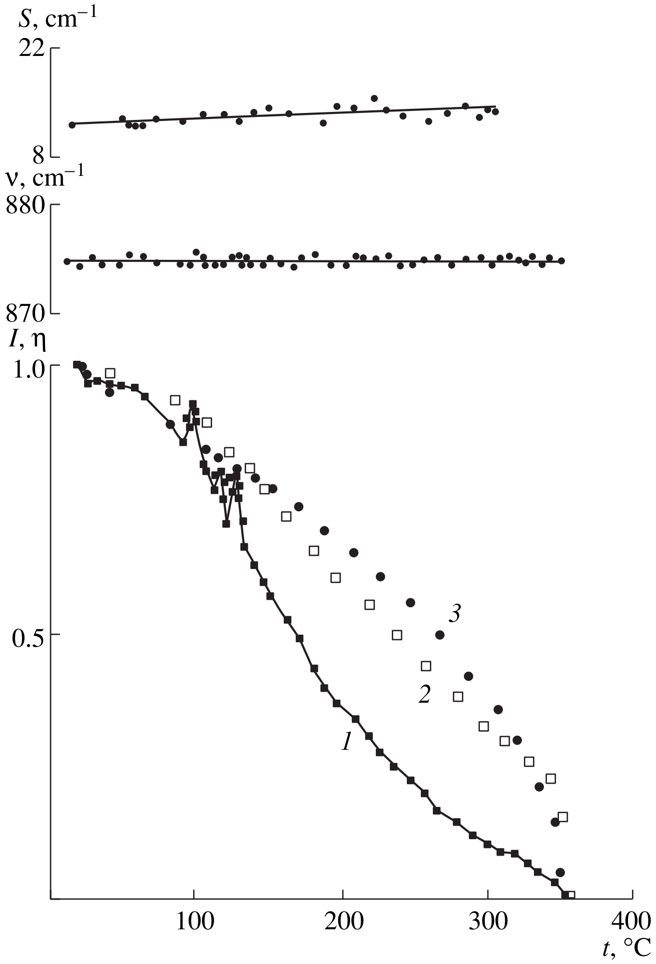

Fig. 2. Temperature dependences in the vicinity of the ferroelectric–antiferroelectric phase transition in the $Li_{0.12}Na_{0.88}Ta_{0.2}Nb_{0.8}O_3$ ceramic solid solution of the intensity I (*1*), width S, and frequency ν of the 875-cm^{-1} Raman line due to bridge stretching vibrations of oxygen atoms (B–O–B) in octahedral BO_6 anions; (*2*) the order parameter η calculated from experiment; and (*3*) the order parameter η calculated for the second-order phase transition within the Landau theory.

(see Fig. 1), the anharmonicity of vibrations of cations in octahedral voids is increased preferentially. However, the initial peculiarities of the structural disordering in $Li_{0.12}Na_{0.88}Ta_{0.2}Nb_{0.8}O_3$ should also be taken into account.

In the case under consideration, we are dealing with a certain level of the compositional disorder in cation sublattices of ferroelectric crystals of complex perovskites at isovalent substitution (Na^+ to Li^+ and Nb^{5+} to Ta^{5+}) (when compounds or solid solutions with a moderate degree of compositional long-range order are formed [12]) rather than with the dipole (electric) ordering. In such systems, which are characterized by a high disorder in cation arrangement and by anharmonicity, the structural units of a crystal have several, rather than one, equilibrium positions in the lattice sites [13–18]. The potential energy of such a crystal exhibits several minima for a structural unit; the motion of these units in the lattice is substantially complicated due to anharmonic jumps between the minima.

In the ceramic solid solution $Li_xNa_{1-x}Ta_yNb_{1-y}O_3$, according to the vibrational-spectroscopy data, a static (hard) disordering of cation sublattices and, possibly, clusterization of cations are initially observed [1–6, 8]. With this disorder, the structural units of the crystal may have several positions (or orientations) in the lattice. These positions are separated by energy barriers that are so high that transitions of a structural unit from one position (orientation) to another are practically ruled out [15, 16]. In this case, the broadening of the lines in the spectrum of a statically disordered crystal may result from both the scattering of phonons by static defects and the phonon–phonon interaction due to the increase in the anharmonicity of some types of vibrations [15, 16].

A slight and linear increase in the width of the 875-cm^{-1} line with increasing temperature (Fig. 2) confirms the presence of static (hard) disordering of niobium and tantalum ions in the antiferroelectric phase. In addition, orientational static disordering (hard disordering) of the oxygen octahedra as a whole is also possible in the crystal lattice. This disordering manifests itself in significant broadening and merging (into a wide band) of the lines due to vibrations of the oxygen framework of the solid solution in the range 550–700 cm^{-1} (Fig. 1).

In terms of the Landau theory of phase transitions, the properties of a crystal system undergoing a structural phase transition can be described phenomenologically with the aid of the order parameter. The latter is zero above the transition point (in the symmetric phase) and differs from zero below the point (in the nonsymmetric phase) [19]. Within the Landau theory, the nature of the order parameter is not specified; in different systems, the order parameter can be associated with different physical quantities.

Experimental studies of phase transitions in crystal systems of various natures with the aid of vibrational spectra (see review in [15]) have shown that not only the frequency (soft mode), but also the intensity of some "hard" lines in the spectrum, can serve as a function of the order parameter of the phase transition. In [20], the relationship between the line intensity and the order parameter η was justified theoretically. From the analysis of the change in the symmetry of normal coordinates, which determines variations in vibrational spectra, it was found in [20] that, in the close vicinity of the transition, the intensity of some "hard" vibrational modes is proportional to the square of the order parameter. Being practically constant in the immediate vicinity of the phase transition, the frequency of the 875-cm^{-1} line (Fig. 2) cannot be considered as a soft mode. In this case, however, the temperature dependence of the intensity of this line can be used as a function of the order parameter of the phase transition.

As can be seen from Fig. 2, the order parameter η determined from the temperature dependence of the intensity of the line at 875 cm^{-1} in the immediate vicinity of the transition is closely approximated by the formula $\eta = \sqrt{I} = (T_C - T)^{\beta/2}$, ($\beta = 1.0 \pm 0.2$). For a second-order phase transition, $\beta = 1$ [15, 19]. Near the phase transition ($t \sim 350°\text{C}$), there is a rather abrupt decrease in the dependence $\sqrt{I}(T)$. These facts, as well as a significant temperature hysteresis and heat release at the phase transition [1], suggest that the ferroelectric phase transition in $Li_{0.12}Na_{0.88}Ta_{0.2}Nb_{0.8}O_3$ is the first-order phase transition, which is similar to second-order phase transitions. This transition is due to the preferential increase in the anharmonicity of the vibrations of intraoctahedral cations in a statically disordered system.

ACKNOWLEDGMENTS

This work was supported in part by the Russian Foundation for Basic Research (RFBR) and the Belarussian Republican Foundation for Basic Research (BRFBR) (project RFBR-BRFBR nos. 02-03-81001 and 00-03-32652).

REFERENCES

1. M. N. Palatnikov, N. V. Sidorov, and V. T. Kalinnikov, *Ferroelectric Solid Solutions Based on Niobium and Tantalum Oxide Compounds: Synthesis, Study of Structural Ordering and Physical Characteristics* (Nauka, St. Petersburg, 2001).
2. N. V. Sidorov, M. N. Palatnikov, and V. T. Kalinnikov, Neorg. Mater. **35**, 213 (1999).
3. N. V. Sidorov, M. N. Palatnikov, N. N. Mel’nik, and V. T. Kalinnikov, in *Proceedings of IV International Conference on Crystals: Growth, Properties, Real Structure, and Application* (VNIISIMS, Aleksandrov, 1999), Vol. 2, p. 654.
4. N. V. Sidorov, M. N. Palatnikov, N. N. Mel’nik, and V. T. Kalinnikov, Zh. Prikl. Spektrosk. **67**, 192 (2000).
5. M. N. Palatnikov, N. V. Sidorov, N. N. Mel’nik, *et al.*, in *Proceedings of V International Conference on Crystals: Growth, Properties, Real Structure, and Application* (Aleksandrov, 2001), p. 324.
6. M. N. Palatnikov, N. V. Sidorov, N. N. Mel’nik, and V. T. Kalinnikov, Zh. Prikl. Spektrosk. **68**, 491 (2001).
7. S. Yu. Stefanovich, in *Proceedings of II International Conference on Real Structure and Properties of Acentred Crystals* (VNIISIMS, Aleksandrov, 1995), p. 48.
8. N. V. Sidorov, M. N. Palatnikov, and V. T. Kalinnikov, in *Proceedings of II International Conference on Crystals: Growth, Properties, Real Structure, and Application* (Aleksandrov, 1997), Vol. 1, p. 375.
9. M. N. Palatnikov, V. A. Sandler, Yu. A. Serebryakov, *et al.*, Neorg. Mater. **28**, 1995 (1992).
10. M. Palatnikov, V. A. Sandler, Yu. A. Serebryakov, *et al.*, Ferroelectrics **131**, 293 (1992).
11. A. V. Ulenzheev, V. G. Smotrakov, and O. E. Fesenko, in *Abstracts of 12th All-Union Conference of Physics of Ferroelectrics* (Rostov-on-Don, 1989), Vol. 1, p. 90.
12. V. A. Isupov, Izv. Akad. Nauk SSSR, Ser. Fiz. **47** (3), 559 (1983).
13. A. D. Bruce and R. A. Cowley, *Structural Phase Transitions* (Taylor and Francis, London, 1981; Mir, Moscow, 1984).
14. A. I. Levanyuk and D. G. Sannikov, Usp. Fiz. Nauk **132**, 693 (1980) [Sov. Phys. Usp. **23**, 868 (1980)].
15. G. N. Zhizhin and E. I. Mukhtarov, in *Vibrational Spectra and Structure*, Ed. by J. R. Durig (Elsevier, Amsterdam, 1995), A Series of Advances, Vol. 21.
16. N. G. Parsonage and L. A. Stavely, *Disorder in Crystals* (Oxford Univ. Press, Oxford, 1979; Mir, Moscow, 1982), Vols. 1 and 2.
17. Yu. S. Kuz’minov, *Electrooptical and Nonlinear Optical Lithium Niobate Crystal* (Nauka, Moscow, 1987).
18. R. Blinc and B. Zeks, *Soft Modes in Ferroelectrics and Antiferroelectrics* (North-Holland, Amsterdam, 1974; Mir, Moscow, 1975).
19. L. D. Landau and E. M. Lifshitz, *Course of Theoretical Physics*, Vol. 5: *Statistical Physics*, 2nd ed. (Nauka, Moscow, 1964; Pergamon Press, Oxford, 1980).
20. J. Petzelt and V. Dvorak, J. Phys. Chem. **9**, 1571 (1976).

Translated by A. Zolot’ko

Crystallography Reports, Vol. 49, No. 4, 2004, pp. 664–667. Translated from Kristallografiya, Vol. 49, No. 4, 2004, pp. 743–746.
Original Russian Text Copyright © 2004 by Mamaluĭ, Siryuk, Bezus.

LATTICE DYNAMICS AND PHASE TRANSITIONS

Phase Transitions in Bubble Domain Structures upon Spin Reorientation near the Compensation Point in Ferrite-Garnet Films

Yu. A. Mamaluĭ, Yu. A. Siryuk, and A. V. Bezus

Donetsk National University, ul. Universitetskaya 24, Donetsk, 83055 Ukraine

e-mail: uam@mail.donbass.com

Received January 31, 2003

Abstract—The behavior of a hexagonal lattice of bubble domains in a uniaxial thin film of $(BiTm)_3(FeGa)_5O_{12}$ ferrite garnet with a compensation temperature of 120 K was studied experimentally in a range of change in anisotropy from the easy magnetization axis to the easy magnetization plane. It is shown that the spin reorientation occurs in the temperature range 185–160 K, in which the angular phase (either $\Phi_{\langle 1\bar{1}\bar{1}\rangle}$ or $\Phi_{\langle \bar{1}11\rangle}$) and the axial phase $\Phi_{\langle 111\rangle}$ coexist. At 172 K, when the percentages of the angular and axial phases are equal, the lattice parameters of the bubble domains and the domain-wall width change stepwise. At $T < 160$ K, only a plane magnetic phase exists. *© 2004 MAIK “Nauka/Interperiodica”.*

When changing temperature, uniaxial thin films of ferrite garnets undergo spin-reorientation phase transitions (SRPTs) accompanied by a change in the magnetization orientation with respect to the $\langle 111\rangle$ axis. Upon an SRPT, rearrangement of the film domain structure occurs. The domain structure near an SRPT was studied visually in a thin ferrite-garnet film using the magneto-optical Faraday effect. The parameters of the serpentine-like domain structure were determined by magneto-optical diffraction [1, 2]. It was found that the magnetization reorientation leads to a stepwise increase in the period of the domain structure. An SRPT from the easy-axis to easy-plane anisotropy occurs without hysteresis but is accompanied by a coexistence of two phases at temperatures near 3 K.

Except for the SRPT region, significant changes of the domain structure of ferrite garnets are observed in the vicinity of the magnetic compensation temperature (T_C). The most interesting situation is observed when the temperature of the SRPT is close to or coincides with T_C. In [3, 4], the domain structure in the temperature range including T_C and the SRPT temperature was studied both in the absence of an external magnetic field (spontaneous transitions) and in magnetic fields of different strengths (induced transitions). In [3], the domain structure was studied using the magneto-optical Faraday effect with a phase identification by the color-contrast method. Study of the domain structure revealed that, for $Er_3Fe_5O_{12}$, the temperature of the first-order SRPT between the phases with magnetization orientated along the $\langle 111\rangle$ and $\langle 100\rangle$ axes coincides with T_C [4]. In [3], it was also established that the temperature ranges of magnetic compensation in a substituted erbium–iron garnet overlap.

The aim of this work is to study the behavior of the hexagonal lattice of bubble domains when changing the film temperature in the range corresponding to spin reorientation near T_C. A uniaxial film of ferrite garnet $(BiTm)_3(FeGa)_5O_{12}$ ($4\pi M_s = 160$ G), in which a bubble-domain lattice could be formed, was studied at room temperature. The $\langle 111\rangle$ axis was normal to the film plane. The bubble-domain lattice was formed using a unipolar pulsed magnetic field with a frequency of 400 Hz and a strength of 60 Oe without a bias field; then, the field was switched off. The spin reorientation in the film with the compensation temperature $T_C = 120$ K occurred in the temperature range 185–160 K. The domain structure was observed by the Faraday effect. Color SRPT recording was performed visually.

There are two ways of studying the characteristics of a bubble-domain lattice. In the first variant, a lattice is formed at different temperatures to obtain the temperature dependences of the lattice period a and the bubble-domain diameter d. Both $a(T)$ and $d(T)$ are continuous functions of temperature. Such lattices are at an equilibrium at the temperature of formation; i.e., their parameters correspond to a minimum energy. The parameter $y = d/a = 0.74$ remains constant within the entire temperature range in which the equilibrium lattice may exist [5]. Another character of the $a(T)$ and $d(T)$ dependences is observed when the bubble-domain lattice is formed at some fixed temperature and, then,

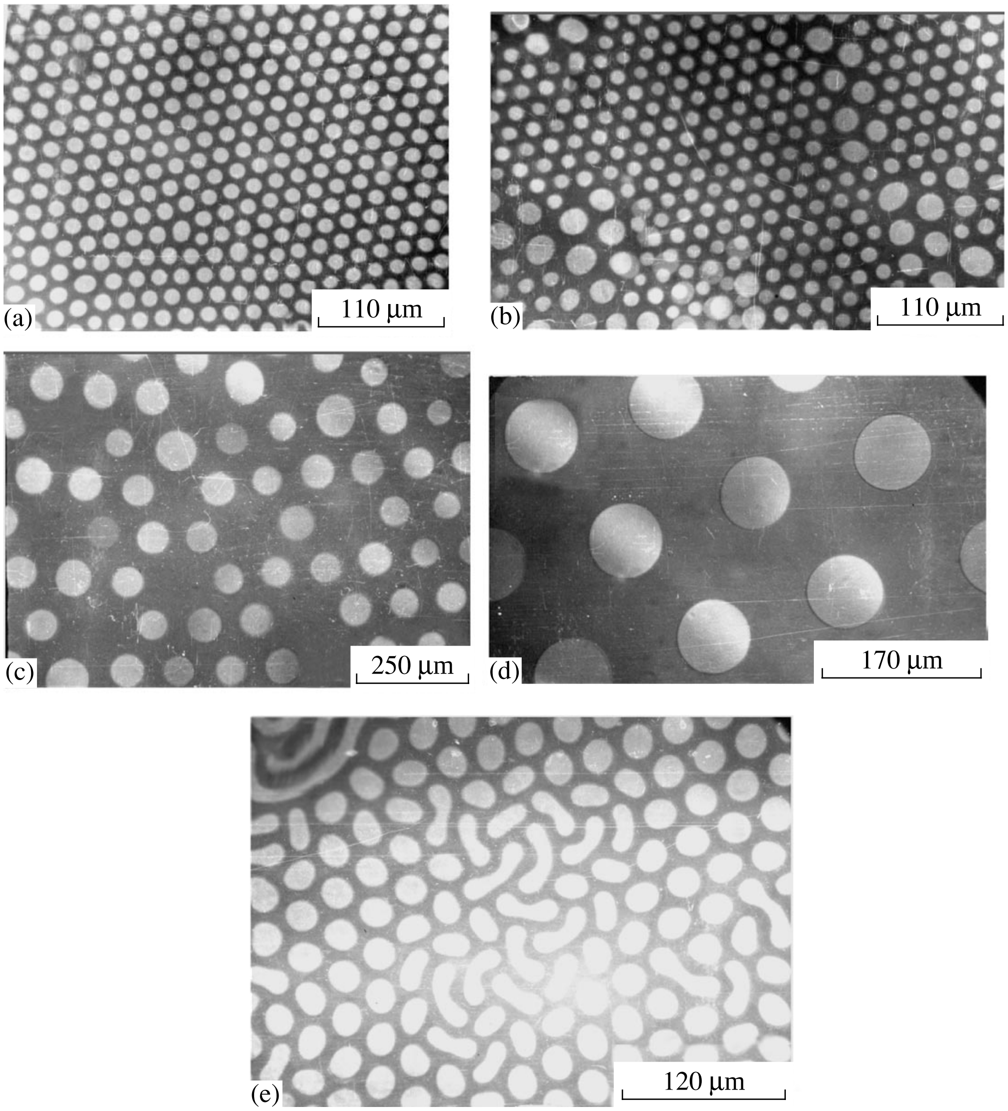

Fig. 1. Domain structure of a $(BiTm)_3(FeGa)_5O_{12}$ film at (a) 300; (b) 215; (c, d) 172; and (e) 205 K.

the film temperature is varied. In this case, the lattice remains the same in a certain temperature range and, then, a spontaneous phase transition to a lattice with new parameters corresponding to an equilibrium lattice at the transition temperature occurs. The latter variant was used in this study.

Let us consider phase transitions in a bubble-domain lattice caused by film cooling. The lattice was formed at T = 300 K (Fig. 1a). Initially, two collinear magnetic phases with magnetization vectors normal to the film plane were observed: the phase $\Phi_1\langle 111\rangle$ corresponding to bubble domains (orange) and the phase $\Phi_2\langle\bar{1}\bar{1}\bar{1}\rangle$ (brown background). The lattice with a = 18 μm remained unchanged up to 215 K; i.e., the value of a remained constant. Then, a transition to a new lattice with a larger parameter occurred. At this transition, some bubble domains were compressed and disappeared, while others increased in diameter and occupied the neighboring sites (Fig. 1b). After an action of a pulsed field, an equilibrium bubble-domain lattice with a larger parameter (a = 25 μm) and a smaller number of bubble domains was formed. The magnetic phases Φ_1 and Φ_2 were still present. At 185 K, some background areas changed their color from brown to green, and some bubble domains changed in color from orange to white. This phenomenon indicated the beginning of spin reorientation and the appearance of two new phases with magnetization vectors directed obliquely to the film plane: the phase $\Phi_3\langle 1\bar{1}\bar{1}\rangle$ of bubble domains (white) and the phase $\Phi_4\langle\bar{1}11\rangle$ (green background). At 172 K, the bubble-domain lattice col-

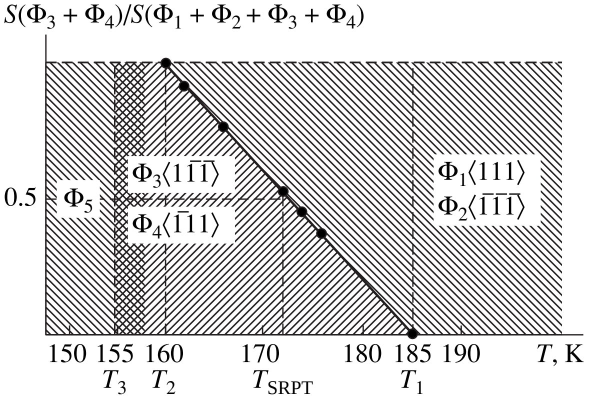

Fig. 2. Temperature dependence of the ratio of the area occupied by the domain phases Φ_3 and Φ_4 to the area occupied by the phases Φ_1 and Φ_2.

lapsed (Fig. 1c). Then, a lattice with parameter a = 118 μm and a wide, very contrasting, domain wall was formed by a pulsed field (Fig. 1d). In this case, the bubble domains changed stepwise in size: the diameter increased threefold with respect to that observed at 185 K. The bubble-domain width also changed stepwise: it increased fivefold with respect to the corresponding value at 185 K. All the four phases were observed, and the total area of the Φ_3 and Φ_4 phases was equal to the total area of the Φ_1 and the Φ_2 phases (Fig. 2). With decreasing temperature, the ratio of areas changed in favor of the Φ_3 and Φ_4 phases; the green background areas increased in size, gradually replacing the brown ones; and almost all the bubble domains became white. At T_2 = 160 K, large isolated bubble domains of bright, white color with wide, clearly pronounced, dark walls were observed against a bright green background, i.e., only two angular phases—Φ_3 and Φ_4—were present. At 158 K, the bubble domains became unstable and drifted continuously, changing their shapes. In this case, the domain-wall width proved to be different for different domain parts. With a further decrease in temperature, the contrast becameimpaired due to the decrease in the Faraday rotation and, at 150 K, the domain structure was no longer observed. This fact indicates that a plane anisotropy may arise; i.e., that only the magnetic phase Φ_5 was present.

Upon film heating, a large strip domain of uncertain (somewhat whitish) color appeared at 155 K. As a result of the action of a pulsed field at 160 K, unstable and isolated white bubble domains were formed against the green background; i.e., Φ_3 and Φ_4 phases arose. In this case, few orange and brown areas of small size (Φ_1 and Φ_2 phases) were observed. Upon film heating up to 172 K, the bubble domains lost their shape, transforming into stripes. At 172 K, a bubble-domain lattice with a smaller parameter (a = 166 μm) and narrow domain walls was formed by a pulsed field. Upon further heating, we observed that some bubble domains changed their color from white to orange and that the green background became partially brown; i.e., the total area of the Φ_1 and Φ_2 phases increased. At 185 K, white and green colors were hardly observed, i.e., the angular Φ_3 and Φ_4 phases tended to disappear, the bubble domains lost their shape, and the bubble-domain lattice was destroyed. At 185 K, a new lattice with a smaller parameter (a = 120 μm), which contained only the collinear Φ_1 and Φ_2 phases (orange bubble domains and brown background), was formed by a pulsed field. This lattice remained unaltered up to 205 K. Then, the lattice decomposed into blocks of a new bubble-domain lattice, separated by stripes, with a smaller parameter (a = 40 μm), corresponding to the equilibrium lattice at a given temperature (Fig. 1e). This situation corresponds to a phase transition upon which the number of domains does not change. Under the action of a pulsed field, the lattice with a smaller parameter occupied all the visible region of the film. As the temperature decreased from $T_{\rm C}$, several phase transitions of this type were observed.

We can generalize the results as follows. In the temperature range above T_1, two magnetic collinear phases—$\Phi_1\langle 111\rangle$ and $\Phi_2\langle \bar{1}\bar{1}\bar{1}\rangle$—exist (Fig. 2). In this range, a hexagonal lattice of bubble domains with the equilibrium parameter y = 0.74 and narrow Bloch walls is formed. The lattice remains stable in a certain temperature range. At one end of the range of stability, when the temperature approaches $T_{\rm C}$, a phase transition to an equilibrium bubble-domain lattice with large parameters, accompanied by a collapse of some domains, occurs. At the other end of the range of stability, when the difference between the film temperature and the value of $T_{\rm C}$ increases, a phase transition from a bubble-domain lattice to a two-phase structure consisting of blocks of a new bubble-domain lattice and areas of stripe domains occurs, with retention of the total number of domains. Despite a qualitative difference, both phase transitions in the lattice occur spontaneously and stepwise within a temperature range of 2–3 K. In this case, a hysteresis is observed: the temperature and character of decomposition of the bubble-domain lattice are different for heating and cooling.

In the temperature range from T_1 to T_2 (Fig. 2), four magnetic phases coexist: collinear phases $\Phi_1\langle 111\rangle$ and $\Phi_2\langle \bar{1}\bar{1}\bar{1}\rangle$ and angular phases $\Phi_3\langle 1\bar{1}\bar{1}\rangle$ and $\Phi_4\langle \bar{1}11\rangle$. At $T_{\rm SRPT}$ = 172 K, the phases have the same percentages. In this case, a stepwise change in the phase volume in the bubble-domain lattice occurs, due to the change in the parameters a and d. The equilibrium parameter y decreases from 0.74 to 0.45. In the temperature range from T_1 to $T_{\rm SRPT}$, the domain-wall width gradually increases. At T_{SRPT}, the domain-wall width changes stepwise, which corresponds to the transition from the Bloch type of domain wall to the Néel type. If only the angular Φ_3 and Φ_4 phases are present (at T_2), the bubble-domain lattice is not formed and only isolated bubble domains are observed.

REFERENCES

1. A. I. Belyaeva, A. V. Antonov, and V. P. Yur'ev, Fiz. Tverd. Tela (Leningrad) **22** (6), 1621 (1980) [Sov. Phys. Solid State **22**, 947 (1980)].
2. A. I. Belyaeva, A. V. Antonov, G. S. Egiazaryan, and V. P. Yur'ev, Fiz. Tverd. Tela (Leningrad) **24** (7), 2191 (1982) [Sov. Phys. Solid State **24**, 1247 (1982)].
3. G. S. Kandaurova and L. A. Pamyatnykh, Fiz. Tverd. Tela (Leningrad) **31** (8), 132 (1989) [Sov. Phys. Solid State **31**, 1351 (1989)].
4. A. I. Belyaeva, V. P. Yur'ev, and V. A. Potakova, Zh. Éksp. Teor. Fiz. **83** (3), 1104 (1982) [Sov. Phys. JETP **56**, 626 (1982)].
5. V. A. Zablotskiĭ, Yu. A. Mamaluĭ, and Yu. A. Siryuk, Ukr. Fiz. Zh. **33** (3), 403 (1988).

Translated by T. Dmitrieva

Crystallography Reports, Vol. 49, No. 4, 2004, pp. 668–675. Translated from Kristallografiya, Vol. 49, No. 4, 2004, pp. 747–754.
Original Russian Text Copyright © 2004 by Golovin.

PHYSICAL PROPERTIES OF CRYSTALS

Magnetoplastic Effects in Crystals in the Context of Spin-Dependent Chemical Kinetics

Yu. I. Golovin
Tambov State University, Tambov, 392622 Russia
e-mail: golovin@tsu.tmb.ru

Received November 25, 2002

Abstract—Possible mechanisms of a number of magnetoplastic effects in magnetically disordered crystals are analyzed in the context of the chemical kinetics of reactions occurring in a system of structural defects upon plastic deformation. Particular attention is given to spin-dependent reactions between real-structure elements containing paramagnetic centers (dislocation cores, impurity centers, electronic excitations, and so on). It is shown that reactions of several types may occur between these elements, and, in some cases, the relative deformation rate can be related to the rate constants of intracrystalline spin-dependent reactions. *© 2004 MAIK "Nauka/Interperiodica".*

Magnetoplastic effects were first found in ferromagnetic materials and interpreted as the result of interaction between dislocations and domain walls upon magnetization reversal of a crystal [1–3]. Almost at the same time, the effects of magnetic fields with induction B up to ~10 T on macroplastic properties of pure diamagnetic materials at liquid-helium temperatures T_H were intensively investigated [4–6]. The effects of strong magnetic fields (at $B \sim 10$ T and $T_H \sim 4$ K, the following relation $\mu_B B \gg kT_H$, where μ_B is the Bohr magneton and k is the Boltzmann constant, is valid) on the strain-hardening coefficient were attributed to the change in the viscosity of an electron gas for dislocations moving in this gas upon active deformation [7].

Occasional attempts to observe the action of weak magnetic fields with $B \sim 1$ T on magnetically disordered (nonmagnetic) materials at room temperature T_R ($\mu_B B \ll kT_R$) [8–10] had been considered for a long time as having no physical basis, and the results of these studies were regarded by most experts as artifacts.

A new stage in studying magnetoplastic effects was opened in 1987 by Alshits *et al.* [11]. Over the next decade, a large number of magnetoplastic effects were revealed in nonmagnetic solids—ionic crystals (NaCl, KCl, LiF), metals and alloys (Al, Zn, bronze, metal glasses), covalent and ionic–covalent crystals (Si, ZnS), molecular crystals (C_{60}), polymers (polymethyl methacrylate), and other materials (see review [12]). Constant, pulsed, and microwave fields with induction from several mT to 30 T, as well as various combinations of them, were used. During the last decade, about 200 works were published that experimentally studied and theoretically analyzed the effects of magnetic fields on the characteristics of internal friction, mobility of individual dislocations, yield point, hardening coefficient, creep rate, microhardness, acoustic emission, deformation luminescence, and other properties of nonmagnetic materials (see Fig. 1). With respect to their character and duration, the effects of magnetic fields on physicochemical properties of materials can all be divided into three large groups (Fig. 2): (i) the *in situ* action of a magnetic field, arising and vanishing during small fractions of a second at switching on and off a field; (ii) the irreversible aftereffect of a magnetic field, which is retained over the full time of observation (at least months at room temperature); and (iii) the reversible aftereffect of a field, which is retained for some time after switching the field off but, gradually (for many hours or days), relaxes to zero at room temperature.

In recent years, a specific nonadditive action of magnetic fields in combination with illumination,

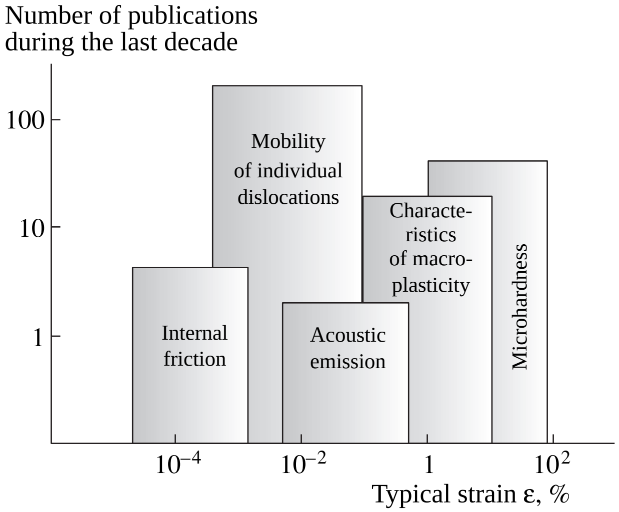

Fig. 1. Methods for studying the effect of magnetic fields on the physicomechanical properties of solids.

X-ray irradiation, and irradiation by β particles on the plastic properties of diamagnetic crystals NaCl, C_{60}, and other objects has been revealed [13–15].

This abundance and variety of the experimental data obtained independently by several groups of researchers using fundamentally different techniques leave no doubt that fairly weak magnetic fields have an anomalously large (and paradoxical, at first glance) effect on the mechanical properties of nonmagnetic materials. In this context, the nature of these phenomena is of fundamental importance. Can they be explained in terms of one universal mechanism (or, at least, using the same approach), or are different reasons responsible for these phenomena in different materials and under different experimental conditions?

Early attempts to interpret magnetoplastic effects using the concepts of Lorentz forces exerted by a magnetic field on moving charged dislocations, a vortex electric field accompanying the switching on and off of magnetic fields, forces caused by magnetization of ferromagnetic precipitates in a diamagnetic matrix, forces related to a gradient of magnetic susceptibility due to the lattice strain near the dislocation core, and so on had no success.

All the aforementioned models for magnetoplastic effects encounter insurmountable difficulties even in the first stage of consideration. They are related to the smallness of forces and energies $U_M \sim \mu_B B$ transferred from a field with induction $B \sim 1$ T to any structural element in a magnetically disordered medium, due to which the magnetic field cannot significantly change the state of a thermodynamically equilibrium system under these conditions. In particular, a magnetic field cannot affect the probability of overcoming stoppers by dislocations, since the activation energy U_A of this process is $U_A \gg kT_R \gg \mu_B B$. One might expect only effects of the same order of magnitude as $\mu_B B/kT_R \sim 10^{-2}$ or $(\mu_B B/kT_R)^2 \sim 10^{-4}$ (in different models), whereas the magnitude of the actually observed effects can be as high as tens or hundreds of percentage points of the initial value of the characteristic under study.

Another group of difficulties in the interpretation of magnetoplastic effects is related to the high complexity and multistage character of the mechanisms of plastic flow and a large “spacing” between the generally recorded macroscopic responses and elementary events, the dynamics of which could, in principle, be influenced by a magnetic field. Changes in the state of electrons (the only objects that can be affected by a magnetic field) and, for example, the yield point (or even the mobility of individual dislocations) are separated by several poorly studied hierarchical levels of the dynamics of the defect structure of a solid. Here is a (far from complete) list of them: changes in the spin and spatial quantum numbers of electrons in interacting defects; atomic rearrangement in the quasi-molecule formed by a stopper and a short dislocation fraction that comes into contact with the stopper, interacting with it; detachment of the dislocation from the stopper; motion of the dislocation to another large stopper; multiplication and interaction of moving dislocations; and macroscopic response of a measuring system. The dynamics of several first stages from the above list, the durations of which are very short (~10^{-12}–10^{-6} s), has been very little studied in the physics of plasticity, if at all, whereas these dynamics are the only ones that can be affected by a magnetic field.

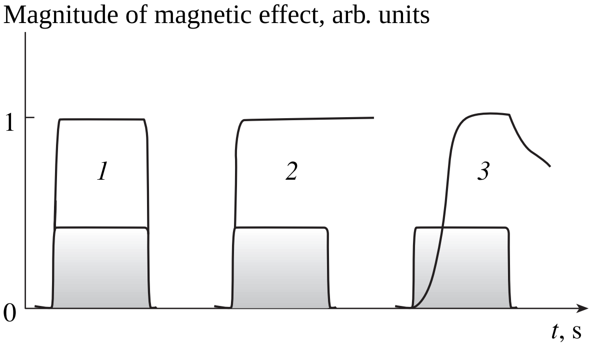

Fig. 2. Three main types of magnetoplastic effects: (*1*) *in situ* effects, (*2*) irreversible aftereffects, and (*3*) reversible aftereffects with delayed kinetics. The shaded rectangles denote the procedure of exposure of samples in a magnetic field.

The problems related to interpreting magnetoplastic effects that could not be overcome within the framework of the aforementioned elementary approaches have caused researchers to appeal to closely related areas of science: chemical kinetics, chemical physics, and the theory of catalysis of chemical reactions, which have been widely and successfully used in the interpretation of strong magnetic effects in nonmagnetic media. For example, in order to explain some magnetic phenomena in chemistry (the effect of a weak constant magnetic field on the kinetics and yield of some radical reactions, the even stronger effect of crossed constant and microwave magnetic fields satisfying the condition for appearance of spin resonance on these characteristics, the polarization of electronic and nuclear spins as a result of chemical reactions, radio emission during the relaxation of chemically polarized spin subsystems, spin catalysis, and so on), a powerful theory of spin-dependent phenomena in chemistry has been developed [16–19].

As applied to the kinetics of radical reactions, this theory is based on principles that follow from the law of conservation of angular momentum in a closed system and the Pauli exclusion principle (which forbids two electrons from occupying the same state):

(i) the total spin of an isolated system should not change. Therefore, only thermodynamically possible reactions satisfying this principle may occur;

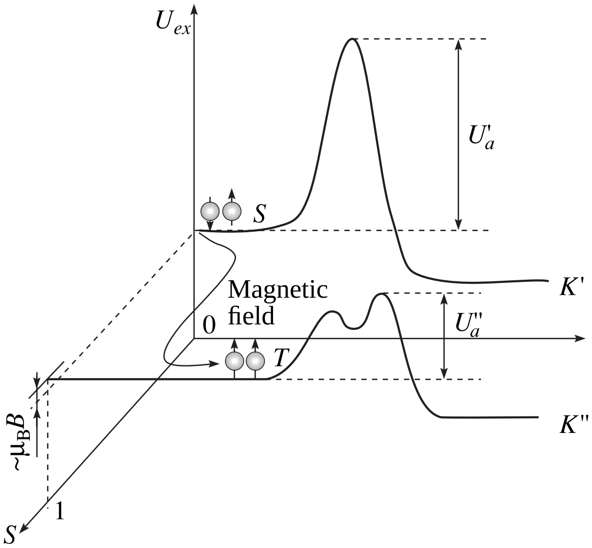

Fig. 3. Change in the rate constant of spin-selective chemical reaction K due to the spin conversion in a radical pair under the action of an external magnetic field. U'_a and U''_a are the activation energies of the molecule decay from the S and T states, respectively.

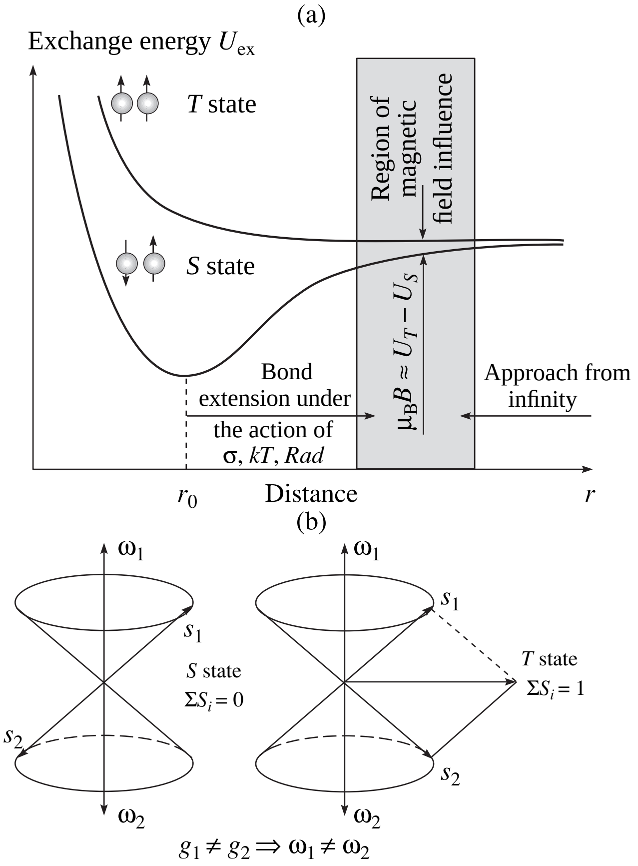

Fig. 4. Mechanisms of spin conversion in an external magnetic field: (a) change in the multiplicity in an excited short-lived radical pair and (b) Δg mechanism of spin conversion in a radical pair. ω_1 and ω_2 are the precession frequencies of paramagnetic centers with g factors g_1 and g_2, respectively.

(ii) the interaction of electrons that have been located for some time in the reaction cell with the environment, including an external magnetic field or intrinsic nuclear one, can partially or completely lift the spin forbiddenness of some possible reaction channels, which, in turn, may change the rate constants of the reactions and the yield ratios for individual products;

(iii) a weak magnetic field can act efficiently only on nonequilibrium systems (spin and molecular ones) evolving via short-lived excited states in which the multiplicity can be changed; and

(iv) the reaction should have several possible alternative thermodynamically allowed channels.

Thus, a magnetic field can affect a reaction by lifting the spin forbiddenness rather than changing its energy (Fig. 3). As a result, the apparent contradiction between the smallness of the energy of interaction between the magnetic field and material and the effect scale is removed.

However, in reality, this can occur only when several conditions are satisfied simultaneously. First, such mechanisms should not contradict thermodynamical principles. Obviously, they cannot be implemented in a thermodynamically equilibrium system and work only in situations where there is a gain in the thermodynamic potential of the final state of the system. Second, significant changes in the reaction rate and channeling may occur only as a result of complex interaction between spin, chemical, and molecular transformations. Depending on the mutual orientation of spins, the simplest pair of radicals with spins $s = \pm 1/2$ in the reaction cell can be in one of two possible states: singlet state S, when $\sum_{1,2} s_i = 0$, and triplet state T, when $\sum_{1,2} s_i = 1$ (Fig. 4a). The difference in the exchange energies of these states at distances r_0 of the same order of magnitude as interatomic distances in condensed media is about 1 eV. Obviously, a magnetic field with $B \sim 1$ T cannot change the state of a radical pair in this situation. At large distances ($r \gg r_0$), $U_T - U_S = 0$; thus, a weak magnetic field cannot affect anything either. A weak field can induce spin conversion only at intermediate distances $r_0 \le r \le 2r_0$, at which $U_M \sim \mu_B B \sim U_T - U_S$. A pair of radicals may find themselves in this position only due to the excitation from the ground state under the action of thermal fluctuations, mechanical bond deformation, ionizing irradiation, or other external factors, as well as during the approach of radicals to each other from infinity. On the one hand, lifetime τ^* in this intermediate state should exceed spin-conversion time τ_c in the magnetic field to make for it to be possible for the spin conversion to occur; on the other hand, τ^* for the solid should be shorter than spin–lattice relaxation time τ_{SL} to prevent field-induced population of states

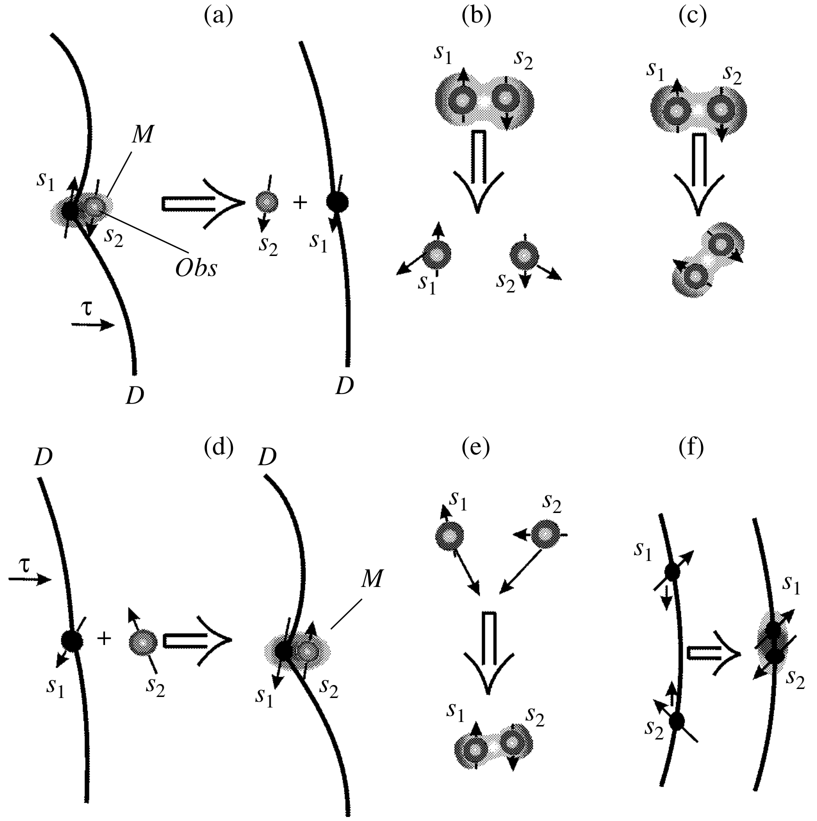

Fig. 5. Plastic deformation as a solid-state chemical reaction: (a–c) monomolecular reactions of detachment of a dislocation from a stopper, decay of a complex of point defects, and its reorientation, respectively; and (d–f) bimolecular reactions of attachment of a dislocation at a stopper, formation of a complex of point defects, and recombination of paramagnetic centers in the dislocation core, respectively. τ are stresses, D is a dislocation, *Obs* is an obstacle, and M is a quasi-molecule formed by two paramagnetic centers belonging to different defects.

from thermalization. Thus, a weak magnetic field can significantly affect a reaction only when the condition $\tau_c < \tau^* < \tau_{SL}$ is satisfied.

Up to this point, we have only discussed a possible scheme of the action of a magnetic field on the kinetics of relaxation from a metastable state (or unstable equilibrium). However, the question of the specific mechanisms of spin conversion in a magnetic field remains open. About ten different mechanisms have been proposed at different times in the theory of spin-dependent chemical reactions. These can be reduced to three main ones (now referred to as Δg, HFI, and ΔJ mechanisms) or combinations thereof [20, 21].

In the Δg mechanism, the spin state of a pair changes in an external magnetic field due to the difference in the g factors of the two interacting radicals. The HFI mechanism, considering the hyperfine interaction, takes into account the effect of the magnetic moments of the atomic nuclei of the radicals on the spin state of electrons. Finally, the ΔJ mechanism considers the spin catalysis of transformations in a pair of radicals induced by a third spin carrier approaching the pair.

For a number of reasons, the Δg mechanism of spin conversion in magnetoplastic effects at $B \sim 1$ T is considered to be the most likely: due to a difference in the g factors of the two radicals (generally by 10^{-3}–10^{-4}), the angular velocities of their precessions in a magnetic field are slightly different and a pair with a frequency $f \sim \mu_B \Delta g B/h \sim 10^8$–$10^9$ s^{-1} passes from the S to T state and vice versa (Fig. 4b).

In order to make the spin conversion in a spin system irreversible and continuous and prevent saturation of the system, the reaction product should be quickly removed from the reaction zone; i.e., the molecular motion should not lag behind the spin and chemical transformations.

If at least one of these conditions is not satisfied, a magnetic field will not act efficiently according to the above scheme.

In the beginning of the 1990s, Alshits and Molotskiĭ proposed using these concepts in plasticity physics [22, 23] to explain, in particular, the nature of magnetoplastic effects. There was not enough justification for doing so at that time; however, it was known that dislocation cores always contain some paramagnetic centers (not only in covalent crystals, where this is quite obvious due to the presence of dangling bonds, but also in ionic, metal, and ionic–covalent crystals, as a result of

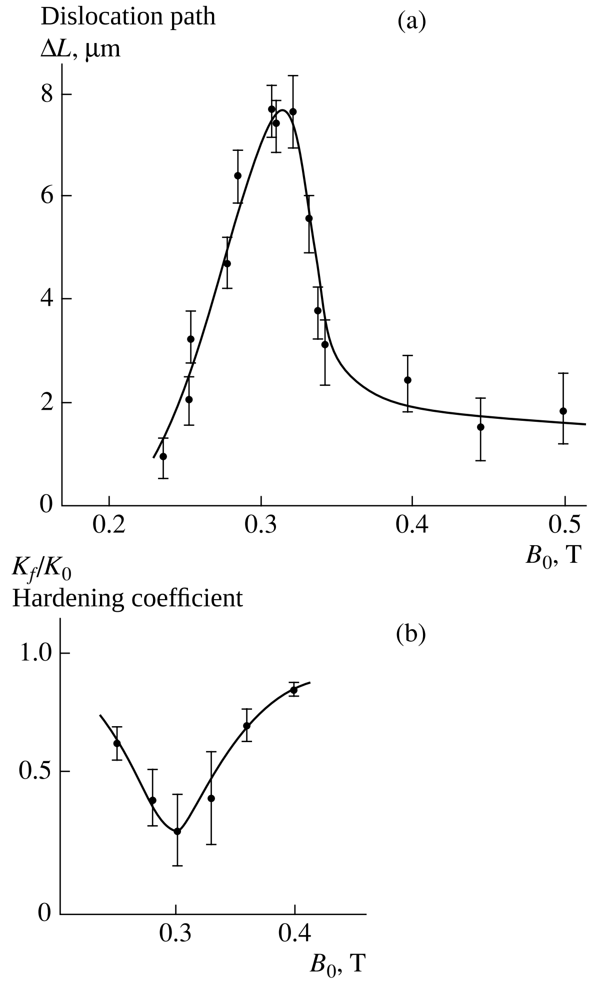

Fig. 6. Softening under the action of electron spin resonance: (a) resonance increase in the dislocation mobility in a NaCl:Eu single crystal after preliminary exposure in crossed constant and microwave magnetic fields and (b) resonance macroscopic softening (decrease in the strain-hardening coefficient) in a NaCl:Ca single crystal upon active deformation and simultaneous action of crossed constant and microwave magnetic fields. K_f is the hardening coefficient upon joint action of microwave and constant magnetic fields and K_0 is the hardening coefficient in the absence of a microwave magnetic field.

trapping of electrons at steps, kinks, and other core features), the concentration of which generally increases with strain enhancement [24–31]. Similar data are also available for paramagnetic centers in impurity–vacancy complexes in ionic and ionic–covalent crystals, glasses, and so on. Therefore, these macroscopically diamagnetic materials always contain a number of paramagnetic particles (radicals, in terms of chemistry) that may be involved in the exchange interaction. An active plastic deformation or relaxation of a structure under the action of internal stresses causes formation, motion, interaction, annihilation, and other transformations of the crystal defect structure, which can be considered as a set of chemical reactions between different reagents or as a change in the conformation of one giant quasimolecule (Fig. 5).

The above point of view was first confirmed by different indirect pieces of evidence and modeling [32–34]. Then, division of the process of field-induced structure relaxation into separate stages and analysis of their kinetics made it possible to reveal that, in impurity ionic crystals containing metastable complexes of point defects, a magnetic field first initiates monomolecular reactions of decay of these complexes and, then, bimolecular reactions of their aggregation into new complexes, even in the absence of new dislocations [35]. Finally, at the end of the 1990s, direct experiments were carried out to reveal the magnetic resonance disordering predicted in [38] and, thus, to prove the spin-dependent nature of magnetoplastic effects in impurity NaCl:Eu (with a Eu concentration of 100 ppm) and NaCl:Ca crystals. The results shown in Fig. 6, related both to the action of a magnetic field *in situ* and to its aftereffect (see, for example, [36–38]), directly indicate that the magnetic field affects particles with spins 1/2 and 3/2 and that this effect is significantly enhanced under conditions of spin resonance under joint action of constant and microwave ($\nu \sim 9.5$ GHz) magnetic fields. From the point of view of classifying the magnetic effects accepted in chemical physics, the revealed effects of resonance softening of crystals in the magnetic field can be considered a further expansion of the terms of reaction yield detected magnetic resonance (RYDMR) spectroscopy [17, 18]. For a number of reasons, the sensitivity of this method for studying short-lived paramagnetic states (actually, in this case, a variation in some plastic characteristic or other—dislocation mobility, strain hardening coefficient, and so on—serves as a response, rather than the decay of an electromagnetic wave in an object) exceeds—by many orders of magnitude—that of conventional electron spin-resonance spectroscopy. This will be shown below using simple considerations.

Let us assume that all the stoppers and dislocation cores have paramagnetic properties. Then, in an area dS_N, the Nth dislocation interacts with $dn \simeq adS_NC$ stoppers, where a is the lattice parameter and C is the volume concentration of the stoppers. With regard to this fact, the relative strain rate can be expressed in terms of the rate constant $K = dn/Cdt$ of the monomolecular reaction of breaking the bond between a paramagnetic center in the dislocation core R_D and a stopper $R_{Obs}(M \longrightarrow \dot{R}_D + \dot{R}_{Obs})$ as follows:

$$d\varepsilon/dt = \sum_N A\frac{dS_N}{dt} = \sum_N A\frac{dn}{aCdt} = \alpha K.$$

Here, $\alpha = A/a$ is a geometric constant.

Thus, a measurement of the dislocation mobility or the macroscopic flow velocity is equivalent to the determination of the rate constant of destruction of quasimolecules M formed by dislocations and stoppers.

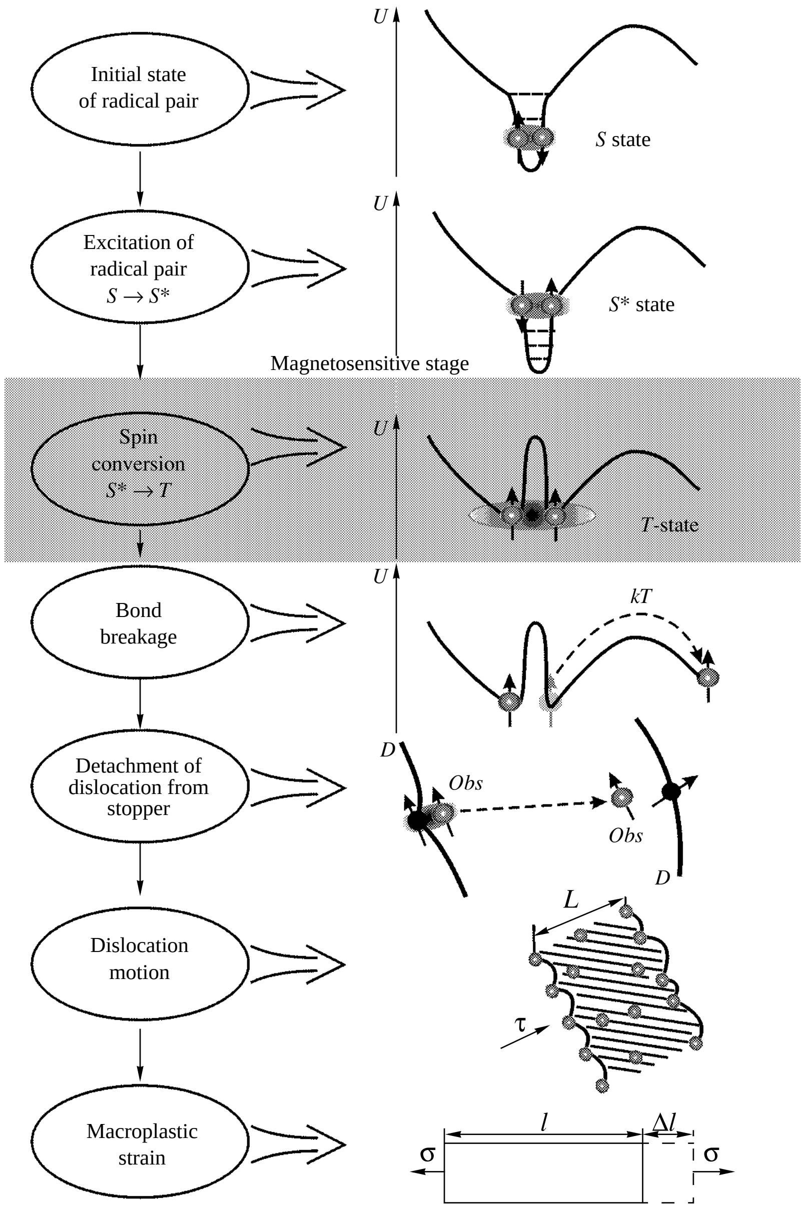

Fig. 7. Step-by-step scheme of a magnetoplastic effect arising due to enhancement of detachment of dislocations from stoppers in a magnetic field.

Obviously, a stricter consideration should also take into account the presence of nonparamagnetic stoppers and the probability of purely elastic interaction of dislocations with these stoppers, as well as the diffusion mobility of paramagnetic centers both in the crystal bulk and along the dislocation core. The resolution of modern methods for measuring the characteristics of the mobility of individual dislocations is sufficient to determine the magnetic-field-induced variations in K in individual events of the reaction $M \longrightarrow \dot{R}_D + \dot{R}_S$.

Obviously, the conditions for the reactions between structural defects in a crystal occur, and, between reagents in the liquid or gaseous phase, they are significantly different, for the following reasons.

(i) In contrast to the case of a chemical reaction in a test tube, a real crystal contains many different reagents capable of reacting with one another, especially under conditions of plastic deformation (point defects, their complexes and aggregates, dislocations of different types, defects captured by dislocation cores, and so on). Many cannot be considered invariable, as they are complex quasi-molecules capable of changing their conformation and even composition.

(ii) All the structural defects are in a close environment, which strongly affects their properties through changes in the electronic structure and limitation of possible orientations, positions, and mobility.

(iii) The residence time of two radicals (belonging to the set of interacting defects) in a reaction cell is determined to a larger extent by the action of external and internal stresses rather than chaotic thermal motion.

(iv) The spin–lattice relaxation in crystals destroys the spin correlation in pairs more rapidly.

In summing up the above considerations, we can imagine the following scenario of events in which a weak magnetic field can significantly affect the mechanical properties of macroscopically diamagnetic crystals containing paramagnetic centers in structural defects (Fig. 7). Some stages, especially those determined by fast electron–spin interactions, should be purposefully and systematically studied by high-resolution methods, since their kinetics—and even existence—manifest themselves only indirectly. This should be done not only because electron–spin dynamics lies at the basis of magnetoplasticity physics, but also because it is involved in the formation of macroscopic properties of real crystals in the absence of magnetic fields.

The results obtained, along with their fundamental importance for condensed-matter physics in general and plasticity physics in particular (where it was shown for the first time by direct methods that the spin degrees of freedom of structural defects play an important role in the formation of mechanical properties of nonmagnetic materials and the sensitivity of other macroscopic properties to magnetic fields), may be useful in closely related fields of knowledge. Thus, the question of the regularities and physical mechanisms of the effect of weak magnetic fields on different properties of solids can be considered a part of the major problem of the weak influence of irradiation, chemical action, electromagnetic fields, and other factors on open nonequilibrium systems in animate and inanimate nature, whereas the influence itself can be regarded as an important environmental factor. For example, models in geodynamics and tectonics should, it appears, take into account the possibility of softening of materials of the earth's crust as a result of combined action of the constant magnetic field of the earth and its high-frequency fluctuations. It is possible that the concepts and physical models developed and verified for simple crystalline systems can also be used in magnetobiology and biochemistry. In any case, progress in the study of magnetoplasticity has already given impetus to investigations of other magnetosensitive (electric, optical, and luminescence) properties of diamagnetic materials with important applications (semiconductors, polymers, fullerites, and so on).

ACKNOWLEDGMENTS

I am grateful to V.L. Berdinskiĭ and N.L. Klyachko for their helpful participation in discussions of the chemical and biochemical aspects of the magnetosensitivity of chemical reactions.

This study was supported by the Russian Foundation for Basic Research (project no. 00-02-16094), the Ministry of Education of the Russian Federation (grant no. E00-34-552), and the federal target programs "Universities of Russia–Basic Research" (grant no. UR.01.01.013) and "Fullerenes and Atomic Clusters" (grant no. 40.012.1.1.11.47).

REFERENCES

1. L. A. Chebotkevich, A. A. Urusovskaya, and V. V. Veter, Kristallografiya **10** (5), 688 (1965) [Sov. Phys. Crystallogr. **10**, 578 (1965)].
2. S. Hayashi, S. Takahashi, M. Yamamoto, *et al.*, J. Phys. Soc. Jpn. **30**, 381 (1971).
3. V. S. Bobrov and M. A. Lebedkin, Fiz. Tverd. Tela (Leningrad) **27** (3), 820 (1985) [Sov. Phys. Solid State **27**, 503 (1985)].
4. V. P. Lebedev and V. S. Krylovskiĭ, Pis'ma Zh. Éksp. Teor. Fiz. **36** (1), 3 (1982) [JETP Lett. **36**, 1 (1982)].
5. V. I. Startcev, in *Dislocations in Solids*, Ed. by F. R. N. Nabarro (North-Holland, Amsterdam, 1983), Vol. 6, p. 143.
6. J. M. Galligan and C. S. Pang, J. Appl. Phys. **50** (10), 6253 (1979).
7. M. I. Kaganov, V. Ya. Kravchenko, and V. D. Natsik, Usp. Fiz. Nauk **111** (4), 655 (1973).
8. N. V. Zagoruĭko, Kristallografiya **10** (1), 81 (1965) [Sov. Phys. Crystallogr. **10**, 63 (1965)].
9. S. T. Kishkin and A. A. Klypin, Dokl. Akad. Nauk SSSR **211** (2), 325 (1973) [Sov. Phys. Dokl. **18**, 502 (1973)].
10. G. I. Distler, V. M. Kanevskiĭ, V. V. Moskvin, *et al.*, Dokl. Akad. Nauk SSSR **268** (3), 591 (1983) [Sov. Phys. Dokl. **28**, 43 (1983)].
11. V. I. Al'shits, E. V. Darinskaya, G. M. Perekalina, and A. A. Urusovskaya, Fiz. Tverd. Tela (Leningrad) **29** (2), 467 (1987) [Sov. Phys. Solid State **29**, 265 (1987)].
12. Yu. I. Golovin and R. B. Morgunov, Materialovedenie, Nos. 3–6, 2 (2000).
13. V. I. Al'shits, E. V. Darinskaya, and O. L. Kazakova, Pis'ma Zh. Éksp. Teor. Fiz. **62** (4), 352 (1995) [JETP Lett. **62**, 375 (1995)].
14. Yu. I. Golovin, R. B. Morgunov, and S. Z. Shmurak, Dokl. Akad. Nauk **360** (6), 753 (1998) [Dokl. Phys. **43**, 340 (1998)].
15. Yu. I. Golovin, A. A. Dmitrievskiĭ, I. A. Pushnin, and R. K. Nikolaev, Dokl. Akad. Nauk **385** (1–3), 485 (2002) [Dokl. Phys. **47** (7), 485 (2002)].
16. A. L. Buchachenko, R. Z. Sagdeev, and K. M. Salikhov, *Magnetic and Spin Effects in Chemical Reactions* (Nauka, Novosibirsk, 1978).
17. K. M. Salikhov, Yu. N. Molin, R. Z. Sagdeev, and A. L. Buchachenko, *Spin Polarization and Magnetic Effects in Radical Reactions* (Nauka, Novosibirsk, 1978; Elsevier, Amsterdam, 1984).
18. A. L. Buchachenko, Chem. Rev. **95** (7), 2507 (1995).

19. B. Ya. Zel'dovich, A. L. Buchachenko, and E. L. Frankevich, Usp. Fiz. Nauk **155** (1), 3 (1988) [Sov. Phys. Usp. **31**, 385 (1988)].
20. U. E. Steiner and T. Ulrich, Chem. Rev. **89**, 51 (1989).
21. A. L. Buchachenko and V. L. Berdinsky, J. Phys. Chem. **100**, 18292 (1996).
22. V. I. Al'shits, E. V. Darinskaya, and E. A. Petrzhik, Fiz. Tverd. Tela (Leningrad) **33** (10), 3001 (1991) [Sov. Phys. Solid State **33**, 1694 (1991)].
23. M. I. Molotskiĭ, Fiz. Tverd. Tela (Leningrad) **33** (10), 3112 (1991) [Sov. Phys. Solid State **33**, 1760 (1991)].
24. V. V. Zyryanov, Izv. Sib. Otd. Akad. Nauk SSSR, Ser. Khim. Nauk **6** (19), 9 (1988).
25. P. Yu. Butyagin, A. A. Berlin, A. É. Kalmanson, and L. A. Blyumenfel'd, Vysokomol. Soedin. **1**, 865 (1959).
26. V. R. Regel', A. I. Slutsker, and É. E. Tomashevskiĭ, *Kinetic Nature of Strength of Solids* (Nauka, Moscow, 1974).
27. P. Yu. Butyagin, A. M. Dubinskaya, and V. A. Radtsig, Usp. Khim. **36**, 593 (1969).
28. M. V. Vlasova and N. G. Kakazeĭ, *Electron Paramagnetic Resonance in Mechanically Destroyed Solids* (Naukova Dumka, Kiev, 1979).
29. J. J. Gilman and H. C. Tong, J. Appl. Phys. **42**, 3479 (1971).
30. V. A. Radtsig, Kinet. Katal. **20** (2), 456 (1979).
31. V. A. Zakrevskiĭ, Fiz. Khim. Stekla **14** (2), 256 (1988).
32. M. I. Molotskii, R. E. Kris, and V. Fleurov, Phys. Rev. B **51** (20), 12531 (1995).
33. M. I. Molotskii and V. Fleurov, Philos. Mag. Lett. **73**, 11 (1996).
34. Yu. I. Golovin and R. B. Morgunov, Dokl. Akad. Nauk **354** (5), 632 (1997).
35. Yu. I. Golovin and R. B. Morgunov, Zh. Éksp. Teor. Fiz. **115** (2), 605 (1999) [JETP **88**, 332 (1999)].
36. Yu. I. Golovin, R. B. Morgunov, A. I. Tyurin, and V. I. Ivolgin, Dokl. Akad. Nauk **361** (3), 352 (1998).
37. Yu. I. Golovin, R. B. Morgunov, V. E. Ivanov, *et al.*, Pis'ma Zh. Éksp. Teor. Fiz. **68** (5), 400 (1998) [JETP Lett. **68**, 426 (1998)].
38. Yu. I. Golovin, R. B. Morgunov, V. E. Ivanov, and A. A. Dmitrievskiĭ, Zh. Éksp. Teor. Fiz. **117** (6), 1080 (2000) [JETP **90**, 939 (2000)].

Translated by Yu. Sin'kov

Crystallography Reports, Vol. 49, No. 4, 2004, pp. 676–679. Translated from Kristallografiya, Vol. 49, No. 4, 2004, pp. 755–758.
Original Russian Text Copyright © 2004 by Pantyukhina, Obrosov, Stepanov, Voronin, Batalov.

PHYSICAL PROPERTIES OF CRYSTALS

Study of Ion Transport in Li_2ZrO_3 Solid Electrolytes with Different Lithium Isotope Ratios

M. I. Pantyukhina*, V. P. Obrosov*, A. P. Stepanov,
V. I. Voronin**, and N. N. Batalov***

* *Institute of High-Temperature Electrochemistry, Ural Division, Russian Academy of Sciences,
ul. S. Kovalevskoi 20, Yekaterinburg, 620219 Russia*
** *Institute of Metal Physics, Ural Division, Russian Academy of Sciences,
ul. S. Kovalevskoi 18, Yekaterinburg, 620219 Russia*

Received January 31, 2003

Abstract—Lithium ionic conductivity and spin-lattice relaxation rates were measured in Li_2ZrO_3 solid electrolytes with different ^6Li and ^7Li ratios. It is found that single-isotope electrolytes undergo a transition to the superionic state in the temperature range of 430–450 K, accompanied by an abrupt increase in conductivity. As a result of introduction of the other type of the isotope, the conductivity jump disappears in this temperature range. The transition to the superionic state is attributed to the redistribution of lithium ions over energetically nonequivalent lattice sites. © *2004 MAIK "Nauka/Interperiodica".*

INTRODUCTION

Previous measurements of the electrical characteristics of the solid electrolyte Li_2ZrO_3 [1, 2] revealed a transition to the superionic state in the temperature range 430–450°C. The transition is accompanied by a significant decrease in the activation energy from 88 to 13 kJ/mol. Since this electrolyte is promising for applications, we continued to study the mechanism of ion transport in it. The results obtained are discussed here. We reported the methods of preparing samples and controlling their phase composition in [2].

Thus, we here report experimental data on the ionic conductivity and the rates of spin-lattice relaxation of ^7Li nuclei in Li_2ZrO_3 samples with different $^6Li : {}^7Li$ ratios. We have also refined some structural details at room and elevated temperatures by neutron diffractometry and measured the NMR spectra.

Conductivity was measured on samples with silver electrodes using an R-5058 ac bridge at a working frequency of 10 kHz. The temperature dependence was measured upon both heating and cooling with the interruptions made that are necessary in performing measurements. The results obtained are shown in Fig. 1.

The NMR spectra and the rates of spin-lattice relaxation of ^7Li nuclei were measured for Li_2ZrO_3 on a pulsed coherent NMR spectrometer at 35 MHz. The results were processed using the Bloembergen–Purcell–Pound model with a single correlation time. The obtained data are shown in Fig. 2. The results of neutron diffraction studies are listed in Table 1.

RESULTS AND DISCUSSION

The temperature dependences of the electrical conductivity of Li_2ZrO_3 samples with different lithium isotope ratios have several characteristic features. In samples with a maximum content of ^7Li or ^6Li, high activation energies are observed at relatively low temperatures (up to 430°C): 99.2 and 91.5 kJ/mol, respectively. With a further increase in temperature, the

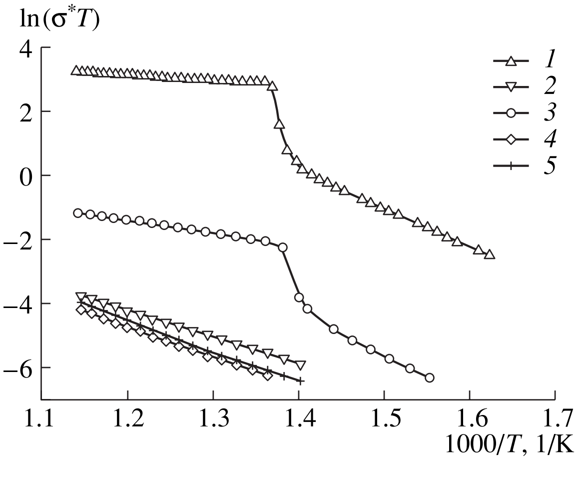

Fig. 1. Temperature dependences of the conductivity of Li_2ZrO_3 samples with different $^6Li : {}^7Li$ ratios: (*1*) 89.5; (*2*) 7.5; (*3*) 25; (*4*) 50; and (*5*) 75 at % of ^6Li.

1063-7745/04/4904-0676$26.00 © 2004 MAIK "Nauka/Interperiodica"

conductivity abruptly increases by about 1.5 orders of magnitude. This conductivity jump is accompanied by a drop in the activation energy to 13.2 and 34.1 kJ/mol, respectively. With an increase in the content of one of the noted isotopes in the solid electrolyte, the conductivity jump disappears, at least at temperatures up to 600°C. In the temperature range in which the drop in activation energy was observed, this parameter remains rather high: 81.1, 93.3, and 81.4 kJ/mol for samples with 25.0, 50.0, and 75.0 at % of ^{6}Li, respectively. These activation energy values are comparable to those characteristic of nearly pure Li_2ZrO_3 samples (with respect to ^{6}Li or ^{7}Li isotopes) in the low-temperature range. In other words, an introduction of large amounts of one of the isotopes into the system of lithium charge carriers removes the transition to the superionic state. These facts indicate a strong effect of lithium isotopes on the dynamics of charge carriers moving in the crystal lattice of Li_2ZrO_3. Note that the conductivity of lithium metazirconate with a prevailing ^{6}Li content is lower than that of Li_2ZrO_3 with ^{7}Li in the entire temperature range under study. On the other hand, as compared to the ^{7}Li-containing samples, the activation energy of the samples with ^{6}Li is slightly lower in the low-temperature range and greater at high temperatures.

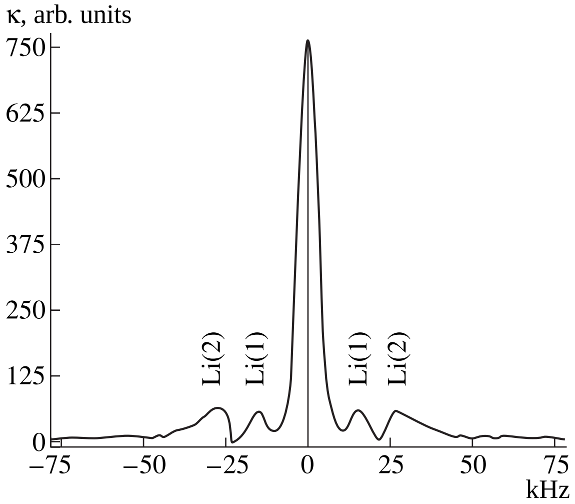

Fig. 2. NMR spectrum for ^{7}Li nuclei in Li_2ZrO_3 at room temperature.

Figure 2, which is typical of all samples with mixed isotopic composition, shows that the NMR spectrum has a central peak that narrows with an increase in temperature and two pairs of satellite peaks that disappear at higher temperatures. This feature is observed at all concentrations of the isotopes under study. It is well known that satellites in the spectra of ^{7}Li nuclei, which have quadrupole moments, are indicative of two nonequivalent positions in the electrolyte sublattice that are occupied by lithium cations. Indeed, the monoclinic Li_2ZrO_3 lattice is characterized by the sp. gr. *C*2/*c*, where lithium cations occupy two different positions, Li(1) and Li(2). Each lithium site is surrounded by six oxygen ions forming two types of octahedra having different sizes and characterized by different values of the electric field gradient at ^{7}Li nuclei. The integrated intensities of the satellite peaks are nearly the same, which indicates that the occupancies of positions (1) and (2) are close to each other. This result is in qualitative agreement with the data of [3].

Table 1. Neutron diffraction data for Li_2ZrO_3 samples with a natural content of the ^{6}Li isotope (7.5 at %) and enriched up to 25 at % of ^{6}Li

Parameters	$Li^7_2ZrO^*_3$	$Li^7_2ZrO_3$ $t = 575°C$	$Li^6_2ZrO^*_3$	$Li^6_2ZrO_3$ $t = 450°C$	$Li^6_2ZrO_3$ $t = 600°C$
a, Å	5.4239(9)	5.5208(5)	5.4265(6)	5.5000(9)	5.5260(9)
b, Å	9.0312(1)	9.0759(1)	9.0265(1)	9.067(1)	9.086(1)
c, Å	5.4221(9)	5.4758(5)	5.4267(7)	5.4650(9)	5.4830(9)
β, deg	112.673	112.485	112.722	113.23(1)	113.42(1)
V, Å^3	245.07	251.65	245.18	250.44	252.62
Occupancy (*N*) for	0.90(1)	0.84(4)	0.58(4)	0.62(4)	0.57(4)
^{6}Li, at %	7.5	7.5	29	27	30
^{7}Li, at %	92.5	92.5	71	73	70
Occupancy (*N*) for	0.92(1)	0.99(3)	0.75(4)	0.75(4)	0.78(4)
^{6}Li, at %	7.5	7.5	22	22	21
^{7}Li, at %	92.5	92.5	78	78	79

* The data correspond to room temperature.

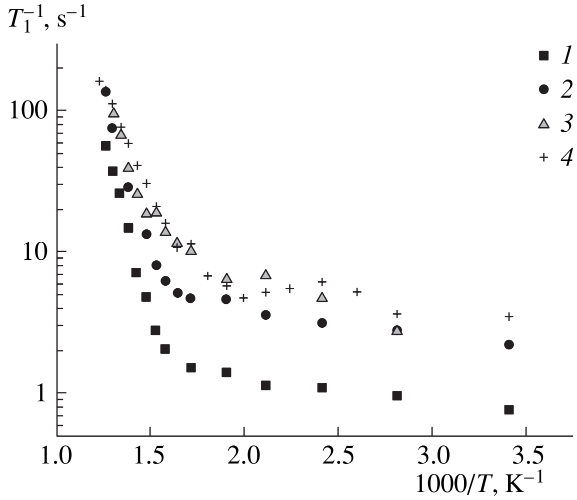

Fig. 3. Spin-lattice relaxation rates for ^{7}Li nuclei in Li_2ZrO_3 with different contents of ^{6}Li: (*1*) 90; (*2*) 75; (*3*) 50; and (*4*) 25 at % of ^{6}Li.

With an increase in temperature, satellite lines broaden and disappear at different rates. The pair of peaks corresponding to the Li(1) positions is the first to disappear. It means that lithium ions occupying these sites are more mobile and quadrupole interactions are averaged out at lower temperatures. The second pair of satellites disappears only at temperatures exceeding 500°C. In addition, the spin-lattice relaxation rate of ^{6}Li nuclei decreases with an increase in the ^{6}Li content (see Fig. 3). To reveal the characteristic features of the changes in the lattice of Li_2ZrO_3 with a high ^{6}Li content, we performed neutron diffraction measurements supplementing those reported in [4]. The obtained data are listed in Table 1.

For the Li_2ZrO_3 samples with a low ^{6}Li content, the data of Table 1 show that lithium cations pass from Li(1) to Li(2) positions with an increase in temperature. As a result, the latter positions are fully occupied. At the same time, about 16 at % of vacancies arise at the Li(1) sites. The transition of lithium cations causes a sharp increase in the conductivity and reduces the activation energy in electrolytes with a prevailing content of one of the isotopes. This manifests itself in the temperature dependences of the conductivity of metazirconate samples with a natural content of ^{6}Li and of those maximally enriched with the ^{6}Li isotope (Fig. 1). The data obtained suggest the following mechanism of the ion transport in single-isotope Li_2ZrO_3 samples after their transition to the superionic state. Lithium ions follow the path “octahedron–tetrahedron–empty octahedron” meeting no significant hindrances and almost not interacting with each other. Moreover, in this case, the values of the activation energies for the long-range motion calculated on the basis of the conductivity measurements are close to those for the short-range motion determined using the data from Fig. 2. This is an additional indication of a small contribution of Coulomb correlations between charge carriers in single-isotope electrolytes. Another state of affairs is observed for a mixture of ^{6}Li and ^{7}Li isotopes that are both of high concentrations. It can be seen from Table 1 that, in such a mixture, the Li(1) sites are occupied mainly by ^{6}Li ions and the redistribution of this isotope between different positions does not occur up to high temperatures. The motion of charge carriers is hindered by individual ^{6}Li ions remaining in Li(1) sites. Thus, the “octahedron–tetrahedron–empty octahedron” chain of easy motion is broken. The breakage of the migration path destroys the superionic state of the electrolyte and leads to the increase in the activation energies for the short- and long-range motion with an increase in the ^{6}Li content, as can be seen from Table 2.

Table 2. Activation energies for the long-range motion (according to the conductivity data) and for the short-range motion (according to the NMR data) for Li_2ZrO_3 samples with different isotope ratios

Content of ^{6}Li, at %	E_a, kJ/mol (according to the conductivity data)	E_a, kJ/mol (according to the NMR data)
7.5	13.2	21.00
7.5	13.2	25.84
25	81.1	56.22
50	93.3	80.70
75	81.4	86.74
89.5	34.1	97.26

The activation energies for these two types of motion do not coincide. It is probable that this difference is because the height of the potential barrier for the short-range motion (i.e., for intersite jumps of charge carriers) increases with an increase in the content of ^{6}Li ions remaining in Li(1) sites. For the long-range motion, statistical effects should be taken into account that are due to the fact that ^{6}Li ions, on average, occupy vacant sites more often, preventing mobile charge carriers from coming to them.

CONCLUSIONS

The ionic conductivities of Li_2ZrO_3 solid electrolyte samples with different lithium isotope ratios were measured. It was shown that introduction of ^{6}Li into a system of charge carriers leads to the breakage of the superionic state in the electrolyte. The NMR spectra and spin-lattice relaxation rates were also measured for the system of lithium charge carriers. It was shown that lithium ions in Li_2ZrO_3 occupy two types of energetically nonequivalent sites and that the spin-lattice relaxation rate of ^{7}Li nuclei decreases with an increase in the ^{6}Li content. The structural details of Li_2ZrO_3 were refined for samples with different ^{7}Li : ^{6}Li ratios at room and elevated temperatures. It was shown that heating leads to the redistribution of lithium ions between Li(1) and Li(2) sites.

ACKNOWLEDGMENTS

This study was supported by the Russian Foundation for Basic Research (project no. 02-02-16406) and the State Research and Development Program “Advances in the Physics of Condensed Matter. Neutron Studies of Condensed Matter” (project no. 40.012.1.1.11.50).

REFERENCES

1. E. E. Hellstrom and W. Van Gool, Solid State Ionics **2**, 59 (1981).
2. O. A. Andreev, M. I. Pantyukhina, B. D. Antonov, and N. N. Batalov, Élektrokhimiya **36**, 1507 (2000).
3. J. L. Hodeau, M. Marezio, A. Santoro, and R. S. Roth, J. Solid State Chem. **45**, 170 (1982).
4. M. I. Pantyukhina, O. A. Andreev, V. G. Zubkov, *et al.*, Zh. Neorg. Khim. **46**, 1716 (2001).

Translated by K. Kugel

Crystallography Reports, Vol. 49, No. 4, 2004, pp. 680–692. Translated from Kristallografiya, Vol. 49, No. 4, 2004, pp. 759–772.
Original Russian Text Copyright © 2004 by Kapustina.

For the 100th Anniversary of the Birth of A.P. Kapustin

Liquid Crystal Acoustics: A Modern View of the Problem

O. A. Kapustina

Andreev Institute of Acoustics, Russian Academy of Sciences, ul. Shvernika 4, Moscow, 117036 Russia
e-mail: bvp@akin.ru

Received October 21, 2003

Abstract—The main results of investigations in the fields of modern liquid crystal acoustics that originate from and continue the pioneering works of Prof. A.P. Kapustin are systematized and generalized. The following aspects of the problem are considered: acoustooptic phenomena, acoustoelectric interactions, acoustically induced domains, and effects of acoustical memory in liquid crystals. Acoustic devices based on liquid crystals are reviewed. *© 2004 MAIK "Nauka/Interperiodica".*

INTRODUCTION

The acoustics of liquid crystals (LCs) are based on progress in various fields of science (acoustics, crystal physics, optics, mathematics, chemistry, and electronics). On the one hand, this makes investigation of LCs a rather complex problem; on the other, this circumstance is highly favorable for the appearance of new and unexpected concepts.

The coming into being and development of modern LC acoustics are closely connected with the name of Prof. A.P. Kapustin (1904–1984). In the beginning of the 1960s, LCs were considered to promise little, and only a few enthusiasts, such as Kapustin, were carrying out investigations in this field. Even at that time, Kapustin was able to evaluate the importance of the fundamental property of LCs: the presence of an orientational degree of freedom that gives rise to a unique mesophase sensitivity to any external effect, including acoustic ones. For example, it was Kapustin who discovered the phenomenon of oscillation of the director in an LC under the action of low-frequency mechanical strains [1], and that he had been the first to see this was confirmed by an inventor's certificate (in 1968) [2]. In the 1990s, this finding stimulated investigations aimed at developing acoustic LC-based devices for seismology, electroacoustics, and hydroacoustics. In his early studies, Kapustin obtained, for the first time, quantitative data on the interrelation between the optical response of nematic LCs (NLCs) and a low-frequency mechanical strain rate and the thickness and temperature of a mesophase layer [3] and formulated the hypothesis of the hydrodynamic nature of the mechanism of the destabilizing effect of sound on LCs, which is generally accepted today. Later, these results gave an impetus to wide theoretical and experimental investigations of acoustooptic phenomena in LCs both in our country and abroad. Kapustin was the first to observe the effect of acoustically induced dynamic light scattering in LCs [4], which was discovered anew abroad almost ten years later [5]. One of the most significant of Kapustin's findings is the observation of the transition of an unordered polycrystalline LC texture into a regular system of domains in an ultrasonic field [4] that is similar to the well-known Kapustin–Williams domains [6, 7] forming in the electric field. Thereafter, this phenomenon also became a subject of intense experimental and theoretical investigations and made it possible to reveal many spatially modulated structures. The description of the effect of acoustical memory in smectic LCs (SLCs) at an action of ultrasound, observed for the first time by Kapustin [4], stimulated the search for this effect in mesophases of other types. Kapustin's studies devoted to acoustoelectric interactions in NLCs [8–11] proved to be very promising. At the end of the 1990s, these works attracted a great deal of attention and stimulated further investigations in this field of LC acoustics. In the mid-1970s, almost simultaneously with the American physicist J. Fergason, Kapustin independently established in an experiment that mechanical strains affect the wavelength of selective light reflection in cholesteric LCs (CLCs) [1]. In the mid-1980s, investigations of this effect were continued and led to the development of thermooptical ultrasonic receivers based on CLCs [12]. At present, the cycle of Kapustin's works on application of methods of ultrasonic spectroscopy to analysis of the properties of LCs near phase transitions and the pretransition states is no less promising. Even in the 1960s, a number of anomalies were found that manifest themselves during the propagation of ultrasonic waves in LCs and are related to relaxation phenomena in a medium: the dispersion of phase velocity and deviation of the frequency dependence of the ultrasonic absorption coefficient α from the classical law α/f^2 = const, where f is the ultrasonic frequency. It was found that these anomalies are most pronounced near phase transitions and in the MHz range. Kapustin was one of the first researchers to carry out systematic investigations of these anomalies in different LC mesophases. The main results of these studies were generalized in [13–15].

The purpose of this review is to systematize and generalize the results of investigations in those fields of the modern LC acoustics that originate from and continue the first studies of Kapustin, specifically:

(1) acoustooptic phenomena in LCs,

(2) acoustically induced structural transformations in LCs accompanied by formation of domains,

(3) acoustoelectric interactions in LCs,

(4) effects of acoustical memory in LCs, and

(5) LC-based acoustic devices.

The most important results and concepts reflecting the main landmarks in this field of research have been fully reported in reviews [12, 16, 17–19], monographs [13–15, 20], and books [21–23] that cover the long period of time from the early, pioneering studies up to the 1990s. The studies cited here do not exhaust all the available data on the subject and are not focused on the most important problems. However, their results make it possible to understand the overall state of affairs, analyze achievements therein, and attempt to formulate a number of new problems.

ACOUSTOOPTIC PHENOMENA IN LCS

Structural transformations in LCs in the mechanical-strain field generated by elastic waves of different types (longitudinal, surface, shear waves) lead to radical changes in the properties of LC objects. The optical characteristics of LCs change quite radically [22]. This circumstance determines the practical viability of such materials and has led to very rapid development of LC acoustooptics, which have become a promising line of development in the modern LC acoustics.

To date, the main regularities and mechanisms of structural transformations have been established for the conditions and geometry of experiments differing in the mutual orientation of the director **n** and one of the wave vectors (**k**, $\mathbf{k}_R$, $\mathbf{k}_S$) of elastic waves (see the simplified schematic diagram in Fig. 1). In these experiments, the optical response of an LC to the effect of elastic waves was measured in passing or reflected light. A cell with an LC was placed between crossed polarizers. It was found that the acoustooptical phenomena that correspond to structural transformations, as well as their interpretation and theoretical description, depend on various factors: LC type, layer geometry, initial orientation of molecules, wave-field structure, and so on. Interpreting experimental results is ambiguous. Generally, it is sufficient to use the Leslie–Ericksen hydrodynamical equations to analyze acoustooptical effects at low frequencies [24]. The explanation of some phenomena observed at high frequencies is beyond the scope of classical hydrodynamics; thus, statistical methods and the apparatus of nonlinear nonclassical hydrodynamics should be used for their description. In this context, it is convenient to choose vibration frequency as one of the criteria in classifying acoustooptical effects in LCs and introduce a frequency-dependent parameter—viscous wavelength λ_v in an LC. According to the relation between the viscous wavelength and the thickness of an LC layer d, three frequency ranges are distinguished: high ($\lambda_v \ll d$), low ($\lambda_v \gg d$), and intermediate ($\lambda_v \sim d$). In what follows, we will consider the two physical situations that have been must thoroughly studied: the structural transformations and optical response of a homeotropic NLC layer in an elastic-wave field at high and low frequencies.

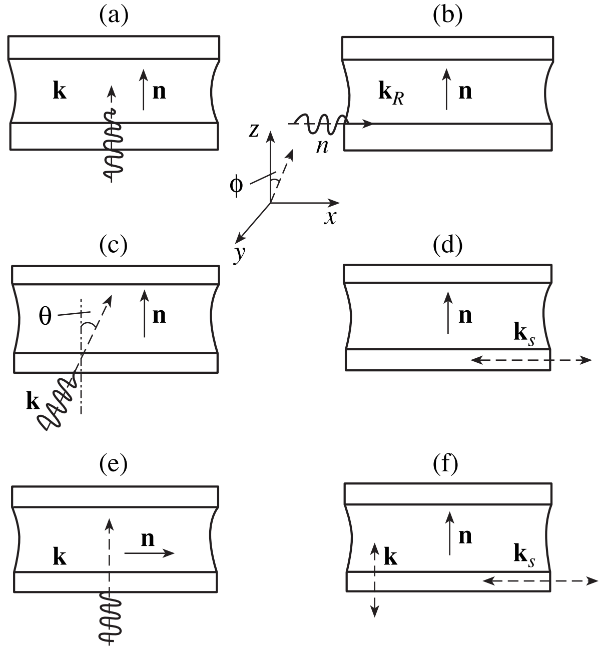

Fig. 1. Geometry of experiments aimed at studying the effect of oscillations of different types on LCs: (a) longitudinal (compression) waves, $\mathbf{k} \parallel \mathbf{n}$; (b) surface acoustic waves, $\mathbf{k}_R \perp \mathbf{n}$; (c) longitudinal waves, $\mathbf{k} \parallel \mathbf{n}$, $\theta \neq 0$; (d) shear vibrations, $\mathbf{k}_S \perp \mathbf{n}$; (e) longitudinal waves, $\mathbf{k} \perp \mathbf{n}$; and (f) shear and piston vibrations, $\mathbf{k}_S \perp \mathbf{n}$, $\mathbf{k} \parallel \mathbf{n}$. Here, **n** is the director, θ is the angle of incidence of an ultrasonic wave on an LC layer; **k**, $\mathbf{k}_R$, and $\mathbf{k}_S$ are the wave vectors of longitudinal, surface, and shear waves, respectively. A beam of polarized light (not shown) is incident normally on the layer (along the z axis).

High Frequencies

By generalizing the results of experimental studies of acoustooptical effects in NLCs at ultrasonic frequencies under the conditions shown in Figs. 1a–1c, we will formulate the basic principles that reflect the features of optical response of NLCs in these frequency ranges:

(1) structural transformations have a nonthreshold nature;

(2) at a certain intensity of elastic waves J_c, the effect of ultrasound causes clearing of an LC layer [25–29];

(3) an increase in the layer thickness leads to a decrease in the value of J_c: $J_c \sim 1/d^2$ [27, 30, 31];

(4) the dependence of J_c on frequency obeys the following law: $J_c \sim f^{-1/2}$ [16, 28, 30];

(5) the optical transparency m of a layer is nonlinearly related to the ultrasonic intensity ($m = \sin^2(\mathrm{const}J^2)$) and shows a number of maxima determined by the interference of ordinary and extraordinary light waves [31, 32]; hereinafter, we regard the optical transparency as the ratio of intensity I of the light flux passed through the system to intensity I_0 of the light flux incident on an LC layer after the polarizer;

(6) the optical transparency of a layer depends on the type of acoustic boundary conditions (a cell with either free [27] or fixed [31] edges);

(7) the optical pattern of layer clearing consists of alternating light and dark fringes, the width and contrast of which depend on the ultrasonic intensity, and the spatial period of the fringes correlating with the ultrasonic wavelength [25, 27–37]; and

(8) the configuration of fringes is determined by the type of acoustic boundary conditions, the cell geometry, and the mutual orientation of the wave vector and the director [22, 23].

Models for describing the mechanism of the effect of ultrasound on the structure of a homeotropically oriented NLC layer using the Leslie–Ericksen hydrodynamical equations, developed in well-known research centers in France [18, 29, 32], Canada [38, 39], Japan [29, 30], the United States [26, 31, 35], and Russia [40–44], are considered and analyzed in detail in [15, 16, 18, 22, 23]. At present, the approach developed in [40–44], according to which the real strain in such a structure is attributed to the action of acoustic streamings, seems to be the most justified. The mechanism of occurrence of acoustic streamings is related to either inhomogeneity of a layer compression in an ultrasonic wave or finite sizes of the layer. The theoretical models developed within this approach consider the following situations:

(1) an NLC layer with free ends [40];

(2) an NLC layer with fixed ends [41];

(3) a limited ultrasonic beam incident normally on an NLC layer;

(4) an uniform ultrasonic wave or a limited ultrasonic beam with a circular cross section incident obliquely on an NLC layer [43, 44]; and

(5) an ultrasonic wave, uniform over the cross section, incident normally on an NLC layer [45].

Specific features of the cell geometry and the effect of ultrasound on NLCs account for some differences between the proposed mechanisms of formation of acoustic streamings in the models [40–44]. Compression of a layer with free ends is transformed into a periodic motion of the fluid in the form of longitudinal waves, which, propagating over the layer, generate viscous waves that penetrate the layer bulk. Convective stresses, proportional to the product of the vibrational velocity in viscous-wave field by the layer-compression rate in the initial ultrasonic-wave field, lead to a steady fluid flow. In a layer with fixed ends, the compression inhomogeneity caused by inhomogeneity of the plate deflection near the ends serves as a source of longitudinal waves. When a limited ultrasonic beam is incident normally on the layer, longitudinal waves arise due to inhomogeneous compression near the beam boundaries; these waves propagate from the beam boundaries both deeply into and beyond the ultrasound-irradiated region. However, acoustic streamings arise only in the irradiated region, where the layer is compressed by the ultrasonic wave. In the case of oblique incidence of a uniform ultrasonic wave on an NLC layer, the occurrence of viscous waves is due to the difference in the mechanical properties of the plates (cell and nematic fluid), while the optical effect depends on the angle of incidence.

Wave patterns and fields of steady-flow velocities in NLC layers, strains in the homeotropic macrostructure, and optical transparencies of NLC layers were calculated in [40–44] for different cell and ultrasonic beam geometries. Calculations were performed on the basis of the above hypotheses in terms of linear hydrodynamics. In the cases under consideration, the optical transparency of an NLC layer and the ultrasonic intensity are related as

$$m = \sin^2\{\Delta n k_0 d^3 \eta_1 B J^2 / K_3 \rho \omega c^2\} \sin^2 2\varphi,$$

where Δn is the optical anisotropy, k_0 is the wave number of an ordinary light wave, $\omega = 2\pi f$, ρ is the NLC viscosity density, η_1 is the NLC viscosity, K_3 is the Frank elastic constant, c is the speed of sound in the NLC, B is the numerical parameter determined by the geometry of the cell and ultrasonic beam, and φ is the angle determining the orientation of polarizers with respect to the plane of acoustic streamings. The theory yields the following features of the effects under consideration: at low ultrasonic intensities, $m \sim J^4$; for an ultrasonic beam with a circular cross section, the effect may be most pronounced near the layer midpoint, where longitudinal waves are focused and the clearing is highest (Fig. 2); the typical ultrasonic intensity value at which the effect can be observed is 1 mW/cm^2; and, for oblique incidence of a uniform ultrasonic wave on a cell with an LC placed in an immersion medium (which corresponds to the real conditions of most experiments), the optical and acoustic transparencies of the layer attain maximum values at the same angle of incidence of ultrasound, and, in the maxima of acoustic transparency, the optical effect can be observed at an ultrasonic intensity of 0.01 mW/cm^2. The theoretical pattern of the effect; the calculated dependences of the layer optical transparency on ultrasonic intensity, angle of wave incidence, ultrasonic frequency, and layer thickness; and the lowest values of ultrasonic intensity at which the effect can be observed [40–44] are consistent with the experimental data [18, 26–31], which confirms the reliability of the hypothesis of the flow mechanism of reorientation of NLC molecules in the ultrasonic field. The only exception is in the case of normal incidence of an ultrasonic wave that is uniform over the cross section. An attempt to describe the reorientation of molecules in terms of linear hydrodynamics as a threshold effect arising in a system with periodically changing parameters of a medium (an analog of the Freedericksz transition [24]) was not successful: the effect is predicted to occur at ultrasonic intensities three orders of magnitude greater than the experimental ones. Only by considering this phenomenon in terms of nonlinear hydrodynamics was it possible to explain it: flows and moments that are quadratic with respect to the strain of a medium arise in the ultrasonic field and tend to reorient molecules perpendicularly to the direction of wave propagation. The joint action of these factors at ultrasonic intensities above the threshold value $J^{th} = C(\omega\tau)^2/d^2[1 + (\omega\tau)^2]$ leads to a distortion of the layer macrostructure [45]. Here, C is a combination of the parameters of an NLC (weakly dependent on temperature) and τ is the relaxation time of the orientational order parameter. The conclusions of the theory regarding strain homogeneity, dependence of the threshold intensity on layer thickness, and the value of the threshold intensity (~0.01 W/cm^2) are in agreement with the experimental data [28].

Low Frequencies

The mechanism of reorientation of molecules in homeotropic NLC layers at low frequencies is determined by oscillating hydrodynamic flows either at shear vibrations of one of the cell plates or in the presence of oscillating gradient pressure on the cell (Couette and Poiseuille flows, respectively). According to modern understandings [15, 46], an oscillating flow "tears" the director from the surface and the latter begins to oscillate with respect to the initial equilibrium position (the z axis in Fig. 1) at angles equal to $\Phi(t) = (\alpha_2\xi_0/\gamma d)\exp(i\omega t)$ (in a Couette flow) [46] and $\Phi(t) = \alpha_2\xi_0(1 - 2z/d)\exp(i\omega t)$ (in a Poiseuille flow) [47]. Here, γ is the rotational viscosity, α_2 is the Leslie viscosity coefficient, and ξ_0 is the amplitude of oscillations. The optical transparency of a layer is related to the phase difference of ordinary and extraordinary waves by the well-known expression $m = \sin^2(0.5\Delta)$.

In generalizing the published theoretical and experimental data, we will note the main features of this optical effect: the light flux passed through the polarizer–NLC-layer–analyzer system contains constant (m_0) and variable (m_{2l}) components, the latter being the sum of even harmonics ($l = 1, 2, 3, \ldots$); in a cell with fixed ends, the relation of m_0 and m_{2l} with the sound pressure amplitude P is quadratic under conditions of oblique incidence of light, and m_0 and m_{2l} are proportional to P^4 in the case of normal incidence [48]; in a cell with free ends, m_0 and m_{2l} nonlinearly depend on the amplitude of oscillations; when an optical signal is read at angles equal to $\pm[\pi(i + 0.5)/k_0\Delta nd]$ [46], m_0 and m_l are proportional to ξ_0 and the spectrum of an optical signal contains even and odd harmonics [46] ($i = 0, 1, 2, \ldots$).

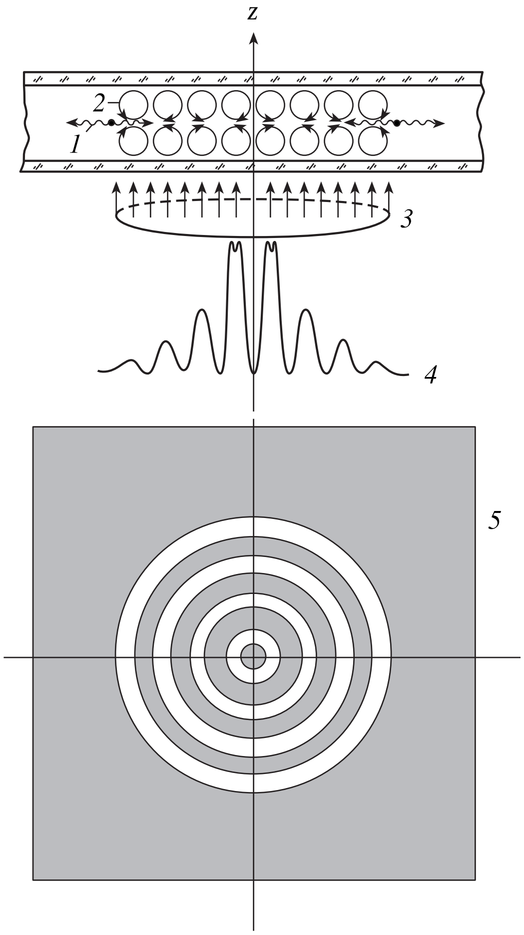

Fig. 2. Schematic of the mechanism of director reorientation for an infinitely wide NLC layer and limited ultrasonic beam of circular cross section, according to the model [42]: (*1*) longitudinal wave, (*2*) steady flow, (*3*) ultrasonic beam, (*4*) optical transmission curve, (*5*) pattern of layer clearing (view from above).

In the context of systematizing and developing a unified approach to the description of orientational phenomena in NLCs in a field of low-frequency mechanical strains, the generalized model [49] seems to be most reliable. This model, which was developed in terms of linear hydrodynamics, predicts a new mechanism of steady-state distortions of the macrostructure of a homeotropic layer related to the nonlinear interaction between the oscillations of the LC director and the velocity field under the conditions of a binary acousto-hydrodynamical effect. This effect can be implemented in the presence of simultaneous excitation of piston (along the z axis) and shear (along the x axis) plate

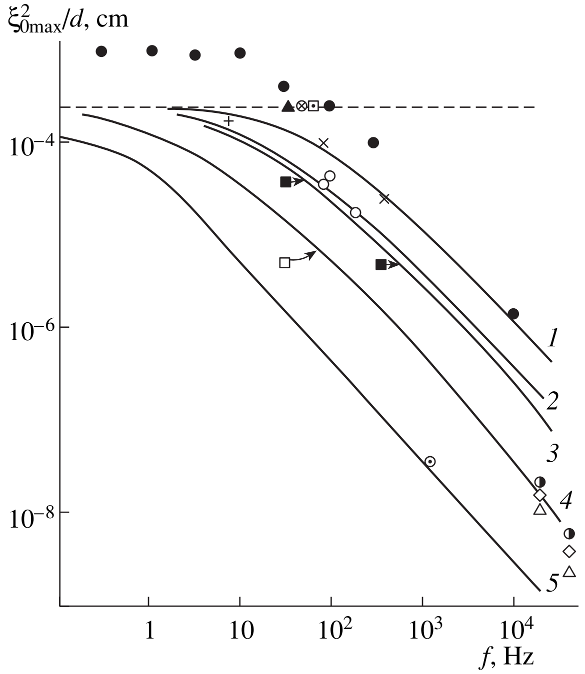

Fig. 3. Frequency dependence of the constant component of an optical signal at different values of the ellipticity parameter and layer thickness d. Linear range: theory (dotted line) and experiment for d = (▲) 37.5, (⊗) 75, (⊡) 25, and (+) 60 μm [49]. Nonlinear range: (*1–5*) theory and experiment: (×) (d = 15 μm, β = 0.02) [49]; (○) (d = 50 μm, β = 0.01) [49]; (■) (d = 15 μm, β = 0.1) [49]; (□) (d = 50 μm, β = 0.08) [49]; (⊙) (d = 50 μm, β = 0.9) [49]; (●) (d = 55 μm) [50]; (△), (◇), (◑) (d = 60, 105, and 155 μm, respectively) [51] (the values of β were not measured in [50, 51]).

vibrations in a free-end cell (Fig. 1f) at the same frequency but with a phase shift. If the amplitudes of the velocities of shear (V_0) and piston (βV_0) vibrations are such that $\beta \ll 1$, the optical response of the layer is affected by both linear and nonlinear factors. It is important that specifically nonlinear effects manifest themselves at high values of the parameter $h = 0.1\beta\gamma\omega\xi_0 d/K_3$ and become dominant at $h \gg 1$, while the optical transparency of the layer is determined by the expression $m = \sin^2(0.5p_0 + p_1\sin\omega t)$ [49]. In this range of h, the behavior of the constant and variable components of an optical signal, $m_0[p_0, J_0(p_1)]$ and $m_l[p_0, J_l(p_1)]$, respectively (the latter being the sum of the even and odd harmonics) is determined by the parameters p_0 and p_1, which depend on the viscoelastic constants of the NLC, the anchoring energy, the light wavelength, and the amplitude and frequency of vibrations. At $h \ll 1$, the nonlinear effects disappear and the optical transparency of the layer is described by the expression $m = \sin^2[0.5p_2(1 - \cos 2\omega t)]$, while the values of the constant and variable components, $m_0[p_2, J_0(p_2)]$ and $m_{2l}[p_2, J_{2l}(p_2)]$, are determined by the parameter $p_2 = 0.5\Delta n k_0 \xi_0^2 (1 - 12\beta^2 x^2/d^2)/d$, which is independent of the vibration frequency. The spectrum of a signal contains only even harmonics. Calculations show that situations can be implemented when, at $h \ll 1$, nonlinear effects manifest themselves at smaller vibration amplitudes than linear ones. This conclusion is confirmed by the set of theoretical frequency dependences of the parameter $p_2/0.5\Delta n k_0 \sim \xi_0^2/d$ (Fig. 3, curves *1–5*) calculated for $x = 0$ and the amplitude of oscillations $\xi_0^{\max}$, for the following values of the ellipticity parameter: 0.018 and 0.1 (for d = 15 μm) and 0.01, 0.08, and 0.9 (for d = 50 μm). The dotted line shows the behavior of the same parameter at $\beta = 0$. The amplitude $\xi_0^{\max}$ corresponds to the position of the first maximum of the function $m_0 = f(\xi_0^2/d)$. The correlation between the experimental results [49–51] and the theoretical data confirms the reliability of the generalized theoretical model [49].

ACOUSTICALLY INDUCED DOMAINS IN LIQUID CRYSTALS

The problem of orientational instability of the LC macrostructure in acoustic fields, which is part of the more general fundamental problem of the effect of elastic waves on dissipative anisotropic systems, deals with the formation of spatially modulated structures (domains). This is a threshold effect that is general for all types of LCs. The scale and configuration of domains depend on the initial orientation of molecules in an LC layer, the cell geometry, and the type and frequency of vibrations [15, 16, 22, 23]. In the present state of the art in this field of LC acoustics, there are two approaches to analyzing this phenomenon: classical hydrodynamics and nonequilibrium hydrodynamics. In the former approach, the mechanism of domain formation in oscillating flows of a nematic fluid, induced by low-frequency shear or piston vibrations, has been analyzed for layers with initial homeotropic or planar orientations of molecules. The latter approach makes it possible to interpret steady-state distortions in the form of domains of planar macrostructure in NLCs and CLCs caused by ultrasound.

Low-Frequency Acoustic Domains

Let us consider the properties of domains arising as a result of instabilities of different types that exist in NLCs in the low-frequency range ($\lambda_v \gg d$). We will distinguish several particular cases differing in the initial orientation of molecules in the layer and the strain type.

Homeotropically oriented layer in an oscillating Couette flow; planar periodic shear [52–59]. Under these conditions, a regular system of linear domains oriented perpendicular to the shear direction is formed in a layer. A theoretical analysis of this phenomenon was given in [53–59]. However, various simplifying assumptions (in the formulation of either initial equations [53, 54, 60] or boundary conditions [54]) led to errors in the estimations of the threshold of appearance of domains and their period and did not make it possible to obtain an exact description of the configuration of streamings and strains in the structures under consideration. In particular, computer simulation of the domain structure disregarding the inertia of a medium [57] gave values of the period of domains and the threshold of their appearance correlating with the experimental data [57] only at frequencies below 100 Hz. At higher frequencies, there were both qualitative and quantitative discrepancies. The most complete theoretical description of domains—adequate to the results of experiments known to date—was given in [59]. The analysis of this phenomenon was based on the linear hydrodynamical equations, in which the quadratic terms proportional to the product of the angle of rotation of molecules by the velocity of the fluid are retained. It was found that steady-state stresses and moments, which destabilize the initial structure, are nonzero if the velocity of fluid in vortex oscillating flows is phase-delayed with respect to the velocity of fluid in the Couette flow. This lag is determined by the inertial properties of a medium and the elastic moments acting on the director in thin (of the same order of magnitude as the wavelength of the orientational wave) boundary LC layers. These effects manifest themselves in different frequency ranges (the boundary effects are observed at low frequencies, whereas the inertia of the medium manifests itself at higher frequencies) and are characterized by different threshold amplitudes ($\xi_0^{th} \sim 1/(\omega d^2)^{1/4}$ and $\xi_0^{th} \sim 1/\omega d^2$ at low and high frequencies, respectively) and domain periods ($\Lambda \sim 0.6d$ and $\Lambda' \sim 1.01d$, respectively). Although experimental data on the threshold characteristics of domains have been obtained for wide frequency ranges (0.01–200 Hz [55, 57] and 0.1–100 kHz [52]), their comparison with the results of calculations encounters certain difficulties. The point is that the data obtained by different researchers for the same layer thickness not only differ by several times, but also contradict each other. Therefore, one cannot draw unambiguous conclusions from numerical comparison of the theory with experiment. At the same time, numerical calculation of the dependences of the threshold amplitude on parameter $\omega\tau_0$ ($\tau_0 = \gamma d^2/K_3$ is the time of relaxation of the perturbed NLC director to its initial state) is in agreement with the experimental data [55, 57], but contradicts the results of previous experiments [52]. Different threshold amplitudes were obtained by different researchers [52, 55, 57] for the same values of $\omega\tau_0$. For more detailed comparison of the theoretical and experimental data, additional investigations on samples about 100 μm thick at frequencies above 100 Hz are required. The theoretical dependence of the reduced domain period Λ/d on $\omega\tau_0$ is consistent with the experimental data [55, 57] only at higher frequencies. At low frequencies, the theoretical value of the domain period is smaller than the experimental one by a factor of 1.5. Note that, in the calculations performed in [59], a real velocity profile for an unperturbed Couette flow and exact boundary conditions for velocities of vortex oscillating flows were used for the first time, which made it possible to obtain, at higher frequencies, values of threshold amplitudes exceeding those obtained by simplified calculations [54] threefold. According to the theory [59], in going from rigid to weak anchoring of molecules, the threshold characteristic of domains change only weakly. This suggests that the boundary conditions are not decisive in determining the steady angle of rotation of the director.

Homeotropic structure of an NLC under the conditions of elliptical shear. The cell plates vibrate in the *xy* plane in mutually perpendicular directions (along the *x* and *y* axes) with a phase shift of 0.5π [57, 61–65]. Under these conditions, a system of linear domains is formed with a period that is proportional to the layer thickness; the domains are located in the *xy* plane, making an angle determined by the ratio of the ellipse components with the *x* axis. The first experimental data on these domains (often referred to as roll domains) and their threshold characteristics in the frequency range from 200 to 500 Hz for layers 20–100 μm thick, reported in [61], were explained in the theoretical studies of the Orsay group [62, 63]. The mechanism of domain formation under these conditions is the same as in the case of a planar oscillating shear: the enhancement of an initial random orientational distortion at an interaction of the velocity field with the LC-director field. The experimental data suggest that the form of the threshold diagram, which shows the ratios of the amplitudes of the *x* and *y* components of motion, depends on the layer thickness. In thick layers, this diagram can be approximated by the expression $\omega\xi_{0x} \cdot \xi_{0y} = \text{const}$ [64]. Investigations of the instability dynamics showed that, at a critical value of the combination of parameters $\omega\xi_{0x}\xi_{0y}/D$, roll domains become distorted and a structure composed of regular (hexagonal and square) elements arises in the layer [65]. Here, D is the orientational diffusivity of the NLC [24]. A further increase in the vibration amplitude results in the melting of these elements and the formation of a polycrystalline fluctuating structure.

Planar structure of an NLC in an oscillating Couette flow induced by a planar shift [19, 66–70]. Under these conditions, the formation of a system of linear domains oriented along the shear direction is determined by a mechanism known as Guyon–Pieranski roll instability [19, 66, 67]. This type of domain was first observed and systematically studied for the case of a director oriented perpendicularly to the velocity vector of an oscillating flow [66]. These experiments were focused on the change in the threshold characteristics of domains in the frequency range 0.4–0.7 Hz under the action of stabilizing electric and magnetic fields. This change is due to the evolution of roll instabilities of different types. Data on the structures forming in planar NLC layers in the case of parallel orientation of the director and the velocity vector are very limited [68]. The formation of domains in the case of an arbitrary angle θ_0 between the LC director and the flow direction was considered for the first time in [69]. Analysis of the linearized system of equations for the angles between the director and the flow velocity vector—isolated from the Leslie–Ericksen equations—for the existence of periodic undamped solutions leads to following expression for determination of the domain threshold characteristics:

$$[S^{th}(q)]^2 = \{2b_1^2b_2^2 + a_1a_2\omega^2[b_1^2 + b_2^2 \pm (b_1^2 - b_2^2)]\}/c_1c_2b_1b_2.$$

Here, a_1, a_2, b_1, b_2, c_1, and c_2 are the coefficients depending on the angle θ_0, Frank elastic constants, Leslie viscosity coefficients, and the distortion wave numbers $q = 2\pi/\Lambda$, $p = 2\pi/d$, and S^{th} is the threshold gradient of the flow velocity. The results of numerical calculation of the threshold characteristics of domains [69] are in agreement with the experimental data obtained for NLC layers 10–150 μm thick in the frequency range 1–20 Hz for the angle θ_0 varied from 0° to 90° [70]. Experiments confirmed the predictions of the theory about the formation of structures of two types (previously known Guyon–Pieranski domains with period $\Lambda \sim d$ [66] and new structures with period $\Lambda < d$), as well as the existence of a critical angle, $\theta_0 = f(\alpha_2, \alpha_3, \alpha_5)$, separating the regions where structures of different types are formed. Note that an unambiguous conclusion about the universality of the model [69] requires additional experimental studies in a wider frequency range.

High-Frequency Domains

Let us now consider the domains arising in planar NLC and CLC layers under the action of ultrasound. As was mentioned above, in the high-frequency range ($\lambda_v \ll d$), explanation of the phenomenon of orientational instability is beyond classical hydrodynamics. We will consider two particular cases that differ in mesophase type.

Planar NLC layer in the ultrasonic compression field; the director and wave vector k (Fig. 1d) are orthogonal [71–73]. Under these conditions, one-dimensional (1D) domains arise, forming a set of light and dark fringes perpendicular to the director; the period of these fringes is determined by the layer thickness and is independent of the ultrasonic frequency [72]. The mechanism of formation and the threshold characteristics of this system of domains can only be described in terms of a new physical approach based on the concepts of nonequilibrium hydrodynamics. This conclusion was substantiated experimentally for the first time in [72]. The theoretical model [73] developed within the new approach takes into account two relaxation processes (critical and normal [14]) and postulates the following physical mechanism of the domain formation: at a random and nonuniform along the layer length (x axis) deviation of molecules from their initial position in the xz plane at angle Φ, compression of the medium in an ultrasonic wave causes anisotropic shear stresses $\sigma_{ij}(\Phi, \mu_3, \Delta E, U_{zz}, V_{zz})$, which give rise to oscillating vortex flows that are periodic along the layer. These flows interact with the ultrasonic field, generating shear stresses $\langle\sigma_{ij}\rangle$, which, in turn, give rise to steady flows that enhance the initial distortion. At the effect threshold, the action of viscosity moments compensates stabilizing elastic Frank moments. Here, μ_3 and ΔE are the second coefficient of viscosity and the anisotropy of the dynamic modulus of elasticity of an NLC, respectively, and U_{zz} and V_{zz} are the compression and compression rate in an ultrasonic wave. According to the theory, the general form of the threshold characteristics of domains can be described by the expressions $V^{th} = 0.5\pi c[\eta F(s_{\min})K_3/\gamma\Delta E]^{1/2}/d$ and $\Lambda = d/(s_{\min})^{1/2}$, where $s_{\min}$ is the value of the parameter $s = (q/p)^2$ minimizing the function $F(s)$. Numerical calculations yield $s_{\min} = 3.7$ and 4.8 for low and high ultrasonic frequencies, respectively, and, accordingly, the domain periods $0.52d$ and $0.48d$. The latter values are in good agreement with experiment [72]. It follows from the theory that the period of domains is frequency-independent and the threshold vibrational velocity decreases insignificantly with an increase in the layer thickness. In the frequency range 1–10 MHz, these facts are also consistent with the experimental data [71]. Since domains were not observed in planar NLC layers at higher ultrasonic frequencies, we cannot make an unambiguous conclusion about the universality of the model [73].

Planar CLC layer in the field of ultrasonic-wave compression. The helix axis and the wave vector **k** are parallel, and the helix pitch is much smaller than the layer thickness [16, 74–82]. Under these conditions, two-dimensional (2D) domains arise in the form of a set of equidistant bright fringes that are parallel and perpendicular to the layer director (the so-called square grid, the period of which correlates with the layer thickness and the helix pitch) [16, 74]. An attempt to describe this phenomenon in terms of linear hydrodynamics [75] showed such a significant quantitative discrepancy between the results of calculation and the experimental data [76, 77] that the necessity of using other conceptions became evident. Taking into account the processes of relaxation of the orientational order parameter in the ultrasonic field, which lead to anisotropy of the dynamic modulus of elasticity of a medium and change the character of the fluid motion, made obtaining a more adequate theoretical description possible [78]. The new approach was developed in [79, 80], where an even subtler effect (manifesting itself at higher frequencies) was taken into consideration: shear lag in oscillating flows due to the relaxation in a medium and the viscoelastic character of the LC strain. By generalizing the theoretical results [78–80], we can predict two mechanisms of destabilization of a planar CLC structure in the ultrasonic field: vortex and relaxation ones. The vortex theory is based on the classical hydrodynamical equations; nevertheless, it takes into account the above-mentioned shear lag in vortex oscillating flows at ultrasonic frequencies. The mechanism of domain formation is similar to that described above: it consists in the enhancement of a random and periodic over the layer deviation of the director from the equilibrium orientation. The vortex mechanism is most efficient in the frequency ranges satisfying the condition $1/a \ll \omega \ll 1/\tau$, where $a = \rho/(\eta\tau q_0^2)$ and q_0 is the wave number of domains with period Λ_0 that are formed at a static stretching of a CLC layer along the helix axis at a critical value [24, 75]. The threshold characteristics of vortex domains are determined by the relations

$$M^{th} \sim (q_0/q)\{A(3+b)(1-\delta)/\tau\Delta E\},\ \Lambda = \Lambda_0 = 2\pi/q_0. \quad (1)$$

Here, $b = K_2/K_3$, K_2 is the Frank elastic constant, A is the numerical parameter that relates the viscoelastic characteristics of a CLC, M^{th} is the threshold compression, and δ is the ratio of the layer stretching to the critical value δ_0. It can be seen that, in the frequency range limited by the above inequality, the threshold domain period and the threshold compression are independent of ultrasonic frequency; beyond this frequency range, the threshold compression increases with both increasing and decreasing frequency. The nonlinear relaxation theory of destabilization of a planar CLC structure takes into account the nonlinear corrections in the hydrodynamical equations that are related to the processes of structural relaxation of the mesophase. The point is that the Leslie viscosity coefficients depend on the degree of orientational order and change with a change in the orientational order when ultrasonic and viscous waves strain the medium. The relaxation delay of these changes with respect to the strain of the medium in an external ultrasonic field leads to the occurrence of steady stresses and moments that have a relaxation nature and are not related to the occurrence of additional vortex flows in the medium. When only the relaxation nonlinear mechanism works, the expressions for the threshold compression and the domain period have the form

$$\begin{gathered} M^{th} \sim \{B(3+b)q_0^2(1-\delta)[1+(\omega\tau)^2]/(\omega\tau)^2\}^{1/2}, \\ \Lambda = \Lambda_0 = 2\pi[2b/(3+b)]^{1/4}/(P_0 d)^{1/2}. \end{gathered} \quad (2)$$

Here, B is the combination of the viscoelastic parameters of a CLC and the parameters determined by the cell geometry. The action of the nonlinear mechanism is most efficient at frequencies $\omega > 1/\tau$. It follows from comparison of formulas (1) and (2) that two independent mechanisms lead to the formation of domains with the same frequency-independent period, and, thus, they cannot be distinguished visually. However, there is a difference in the relationship between the threshold instability and the helix pitch: $M^{th} \sim P_0^{1/2}$ and $M^{th} \sim 1/P_0^{1/2}$ for the vortex and nonlinear mechanisms, respectively. This makes it possible to identify the action of different mechanisms in an experiment. It is important that these mechanisms, being dominant in different frequency ranges, supplement each other, this leading to a weak dependence of the threshold compression on the ultrasonic frequency (Fig. 4) and significantly expanding the frequency range in which this effect can manifest itself. The experimental data are in agreement with the results of numerical calculations. The value of the boundary frequency separating the regions where different mechanisms work is $\omega_0 \sim 0.023 d\tau/P_0$ [80]. As observations show, sometimes domains arise in CLC layer regions stretched along the helix axis. In planar layers, these are regions limited by pair disclinations [24, 74, 81]; in layers with nonparallel boundaries, these are regions near Grangin lines [24, 76]. The theory takes this factor into account via the parameter δ.

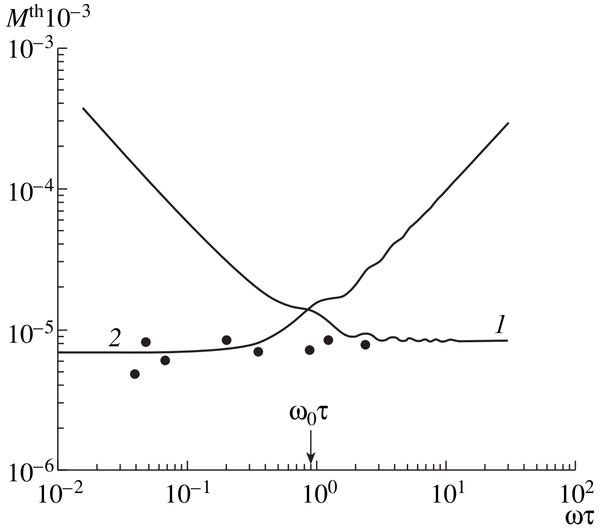

Fig. 4. Comparison of theoretical and experimental dependences of the threshold compression of CLCs in the elastic-wave field on the reduced ultrasonic frequency: (*1*) relaxation mechanism, (*2*) vortex mechanism (theory: d = 100 μm, P_0 = 10 μm, δ = 0.8, $\tau = 3 \times 10^{-8}$); and (●) experimental data for the frequency range 0.35–14.5 MHz, δ = 0.7, d = 80 μm [81].

The correlation of the theory that takes into account the relaxation processes in a medium with the experimental results indicates that these processes may play a key role in the formation of domains in CLCs under the action of ultrasound and should be taken into account in analysis of orientational phenomena.

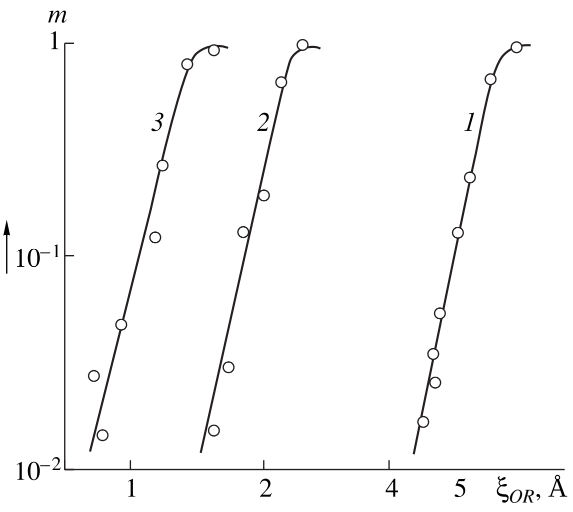

Fig. 5. Optical transmittance of an NLC layer 40 μm thick as a function of the surface-wave amplitude at a frequency of 6 MHz in a transverse electric field at voltages close to the Freedericksz transition threshold: (*1*–*3*) theory for (*1*) zero electric field and voltages of (*2*) 4.5 and (*3*) 4.6 V and (○) experimental data for the same conditions.

A new acoustic method [82] has been developed to estimate the relaxation time τ, which is simpler than conventional methods of ultrasonic spectroscopy.

ACOUSTOELECTRIC INTERACTION IN LIQUID CRYSTALS

Investigations in the field of LC electroacoustics are, to a large extent, related to the search for methods for controlling and optimizing the functional characteristics of acoustooptical LC-based devices designed for information mapping systems. By analyzing the results of these studies (which are reported in greater detail in [15]), we can classify according to two criteria: the geometry of the experiment and the sign of dielectric anisotropy $\Delta\varepsilon$:

(1) the transverse electric field (the director and vector **E** are parallel to the *z* axis), $\Delta\varepsilon > 0$ [28, 36, 83–91];

(2) the transverse electric field, $\Delta\varepsilon < 0$ [18, 92–94]; and

(3) the longitudinal electric field (the director parallel to the *z* axis and the vector **E** parallel to the *x* axis), $\Delta\varepsilon < 0$ [95].

The physics and specific features of orientational phenomena in NLCs under conditions of the joint effect of electric and acoustic fields were investigated in [85–94]. Among these studies, those devoted to secondary phenomena deserve particular attention. For example, the effect of local rotation of the director was found experimentally in homeotropic NLC layers in a transverse electric field under the action of mechanical strains (in-plane shear [87, 93], elliptical shear [57, 94], and compression [57]) at sound (50–500 Hz) and ultrasonic frequencies (1–100 kHz). From the results of systematic experimental and theoretical investigations of the effect of surface acoustic waves (in the frequency range 6–30 MHz) on NLC layers in a transverse electric field (with a frequency of ~50 Hz), we report a set of curves illustrating the relationship between the optical transparency of an NLC layer and the wave amplitude in the absence of the electric field and at voltages of 4.5 and 4.6 V (Fig. 5). What is of importance is that, near the Freedericksz transition [24], the sensitivity of NLCs to the acoustic effect increases by more than an order of magnitude. According to the theory in [92], there is a relation—$m(E) = m(0)E_0^4/\pi^4(E_0 - E)^4$—that is in good agreement with the experimental data. Here, E_0 corresponds to the Freedericksz transition threshold.

EFFECT OF ACOUSTIC MEMORY

Among the effects that are known to date of acoustic memory in LCs, the following should be noted:

(1) acoustic memory in CLCs—an analog of the electrooptical effect of dynamic light scattering with memory [96];

(2) acoustic memory in CLCs, related to the formation of bubble domains [97–100]; and

(3) acoustic memory at the NLC–SLC phase transition [10].

Acoustic Dynamic Light Scattering with Memory

There is only a small amount of experimental data on this effect [83, 96]. In plane CLC layers with a large helix pitch, the effect of mechanical strains generated by ultrasonic waves leads to the occurrence of a residual strain due to the reconstruction of the initial macrostructure. The mechanism of this phenomenon is related to the nonlinear acoustic effect—the occurrence of acoustic streamings. At high intensities of ultrasound, these streamings lead to the formation of a polydomain structure that can scatter light intensively (acoustic dynamic light scattering [27]). The nature of the slow reconstruction of the planar macrostructure (this process is referred to as the acoustic memory of an LC) has not been studied. However, it is known that the reconstruction of the initial planar orientation can be enhanced by an ac electric field (~20 kHz). It has been ascertained experimentally that the residual light scattering is about 0.5*K*, where *K* is the coefficient of attenuation of a specularly reflected light beam, the value of which is determined by the ultrasonic intensity [96]. We should note that this effect can be used in acoustic-information mapping systems if the processes of recording of an acoustic image and its analysis need to be separated in time and space [15].

Bubble Domains in CLCs

The physical nature of another mechanism of acoustic memory is related to the formation of a stable inhomogeneous structure in the form of a system of bubble domains that intensively scatter light in a layer with homeotropic boundary conditions [97] in the stage of CLC relaxation after the action of ultrasound. This effect occurs only if, during the irradiation, the ultrasound intensity attains the threshold value corresponding to the occurrence of acoustic dynamic light scattering [27]. There exists a certain relationship between diameter D of bubble domains, the layer thickness, and the helix pitch (Fig. 6a); the change in the ultrasonic frequency in the range 0.5–3 MHz does not affect the form of the function $D(d, P_0)$. The experimental data are in good agreement with the theory given in [99], which attributes the formation and relatively high stability of bubble domains to the presence of defects (disclinations [24]) that fix bubble domains. The correlation of the theoretical results (curve I) with the experimental data (especially at $d/P_0 < 1.5$) is quite satisfactory. Some discrepancy at $d/P_0 > 1.5$ is due to the increase in the packing density of bubble domains under these conditions and their interaction with each other, which is disregarded in the theory [99]. The free energy $F_{\min}$ of a stable bubble domain fixed by disclinations also depends on d/P_0 (curve II). At $d/P_0 < 0.5$, the homeotropic orientation is more stable than the texture with a system of bubble domains, since $F_{\min}/F_r > 1$ (F_r is the free energy of the homeotropic macrostructure). The forced reconstruction of the initial homeotropic structure is performed by applying an ac electric field.

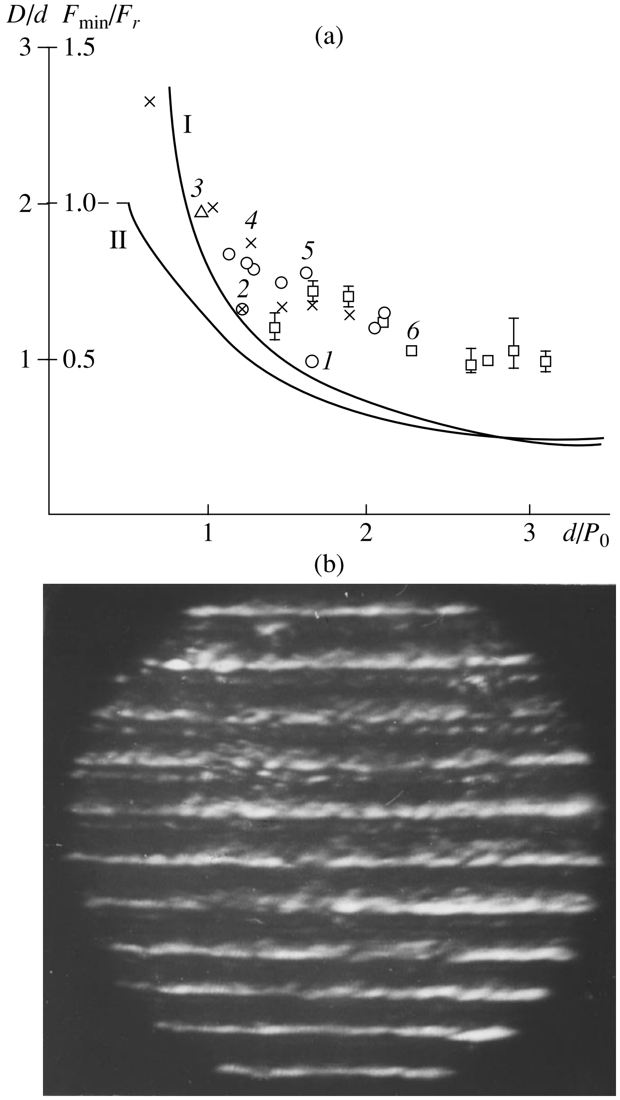

Fig. 6. Effect of acoustic memory in LCs of different types. (a) Dependences of the (I) diameter and (II) free energy of a bubble domain in CLCs on helix pitch; comparison of the theoretical and experimental data: (*1*–*4*) for samples with a helix pitch of 3, 4.2, 10.5, and 48 μm, respectively, at a frequency of 0.22 MHz; (*5*), (*6*) for samples with a helix pitch of 48 μm at frequencies of 0.5 and 3 MHz, respectively; the layer thickness was varied within 10–150 μm; dashed straight line: $F_{\min} = F_r$. (b) Optical phase grating formed at the NLC–SLC-A phase transition in a nonuniformly heated sample.

Acoustic Memory at the Phase Transition in a Nonuniformly Heated LC layer

If a temperature gradient is formed in a plane LC layer along the x axis ($\partial T/\partial x = b$), the bulk modulus $K(x)$ will be inhomogeneous along the same direction: $\partial K/\partial x = b\partial K/\partial T$. A uniform strain in the layer $\Delta V/V$ leads to nonuniform distribution of pressure $P(x)$ over the layer as a result of the dependence $K(x)$. Here, ΔV is a change in the volume V with a change in the pressure by ΔP. Thus, a compression of a nonuniformly heated CLC layer gives rise to volume force $F(x)$, which causes motion of the fluid, rotation of the director by an angle of $\Phi(x, z) \sim \text{const}(0.25d^2 - z)zF(x)$, and clearing of a certain portion of the layer. This unique effect was observed in a homeotropic LC layer having a nematic phase and three smectic phases in the temperature range of the existence of the nematic phase upon cooling the LC from the isotropic state [10]. If the layer is subjected to compression at a temperature close to that of the NLC–SLC A phase transition, the orientational distortion is retained after the strain removal, manifesting itself as a bright fringe. It is a matter of importance that, although the layer is compressed over the entire plane, this fringe arises only in a certain region, the position of which is set by the temperature distribution over the layer, and changes with time. In this region, tilted molecules do not return to the initial homeotropic position due to the increase in the fluid viscosity with decreasing temperature and, as phase A forms, they are “frozen” in this state. By using multiple applications and removals of compression, one can form a system of parallel bright fringes in a layer, the number of which is determined by the repetition frequency of compression cycles and the rate of temperature variation over the layer. The width of the fringes is determined by the force and duration of compressions (Fig. 6b). With a decrease in temperature, the layer, passing successively through different smectic phases, demonstrates another texture. However, after the transition between the second and third low-temperature smectic phases, the pattern of regular fringes in the layer becomes completely reconstructed and remains the same even at layer solidification. These effects are interesting and important from a practical point of view—for development of phase gratings with a step determined and controlled by an external acoustic effect.

ACOUSTIC DEVICES BASED ON LIQUID CRYSTALS

During recent decades, applied aspects of LC acoustics have been the focus of the attention of physicists and engineers. In our opinion, the work that has aimed at designing LC-based acoustooptical devices for reception, analysis, transformation, and transfer of information has been most significant. Since the body of applied data stored to date is extremely large, we refer those who are interested to [12, 15, 17, 18] and restrict ourselves only to a brief description of the group of devices based on the method of measurement of perturbations claimed in Kapustin's invention [2]. These are parametric acoustooptical devices based on the same physical principle (polarization modulation of light), with a sensitive element in the form of an NLC layer with homeotropic or quasi-homeotropic orientation of molecules. These devices are designed for different purposes but have the same functional scheme including, along with a sensitive element, a light-emitting diode, a photodiode, a communication line (optical or electric), and a quantum-electronic module for analog signal processing. Acoustooptical transformation can be linearized in two ways: by either reading data at optimum angles ($\beta_i = \pm\pi[(i + 0.5)/k_0\Delta nd)$ for homeotropic orientation of molecules [46, 101] or creating an initial static distortion of the orientation $\Phi(z) \sim 2z/d$ in the layer, reproducing its dynamic distortion in the oscillating hydrodynamic flow formed by an external effect [102]. With a proper design of the sensitive element [46, 103, 104], NLC-based acoustooptical devices can detect variations in the main physical parameters characterizing the state of environment. Various devices have been developed to measure variations in pressure, rates of temperature fluctuations, and angular and linear vibrational velocities and accelerations. These devices operate in the dynamic range ~100 dB and have a planar or descending (as $1/f$) amplitude–frequency characteristic. Their advantages are compatibility with the modern optical element base, the possibility of using multimode optical fibers and nonmonochromatic light sources, simple and universal constructions, low thresholds of signal detection, wide frequency ranges (from 0.001 to 100 Hz), the ability to adapt to changing external conditions within certain limits, and high selectivity to measurable parameters. The field of application of these devices is very wide: seismology (including vector seismology), vibrometry, electroacoustics, navigation (including orientation of a moving object in space), criminology, acoustic measurements, meteorology (including dynamic microbarometry and field temperature measurements), and so on.

REFERENCES

1. A. P. Kapustin, Izv. Vyssh. Uchebn. Zaved., Fiz., No. 11, 55 (1967).
2. A. P. Kapustin, Byull. Izobrer., No. 224102, 25 (1968).
3. A. P. Kapustin, Z. Kh. Kuvatov, and A. I. Trofimov, Izv. Vyssh. Uchebn. Zaved., Fiz., No. 4, 150 (1971).
4. A. P. Kapustin and L. M. Dmitriev, Kristallografiya **7** (2), 332 (1962) [Sov. Phys. Crystallogr. **7**, 263 (1962)].
5. L. W. Kessler and S. P. Sawyer, Appl. Phys. Lett. **17** (10), 440 (1970).
6. G. E. Zvereva, in *Application of Ultrasonics for Studying Substance* (MOPI, Moscow, 1961), Vol. 15, p. 69.
7. R. Williams, J. Chem. Phys. **39**, 384 (1963).
8. A. P. Kapustin, Kristallografiya **14** (5), 943 (1969) [Sov. Phys. Crystallogr. **14**, 819 (1969)].
9. A. P. Kapustin and D. Demus, Kristallografiya **23** (2), 430 (1978) [Sov. Phys. Crystallogr. **23**, 241 (1978)].
10. A. P. Kapustin and S. A. Pikin, Pis'ma Zh. Éksp. Teor. Fiz. **33**, 332 (1981) [JETP Lett. **33**, 316 (1981)].
11. A. P. Kapustin and S. S. Yakovenko, Kristallografiya **28** (3), 609 (1983) [Sov. Phys. Crystallogr. **28**, 361 (1983)].
12. F. F. Legusha, Usp. Fiz. Nauk **144** (3), 509 (1984) [Sov. Phys. Usp. **27**, 887 (1984)].
13. A. P. Kapustin, *Electrooptical and Acoustic Properties of Liquid Crystals* (Nauka, Moscow, 1973).
14. A. P. Kapustin, *Experimental Studies of Liquid Crystals* (Nauka, Moscow, 1978).
15. A. P. Kapustin and O. A. Kapustina, *Acoustics of Liquid Crystals* (Nauka, Moscow, 1985).
16. O. A. Kapustina, Mol. Cryst. Liq. Cryst. **112** (1–2), 112 (1982).
17. K. Miyano and J. Ketterson, Phys. Rev. A **12**, 615 (1975).
18. J. N. Perbet, M. Harang, S. Le Berre, and B. Mourrey, Rev. Tech. Thomson–CSF **11**, 837 (1979).
19. E. Dubois-Violette, E. Guyon, I. Janossy, *et al.*, J. Mec. **16**, 733 (1977).
20. P. Khabibullaev, E. Gevorkyan, and A. Lagunov, *Reology of Liquid Crystals* (Allerton, New York, 1994), Chaps. 3.2, 6.3, 6.4.
21. *Advances in Liquid Crystals*, Ed. by G. Brown (Gordon and Breach, New York, 1978), Vol. 3, p. 163.
22. *Handbook of Liquid Crystals*, Ed. by D. Demus *et al.* (Wiley–VCH, Weinheim, 1998), Vol. 1, p. 549.
23. *Physical Properties of Liquid Crystals*, Ed. by D. Demus, J. Goodby, G. W. Gray, H. W. Spiess, and V. Vill (Wiley, Weinheim, 1999), p. 447.
24. P. de Gennes, *The Physics of Liquid Crystals* (Clarendon Press, Oxford, 1974; Mir, Moscow, 1977).

25. L. E. Devis and J. Chambers, Electron. Lett. **7**, 287 (1971).
26. H. Mailler, L. L. Likins, T. R. Teilor, and J. L. Fergason, Appl. Phys. Lett. **18**, 105 (1971).
27. O. A. Kapustina and V. N. Lupanov, Akust. Zh. **23** (3), 390 (1977) [Sov. Phys. Acoust. **23**, 218 (1977)].
28. S. Nagai and K. Iizuka, Jpn. J. Appl. Phys. **13**, 189 (1974); Jpn. J. Appl. Phys. **17**, 723 (1978); Mol. Cryst. Liq. Cryst. **45**, 83 (1978).
29. S. Nagai, A. Peters, and S. Candau, Rev. Phys. Appl. **12**, 21 (1977).
30. T. Hatakeyama and Y. Kagawa, J. Acoust. Soc. Jpn. **32**, 92 (1976); J. Sound Vibr. **46**, 551 (1976).
31. Ch. Sripaipan, Ch. F. Hayes, and G. T. Fang, Phys. Rev. A **15**, 1297 (1977).
32. I. Lebran, S. Candau, and S. Letcher, J. Acoust. Soc. Am. **63**, 55 (1978); J. Phys. (Paris) **40**, 298 (1979).
33. A. P. Kapustin and O. A. Kapustina, Krist. Tech. **8**, 237 (1973).
34. O. A. Kapustina and A. A. Talashev, Akust. Zh. **19**, 626 (1973) [Sov. Phys. Acoust. **19**, 397 (1973)].
35. K. Miyano and Y. R. Shen, Appl. Phys. Lett. **28**, 473 (1976); Appl. Phys. Lett. **28**, 699 (1976); Phys. Rev. A **15**, 2471 (1977).
36. S. Sato and H. Uedo, Jpn. J. Appl. Phys. **20**, 511 (1981).
37. D. I. Anikeev, Yu. V. Bocharov, O. A. Kapustina, and A. D. Vuzhva, Akust. Zh. **35**, 966 (1989) [Sov. Phys. Acoust. **35**, 563 (1989)].
38. J. L. Dion and A. D. Jacob, Appl. Phys. Lett. **31**, 490 (1977); IEEE Trans. Ultrason. Ferroelectr. Freq. Control **34**, 550 (1987).
39. J. L. Dion, A. Le Blanc, and A. D. Jacob, Acoust. Imaging **10**, 151 (1982).
40. E. N. Kozhevnikov, Akust. Zh. **27**, 533 (1981) [Sov. Phys. Acoust. **27**, 297 (1981)].
41. E. N. Kozhevnikov and N. K. Gus’kov, Akust. Zh. **29**, 38 (1983) [Sov. Phys. Acoust. **29**, 21 (1983)].
42. E. N. Kozhevnikov, Zh. Éksp. Teor. Fiz. **82** (1), 161 (1982) [Sov. Phys. JETP **55**, 96 (1982)].
43. E. N. Kozhevnikov, Akust. Zh. **28**, 136 (1982) [Sov. Phys. Acoust. **28**, 84 (1982)].
44. E. I. Zhukovskaya, E. N. Kozhevnikov, and V. M. Podol’skiĭ, Zh. Éksp. Teor. Fiz. **83**, 207 (1982) [Sov. Phys. JETP **56**, 113 (1982)].
45. E. N. Kozhevnikov and N. G. Dolmatova, Vestn. Samar. Gos. Univ., No. 2(4), 142 (1997).
46. É. L. Vinogradova, O. A. Kapustina, V. N. Reshetov, *et al.*, Akust. Zh. **31**, 101 (1985) [Sov. Phys. Acoust. **31**, 10 (1985)].
47. L. M. Blinov, S. A. Davidyan, V. N. Reshetov, and D. B. Subachyus, Zh. Éksp. Teor. Fiz. **97** (5), 1597 (1990) [Sov. Phys. JETP **70**, 902 (1990)].
48. E. N. Kozhevnikov, Akust. Zh. **28**, 238 (1982) [Sov. Phys. Acoust. **28**, 143 (1982)].
49. O. A. Kapustina, E. N. Kozhevnikov, and G. N. Yakovenko, Zh. Éksp. Teor. Fiz. **87** (3), 849 (1984) [Sov. Phys. JETP **60**, 483 (1984)].
50. H. Bruchmuller, Acustica **40**, 155 (1978).
51. Y. Kagawa, T. Hatakeyama, and Y. Tanaka, J. Acoust. Soc. Jpn. **31**, 81 (1975).
52. G. N. Belova and E. I. Remizova, Akust. Zh. **31**, 289 (1985) [Sov. Phys. Acoust. **31**, 171 (1985)]; Kristallografiya **31**, 517 (1976) [Sov. Phys. Crystallogr. **31**, 304 (1976)].
53. E. N. Kozhevnikov, Zh. Éksp. Teor. Fiz. **91**, 1346 (1986) [Sov. Phys. JETP **64**, 793 (1986)].
54. S. J. Nogan, T. Mullen, and P. Woodford, Proc. R. Soc. London, Ser. A **441**, 559 (1993).
55. T. Borsonyi, A. Buka, A. P. Krekhov, and L. Kramer, Phys. Rev. E **58**, 7419 (1998).
56. O. S. Tarasov and A. P. Krekhov, Kristallografiya **44** (6), 1121 (1999) [Crystallogr. Rep. **44**, 1050 (1999)].
57. F. P. Krekhov, T. Borsonyi, P. Totch, *et al.*, Phys. Rep. **337**, 171 (2000).
58. A. P. Krekhov and L. Kramer, Phys. Rev. E **53** (5), 4925 (1996).
59. E. N. Kozhevnikov, Vestn. Perm. Univ., Fiz., No. 1, 63 (2002).
60. I. A. Chaban, Akust. Zh. **24**, 260 (1978) [Sov. Phys. Acoust. **24**, 145 (1978)]; Akust. Zh. **31**, 132 (1985) [Sov. Phys. Acoust. **31**, 77 (1985)].
61. P. Pieranski and E. Guyon, Phys. Rev. Lett. **39**, 1280 (1977).
62. F. Rothen and E. Dubois-Violette, J. Phys. (Paris) **38**, 1039 (1978).
63. J. Sadik, F. Rothen, and W. Bestgen, J. Phys. (Paris) **42**, 915 (1981).
64. J. M. Dreyfus and E. Guyon, J. Phys. (Paris) **42**, 283 (1981).
65. E. Guazzelli and E. Guyon, J. Phys. (Paris) **43**, 985 (1982); C. R. Acad. Sci. **292**, 142 (1981).
66. P. Pieranski and E. Guyon, Solid State Commun. **13**, 435 (1973); Phys. Rev. A **9**, 404 (1974).
67. P. Manneville and E. Dubois-Violette, J. Phys. (Paris) **37**, 285 (1976).
68. M. Clark, F. Saunders, I. Shenks, and F. Leslie, Mol. Cryst. Liq. Cryst. **70**, 195 (1981).
69. V. N. Reshetov, Akust. Zh. **31**, 639 (1985) [Sov. Phys. Acoust. **31**, 383 (1985)].
70. D. I. Anikeev and O. A. Kapustina, Zh. Éksp. Teor. Fiz. **110** (4), 1328 (1996) [JETP **83**, 731 (1996)].
71. O. A. Kapustina and V. N. Lupanov, Zh. Éksp. Teor. Fiz. **71**, 2324 (1976) [Sov. Phys. JETP **44**, 1225 (1976)].
72. D. I. Anikeev, O. A. Kapustina, and V. N. Lupanov, Zh. Éksp. Teor. Fiz. **100**, 197 (1991) [Sov. Phys. JETP **73**, 109 (1991)].
73. E. N. Kozhevnikov, in *Abstracts of VI All-Union Conference on Liquid Crystals* (Chernigov, 1988), Vol. 1, p. 121.
74. O. A. Kapustina and O. V. Romanova, Kristallografiya **46** (1), 112 (2001) [Crystallogr. Rep. **46**, 103 (2001)].
75. E. N. Kozhevnikov, Zh. Éksp. Teor. Fiz. **92**, 1306 (1987) [Sov. Phys. JETP **65**, 731 (1987)].
76. I. N. Gurova and O. A. Kapustina, Akust. Zh. **43** (3), 338 (1997) [Acoust. Phys. **43**, 290 (1997)].
77. I. N. Gurova and O. A. Kapustina, Pis’ma Zh. Éksp. Teor. Fiz. **63** (11), 866 (1996) [JETP Lett. **63**, 907 (1996)].
78. E. N. Kozhevnikov, Akust. Zh. **47** (4), 501 (2001) [Acoust. Phys. **47**, 430 (2001)].

79. E. N. Kozhevnikov, Akust. Zh. **48** (3), 425 (2002) [Acoust. Phys. **48**, 371 (2002)].
80. E. N. Kozhevnikov, Akust. Zh. **48** (6), 777 (2002) [Acoust. Phys. **48**, 687 (2002)].
81. O. A. Kapustina, N. A. Kolesnikova, and O. V. Romanova, Akust. Zh. **50** (1), 77 (2004) [Acoust. Phys. **50**, 66 (2004)].
82. O. A. Kapustina, N. A. Kolesnikova, and O. V. Romanova, Akust. Zh. **48** (4), 512 (2002) [Acoust. Phys. **48**, 448 (2002)].
83. I. N. Gurova, O. A. Kapustina, and V. N. Lupanov, in *Advances in Liquid Crystal Research and Applications*, Ed. by L. Bata (Pergamon Press, Oxford, 1980), p. 395.
84. T. F. North and G. F. Britten, in *Proceedings of Ultrasonic International Conference* (London, 1975), p. 120.
85. H. Hakemi, J. Appl. Phys. **53**, 6137 (1982).
86. Y. Kagawa, T. Hatakeyama, and Y. Tanaka, J. Sound Vibr. **36**, 407 (1974).
87. D. I. Anikeev, Yu. V. Bocharov, and A. D. Vuzhva, Zh. Tekh. Fiz. **58**, 1554 (1988) [Sov. Phys. Tech. Phys. **33**, 933 (1988)]; Liq. Cryst. **6**, 593 (1989).
88. S. Ezhov, S. Pasechnik, and V. Balandin, Pis’ma Zh. Tekh. Fiz. **10**, 479 (1984) [Sov. Tech. Phys. Lett. **10**, 202 (1984)].
89. C. F. Hayes, in *Liquid Crystals and Ordered Fluids* (Plenum, New York, 1978), p. 482.
90. A. Strigazzi and G. Barbero, Mol. Cryst. Liq. Cryst. Lett. **82**, 5 (1982).
91. R. S. Akopyan, B. Ya. Zel’dovich, and N. V. Tabiryan, Akust. Zh. **34**, 583 (1988) [Sov. Phys. Acoust. **34**, 337 (1988)].
92. Yu. V. Bocharov and A. D. Vuzhva, Pis’ma Zh. Tekh. Fiz. **15** (3), 84 (1989) [Sov. Tech. Phys. Lett. **15**, 242 (1989)]; Pis’ma Zh. Tekh. Fiz. **14**, 1460 (1988) [Sov. Tech. Phys. Lett. **14**, 635 (1988)].
93. A. N. Chuvyrov, Zh. Éksp. Teor. Fiz. **82**, 761 (1982) [Sov. Phys. JETP **55**, 451 (1982)].
94. J. M. Dreyfus and P. Pieranski, J. Phys. (Paris) **42**, 459 (1981).
95. G. N. Belova, Akust. Zh. **34**, 24 (1988) [Sov. Phys. Acoust. **34**, 13 (1988)].
96. O. A. Kapustina, V. N. Lupanov, and G. S. Chilaya, Akust. Zh. **24** (1), 136 (1978) [Sov. Phys. Acoust. **24**, 76 (1978)].
97. I. N. Gurova and O. A. Kapustina, Akust. Zh. **35** (3), 446 (1989) [Sov. Phys. Acoust. **35**, 262 (1989)].
98. I. N. Gurova and O. A. Kapustina, Liq. Cryst. **6**, 525 (1989).
99. T. Akahane and T. Tako, Mol. Cryst. Liq. Cryst. **38**, 251 (1977).
100. M. Kawaachi, O. Koguri, and Y. Kato, Appl. Phys. Lett. **13** (9), 1457 (1974).
101. V. N. Reshetov, I. V. Sytin, and G. N. Yakovenko, in *Problems in Ship Building* (TsNII RUMB, Moscow, 1985), No. 20, p. 59.
102. O. A. Kapustina and V. N. Reshetov, Akust. Zh. **37** (3), 497 (1991) [Sov. Phys. Acoust. **37**, 254 (1991)].
103. Yu. V. Bocharov, O. A. Kapustina, and V. N. Reshetov, Akust. Zh. **38** (4), 616 (1992) [Sov. Phys. Acoust. **38**, 340 (1992)].
104. Yu. Bocharov, O. Kapustina, and V. N. Reshetov, Mol. Cryst. Liq. Cryst. **209**, 19 (1991).

Translated by Yu. Sin’kov

Crystallography Reports, Vol. 49, No. 4, 2004, pp. 693–697. Translated from Kristallografiya, Vol. 49, No. 4, 2004, pp. 773–777.
Original Russian Text Copyright © 2004 by Soboleva, Voloshin.

Me_2O–P_2O_5–H_2O Solubility Phase Diagrams and Growth of MeH_2PO_4 Single Crystals (Me = Li, Na, K, Rb, Cs, NH_4)

L. V. Soboleva and A. E. Voloshin

Shubnikov Institute of Crystallography, Russian Academy of Sciences, Leninskiĭ pr. 59, Moscow, 119333 Russia
e-mail: lab.sol@ns.crys.ras.ru

Received March 28, 2001; in final form, May 15, 2003

Abstract—The Me_2O–P_2O_5–H_2O solubility phase diagrams are used to determine the optimum compositions and the temperatures for growing crystals of MeH_2PO_4 solid phases (Me = Li, Na, K, Rb, Cs, NH_4). The optimum conditions for dynamic growth of dihydrophosphates of the elements of the first group and ammonium are determined. LiH_2PO_4, NaH_2PO_4, $NaH_2PO_4 \cdot 2H_2O$, $NaH_2PO_4 \cdot H_2O$, KH_2PO_4, $K(H,D)_2PO_4$, RbH_2PO_4, CsH_2PO_4, and $(NH_4)H_2PO_4$ single crystals are grown on seed from aqueous solutions by the methods of temperature lowering and isothermal evaporation. *© 2004 MAIK “Nauka/Interperiodica”.*

INTRODUCTION

Earlier [1], we suggested a general approach to selection of the crystallization conditions for growth of complicated compounds of various chemical classes based on preliminary analysis of solubility phase diagrams of ternary systems. In these systems, each solid phase is characterized by the corresponding crystallization region, with the solubility curve having specific invariant (eutonic, transient) points. In these regions, two solid phases with different compositions are crystallized simultaneously. It is shown that a solid phase may crystallize only if the optimum composition of the solution is at the maximum distance from the points of invariant equilibria. In this case, no simultaneous crystallization of adjacent phases or transition to the crystallization region of a solid phase with different composition can take place.

The characteristic feature of this approach is the preparation of mother liquors from the simple components of the system. This allows one to prepare solution of any required composition, which is very important for performing the crystallization process according to selected (optimum) scheme. Using this approach, we have already grown the following single crystals: LiH_2PO_4 (LiDP) [2], NaH_2PO_4 (NaDP), $NaH_2PO_4 \cdot 2H_2O$ (NaDP · $2H_2O$), $NaH_2PO_4 \cdot H_2O$ (NaDP · H_2O) [3], KH_2PO_4 (KDP) [4], and $K(D_xH_{1-x})_2PO_4$ (DKDP) [5], where D is deuterium.

The present study is aimed at (1) the development of methods for growing RbH_2PO_4, CsH_2PO_4, and $NH_4H_2PO_4$ crystals using data on the Me_2O–P_2O_5–H_2O phase diagrams (Me = Rb, Cs, and NH_4) and growth of the respective single crystals on seeds in the dynamic mode and (2) comparative analysis of the solubility phase diagrams of the ternary Me_2O–P_2O_5–H_2O and K_2O–P_2O_5–$(D_xH_{1-x})_2O$ systems and the conditions for growth of $MeH_2PO_4 \cdot nH_2O$ and $K(D_xH_{1-x})_2PO_4$ single crystals (Me = Li, Na, K, Rb, Cs, NH_4, n = 0, 1).

ANALYSIS OF THE PHYSICAL–CHEMICAL FEATURES OF THE SOLUBILITY PHASE DIAGRAMS OF TERNARY Me_2O–P_2O_5–H_2O (Me = Rb, Cs, NH_4) SYSTEMS AND COMPOSITIONS OF MOTHER LIQUORS USED FOR GROWTH OF THE CORRESPONDING MeH_2PO_4 CRYSTALS

Unlike solubility phase diagrams of the ternary Me_2O–P_2O_5–H_2O systems (Me = Li, Na, K, NH_4), systems with Rb and Cs have been studied only partly. In the latter systems, the regions of the RbH_2PO_4 and CsH_2PO_4 crystallization are established only partly, so that the positions of invariant points are not known.

Figure 1 shows the solubility isotherms of RbH_2PO_4 in the Rb_2O–P_2O_5–H_2O system at the temperatures t = 25 and 50°C. These isotherms are characterized by a congruent nature of solubility: the RbH_2PO_4–H_2O singular secant passes through the crystallization region of rubidium dihydrophosphate. In the whole existence region, tetragonal RbH_2PO_4 crystals with a habit similar to the habit of KH_2PO_4 crystals are formed in the whole crystallization region. The specific feature of this system is the nonlinearity of the acid and alkali branches of the solubility curve in the region of RbH_2PO_4 crystallization. This allows one to vary the solution composition along the solubility curve practically at a constant concentration of one of the system components.

At the same time, the known data on phase formation in the systems with RbH_2PO_4 and CsH_2PO_4 are inconsistent. Contrary to some data [6], it was established [7] that, at $t < 85$°C RbH_2PO_4 is crystallized in the monoclinic system with the lattice parameters a =

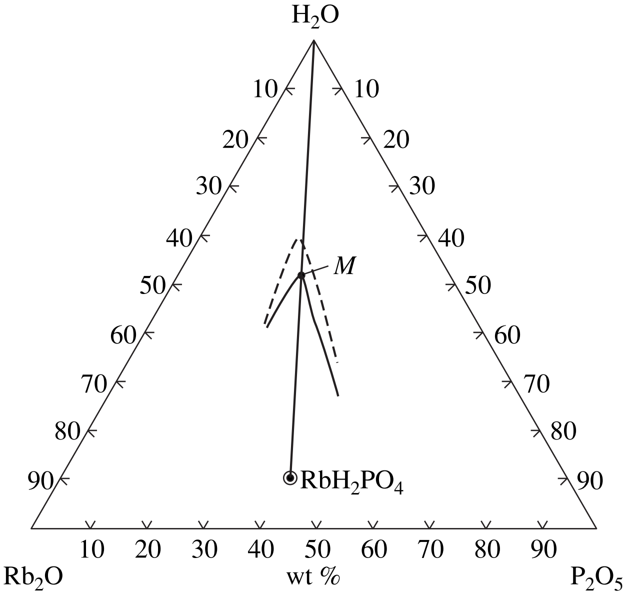

Fig. 1. Solubility isotherms of RbH_2PO_4 in the Rb_2O–P_2O_5–H_2O system at 25°C (dashed line) and 50°C (solid line). *M* is the composition of the mother liquor for growth of RbH_2PO_4 crystals. The H_2O–RbH_2PO_4 line is a singular secant.

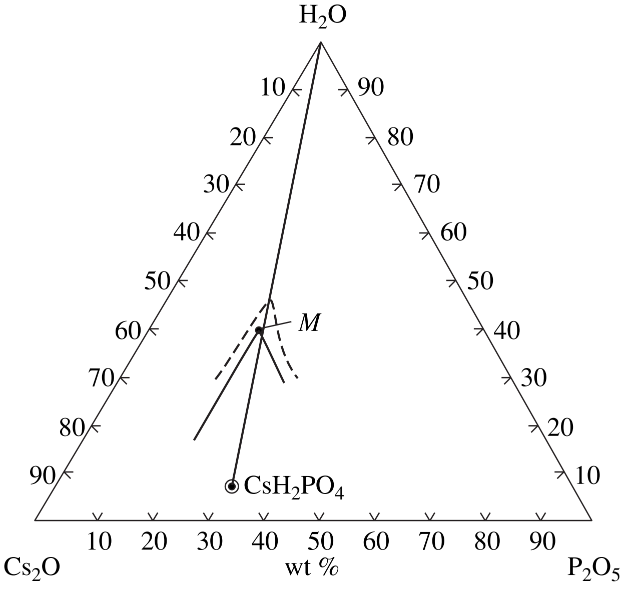

Fig. 2. Solubility isotherms of CsH_2PO_4 in the Cs_2O–P_2O_5–H_2O system at 25°C (dashed line) and 50°C (solid line). *M* is the composition of the mother liquor for growth of CsH_2PO_4 crystals. The H_2O–CsH_2PO_4 line is a singular secant.

7.06 Å, $b = 6.30$ Å, $c = 5.21$ Å, $\beta = 107.95°$, $Z = 2$, whereas, at $t > 85°C$, tetragonal crystals are formed. The latter crystals exist for quite a long time during system cooling to room temperature [7].

The Cs_2O–P_2O_5–H_2O system at $t = 25$ and 50°C (Fig. 2) [8] also has the region of the congruently dissolving CsH_2PO_4 solid phase crystallizing in the monoclinic system [7]. The alkali and acid branches of the solubility curve in the CsH_2PO_4 crystallization region are almost linear and have no singular points. The possibility of growth of tetragonal CsH_2PO_4 crystals depending on the solution temperature and CsOH and H_3PO_4 content was considered in [7].

It was established that, in the temperature range $-5 < t < +80°C$ and solution acidity pH = 2–8, only monoclinic crystals with a habit dependent on the crystallization conditions can grow. The tetragonal phase is formed only after prolonged heating of CsH_2PO_4 at 150–160°C, with the stability of this phase at room temperature being considerably lower than the stability of RbH_2PO_4. Table 1 indicates the temperatures and the character of the polymorphous transformations in RbH_2PO_4 and CsH_2PO_4 and, for comparison, also in KH_2PO_4 [7].

In accordance with the approach developed in [1–5], the compositions of the mother liquors for growth of Li, Na, and K dihydrophosphates were determined from the compositions of the points on the solubility curve lying at the maximum distance from the invariant equilibria. However, this approach is invalid for the Me_2O–P_2O_5–H_2O systems (*Me* = Rb, Cs) because the compositions of the invariant points are unknown. Nevertheless, the physical–chemical characteristics of the solubility curves of RbH_2PO_4 and CsH_2PO_4 in the $Rb_2O(Cs_2O)$–P_2O_5–H_2O systems (these are the location of the maxima on the solubility curves or the singular points in the vicinity of the singular $Rb(Cs)H_2PO_4$–H_2O secants) lead to the assumption that the optimum compositions of the mother liquors for growth of Rb and Cs

Table 1. Temperatures and character of polymorphous transformations in KH_2PO_4, RbH_2PO_4, and CsH_2PO_4

Solid phase	Temperature and character of transformations*
KH_2PO_4	Tetragonal (25°C) $\xrightarrow{192°C}$ monoclinic
RbH_2PO_4	Monoclinic (25°C) $\xrightarrow{85°C}$ tetragonal $\xrightarrow{128°C}$ monoclinic
CsH_2PO_4	Monoclinic (25°C) $\xrightarrow{150–160°C}$ tetragonal $\xrightarrow{186°C}$ monoclinic

* The inverse transition requires a long period of time.

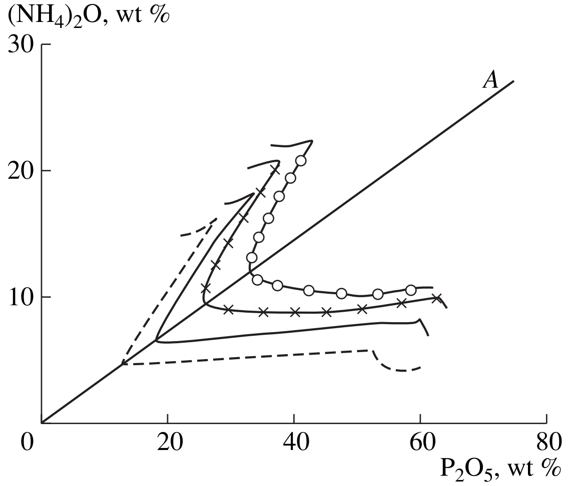

Fig. 3. Solubility isotherms of $NH_4H_2PO_4$ in the $(NH_4)_2O$–P_2O_5–H_2O system at 25°C (dashed line), 50°C (solid line), 75°C (–×–×–×–), and 100°C (–○–○–○–). The O*A* line is the H_2O – $NH_4H_2PO_4$ singular secant.

dihydrophosphates should be close to the solution compositions at the point *M* (Figs. 1, 2).

To grow RbH_2PO_4 crystals, we used the mother liquor of the composition (in wt %): $Rb_2O = 27.00$, $P_2O_5 = 22.00$, and $H_2O = 51.0$. To grow CsH_2PO_4 crystals, we used the mother liquor of the composition (in wt %): $Cs_2O = 40.70–43.00$, $P_2O_5 = 29.40–19.60$, and $H_2O = 39.90–37.40$. The temperature range of crystallization was $25 < t < 50$°C.

The $(NH_4)_2O$–P_2O_5–H_2O system was studied at several temperatures $t = 25$, 50 [9, 10], 75 [11], and 100°C [12] (Fig. 3). It should be emphasized that this system contained lower amounts of hydrates and double salts than the corresponding systems with Na and K. Figure 4 shows a part of the $(NH_4)_2O$–P_2O_5–H_2O diagrams in which the solubility isotherms of $NH_4H_2PO_4$ at $t = 25$, 50°C have linear branches, the singular points at 25°C, and a diffuse maximum at 50°C. In this system, only one congruently dissolving tetragonal phase of the composition $NH_4H_2PO_4$ is crystallized with the habit typical of KH_2PO_4. By analogy with data in [1–5], we may state that the composition of the mother liquor for growing $NH_4H_2PO_4$ crystals should correspond to the point *M* of the saturated solution (Fig. 4), namely, $P_2O_5 = 45.40$, $(NH_4)_2O = 13.50$, and $H_2O = 41.40$ wt %. The temperature ranges of crystallization varied from 50 to 25°C.

EXPERIMENTAL

To prepare the mother liquor we used extra pure Rb_2CO_3, Cs_2CO_3, $NH_4H_2CO_3$, and H_3PO_4 chemicals, reagent grade RbOH and CsOH chemicals, and twice-distilled water. We added small portions of the H_2O solution into a cooling, constantly stirred Me_2CO_3 or *Me*OH solution, with the reagents being taken in the amounts corresponding to the chosen compositions of the mother liquors.

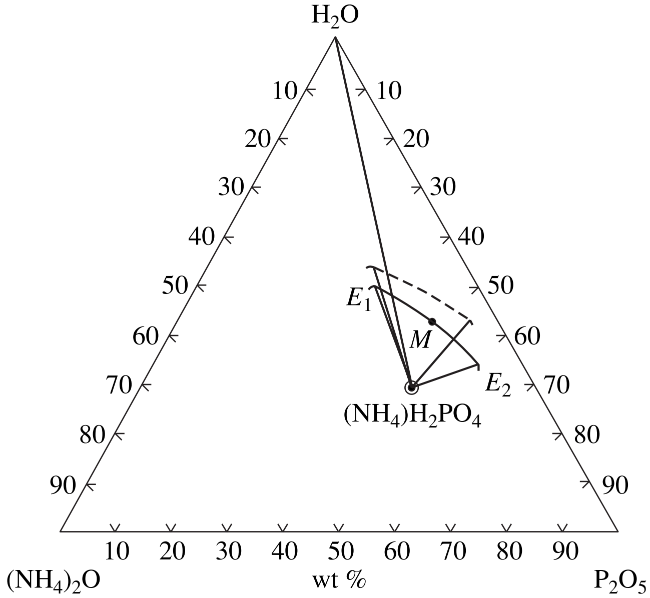

Fig. 4. Solubility isotherms of $NH_4H_2PO_4$ in the $(NH_4)_2O$–P_2O_5–H_2O system at 25°C (dashed line) and 50°C (solid line). The point *M* is the composition of the mother liquor for growth of $(NH_4)H_2PO_4$ crystals. The H_2O–$(NH_4)H_2PO_4$ line is a singular secant; E_1 and E_2 are the eutonic points.

The interaction between the components in the solution proceeds according to the exothermal reaction with the formation of dihydrophosphates, e.g., by the reaction

$$\mathrm{Rb_2CO_3(Cs_2CO_3) + 2H_3PO_4}$$

$$\xrightarrow[100°C]{H_2O} \mathrm{2RbH_2PO_4(CsH_2PO_4)} + \uparrow \mathrm{CO_2} + \uparrow \mathrm{H_2O}.$$

The RbH_2PO_4, CsH_2PO_4, and $NH_4H_2PO_4$ crystals were grown on seed by the methods of isothermal evaporation at 50°C and lowering of temperature (50–25°C). The seeds were prepared by spontaneous crystallization from the corresponding mother liquors.

We grew 25 × 20 × 18-mm^2-large transparent RbH_2PO_4, CsH_2PO_4, and $NH_4H_2PO_4$ single crystals.

The crystals grown were identified by their X-ray diffraction patterns using ASTVL cards. X-ray phase analysis showed that the RbH_2PO_4 and $NH_4H_2PO_4$ crystals were tetragonal, whereas CsH_2PO_4 crystals were monoclinic.

SPECIFIC FEATURES OF PHASE FORMATION IN DIHYDROPHOSPHATES IN THE Me_2O–P_2O_5–H_2O SYSTEMS (*Me* = Li, Na, K, Rb, Cs, AND NH_4)

Comparing the physical–chemical characteristics of the Me_2O–P_2O_5–H_2O (*Me* = Li, Na, K, Rb, Cs, NH_4) and K_2O–P_2O_5–$(D,H)_2O$ systems, we see a close rela-

Table 2. Optimum conditions for growth of $MeH_2PO_4 \cdot nH_2O$ crystals (Me = Li, Na, K, Rb, Cs, NH_4, n = 0–2)

System	Grown crystal	Growth conditions		Characteristics of crystals	
		solution composition, wt %	t, °C	sp. gr. and symmetry class	dimensions, mm
$Li_2O–P_2O_5–H_2O$	LiH_2PO_4	Li_2O = 6.62 P_2O_5 = 43.50 H_2O = 49.88	50.00	$P_{na}2_1$ $mm2$	35 × 27 × 30
$Na_2O–P_2O_5–H_2O$	NaH_2PO_4	Na_2O = 15.00 P_2O_5 = 36.50 H_2O = 48.50	60.00	$P2_1\|C$ $2\|m$	25 × 22 × 18
	$NaH_2PO_4 \cdot H_2O$	Na_2O = 14.66 P_2O_5 = 33.62 H_2O = 51.72	47.50	$Pna2_1$ $mm2$	35 × 30 × 35
	$NaH_2PO_4 \cdot 2H_2O$	Na_2O = 13.00 P_2O_5 = 29.80 H_2O = 57.20	35.20	$P2_12_12_1$ 222	35 × 30 × 18
$K_2O–P_2O_5–H_2O$	KH_2PO_4	K_2O = 10.00 P_2O_5 = 15.00 H_2O = 75.00	50.10	$1\bar{4}2d$ $\bar{4}2m$	40 × 30 × 28
$K_2O–P_2O_5–(D,H)_2O$	$K(D_xH_{1-x})_2PO_4$	KH_2PO_4 = 36.65 D_2O = 63.35	50.00	$1\bar{4}2d$ $\bar{4}2m$	15 × 20 × 10
$Rb_2O–P_2O_5–H_2O$	RbH_2PO_4	Rb_2O = 27.00 P_2O_5 = 22.00 H_2O = 51.00	50.00	$1\bar{4}2d$ $\bar{4}2m$	25 × 20 × 18
$Cs_2O–P_2O_5–H_2O$	CsH_2PO_4	Cs_2O = 40.00 P_2O_5 = 20.00 H_2O = 40.00	50.00	$P2\|m$ $2\|m$	25 × 18 × 20
$(NH_4)_2–P_2O_5–H_2O$	$(NH_4)H_2PO_4$	$(NH_4)_2O$ = 13.50 P_2O_5 = 45.40 H_2O = 41.40	50.00	$1\bar{4}2d$ $\bar{4}2m$	28 × 20 × 18

tion of the systems with KH_2PO_4, $K(D_xH_{1-x})_2PO_4$, $NH_4H_2PO_4$ and RbH_2PO_4, CsH_2PO_4—they have similar solubility isotherms, close dimensions of the crystallization fields, congruent nature of solubility, close concentration and temperature limits of crystallization, etc.

Above, we indicated the discrepancies in the existence region of the tetragonal RbH_2PO_4 phase in [6 and 8]. We also synthesized the tetragonal RbH_2PO_4 phase at t = 50–25°C. Our results confirm the conclusions drawn in [6]. Possibly, the controversy indicated above is explained by insufficient knowledge on this system and may be explained by the dependence of the existence regions of various solid phases on the solution composition and other crystallization conditions.

The concentration and temperature conditions for crystallization in the systems of K, Rb, Cs, and NH_4 dihydrophosphates are rather favorable and, therefore, growth of single crystals in these systems meets with no serious difficulties. Single crystals can be grown from the solutions of both stoichiometric and nonstoichiometric compositions over wide temperature ranges. We should like to emphasize the unique properties of the $K_2O–P_2O_5–H_2O$ system, which possesses extremely wide and stable temperature and concentration ranges of the components that ensure the successful KH_2PO_4 crystallization. To a large extent, this made KH_2PO_4 an extremely convenient material for studying growth from solutions, because it allows the variation of the growth conditions over the wide ranges.

At the same time, the systems with Li and Na dihydrophosphates considerably differ from the above systems by the incongruent nature of LiH_2PO_4 solubility at 25°C and the change of the incongruent NaH_2PO_4 solubility at 25 and 40°C to the congruent solubility at 60°C. Unlike all the other systems, the system with sodium forms two new hydrate phases—$NaH_2PO_4 \cdot H_2O$ and $NaH_2PO_4 \cdot 2H_2O$—with different solubility natures. The systems with Li and Na are characterized by narrow concentration and temperature ranges of dihydrophosphate crystallization. Unlike the systems with K, Rb, Cs, and NH_4, LiH_2PO_4, NaH_2PO_4, $NaH_2PO_4 \cdot H_2O$, and $NaH_2PO_4 \cdot 2H_2O$ crystals with an incongruent nature of solubility can be grown only based on data on their solubility diagrams. This does not allows one to use the LiH_2PO_4 and NaH_2PO_4 solutions for crystal growth and requires thorough selection not only of the mother-liquor composition the but also of the crystallization conditions. In these cases, the approach described above becomes the only method for growth of lithium and sodium dihydrophosphates.

Table 2 indicates the growth conditions of $MeH_2PO_4 \cdot nH_2O$ ($n = 0$–2 and $K(D_xH_{1-x})_2PO_4$ crystals, the compositions of the mother liquors, and the initial crystallization temperature established from the solubility diagrams in the Me_2O–P_2O_5–H_2O and K_2O–P_2O_5–$(D_xH_{1-x})_2O$ systems (Me = Li, Na, K, Rb, Cs, and NH_4) as well as the space groups, symmetry classes, and the dimensions of the crystals grown.

CONCLUSIONS

The present study concludes the cycle of studies on growth of crystals of the homologous series of alkali metal and ammonium dihydrophosphates with the use of the approach based on the consideration of the solubility phase diagrams of ternary systems developed in [1–5].

We determined the crystallization conditions for RbH_2PO_4, CsH_2PO_4, and $NH_4H_2PO_4$ in the Me_2O–P_2O_5–H_2O ternary systems (Me = Rb, Cs, and NH_4) at $t = 50$–25°C and grew single crystals of these compounds, which are the last representatives of the class of compounds not studied earlier.

As a result, we demonstrated the applicability of the above approach to the KH_2PO_4, $K(D_xH_{1-x})_2PO_4$, RbH_2PO_4, CsH_2PO_4, and $NH_4H_2PO_4$ crystals synthesized earlier by other authors by the traditional method. The high efficiency of the method suggested above is confirmed by synthesis of new crystals—LiH_2PO_4, NaH_2PO_4, $NaH_2PO_4 \cdot H_2O$, and $NaH_2PO_4 \cdot 2H_2O$ with incongruent nature of solubility. All the above facts allow us to state that the analysis of phase diagrams in combination with the use of mother liquors having compositions far from the points of the invariant equilibria is a universal approach that can be used for growth of single crystals of complicated compounds.

REFERENCES

1. L. V. Soboleva, Neorg. Mater. **31** (85), 614 (1995).
2. L. V. Soboleva and I. L. Smol'skiĭ, Kristallografiya **42** (4), 762 (1997) [Crystallogr. Rep. **42**, 700 (1997)].
3. L. V. Soboleva and A. É. Voloshin, Kristallografiya **47** (5), 937 (2002) [Crystallogr. Rep. **47**, 871 (2002)].
4. L. V. Soboleva, Neorg. Mater. **32** (8), 1007 (1996).
5. L. V. Soboleva, A. É. Voloshin, V. A. Kirikov, and M. V. Biglova, Kristallografiya **47** (1), 140 (2002) [Crystallogr. Rep. **47**, 130 (2002)].
6. L. N. Rashkovich and R. Sh. Momtats, Zh. Neorg. Khim. **23** (5), 1349 (1978).
7. B. M. Zhigarnovskiœ, Yu. A. Polyakov, V. I. Bugakov, *et al.*, Neorg. Mater. **20** (8), 1243 (1984).
8. L. N. Rashkovich, K. B. Meteva, and Ya. V. Shevchik, Zh. Neorg. Khim. **22** (7), 1982 (1977).
9. L. N. Rashkovich, *KDP-Family Single Crystals* (Adam Hilger, Bristol, 1991).
10. V. A. Muromtsev and L. A. Nazarova, Byull. Akad. Nauk SSSR, Ser. Khim., No. 1, 177 (1938).
11. I. C. Brosheer and I. F. Anderson, J. Am. Chem. Soc. **68**, 92 (1946).
12. I. Wengu, J. Chengdu Univ. Sci. Technol., No. 2, 41 (1985).

Translated by L. Man

Crystallography Reports, Vol. 49, No. 4, 2004, p. 698. Translated from Kristallografiya, Vol. 49, No. 4, 2004, p. 778.
Original Russian Text Copyright © 2004 by the Editorial Board.

JUBILEES

Aleksandr Borisovich Gil’varg (On the Occasion of His 90th Birthday)

Aleksandr Borisovich Gil’varg, a well-known Russian expert in the mechanical treatment of crystals and the oldest employee of the Shubnikov Institute of Crystallography of the Russian Academy of Sciences, turned 90 on May 1, 2004.

Gil’varg has worked at the Institute of Crystallography since the day of its foundation. As a student at a technical secondary school of optics and mechanics, he started working as an optical mechanic under the supervision of A.V. Shubnikov at the Laboratory of Crystallography of the Lomonosov Institute of the Academy of Sciences of the Soviet Union in 1935. Shubnikov appraised his abilities highly and, in June 1938, Gil’varg was appointed a junior research worker. In October 1941, Gil’varg, along with some of his colleagues, was evacuated to Sverdlovsk oblast (to the village of Filatovo, Sukhologskiĭ region), where he worked as a technological engineer in workshops producing piezoelectric quarz resonators (which were main parts of field telephones). After the war, Gil’varg took part in the development of the technology of fabrication of scintillation crystals, narrow-band polarization interference filters for astrophysics, and analyzing crystals for X-ray spectroscopy. For successful development of the area, Gil’varg was awarded the Prize of the Presidium of the Academy of Sciences of the Soviet Union. His contribution in the organization of the production of laser crystals can hardly be overestimated. Gil’varg, with his vast knowledge and experience, played a key role in the organization of the workshop for the mechanical treatment of such crystals at the Special Design Bureau. That all post graduate students at the Institute of Crystallography studied crystal treatment directly under Gil’varg’s supervision was a fine tradition.

Presently, Gil’varg is working as actively as ever on the problem of improving the mechanical treatment of leucosapphire crystals. He has many students who are deeply grateful to him for his help in mastering the profession of optical mechanic.

Gil’varg is a great authority, not only for his colleagues at the Laboratory of High-Temperature Crystallization, but also among all the employees of the Institute of Crystallography. From time to time, he consults with researchers from other organizations. As one of the most skilled experts in the mechanical treatment of crystals for astrophysical experiments, Gil’varg devotes particular attention to problems of astrophysics.

The colleagues of Aleksandr Borisovich Gil’varg from the Institute of Crystallography and the editorial board of *Kristallografiya* (Crystallography Reports) congratulate him on his jubilee and wish him good health and new creative achievements. We are proud that we have been so privileged as to know this unique expert, who has been working continuously and fruitfully for the welfare of domestic science for 70 years.

Translated by Yu. Sin’kov

Crystallography Reports, Vol. 49, No. 4, 2004, pp. 699–700. Translated from Kristallografiya, Vol. 49, No. 4, 2004, pp. 779–780.

JUBILEES

Khachik Saakovich Bagdasarov (on the Occasion of His 75th Birthday)

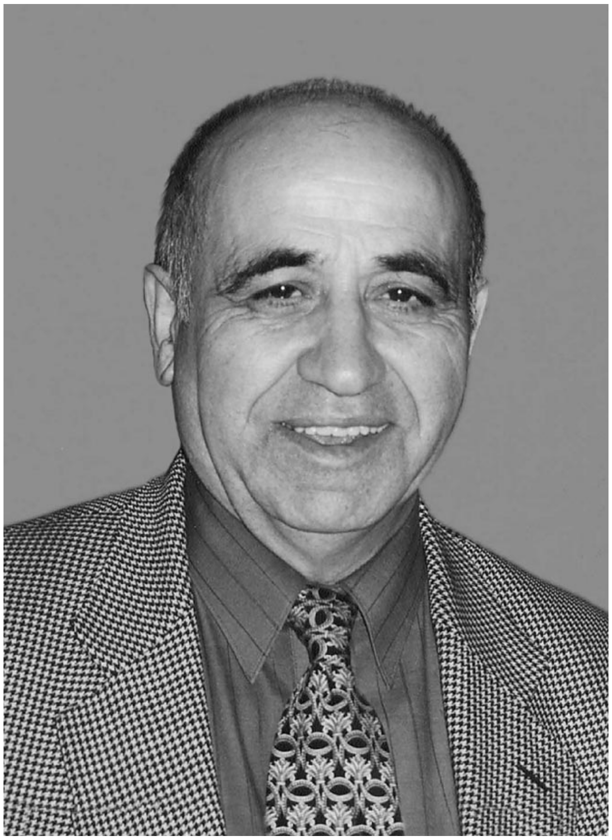

On May 21, 2004, Prof. Khachik Saakovich Bagdasarov celebrated his 75th birthday. A Doctor in Physics and Mathematics, corresponding member of the Russian Academy of Sciences, and full member of the Academy of Engineering Sciences, Bagdasarov was awarded the title of Honorary Scientist of the Russian Federation and State Prizes of the Soviet Union and the Russian Federation.

Bagdasarov, a student of Academician Aleksei Vasil’evich Shubnikov, follows in the traditions of the Russian school of crystallography. He has made a considerable contribution to both fundamental and applied research in crystallography.

Bagdasarov started his scientific activity as a postgraduate student at the Institute of Crystallography fifty years ago (in December 1953). He established the influence of ultrasound on crystallization, developed an original method for detecting dislocations in single crystals, and discovered the effect of strengthening of zinc single crystals during their growth in an ultrasonic field.

Bagdasarov’s main interest is high-temperature crystallization and development of original growth methods for synthesis of technologically important single crystals. Solving various problems of high-temperature crystallization, Bagdasarov pays his main attention to high-temperature chemical processes occurring during melting and crystallization of various materials. This approach allowed him to elaborate a new method for growing single crystals—the so-called Bagdasarov method—now widely used in many countries. This method allowed Bagdasarov and a group of designers to develop a number of new crystallization setups now manufactured by many industrial enterprises of the Russian Federation and other countries of the Commonwealth of Independent States.

Bagdasarov also made an important contribution to the theory of synthesis of high-quality optical single crystals. Together with Academician A.M. Prokhorov, he developed concepts that allowed them to use a ruby crystal and obtain, within a short time, stimulated radiation in the optical range. The solution of this problem was extremely important and timely because of serious attempts to solve this problem made simultaneously by the scientists in the Soviet Union and United States. The designed ruby-based optical generator allowed our scientists to solve a number of important problems including the design and construction of special rangers and perform, under the guidance of Academician N.G. Basov, lunar laser ranging. The latter was important not only because it was the first attempt to determine the distance between the earth and its natural satellite within a decimeter accuracy, but also because it proved the great possibilities of optical ranging and communication. Bagdasarov headed the solution of other problems of laser technology, such as the creation of unique lasing elements based on neodymium-activated yttrium aluminum garnet (YAG) and yttrium aluminate, yttrium erbium aluminum garnet (YEAG), etc. These facts were soon used to start industrial production of lasing crystals. The growth apparatus based on the Bagdasarov method and the respective licenses were bought by a number of countries, including Japan, France, Switzerland, South Korea, and Bulgaria.

Bagdasarov also made a great contribution to synthesis of high-quality single crystals, work for which he was awarded the Soviet Union State Prize in 1972. The crystals grown by Bagdasarov have record Q-factors in the SHF range. He actively studied the radiation stability of sapphire and developed an original method of radiation-induced strengthening of single crystals.

Bagdasarov is a well known organizer of scientific events and work. He finds new, original technical solutions to growth problems and puts them into practice. He used sapphire single crystals in systems operating under the extreme conditions; in particular, he designed and constructed an optically transparent internal-combustion engine especially important for design and construction of ecologically pure engines.

Bagdasarov played an active role in the organization of large centers for growing single crystals and manufacturing crystallization setups, such as the scientific and research enterprise Lasernaya Tekhnika in Erevan, department of technological lasers at the Moscow production enterprise Zavod Vladimira Il'icha, Lyuminofor plant in Stavropol, All-Union Research Institute of Single Crystals in Kharkov, All-Union Research Institute of Electrothermal Equipment in Moscow, Plant of Electrothermal Equipment in Taganrog, and Plant of Electronic Engineering in Lugansk. The Laboratory of High-Temperature Crystallization founded by Bagdasarov at the Institute of Crystallography in 1964 has been transformed into a large department solving fundamental and applied problems of crystal growth. Bagdasarov's organizational gift has manifested itself especially clearly in the last decade, a period hard for our science. He managed to preserve his actively working research group.

In 2000, Bagdasarov was awarded the State Prize of the Russian Federation for the development of powerful technological solid-state lasers and their industrial manufacture. At present, Bagdasarov is engaged in growth of very large refractory single crystals. The state of the art, engineering developments, and new technological concepts in this field are considered in detail in his recently published monograph High-Temperature Crystallization from Melts.

Bagdasarov is a member of the editorial board of the journal Kristallografiya (*Crystallography Reports*). For more than 20 years, he served as an expert of the State Certifying Commission in Physics. He published 6 monographs and more than 300 other scientific publications. He has more than 200 Inventor's Certificates. Bagdasarov has been awarded several orders and medals of the Soviet Union and Russian Federation.

Today, Bagdasarov actively works on synthesis of new technological single crystals, finds novel fields of their application, and puts into practice his new ideas. He has numerous offers to cooperate with many research centers in the United States, France, China, Israel, Greece, etc. In 2003, his activity was highly recognized once again—he was awarded the Fedorov Prize of the Russian Academy of Sciences.

The editorial board of Kristallografiya, Russian crystallographers, and numerous students and colleagues congratulate Prof. Bagdasarov on his 75th birthday and wish him good health, happiness, and great success in putting all his plans into practice.

Translated by L. Man

Crystallography Reports, Vol. 49, No. 4, 2004, pp. 701–702. Translated from Kristallografiya, Vol. 49, No. 4, 2004, pp. 781–782.

JUBILEES

Boris Viktorovich Mchedlishvili (On the Occasion of His 60th Birthday)

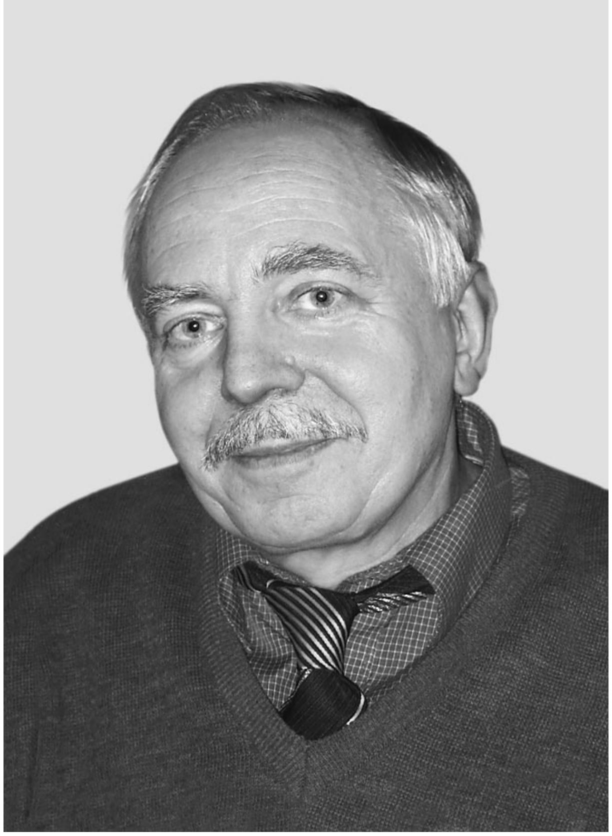

Boris Viktorovich Mchedlishvili was born in Leningrad on October 1, 1944. In 1969, he graduated from the Faculty of Physics and Mechanics of the Kalinin Leningrad Polytechnical Institute (now, St. Petersburg State Technical University) with a degree as an engineering physicist. From 1969 to 1984, he worked at the Chair of Physics of Isotopes and the Chair of Biophysics of this institute.

In 1983, a laboratory for the development of nuclear filters (track membranes) was organized at the Shubnikov Institute of Crystallography by a decree of the Presidium of the Academy of Sciences of the Soviet Union, initiated by academicians B.K. Vaĭnshteĭn, G.N. Flerov, A.P. Aleksandrov, and A.M. Prokhorov. Mchedlishvili moved to Moscow in 1984 and, since then, has headed this department of the Institute of Crystallography (now, the Department of Membrane Technologies).

In 1990, Mchedlishvili defended his doctoral dissertation in chromatography and became a professor of biophysics in 1992. From 1997 to 1999, he was the deputy chief for research at the Institute of Crystallography.

The range Mchedlishvili's scientific interests includes condensed-matter physics, high-energy physics and chemistry, X-ray diffractometry, problems of physical and colloidal chemistry related to processes of separation of complex mixtures by nanomaterials with calibrated porosity, and problems of biophysics (interaction of biopolymers and viruses with a surface and their spectroscopy).

One of his well-known developments is a new chromatographic technique—the exclusive chromatography of colloidal particles (first and foremost, viruses). During its development, it was demonstrated both theoretically and experimentally that the essential feature of this method is its nonequilibrium nature, which

1063-7745/04/4904-0701$26.00 © 2004 MAIK “Nauka/Interperiodica”

makes it radically different from conventional chromatographic techniques. In 1984, Mchedlishvili and his colleagues were awarded the Prize of the Council of Ministers of the Soviet Union for this research and the practical application of the results obtained.

Being a student of Academician Flerov, Mchedlishvili, together with his teacher, has been working since 1973 on the problems of research, production, and application of track membranes. The laboratory headed by Mchedlishvili at the Institute of Crystallography is a unique one both in our country and abroad. Experts in membranes know the pioneer Mchedlishvili's works on the synthesis, structure, and properties of track membranes well. The data obtained by Mchedlishvili are now widely used in the production of track membranes and items based on them, as well as in membrane technologies, in St. Petersburg, Dubna, Obninsk, Novosibirsk, and Tomsk. The creation of the track membrane industry in Russia is one of the results of his scientific activity over 1984–2004.

Over the past two decades, Mchedlishvili has also been engaged in research and pedagogical work. The translation into Russian of the well-known book *Membrane Filtration* by Brock was edited by Mchedlishvili. Along with Prof. V.M. Kolikov, he published the monograph *Macroporous Silicas in Chromatography of Biopolymers*. Mchedlishvili has supervised eight candidate's and eight doctoral dissertations. He is a member of several scientific and expert councils and committees of the Russian Academy of Sciences; Ministry of Industry, Science, and Technology of the Russian Federation; Mendeleev Russian Chemical Society; and Ministry of Education of the Russian Federation. Since 1993, Mchedlishvili has been deputy chairman of the Dissertation Council on Biophysics of the St. Petersburg State Technical University. Mchedlishvili also supervises the Scientific Methodical Laboratory of Track Membranes and the Russian Seminar on Track Membranes. He is the author of more than 200 articles that have been published in leading scientific journals in Russia and abroad.

The editorial board of *Kristallografiya* (Crystallography Reports), along with all his colleagues and friends, wish Boris Viktorovich Mchedlishvili good health and further success in his scientific work.

Translated by Yu. Sin'kov

Crystallography Reports, Vol. 49, No. 4, 2004, pp. 703–704. Translated from Kristallografiya, Vol. 49, No. 4, 2004, pp. 783–784.
Original Russian Text Copyright © 2004 by Kapustina.

MEMORIAL DATA

On the Occasion of the 100th Birthday of Professor A. P. Kapustin

O. A. Kapustina

On August 20, 2004, 100 years had passed since the birth of the world-renowned scientist Prof. Aleksandr Pavlovich Kapustin, a doctor of physics and mathematics and one of the pioneers in the field of the physics of liquid crystals.

Kapustin was born in Saratov into the family of a railroad fitter. Because of material difficulties, he failed to graduate from the higher municipal school and, at the age of 14, he began to work as a coupon checker in the Saratov Transport Consumer's Society. However, his natural intellectual curiosity, love of books, and keen interest in technique helped him, despite the hard conditions and instability of his life, to graduate from a program of radio-telegraph courses (1923), a *rabkor* (proletarian correspondent) school (1924), and a school for adults, after which he managed to obtain the job of head librarian in the Communication Union Club. This occupation was of greater interest to him. In 1927, he successfully passed the entrance examinations for the Faculty of Physics and Technology of Chernyshevsky Saratov University. From 1930 to 1933, Kapustin was a post-graduate student at the Chair of General Physics of Saratov University. At the same time, he began to work as a lecturer at the Saratov Pedagogical Institute, and his lecturing activity at this institute lasted until the end of his life. After Kapustin graduated from his postgraduate course, he was sent to the Magnitogorsk Pedagogical Institute, where he worked until 1952, first as the head of the Chair of General Physics and then as a deputy director for research and education. At that time, Kapustin's talents manifested themselves in his vigorous and enthusiastic work in a great variety of fields. He gave lecture courses in general and theoretical physics, organized and carried out practical studies in physics in the laboratory, and successfully continued his research at the Laboratory of Oscillations of the Faculty of Physics of Moscow State University at the same time as conducting long-term business trips. In 1940, based on the results of this research, he defended his candidate's dissertation, *Application of the Drude Method to Permittivity Measurements and Determination of Dipole Moments at Wavelength* $\lambda = 10$ *cm*. The range of his scientific interests constantly expanded. In 1945–1948, Kapustin performed a series of investigations of the effect of ultrasound on the kinetics of crystallization of metals at the Central Plant Laboratory of the Magnitogorsk Metallurgical Plant. The results obtained proved to be so promising that Kapustin was sent on to a doctorate course of study at the Institute of Crystallography of the Academy of Sciences of the Soviet Union (1948–1951) to continue this work. In October 1951, Kapustin defended his doctoral dissertation in physics and mathematics at the Institute of Physical Chemistry of the Academy of Sciences brilliantly. A year later, in 1952, he was appointed head of the Chair of General Physics at the Lenin Moscow Pedagogical Institute, where he worked until 1959. At the same time, Kapustin continued his research in Moscow: in 1952, Academician A.V. Shubnikov offered that he work as a senior researcher at the Institute of Crystallography, where he was employed until the end of his life. Kapustin had many new ideas and creative plans. His main scientific interests dealt with the physics of liquid crystals. And, along with Shubnikov, Kapustin was one of the founders of this field of science in our country. In the 1960–1970s, he carried out a series of investigations of the electrooptical properties of liquid crystals, which led to the discovery of the spatially modulated structures now referred to as Kapustin–Williams domains. This discovery initiated wide experimental and theoretical investigations of this phenomenon both in our country and abroad. The studies performed by Kapustin in the 1980s anticipated many ideas of modern acoustics of liquid crystals. For example, his name is associated with the foundation and development of acoustic spectroscopy of liquid crystals (one of the most fruitful methods for studying their structure) in our country. Another fundamental work of that period, which initiated a new line of investigations of acoustooptical properties of liquid crystals, was the study of orientational phenomena in liquid crystals in ultrasonic fields performed by Kapustin in collaboration with L.M. Dmitriev. It was precisely this, along with a number of other studies of the effect of mechanical strains generated by acoustic waves on liquid crystals, that made the solution of several problems of hydroacoustics, seismology, and nondestructive testing with the use of liquid-crystal sensors possible.

In recent years, Kapustin, along with S.A. Pikin, studied with much success the effect of periodic mechanical strains on polymorphic liquid crystals under certain temperature conditions. The results of these studies allowed him to propose a new approach to solving a number of special problems relating to construction of liquid-crystal optical phase gratings with a controlled period and memory. The results of Kapustin's investigations in the field of the physics of liquid crystals have been reported in several monographs based on the original materials. One of these monographs was published in the United States.

They say that style is the man, and Kapustin's style could not be called anything other than classic: a deep and broad approach, along with accuracy, was characteristic, not only of all his research, but also of his attitude to any problem. Another feature, which is not quite typical of modern researchers, was his desire to establish, first of all, qualitative relationships between the macroscopic characteristics of a phenomenon under study. He almost always set up experiments himself, liked to work with his own hands, and understood where an experimenter may encounter a "perfidy of nature, error or, probably, miscalculation."

Kapustin was a brilliant representative of those people who participate fully in the life of their country. Along with his intense scientific and pedagogical activity, he was continually involved in all the aspects of public life. His adherence to principles, straightforwardness, keen interest in all scientific developments, inexhaustible erudition, invariable benevolence and cordiality, optimism, and rare charm always attracted other people to him. His extensive international relations are also indicative of this. Profs. G. Brown, N. Felici, E. Guyon, S. Chandrasekar, H. Zackmann, D. Demus, H. Zaschke, A. Derzhanski, A. Petrov, and I. Myll make up a far from complete list of the well-known foreign physicists with whom Kapustin communicated and was in correspondence. He would give lecture courses on the physics of liquid crystals in universities on our country, Germany, Czechoslovakia, and Bulgaria and actively participated in international conferences and symposia on liquid crystals. Science was always a source of the deepest and happiest experiences for him.

Kapustin passed away on October 27, 1984, in the 81st year of his life, most of which he devoted to the science of liquid crystals.

Translated by Yu. Sin'kov